D5.7 BEACON Bentonite Mechanical Evolution

Synthesis of the results obtained from all tasks in WP5
Final report for WP5

Beacon Deliverable D5.7

Report

Authors: Jean Talandier[1], Ola Kristensson[2], Daniel Malmberg[2], Asta Narkuniene[3], Darius Justinavicius[3], Lidija Zdravkovic[4], Veli-Matti Pulkkanen[5], Heidar Gharbieh[5], Alessio Ferrari[6], Jose Bosch Llufriu[6], Vinay Kumar[7], Steffen Beese[7], Antonio Gens[8], Robert Charlier[9], Rebecca Newson[10], Mattias Åkesson[11], Gianvito Scaringi[12], David Masin[12], Olivier Leupin[13]

[1]Andra, France; [2]Clay Technology, Sweden; [3]LEI, Lithuania; [4]ICL, United Kingdom; [5]VTT, Finland; [6]EPFL, Switzerland; [7]BGR, Germany; [8]UPC, Spain;[9]ULg, Belgium;[10]Quintessa, United Kingdom, [11]SKB, Sweden, [12] CU/CTU, Czech Republic, [13]Nagra, Switzerland

Reporting period: 01/06/2020 – 31/05/2022

Date of issue of this report: **15/01/2022**

Start date of project: **01/06/17** Duration: 60 Months

This project receives funding from the Euratom research and training programme 2014-2018 under grant agreement No 745 942		
Dissemination Level		
PU	Public	

REVIEW

Name	Internal/Project/External	Comments
All Beacon partners	Internal	

DISTRIBUTION LIST

Name	Number of copies	Comments
Seifallah BEN HADJ HASSINE(EC)	Digital	
Beacon partners	Digital	

Content

1 Introduction

This report concerns the results obtained on the last task of WP5 (task 5.4) dedicated to assessment case. Three cases have been proposed and have been built based on repository designs. 1) a tunnel plug based on the Andra design, 2) a disposal cell from the Nagra concept, 3) the KBS-3 deposition tunnel backfill. One of the main interests of these test cases, apart from the fact that they approach real structures, is the introduction of heterogeneities in the bentonite or in boundary conditions that may lead to residual heterogeneities after full water saturation.

The test cases are designed to evaluate the capacity of the models to predict the hydromechanical evolution of the bentonite barrier and the resulting performance of the barrier. The results at the end can be analysed in the way to verify if the long-term performance expectations are fulfilled.

This report is dedicated to the presentation of the results obtained by the participants on the three tests. The analysis concerning the evaluation of these results in regards of the expectation in terms of safety assessment and the recommendations that could be deduced for the modelling or the installation of bentonite component will be presented in the report D3.1 produced under the framework of WP1.

The specifications of the tests are presented in a document wrote by partners involved in WP1 (Assessment Cases for the Evaluation of the Degree of Heterogeneity – Leupin et al, 2020). Ten teams participated to this task. The partners involved and the tests on which they work are indicated in Table 2.1-1. Each test was performed by at least 3 teams.

Table 2.1-1 List of partners involved in Task 5.4 and performed tests

Test	Partner
KBS3 – backfill homogenization	Clay Technology
	LEI
	VTT/UCLM
	ICL
Nagra - Nearfield for high-level waste	EPFL
	UPC
	BGR
Andra – Tunnel sealing	Ulg
	Quintessa
	Andra

This report contains also a contribution from all the partners involved in WP5 describing the main lessons learned during the project, the progress made based on the participations in the 10 test cases proposed under task 5.1, 5.2 and 5.3. The partners also propose some perspectives to go further. Due to the evolution of the numerical tools during the project, it was proposed to the partners to revisit some of the previous tests showing the improvement of the models. This is the purpose of §5 of this document.

2 SKB assessment case

2.1 Clay Technology

The SKB assessment case was modelled using the Hysteresis Based Material (HBM) model implemented in COMSOL Multiphysics (see, for example D3.3 for a description of the material model). The modelling consisted of fully coupled hydro-mechanical simulations of tunnel backfill during the transient water-uptake phase.

2.1.1 Description of the models

The SKB assessment case was represented using a 2D axisymmetric geometry, identical to the geometry defined in the task description. Only the buffer components (block and pellets) were considered, the water transport through the surrounding rock mass was not included in the model. Water inflow to the bentonite clay was instead handled using hydraulic boundary conditions.

The simulations were run until full water saturation was achieved and both hydraulic and mechanical evolutions had reached steady state.

2.1.2 Geometry and discretization

The geometry used in the models is shown in Figure 2.1-1 (left panel) and the discretization of the geometry, e.g. the finite element mesh, is shown in the right panel of Figure 2.1-1. The mesh consists of 1000 quadrilateral elements with a total of 1066 nodes.

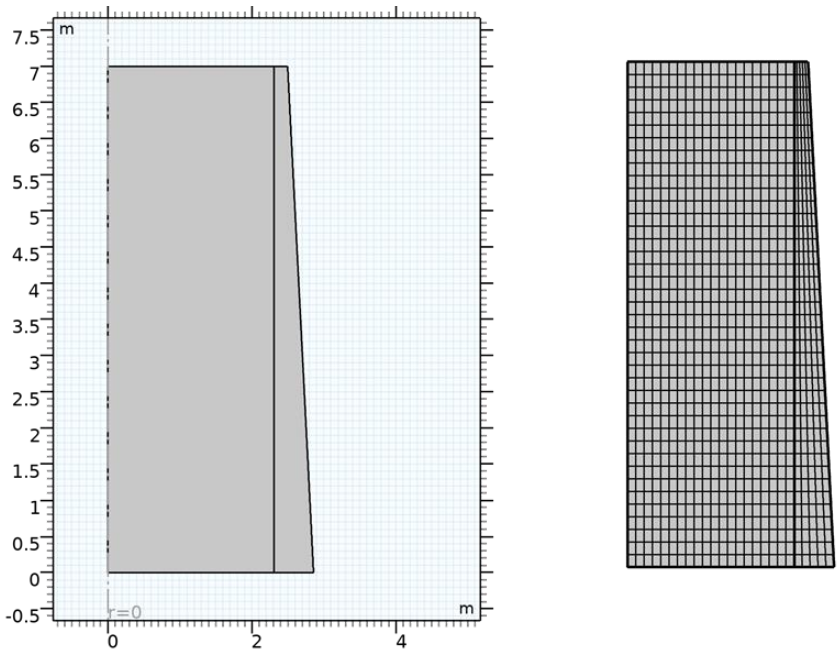

Figure 2.1-1. Geometry and mesh used when simulating the SKB Assessment case using HBM in COMSOL Multiphysics

2.1.3 Input parameters

The HBM model requires few inputs:

- Parameters of two clay potential functions (eight for the present case)
- Three parameters for the evolution of the path dependent variable
- One parameter for the contact area fraction
- Two parameters for the micro void ratio evolution

Clay potential, Ψ

The parameterisation used was that for MX-80 bentonite, previously determined in the modelling of the homogenisation test (D5.1.2, Test 1B). In that parametrisation the clay potential functions are given by:

$$\Psi = exp(c_3 e^3 + c_2 e^2 + c_1 e + c_0) \tag{2-1}$$

Both an upper and lower clay potential curve are needed, and the coefficients used are given in Table 2.1-2.

Path variable

The path dependence seen in the behaviour of bentonite is included in the HBM model using the path dependent variable $\boldsymbol{f}$, given by:

$$d\boldsymbol{f} = \frac{\partial \boldsymbol{f}}{\partial \boldsymbol{\varepsilon}} d\boldsymbol{\varepsilon} \tag{2-2}$$

where the differentials are given by:

$$\frac{\partial f_{\alpha\beta}}{\partial \varepsilon_{\alpha\beta}} = -K_{\alpha\beta}\left[\sqrt{\left(\frac{\varphi_{\alpha\beta}}{2}\right)^2 - \omega_{\alpha\beta}} + \mathrm{sgn}\left(\dot{\varepsilon}_{\alpha\beta}\right)\left(\frac{\varphi_{\alpha\beta}}{2} + f_{\alpha\beta}\right)\right] \tag{2-3}$$

In the present formulation $K_{\alpha\beta}$ has two possible values, one for $\alpha = \beta$ and another for $\alpha \neq \beta$, respectively. The expressions for $\varphi_{\alpha\beta}$ and $\omega_{\alpha\beta}$ are given in Table 2.1-1.

Table 2.1-1 Terms present in the HBM path variable evolution law.

α,β	$\varphi_{\alpha\beta}$	$\omega_{\alpha\beta}$
1,1	$-0.7(f_{22}+f_{33})$	$f_{22}{}^2+f_{33}{}^2-0.7f_{22}f_{33}+2.7(f_{13}{}^2+f_{23}{}^2+f_{12}{}^2)-0.9R^2$
2,2	$-0.7(f_{11}+f_{33})$	$f_{11}{}^2+f_{33}{}^2-0.7f_{11}f_{33}+2.7(f_{13}{}^2+f_{23}{}^2+f_{12}{}^2)-0.9R^2$
3,3	$-0.7(f_{11}+f_{22})$	$f_{11}{}^2+f_{22}{}^2-0.7f_{11}f_{22}+2.7(f_{13}{}^2+f_{23}{}^2+f_{12}{}^2)-0.9R^2$
2,3	0	$\frac{10}{27}(f_{11}{}^2+f_{22}{}^2+f_{33}{}^2)-\frac{7}{27}(f_{11}f_{22}+f_{22}f_{33}+f_{11}f_{33})+(f_{13}{}^2+f_{12}{}^2)-\frac{R^2}{3}$
1,3	0	$\frac{10}{27}(f_{11}{}^2+f_{22}{}^2+f_{33}{}^2)-\frac{7}{27}(f_{11}f_{22}+f_{22}f_{33}+f_{11}f_{33})+(f_{23}{}^2+f_{12}{}^2)-\frac{R^2}{3}$
1,2	0	$\frac{10}{27}(f_{11}{}^2+f_{22}{}^2+f_{33}{}^2)-\frac{7}{27}(f_{11}f_{22}+f_{22}f_{33}+f_{11}f_{33})+(f_{13}{}^2+f_{23}{}^2)-\frac{R^2}{3}$

Parameter values are needed for K_{aa} (e.g. when $\alpha=\beta$), K_{ab} (eg when $\alpha\neq\beta$) and R. The values used in the models of the SKB assessment case are given in Table 2.1-2.

Contact area fraction and micro void ratio evolution

The micro void ratio e_μ is governed by the differential,

$$e_\mu=\frac{\partial e_\mu}{\partial e}de+\frac{\partial e_\mu}{\partial s}ds \tag{2-4}$$

Here the micro-void ratio evolution dependence on the total void ratio is given by:

$$\frac{\partial e_\mu}{\partial e}=\tilde{\alpha}(e,e_\mu) \tag{2-5}$$

The suction dependence in the micro void ratio is given by

$$\frac{\partial e_\mu}{\partial s}=\begin{cases}\dfrac{(e-e_\mu)\Psi_M(e_\mu)}{\max(s,s_{min})}\dfrac{1}{(e-e_\mu)\dfrac{\partial\Psi_M}{\partial e_\mu}-\Psi_M(e_\mu)} & \text{if } \dot{s}<0\\ \dfrac{-e_{step}}{\left|s-\Psi_M(e_\mu-e_{step})\right|} & \text{otherwise}\end{cases} \tag{2-6}$$

The parameter s_{min}, limiting the minimum suction value in the denominator of equation 2-6 when $\dot{s}<0$ was introduced to avoid numerical problems. e_{step} sets the shrinking limit of the material. Furthermore, the partial differential $\frac{\partial e_\mu}{\partial s}$ was set to zero for negative values of suction in the model.

The contact area function is given by equation 2-7.

$$\alpha = \tilde{\alpha}(e, e_\mu) = \left(\frac{1+e_\mu}{1+e}\right)^\gamma, \tag{2-7}$$

The parameters that needs to be defined are s_{min} and e_{step} in equation 2-6 and the coefficient γ in equation 2-7. The values are given in Table 2.1-2.

Table 2.1-2 HBM parameters used in the models of the SKB assessment case

Parameter	Value	Source
c_0^{low}	5.7035	Beacon D5.1.2 (Test 1B)
c_1^{low}	-6.3234	Beacon D5.1.2 (Test 1B)
c_2^{low}	1.1904	Beacon D5.1.2 (Test 1B)
c_3^{low}	-0.0838	Beacon D5.1.2 (Test 1B)
c_0^{high}	6.6008	Beacon D5.1.2 (Test 1B)
c_1^{high}	-6.6382	Beacon D5.1.2 (Test 1B)
c_2^{high}	1.6239	Beacon D5.1.2 (Test 1B)
c_3^{high}	-0.1463	Beacon D5.1.2 (Test 1B)
$\left(p_{sw}^{low\ \&\ high}\right)_0$	10^6 Pa	For conversion to Pa
γ	7	Beacon D3.1
K_{aa}	40	Beacon D5.1.2 (Test 1B)
K_{ab}	$40\sqrt{2.7}$	Beacon D3.2
R	0.9	Beacon D5.2.2 (obtained from studying small example problems)
e_{step}	0.05	Beacon D5.2.2 (obtained from studying small example problems)

2.1.4 Initial and boundary conditions

When using the HBM model, the initial condition is given by the initial values of:

- Void ratio
- Micro void ratio
- Suction

- Stress
- Path variable

The initial conditions for the two materials included in the simulations (blocks and pellets) are given in

Table 2.1-3.

Table 2.1-3 Initial conditions used in the models of the SKB assessment case

Parameter	Units	Blocks	Pellets
Void ratio	-	0.63529	1.780
Micro void ratio	-	0.48022	0.48022
Suction	MPa	31.102	31.102
Stress[1)]	MPa	0	0
Path variable[1)]	-	0	0

[1)]Isotropic conditions were prescribed

As requested in the task definition, two types of mechanical boundary conditions and two types of hydraulic boundary conditions were considered.

The hydraulic boundary conditions were:

- Free inflow of water through the tunnel wall
- Flux-limited inflow of water through the tunnel wall calibrated such that the time until full saturation in the buffer was 4000 years

The mechanical boundary conditions were

- Roller conditions on all outer boundaries
- Roller conditions on all outer boundaries except on the tunnel wall, where no displacements were allowed.

Table 2.1-4 identifies the resulting four models with the combinations of used boundary conditions.

Table 2.1-4 Initial conditions used in the models of the SKB assessment case

Model ID	Hydraulic boundary	Mechanical boundary
WP5.4_2D_ROLLER_FREE_M03	Free access to water	Roller conditions on tunnel wall
WP5.4_2D_FIXED_FREE_M03	Free access to water	No displacements on tunnel wall
WP5.4_2D_ROLLER_LIMITED_M03	Flux limited inflow	Roller conditions on tunnel wall
WP5.4_2D_FIXED_LIMITED_M03	Flux limited inflow	No displacements on tunnel wall

2.1.5 Results

First, it is worth noting that the models from which the results presented below comes from are not entirely well behaved. During the modelling it was discovered that there is a small drift (e.g. change) in the total solid mass in the models. Significant time was spent in trying to resolve this issue, and while the change in mass in the models presented here could be reduced to less than 1% it could not be eliminated.

Furthermore, the HBM model specifies that the net-mean stress for a given void ratio cannot be larger than the upper bound of the clay potential (Ψ_H) at the void ratio in question. In some parts of the pellets column this criterion was not fulfilled; the net-mean stress slightly exceeded the value of Ψ_H.

While these two features shows that the models are not behaving exactly as desired, the deviations are small and hence the results presented below are not expected to change significantly once they are resolved.

The results presented are the radial dry density profiles at the end sections (where $z = 0$ m and $z = 7$ m, see Figure 2.1-1) of each model, as well as the evolution in net mean stress in 6 points from each model (3 points in each end section). The dry density profiles requested for each model is given in Figure 2.1-2 - Figure 2.1-5. The dry density profiles are compared and discussed in 2.1.6. It should be noted that the dry density profile from the models with slow water uptake are not well behaved in the pellet's column, in particularly for the model with roller conditions in the tunnel wall. The cause of this probably lies in the accuracy of the numerical solution, but at the time of writing we have not been able to fully determine the cause, nor how to remedy the situation.

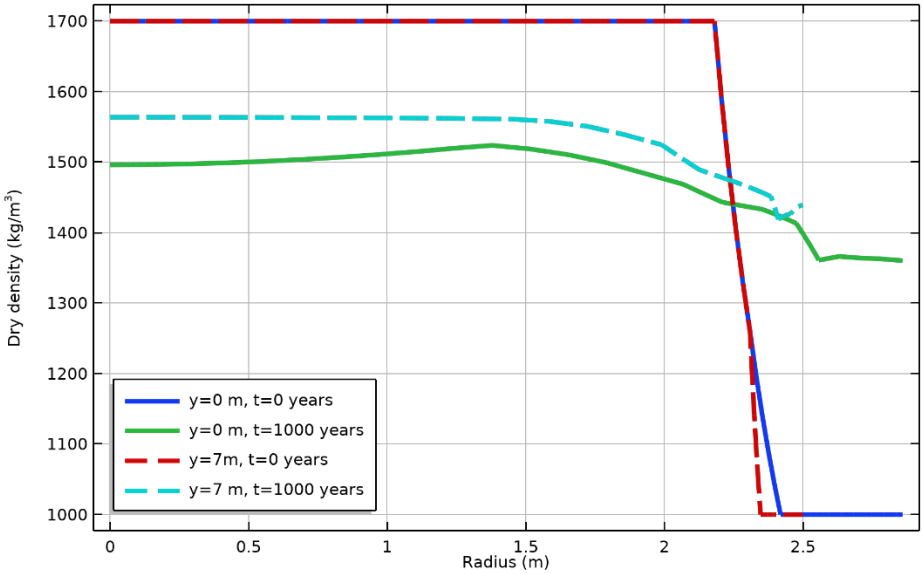

Figure 2.1-2. The dry density profiles from model WP5.4_2D_ROLLER_FREE_M03 e.g. roller boundary on tunnel wall and free access to water.

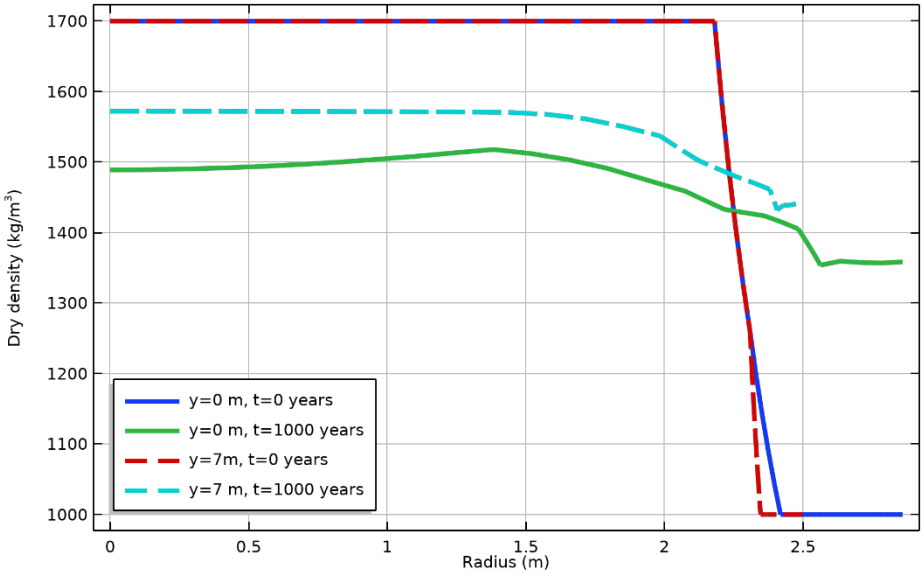

Figure 2.1-3. The dry density profiles from model WP5.4_2D_FIXED_FREE_M03, e.g. no displacement on tunnel wall and free access to water.

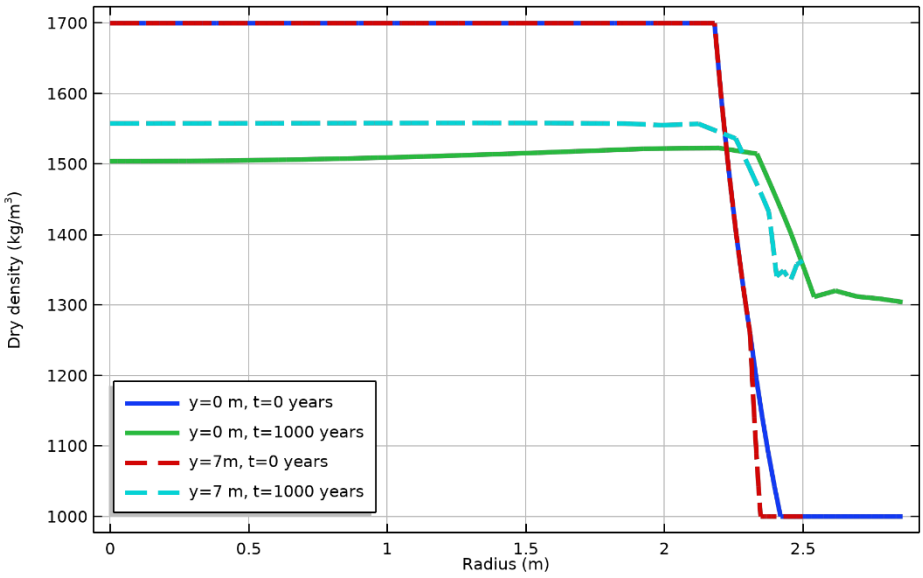

Figure 2.1-4. The dry density profiles from model WP5.4_2D_ROLLER_LIMITED_M03, e.g. roller boundary on tunnel wall and limited access to water.

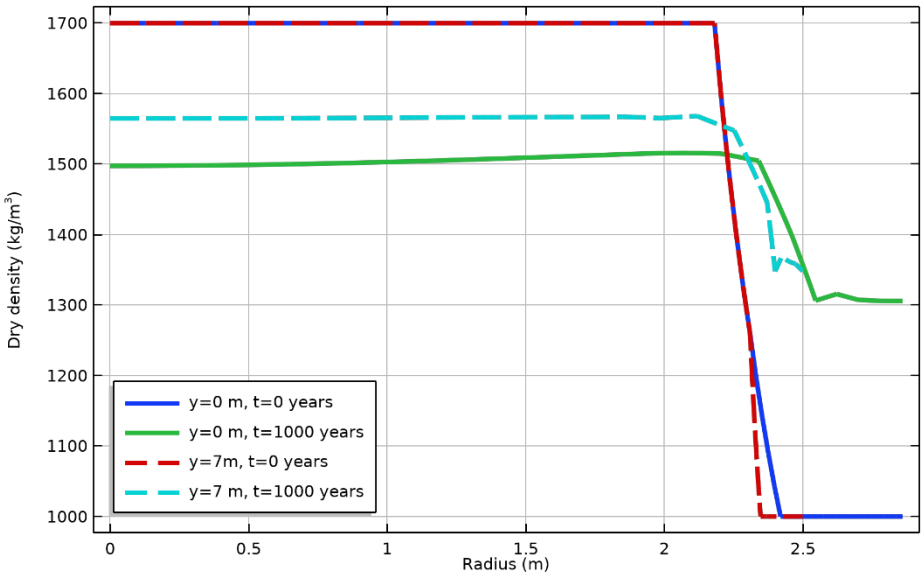

Figure 2.1-5. The dry density profiles from model WP5.4_2D_FIXED_LIMITED_M03, e.g. no displacement on tunnel wall and limited access to water.

In Figure 2.1-6 to Figure 2.1-9 the net mean stress evolution in six different points is shown from all four models. As can be seen in Figure 2.1-8 and Figure 2.1-9 steady state is reached after 4000 years, and the model is continued for 150 years after this. The

maximum stress values in the final state are about 1MPa higher in the models with slow water uptake as compared to the models with free access to water.

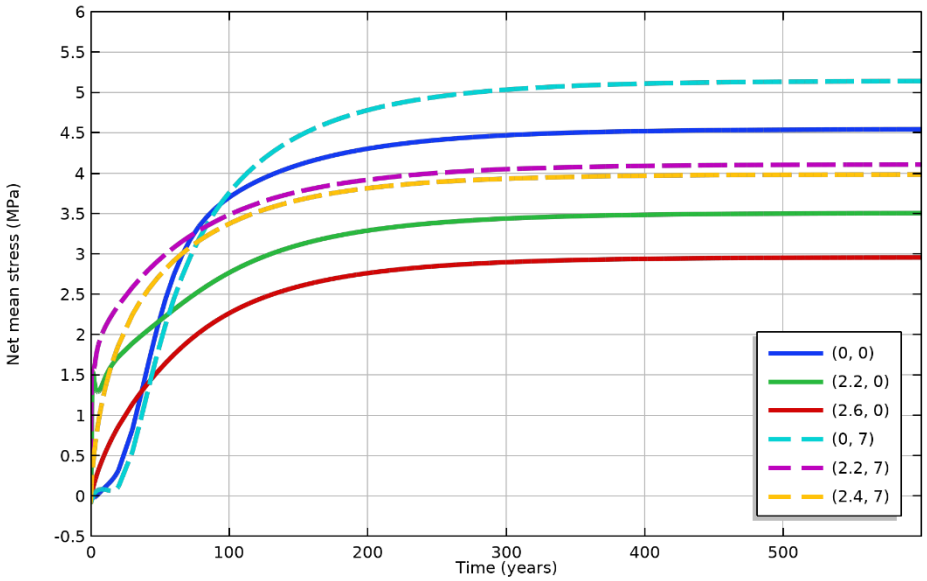

Figure 2.1-6. The net mean stress evolution in six points from WP5.4_2D_ROLLER_FREE_M03, e.g. no displacement on tunnel wall and free access to water.

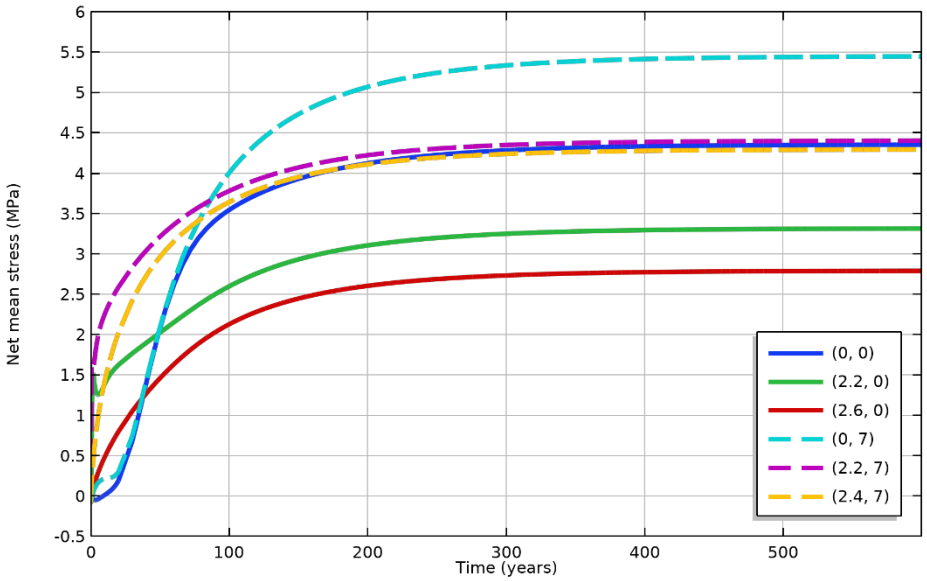

Figure 2.1-7 The net mean stress evolution in six points from WP5.4_2D_FIXED_FREE_M03, e.g. no displacement on tunnel wall and free access to water.

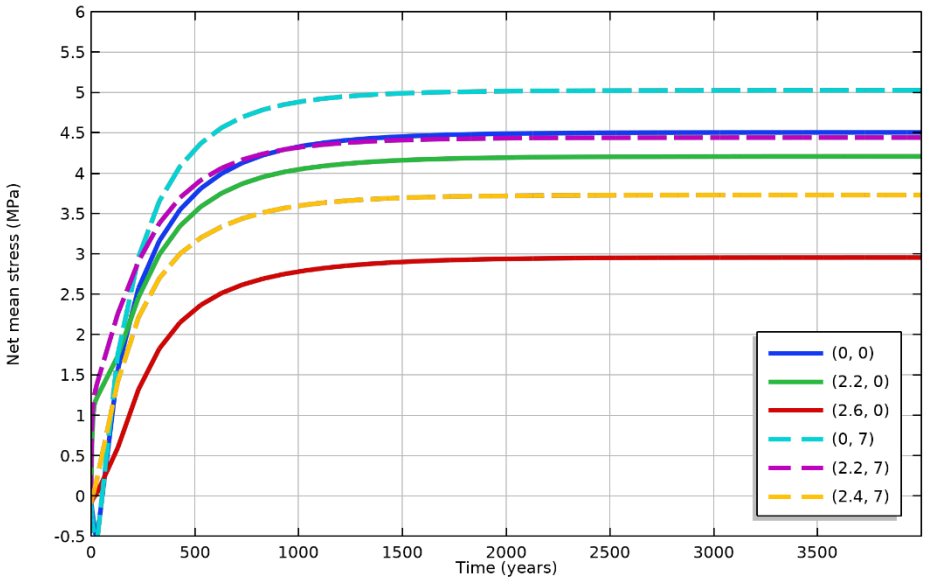

Figure 2.1-8. The net mean stress evolution in six points from model from model WP5.4_2D_ROLLER_LIMITED_M03, e.g. roller boundary on tunnel wall and limited access to water.

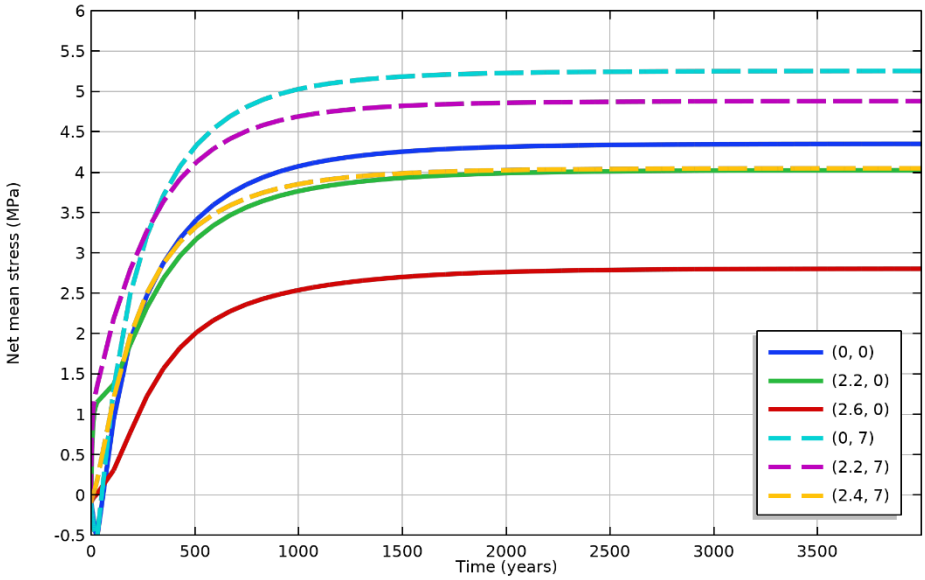

Figure 2.1-9. The net mean stress evolution in six points from model WP5.4_2D_FIXED_LIMITED_M03, e.g. no displacement on tunnel wall and limited access to water

2.1.6 Discussion

Figure 2.1-10 shows a comparison of the dry density profiles from the lower baseline at the end of the simulations and Figure 2.1-11 the same comparison for dry density profiles at the upper baseline in the model geometry. One can clearly see that the mechanical boundary condition has a rather small effect on the results, whereas the hydraulic boundary has a more pronounced effect.

Comparing the fast and slow water uptake models shows that the latter gives rise to a larger heterogeneity in the final dry density profiles as compared to the models with a fast water uptake.

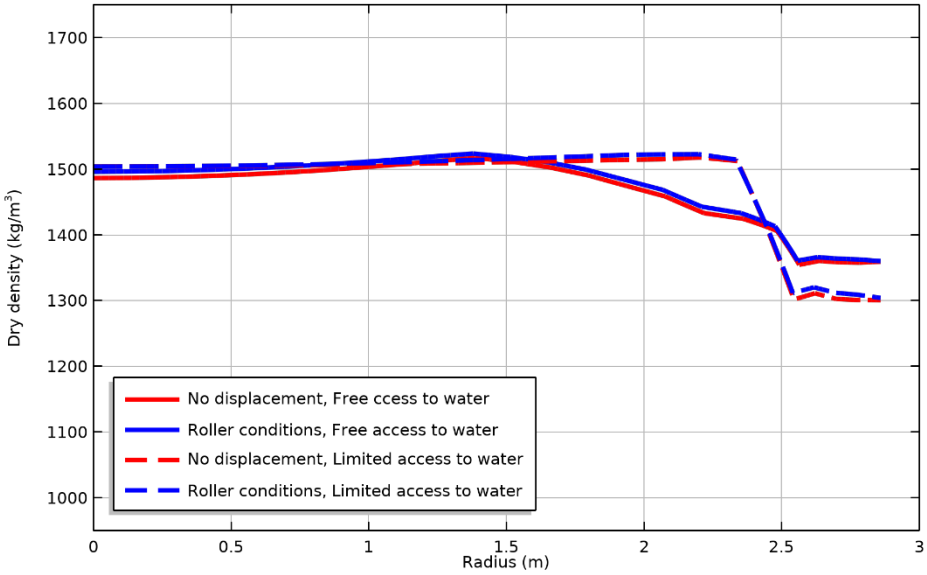

Figure 2.1-10. Comparison of the dry density profiles evaluated at the lower baseline in the geometry (y=0m, see Figure 2.1-1)

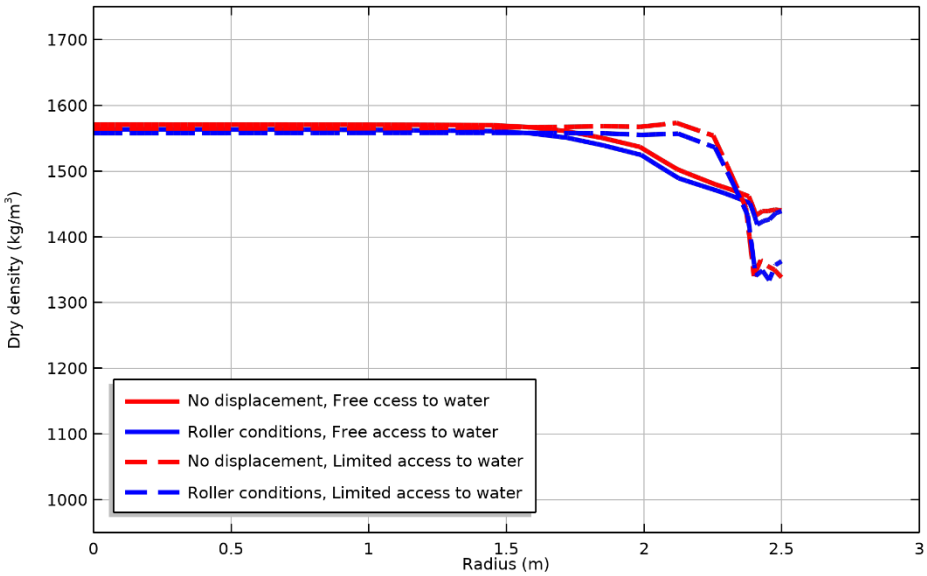

Figure 2.1-11. Comparison of the dry density profiles evaluated at the upper baseline in the geometry (y=7m, see Figure 2.1-1)

Including wall friction in these models are, given the results in Figure 2.1-10, not important. The minor difference in the final state suggests that friction would have a negligible effect on the evolution.

However, understanding the mode and rate of hydration can be very important. One can imagine that given the pronounced effect of the different water uptake rates simulated here, the mode of water uptake (matrix vs fracture) could also play a significant role.

2.2 LEI

2.2.1 Description of the model

Modelling of SKB assessment case was performed with LEI model developed in numerical tool COMSOL Multiphysics v5.6 (for more description see BEACON WP3 deliverable report D3.3. and Narkuniene et al., 2021 - COMSOL Multiphysics is general-purpose platform software for modelling engineering applications. It allows conventional physics-based user interfaces and coupled systems of partial differential equations for simulation with finite element method.

For the modelling of hydro-mechanical (HM) response of hydration of MX-80 bentonite (compacted block and pellets) Richard's equation was considered for the ` flow modelling. It was assumed that bentonite mechanical response in terms of deformation or/and developed swelling pressure are mainly governed by bentonite saturation. Wetting induced swelling was modelled as elastic deformation and its impact on porosity change was assessed. Young's modulus dependency on saturation was considered in the model. HM model included couplings to consider impact of mechanical deformations on water balance, porosity change impact on specific moisture capacity, on storage coefficient and on permeability.

Plastic deformations of bentonite have not been considered in the model.

2.2.2 Geometry and discretization

The backfill is one of the engineered barriers in the KBS-3 repository. The backfill is the material installed in deposition tunnels to fill them. The purpose and function of the backfill in deposition tunnels is to sustain the multi-barrier principle by keeping the buffer in place and restrict groundwater flow through the deposition tunnels. The acceptable dimensions and geometry of KBS-3 deposition tunnels are illustrated in Figure 2.2-1.

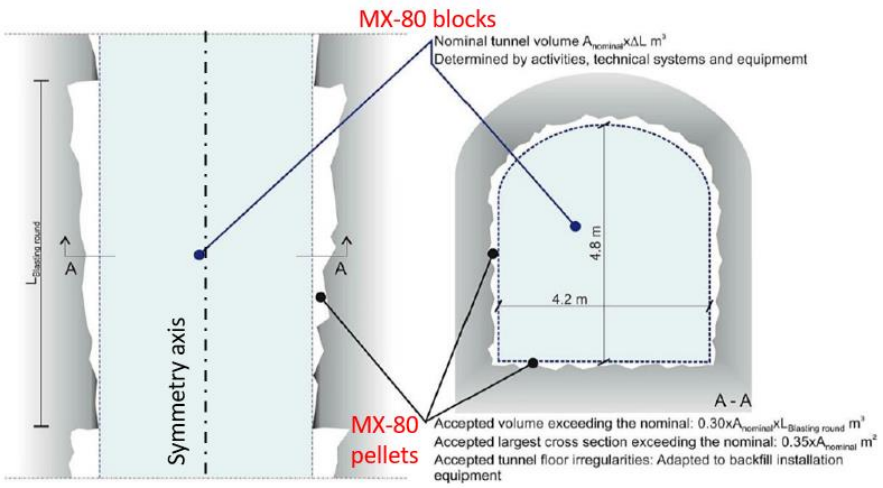

Figure 2.2-1. Dimensions and geometry of KBS-3 deposition tunnel [Leupin et al., 2020]

The installed backfill consist of compacted bentonite blocks (MX-80 type) stacked on a compacted flat bed of bentonite pellets (MX-80 type), and the gap between the blocks and the rock surface filled with bentonite pellets. The section area of the block stack is planned to be constant throughout the deposition tunnel, while the tunnel section area is expected to vary within a certain interval for each blasting round (Leupin et al., 2020). For LEI modelling work this interval was represented with two tunnel sections (theoretical and maximum fallout) in 2D axisymmetric geometry as could be seen in Figure 2.2-2. The analysed domains were discretized into 2486 triangular grid elements.

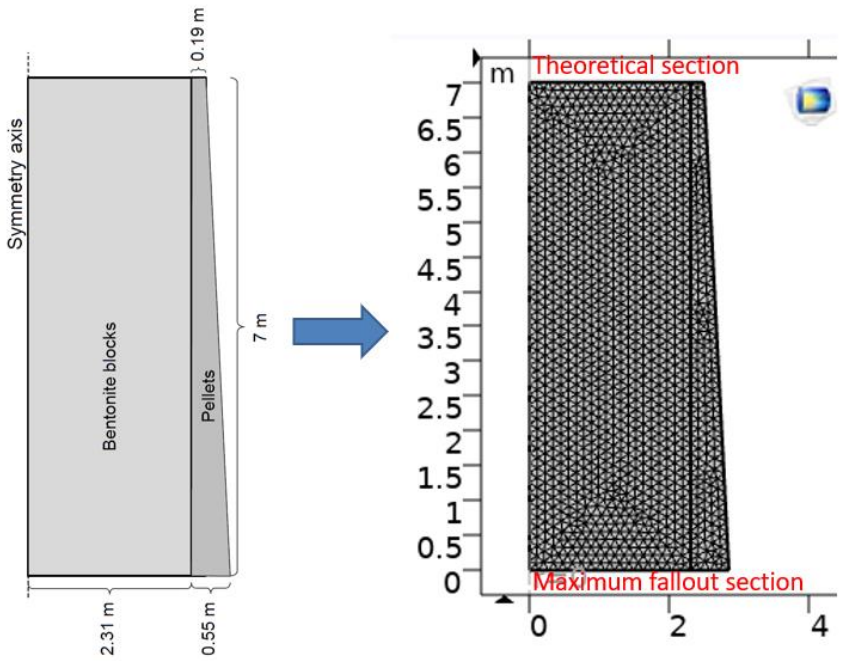

Figure 2.2-2. Geometry and computational grid for 2D axisymmetric model

2.2.3 Input parameters

The initial values and dependencies of HM processes related parameters for bentonite pellets and block considered for SKB assessment case are summarized in Table 2**.2-1**.

Table 2.2-1. Characteristics of MX-80 type bentonite materials considered in LEI model

Parameter	Pellets zone	Block zone
Water retention function, -	Van Genuchten P_0=7 MPa, λ=0.4 (Toprak et al., 2020)	Modified Van Genuchten P_0=f(e), λ=0.38 (Seiphoori et al., 2014) $\Psi(e) = 248.21 \cdot exp(-4.78 \cdot e)$

Parameter	Pellets zone	Block zone
Saturated intrinsic permeability, m^2	$k = k_0 \cdot \exp\{b(n - n_0)\}$ k_0=1.4e^{-18}, n_0=0.35, b=10 (Toprak et al., 2020)	$k = k_0 \cdot \left(\frac{e}{e_0}\right)^{\eta}$ (Akesson et al., 2010) k_0=2.45e^{-20}, e_0=1, η=5.33
Relative permeability function, -	Van Genuchten, λ=0.4	$k_{rel}=S_e^3$
Solid density*, kg/m^3	2780	
Initial dry density*, kg/m^3	1000	1700
Initial porosity *n**, -	0.64	0.388
Initial void ratio e*, -	1.78	0.635
Young modulus E, MPa	$10.293 \cdot S_e - 0.9327$	$1.7745 \cdot \exp(4.0441 \cdot S_e)$
Poisson ration, -	0.3 (Toprak et al., 2020)	0.35 (Toprak et al., 2013)
Swelling coefficient, -	$0.1 \cdot S_e$	$0.2 \cdot S_e$

* - data from Leupin et al., 2020.

The selected water retention curve for bentonite pellets was based on the results presented in (Toprak et al., 2020). For bentonite block van Genuchten relationship was used where air entry pressure was made dependent on void ratio as reported in (Seiphoori et al., 2014). The graphical expression of both dependencies could be seen in Figure 2.2-3.

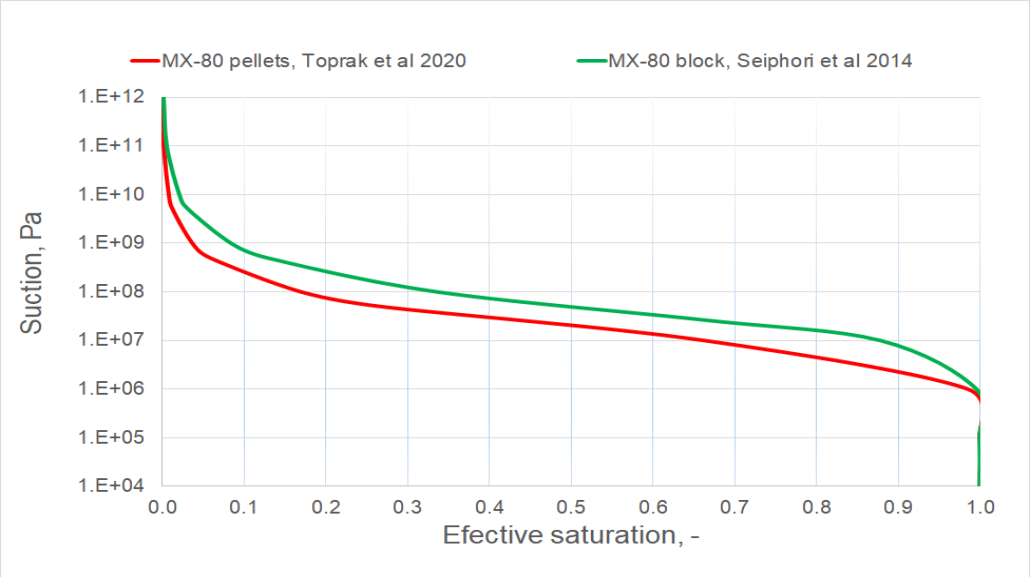

Figure 2.2-3. Water retention curves for bentonite pellets and block considered in LEI model

Saturated intrinsic permeability for bentonite pellets was defined according to exponential dependence on porosity change presented in (Toprak et al., 2020). Saturated intrinsic permeability for bentonite block was assumed to be dependent on void ratio according to empirical relationship reported in (Akesson et al., 2010). The graphical expression of both dependencies as well as initial and final values in both materials is presented in Figure 2.2-4. As it could be seen from the figure, the pellets have much higher saturated intrinsic permeability (about three orders of magnitude) compared to bentonite block.

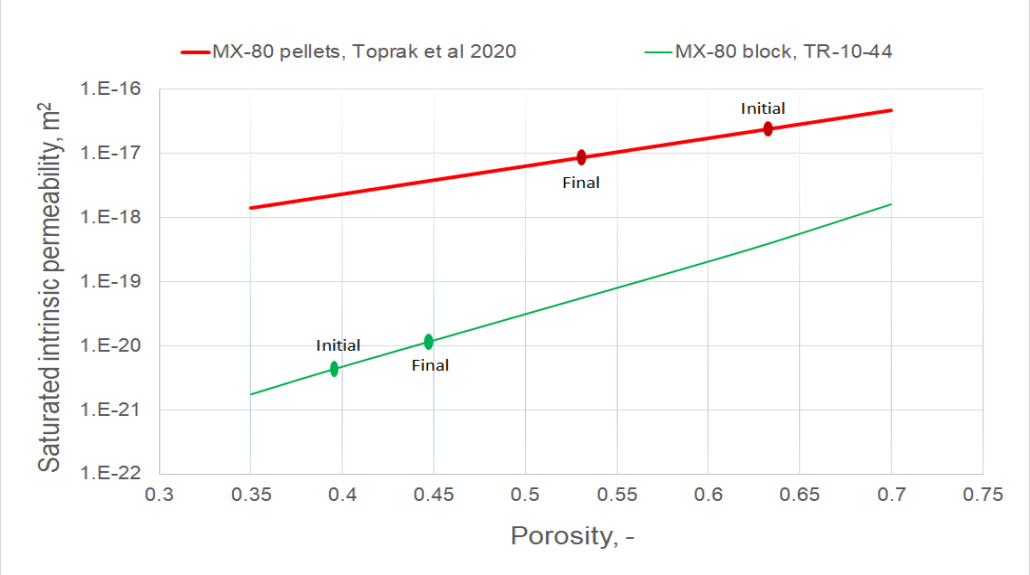

Figure 2.2-4. Saturated intrinsic permeability dependencies on porosity for bentonite pellets and block considered in LEI model

Unsaturated intrinsic permeability is highly dependent on the degree of saturation S_e and was expressed as the product of relative permeability k_r and the saturated intrinsic permeability. The dependency of relative permeability on degree of saturation was expressed as Van Genuchten relationship (λ=0.4) for bentonite pellets and as a power law (with exponent n=3) for block. The graphical expression of both dependencies is presented in Figure 2.2-5.

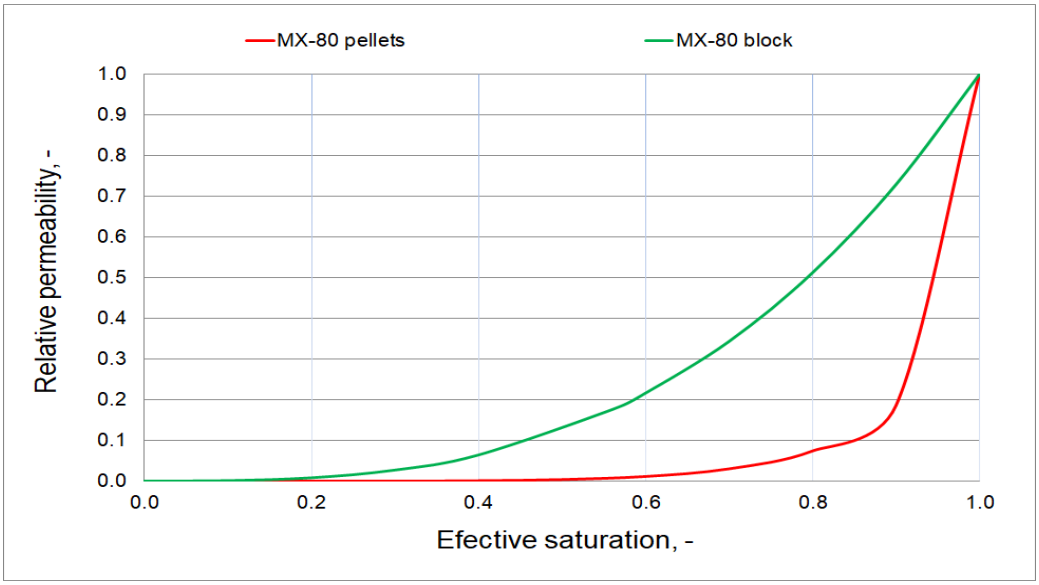

Figure 2.2-5. Relative permeability functions for bentonite pellets and block considered in LEI model

Mechanical parameters required to describe LEI non-linear swelling model are: Young's modulus, swelling coefficient and Poisson ratio. Young's modulus and swelling coefficient in both materials were assumed to be dependent on effective saturation in the model. The minimal and maximal values of Young's modulus for pellets and block were determined from BBM parameter values at unsaturated and saturated conditions presented in (Abed et al., 2016) and (Akesson et al., 2010), respectively. Later these values were interpolated linearly (for pellets) and exponentially (for block). The graphical expression of Young's modulus dependencies on effective saturation in both materials considered in LEI model is presented in Figure 2.2-6. Empirical expressions for swelling coefficients were obtained as a result of model calibration and the values of Poisson ratio were based on literature data.

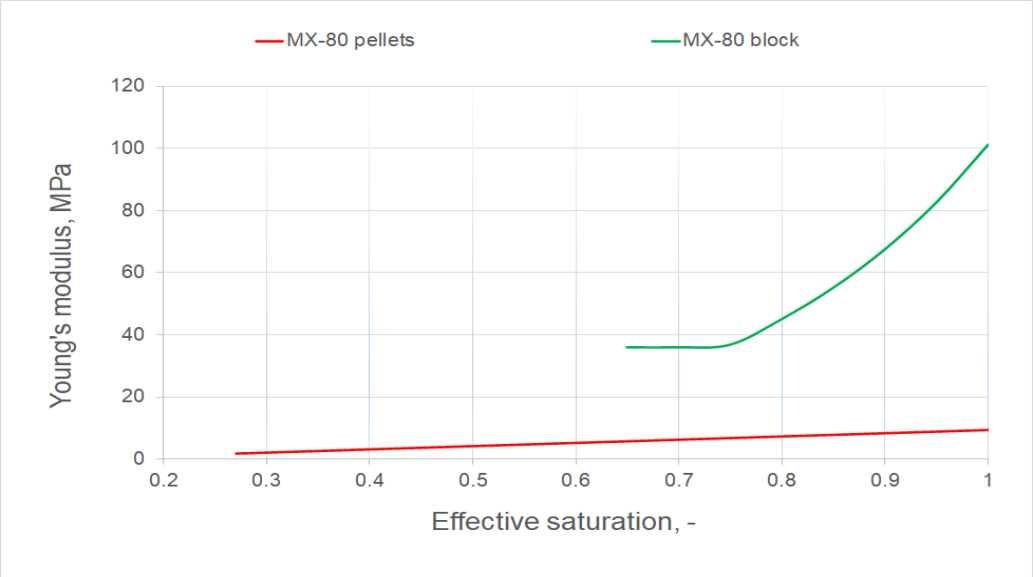

Figure 2.2-6. Young's modulus dependencies on effective saturation for bentonite pellets and block considered in LEI model

2.2.4 Initial and boundary conditions

A constant temperature of 20 °C and a constant gas pressure of 0.1 MPa was assumed in the model. The initial conditions of both materials are presented in Table 2**.2-2**.

Table 2.2-2. Initial characteristics of MX-80 type bentonite materials considered in LEI model

Parameter	Pellets zone	Block zone
Water content*, %	17	
Degree of saturation, -	0.266	0.744
Suction, MPa	-49.9	-26.4
Stress, MPa	0.01	

* - data from Leupin et al., 2020.

Two cases with different hydraulic boundary conditions were modelled:

- Free access of groundwater (simulation time – 250 years). The water pressure at the outer boundary of the pellets filling (blue line in Figure 2.2-7) was prescribed

through step function allowing representation of quick transition from unsaturated state to saturated state:

- $p = \begin{cases} -49.9\ MPa, & t < 0.01\ years \\ 0.1\ MPa, & t \geq 0.01\ years \end{cases}$
- Limited access of groundwater (simulation time – 4500 years). The constant water inflow rate through the outer boundary of the pellets filling (blue line in Figure 2.2-7) was held constant until fully saturated conditions were reached:
- $inward\ flux = \begin{cases} 2.6 \cdot 10^{-9}\ kg/(m^2 \cdot s), & t < 4000\ years \\ 0, & t \geq 4000\ years \end{cases}$

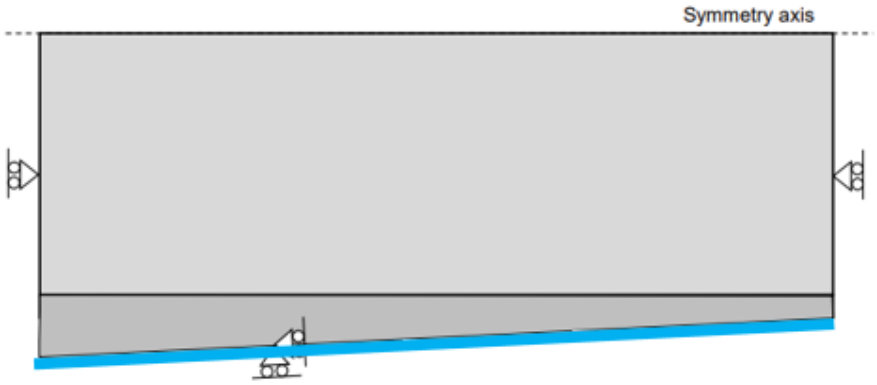

Figure 2.2-7. Hydraulic and mechanical boundary conditions considered in LEI model

Roller boundary conditions were applied to all mechanical boundaries and friction was not taken into account in the model.

2.2.5 Results

Time evolution of HM parameters

Average degree of saturation

The time evolution of average degree of saturation in modelled domain using different hydraulic boundary conditions are presented in Figure 2.2-8. As it could be seen, the much faster saturation was obtained in the case of free access of groundwater – the pellet zone was saturated during the first year as the block zone was saturated after about 170 years (Figure 2.2-8a). In the case of limited access of groundwater, the obtained trends in time were different, however the fully saturation in both materials was reached at the same time – after about 4000 years (Figure 2.2-8b).

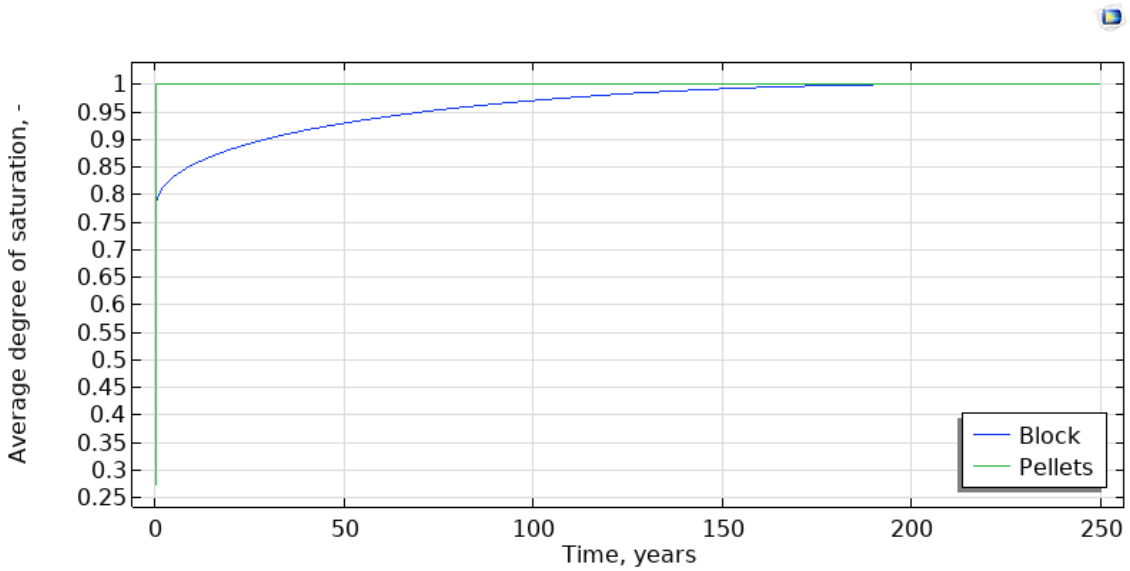

(a)

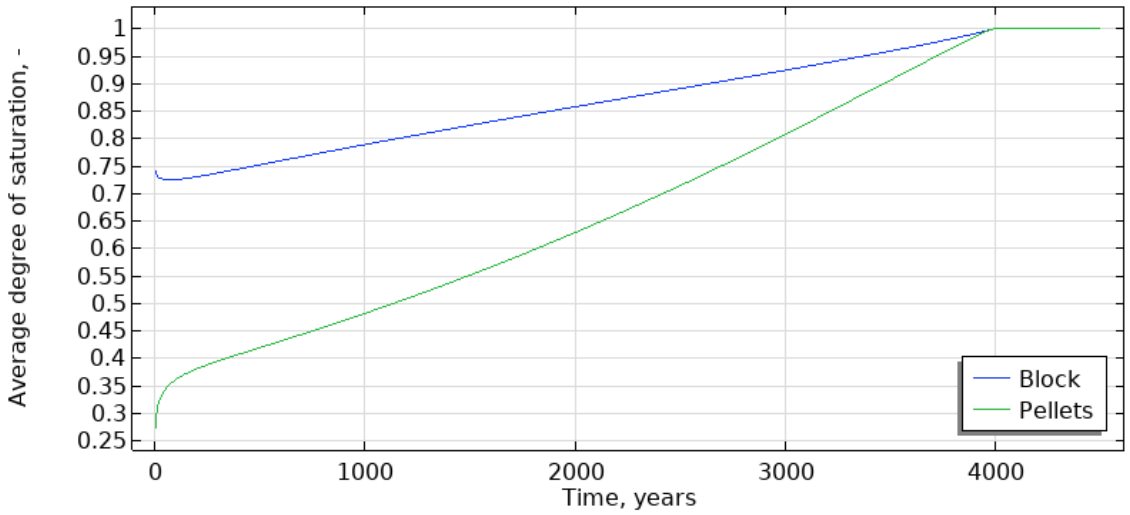

(b)

Figure 2.2-8. Time evolution of average degree of saturation in modelled domain; a) free access of groundwater case; b) limited access of groundwater case

Mean stress

Time evolution of mean stress at selected points along the base lines using different hydraulic boundary conditions are presented in Figure 2.2-9. Several aspects could be concluded from the figure:

- the peak stress at selected points was determined at the time when fully saturated conditions were reached in materials and later remained stable;
- despite different trends of mean stress in time were obtained at the same points in both analysed cases, the peak values were equal at the same points;

- wide range of mean stresses (from 3.6 up to 7.5 MPa) were obtained in analysed domain at saturated conditions;
- higher stresses were determined in theoretical section (points B1-B3) compared to maximum fallout section (points A1-A3):
    - the determined peak stress in pellets – about 4.8 MPa (point B3);
    - the determined peak stress in block – about 7.5 MPa (point B2).
-

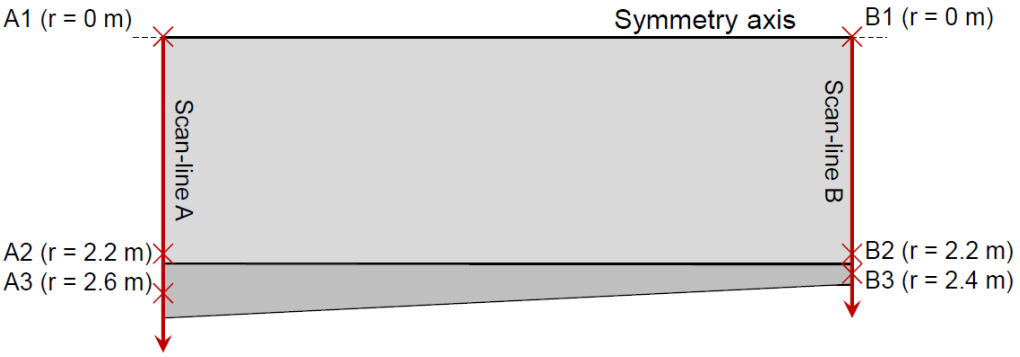

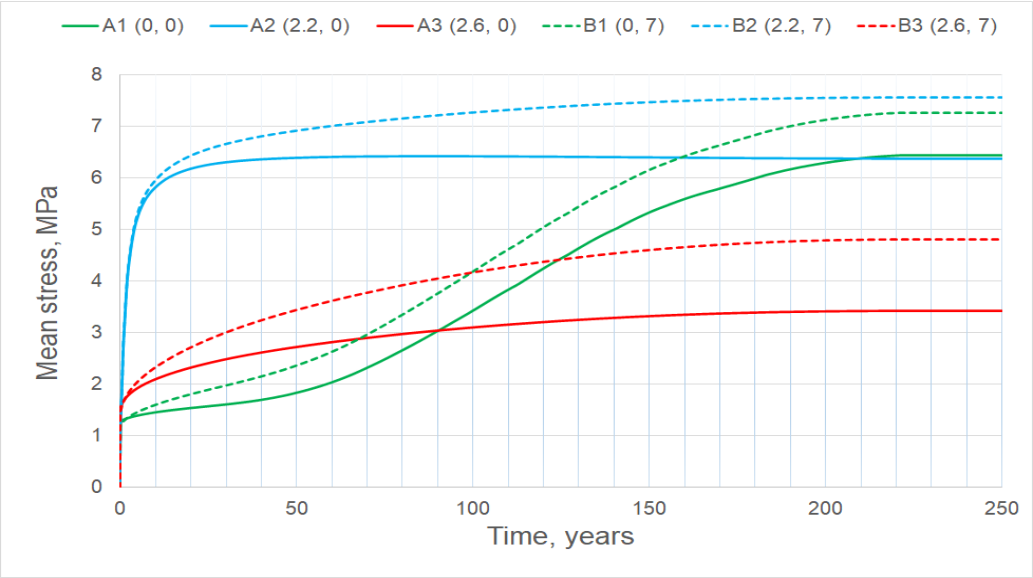

(a)

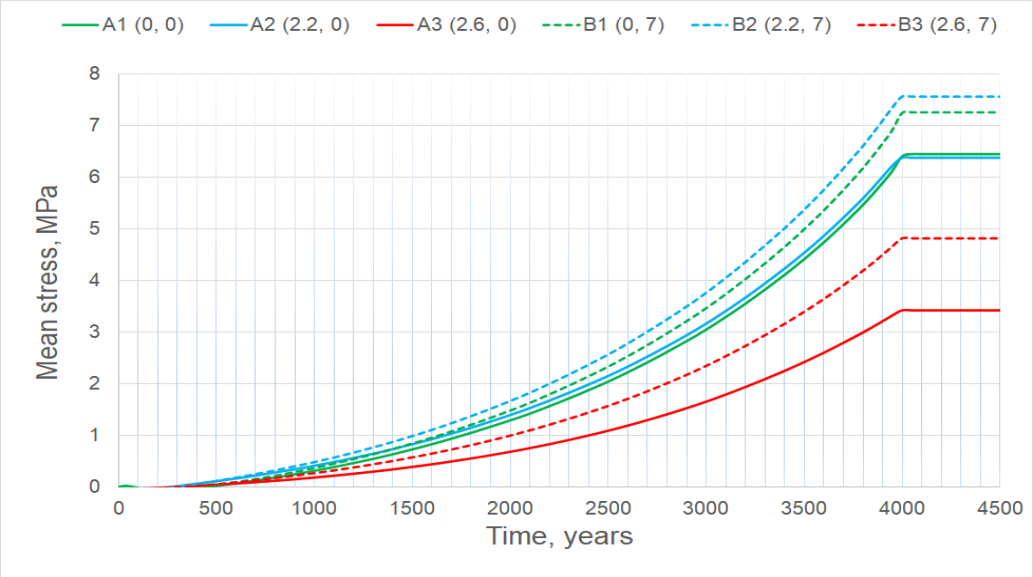

(b)

Figure 2.2-9. Time evolution of mean stress in selected points; a) free access of groundwater case; b) limited access of groundwater case

Final distributions of mechanical parameters

Displacements

Contours of modelled distribution of displacements (in centimetres) in analysed domain at the end of simulations using different hydraulic boundary conditions are presented in Figure 2.2-10. As it could be seen from the figure, both distributions are very similar due to fact that fully saturated conditions were reached in both analysed cases. The peak displacements were fixed in the points of the block near the maximum fallout section and displacement magnitude was of about 12.3 cm.

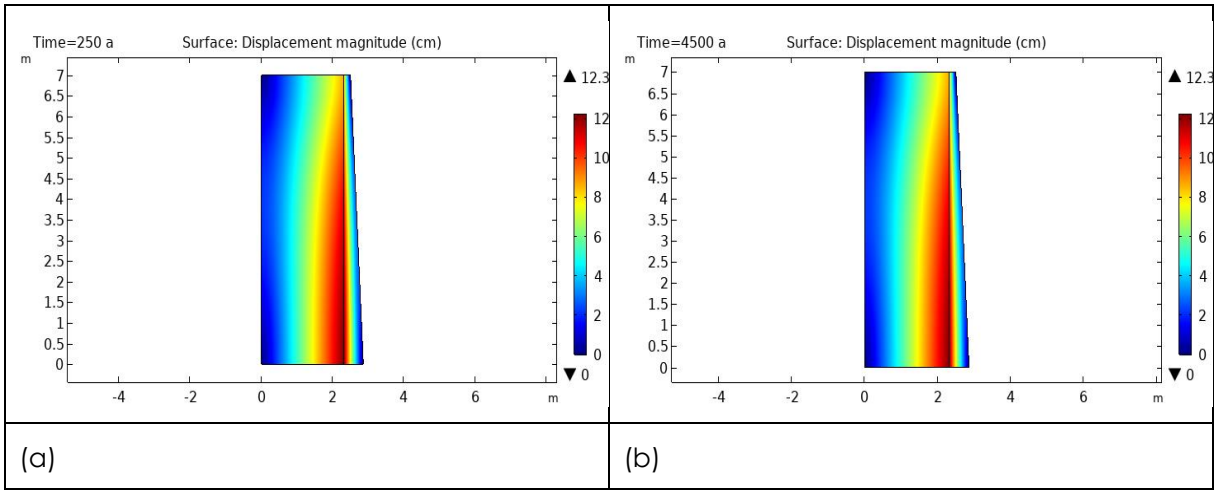

(a) (b)

Figure 2.2-10 Contours of modelled distribution of displacements in analysed domain at the end of simulations; a) free access of groundwater case;
b) limited access of groundwater case

Void ratio

Distribution of void ratio along the base lines at the end of simulations using different hydraulic boundary conditions are presented in Figure *2.2-11*. Despite the fact that simulation time was different, both graphs are almost identical and it is related to the fact what fully saturated condition were reached in both cases. Important aspects could be concluded from the figure:

- significant extent of homogenization was obtained compared to initial distribution of void ratio in both analysed cases. The initial difference of void ratios in both materials is about 200 %;
- higher homogenisation was obtained along the theoretical section (scan-line B) compared to maximum fallout section (scan-line A):
    - about 10 % difference of final average void ratios was determined in theoretical section (the final average void ratio in pellets was around 0.87 while in the block – around 0.79);
    - more than 50 % difference of final average void ratios was determined in maximum fallout section (the final average void ratio in pellets was around 1.22 while in the block – around 0.8).

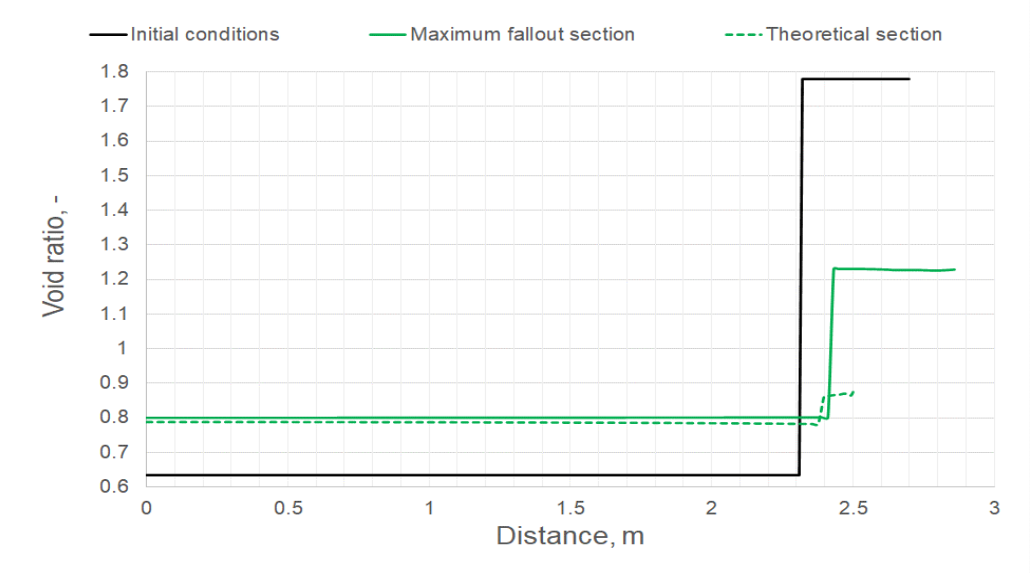

(a)

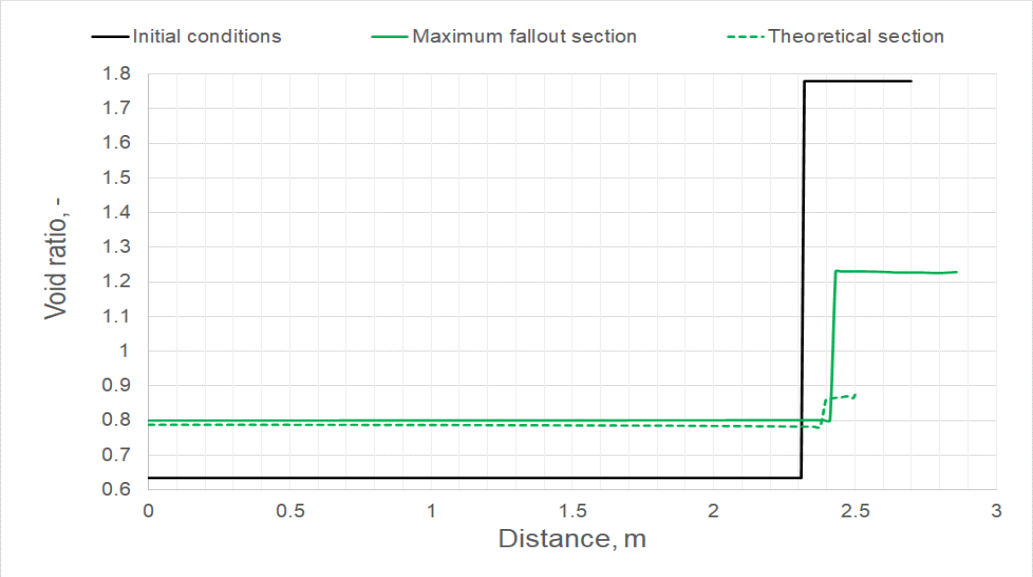

(b)

Figure 2.2-11 Distribution of void ratio along the base lines at the end of simulations; a) free access of groundwater case; b) limited access of groundwater case

2.2.6 Discussion

The modelling results of KBS-3 backfill homogenization test case have been obtained by LEI team applying model developed in BEACON WP3. For hydro-mechanical behaviour of MX-80 bentonite (block and pellets) Richard's equation and non-linear elastic swelling model was coupled in numerical tool COMSOL Multiphysics. The selection of the values of input parameters for bentonite block and pellets were based on available literature. However, empirical expressions for swelling coefficient in both materials were obtained as a result of model calibration.

Two cases using different hydraulic boundary conditions were modelled and fully saturated conditions were obtained after about 170 years (free access of groundwater case) and after about 4000 years (limited access of groundwater case). Wide range of mean stresses (from 3.6 up to 7.5 MPa) were obtained in analysed domain at saturated conditions and higher stresses were determined in theoretical section compared to maximum fallout section. The model indicates that the backfill material will not be completely homogenised. The remaining heterogeneity is of such an extent that the difference between the block and the pellets varies between 10 % and 50 % in analysed sections in terms of void ratio. However, significant extent of homogenization was obtained compared to initial distribution of void ratios in both materials, where initial difference was about 200 %.

2.3 ICL

2.3.1 Description of the models

To simulate the mechanical behaviour of MX-80 bentonite in Task 5.4, the ICL team has applied the constitutive model presented in the Beacon deliverables D3.1 and D3.3, produced as part of the WP3 of the Beacon project.

The model is an extended and modified version of the Barcelona Basic Modelling (BBM) framework (Alonso et al., 1990; Gens & Alonso, 1992), adopting a double-porosity structure and the formulation with net stress and suction as two independent stress variables (Ghiadistri, 2019; Ghiadistri et al., 2018).

The soil water retention (SWR) model used in the simulations is a form of a non-hysteretic Van Genuchten-type (van Genuchten, 1980) model, formulated in terms of the degree of saturation and matric suction and accounting for the variation of the specific volume (Melgarejo Corredor, 2004).

The adopted hydraulic conductivity (permeability) model (Potts & Zdravkovic, 1999; Nyambayo & Potts, 2010) assumes logarithmic variation of permeability with matric suction.

All models were implemented in the finite element software ICFEP (Potts & Zdravkovic, 1999), which has been applied by the ICL team in all numerical simulations for the Beacon project.

Mechanical model

The constitutive model applied in all analyses to represent the mechanical behaviour of MX-80 bentonite is the Imperial College Double Structure Model (ICDSM), Ghiadistri (2019), Ghiadistri et al. (2018). This is an extension of the previous single structure model (ICSSM, Georgiadis et al., 2005; Tsiampousi et al., 2013) which adopts the Barcelona Basic Modelling (BBM) framework (Alonso et al., 1990).

The ICDSM was introduced in detail in the deliverable D.3.1. Consequently, only the part of the model that enhances the simulation of the behaviour of expansive clays, as appropriate for compacted bentonite, is presented here. Overall, the model is formulated for unsaturated clays, adopting two independent stress variables: suction, $s = u_{air} - u_w$, and net stress, $\bar{\sigma} = \sigma_{tot} - u_{air}$, with u_{air} and u_w (the latter also referred as u) being the air and water pressures in the pores, respectively, and σ_{tot} being the total stress.

To enable smooth transition from saturated to unsaturated states and vice versa, the model also introduces an equivalent suction, $s_{eq} = s - s_{air}$, and equivalent stress, $\sigma = \bar{\sigma} + s_{air}$, where s_{air} is the air-entry value of suction for a given soil. As such, the model allows realistic values of s_{air} to be prescribed for any soil and full saturation is reached when $s = s_{air}$. The model is further generalised in the (J, p, θ, s_{eq}) space, where J, p and θ are the invariants of the equivalent stress tensor, representing generalised deviatoric stress, mean equivalent stress and Lode's angle, respectively.

The enhancement of the ICDSM to enable the modelling of unsaturated expansive clays comprises the introduction of a double-porosity structure into the model formulation, in agreement with e.g. Gens & Alonso (1992) and Alonso et al. (1999). This formulation differentiates two levels of structure in the clay: the macro-structure, which is assumed unsaturated and mostly defined by the original ICSSM framework; and the micro-structure, assumed to be elastic, volumetric and fully saturated.

Characteristics of the micro-structure

Assuming the micro-structure to be fully saturated implies that it can be defined in terms of effective stresses, where the mean effective stress is defined as $p' = p + s_{eq}$. The assumptions that it is also volumetric and elastic imply that changes in p' result in elastic volumetric micro-strains, $\Delta\varepsilon_{v,m}^{e}$:

$$\Delta\varepsilon_{v,m}^{e} = \frac{\Delta p'}{K_m} \tag{1}$$

where the micro-structural bulk modulus, K_m, is defined as:

$$K_m = \frac{1 + e_m}{\kappa_m} p' \tag{2}$$

In the above equation, e_m is the micro-structural void ratio and κ_m is the micro-structural elastic compressibility parameter. For consistency, the following must be satisfied:

$$e = e_M + e_m \tag{3}$$

where e_M is the macro-structural void ratio and e is the overall void ratio of the material. The bulk modulus K_m is additional to the two bulk moduli associated with the macro-structure and defined by the ICSSM formulation: $K_{s,M}$, associated with equivalent suction, and $K_{p,M}$, associated with mean equivalent stress, all three defining the overall elastic soil behaviour in the double-structure formulation.

Interaction of the two levels of structure

Although the micro-structural volumetric deformation is elastic, it is assumed to contribute to the macro-structural volumetric plastic strains, $\Delta\varepsilon_{v,\beta}^{p}$, through an additional plastic mechanism:

$$\Delta\varepsilon_{v,\beta}^{p} = f_\beta \cdot \Delta\varepsilon_{v,m}^{e} \tag{4}$$

defined by the interaction function, f_β, between the two levels of structure. The shape of this function is dependent on whether the micro-structure swells or compresses, and is defined as:

$$f_{\beta} = \begin{cases} \begin{cases} c_{c1} + c_{c2}\left(\frac{p_r}{p_0}\right)^{c_{c3}} & if \quad \frac{p_r}{p_0} \geq 0 \\ c_{c1} & if \quad \frac{p_r}{p_0} < 0 \end{cases} & micro-compression \\ \begin{cases} c_{s1} + c_{s2}\left(1 - \frac{p_r}{p_0}\right)^{c_{s3}} & if \quad \frac{p_r}{p_0} \geq 0 \\ c_{s1} + c_{s2} & if \quad \frac{p_r}{p_0} < 0 \end{cases} & micro-swelling \end{cases} \tag{5}$$

in which p_r/p_0 expresses the degree of openness of the structure in terms of the distance between the current stress state (represented by p_r) and the yield surface (represented by p_0), while c_{c1}, c_{c2}, c_{c3} and c_{s1}, c_{s2}, c_{s3} are coefficients defining the shape of the interaction function.

Quantification of the micro-structural evolution

Finally, the ICDSM introduces the void factor, $VF = e_m/e$, to enable the quantification of the micro-structural evolution in the clay. This parameter expresses the degree of dominance of each structural level in the overall clay fabric.

All model parameters are summarised in Table 2.3-1, together with a list of experiments that enable parameter derivation. A double-structure formulation introduces four additional model parameters, as shown in the table.

Table 2.3-1 Summary of ICDSM parameters

	Parameter	Source
Input parameters for IC SSM	Parameters controlling the shape of the yield surface, M_F, α_F, μ_F	Triaxial compression
	Parameters controlling the shape of the plastic potential surface, α_G, μ_G	Triaxial compression; relationship between dilatancy and J/p ratio
	Generalized stress ratio at critical state, M_J	Triaxial compression, related to the angle of shear resistance at critical state ϕ'_{cs}
	Characteristic pressure, p_c (kPa)	Limiting confining stress at which $p_0 = p_0^* = p_c$
	Specific volume at unit pressure related to the initial equivalent suction, $v_1(s_{eq})$	Isotropic compression test at constant equivalent suction s_{eq}
	Fully saturated plastic compressibility coefficient, $\lambda(0)$	Fully saturated isotropic loading
	Elastic compressibility coefficient, κ	Fully saturated isotropic loading/unloading
	Maximum soil stiffness parameter, r	Isotropic compression tests at different constant values of suction
	Soil stiffness increase parameter, β(1/kPa)	Isotropic compression tests at different constant values of suction
	Elastic compressibility coefficient for changes in suction, κ_s	Drying/wetting test at constant confining stress
	Poisson's ratio, ν	Triaxial compression test
	Plastic compressibility coefficient for changes in suction, λ_s	Drying test at constant confining stress
	Air-entry value of suction, s_{air} (kPa)	From the soil water retention curve
	Yield value of equivalent suction, s_0 (kPa)	Drying test at constant confining stress (usually a high value if it is not to be mobilised)
Additional input parameters for IC DSM	Micro-structural compressibility parameter, κ_m	No direct routine test - potentially from micro-structural investigations (e.g. MIP)
	Void factor, VF	No direct routine test – potentially from micro-structural investigations (e.g. MIP)
	Coefficients for the micro swelling function, c_{s1}, c_{s2}, c_{s3}	No direct routine test – potentially from micro-structural investigations (e.g. MIP)
	Coefficients for the micro compression function, c_{c1}, c_{c2}, c_{c3}	No direct routine test – potentially from micro-structural investigations (e.g. MIP)

Soil Water Retention (SWR) model

For the analyses presented in this report, a non-hysteretic Van Genuchten-type (van Genuchten, 1980) SWR model was adopted, formulated in terms of the degree of saturation, S_r, and the matric suction (Melgarejo Corredor, 2004):

$$S_r = \left[\frac{1}{1+\left[\alpha\cdot(v-1)^{\psi}\cdot s_{eq}\right]^{n}}\right]^{m}\cdot(1-S_{r0})+S_{r0} \qquad (6)$$

In the above equation, S_{r0} is the residual degree of saturation, while α, m and n are fitting parameters controlling the shape of the retention curve; ψ is the parameter controlling the effect of the specific volume, v.

Hydraulic conductivity (permeability) model

The variable permeability model (Potts & Zdravkovic, 1999; Nyambayo & Potts, 2010) adopted in all analyses assumes the permeability (hydraulic conductivity) to vary with matric suction according to the expression:

$$\log k = \log k_{sat} - \frac{s-s_1}{s_2-s_1}\cdot\log\frac{k_{sat}}{k_{min}} \qquad (7)$$

where k_{sat} is the saturated value of permeability (m/s), k_{min} its minimum value reached after the prescribed change in matric suction from s_1 to s_2.

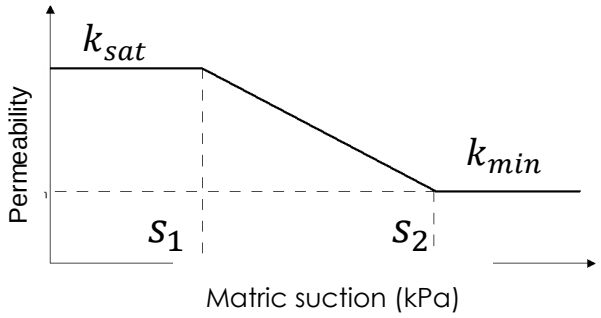

Figure 2.3-1 Variable permeability model.

2.3.2 Geometry and discretization

All the numerical simulations undertaken were hydro-mechanically fully coupled and were carried out with the FE code ICFEP (Potts & Zdravkovic, 1999). Given that the 2 scenarios investigated as part of Task 5.4 refer to (global) constant volume conditions, no significant displacements were expected, and, therefore, the small displacement formulation was adopted.

Due to the axisymmetric nature of the 2 scenarios under investigation (i.e. *free access of water* and *restricted access of water*), 2 two-dimensional (2D) axisymmetric finite element (FE) simulations were undertaken. The domain analysed (maximum length of 2.86 m, height of 7 m) was discretised using 8-noded quadrilateral displacement-based elements, with 4 pore pressure degrees of freedom at the corner nodes. The mesh generated is shown in Figure 2.3-2, together with the mechanical and hydraulic boundary conditions adopted for the 2 scenarios investigated (see details in Section 2.3.4).

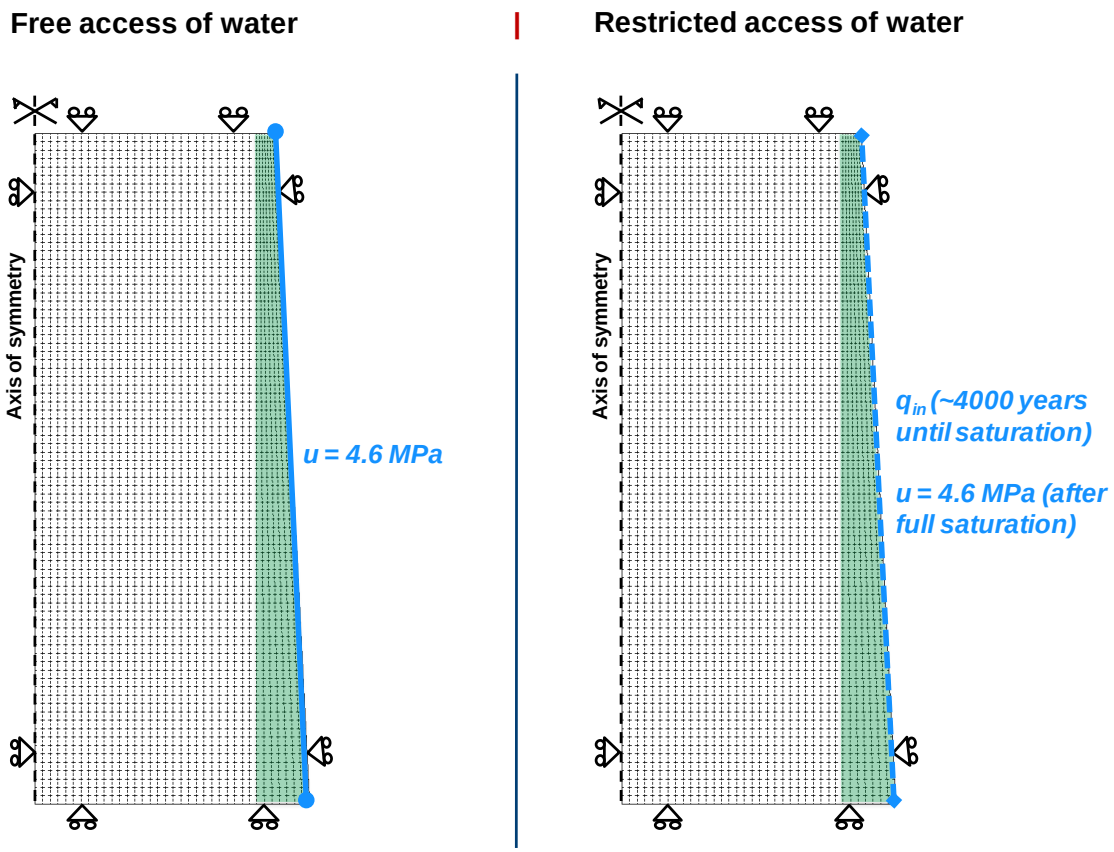

Figure 2.3-2 Meshes generated and boundary conditions adopted in the FE analyses.

2.3.3 Input parameters

The model parameters used in both analyses are reported in Table 2.3-2, Table 2.3-3 and Table 2.3-4, with reference to the Imperial College Double Structure Model (IC DSM), the Soil Water Retention (SWR) model, and the Hydraulic conductivity model, respectively.

For the MX-80 bentonite blocks, the parameters were derived from the laboratory data reported in Marcial et al. (2008), Dueck & Nilsson (2010), Tang & Cui (2010), Seiphoori et al. (2014), and Bosch et al. (2019). For the MX-80 bentonite pellets, the parameters were derived from the laboratory data reported in Hoffman et al. (2007), Alonso et al. (2011), and Toprak et al. (2020).

Table 2.3-2 Input parameters for SWR model

Parameter	Value (block)	Value (pellets)
Fitting parameter, $\boldsymbol{\alpha}$(1/kPa)	0.0001	0.0015
Fitting parameter, $\boldsymbol{m}$	0.47	0.25
Fitting parameter, $\boldsymbol{n}$	1.90	1.05
Fitting parameter, $\boldsymbol{\psi}$	2.0	2.5
Residual degree of saturation, $\boldsymbol{S_{r0}}$	0.05	0.0

Table 2.3-3 Input parameters for Hydraulic conductivity model

Parameter	Value (block)	Value (pellets)
Saturated hydraulic conductivity, $\boldsymbol{k_{sat}}$(m/s)	3×10^{-14}	5×10^{-10}
Minimum hydraulic conductivity, $\boldsymbol{k_{min}}$ (m/s)	3×10^{-15}	5×10^{-10}
Suction, $\boldsymbol{s_1}$(kPa)	1000.0	N/A
Suction, $\boldsymbol{s_2}$(kPa)	41000.0	N/A

Table 2.3-4 Input parameters for IC DSM model

Parameter	Value (block)	Value (pellets)
Parameters controlling the shape of the yield surface, M_F, α_F, μ_F	0.495, 0.4, 0.9	1.00, 0.4, 0.9
Parameters controlling the shape of the plastic potential surface, α_G, μ_G	0.4, 0.9	0.4, 0.9
Generalized stress ratio at critical state, M_J	0.495	1.00
Characteristic pressure, p_c (kPa)	1000.0	50.0
Specific volume at unit pressure related to the initial equivalent suction, $v_1(s_{eq})$	5.847	4.020
Fully saturated plastic compressibility coefficient, $\lambda(0)$	0.515	0.226
Elastic compressibility coefficient, κ	0.0087	0.045
Maximum soil stiffness parameter, r	0.800	0.800
Soil stiffness increase parameter, β(1/kPa)	0.000085	0.0000001
Elastic compressibility coefficient for changes in suction, κ_s	0.142	0.010
Poisson's ratio, ν	0.3	0.2
Plastic compressibility coefficient for changes in suction, λ_s	0.566	0.040
Air-entry value of suction, s_{air} (kPa)	1000.0	0.0
Yield value of equivalent suction, s_0 (kPa)	10^6	10^6
Micro-structural compressibility parameter, κ_m	0.360	0.090
Void factor, VF	0.457	0.163
Coefficients for the micro swelling function, c_{s1}, c_{s2}, c_{s3}	-0.20, 1.20, 3.00	-0.10, 1.10, 3.00
Coefficients for the micro compression function, c_{c1}, c_{c2}, c_{c3}	-0.20, 1.20, 3.00	-0.10, 1.10, 3.00

The predictive capabilities of the models, when adopting the parameters in Table 2.3-2, Table 2.3-3 and Table 2.3-4 to simulate the behaviour of MX-80 bentonite blocks, can be evaluated from Figure 2.3-3. The figure shows the results of a swelling pressure test (a) for a dry density, ρ_d, and an initial gravimetric water content, w, of 1.7 g/cm^3 and 17%, respectively, together with swelling pressure laboratory data (b), as reported in the SKB Report TR-13-21 (Olsson et al., 2013).

Further predictive capabilities of the models can be seen in Figure 2.3-4, where a comparison between experimental and numerical oedometer test data is shown.

The SWR curves employed in the analyses, and the corresponding data used for their calibration, are illustrated in Figure 2.3-5 for both MX-80 blocks (a) and pellets (b).

The Hydraulic conductivity model used for the MX-80 bentonite blocks was defined based on the data reported by Marcial et al. (2008), and was adopted in conjunction with a saturated hydraulic conductivity of 3×10^{-14} m/s, the latter obtained from the SKB Report TR-13-21 (Olsson et al., 2013).

Regarding the pellets, due to their peculiar structure, Hoffman et al. (2007) show that the hydraulic conductivity tends to decrease with suction reductions, contrarily to what is more generally observed in geo-materials.

The Hydraulic conductivity model available (described in Section 2.3.1) cannot reproduce such a variation, and, therefore, a constant hydraulic conductivity of 5×10^{-10} m/s was selected for the pellets, corresponding to the average value of measurements carried out at different suction levels by Hoffman et al. (2007).

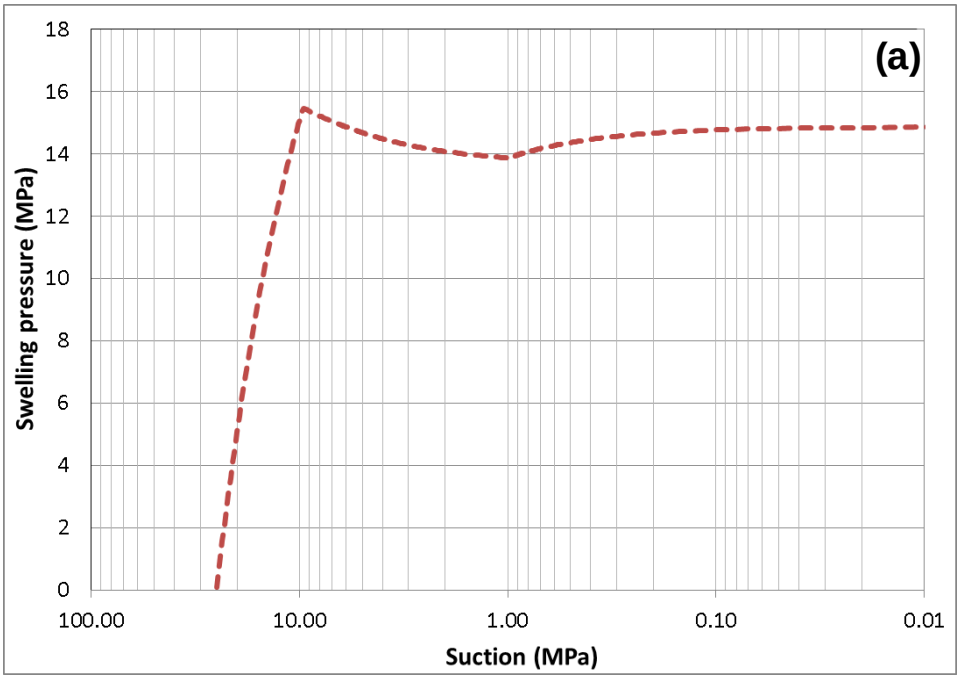

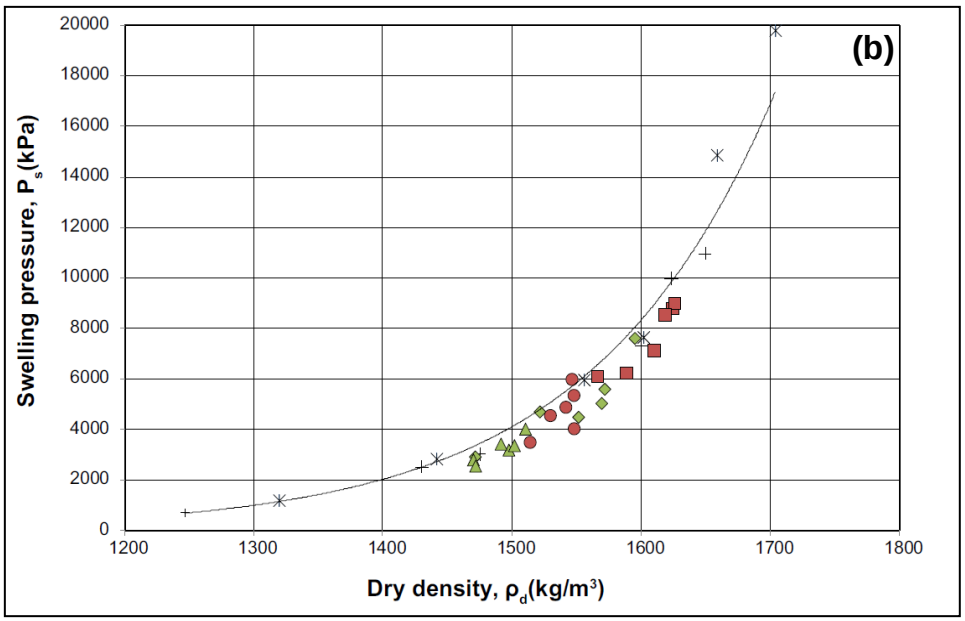

Figure 2.3-3 Swelling pressure test results (ρd=1.7 g/cm3 and w=17%) (a) and swelling pressure laboratory data (b).

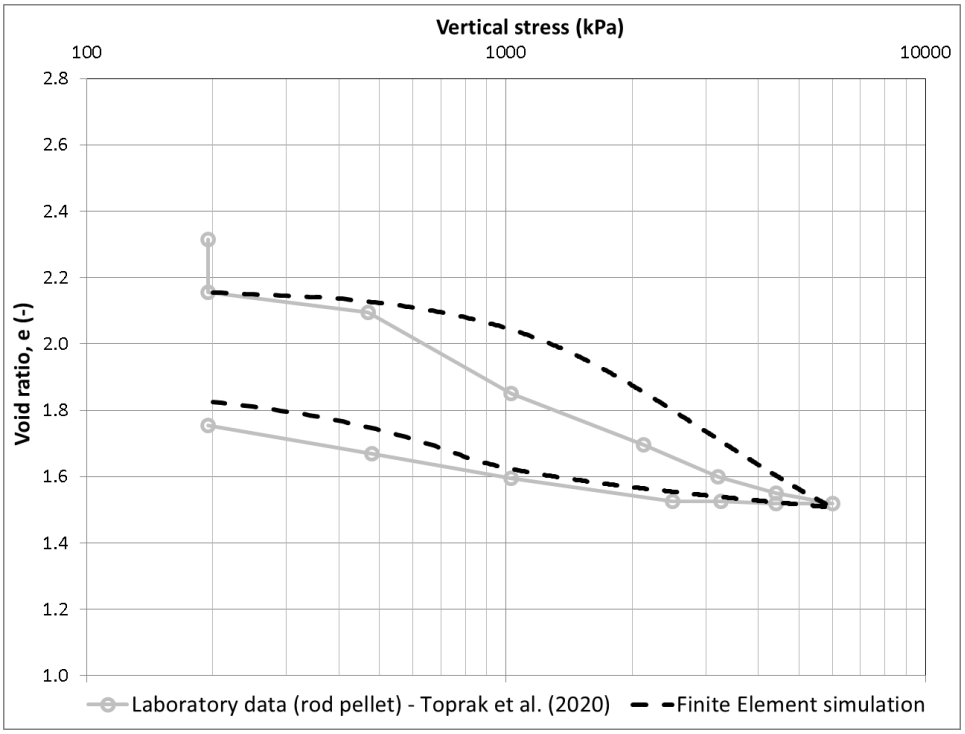

Figure 2.3-4 Comparison between experimental and numerical oedometer test data.

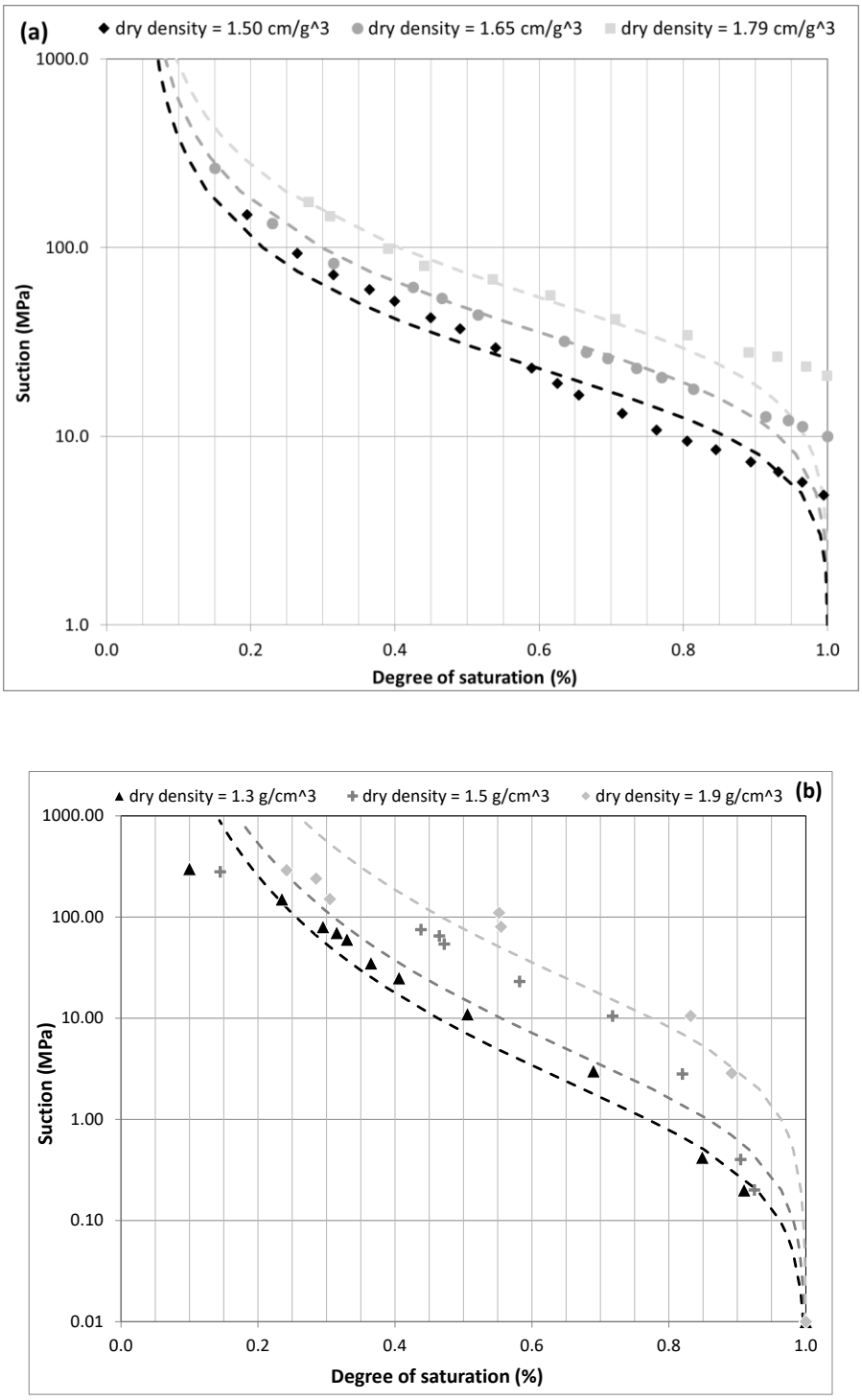

Figure 2.3-5 Comparison between adopted soil water retention curves (dashed lines) and laboratory data (symbols) for bentonite blocks (a) and pellets (b) (laboratory data from Seiphoori et al., 2014, and Alonso et al., 2011, respectively).

2.3.4 Initial and boundary conditions

The initial conditions assumed in the 2 analyses undertaken for Task 5.4, summarised in Table 2.3-5, correspond to those indicated in the modelling specifications for Task 5.4 (Leupin et al., 2020). The initial state of the materials were defined by Leupin et al. (2020) in terms of dry densities and gravimetric water contents, so the initial suctions were directly derived from the water retention curves adopted (Figure 2.3-5). An initial nominal isotropic total stress of 100 kPa was assigned to both materials in both analyses.

Table 2.3-5 Initial conditions adopted in the FE analyses

Material	p (MPa)	w (%)	ρ_d (g/cm^3)	e (-)	S_r (%)	s (MPa)
Pellets	0.1	17.0	1.0	1.780	26.55	24536.0
Block	0.1	17.0	1.7	0.635	74.56	24995.3

The 2 analyses undertaken are representative of 2 different scenarios, named *free access of water* and *restricted access of water* by Leupin et al. (2020).

The *free access of water* scenario was modelled by imposing a positive pore pressure of 4.6 MPa on the mesh boundary representing the contact area between MX-80 pellets and the host rock (Figure 2.3-2). The 4.6 MPa pore pressure, representative of repository depths, was applied gradually, over 1.5 years circa, to avoid large hydraulic gradients at the boundary. The boundary corresponding to the axis of symmetry, as well as the top and bottom boundaries (Figure 2.3-2), were assumed impervious during the entire simulation. The analysis was considered completed when a 4.6 MPa positive pore pressure was observed throughout the whole domain analysed.

The *restricted access of water* scenario was modelled by applying, in the first part of the analysis, a constant in-flow of 2.1×10^{-12} m/s on the mesh boundary representing the contact area between MX-80 pellets and the host rock (Figure 2.3-2). The in-flow magnitude was selected in order to reach full saturation after around 4000 years, the latter identified by Sellin et al. (2017) as a representative saturation period, should access to water be restricted.

At the end of the saturation period of around 4000 years, the hydraulic boundary condition on the right boundary was changed, applying a constant positive pore pressure of 4.6 MPa instead. Also for the second scenario analysed, top, bottom and left boundaries were assumed impervious, and the analysis was stopped when a 4.6 MPa positive pore pressure was observed everywhere in the mesh.

The mechanical boundary conditions applied in both analyses, i.e. no displacements allowed in the directions orthogonal to the model boundaries, are shown in Figure 2.3-2.

2.3.5 Results

For each of the 2 scenarios analysed (i.e. *free access of water* and *restricted access of water*), the following results are reported and discussed:

- Pore water pressure, degree of saturation, mean total stress, and void ratio distributions, at key stages of the analyses, along scan-lines A and B (the scan-lines are indicated in Figure 2.3-6; Leupin et al., 2020).
- Mean total stress and void ratio variations with time, with reference to the points A1, A2, A3 and B1, B2, B3 in Figure 2.3-6 (Leupin et al., 2020).

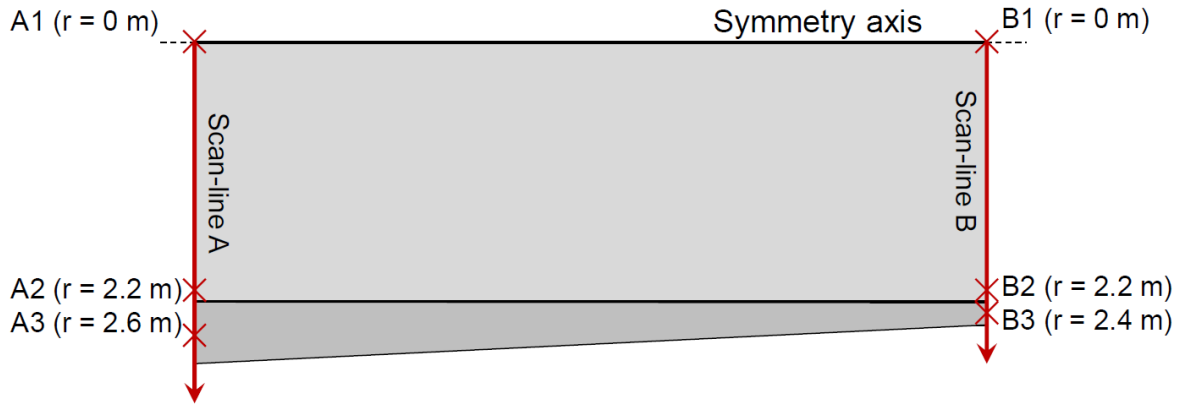

Figure 2.3-6 Reference scan-lines and points considered (Leupin et al., 2020).

Free access of water scenario

Figure 2.3-7a shows the pore water pressure distributions, at key stages of the *free access of water* analysis, along scan-line A (indicated in Figure 2.3-6). The initial pore water pressure profile is consistent with the information reported in Table 2.3-5, indicating the presence of an initial suction close to 25 MPa. After around 1.5 years, the pore pressure in the bentonite pellets corresponds to the one applied at the hydration boundary (i.e. 4.6 MPa), due to the large permeability characterising the pelletised material (see Table 2.3-4). On the other hand, it takes several decades for the hydration front to penetrate the blocks and reach the axis of symmetry, due to the very low permeability characterising the blocks (see Table 2.3-4). As a consequence, the full pore pressure equilibration is only reached after almost 150 years.

Figure 2.3-7b shows the degree of saturation distributions, at key stages of the *free access of water* analysis, along scan-line A. As expected, due to the hydraulic conductivities of the backfill, full saturation is quickly observed for the pellets (after 1.5 years), while the saturation process within the blocks is much slower.

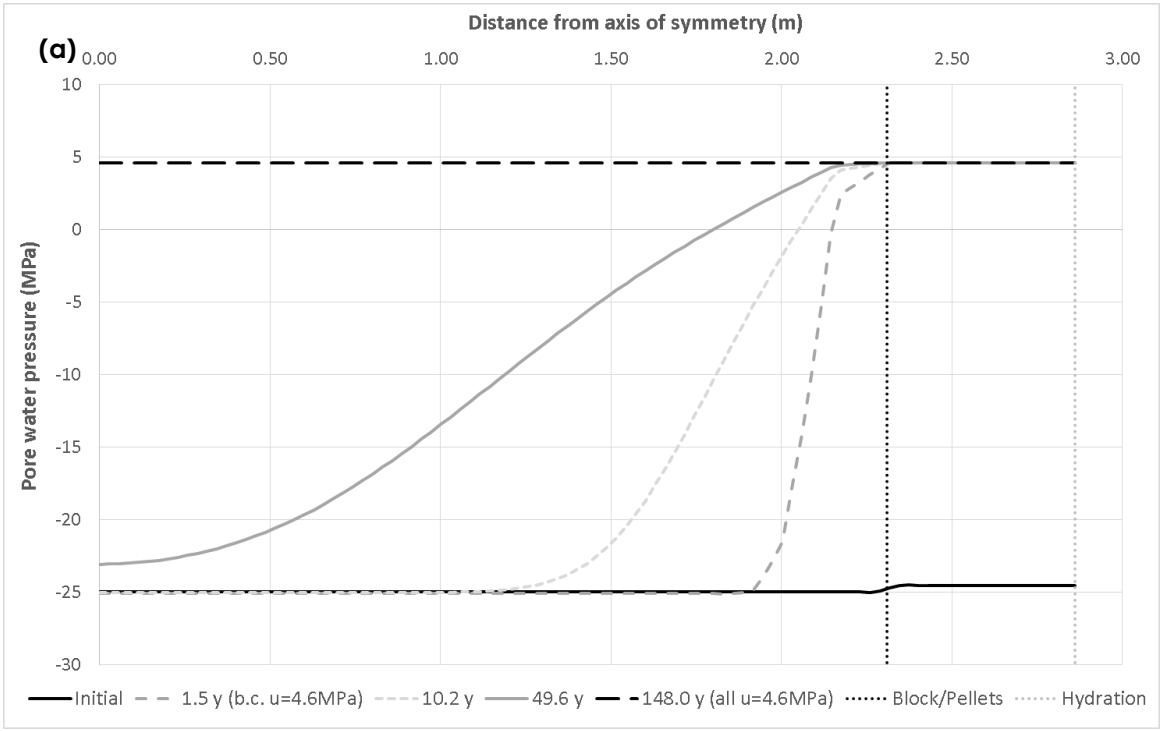

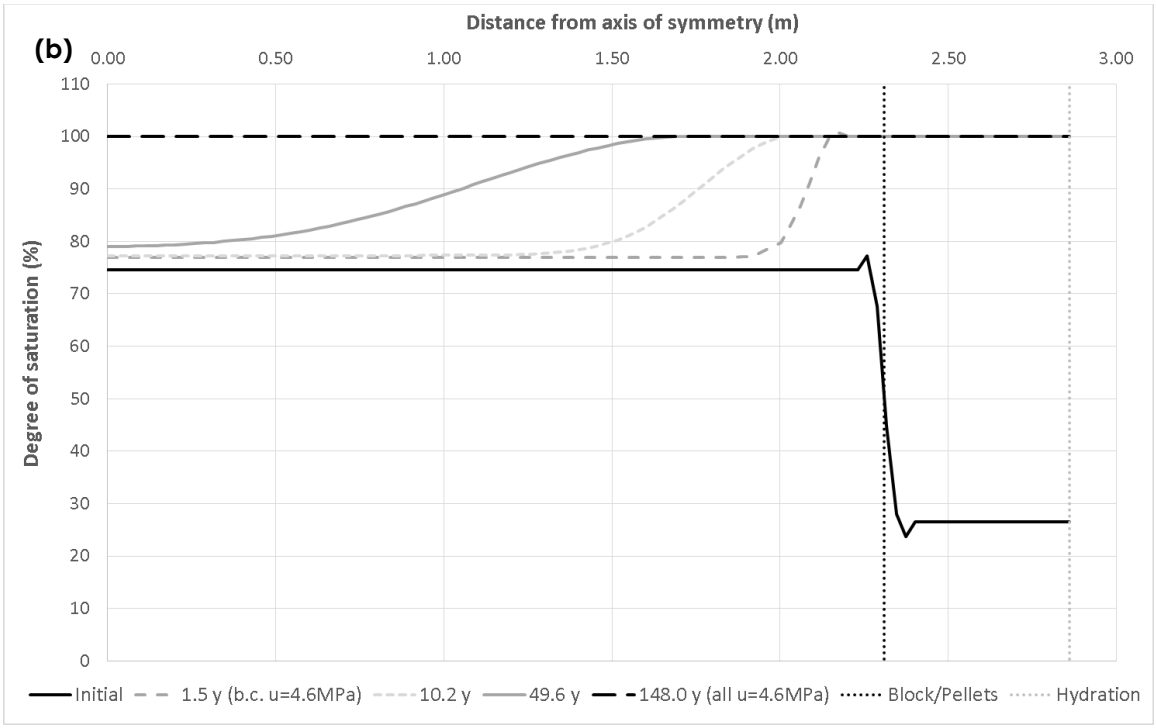

Figure 2.3-7 Pore water pressure (a) and degree of saturation (b) distributions, at key stages of the 'free access of water' analysis, along scan-line A (shown in Figure 2.3-6).

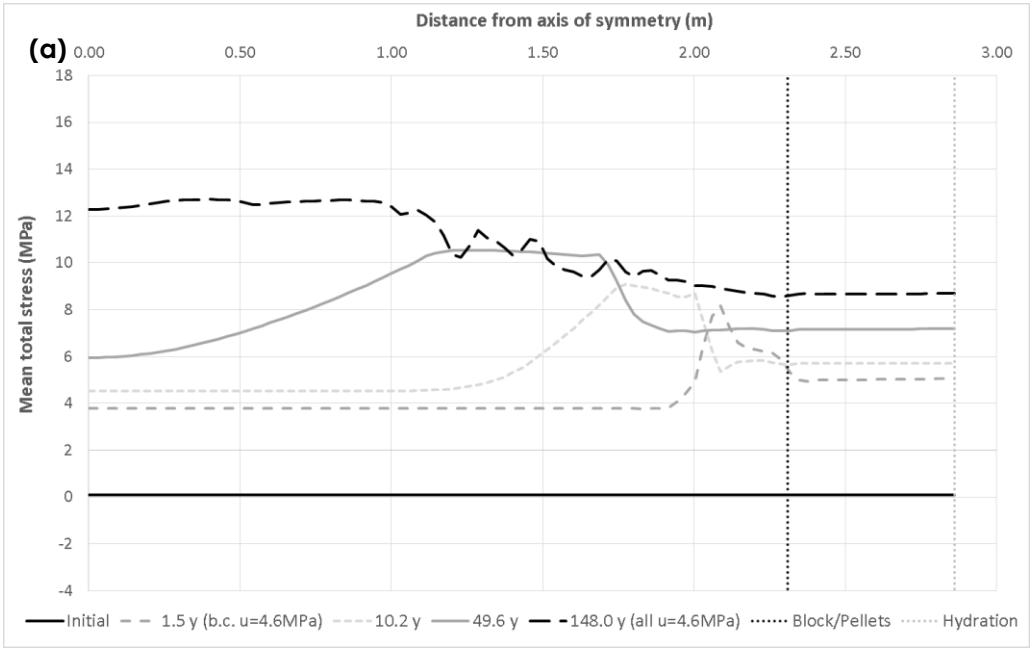

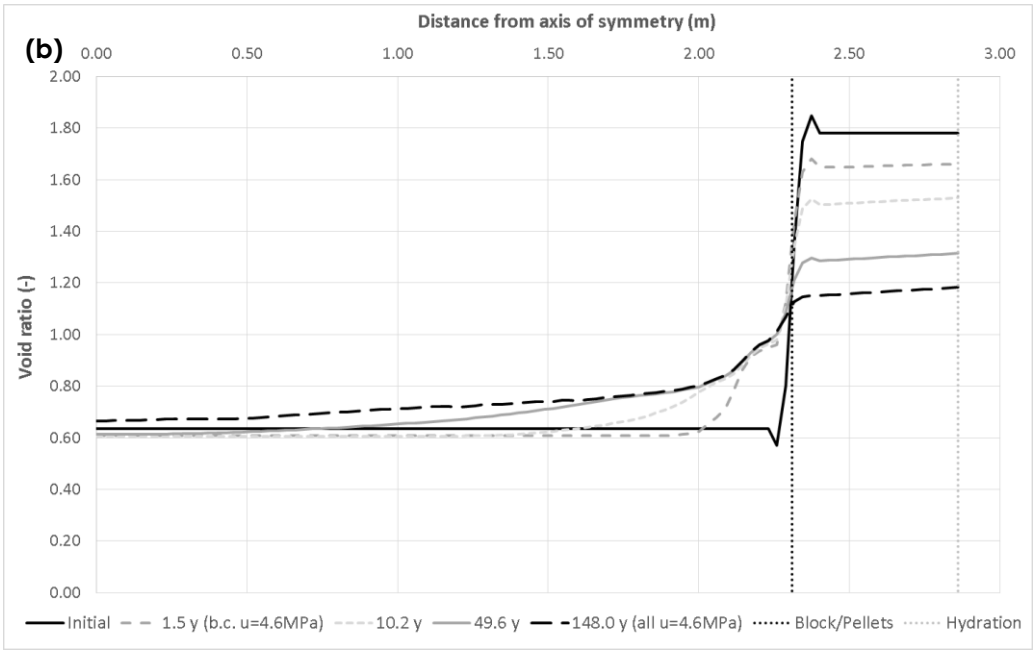

Figure 2.3-8 Mean total stress (a) and void ratio (b) distributions, at key stagesof the 'free access of water' analysis, along scan-line A (shown in Figure 2.3-6).

Figure 2.3-8a shows the mean total stress distributions, at key stages of the *free access of water* analysis, along scan-line A. After 1.5 years, when the pore water pressure at the right boundary of the mesh is increased up to 4.6 MPa, a significant increase in mean total stress is already observed across the whole domain analysed. Such an increase is larger in the area closer to the hydration boundary (particularly for the blocks, as they have a larger swelling potential compared to the pellets). After some decades, the hydration front tends to move towards the axis of symmetry of the mesh, causing a further increase in swelling pressure (>10 MPa after around 50 years). The maximum swelling pressure (12-13 MPa) is predicted at the end of the analysis, i.e. after almost 150 years, when a positive pore pressure of 4.6 MPa is reached everywhere in the mesh.

Figure 2.3-8b shows the void ratio distributions, at key stages of the *free access of water* analysis, along scan-line A. As expected, the hydration process gradually induces the homogenisation of the backfill, which results in significant void ratio reductions for the pellets (from e=1.78 to e<1.20). The blocks, on the other hand, tend to swell during the hydration process, experiencing less pronounced void ratio variations compared to the pellets.

In particular, the void ratio variations appear to be very limited in the proximity of the axis of symmetry, probably because hydration takes place from the outer edge of the domain analysed, so the central area tends to swell almost under fully confined conditions.

Figure 2.3-9 shows the pore water pressure (a) and degree of saturation (b) distributions, at key stages of the *free access of water* analysis, along scan-line B (indicated in Figure 2.3-6). The pore water pressure and degree of saturation variations observed along scan-line B are very similar, in terms of timing and magnitude, to those observed along scan-line A.

More significant differences between scan-line A and scan-line B results are predicted in terms of mean total stress and void ratio variations (shown in Figure 2.3-10a and Figure 2.3-10b, respectively, for scan-line B). The maximum swelling pressure developed along scan-line B at the end of the analysis is around 14 MPa, compared to the 12-13 MPa predicted, at the same stage, along scan-line A. The presence of higher swelling pressures is associated with more significant void ratio reductions in the pellets (where e reduces from 1.78 to values close to 1.00).

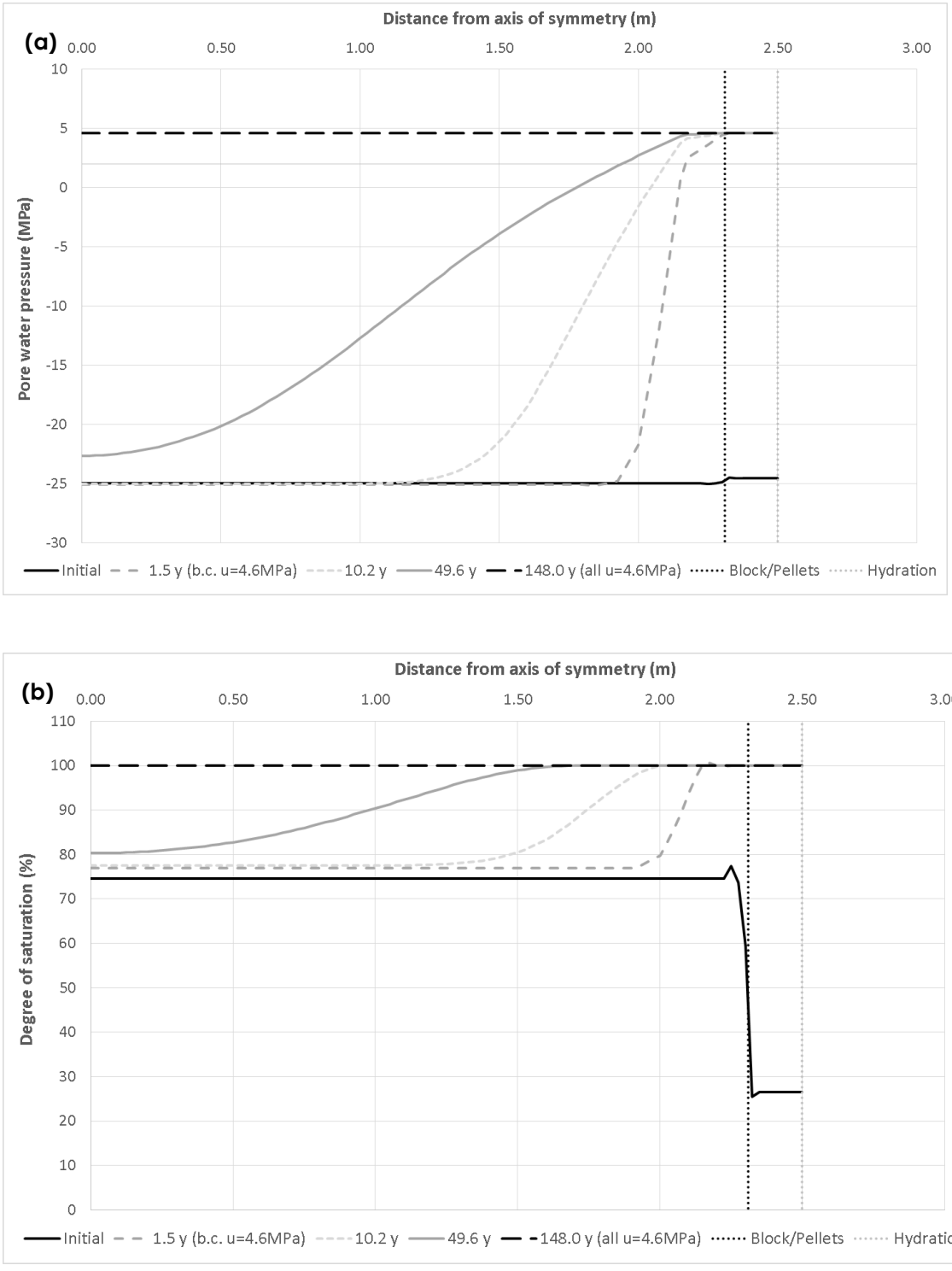

Figure 2.3-9 Pore water pressure (a) and degree of saturation (b) distributions, at key stages of the 'free access of water' analysis, along scan-line B (shown in Figure 2.3-6).

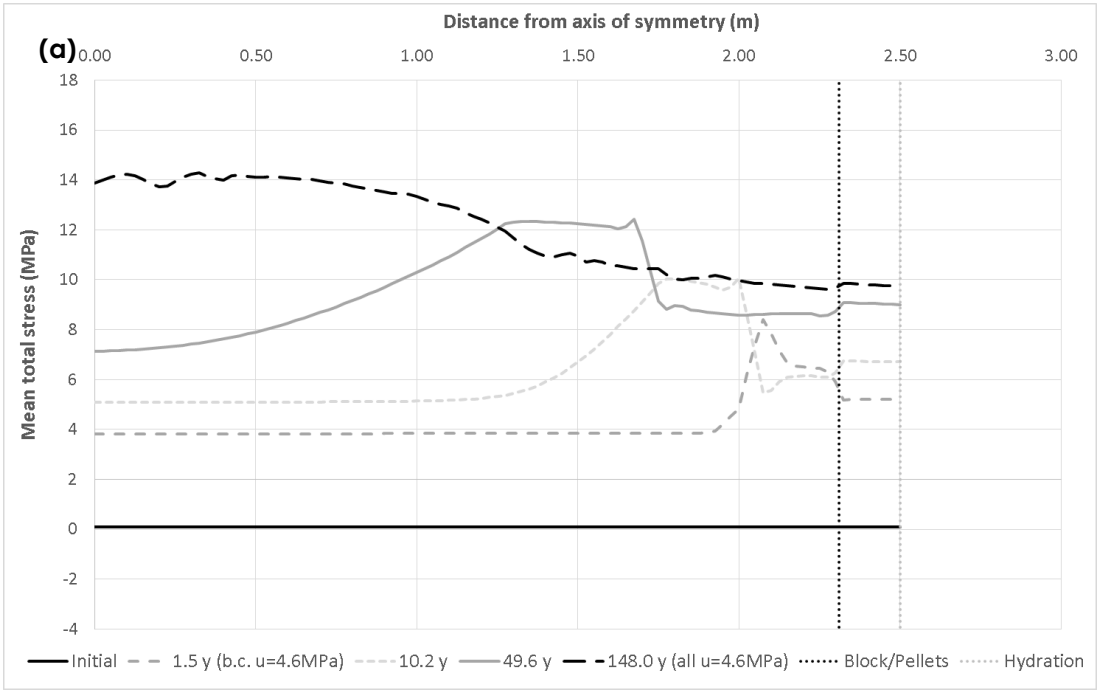

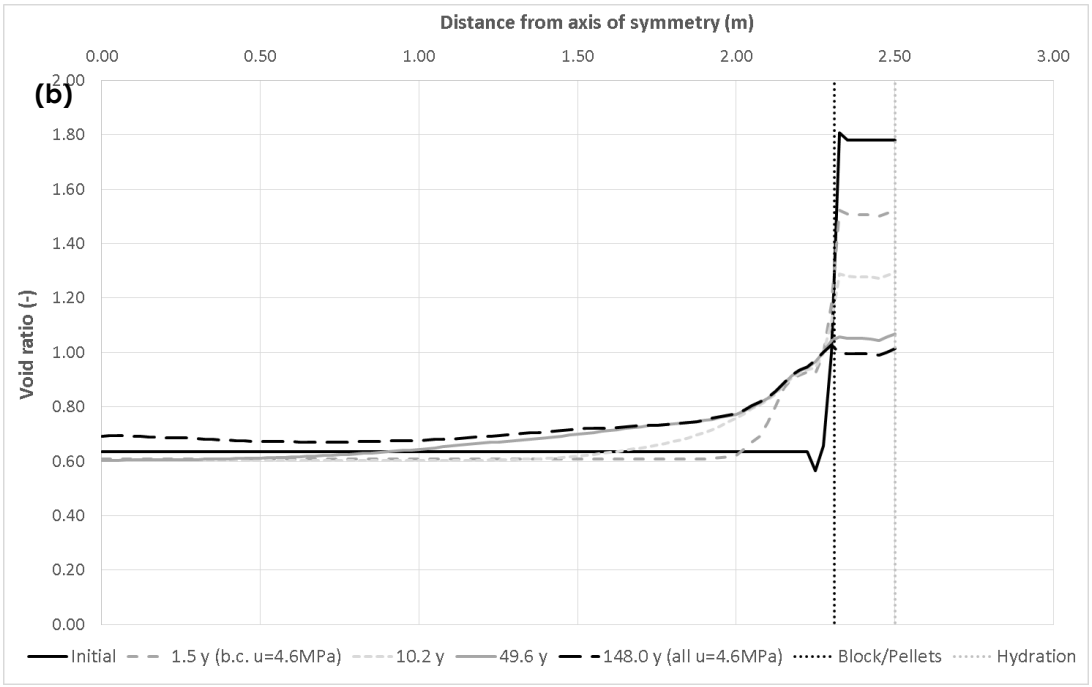

Figure 2.3-10 Mean total stress (a) and void ratio (b) distributions, at key stages of the 'free access of water' analysis, along scan-line B (shown in Figure 2.3-6).

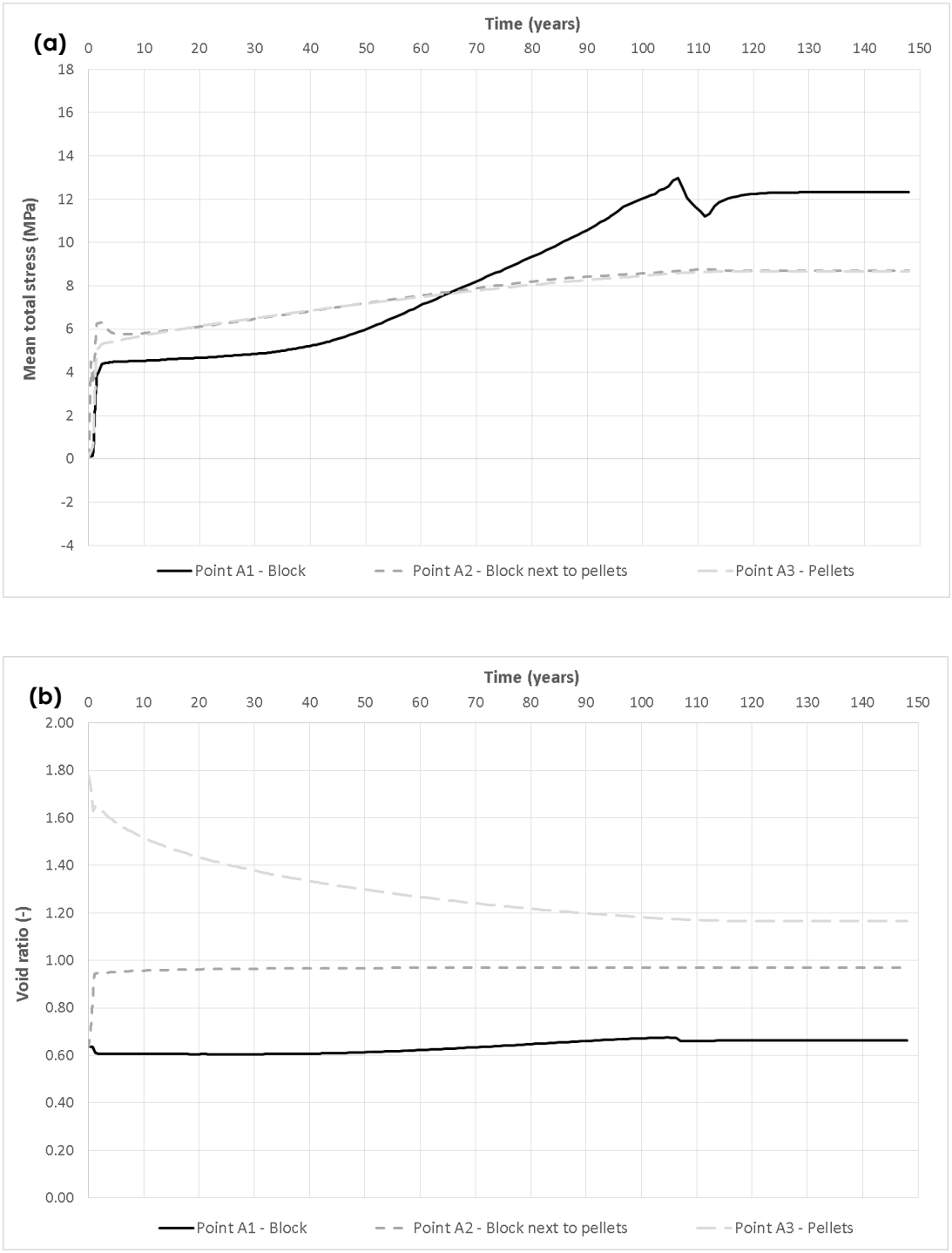

Figure 2.3-11 Free access of water' analysis: mean total stress (a) and void ratio (b) variations with time with reference to points A1, A2, A3 (indicated in Figure 2.3-6).

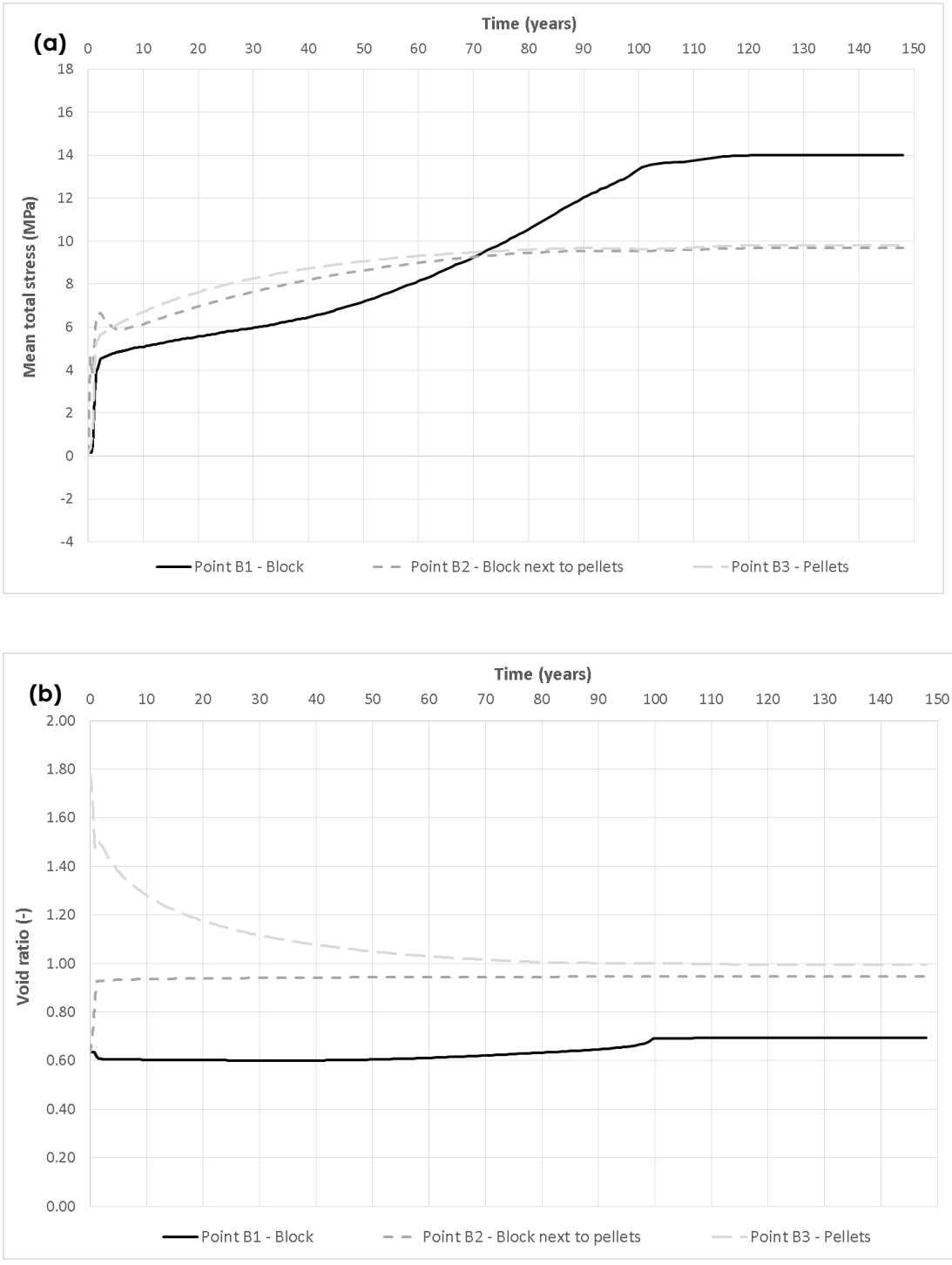

Figure 2.3-12 Free access of water' analysis: mean total stress (a) and void ratio (b) variations with time with reference to points B1, B2, B3 (indicated in Figure 2.3-6).

Figure 2.3-11 and Figure 2.3-12 show the mean net stress and the void ratio variations with time at the points A1, A2, A3 and B1, B2, B3 indicated in Figure 2.3-6.

As already noticed by looking at Figure 2.3-7 to Figure 2.3-10, a rapid increase in mean total stresses is predicted at the beginning of the analysis (while the pore water pressure is increased up to 4.6 MPa at the hydration boundary). Subsequently, a more gradual mean total stress increase is observed both in the pellets and the blocks, with maximum mean total stresses already approached after around 100 year, even though the pore pressure of 4.6 MPa is not reached yet everywhere in the mesh.

The void ratio variations with time (Figure 2.3-11b and Figure 2.3-12b) also reflect what has been already observed in relation to the results plotted in Figure 2.3-7 to Figure 2.3-10. Significant void ratio reductions can be observed for the pellets, while swelling is predicted within the blocks. In particular, the blocks that are closer to the hydration boundary experience more swelling compared to those located in the proximity of the axis of symmetry.

Restricted access of water scenario

Figure 2.3-13 shows the pore water pressure (a) and degree of saturation (b) distributions, at key stages of the *restricted access of water* analysis, along scan-line A (indicated in Figure 2.3-6). In this case, contrarily to what has been observed for the *free access of water* scenario, the pore water pressure increase is significantly slower, as well as more homogeneous throughout the domain (see Figure 2.3-13a). This is a consequence of the inflow rate applied as boundary condition (i.e. 2.1×10^{-12} m/s), which was selected in order to achieve full saturation roughly after 4000 years (see Figure 2.3-13b).

After reaching full saturation everywhere in the mesh, the hydraulic boundary condition was changed, and a positive pore pressure of 4.6 MPa was applied instead. Given that the backfill was already fully saturated when the hydraulic boundary condition was changed, the pore pressure quickly increased everywhere towards the value of 4.6 MPa. More specifically, S_r=1.0 was observed after around 4172 years, and u=4.6 MPa was attained everywhere in the mesh after around 4186 years.

Figure 2.3-14 shows the mean total stress (a) and void ratio (b) distributions, at key stages of the *restricted access of water* analysis, along scan-line A.

The mean total stress increase is very limited in the first 100 years, with the highest values achieved within the blocks located next to the pellets (i.e. closer to the hydration boundary). More significant swelling pressure variations were predicted after around 1000 years, when mean total stresses approach 1 MPa in the pellets and 4 MPa in the blocks. At the end of the saturation stage (i.e. after around 4172 years), the swelling pressure exceeds 11 MPa in the blocks and 9 MPa in the pellets. As expected, the highest mean total stress values are predicted at the end of the analysis (when u=4.6 MPa everywhere in the mesh), when mean total stresses exceeds 14 MPa in the blocks.

The increase in mean total stress with time is associated with a significant void ratio reduction in the pellets and a (more limited) void ratio increase in the blocks (see

Figure 2.3-14b). It is interesting to observe that a much more homogenous void ratio distribution is achieved at the end of the *restricted access of water* analysis compared to the *free access of water* analysis (see Figure 2.3-8b and Figure 2.3-14b). This seems to suggest that a slower hydration process leads to a more homogeneous void ratio distribution in the backfill.

Figure 2.3-15 shows the pore water pressure (a) and degree of saturation (b) distributions, at key stages of the *restricted access of water* analysis, along scan-line B (indicated in Figure 2.3-6). The pore water pressure and degree of saturation variations observed along scan-line B are very similar, in terms of timing and magnitude, to those observed along scan-line A.

As already observed for the *free access of water* analysis, more significant differences between scan-line A and scan-line B results are observed in terms of mean total stress and void ratio variations (shown in Figure 2.3-16a and b, respectively, for scan-line B). The maximum swelling pressure developed along scan-line B at the end of the analysis is close to 16 MPa (see Figure 2.3-16a), compared to the 14-15 MPa predicted, at the same stage, along scan-line A. The presence of higher swelling pressures is associated with more significant void ratio reductions in the pellets, where void ratios even lower than those characterising the blocks are predicted at the end of the analysis.

Figure 2.3-17 and Figure 2.3-18 show the mean net stress and the void ratio variations with time at the points A1, A2, A3 and B1, B2, B3 indicated in Figure 2.3-6.

A gradual increase in mean total stress with time is observed at all points until the slow inflow rate is applied as hydraulic boundary condition. When the hydraulic boundary condition is changed and the pore pressure is rapidly increased to u=4.6 MPa, an abrupt mean total stress increase is observed at all points, consistently with what was already observed with reference to Figure 2.3-14a and Figure 2.3-16a.

The results in Figure 2.3-17b and Figure 2.3-18b show how the void ratios tend to converge, with time, towards an almost unique value, giving an idea of how pronounced can be the homogenisation process when hydration takes place very slowly.

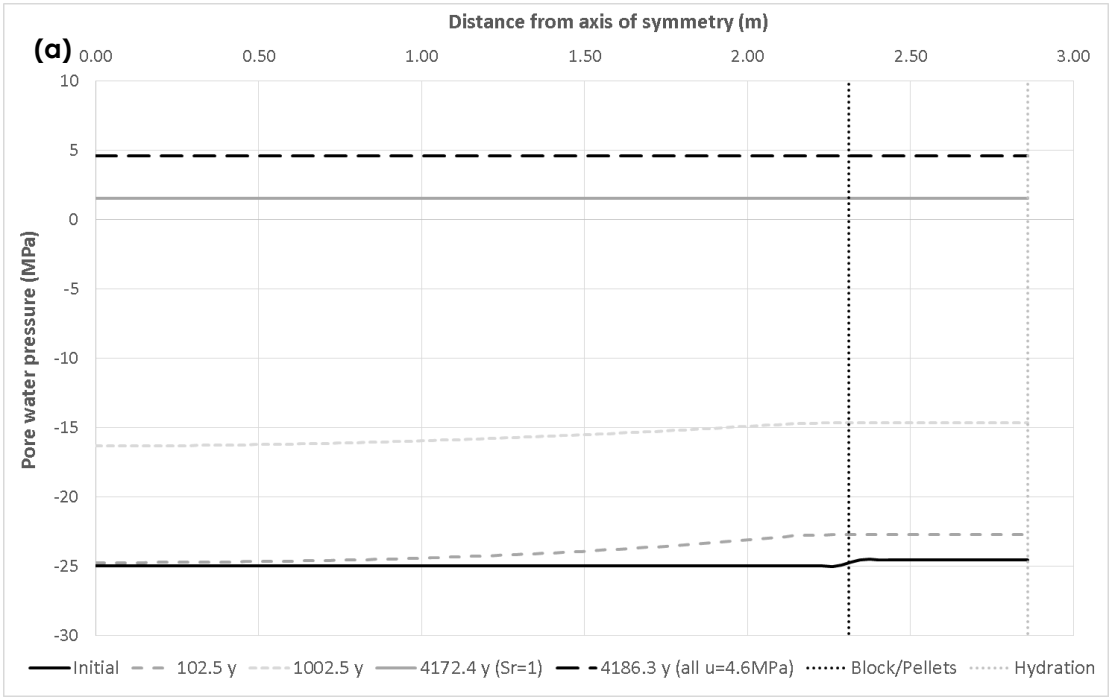

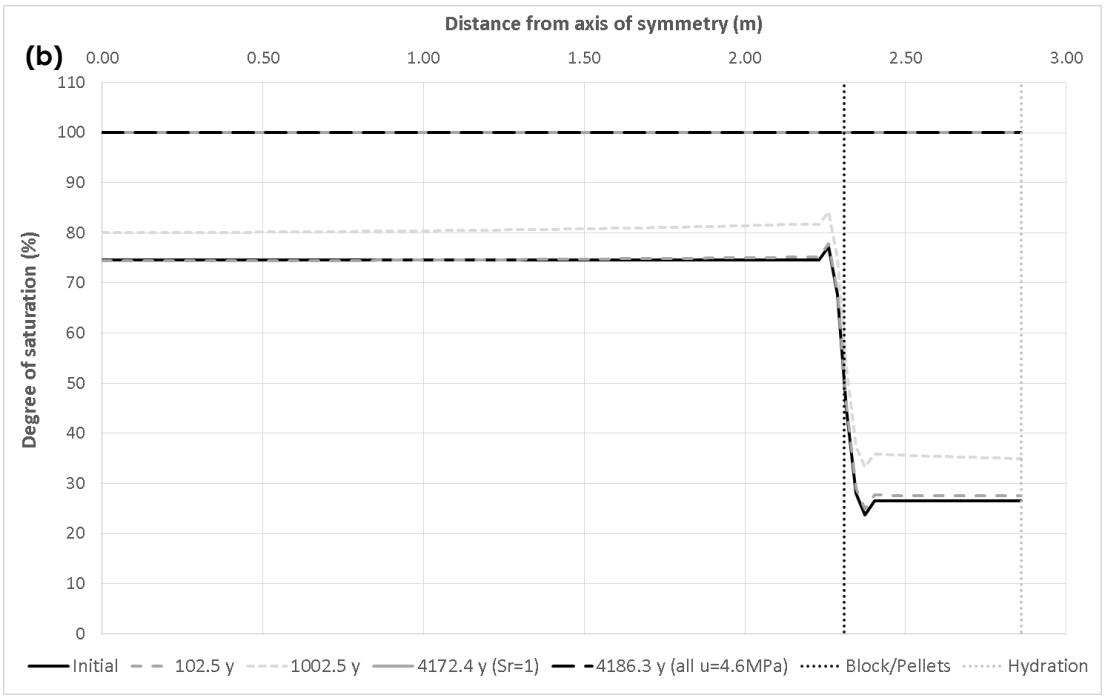

Figure 2.3-13 Pore water pressure (a) and degree of saturation (b) distributions, at key stages of the 'restricted access of water' analysis, along scan-line A (shown in Figure 2.3-6).

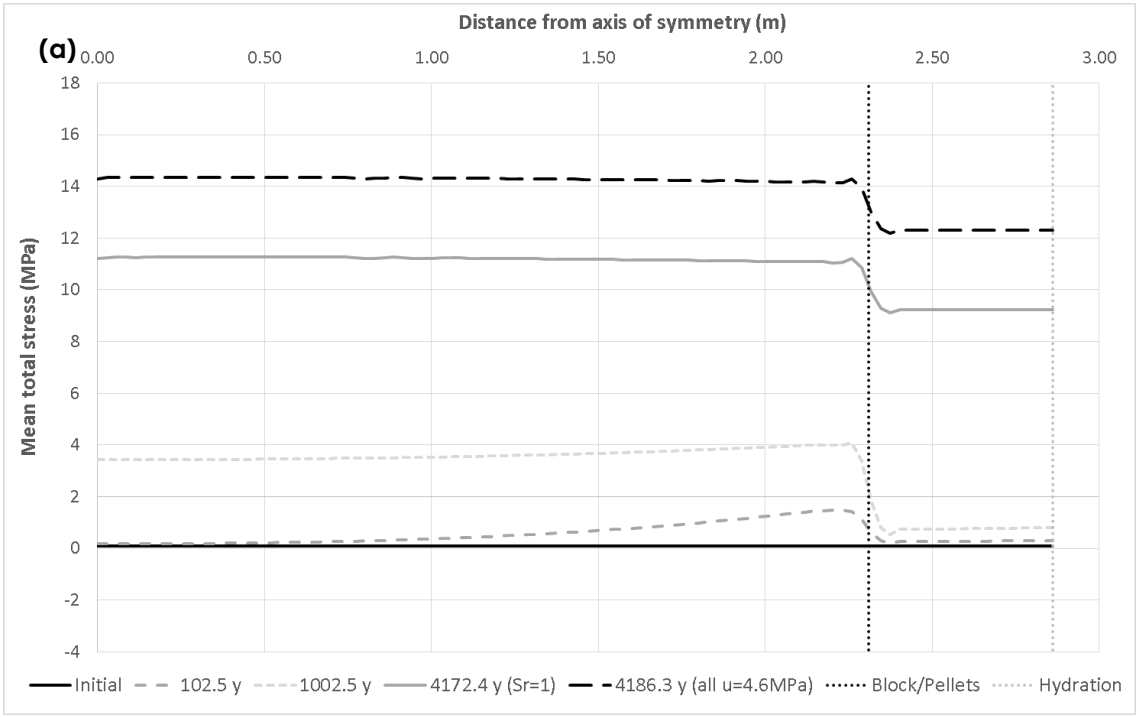

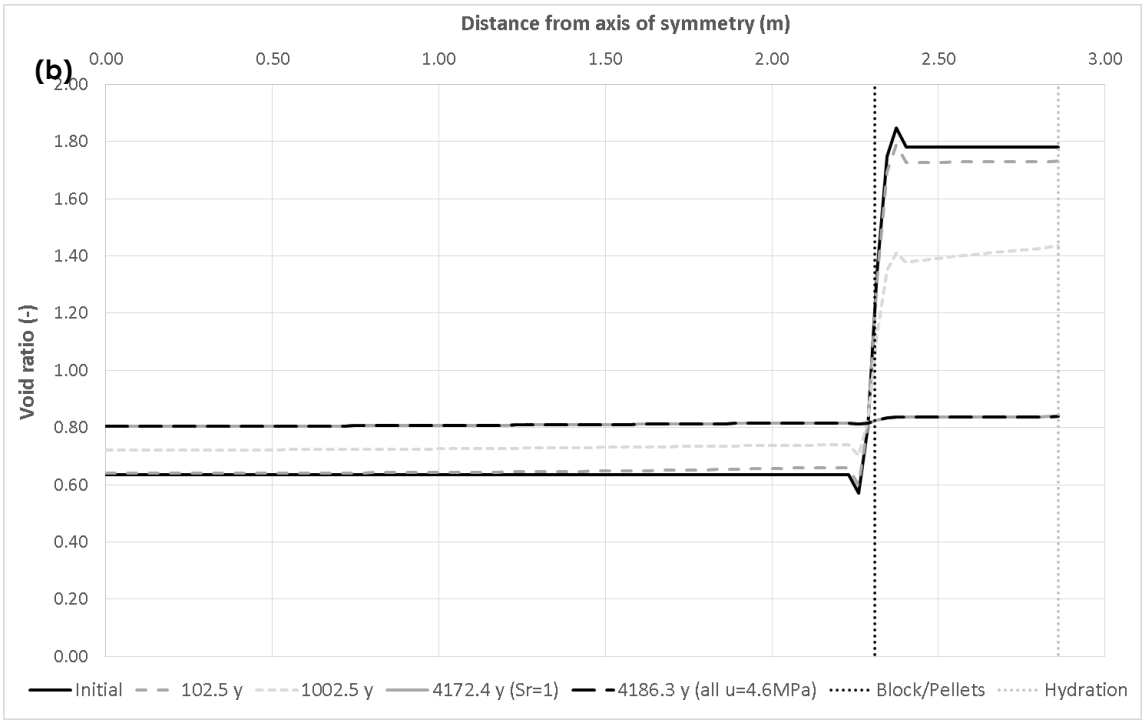

Figure 2.3-14 Mean total stress (a) and void ratio (b) distributions, at key stage of the 'restricted access of water' analysis, along scan-line A (shown in Figure 2.3-6).

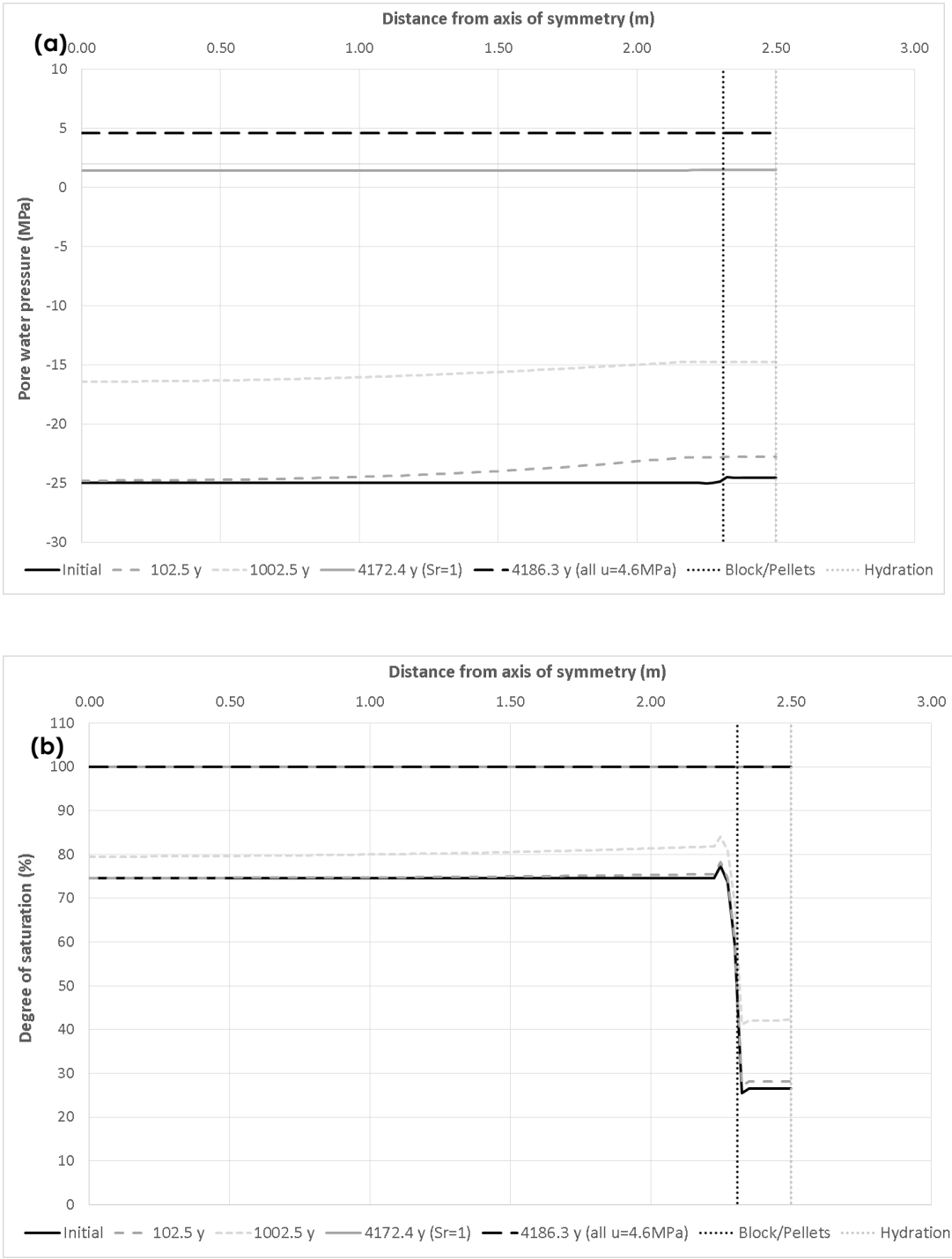

Figure 2.3-15 Pore water pressure (a) and degree of saturation (b) distributions, at key stages of the 'restricted access of water' analysis, along scan-line B (shown in Figure 2.3-6).

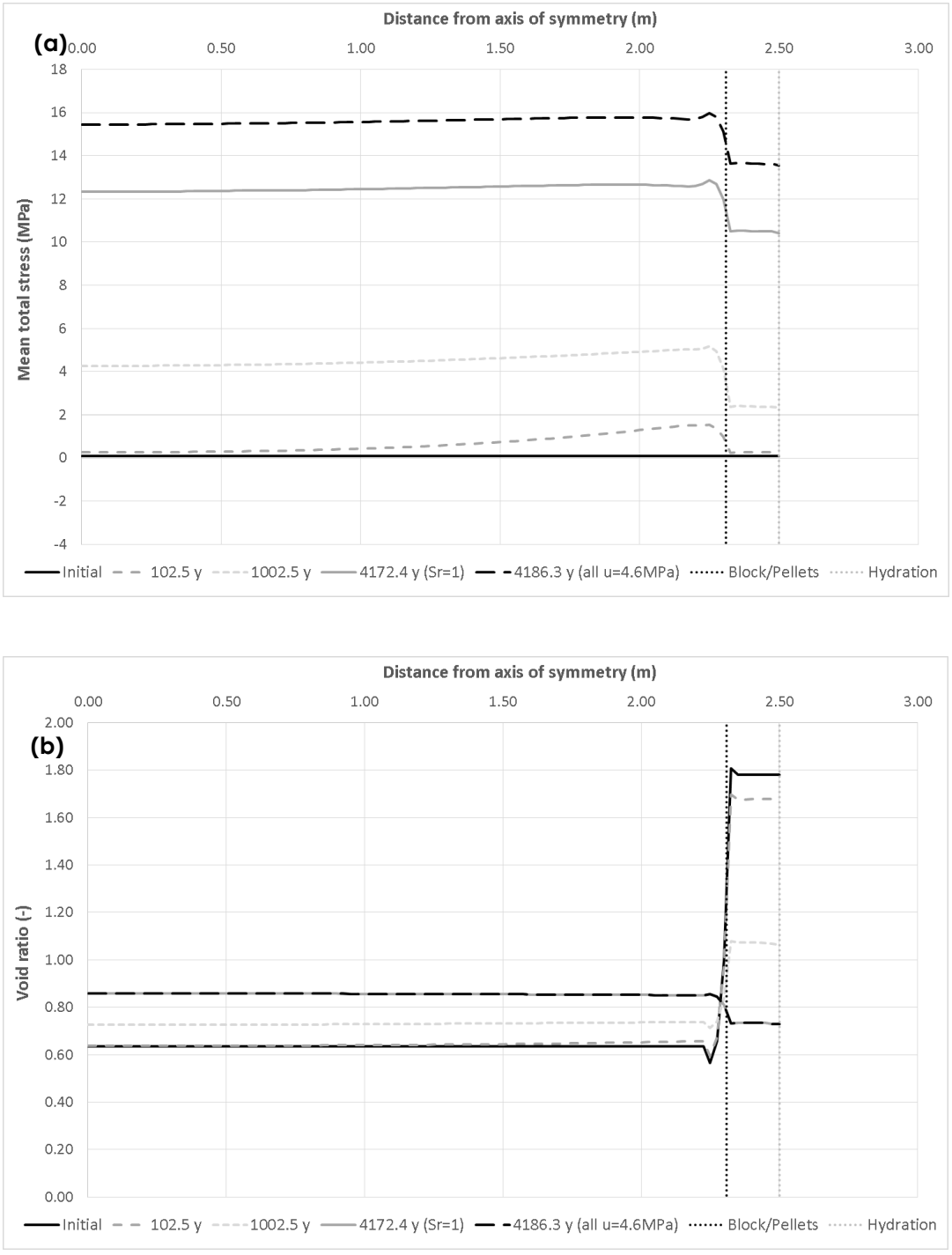

Figure 2.3-16 Mean total stress (a) and void ratio (b) distributions, at key stages of the 'restricted access of water' analysis, along scan-line B (shown inFigure 2.3-6).

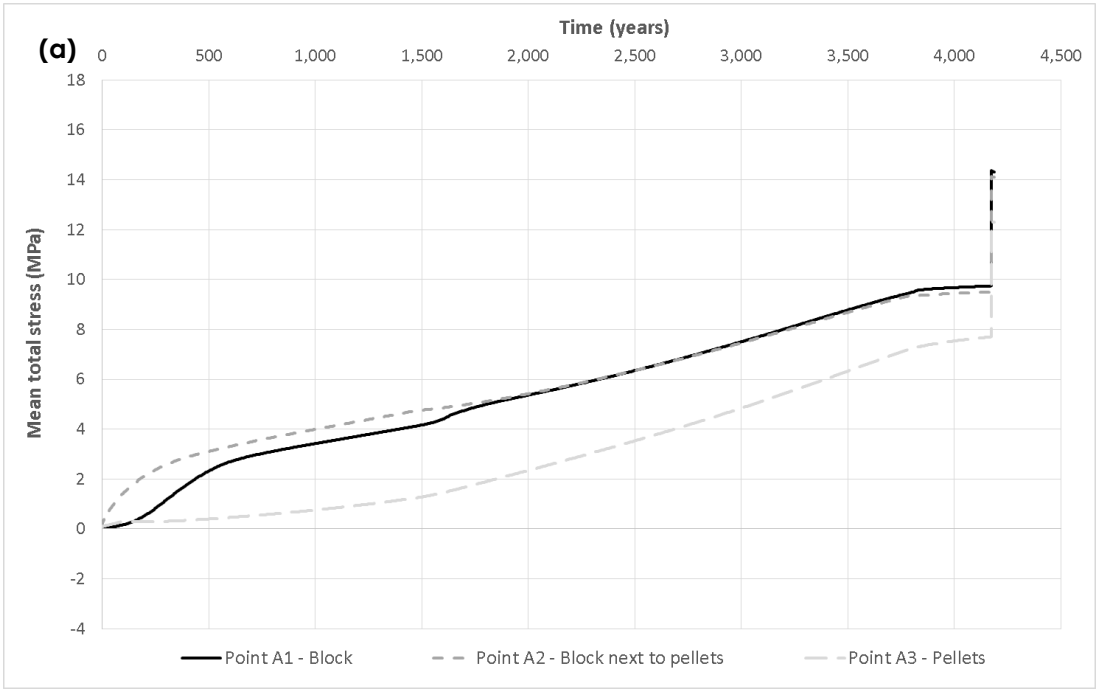

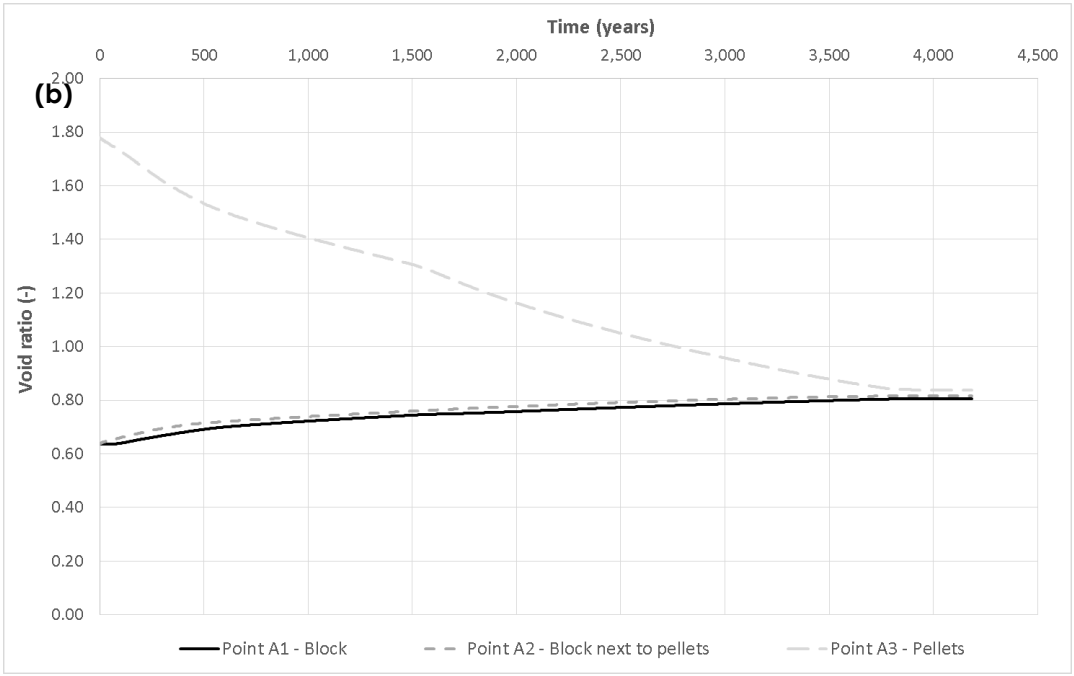

Figure 2.3-17 Restricted access of water' analysis: mean total stress (a) and void ratio (b) variations with time with reference to points A1, A2, A3 (indicated in Figure 2.3-6).

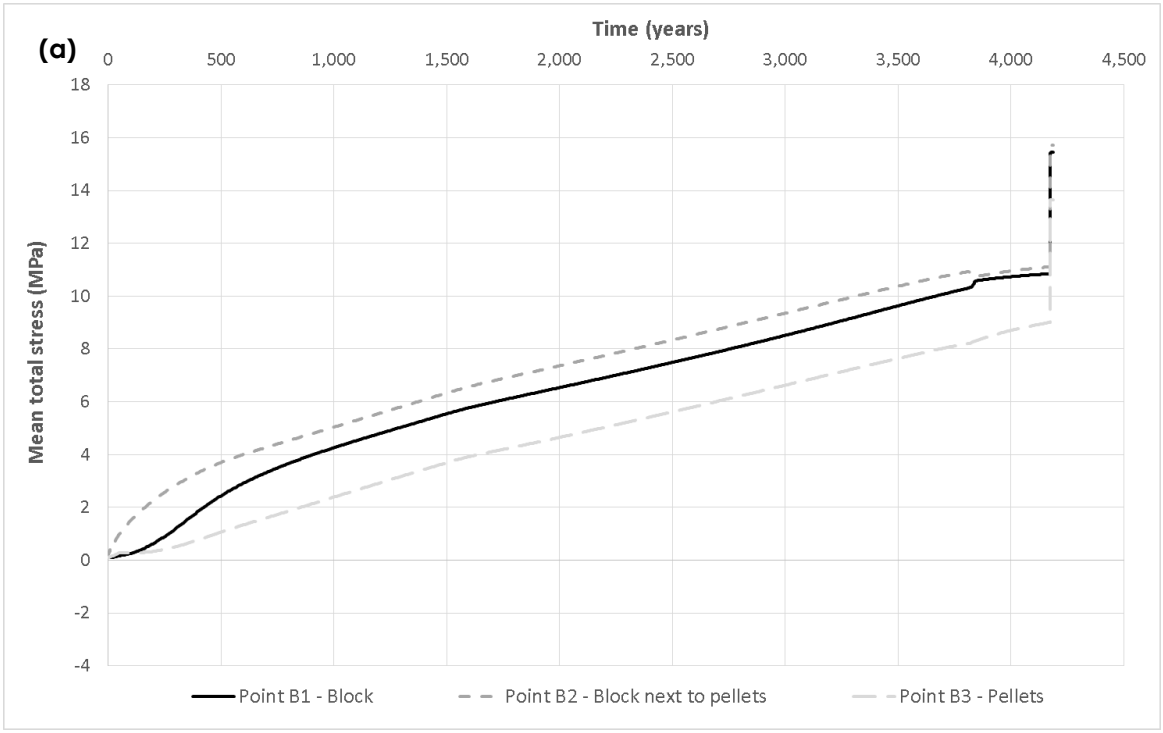

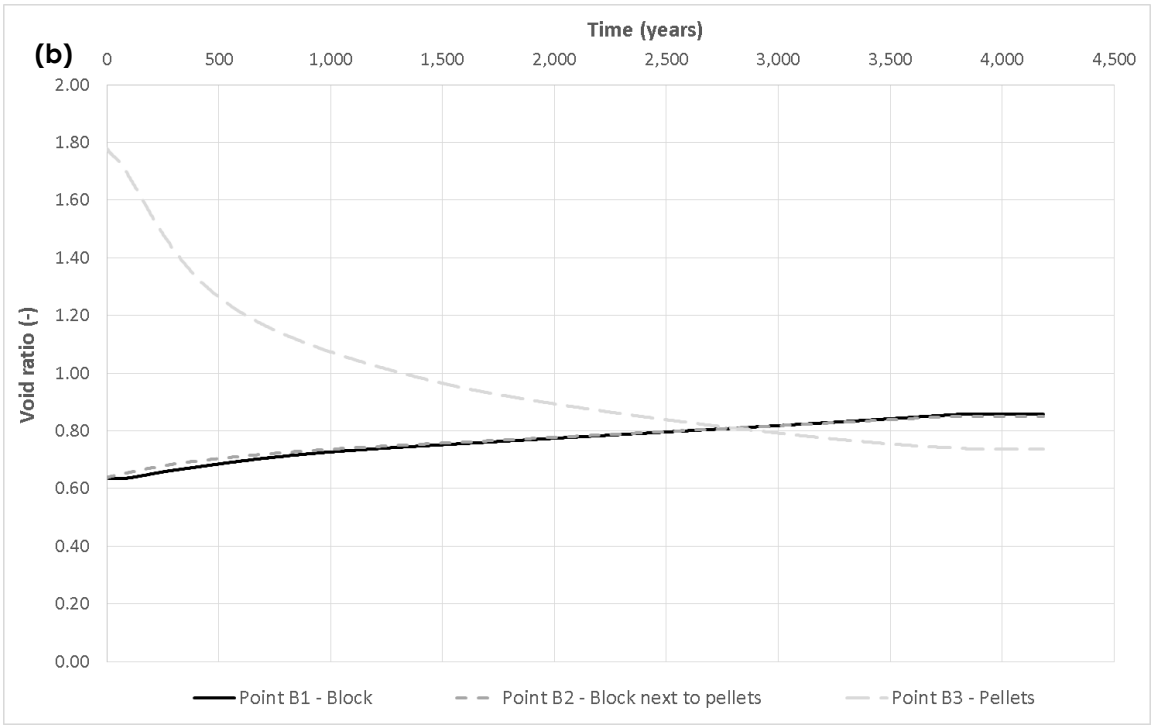

Figure 2.3-18 Restricted access of water' analysis: mean total stress (a) and void ratio (b) variations with time with reference to points B1, B2, B3 (indicated in Figure 2.3-6).

2.3.6 Discussion

As part of the activities conducted for Task 5.4, the SKB assessment case was analysed by the ICL team. Following Leupin et al. (2020), 2 different scenarios were investigated, namely *free access of water* and *restricted access of water*. In the first scenario, hydration was simulated by applying a constant pore water pressure of 4.6 MPa at the boundary representing the contact area between the host rock and the backfill. In the second scenario, hydration took place by applying a very small water inflow rate (i.e. 2.1×10^{-12} m/s) at the hydration boundary (with the boundary condition changed to u=4.6 MPa after reaching S_r=1.0 everywhere in the mesh).

The results of the 2 FE analyses have been presented and extensively discussed in Section 2.3.5. The following key conclusions can be drawn:

- When access to water is not restricted and the pore water pressure acting on the outer surface of the backfill corresponds to values representative of repository depths (i.e. u=4.6 MPa), the full pore pressure equalisation is achieved after around 150 years.
- The maximum mean total stress predicted in the *free access of water* scenario (representative of the swelling pressures developing within the backfill) is around 14 MPa. In the *restricted access of water* scenario, instead, the maximum mean total stress predicted is around 16 MPa. It is worth highlighting that, in both cases, the mean total stresses are exceeding the limit pressure of 10 MPa suggested in Appendix A2 of the modelling specifications (Leupin et al., 2020).
- During the hydration process, the pellets tend to compress and the blocks tend to swell. This results, in both cases, in a more homogeneous void ratio distribution after hydration. However, the results suggest that a more pronounced homogenisation is likely to be achieved when slower hydration takes place (e.g. *restricted access of water* analysis).

2.4 VTT

The objective is to conduct a sensitivity analysis of SKB assessment case to study the effect of design and model parameters as well as hydraulic boundary conditions on the bentonite mechanical evolution during the wetting phase.

2.4.1 Description of the models

The model described in the journal articles (Navarro et. al 2019, 2020a,b, 2021), in PhD Thesis by Gharbieh (2021) and also in Beacon deliverables D3.1 and D5.1.2 is utilized in the SKB assessment case simulations. In brief, the model consists of a coupled THcM double porosity model for the bentonite blocks and of a triple porosity model for the pellet fill (Navarro et al. 2020a,b). In the assessment case, isothermal and isochemical conditions are assumed.

2.4.2 Geometry and discretization

The model geometry follows SKB assessment case description. The spatial model is 2D axisymmetric and the finite element method is used for the discretization. The element types vary by the phenomena (cf. Gharbieh 2021). Two triangular meshes are used: one for the simulation cases with a constant pressure boundary condition on the bentonite-rock boundary (Figure 2.4-1) and another one for a local fracture inflow boundary condition (Figure 2.4-2). In the latter case, the mesh density close the water inlet at the tunnel section mid-height has been increased.

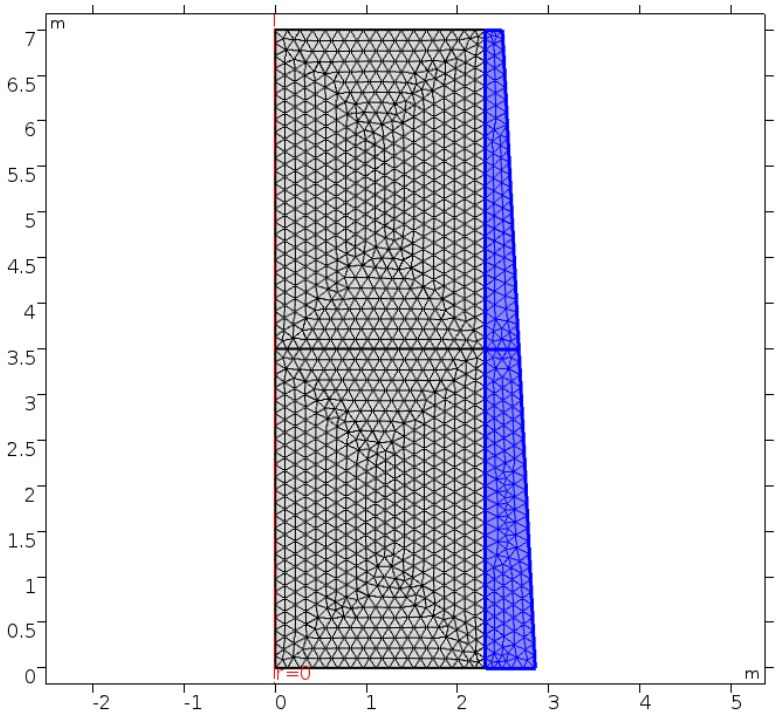

Figure 2.4-1. Meshed geometry of the modelled backfill domain for simulating uniform water inflow. The pellet fill is highlighted in blue.

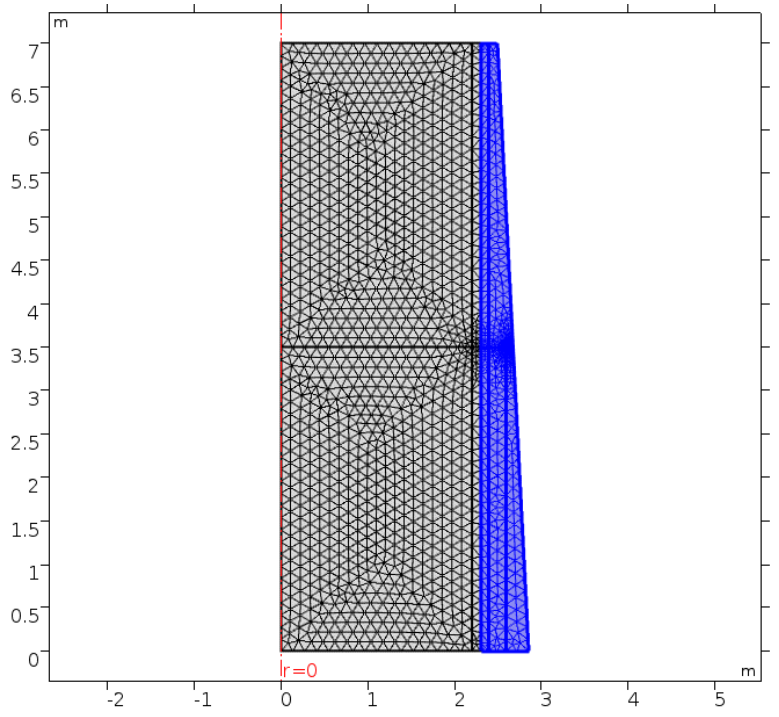

Figure 2.4-2. Meshed geometry of the modelled backfill domain for simulating localised fracture inflow. The pellet fill is highlighted in blue.

Processes	Hydraulic (H) Mechanical (M)
Physics	Macro water mass balance Water mass exchange between macro and micro: kinetic approach Water vapour Mechanical equilibrium
State variables	Liquid pressure P_{L} Displacement field $\boldsymbol{u}$ Net/effective stress $\boldsymbol{\sigma}$ Preconsolidation pressure for saturated condition p_0^* Micro void ratio e_{m} Inter-pellet void ratio e_{M2}
Initial conditions blocks	Hydraulic: $P_{\mathrm{L,init}}$ depends on P1 and P3 (Table 2.4-1). Calculated from the initial water content. Microstructural: $e_{\mathrm{m,init}}$ depends on P1 and P3 (Table 2.4-1). Calculated from the initial water content. Mechanical: $\sigma_{\mathrm{r,init}} = \sigma_{\varphi,\mathrm{init}} = \sigma_{\mathrm{z,init}} = 5 \cdot 10^4$ Pa$\tau_{\mathrm{rz,init}} = 0$ Pa $p_{0,\mathrm{init}}^* = 8 \cdot 10^6$ Pa
Initial conditions pellet fill	Hydraulic: $P_{\mathrm{L,init}}$ depends on depends on P2 and P3 (Table 2.4-1). Calculated from the initial water content. Microstructural: $e_{\mathrm{m,init}}$ depends on P2 and P3 (Table 2.4-1). Calculated from the initial water content. Mechanical: $\sigma_{\mathrm{r,init}} = \sigma_{\varphi,\mathrm{init}} = \sigma_{\mathrm{z,init}} = 5 \cdot 10^4$ Pa$\tau_{\mathrm{rz,init}} = 0$ Pa $p_{0,\mathrm{init}}^* = 8 \cdot 10^6$ Pa

Boundary conditions	Hydraulic: $P_{\mathrm{L,Rock}} = 0$ Pa applied either at the lateral rock-backfill boundary representing high water availability or locally at the center of the modelled tunnel section simulating fracture inflow (P7 in Table xyz). No flow on top and bottom boundary: $-\hat{\boldsymbol{l}}_{\mathrm{MW}} \cdot \boldsymbol{n} = 0$ $\frac{\mathrm{kg}}{\mathrm{m^2 s}}$ Mechanical: Roller on top, bottom and rock boundary: $\boldsymbol{u} \cdot \boldsymbol{n} = 0$ m
Geometry	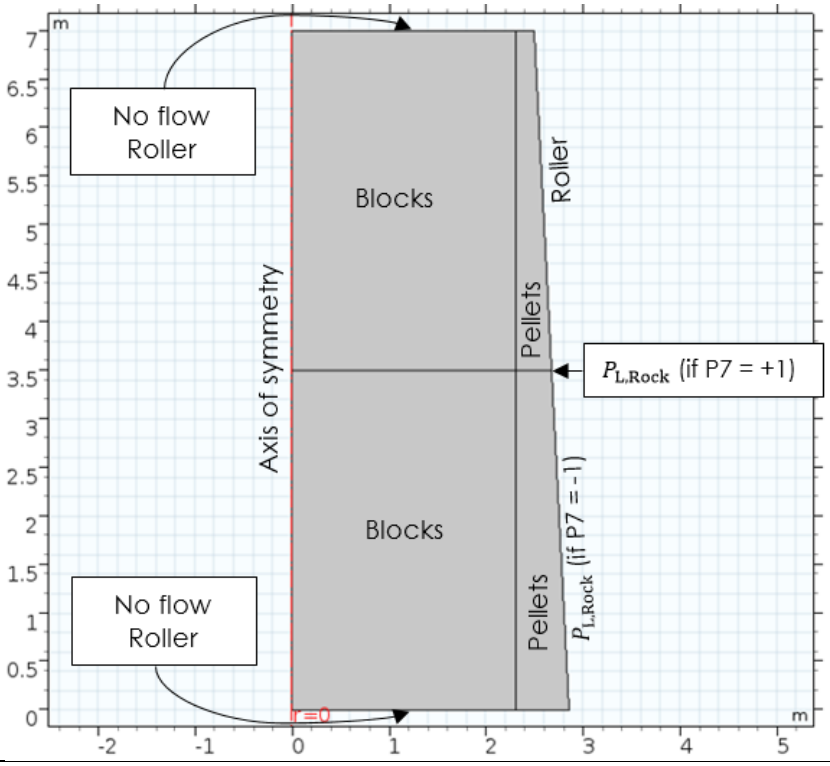
Parameters	Remaining microstructural void ratio under dry conditions: $e_{\mathrm{m,R}} = 0$ See Table 2.4-1 for the parameters included in the sensitivity analysis

2.4.3 Sensitivity analysis - General idea and objectives

The idea of sensitivity analysis is to estimate how variations in the input parameters change the output variables. In the performed analysis, the varied input parameters are the design and model parameters as well as boundary conditions and the output variables are the density heterogeneity and swelling pressure of the bentonite. In practise, a number of simulations are run such that the chosen input parameters are

varied simultaneously and the change in the output variable is measured. To estimate the individual effect of each input parameter and the combined effects, a multidimensional polynomial regression model is fitted to the obtained data set (the variations in the input parameters vs the change in output variables) with Ordinary Least Squares (OLS). The wellness of the fit is estimated with various statistical measures.

The main objective of the performed sensitivity analysis is to screen the parameters that affect the bentonite density homogeneity, that is, the objective is not to give precise quantitative information on the sensitivities. Consequently, the particular interest on the regression model is on the linear main effects, which means that the second order effects (the two-factor interaction terms and the quadratic terms) and the higher order effects are considered less important. In line with this, it is assumed that third- and higher-order effects are negligible.

In sensitivity analysis, it is generally accepted that

1. only a small number of the candidate effects are important (effect heredity),
2. linear main effects are more important than second-order effects and so forth for high-order effects (effect hierarchy), and that
3. higher-order effects are only relevant when the corresponding lower-order effects are identified as important (effect heredity).

These principles held when analysing the results. The methodology is presented in detail in Appendix 1.

2.4.4 Output variables and input parameters

Output variables

For the evaluation of the mechanical evolution process of the SKB assessment case, three output variable have been defined

- the heterogeneity degree of the whole tunnel section δ_{vol};
- the heterogeneity degree of the tunnel cross section at half-a-way in the tunnel section (mid-plane) which is also the fracture locationδ_{mid};
- the mean stress averaged over the tunnel section volume $\bar{p}_{\mathrm{mean}}$.

Using the results from the model runs described in

Table 6.10-1, a regression model is fitted for each output variable. The coefficients of each regression model indicate the effect of variation in the input parameters on the particular output variable.

The heterogeneity degree is a measure for the deviation from the theoretical fully homogenised state. The heterogeneity degree is calculated by integrating the absolute value of the difference between the simulated dry density ρ_{dry} and the average dry density $\rho_{\mathrm{dry,avg}}$ (i.e., the volume-weighted initial dry density) and normalising it by division by the integral of the average dry density. Mathematically expressed, the whole tunnel section and the mid-plane heterogeneity degrees are:

$$\delta_{\mathrm{vol}} = \frac{\int \mathrm{abs}\left(\rho_{\mathrm{dry}} - \rho_{\mathrm{dry,avg}}\right)\mathrm{d}V}{\int \rho_{\mathrm{dry,avg}}\,\mathrm{d}V}$$

$$\delta_{\mathrm{mid}} = \frac{\int \mathrm{abs}\left(\rho_{\mathrm{dry}} - \rho_{\mathrm{dry,avg}}\right)\mathrm{d}A}{\int \rho_{\mathrm{dry,avg}}\,\mathrm{d}A}$$

The heterogeneity degree may be low indicating low level of remaining density differences, but simultaneously the average dry density may be insufficiently low. Therefore, the analysis of remaining density differences using the heterogeneity degrees defined above is complemented by the average mean stress over the tunnel section, $\bar{p}_{\mathrm{mean}}$. The average mean stress provides a measure for the confinement of the system and is relevant for the assessment of the buffer performance in terms of swelling pressure and related safety functions.

For each simulation, the temporal evolution of the output variables is evaluated. However, only the final values at the end of the simulations are used for calculating the effects of the different parameters and for evaluating the homogenisation process. The simulation times are chosen to ensure a fully saturated tunnel section.

Input parameters

The varied input parameters are listed in Table 2.4-1. The first two, block and pellet dry densities, are related to the tunnel backfill design. The value range is twice the design tolerance. The state function (P3) indicates how much the structure of the bentonite swells during saturation (Figure 2.4-3). Parameters P4 and P5 specify the mechanical (elastic) stiffness of the blocks and the pellets, respectively. Parameter P6 is related to the water permeability of the bentonite. The value ranges for P3-P6 is ±20% of the centre value. P7 is a categorical parameter that defines whether the water saturates the bentonite uniformly from the rock or through a single fracture at the mid-plane of the tunnel section.

The rest of the model parameters follow the values used in previous Beacon simulations described in Deliverable D5.1.2 (see also Gharbieh 2021).

Table 2.4-1. Sensitivity analysis input parameters and value ranges considered in the sensitivity analysis.

	Parameter	Symbol	Units	Low (-1)	Center (0)	High (+1)	Comment
P1	Block dry density	$\rho_{\mathrm{dry,B}}$	$\frac{\mathrm{kg}}{\mathrm{m}^3}$	1600	1700	1800	Twice the design tolerance (SKB TR-10-16)
P2	Pellet fill dry density	$\rho_{\mathrm{dry,PF}}$	$\frac{\mathrm{kg}}{\mathrm{m}^3}$	900	1000	1100	Design tolerance (SKB TR-10-16)
P3	State surface defining the micro-structural volumetric constitutive model	$e_{\mathrm{m}}(\pi_{\mathrm{m}})$	–	see Figure 2.4-3			±20%
P4	Elastic stiffness for changes in net mean stress for saturated conditions	κ_0	–	0.08	0.10	0.12	±20%
P5	M2 elastic stiffness for changes in net mean stress	κ_{M2}	–	0.46	0.6	0.2	±20%
P6	Reference intrinsic permeability	$K_{\mathrm{int,L,ref}}$	m^2	$9.36 \cdot 10^{-21}$	$1.17 \cdot 10^{-20}$	$1.40 \cdot 10^{-20}$	±20%
P7	Hydraulic boundary condition	BC_{hyd}	–	Uniform inflow	–	Localised fracture inflow	Binary categorical variable

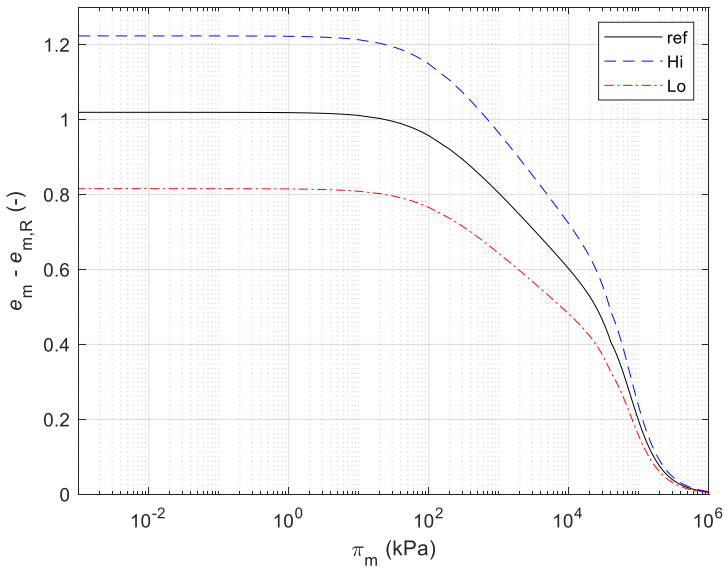

Figure 2.4-3. Considered variability of the state surface defining the microstructural volumetric constitutive model. The parameter $e_{m,R}$ defines the remaining microstructural void ratio under dry conditions.

2.4.5 Results and discussion

The output variables from the sensitivity analysis simulations runs (in Table 2 1) have been collected to Table 2.4-2.

Table 2.4-2. Data of the output variables collected for the sensitivity analysis.

Run	δ_{vol} [1]	δ_{mid} [1]	$\bar{p}_{mean}$ [kPa]
1	0.0266	0.0358	5885
2	0.0426	0.0410	1335
3	0.0173	0.0105	681
4	0.0718	0.0644	6124
5	0.0742	0.0703	5420
6	0.0211	0.0205	1581
7	0.0217	0.0122	8897
8	0.0234	0.0233	775
9	0.0575	0.0537	7113
10	0.0265	0.0200	1850
11	0.0446	0.0442	1099
12	0.0376	0.0406	8614
13	0.0345	0.0458	7725
14	0.0258	0.0246	1044
15	0.0903	0.0502	882
16	0.0781	0.0750	10379
17	0.0152	0.0167	2794
18	0.0393	0.0378	3650

For each output variable, the results of the regression model fitting and the statistical analysis are presented in the following sections.

Heterogeneity degree of the whole tunnel section

The basic statistics of the whole tunnel section heterogeneity data obtained from the sensitivity analysis simulation runs is presented in Table 2.4-3. The AD test p-value is

above the significance level (0.05), which means that normal distribution can be used to approximate the heterogeneity degree data. Normal probability plot of the Box-Cox transformed data is also illustrated in Figure 2.4-4.

Table 2.4-3. Basic statistics of the data of the final heterogeneity degree of the modelled backfill domain. AD indicates the p-value of Anderson-Darling test to check the normality of the Box-Cox transformed data.

Mean (%)	std. dev (%)	min (%)	max (%)	AD (-)
4.1	2.3	1.5	9.0	0.61

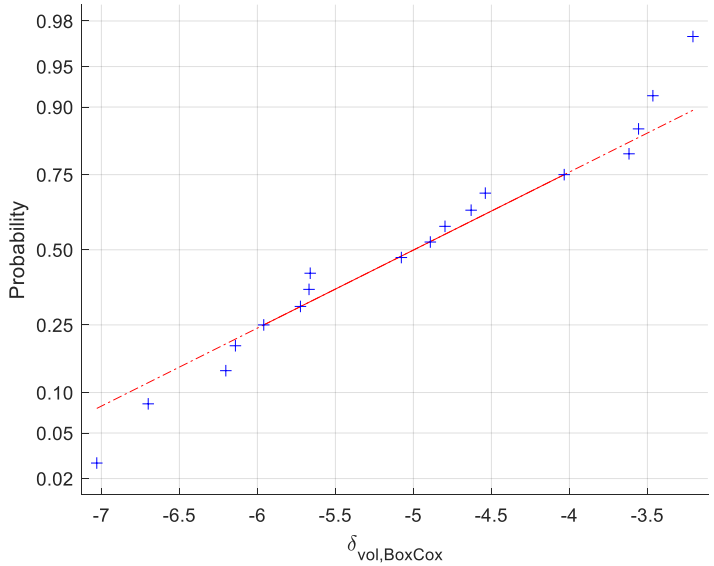

Figure 2.4-4. Normal probability plot of the final heterogeneity degree of the modelled backfill domain after Box-Cox transformation with $\lambda = -0.229$.

Linear regression model

A first-order main effect model is fitted to the whole tunnel section heterogeneity degree data. The analysis of variance (ANOVA) numbers of the fit is presented in Table 2.4-4 and the standardized effects are illustrated in Figure 2.4-5. The effects state the significance and the relative importance of the input parameters for the tunnel section dry density homogeneity. The hydraulic boundary condition (BC_hydr) seems to be the most important and the only statistically significant input parameter (the standardized effect is above the critical t-value). The second most important parameters is the water intrinsic permeability (which represents the hydraulic properties of the material) and the third most important parameter is the swelling function, which are, however, statistically not significant based on the analysis.

The F-test p-value in Table 2.4-4 (0.2 > 0.05 which is the used significance level) suggests that the regression model is not statistically significant as whole, which further suggests that interpretation of the individual effects is also questionable. However, the p-value depends on the used regression model and could be made smaller by revising the regression model. If the model was changed, the individual effect values could change, but the orthogonality of the DSD would make the relative importance of the main effects unchanged. Consequently, the first-order main effect model is valid for the screening purpose of this sensitivity analysis, that is, figuring out which input parameters are the most important.

Table 2.4-4. ANOVA of the first-order main effect model of the final heterogeneity degree of the modelled backfill domain.

ANOVA	SS	df	MS	Num. obs.	18
Total	23	17	1.4	F(7, 10)	1.6
Model	12	7	1.7	p-value	0.23
Residual	11	10	1.1	R^2	0.53

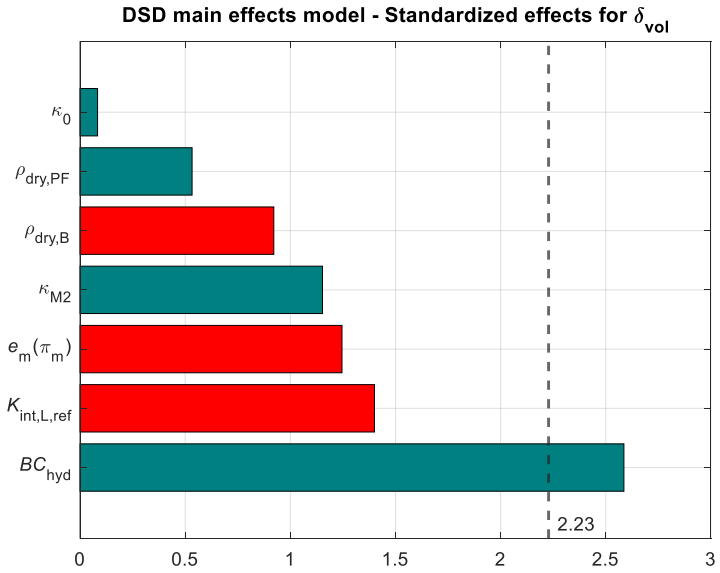

Figure 2.4-5. Pareto chart of standardized effects for the final heterogeneity degree of the modelled backfill domain. The dashed vertical line represents the critical t-value which corresponds to 0.05 significance level.

The residual analysis (Figure 2.4-6 and Table 2.4-5) shows that the residuals (difference between the fit and the actual values) can be considered normally distributed (see normality plot in Figure 2.4-6 and AD test p-value in Table 2.4-5 is above the 0.05 significance level) and there is no obvious symmetry pattern in the residual-vs-fitted value plot. Consequently, the residual analysis suggests that the OLS assumptions of

zero conditional mean (the regression model fit does not correlate with the errors) and homoscedasticity (the residuals have constant variance, which means that OLS is efficient fitting method) are met and the OLS can be said to be adequate regression model fitting method.

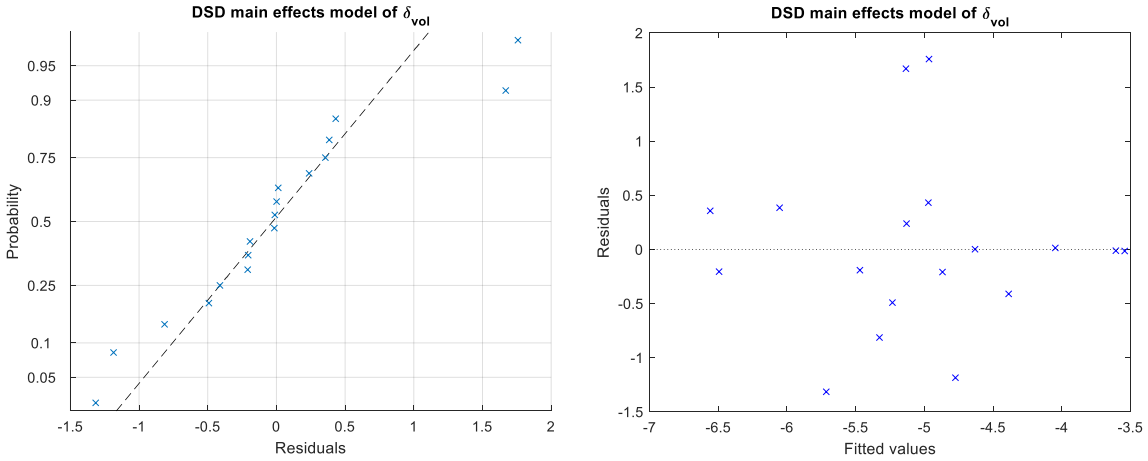

Figure 2.4-6. Normal probability plot of the residuals (left) and residuals-vs-fitted values plot (right) of the first-order main effect model of the final heterogeneity degree of the modelled backfill domain.

Table 2.4-5. Residual AD test of the linear regression model for the whole tunnel homogeneity degree.

AD residuals (-)
0.07

Stepwise regression model

In order to improve the first-order main effect regression model, stepwise regression is used starting from the linear main effects only model and using p-enter = p-remove = 0.25 for inclusion and exclusion of model terms (considering linear, 2fi and quadratic terms), respectively. The F-test p-value in the ANOVA data of the regression model (Table 2.4-6) is below the used significance level (0.05) and the regression model can be said to be significant as whole, which was not the case with the first-order main effect model. The Pareto chart of the standardized effects (Figure 2.4-7) shows that, again, the hydraulic boundary condition is the only statistically meaningful parameter for the whole tunnel section heterogeneity degree. The combined effects $K_{int,L,ref}$:BC_{hyd} and κ_{M2}: $K_{int,L,ref}$ improve the regression fit, but the main effects are of the main interest in the performed sensitivity analysis.

Table 2.4-6. ANOVA of the model of the final heterogeneity degree of the modelled backfill domain obtained by stepwise regression considering first-order main effects and second-order 2fi and quadratic effects.

ANOVA	SS	df	MS	Num. obs.	18
Total	23	17	1.4	F(9, 8)	5.1
Model	20	9	2.2	p-value	0.015
Residual	3.4	8	0.42	R^2	0.85

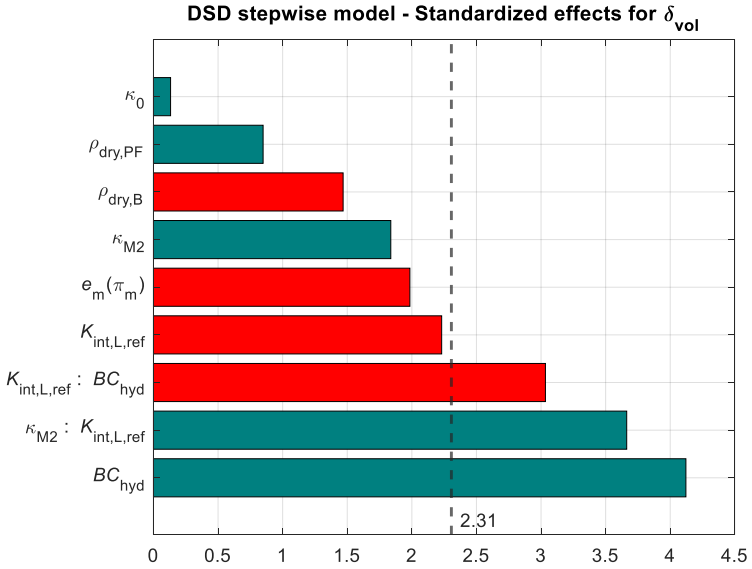

Figure 2.4-7. Pareto chart of standardized effects for the final heterogeneity degree of the modelled backfill domain obtained from stepwise regression considering first-order main effects and second-order 2fi and quadratic effects. The colon represents combined effects of two parameters. The dashed vertical line represents the critical t-value, above which the effects are statistically significant.

The residual analysis (Figure 2.4-8 and Table 2.4-7) shows that the residuals can be considered normally distributed (Figure 2.4-8 normality plot and AD test p-value in Table 2.4-7 is above the 0.05 significance level) and there is no obvious pattern in the residual-vs-fitted value plot. Consequently, the residual analysis suggest that the OLS assumptions of zero conditional mean (the regression model fit does not correlate with the errors) and homoscedasticity (the residuals have constant variance, which means that OLS is efficient fitting method) are met. Therefore, OLS can be considered as an adequate regression model fitting method.

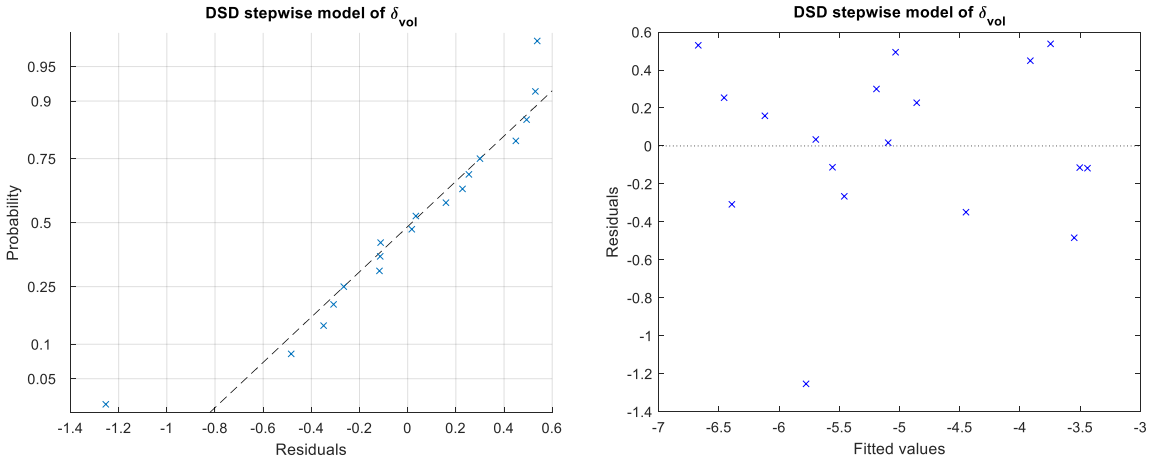

Figure 2.4-8. Normal probability plot of the residuals (left) and residuals-vs-fitted values plot (right) of the stepwise regression model of the final heterogeneity degree of the modelled backfill domain.

Table 2.4-7. Residual AD test of the stepwise regression model for the whole tunnel homogeneity degree.

AD residuals (-)
0.28

Heterogeneity degree at the backfill mid-plane

The basic statistics of the mid-plain heterogeneity data obtained from the sensitivity analysis simulation runs is presented in Table 2.4-8. The AD test p-value is above the significance level (0.05), which means that normal distribution can be used to approximate the heterogeneity degree data. Normal probability plot of the Box-Cox transformed data is also illustrated in Figure 2.4-9.

Table 2.4-8. Basic statistics of the data of the final heterogeneity degree of the backfill at the simulated fracture.

Mean (%)	std. dev (%)	min (%)	max (%)	AD (-)
3.8	2.0	1.1	7.5	0.68

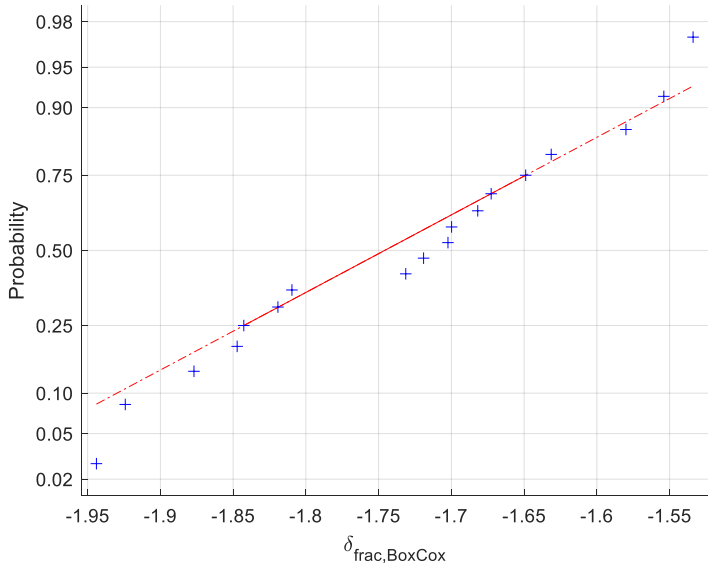

Figure 2.4-9. Normal probability plot of the final heterogeneity degree of the backfill at the simulated fracture after Box-Cox transformation with $\lambda = 0.447$.

Linear regression model

A first-order main effect model is fitted to the mid-plain heterogeneity degree data. The analysis of variance (ANOVA) of the fit is presented in Table 2.4-9 and the standardized effects are illustrated in Figure 2.4-10. The effects state the significance and the relative importance of the input parameters for the tunnel mid-plane dry density homogeneity. The hydraulic boundary condition (BC_{hydr}) and the state surface (which defines the swelling of clay in the model) seem to be the most important input parameters that are also statistically significant (the standardized effect is above the critical t-value). The third most important parameter is the water intrinsic permeability (which represents the hydraulic properties of the material), which is also almost statistically significant.

The F-test p-value in Table 2.4-9 (0.096 > 0.05 which is used the significance level) suggests that the regression model is not statistically significant as whole, which further suggests that interpretation of the individual effects is also questionable. However, the p-value depends on the used regression model and could be made smaller by revising the regression model. If the model was changed, the individual effect values could change, but the orthogonality of the DSD would make the relative importance of the main effects unchanged. Consequently, the first-order main effect model is valid for the screening purpose of this sensitivity analysis, that is, figuring out which input parameters are the most important.

Table 2.4-9. ANOVA of the first-order main effect model of the final heterogeneity degree of the backfill at the simulated fracture domain.

ANOVA	SS	df	MS	Num. obs.	18
Total	0.26	17	0.015	F(7, 10)	2.5

Model	0.17	7	0.024	p-value	0.096
Residual	0.096	10	0.010	R^2	0.63

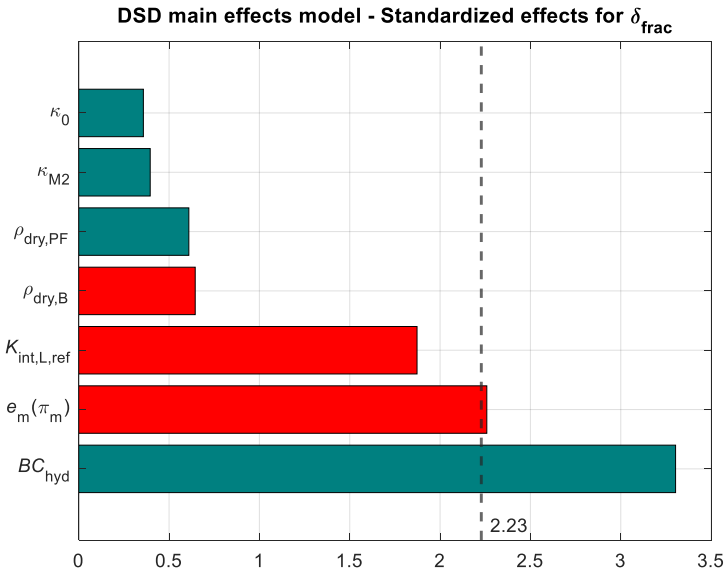

Figure 2.4-10. Pareto chart of standardized effects for the final heterogeneity degree of the backfill at the simulated fracture. The dashed vertical line represents the critical t-value.

The residual analysis (Figure 2.4-11 and Table 2.4-10) shows that the residuals (difference between the fit and the actual values) can be considered normally distributed (Figure 2.4-11. normality plot and AD test p-value in Table 2.4-10 is above the 0.05 significance level), but a mirror symmetry pattern (left vs right) can be noticed in the residual-vs-fitted value plot. Although the residual analysis suggest that the OLS assumptions of zero conditional mean (the regression model fit does not correlate with the errors) is met, the symmetry pattern indicates heteroscedasticity which in turn suggest that the regression model specification is not optimal. Likely, including the second-order terms to the regression model would improve the fit.

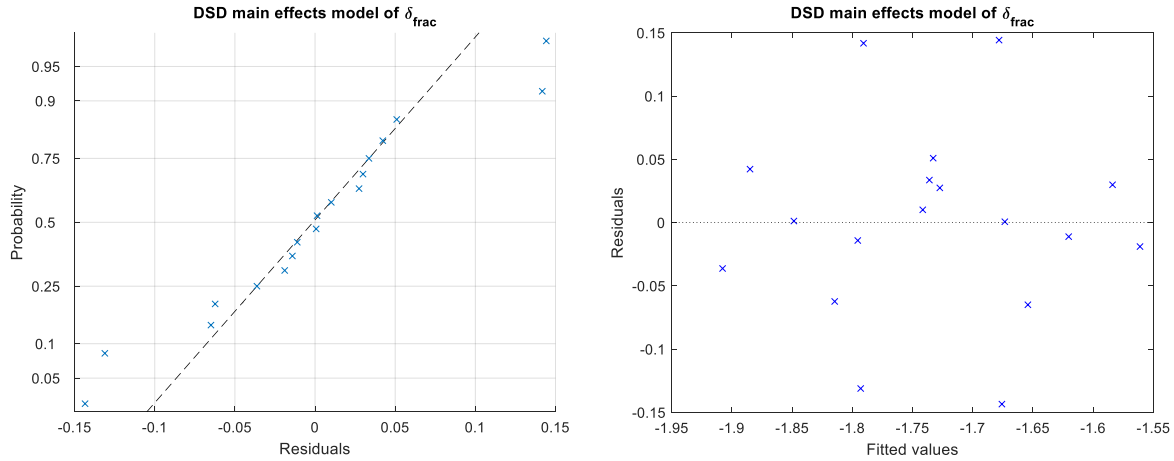

Figure 2.4-11. Normal probability plot of the residuals (left) and residuals-vs-fitted values plot (right) of the first-order main effect model of the final heterogeneity degree of the backfill at the simulated fracture.

Table 2.4-10. Residual AD test of the linear regression model for the tunnel mid-plane homogeneity degree.

AD residuals (-)
0.30

Stepwise regression model

In order to improve the first-order main effect regression model, stepwise regression is used starting from the linear main effects only model and using p-enter = p-remove = 0.25 for inclusion and exclusion of model terms (considering linear, 2fi and quadratic terms), respectively. The F-test p-value in the ANOVA data of the regression model (Table 2.4-11) is below the used significance level (0.05) and the regression model can be said to be significant as whole, which was not the case with the first-order main effect model. Moreover, the high R^2 value indicates good fit.

The Pareto chart of the standardized effects (Figure 2.4-12) shows now that the hydraulic boundary condition, the state surface (that defines the swelling of the clay in the model) and the intrinsic permeability are the statistically significant input parameters that affect the mid-plain heterogeneity degree. The combined effects (marked with colon) improve the regression fit, but the main effects are of the main interest in the performed sensitivity analysis.

Table 2.4-11. ANOVA of the model of the final heterogeneity degree of the backfill at the simulated fracture obtained by stepwise regression considering first-order main effects and second-order 2fi and quadratic effects.

ANOVA	SS	df	MS	Num. obs.	18

Total	0.261	17	0.0154	F(10, 7)	13.872
Model	0.249	10	0.0249	p-value	0.001
Residual	0.013	7	0.0018	R^2	0.952

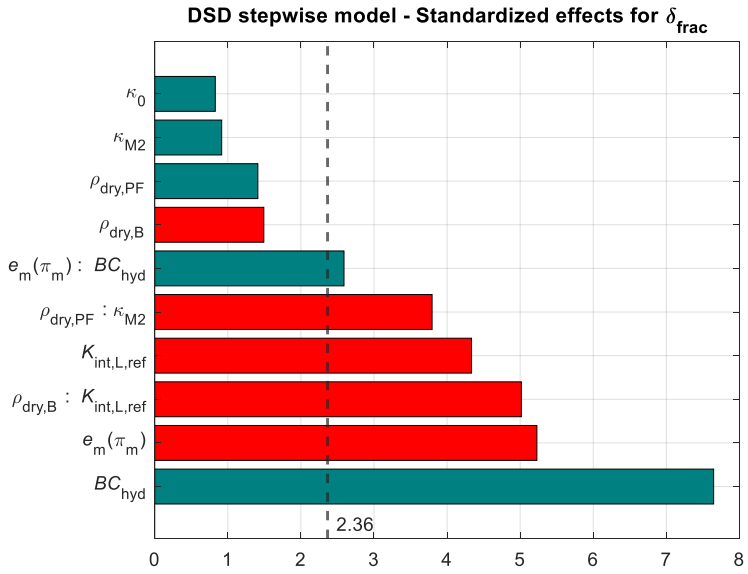

Figure 2.4-12. Pareto chart of standardized effects for final heterogeneity degree of the backfill at the simulated fracture obtained from stepwise regression considering first-order main effects and second-order 2fi and quadratic effects. The dashed vertical line represents the critical t-value.

The normality plot (Figure 2.4-13) suggests that the residuals can be considered normally distributed, but the AD test p-value in Table 2.4-12 is below the 0.05 significance level which suggests the opposite. Consequently, the regression model coefficients may correlate with the residuals and the regression model could be biased. However, due to DSD orthogonality, the main effects remain unbiased and the regression model is valid for screening purpose of the performed sensitivity analysis. The two outliers seen in the down left corner of the normality plot likely cause the discrepancy. It is noteworthy that the residual values are small when compared to fitted values, which also likely has an effect on the normality test. In the residual-vs-fitted value plot, there is no obvious pattern meaning that homoscedasticity assumption (the residuals have constant variance, which means that OLS is efficient fitting method) is met.

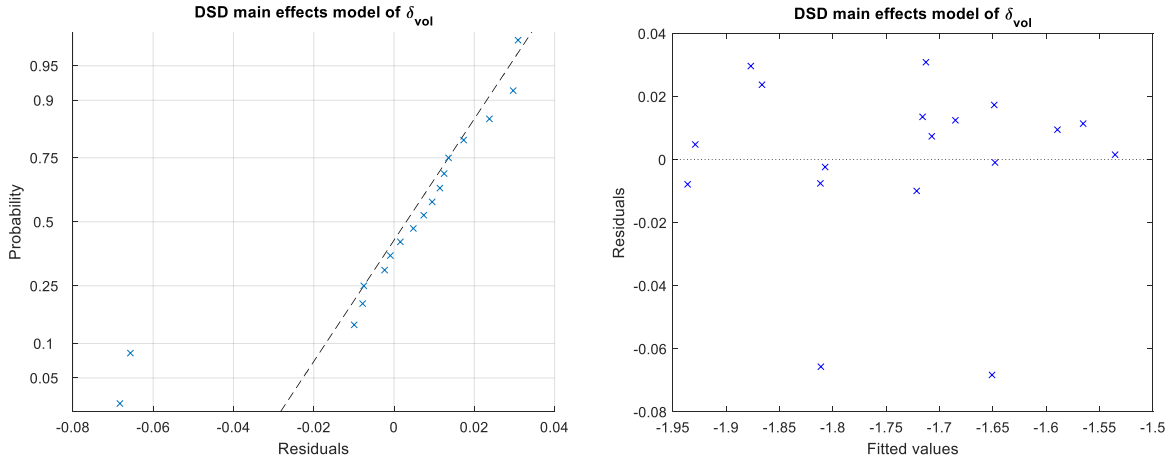

Figure 2.4-13. Normal probability plot of the residuals (left) and residuals-vs-fitted values plot (right) of the stepwise regression model of the final heterogeneity degree of the backfill at the simulated fracture.

Table 2.4-12. Residual AD test of the stepwise regression model for the tunnel mid-plane homogeneity degree.

AD residuals (-)
< 0.005

Average mean stress in the backfill domain

The basic statistics of the average mean stress data obtained from the sensitivity analysis simulation runs is presented in Table 2.4-13. The AD test p-value is above the significance level (0.05), which means that normal distribution can be used to approximate the mean stress data. The p-value is, however, close to the significance level and the normal probability plot of the Box-Cox transformed data (Figure 2.4-14) indicates deviation from normality. The high variability in the means stress (min vs max value) should be noted.

Table 2.4-13. Basic statistics of the data of the average mean stress in the modelled backfill domain.

Mean (MPa)	std. dev (MPa)	min (MPa)	max (MPa)	AD (-)
4.2	3.3	0.7	10.4	0.06

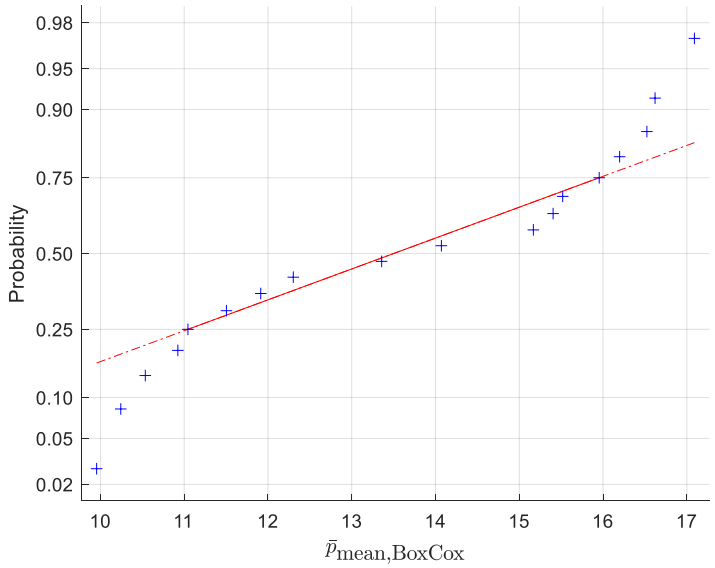

Figure 2.4-14. Normal probability plot of the final average mean stress in the modelled backfill domain after Box-Cox transformation with $\lambda = 0.122$.

A first-order main effect model is fitted to the average mean stress data. The analysis of variance (ANOVA) of the fit is presented in Table 2.4-14 and the standardized effects are illustrated in Figure 2.4-15. The effects state the significance and the relative importance of the input parameters for the mean stress. The state function (which defines the swelling in the model) has by far the highest effect on the mean stress. The mechanical parameters (the block and pellet stiffness) and pellet fill initial dry density have also statistically meaningful effect on the mean stress.

The F-test p-value in Table 2.4-14 (0 < 0.05 which is used the significance level) suggests that the regression model is statistically significant as whole and the high R^2 value suggest a good fit. In this view, the linear main effect model can be considered adequate regression model for the average mean stress.

Table 2.4-14. ANOVA of the first-order main effect model of the final average mean stress in the modelled backfill domain.

ANOVA	SS	df	MS	Num. obs.	18
Total	110	17	6.4	F(7, 10)	60
Model	110	7	15	p-value	0.000
Residual	2.5	10	0.25	R^2	0.98

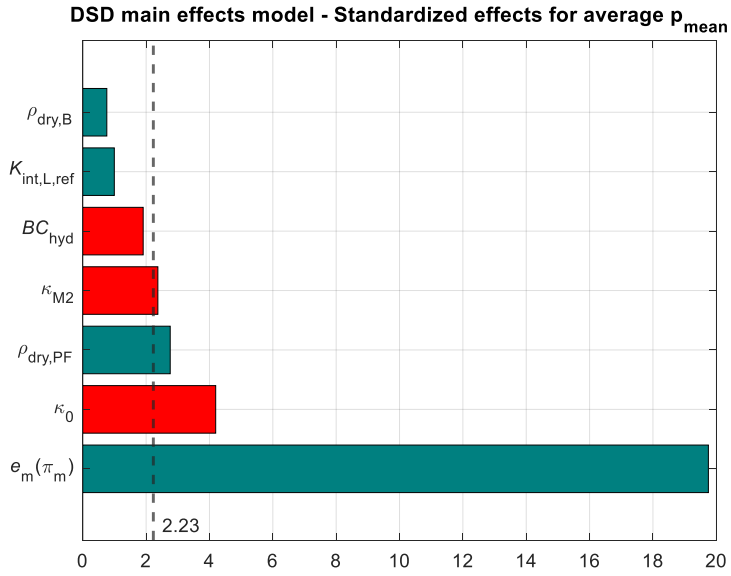

Figure 2.4-15. Pareto chart of standardized effects for the average mean stress in the modelled backfill domain. The dashed vertical line represents the critical t-value.

The residual analysis (Fig and Table 2.4-15) shows that the residuals can be considered normally distributed (Figure 2.4-16 normality plot and AD test p-value in Table 2.4-15 is above the 0.05 significance level) and there is no obvious pattern in the residual-vs-fitted value plot. Consequently, the residual analysis suggest that the OLS assumptions of zero conditional mean (the regression model fit does not correlate with the errors) and homoscedasticity (the residuals have constant variance, which means that OLS is efficient fitting method) are met. Therefore, OLS can be considered as an adequate regression model fitting method.

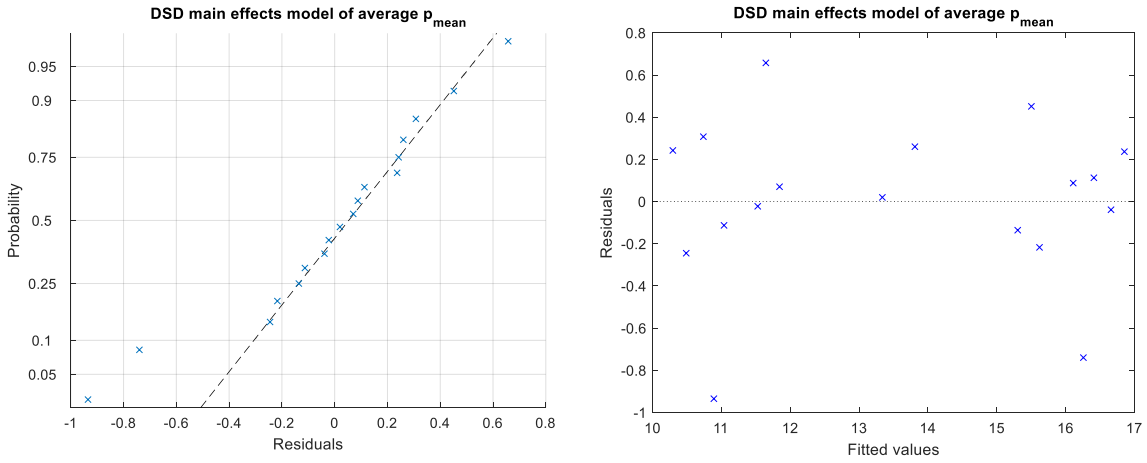

Figure 2.4-16. Normal probability plot of the residuals (left) and residuals-vs-fitted values plot (right) of the first-order main effect model of the final average mean stress in the modelled backfill domain.

Table 2.4-15. Residual AD test of the stepwise regression model for the average mean stress.

AD residuals (-)
0.15

Requested results

The centre point runs in the DSD with run no. 18 (uniform water inflow) and 17 (fracture inflow) provide the requested SKB assessment case results (Figure 2.4-17 to Figure 2.4-22) for comparison to other models.

Uniform water inflow

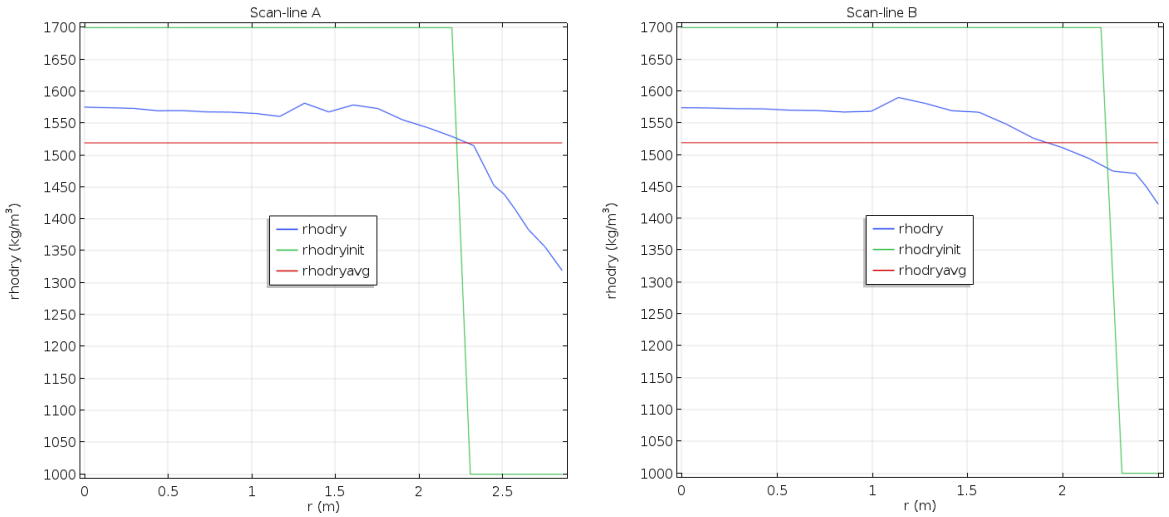

Figure 2.4-17. Final dry density profiles (blue lines) at scan-line A (left) and B (right) with uniform water inflow (run no. 18). The green and red lines represent the initial dry density and the dry density corresponding to the theoretically fully homogenised state, respectively.

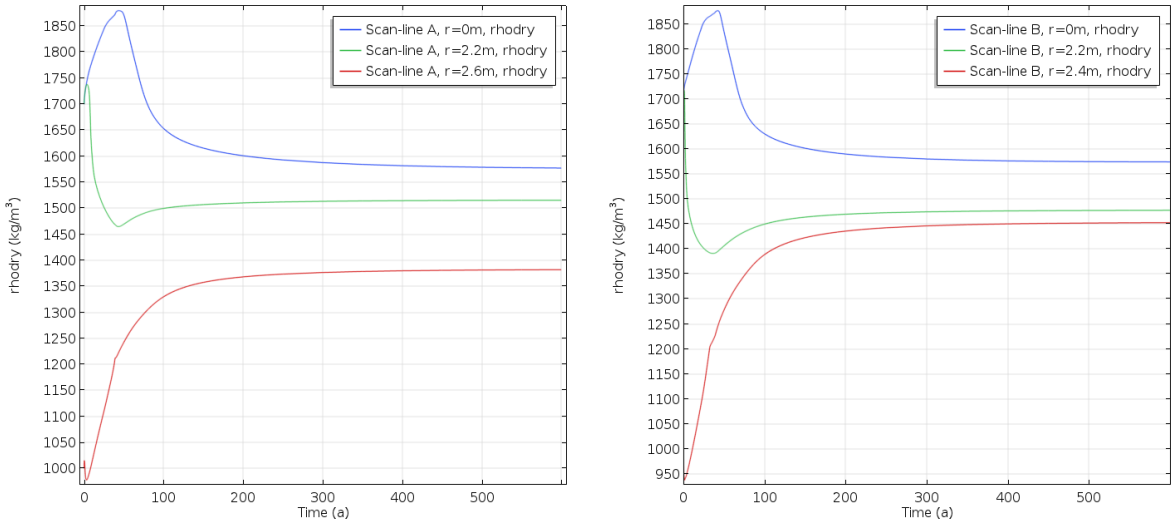

Figure 2.4-18. Temporal dry density evolution at different points on scan-line A (left) and B (right) with uniform water inflow (run no. 18).

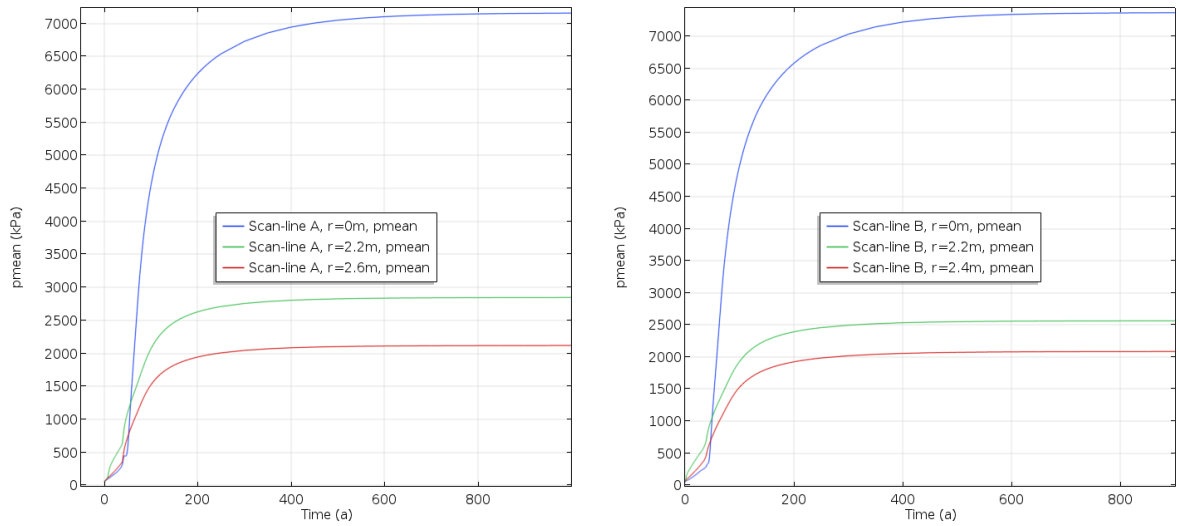

Figure 2.4-19. Temporal mean stress evolution at different points on scan-line A (left) and B (right) with uniform water inflow (run no. 18).

With uniform water flow, the pellet fill saturates first and pushes the bentonite blocks such that their dry density increases (see the initial peaks in the blue graphs in Figure 2.4-18 and also the green graphs on left), but the dry density differences begin to narrow when the wetting process proceeds. At the fully saturated state, the dry density differences at the tunnel section end with less pellet fill (scan-line B) are smaller than in the tunnel section end with more pellet fill (scan-line A) as can be expected (Figure 2.4-17 and the final time of Figure 2.4-18). The swelling pressures seem to settle to acceptable limit (Figure 2.4-19).

Localized fracture inflow

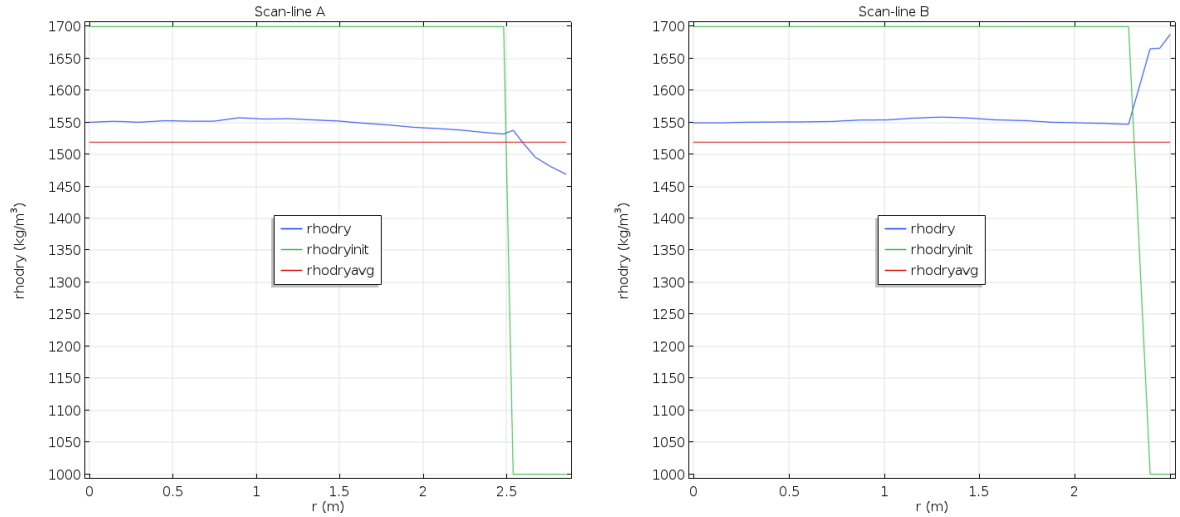

Figure 2.4-20. Final dry density profiles (blue lines) at scan-line A (left) and B (right) with localised fracture inflow (run no. 17). The green and red lines represent the initial dry density and the dry density corresponding to the theoretically fully homogenised state, respectively.

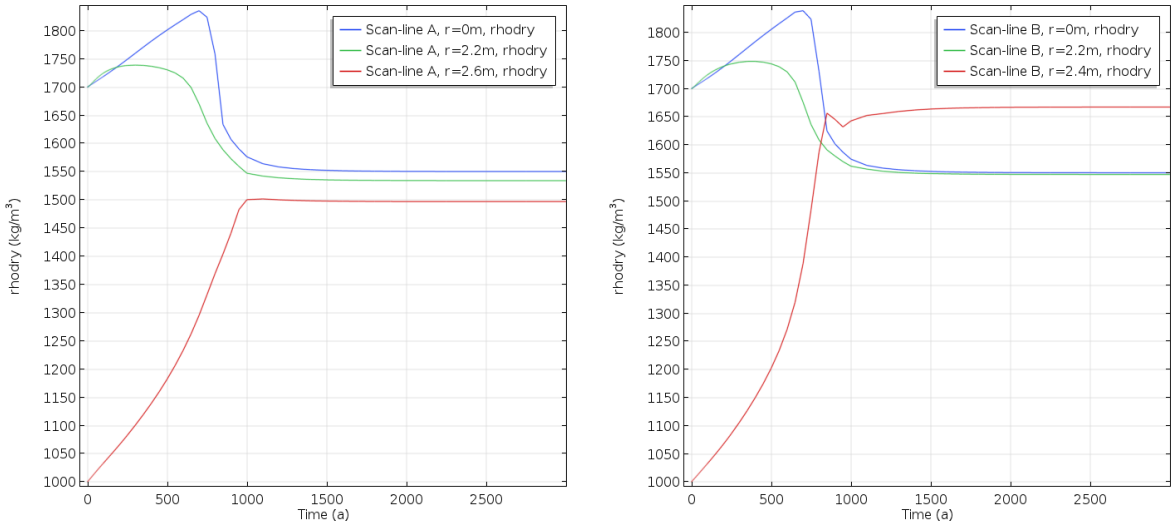

Figure 2.4-21. Temporal dry density evolution at different points on scan-line A (left) and B (right) with localised fracture inflow (run no. 17).

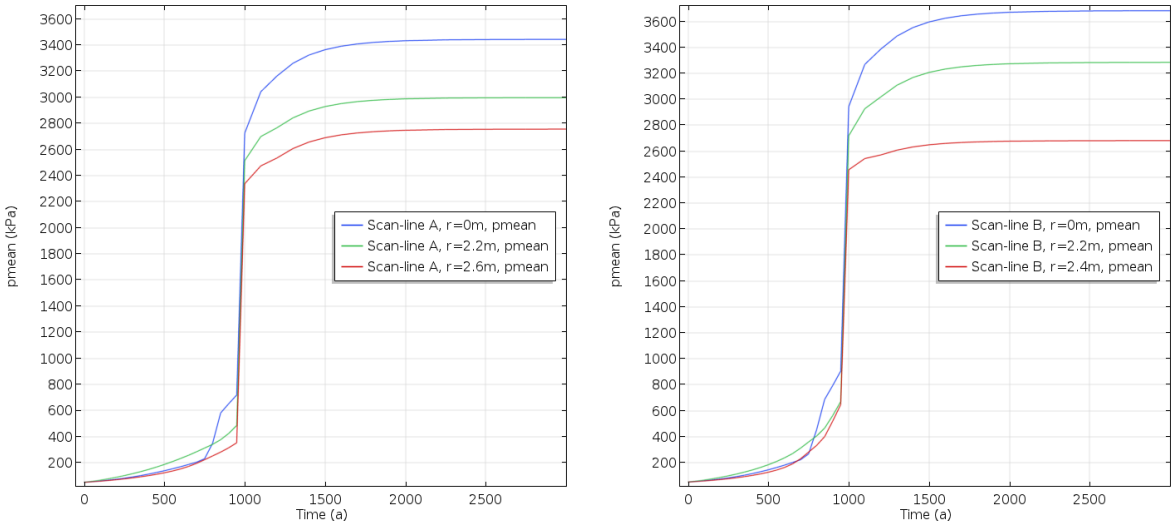

Figure 2.4-22. Temporal mean stress evolution at different points on scan-line A (left) and B (right) with localised fracture inflow (run no. 17).

With fracture inflow from the mid-plane of the tunnel section, the pellet fill close to the inflow fill saturates first and the saturation begins to spread in the pellet fill towards the tunnel section ends. Consequently, the pellet fill pushes the bentonite blocks towards the middle axis of the tunnel and also towards the tunnel ends (scan-lines A and B) such that the point-wise block dry densities increases according to Figure 2.4-21 (the blue graph is the centre axis block dry density and the green the block dry density close to the pellet fill). This swelling behaviour is much more complex than with the uniform inflow. The uneven swelling towards the narrow tunnel end (scan-line B) and the wide tunnel end (scan-line A) can be noticed especially in the pellet dry densities: the pellet fill dry density becomes even higher than the block dry density at the scan-

line B (Figure 2.4-20 and Figure 2.4-21). Technically, the effect is a consequence of the model configuration, which may require elaborating based on new experiments.

During the saturation, the dry density differences decrease more in the fracture inflow case than in the uniform inflow case, but the saturation takes significantly (thousand vs a few hundred years). The swelling pressures also seems to be more even with the fracture inflow than with the uniform inflow (Figure 2.4-22).

2.4.6 Conclusions

A sensitivity analysis of the SKB assessment case was successfully performed with a double (blocks) to triple (pellets) porosity hydromechanical model for bentonite. The chosen input parameters cover the design (block and pellet installation dry densities), the mechanical model (elastic stiffnesses of the blocks and the pellets), the hydraulic model (intrinsic water permeability), the swelling model (the state surface) and the water intake (uniform wetting from the surrounding bedrock or through a fracture). The output (response) variables are the tunnel section heterogeneity degree (the integrated deviation from the average dry density in the whole tunnel section), the tunnel mid-plane heterogeneity degree (integrated deviation from the average density at the fracture location) and the mean stress.

The statistical analysis of the results show that the chosen Definitive Screening Designs with Ordinary Least Squares fitted regression models suit to screen the most important parameters for the mechanical evolution of the tunnel section. The use of different regression model selection techniques could, however, further improve the quality of the fits. Overall, the outcome of the sensitivity demonstrates that a statistically sound sensitivity analysis is a powerful method to analyse the relative effects of different phenomena in complex systems. Even though the analysis was performed for modelled system in this work, the method is applicable also to analysis and design of experiments

The sensitivity analysis suggests that the hydraulic boundary condition, the swelling capacity and the intrinsic water permeability are the most important parameters for the density homogenisation of the tunnel section. On the contrary, the design parameters with the used variation range (double the current design tolerances) seem to be less important for the density homogenisation. Consequently, a possible elaborated sensitivity analysis of the assessment case should allow more variations in the boundary conditions (for example, number of fractures and their locations could be varied) as wells as include more water transport and swelling related parameters. Moreover, the plastic model related parameters could also be considered besides the now used elastic parameters.

In addition to the elaboration of the sensitivity analysis, the underlying hydromechanical model also could be improved in various ways. For example, the parameters of the mechanical model could be directly measured such that statistical information of them would be available. In more complicated than isothermal and isochemical conditions (in the tunnel assessment case), the model details would also require further inspection in the light of experiments.

2.5 Synthesis of results – key lessons (SKB + all participants in the SKB test)

2.5.1 Contributions

Four modelling teams have contributed to this assessment case. An overview of the different codes and models used by these teams are shown in Table 2.5-1.

It can be noted that ICL was the only team that used a hydrostatic pressure level for their boundary conditions, and this has been accounted for in the evaluation below. VTT presented a sensitivity analysis with 18 different models. However, the case with restricted access of water in the task description was replaced by a test case in which water was supplied through a fracture in the mid-section of the analysed tunnel section. This is quite different from the assessment case and it may therefore not be fully relevant to compare this case with corresponding results from the other teams. Finally, CT presented models with two different mechanical boundary conditions; with roller boundary or a fixed boundary. For this comparison, the model cases with a fixed boundary were selected.

Table 2.5-1 Contributing modelling teams and used codes and material models

Partner	Code/model	Comments
LEI	Comsol/Elastic	-
ICL	ICFEP/ICDSM	Hydrostatic boundary conditions
VTT	Comsol/Double-triple porosity framework	Sensitivity analysis (model 17 and 18 in this evaluation)
CT	Comsol/HBM	Different mechanical BS's. Cases with fixed boundary in this evaluation.

2.5.2 Final density distributions

A compilation of the final void ratio distributions for the two scan-lines (as requested in the task description, see Figure 2.5-1) from the different teams and different test cases is shown in Figure 2.5-2. The minimum dry density found along these two scan-lines has been used as a simple measure of the remaining heterogeneity of each model. A compilation of these dry density values is shown in Table 2.5-2.

The results presented by LEI display a quite extensive remaining heterogeneity of the A-section, with a minimum dry density of 1246 kg/m^3. Moreover, the results for the two cases (i.e. free and restricted access of water) are identical and this seems to be a consequence of the elastic model used by this team.

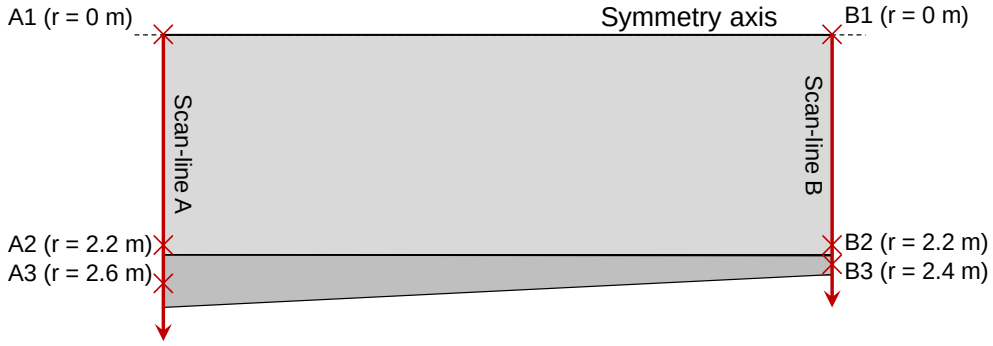

Figure 2.5-1 Positions for requested modelling results: scan-lines (→) and point analyses (×).

The results for the case with free access of water presented by ICL also display a quite extensive remaining heterogeneity of the A-section, with a minimum dry density of 1273 kg/m^3. For the case with restricted access of water, however, the final void ratio distribution is much more homogenous, and display a minimum dry density of 1495 kg/m^3 along the tunnel axis.

The results for the case with free access of water presented by VTT display a fairly moderate remaining heterogeneity of the A-section, with a minimum dry density of 1319 kg/m^3. For the case with restricted access of water (No 17), however, the final void ratio distribution is much more homogenous, and display a minimum dry density of 1469 kg/m^3.

Finally, the results for the case with free access of water presented by CT also display a fairly moderate remaining heterogeneity of the A-section, with a minimum dry density of 1354 kg/m^3. For the case with restricted access of water, the final void ratio distribution is slightly more heterogeneous and display a minimum dry density of 1301 kg/m^3. It can be noted that the models presented by both VTT and ICL displayed higher dry density levels in the pellets than in the blocks along the B-section in case with restricted inflow.

The final minimum dry density values for the different teams and the different cases are illustrated in Figure 2.5-3, and two main observations can be made from this graph:

- There is a significant variation in the minimum dry density in the cases with free access of water presented by the different teams (with values ranging from 1246 to 1354 kg/m^3).
- Different teams have obtained different results regarding the influence of a restricted access of water. LEI found no change, ICL found an increasing minimum dry density, whereas CT found a decreasing minimum dry density. VTT found an increasing minimum dry density, however, as mentioned above, the VTT case (No 17) cannot readily be used for comparisons for the case with restricted water access.

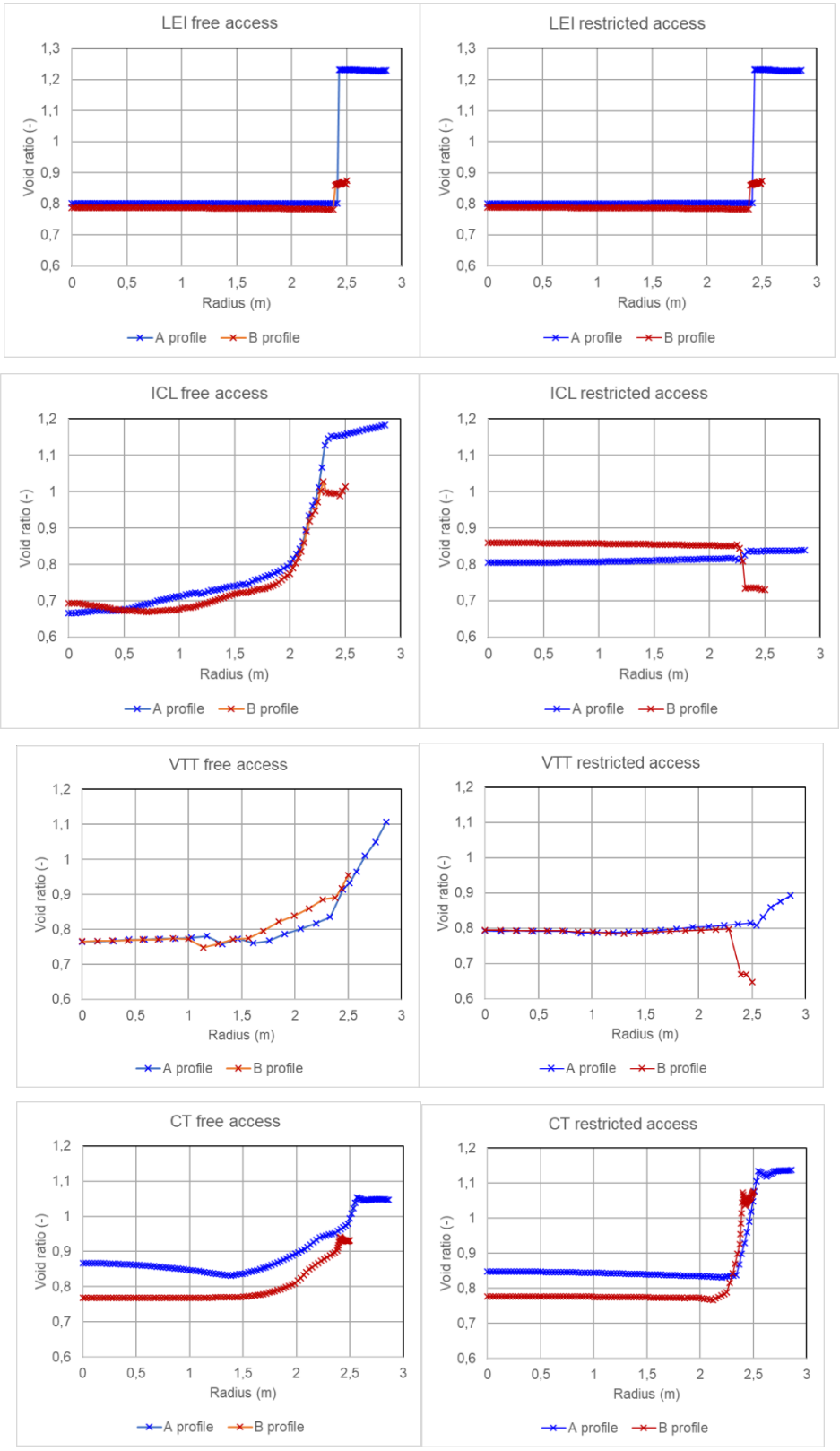

Figure 2.5-2 Final void ratio distributions from different teams and different cases.

Table 2.5-2 Final minimum dry density (kg/m³) for different teams and different cases.

Partner	Free access	Restricted access
LEI	1246	1246
ICL	1273	1495
VTT	1319	1469
CT	1354	1301

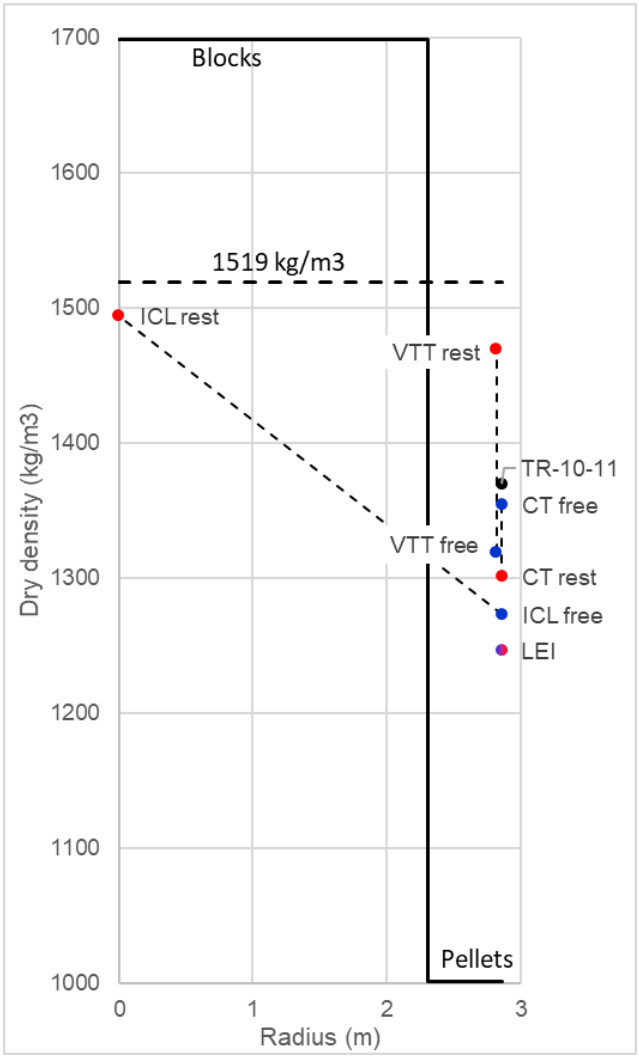

Figure 2.5-3 Schematic illustration of the final minimum dry density for different teams and for different cases (free or restricted access of water). Point marked "TR-10-11" shows the minimum dry density in the backfill homogenisation models with free access of water presented by Åkesson et al. (2010). The solid line represents the initial dry density profile, while the dashed line represents a completely homogenised backfill for this geometry and initial conditions.

2.5.3 Model validation

This scatter in the results from the different teams has motivated an attempt to validate the different models, and from this identify the most likely outcome of either a free access or a restricted access of water investigated in this assessment case.

A schematic illustration of a modelling task with an assessment case such as the one analysed here is shown in Figure 2.5-4. The modelling task defines the geometry, the initial conditions and the boundary conditions, whereas experimental data are used for calibration (i.e the parameter value adoption) of the model. If the task does not provide any measured results (such as in this assessment case), then the only way to validate the model is to compare the model results with experimental data at hand. Different quantities can be investigated for this purpose, e.g. the swelling pressure and the shear strength. The swelling pressure and its relation with the dry density may be regarded as the most important property of the bentonite. For instance, the translation of a performance target (defined in terms of a limiting swelling pressure) and a technical design requirement (defined in terms of liming dry density) relies on material specific relations between dry density and swelling pressure (e.g. Posiva SKB 2017).

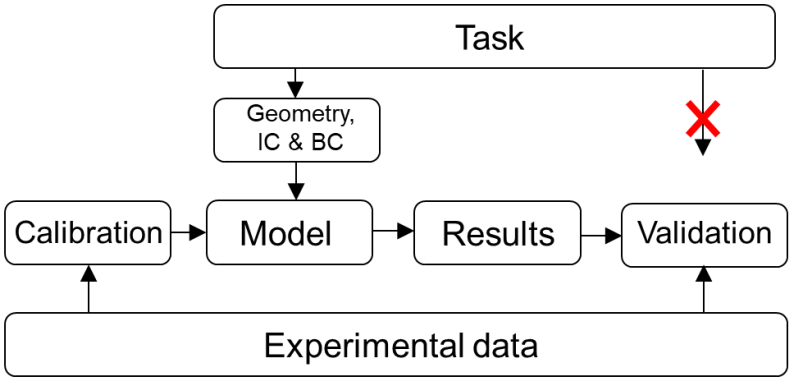

Figure 2.5-4 Final minimum dry density from different teams and different cases.

The assessment case in question is fairly simple in the sense that it doesn´t include any dehydration due to heating. Moreover, since the same initial water content was specified for the blocks and the pellets, this means that these components can be expected to be in equilibrium at the start. The models should therefore exhibit fairly simple stress paths. It is thus relevant to compare the final state (i.e. when the liquid pressure in the model has equilibrated with the boundary pressure) regarding the net mean stress (or effective stress) and the dry density in the different models with swelling pressure measurements and data from saturated oedometer tests. Plots of such final states at three point along each scan-line (see Figure 2.5-1) is shown in Figure 2.5-5 for the different teams and different cases. The final state for points in the backfill blocks (especially in the central parts) should preferably be consistent with swelling pressure measurements. Correspondingly, the final state for points in the backfill pellets (especially in the case with free access with water in which the pellets are saturated

at an early stage) should be consistent with results from saturated oedometer tests. Two reports with such experimental data (swelling pressure in Olsson et al. 2013, and the saturated oedometer tests in Börgesson et al. 2015), which were specified in the task description, can thus be regarded as relevant data sets used for model validation and are therefore included in Figure 2.5-5. It should be noted that only the axial stress measured in the oedometer test (denoted KMXAR4) were included in this analysis. If the mean stress were used instead, then the interval between the compression line and the swelling line would be more narrow.

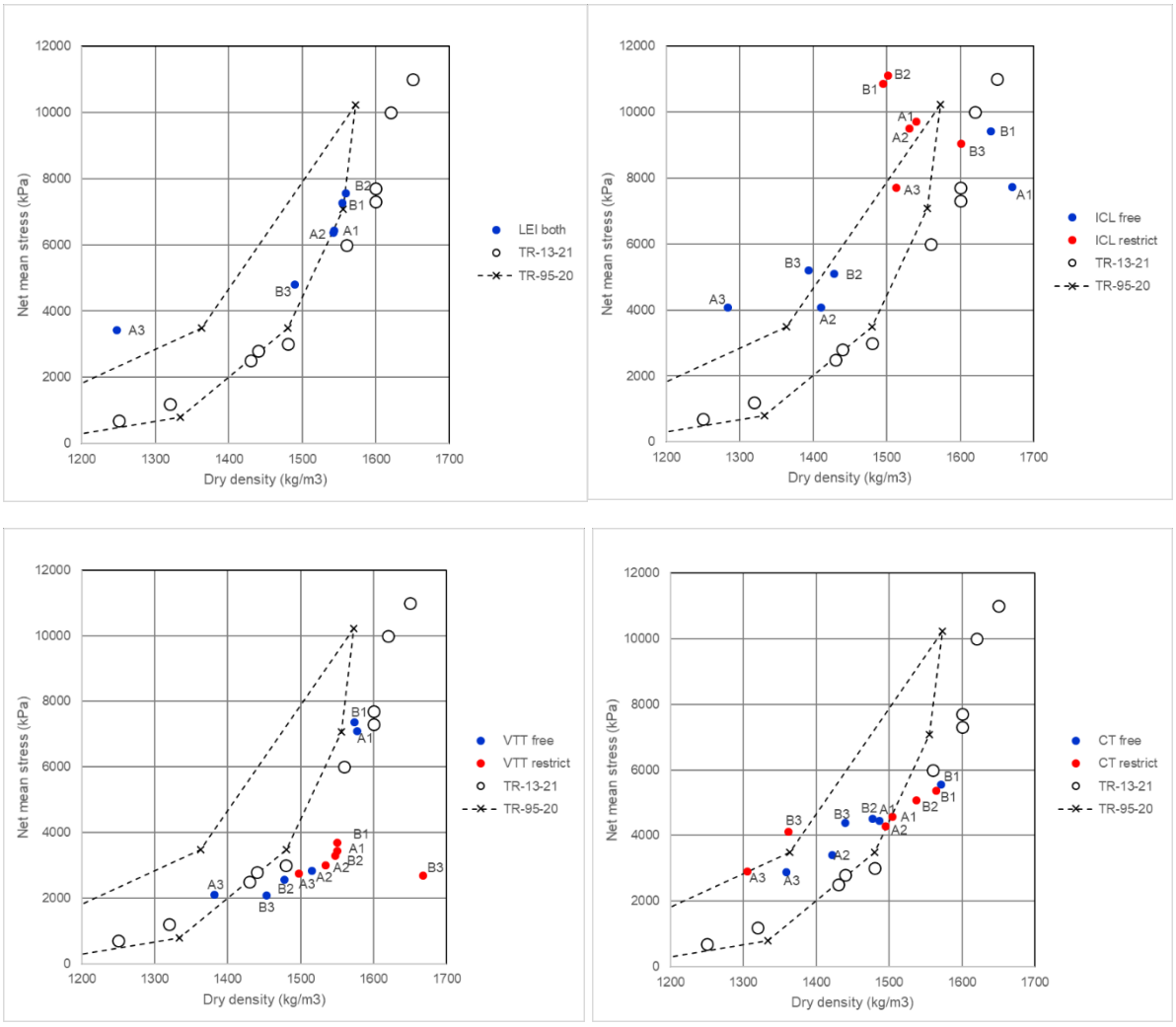

Figure 2.5-5 Final states regarding net mean stress and dry density at six points in each model. Experimental data regarding swelling pressure measurements on reference samples in the Prototype project (O) and saturated oedometer test results (×) are shown for comparison.

From this analysis it can be observed that:

- Point A3 (in the pellets) in both the LEI models which appear to be identical in their final states, as well as in the ICL model with free access of water, display a mean stress which significantly exceeds the compressions line in the oedometer data for the same dry density level. This appears to be main reason for the quite extensive remaining heterogeneity with low minimum dry densities found in these models.
- Point B1 (in the central part of the blocks) in the ICL model with restricted access of water, displays a mean stress which significantly exceeds the swelling pressure for the same dry density level. The final mean effective stress in the six investigated points in this model fall between 8 and 11 MPa, which is approximately twice as high as swelling pressure data for the average dry density in the modelled tunnel section (1519 kg/m^3)
- Point B3 (in the pellets) in the VTT model with restricted access of water, displays a mean stress which is significantly lower than the swelling pressure for the same dry density level.
- Point B3 (in the pellets) in the CT model with restricted access of water, displays a mean stress which slightly exceeds the compression line in the oedometer data for the same dry density level.

2.5.4 Overall assessment

Taken together for the case with free access of water, the models presented by the different teams display a significant variation in the minimum dry density (with values ranging from 1246 to 1354 kg/m^3). However, based on the model validation above, which indicates that the final states in the models presented by VTT and CT are more consistent with experimental data regarding swelling pressure, the minimum dry density is more likely to fall in the upper part of this range (1319 to 1354 kg/m^3).

Regarding the influence of a restricted access of water on the remaining heterogeneity, the models presented by the different teams display very different behaviour. However, based on the model validation above, which shows that the final states in the model presented by CT are more consistent with experimental data, the remaining heterogeneity is likely to increase with a restricted access of water, even though the difference is quite limited.

Still, this is to some extent contradicted by results from lab-scale homogenisation experiments with restricted water uptake. Villar et al. (2022) (D4.3) presented results for tests with either i) swelling of compacted samples into voids, or with ii) homogenisation of binary mixtures with pellets and blocks. Tests were either performed with constant boundary pressure, with suction control or with a constant low inflow rate; and tests were either hydrated from the block side or from the void/pellets side. The test cases most comparable with the assessment case analysed here were the binary mixture large scale oedometer tests with either constant boundary pressure (MGR23), or with constant inflow rate (MGR22). Both these tests were hydrated from the pellets side, and both were hydrated for sufficiently long time in order to saturate completely. The difference between the final dry density profiles was quite small, with

slightly larger density difference in the MGR23 test with constant boundary pressure (Figure 2.5-6), and in this sense it resembles the model results presented by LEI which displayed identical density profiles for the two wetting cases (Figure 2.5-2). However, the relative difference in wetting time (approximately 120 and 220 days respectively to reach an intake of 250 cm^3), was much smaller than the relative difference in wetting time found by the different modelling teams in these analyses, which differed at least with a factor of 10. It would therefore be valuable, if this issue could be further investigated with dedicated scale-tests, in which the duration of a restricted water uptake corresponds to the time-scale of the slow hydration considered in this assessment case.

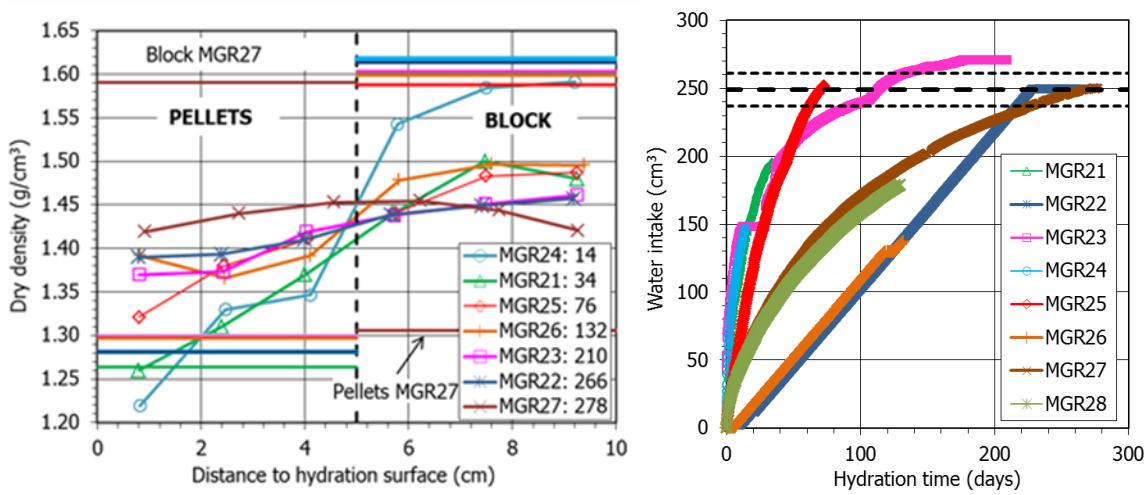

Figure 2.5-6 Final dry density along the samples of MGR tests (left). Water intake evolution in the large-scale oedometer tests (right) (from Villar et al. 2022).

The safety functions that should be upheld for the backfill in a KBS-3 type repository is to limit advective mass transfer and to keep the buffer in place (Posiva SKB 2017). The safety function: "To keep the buffer is place" is mainly affected by the compressibility of the backfill in a dry state and will not be affected by the homogenisation. For the safety function "limit advective mass transfer" the performance targets have been set to a swelling pressure of 0.1 MPa at all points in the tunnel and a hydraulic conductivity of 10^{-10} m/s on average over a section between two deposition holes (6 m).

In this assessment case the properties of MX-80 were assumed for the backfill material. The swelling pressure and hydraulic conductivity as a function of dry density for MX-80 can be found in Figure 2.5-7 and Figure 2.5-8. As can be seen in the figures a dry density of 1200 kg/m^3 is sufficient to reach a swelling pressure of 100 kPa in a very saline solution and 1000 kg/m^3 would be sufficient for all relevant salinities. The hydraulic conductivity is below 10^{-11} m/s at 750 kg/m^3 for salinities up to 1 M.

The lowest calculated dry densities from all teams would still fulfil the performance targets for both hydraulic conductivity and swelling pressure with a reasonable margin. It should however be pointed out that the performance target should be evaluated against the sum of all processes that could affect the hydromechanical

properties of the material. This would include, for example, mass loss from erosion and long-term alteration in addition to the homogenisation process. MX-80 bentonite is also not very likely to be used as tunnel backfill and a more relevant backfill material may have less favourable hydromechanical properties.

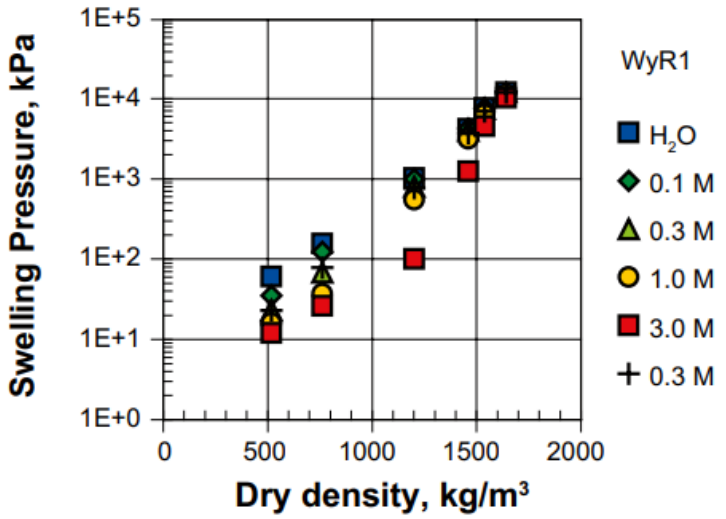

Figure 2.5-7 Swelling pressure of the Wyoming MX-80 reference material (Karnland et al 2006)

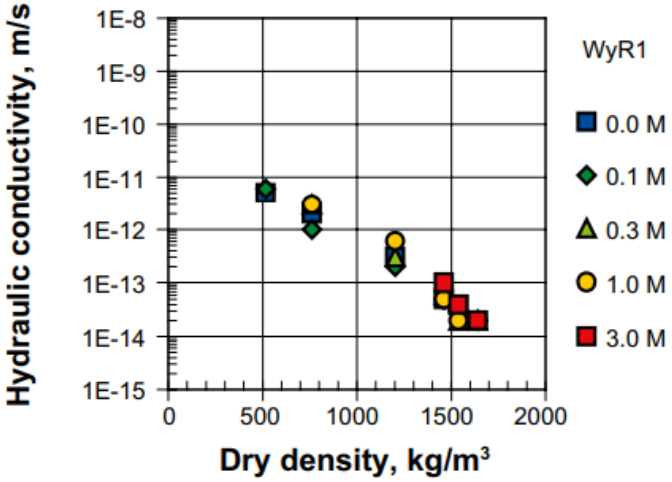

Figure 2.5-8 Hydraulic conductivity of the Wyoming MX-80 reference material (Karnland et al 2006)

3 Nagra assessment case

3.1 EPFL

3.1.1 Description of the models

The constitutive model used by EPFL has been developed within the WP3 of the BEACON project. The complete description is reported in Bosch et al. (2021) and in the deliverable D3.3 of the WP3, including its implementation in the Finite Element code Lagamine (Charlier 1987, Collin 2003) which allows the analysis of thermo-hydro-mechanical processes in porous media. The model equations are summarised in the following.

According to the theory of elasto-plasticity, an explicit distinction is made between elastic (reversible) strains and plastic (irreversible) strains:

$$\mathrm{d}\boldsymbol{\epsilon} = \mathrm{d}\boldsymbol{\epsilon}^e + \mathrm{d}\boldsymbol{\epsilon}^p \tag{1}$$

where $\boldsymbol{\epsilon}$ is the total strain tensor and superscripts e, p denote elastic and plastic strains respectively. The following Bishop-type expression is used for the effective stress $\boldsymbol{\sigma}'$ (Nuth and Laloui 2008):

$$\boldsymbol{\sigma}' = \boldsymbol{\sigma} - [p_a - (p_a - p_w)S_r]\mathbf{I} \tag{2}$$

where $\boldsymbol{\sigma}$ is the total stress tensor, p_a is the pore air pressure, p_w is the pore water pressure and S_r is the degree of saturation.

The equations of the model are written in terms of the following stress invariants:

$$p' = \frac{1}{3}\mathrm{tr}(\boldsymbol{\sigma}'), \qquad q = \sqrt{3}J, \qquad \sin(3\theta) = \frac{3\sqrt{3}\det \mathbf{s}}{2J^3}$$

where $\mathbf{s} = \boldsymbol{\sigma}' - p'\mathbf{I}$ and $J = \sqrt{\frac{1}{2}\mathrm{tr}(\mathbf{s}^2)}$. Likewise, the following strain invariants are defined

$$\epsilon_v = \mathrm{tr}(\boldsymbol{\epsilon}), \qquad \epsilon_d = \sqrt{\frac{1}{3}\mathrm{tr}(\boldsymbol{\gamma}^2)}, \qquad \boldsymbol{\gamma} = \boldsymbol{\epsilon} - \frac{1}{3}\epsilon_v\mathbf{I}$$

The following elastic relationships are used:

$$\mathrm{d}\epsilon_v^e = \frac{p'}{\kappa}\mathrm{d}p' - \frac{1}{3}[\beta_{T0} + \beta_{T1}(T - T_r)]\mathrm{d}T, \qquad \mathrm{d}\epsilon_d^e = \frac{9(1-2\nu)}{2(1+\nu)}\frac{p'}{\kappa}\mathrm{d}q \tag{3}$$

Where T is the current temperature, κ and ν are elastic material parameters, T_r is a reference temperature and β_{T0}, β_{T1} are thermo-elastic parameters (Laloui and François 2009). The yield surface and flow rule derived by Collins and Kelly (2002) are used. The yield surface, f_Y in the stress space takes the following form:

$$f_Y = q^2 - M^2\Pi^2(p'_Y - p')p' = 0 \tag{4}$$

$$\Pi = \alpha + (1-\alpha)\left(\frac{2p'}{p'_Y}\right)$$

where M is the critical stress ratio, which depends on Lode's angle, α is a material parameter, and $p'_Y = p'_Y(\epsilon_v^p, S_r, T)$ corresponds to the yield pressure. A dependency of strength on the stress path is established by taking the critical stress ratio as a function of the Lode's angle (van Eekelen, 1980; Vilarassa et al. 2017):

$$M(\theta) = a_L[1 + b_L \sin(3\theta)]^{n_L} \tag{5}$$

Where a_L and b_L are defined as:

$$a_L = \frac{M_c}{(1+b_L)^{n_L}} \tag{6}$$

$$b_L = \frac{\left({}^{M_c}/_{M_e}\right)^{1/n_L} - 1}{\left({}^{M_c}/_{M_e}\right)^{1/n_L} + 1} \tag{7}$$

$$M_c = \frac{6\sin\phi'_c}{3-\sin\phi'_c}, \qquad M_e = \frac{6\sin\phi'_e}{3+\sin\phi'_e} \tag{8}$$

Where ϕ'_c and ϕ'_e are the shear strength angles at failure for compression paths and extension paths respectively; and $n_L = -0.229$.

The yield pressure, p'_Y evolves with the degree of saturation (Zhou et al. 2012):

$$\frac{p'_Y}{p'_r} = \left(\frac{p'_{TY}}{p'_r}\right)^{\frac{\lambda_s - \kappa}{\lambda(S_r) - \kappa}} \tag{9}$$

Where p'_{TY} is the yield pressure at current temperature, p'_r is a reference stress, λ_s defines the elastoplastic compressibility during yielding for saturated states and $\lambda(S_r)$ is a function expressing the evolution of elastoplastic compressibility with the degree of saturation:

$$\lambda(S_r) = \lambda_s - r(\lambda_s - \kappa)\left(1 - S_r^{\zeta}\right)^{\xi} \tag{10}$$

where parameter r $(0 < r < 1)$ expresses the decrease of elastoplastic compressibility from saturated to dry state $(S_r = 0)$; and ζ and ξ are material parameters. A dependency of yield on temperature is introduced as (Laloui and Cekerevac 2003, Laloui and François 2009):

$$p'_{TY} = p'_{Ys}\left[1 + \gamma_T \ln\left(\frac{T}{T_r}\right)\right] \tag{11}$$

Where p'_{Ys} is the hardening variable (corresponding to the yield pressure at $S_r = 1$ and $T = T_r$) and γ_T is a material parameter.

Volumetric and deviatoric plastic strain increments are given by the flow rule:

$$\mathrm{d}\epsilon_v^p = -\mathrm{d}\Lambda(p' - p'_Y/2), \qquad \mathrm{d}\epsilon_d^p = -\mathrm{d}\Lambda\frac{q}{M^2\Pi^2} \tag{12}$$

The hardening variable, p'_{Ys} evolves according to the hardening law:

$$\frac{\mathrm{d}p'_{Ys}}{p'_{Ys}} = \frac{\mathrm{d}\epsilon_v^p}{\lambda_s - \kappa} \tag{13}$$

The degree of saturation is computed as the ratio between water ratio e_w (ratio of water volume with respect to volume of solids) and void ratio e, i.e. $S_r = \frac{e_w}{e}$.

The water retention model is formulated in terms of the water ratio, e_w which is divided into free water ratio, $e_{w,f}$ (volume of non-adsorbed water with respect to volume of solids) and adsorbed water, $e_{w,a}$ (volume of adsorbed water with respect to volume of solids)as $e_w = e_{w,f} + e_{w,a}$.

The evolution of free water ratio $e_{w,f}$ is modelled as:

$$e_{w,f} = \left(e - e_{w,a}\right)\left[1 + \left(a\left(e - e_{w,a}\right)^b s\right)^n\right]^{1/n-1} \tag{14}$$

where n, a and b are material parameters and s stands for matric suction. $e_{w,a}$ follows a Freundlich isotherm:

$$e_{w,a} = e_{w,a}^C\left[\exp\left(-\frac{M_w}{\rho_{w,a}RT_r}s\right)\right]^{1/m} \tag{15}$$

where $\rho_{w,a}$ is the density of adsorbed water, R = 8.314 J/mol K, is the gas constant, M_w is the molar mass of water, $e_{w,a}^C$ is the adsorption capacity parameter, and m is a material parameter. Note that while free water ratio depends on the current void ratio, the adsorbed water ratio only depends on suction.

The balance equations of mass, energy and momentum implemented in Lagamine are based on the compositional approach and are described in detail in Collin (2003). For the sake of conciseness only the most relevant constitutive relationships will be described here.

Water flow is modelled by means of Darcy's law neglecting the gravitational forces:

$$\mathbf{q}_w = -\frac{k_{rw}\mathbf{k}_f}{\mu_w}[\text{grad}(p_w)] \quad (16)$$

Where $\mathbf{q}_w$ is the vector of water flux, $\mathbf{k}_w$ is the tensor of intrinsic permeability, k_{rw} is the relative permeability and μ_w is the water viscosity. Relative permeability evolves with the degree of saturation, S_r following an exponential law

$$k_{rw} = S_r^{\alpha_k} \quad (17)$$

Where k_{sat} is the permeability at saturated state, and α_k is a material parameter. In the present case it will be considered that the permeability tensor is isotropic, i.e.:

$$\mathbf{k}_f = \mathbf{I}k_f \quad (18)$$

The influence of deformation on the intrinsic permeability is taken into account by means of the Kozeny-Karman formula:

$$k_f = k_{f,0}\frac{(1-n_0)^M}{n_0^N}\frac{n^N}{(1-n)^M} \quad (19)$$

Where $k_{f,0}$ is the initial intrinsic permeability, n stands for porosity, n_0 is the initial porosity and M and N are material parameters.

The effect of temperature on water is important because it controls the change from liquid phase to gas phase in the form of vapor. Vapor in the porous medium is supposed to be in thermodynamic equilibrium with liquid water, thus using Kelvin-Laplace's law as the definition of relative humidity, the following relationship is obtained:

$$\rho_v = \exp\left[\frac{(p_w - p_g)M_v}{RT\rho_w}\right]\rho_{v,0} \quad (20)$$

Where M_v is the gas constant of water vapour, and $\rho_{v,0}$ is the saturated vapor density, that is dependent on temperature. Applying Dalton's law $p_g = p_a + p_v$, where p_g is the gas pressure (mixture of air and vapor) and p_v is the vapor pressure, the overall air density is:

$$\rho_a = \frac{p_g M_a}{RT} - \frac{\rho_v R_v}{R_a} \quad (21)$$

This relationship is used in the vapor diffusion law that is based on Fick's law in a porous medium:

$$\mathbf{i}_v = n(1 - S_r)\tau D\rho_g \mathrm{grad}\left(\frac{\rho_a}{\rho_g}\right) = -\mathbf{i}_a \qquad (22)$$

where $\mathbf{i}_v$ is the vapor flow, D is the diffusion coefficient and τ the tortuosity. Heat transport is governed by both conduction and convection:

$$\mathbf{f}_T = -\Gamma \mathrm{grad}(T) + \left[c_{p,w}\rho_w \mathbf{f}_w + c_{p,a}\left(\mathbf{i}_a + \rho_a \mathbf{f}_g\right) + c_{p,v}\left(\mathbf{i}_v + \rho_v \mathbf{f}_g\right)\right](T - T_0) \qquad (23)$$

where Γ is the thermal conductivity of the mixture and $c_{p,i}$ corresponds to the heat capacity of the phase i. Γ is considered as a function of the degree of saturation.

3.1.2 Geometry and discretization

The finite element mesh of the buffer analysed is shown in Figure 3.2.1, which includes the concrete liner, bentonite pedestal, GBM backfill and canister. The model involves plane-strain conditions, which is representative of a mid-section in the canister. The rock around the tunnel is assumed to be representative of the OPA clay in the Mont-Terri rock laboratory where a marked anisotropy of 33º with respect to the tunnel is present (Müller et al. 2017). As the focus of the study is on the bentonite buffer evolution, the boundaries of the model are defined at 100 m from the tunnel axis, which avoids undesired boundary effects. This also implies that eventual interactions with neighbour disposal drifts are not accounted for.

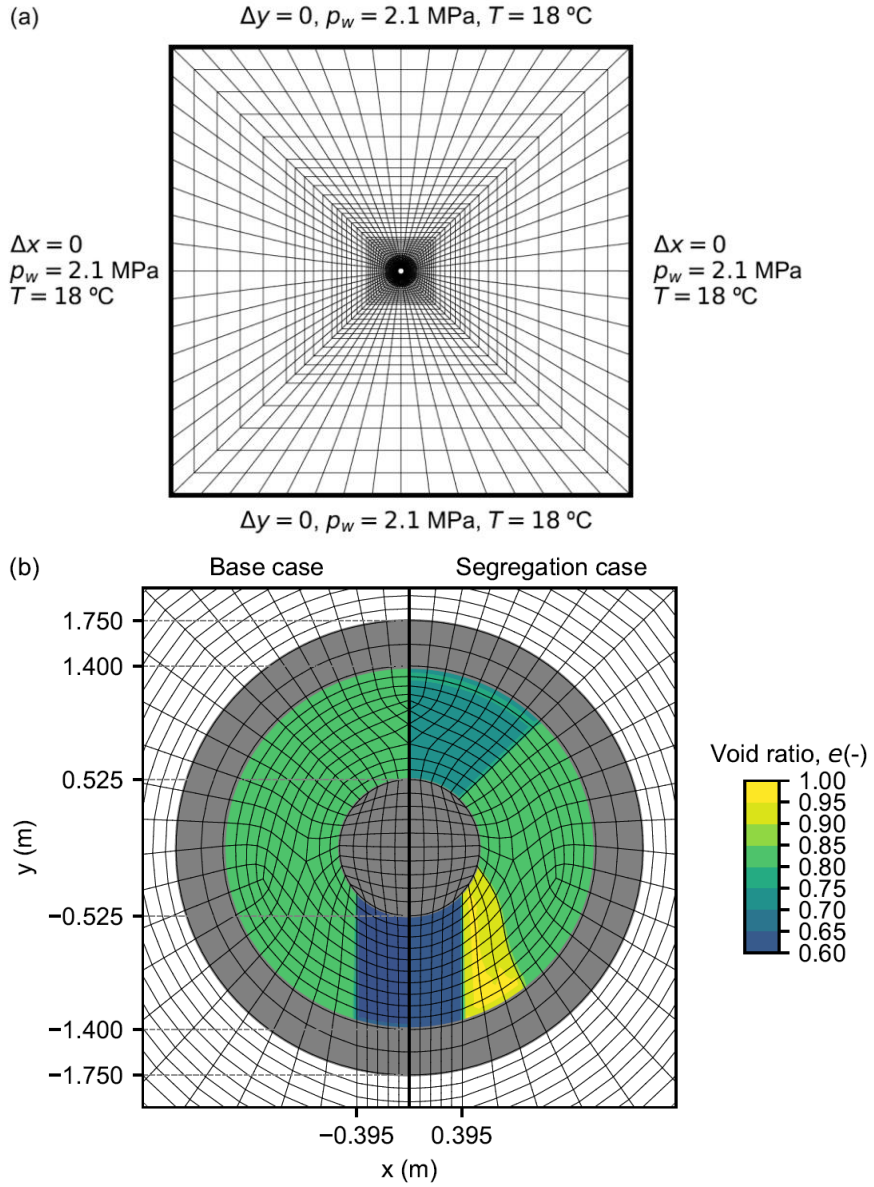

Figure 3.1-1 a) Finite element mesh of the buffer analysed including boundary conditions in the outer zone. b) Detailed view of the buffer mesh, the mesh is symmetric and the left part shows the initial distribution of void ratio, whereas the right side shows the distribution of the case simulating an initial segregation of the granular bentonite.

3.1.3 Input parameters

The water retention behaviour was calibrated with data reported by Seiphoori et al. (2014) for the GBM and by Villar (2005) for the bentonite blocks. The fit obtained with the model is shown in Figure 3.1-2. Although no temperature dependency neither hysteresis is included in the water retention curve, this is justified with the data shown in Figure 3.1-2b, which does not indicate significant differences for different temperatures and drying before wetting tests.

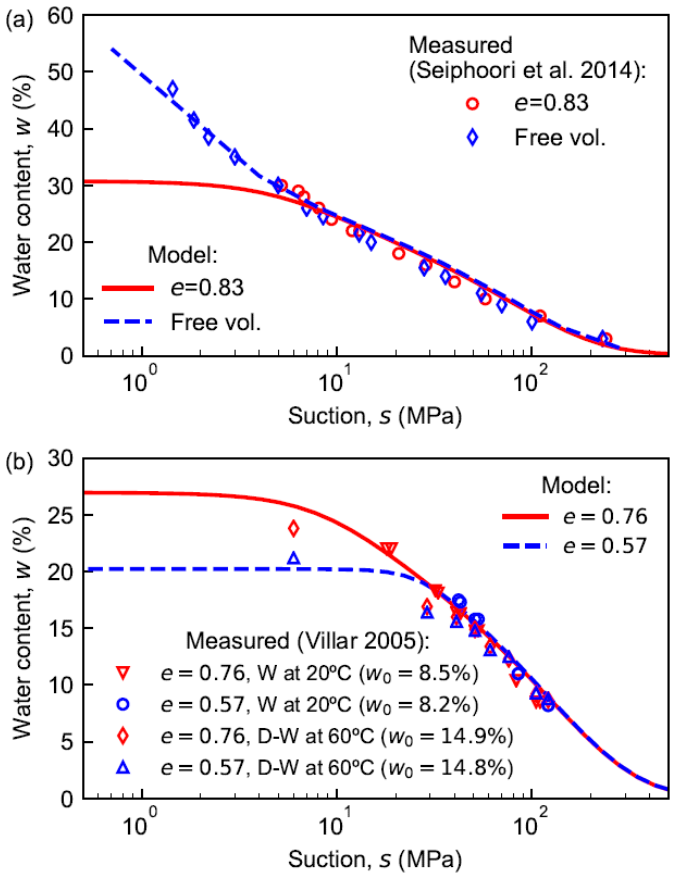

Figure 3.1-2 *a) water retention calibration of granular bentonite (GBM) with data reported by Seiphoori et al. (2014) under constant volume and free volume conditions. b) Water retention of block bentonite calibrated with data obtained by Villar (2005) for different wetting (W) and drying (D) paths at 20ºC and 60ºC.*

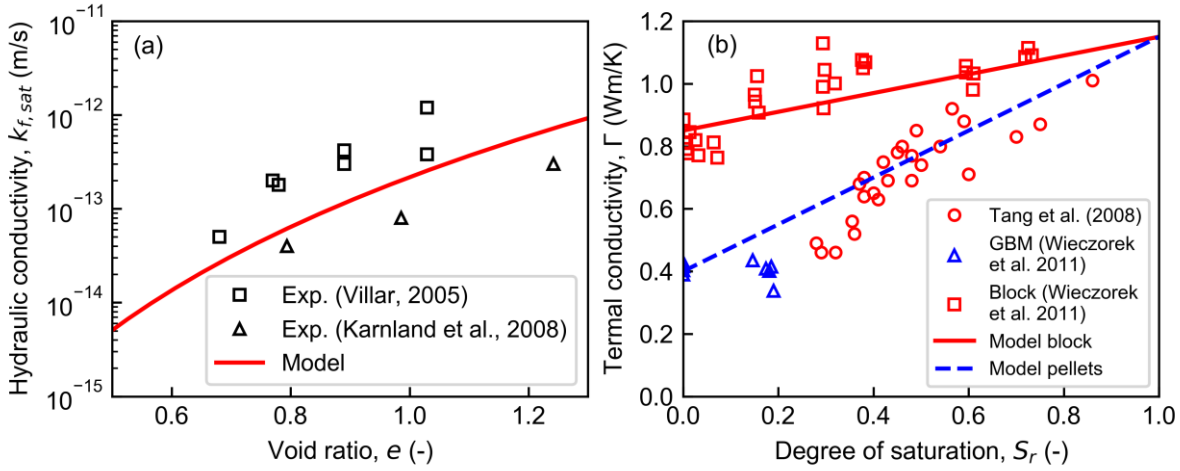

Figure 3.1-3 *a) Calibration of the saturated hydraulic conductivity as a function of void ratio with experimental data (Exp.) from Villar (2005) and Karnland et al. (2008). b) Calibration of the thermal conductivity as a function of the degree of saturation with experimental data from Tang et al. (2008) and Wieczorek et al. (2011).*

The hydraulic conductivity at saturated state is calibrated with the data reported by Villar (2005) and Karnland et al. (2008) as shown in Figure 3.1-3a.

The thermal conductivity of the bentonite as a function of the degree of saturation is derived from data shown in Figure 3.1-3b reported by Wieczorek et al. (2011) on GBM and blocks and Tang et al. (2008) on compacted MX80 at different void ratios. The following expression has been used to fit the data:

$$\Gamma = \Gamma_0 + \Gamma_1 S_r \quad (24)$$

Once the TH properties are defined for the bentonite materials, the mechanical behaviour is calibrated. The same parameters reported in Bosch et al. (2021) for the MX80 at saturated states are used in this study (see Table 1). Swelling pressure tests in mixtures of pellets and powder are used to determine the loading collapse curve parameters of the GBM. In addition, a swelling pressure test in which bentonite was emplaced at two different dry densities is considered. The same tests are used in order to backanalyse k_{rw} using an exponential dependency on S_r:

$$k_{rw} = S_r^{\alpha_k} \quad (25)$$

where α_k is a material parameter.

Figure 3.1-4 shows the calibration of the granular bentonite against the pellets and powder mixture that had an average dry density of 1.49 Mg/m³. The nonlinear development of swelling pressure, which captures well the experimental measurements, results from the coupling between the water retention and the generalised effective stress framework, involving the Bishop-type stress and the dependency of plastic compressibility on S_r.

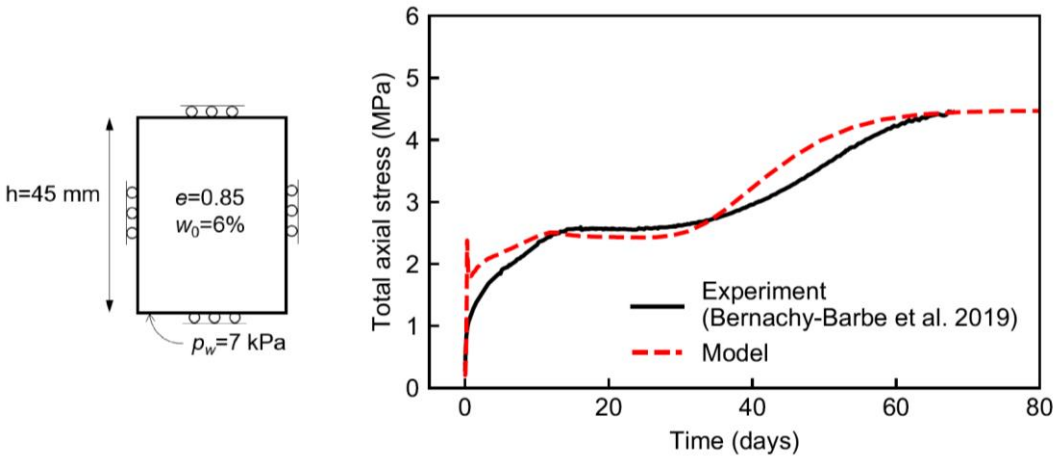

Figure 3.1-4 Calibration of the behaviour of granular bentonite with an initial void ratio $e = 0.85$ subjected to hydration under constant volume at isothermal conditions. Experimental data reported in the Beacon WP4 by Bernachy Barbe et al. (2019, 2021).

Figure 3.2.5 Figure 3.1-5reproduces the swelling pressure test presented by Bernachy-Barbe (2021) that consisted of two compacted blocks at densities of 1.4 Mg/m³ and 1.56 Mg/m³ placed in the same oedometer ring. This test is of interest because these

densities are close to the upper and lower bounds of dry density that was measured in the backfill emplacement test. The lower density block was placed at the bottom which is the side from which hydration took place by means of constant water pressure.

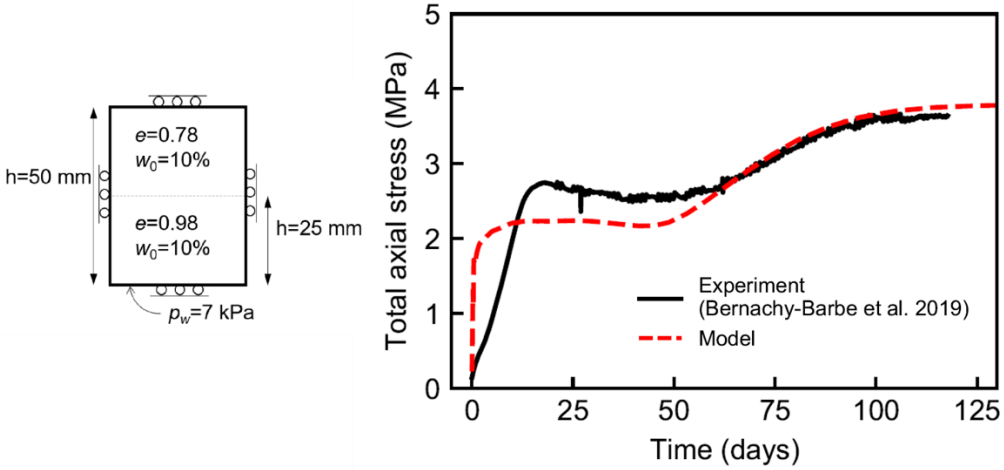

Figure 3.1-5 Calibration of the behaviour of bentonite with an initial void ratio $e = 0.78$ and $e = 0.98$ subjected to hydration from the side at $e = 0.98$ under overall constant volume at isothermal conditions. Experimental data reported by Bernachy Barbe (2021).

The behaviour of the bentonite pedestal is calibrated as shown in Figure 3.1-6 with a swelling pressure test reported by Pusch (1980) on a oedometric sample with a void ratio of around 0.63, that is representative of the overall void ratio of the pedestal including gaps between the blocks. Only the loading collapse curve parameters (ζ, ξ and r) differ from the GBM.

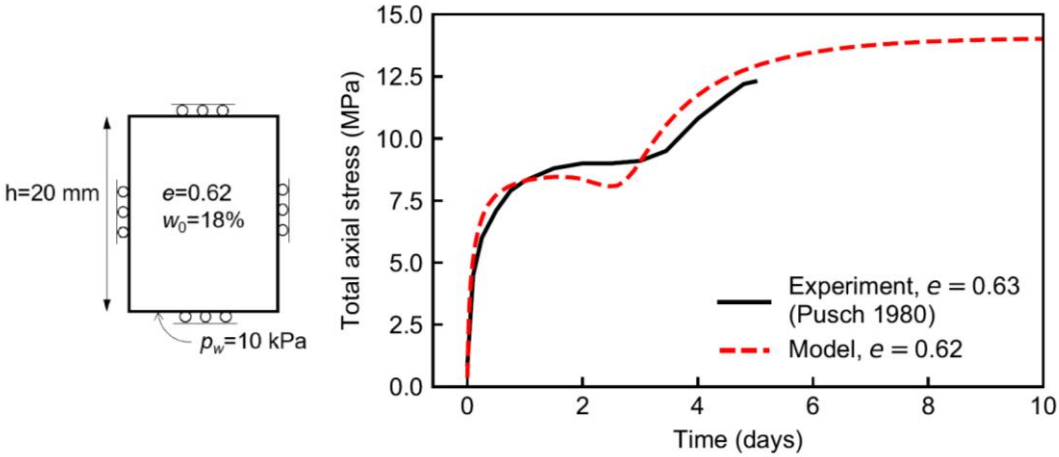

Figure 3.1-6 Calibration of the behaviour of the bentonite pedestal with an initial void ratio $e = 0.62$ subjected to hydration under constant volume at isothermal conditions. Experimental data reported by Pusch on MX80 bentonite (1980).

For both GBM and pedestal blocks, a thermal plasticity parameter of $\gamma_T = 0.15$ is used, which implies a decrease of swelling pressure of 20% at $T = 70$ °C as reported by (Pusch et al. 2003). All intrinsic material parameters for the bentonite are reported in Table 3.1-1, while Table 3.1-2 summarises the parameters that depend on its initial state.

Table 3.1-1 List of intrinsic material parameters for the MX80 bentonite

Parameter	Value	Parameter	Value
κ	0.068	a	0.9 MPa^{-1}
ν	0.35	b	1.5
λ_s	0.112	n	1.8
p'_{NCL} $(e = 1, S_r = 1, T = T_r)$	2.2 MPa	e_{ads}	0.55
ϕ'	11^{o}	$k_{f,0}(e_0 = 0.85)$	10^{-20} m^2
α	0.38	M	6
p'_r	1 Pa	N	5
γ_T	0.15	τ	0.8
β_{T0}	$1.5 \cdot 10^{-5}$		
β_{T1}	0		

Table 3.1-2 List of parameters used for the pellets/powder mixture and the block bentonite

Parameter		GBM $(e_0 = 0.98)$	GBM $(e_0 = 0.83)$	GBM $(e_0 = 0.78)$	Block $(e_0 = 0.62)$
Γ_0, Γ_1 (Wm/^{o}K)		0.4, 0.75	0.4, 0.75	0.4, 0.75	0.85, 0.3
r		0.35	0.29	0.23	0.22
ζ		2.7	2.1	2.7	2.5
ξ		0.9	0.9	0.8	0.5
α_{kw}		4	4	4	2.9
m		0.65	0.65	0.65	1.0

Constitutive relations and parameters for the canister, liner and host-rock

The main THM parameters for the host rock and the concrete liner are summarised in Table 3.1-3. The mechanical behaviour of the tunnel support and the host rock is assumed to be isotropic linear elastic. The thermal and hydraulic parameters for the host rock are representative of the Opalinus clay in the Mont-Terri rock laboratory (Bossart & Thury 2008, Favero et al. 2016, Crisci et al. 2019). As in the FE experiment an anisotropic thermal conductivity and hydraulic conductivity are considered at 33° with respect to the tunnel horizontal axis. The thermal conductivity of both Opalinus and concrete is assumed to not depend on the degree of saturation. A van-Genuchten form of water retention curve and relative water permeability is adopted for both the Opalinus clay and the concrete support:

$$S_r = \left[1 + \left(\frac{s}{\alpha_{VG}}\right)^{\lambda_{VG}}\right]^{\frac{1}{\lambda_{VG}}-1}$$

$$k_{rw} = \sqrt{S_r}\left[1 - \left(1 - S_r^{\frac{1}{\lambda_{VG}}}\right)^{\lambda_{VG}}\right]^2$$

Properties representative of steel are assigned to the canister, characterised by a thermo-elastic law with $E = 210$ GPa, ν =0.25 and a volumetric thermal expansion coefficient of $4 \cdot 10^{-4}$°C^{-1}.

Table 3.1-3 List of material parameters for the host rock (Opalinus clay) and concrete lining

Parameter	Host rock	Concrete
$\mathbf{k}_f$ (m^2)	$k_{fpar} = 5 \times 10^{-20}$ $k_{fper} = 1 \times 10^{-20}$	$k_f = 1.7 \times 10^{-17}$
$\boldsymbol{\Gamma}$ (Wm/°K)	$\Gamma_{par} = 2.1$ $\Gamma_{per} = 1.2$	$\Gamma = 2$
α_{VG}(MPa)	30	1
λ_{VG}	1.8	1.25
E (GPa)	7	30
ν	0.27	0.20
Initial porosity n	0.183	0.23

3.1.4 Initial and boundary conditions

The initial water pressure and temperature of the host-rock before the excavation takes place is set at 2.1 MPa and 18ºC respectively, that is representative of the FE tunnel and homogeneous all throughout the OPA clay domain. The excavation is simulated assuming that the liner is installed immediately. After excavation, a period of two years of ventilation is considered that is simulated by imposing a p_w on the liner surface consistent with the measured water content of the OPA clay after the FE tunnel ventilation (Müller et al. 2017). The relationship between water content and p_w has been derived from water retention measurements (Favero et al. 2016) using Kelvin's law, resulting to be around p_w =-30 MPa.

After the ventilation period the buffer and canister are emplaced all simultaneously and the heating sequence, controlled by power in the canister is applied. The heating power evolution is shown in Figure 3.1-7 which is scaled down to 75% in order to account for the plane-strain conditions (Dupray and Laloui 2016).

The GBM is emplaced with a w =5% (RH =33%) while the bentonite blocks are emplaced at a higher water content of w =18% (RH =80%). A specific gravity value of $G_s = 2.74$ is considered in order to compute the void ratio, e from the dry density. The initial dry density of the bentonite pedestal is set to 1.69 Mg/m^3 ($e = 0.62$), that is an average considering blocks and the technological gaps between them. In the base case a homogeneous initial dry density of the GBM is set at 1.5 Mg/m^3, ($e = 0.83$). The simulation is performed up to 10^5 years representing the time for the canister to dissipate most of its radioactivity.

The initial distribution of e in the segregation case (Figure 3.1-1b) is based on the estimated profiles of dry density reported in the Assessment case deliverable. On the top of the canister, a higher dry density of 1.54 Mg/m^3 ($e = 0.78$) is achieved as a result of the configuration of the backfilling machine, whereas a lower density of 1.39 Mg/m^3 ($e = 0.98$) is considered around the pedestal. The remaining area is supposed to be filled with a dry density of 1.5 Mg/m^3 ($e = 0.83$).

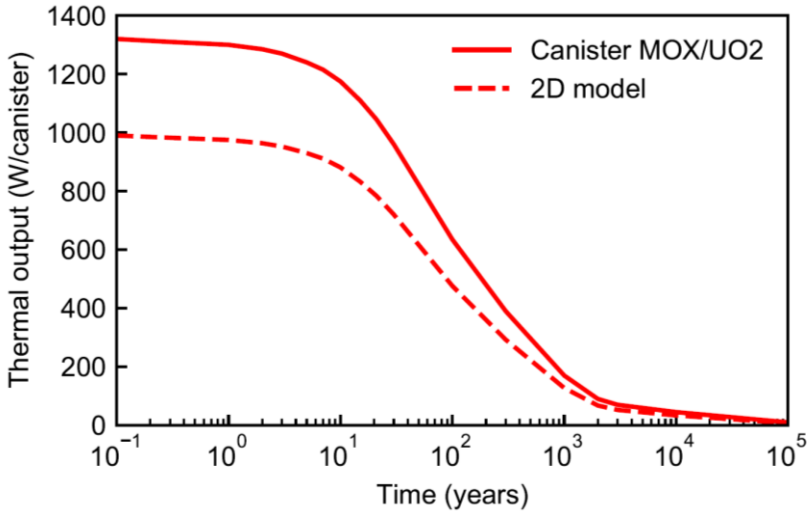

Figure 3.1-7 Heating power emitted by the MOX/UO2 canister and the input sequence of power imposed in the plane-strain model.

3.1.5 Results

Comparison between the FE results and the model.

In this section model results are compared to the temperature, relative humidity and heater displacement measurements that are available from the first years of operation of the FE experiment (NAGRA, 2019).

Temperature and RH measurements close to the heater surface from a section corresponding to the heater #3, are shown in Figure 3.1-8 together with the model predictions. The evolution of temperature and relative humidity are well captured by the model for both the GBM and the pedestal. Figure 3.1-9 shows the monitored heater position together with the model results. It can be seen that the model also predicts the settlement of the heater, which is essentially linked to the strong drying of the bentonite blocks (with higher water content thus subjected to shrinkage when dried) in the early stage. The difference between the top and lower points is due to the dilation of the steel.

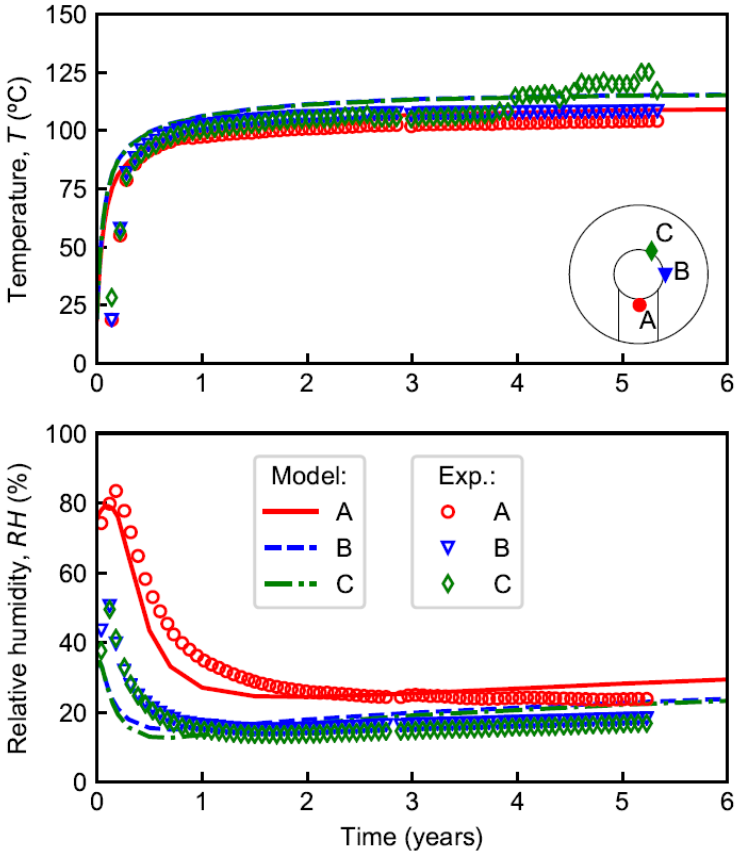

Figure 3.1-8 Experimental results from the FE experiment (Nagra, 2019) at monitoring points close to a heater (denoted by Exp.) and corresponding model results.

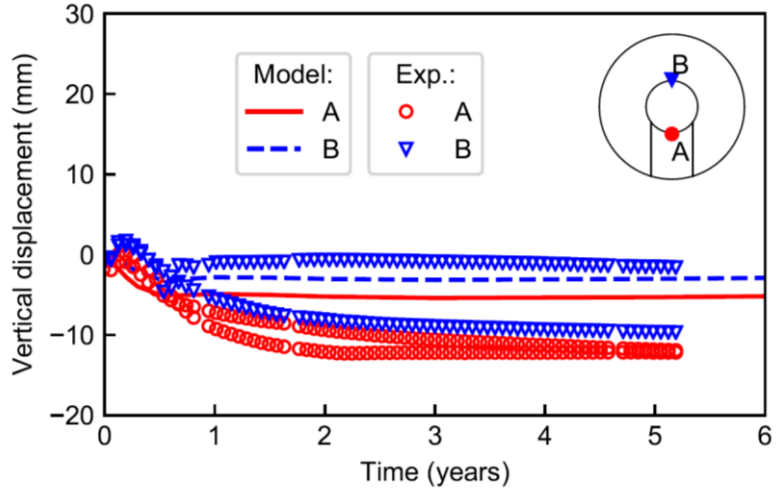

Figure 3.1-9 Measured displacements of one of the heaters in the FE experiment (Nagra 2019) and model results of the upper and lower part of the canister.

The temperature evolution of the buffer in the long term is shown in Figure 3.1-10. The maximum temperature at the canister surface is around 120 °C and it is reached after 3 years. Temperature increases faster in the pedestal as a consequence of the higher initial S_r resulting in higher conductivity. Conversely, in the cooling phases the GBM and the pedestal show similar rates of temperature decrease mostly due to the saturated state that corresponds to a rather homogeneous thermal conductivity.

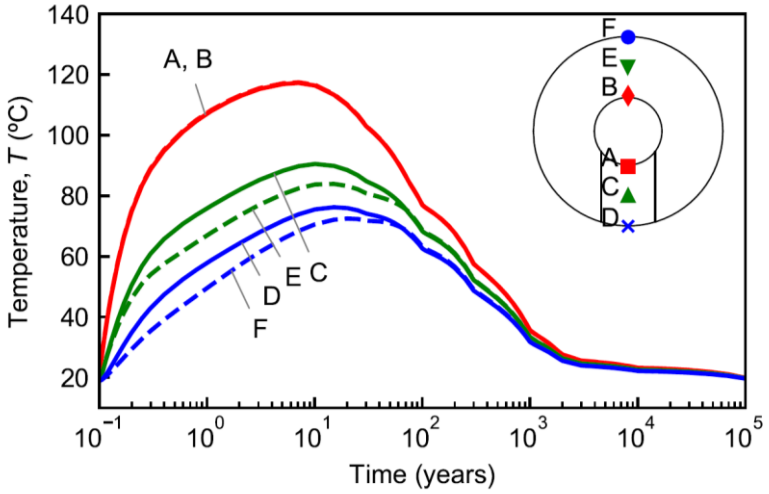

Figure 3.1-10 Long term prediction of the temperature evolution at six points of the buffer.

The predicted evolution of the degree of saturation is shown in Figure 3.1-11. Initially, the pedestal is subjected to a substantial drying from $S_r = 0.8$ up to values lower than $S_r = 0.2$ close to the canister surface. This drying is limited to the first five years after which the buffer is globally hydrated. The complete saturation of the buffer is predicted to be achieved after 80 years of operation.

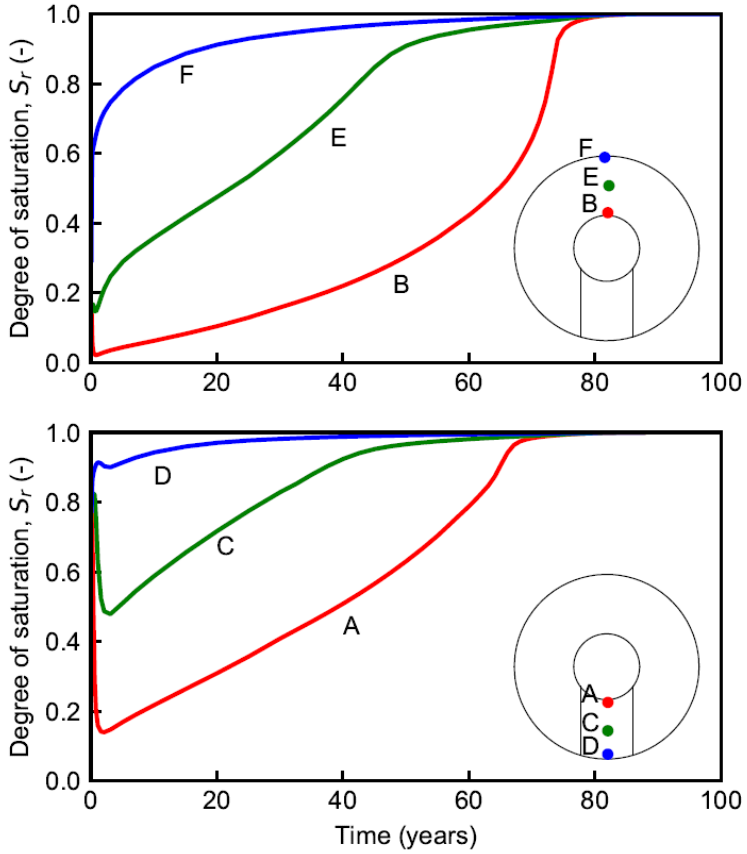

Figure 3.1-11 Predicted evolution of the degree of saturation in the buffer. a) Points corresponding to the granular bentonite. b) Points corresponding to the bentonite pedestal

The development of normal pressure close to the canister and the tunnel liner, is shown in Figure 3.1-12. The pressure development is characterised by a non-monotonic development of stresses in both the granular and pedestal zones. Around the liner (Figure 3.1-12b), the swelling pressure is observed to be practically the same at points C and D, which indicates that the anisotropic thermal and hydraulic conductivity of the host rock do not play a relevant role in its development. At the time of saturation, a significant build-up of stress is observed due to the predicted thermal pressurisation of the pore water. This is a consequence of the very low permeability of both geological and engineered barriers.

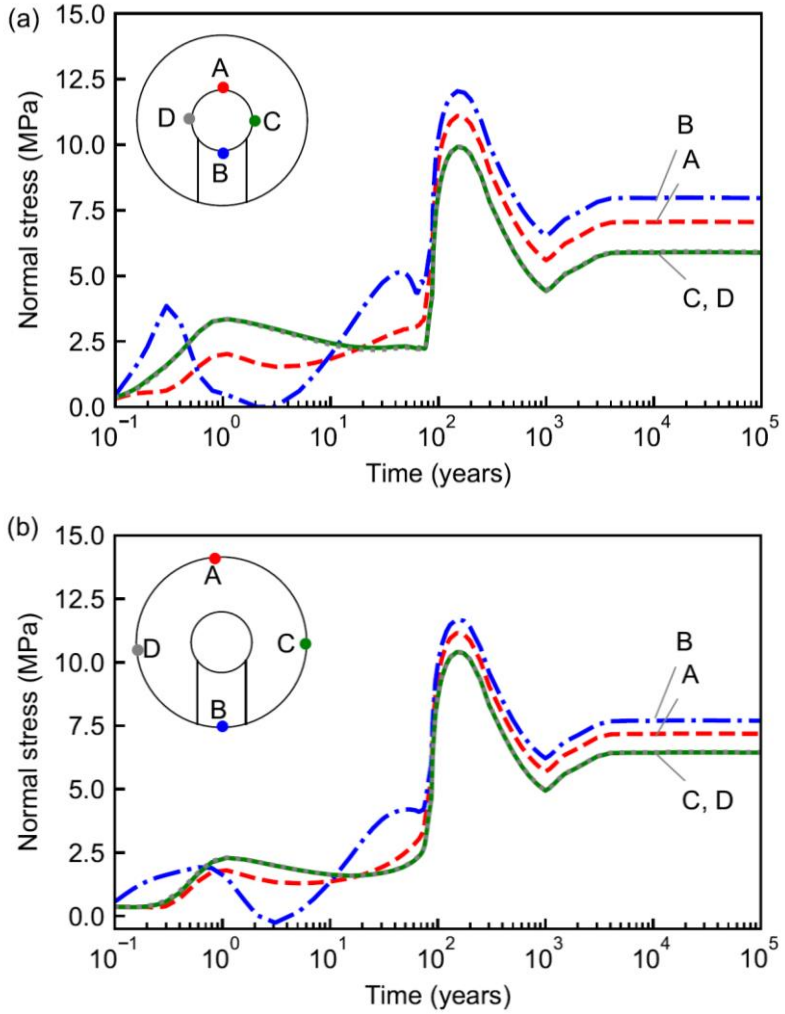

Figure 3.1-12 Predicted developement of total stress (swelling pressure) in the buffer. a) Normal stress acting on the canister. b) Normal stress acting on the concrete liner

Effects of a non-uniform density of granular bentonite

Figure 3.1-13 shows the evolution of S_r in three points close to the canister for both the base case and the segregation case. These results also indicate the sensitivity of the water retention to the saturation time, as the water retention model depends on the void ratio. Given the time scale of the problem, the model predicts minor differences between the base and the segregated case. Indeed, the buffer becomes saturated around 5 years earlier in the case of segregated GBM, without significant differences in the rate of saturation.

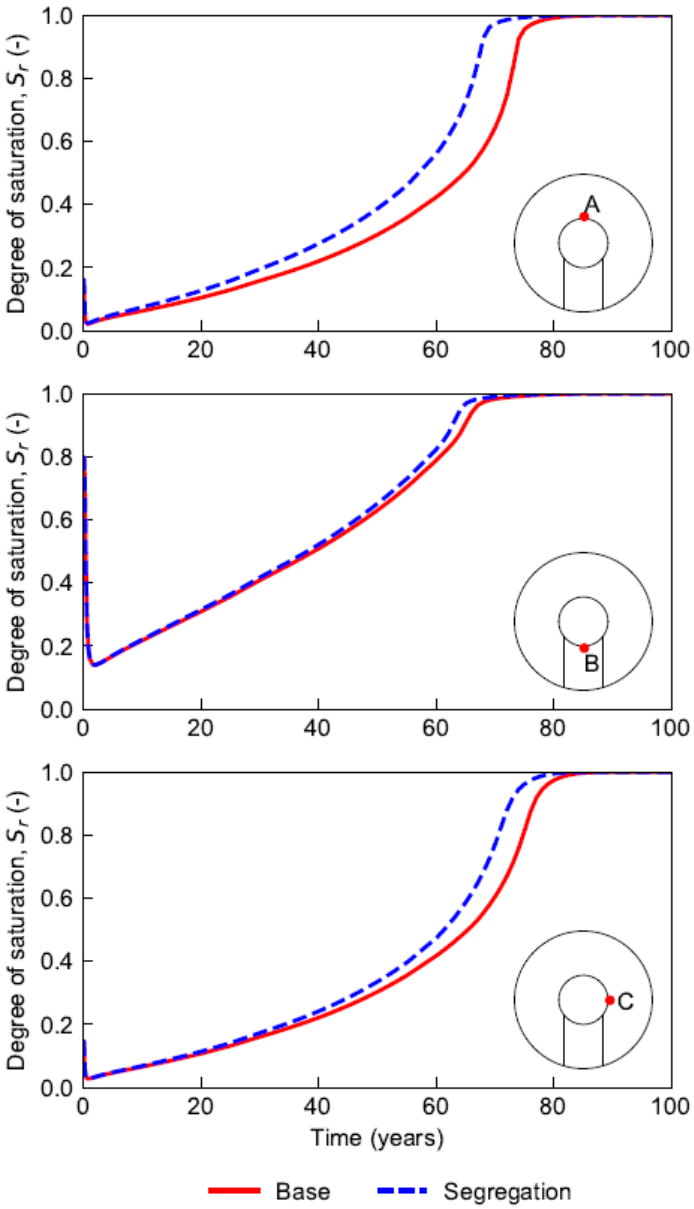

Figure 3.1-13 Evolution of the degree of saturation in the base case and in the segregated granular bentonite case for three points close to the canister

The differences in swelling pressure development between the base case and the segregation case can be seen in Figure 3.1-14. As a consequence of the higher dry density on the top part, the swelling pressure is about 1 MPa higher. The swelling pressure on the pedestal is not affected by the different distribution of the dry density. Conversely, the lateral pressure during the saturation phase is slightly lower in the segregation case despite that the initial dry density is the same at this area in both cases, although this difference is minimized once full saturation is achieved.

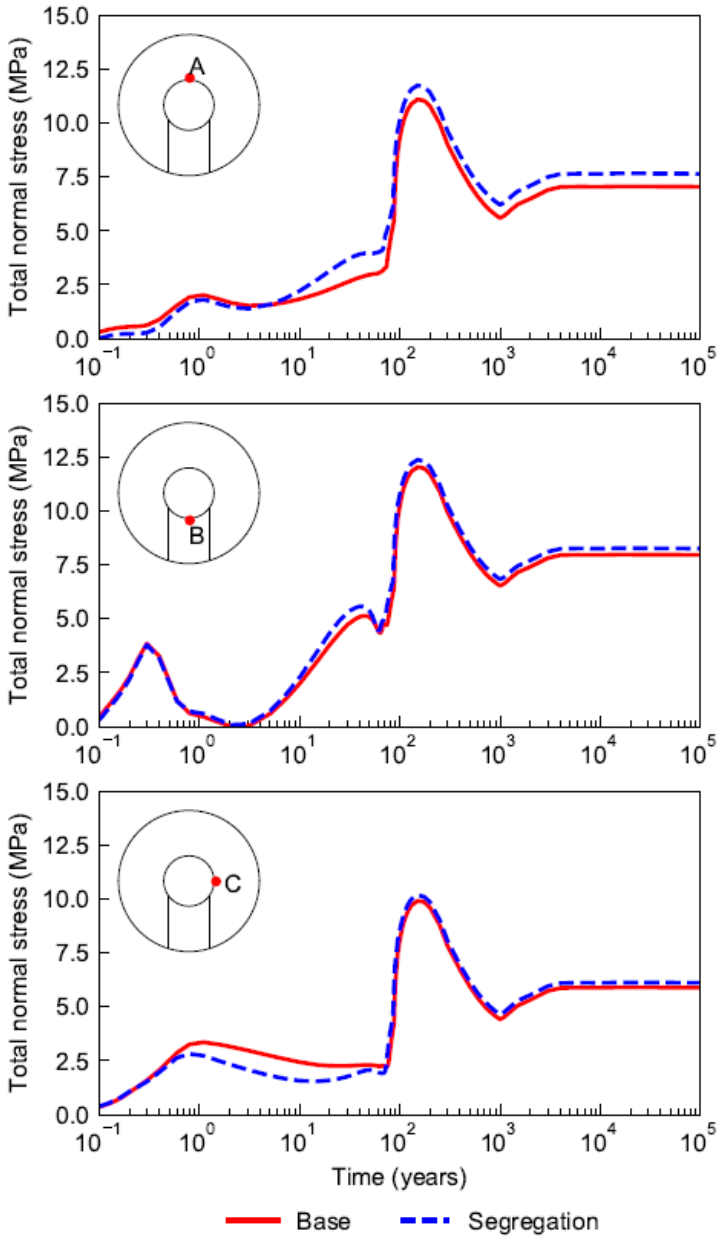

Figure 3.1-14 Evolution of the normal stress on the canister in the base case and in the segregated granular bentonite case at three points

The vertical displacement of the canister in both cases is shown in Figure 3.1-15. While at early stage the displacement is quite similar, it is observed that after saturation the displacement is significantly prevented in the segregation case. It is explained by the fact that at early stage is the thermal process that affects the mechanical response of the pedestal trough drying and shrinkage, while the GBM is practically unaffected due to its lower water content at emplacement. Once full saturation is approached, the higher swelling pressure developed by the upper part (with higher initial density), together with the lower swelling pressure of the GBM close to the pedestal, reduces significantly the canister displacements.

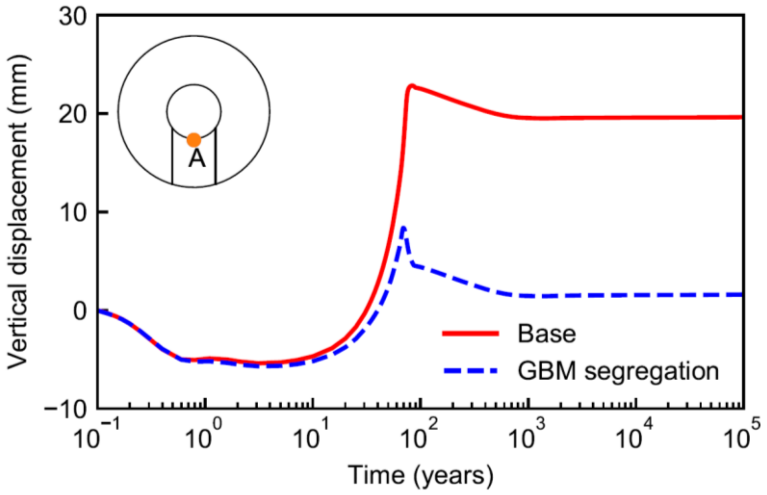

Figure 3.1-15 Canister displacement in the segregated granular backfill case as compared to the base case

Figure 3.1-16 shows the spatial evolution of the overall void ratio and degree of saturation at four times during the saturation phase. The interaction predicted between the pedestal and GBM as well as their trend to homogenise can be visualised. After 40 years of operation no significant differences are observed in terms of void ratio, whereas the spatial variability of S_r is significant, mostly induced by the strong thermal and hydraulic gradients. As the saturation of the buffer proceeds (Figure 3.1-16c) it is observed that the interface between the pedestal and GBM starts to converge in terms of void ratio, as a result of the swelling of the external bentonite although the internal parts have higher stiffness and are only slightly compressed. Once the internal zones of the buffer become saturated, they swell and tend to compress the outer zones. As a result of the stress-path dependency of bentonite behaviour the initial state is not recovered and instead a rather homogeneous distribution is achieved after saturation (Figure 3.1-17d).

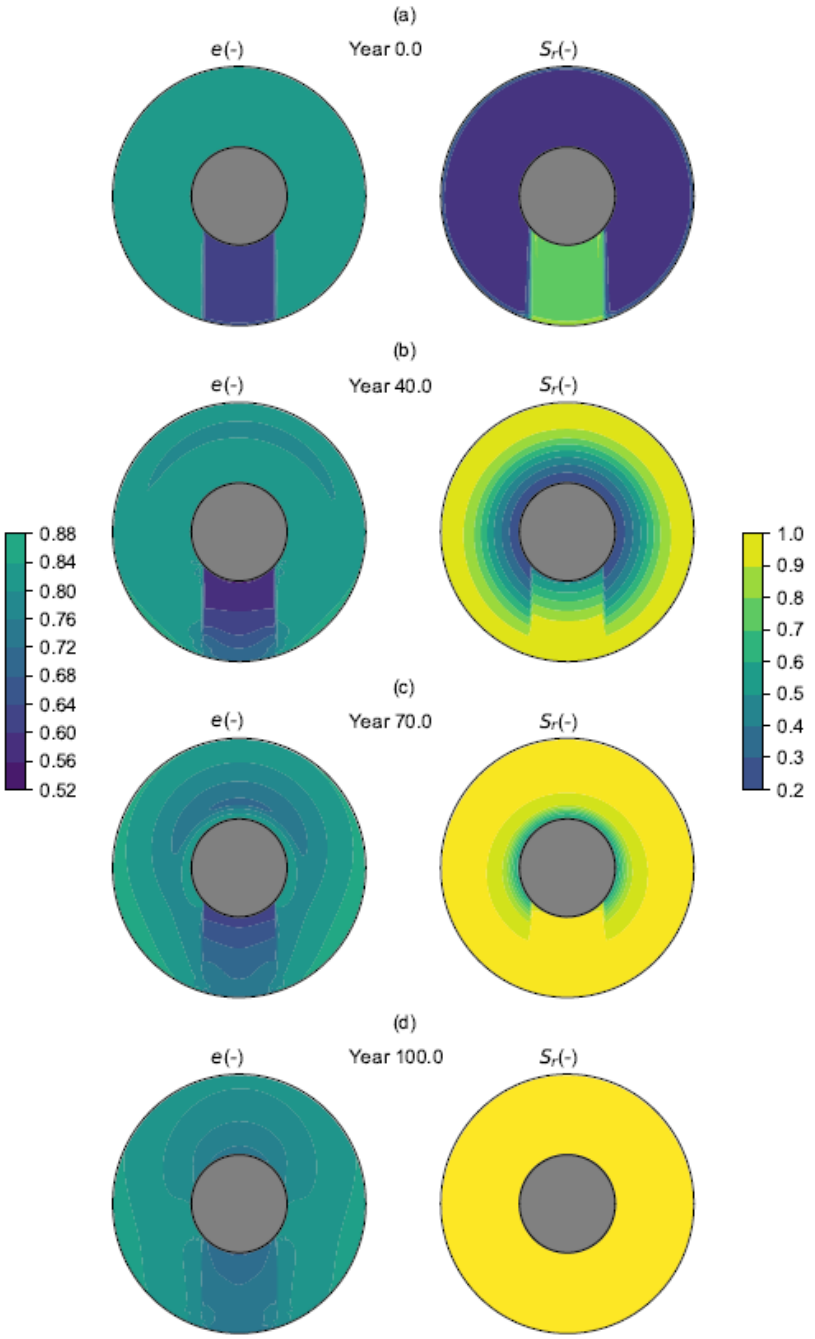

Figure 3.1-16 Predicted evolution of the spatial distribution of the void ratio and degree of saturation. a) initial state. b) After 40 years. c) After 70 years. d) After 100 years

The spatial distribution of the void ratio and the degree of saturation for the initially segregated bentonite is shown in Figure 3.1-17 at t=10, 40, 70 and 100 years. The initial distribution is not significantly modified until S_r approaches 1, although once saturated the void ratio of the granular bentonite has homogenised significantly. Comparing it with the base case it can be concluded that the initial GBM segregation does not

significantly impact the void ratio distribution after saturation and therefore does not affect the buffer performance from a THM point of view.

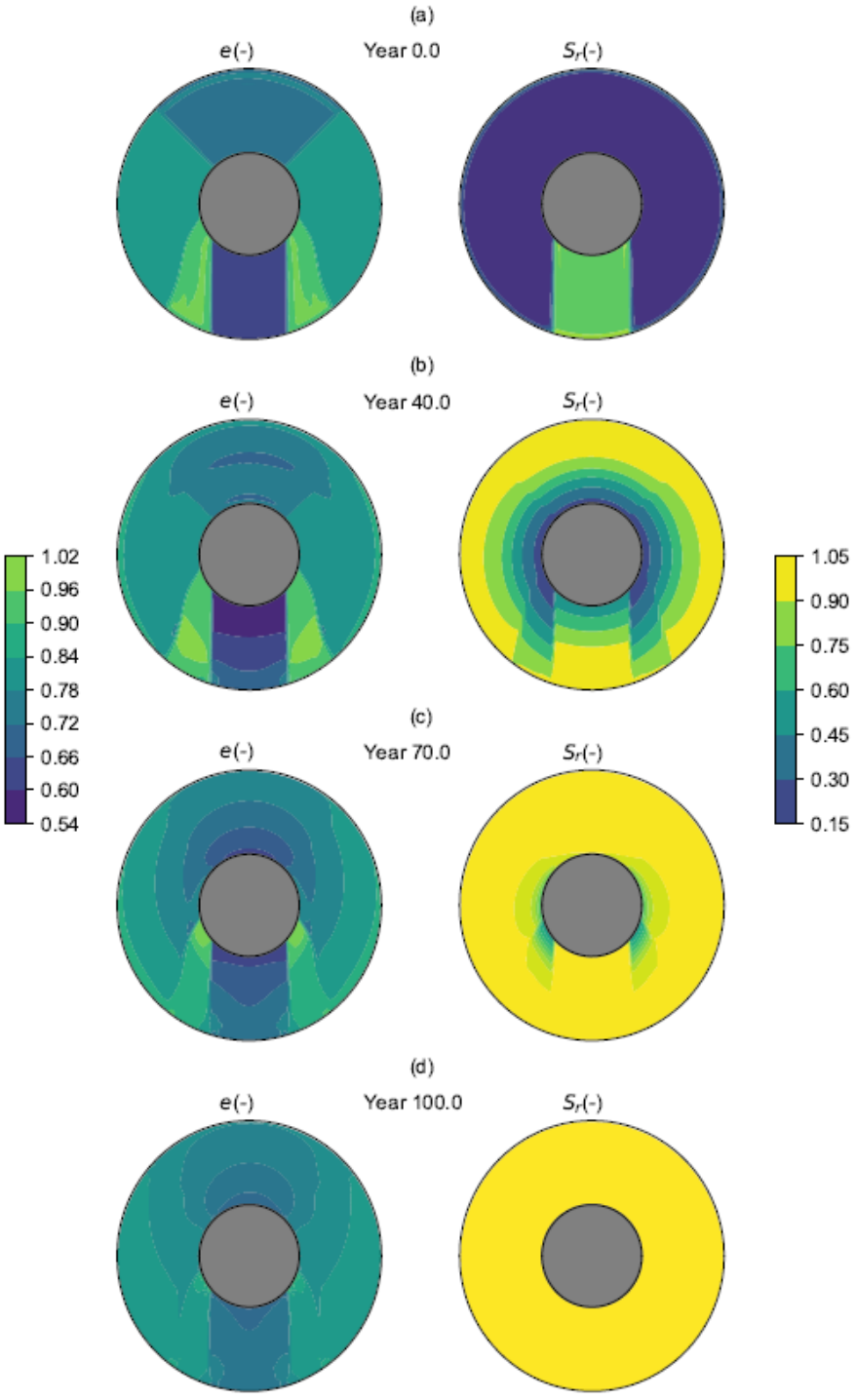

Figure 3.1-17 Evolution of the spatial distribution of the void ratio and degree of saturation in the initially segregated buffer case. a) initial state. b) After 40 years. c) After 70 years. d) After 100 years

3.1.6 Discussion

Two initial distributions of the granular backfill void ratio (or dry density) in the Nagra case have been analysed. The base case scenario supposes that the void ratio distribution of the granular pellet mixture is uniform, while the alternative case assumes a void ratio distribution affected by segregation during the emplacement. The distribution of dry density in the segregated case has been established based on the results from a full scale test. A comparison with the measurements of the FE in-situ test (5 years) provided a satisfactory validation of the model hypothesis.

The modelling predictions indicate that there are minor differences between the initially homogeneous GBM case and the initially segregated GBM case. Full saturation of the buffer is reached after 75 years in the GBM segregated case as compared to 80 years in the homogeneous GBM case. This result implicitly includes the sensitivity of the water retention curve and permeability as they depend on void ratio. In both cases the model predicts a fairly homogeneous distribution of void ratio after saturation, with the upper and lower part of the buffer presenting higher density. As a result, the segregation of the GBM does not influence significantly the magnitude and distribution of swelling pressure after saturation.

Although in both cases the canister moves downwards in the early stage as a result of the drying induced shrinkage of the pedestal, after 10 years the hydration and swelling of the pedestal blocks starts to compensate this settlement. At full saturation, the canister equilibrates about 20 mm above its initial position in the homogeneous GBM case while it remains close to the initial position in the segregated GBM case, therefore the distribution of GBM as emplaced with the backfill machine tends to restrict canister movements due to bentonite swelling.

3.2 BGR

3.2.1 Description of the models

The hydro-mechanical model with all its constitutive relations is discussed in detail in Deliverable D3.3 of the Beacon project. Additional to the balance equations described there, the first law of thermodynamics is considered in the simulations of the assessment cases. This fully coupled thermo-hydro-mechanical (THM) model formulation is analogue to Rutqvist et al. (2001) and was applied .e.g. in Nguyen et al. (2007) for a similar boundary value problem as considered in the present assessment case. Because the thermo-hydraulic coupling for the double porosity model is not implemented yet, only the single-scale hydraulic model is considered for the assessment case. The basic features of the model are:

- Richards approximation for the balance of mass of the fluid phases Richards (1931)
- Balance of linear momentum with effective stress concept and modified Cam-clay constitutive model in a small strain version analogue to Callari, Auricchio, and Sacco (1998)
- Water retention behaviour according to Van Genuchten (1980)
- Orthotropic saturation dependent power law swelling
- Balance of energy for the entire porous medium
- Vapour diffusion model of Philip and De Vries (1957)Thermal expansion of solids and fluids

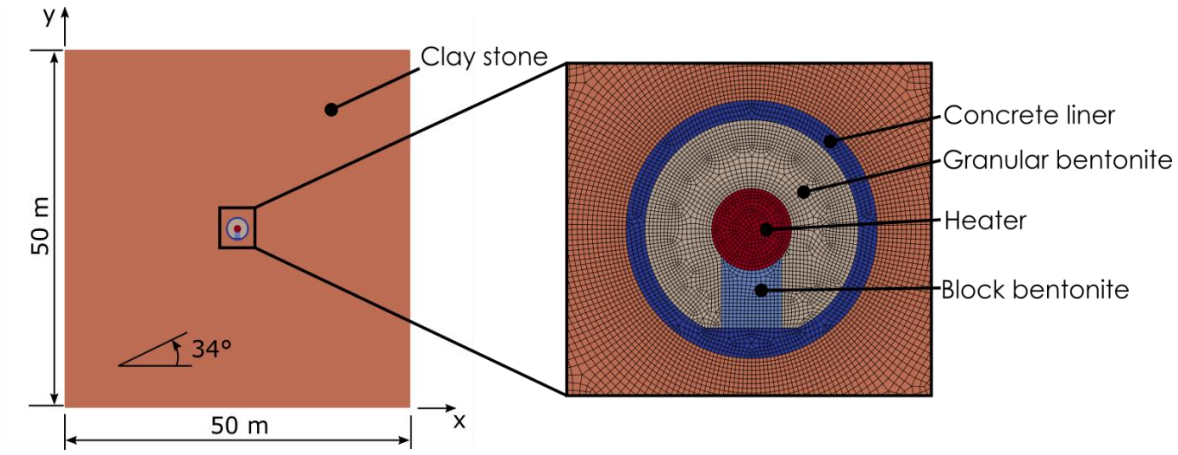

Figure 3.2-1 Simulation domain with bedding angle of 34° (left) and discretization of assessment case (right).

3.2.2 Geometry and discretization

The spent fuel (SF) canister is bedded on a pedestal of bentonite blocks and surrounded by granular bentonite material (GBM). The tunnel wall is reinforced by a concrete liner. Between the liner and the Opalinus clay host rock there is a small gap, which is not considered here. Figure 3.2-1 shows the 2-dimensional idealization of this

geometry. The pedestal is slightly simplified in order to apply a coarser mesh in this area. The dimensions of the detailed model on the right hand side of Figure 3.2-1 is taken from the specification document. The entire simulation domain is a quadrilateral of 50 m edge length. The bedding of the Opalinus clay is 34° according to Müller et al. (2018).

The finite-element model consists of 20664 unstructured Q1P1T1 elements with a plane strain hypothesis.

3.2.3 Input parameters

The input parameters for material characterisation are mainly taken from the specification document and from Senger, Papafotiou, and Marschall (2014). The plastic parameters of the bentonite material are taken from task 3 of work package 3 which itself adapts the parameters from Åkesson, Börgesson, and Kristensson (2010). For the concrete liner the material parameters are taken from Jobmann (2019). The parameters for the water phase are summarized in

Parameter	Viscosity	Specific heat capacity	Thermal conductivity	Thermal expansivity
Unit	$Pa\,s$	$J/(K\,kg)$	$W/(m\,K)$	$1/K$
Value	1e-3	4181.3	0.598	4e-4

Table 3.2-1 and those for the solid materials in Table 3.2-2, respectively. For some material parameters the chosen values slightly deviate from the given sources in order to calibrate the model. The corresponding parameters are highlighted in Table 3.2-2. The tortuosity for the vapour diffusion model is estimated to be 0.8.

Table 3.2-1 Water material parameters for the simulation model.

Parameter	Viscosity	Specific heat capacity	Thermal conductivity	Thermal expansivity
Unit	$Pa\,s$	$J/(K\,kg)$	$W/(m\,K)$	$1/K$
Value	1e-3	4181.3	0.598	4e-4

Table 3.2-2 Solid material parameters for the simulation model.

Parameter	Unit	Clay	GBM	Block	Liner	Heater	Comment
Specific heat capacity	$J/(K\ kg)$	995[1]	893[1]	1058[1]	880[1]	440[1]	[1]grain quantity
Thermal conductivity	$W/(m\ K)$	1.25[1] ∥ [2] 2.15[1] ⊥ [3]	0.3-1.3[1]	0.8-1.3[1]	0.7[1]	52.5[1]	[1]grain quantity [2]paralell to bedding [3]perpendic-ular to bedd.
Thermal expansivity	K^{-1}	1.5e-5	2.5e-5	2.5e-5	1.3e-6	1.2e-5	
Mass density	kg/m^3	2700	2700	2700	2300	7850	
Young's modulus	MPa	6000	100[1]	100[1]	17000	2.10e5[2]	[1]magnitude used in previous tasks [2]steel
Poisson's ratio	-	0.27	0.35[1]	0.35[1]	0.2	0.3	[1](Ballarini, Graupner, and Bauer 2017)
Swelling parameter	MPa	0	20e6	20e6	0	0	
Slope critical state line	-	-	0.24[1]	0.24[1]	-	-	[1]delivarble 3.3
Preconsolidation pressure	MPa	-	5e5	2e6	-	-	[1]delivarble 3.3
Swelling exponent	-	2	2	2	2	2	
Initial porosity	-	0.12	0.45	0.4	0.15[1]	0.0001	[1]estimate
Transport porosity	-	0.08[1]	0.3[1]	0.3[1]	0	0	[1]estimate

Intrinsic permeability	m^2	1e-20 [1] 2e-21 $\perp$ [2]	3.5e-20	2.5e-21	1e-17	1e-50	[2]paralell to bedding [3]perpendic-ular to bedd.
Initial saturation	-	1	0.2	0.63	1	0	
Biot coefficient	-	1	1	1	1	1	
Permeability model	Model:	Exponential porosity dependent			Constant		[1]estimate
	n in -	7[1]	7[1]	7[1]			
Relative permeability	Model:	Van Genuchten[1]					[1]Van Genuchten (1980) [2]shape factor [3]entry pressure [4]minimal permeability
	m [-] [2]	0.4012	0.4012	0.2958	0.55	Constant	
	p_b [MPa] [3]	18e6	10e6	21.9e6	1.5e5		
	ε_{min} [m^2] [4]	1e-6	1e-6	1e-6	1e-6		
Water retention	Model:	Van Genuchten[1]					[1]Van Genuchten (1980) [2]shape factor [3]entry pressure
	m [-] [2]	0.4012	0.4012	0.2958	0.55	Constant	
	p_b [MPa] [3]	18e6	10e6	21.9e6	1.5e5		

3.2.4 Initial and boundary conditions

In order to determine the initial stress state in the host rock a linear-elastic mechanical model is solved prior to the THM simulation. The traction boundary conditions are chosen to yield an initial stress state of $\sigma_x = 4$ MPa and $\sigma_y = 7$ MPa according to the in situ measurements reported in Martin and Lanyon (2003). Additionally the self-weight is considered as external load yielding a compressive stress state in the backfilling. The boundary conditions are shown in Figure 3.2-2. The resulting stress distribution in the host rock is shown in Figure 3.2-3.

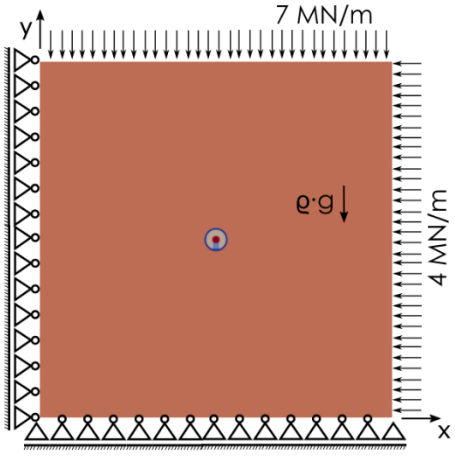

Figure 3.2-2 Linear elastic model for initial stress determination.

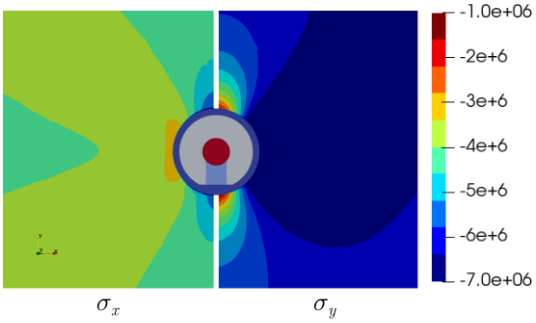

Figure 3.2-3 Stress distribution around excavation.

Measurements in Mont Terri show that the pore pressure p_0 in the undisturbed host rock is about 2 MPa, see e.g. Martin and Lanyon (2003). For the granular bentonite material and the bentonite block material the initial pressure is chosen in order to yield the specified degree of saturation in accordance to the chosen retention behaviour.

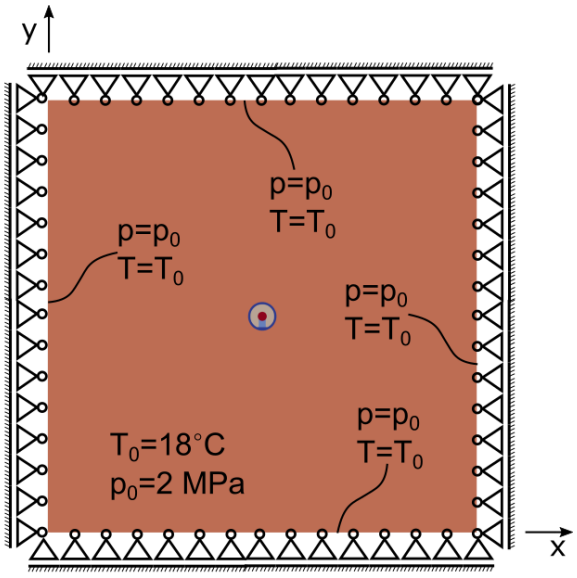

Figure 3.2-4 Boundary and initial conditions for the THM model.

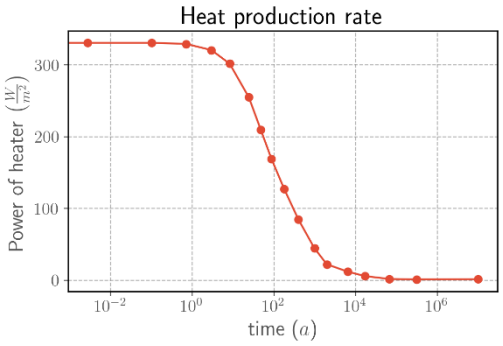

Figure 3.2-5 Heat production rate per unit area over time.

The initial temperature is $T_0 = 18\,°C$ within the host rock. For the bentonite material and the heater domain an initial temperature of $T_0 = 20\,°C$ is considered. In the THM model, zero-displacement is prescribed on the entire outer boundary in the normal direction as depicted in Figure 3.2-4. For the pressure and the temperature degree of freedom,

Dirichlet boundary conditions are applied as well. The heat power generated by the nuclear waste is modelled as thermal source term. The heater curve from Senger, Papafotiou, and Marschall (2014) was digitized and scaled to represent a heat source per unit area and depth. With this approach a canister of infinite length is modelled. Therefore, the resulting curve was scaled by a factor of 0.8 in order to achieve the peak temperature given in the specification document and truncate the length of the canister. The applied heat source curve is displayed in Figure 3.2-5.

Due to the backfilling process the initial dry density or equivalently the porosity of the granular bentonite material is not homogeneous. The initial dry density distribution of the granular bentonite material is computed by an inverse distance weighting function according to Shepard (1968) of 15 sample points taken from figure 12 of the specification document to emulate a non-uniform distribution. The resulting distribution is shown in Figure 3.2-6.

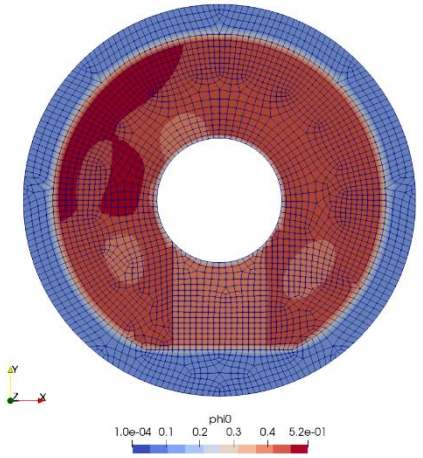

Figure 3.2-6 Initial porosity distribution according to figure 12 of the specification document.

3.2.5 Results

Due to the pressure gradient between host rock and bentonite the fluid flows from the host rock and increases the degree of saturation. Since the clay rock and the concrete liner are assumed to be fully saturated at the beginning, the saturation process in the granular bentonite material is nearly homogeneous as could be seen for two points in the granular material in Figure 3.2-7. The entire saturation process took about 20 years. The evolution of saturation in the bentonite block starts a little bit later because of its reduced intrinsic permeability. The porosity evolution in bentonite block is more pronounced as could be seen in Figure 3.2-7. The porosity in the block increases, so the dry density decreases due to the swelling mechanism. In comparison, the porosity

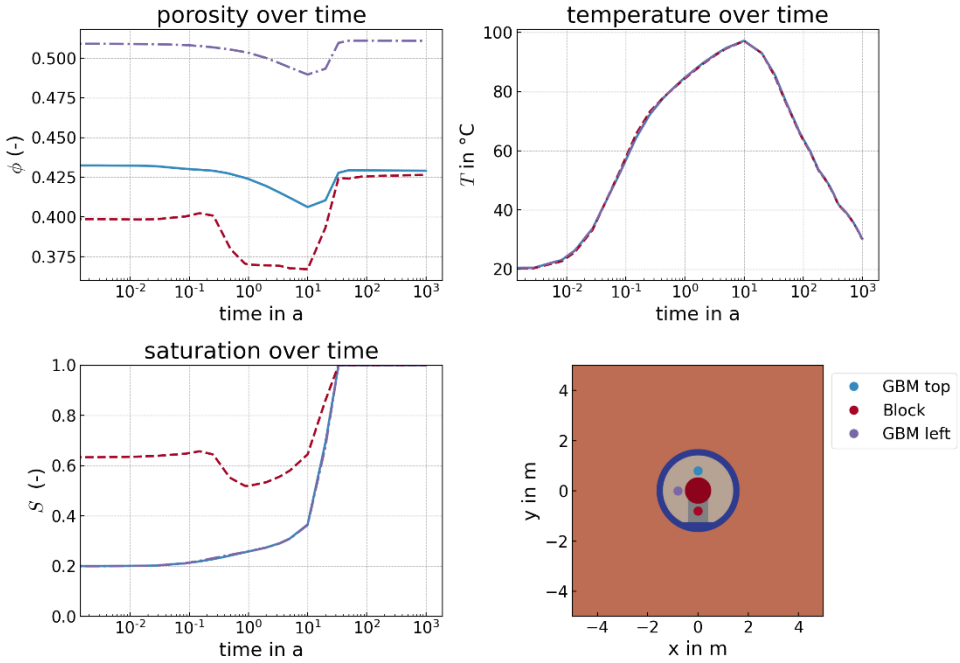

Figure 3.2-7 Time history plots of porosity, temperature and saturation for three points.

of the granular bentonite material decreases only slightly. The porosities between bentonite block and granular bentonite material homogenize over time as could be seen in Figure 8. As shown in Figure 8, the porosity evolution is strongly coupled to the evolution of the degree of saturation.

In Figure 3.**2-8** the profiles along a vertical line through the bentonite are shown. There is no sharp front where the porosity evolves. The increase of porosity is homogeneously distributed over the block. In Figure 3.2-9 the same profiles are shown for the GBM. Here, the initial inhomogeneous porosity distribution is visible. There seems to be no influence of the inhomogeneity on the swelling behaviour.

In Figure 3.**2-10** and Figure 3.**2-11** the degree of saturation is shown for different times

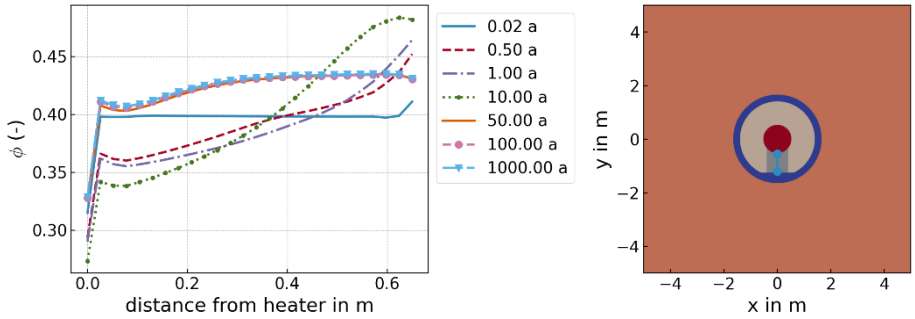

Figure 3.2-8 Porosity profiles for different times in the bentonite block.

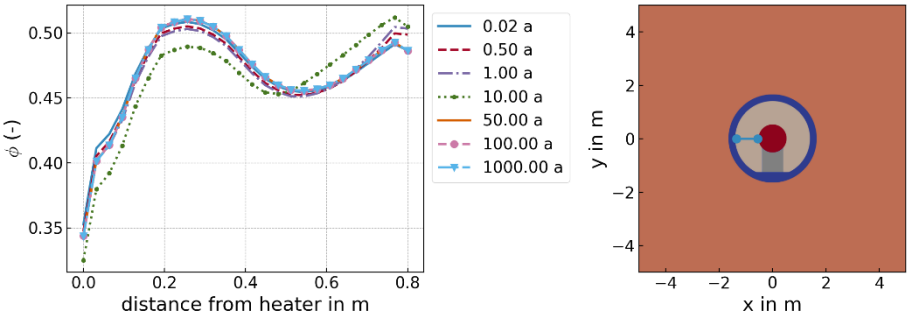

Figure 3.2-9 Porosity profiles for different times in the granular bentonite material.

through the block and through the granular material, respectively. The saturation front rises from the concrete liner. In the vicinity of the heater the bentonite desaturates due to vapour diffusion.

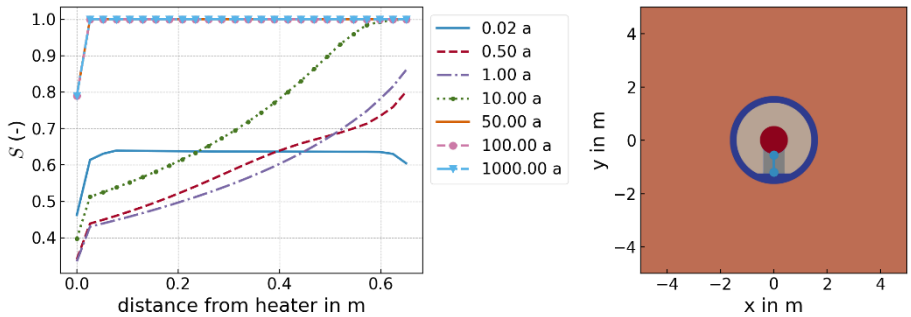

Figure 3.2-10 Saturation profiles for different times in the bentonite block.

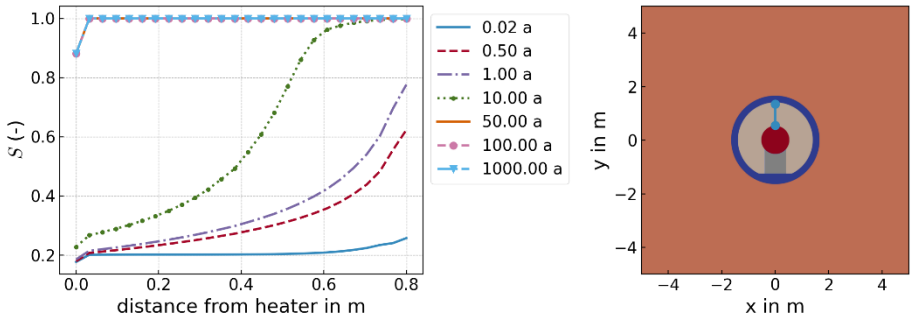

Figure 3.2-11 Saturation profiles for different times in the granular bentonite material.

In Figure 3.2-13, different profiles across the backfilling domain are shown exemplarily for the time of 10 years. A homogeneous behaviour is observed along the lines in the GBM regarding degree of saturation and porosity and temperature. Here again the inhomogeneous porosity distribution seems to have no significant influence onto the saturation process.

If we now focus on the temperature, we can first identify the 34° bedding angle of the Opalinus clay in Figure 3.2-12 due to the orthotropic thermal conductivity applied here. After ca. 10 years the temperature reaches a maximum at the heater surface shown in Figure 3.2-14. The peak temperature is 107 °C. The temperature in the GBM Material is slightly higher due to lower conductivity as can be seen in Figure 3.2-7.

Within the specification document an uplift of the heater was reported. In Figure 3.2-15 the vertical displacement at the heater base is shown predicting an uplift of 1.5 cm after 10 years.

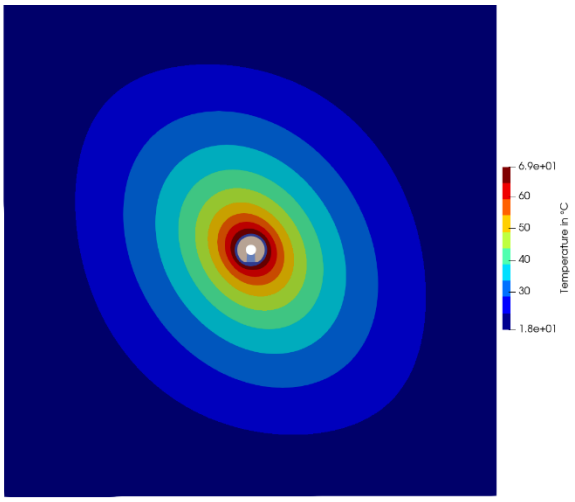

Figure 3.2-12 Temperature distribution at time t=10 a.

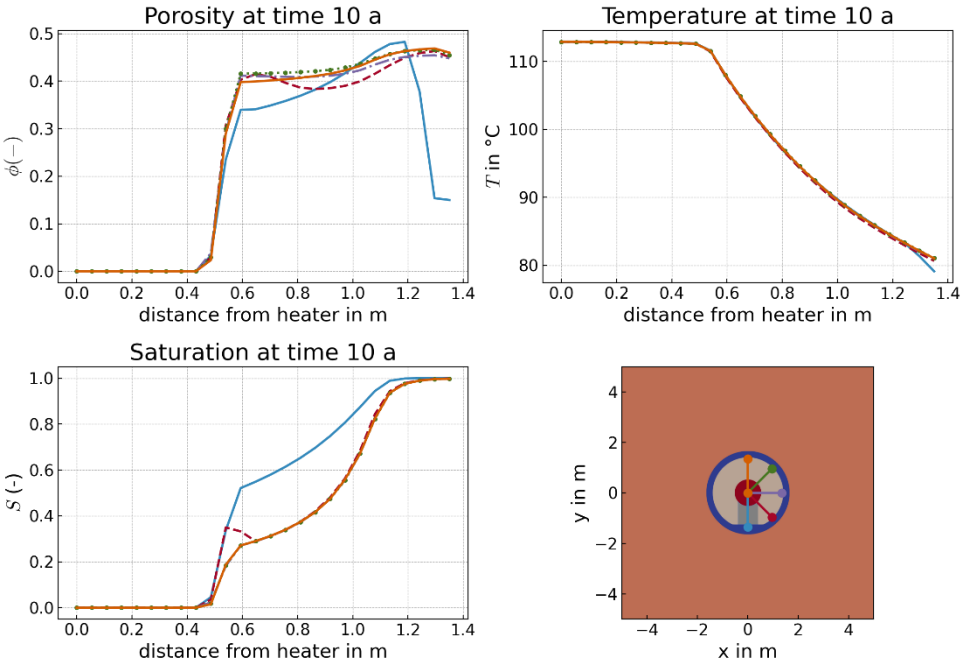

Figure 3.2-13 Profiles of porosity, temperature and saturation over different lines in the backfilling zone.

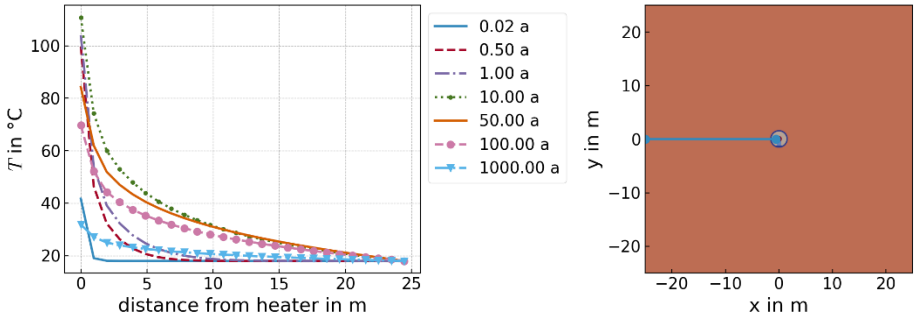

Figure 3.2-14 Temperature evolution in the domain.

In

Figure 3.2-16 the time history plots for liquid pressure, horizontal and vertical stress at three points are shown. In the first year the stresses evolve only due to the thermal expansion of the materials, hence the evolution is slow. When the saturation process becomes faster, swelling of the bentonite materials is the dominating effect. Initially the preconsolidation pressure in the granular bentonite material is one magnitude smaller than the preconsolidation pressure of the block material, the resulting stress curves are nearly coincident. After 1000 years stationarity in the stress fields is not fully reached.

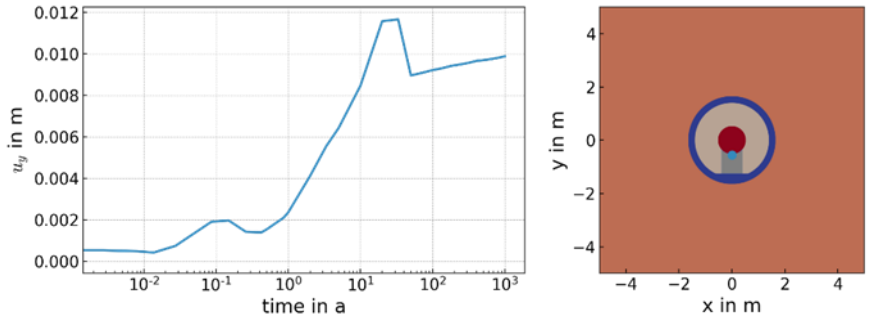

Figure 3.2-15 Uplift of the heater

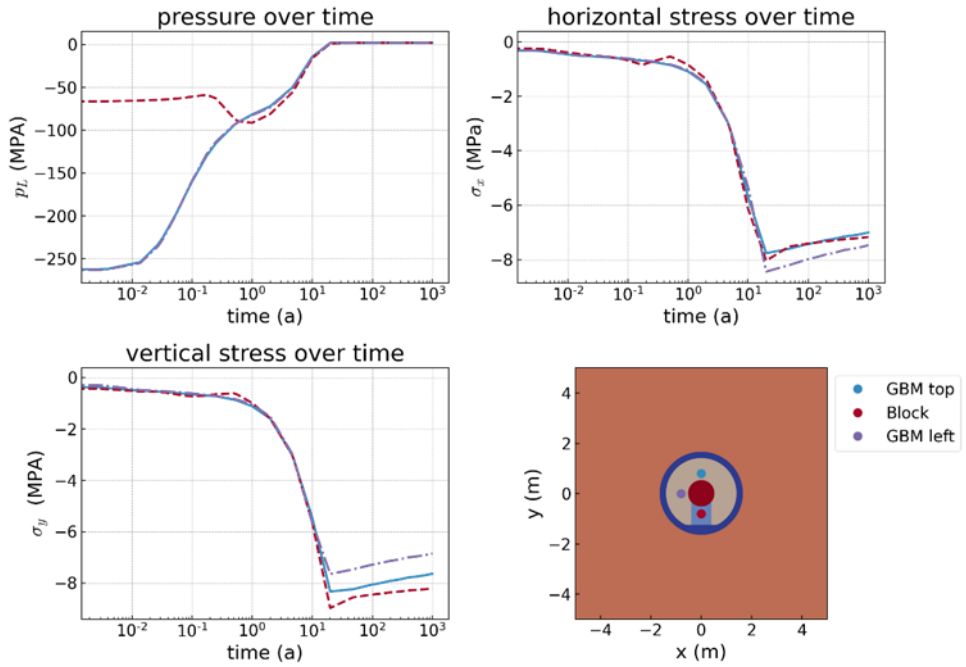

Figure 3.2-16 Time history plot of liquid pressure, vertical and horizontal pressure for three points

3.2.6 Discussion

The model is able to reflect the basic effects of temperature distribution and porosity evolution: increasing in the block material while the porosity in the GBM is reduced. Also, the vertical uplift of the heater and a homogenisation between block and granular bentonite can be simulated.

To improve the results further the initial boundary value problem can be refined. The hydraulic initial conditions have a significant influence on the saturation process in the bentonite material. In the model presented so far, the excavation of the tunnel and the ventilation phase was not explicitly modelled. Therefore, the initial state of a fully saturated host rock and concrete liner is a simplified assumption. In further assessment cases these two emplacement phases should be addressed as well to capture the

initial state of liquid saturation more accurately. Furthermore, the real process is three dimensional and realistic results can only be achieved by a 3D model. In order to study the model and try to reproduce the observed effects the 2D approximation is suitable.

It can be seen from the results, that the evolution of saturation within the GBM is quite homogeneous. This is mainly related through a small exponent ($n = 7$) of the porosity dependent permeability model, because currently this significantly influences the stability of the solution. With the porosity dependent permeability model active a sharp saturation front evolves. This results in high swelling strains and so the permeability is further reduced leading to an almost impermeable layer. By investigating the numerical stability of the porosity dependent permeability model and a comparison of parameters with some previous test cases of BEACON this drawback can be eliminated.

During the modelling of the assessment case we recognized a strong dependence of the results on the parameters of the chosen water retention behaviour. Since the entire process is driven by the saturation of bentonite material, an accurate description of the retention behaviour is necessary. The initial saturation of the bentonite material defines the fluid pressure by the chosen retention curve. This pressure can be seen as a potential for the mechanical work done in the system and therefore has a significant influence on the model.

Via the swelling stress parameter the final porosity can be calibrated. Since the material parameters for the GBM and the bentonite block material are comparable, the resulting volumetric strains directly depend on the amount of swelling strain. Up to now, the swelling strain is only a function of the liquid saturation. Inhomogeneous distributions of the dry density or the porosity, respectively, do not lead to a different evolution of swelling strains. This is not realistic. Therefore, the homogenization process takes only place between the bentonite block and the granular bentonite material and not within the granular bentonite material.

3.3 UPC

3.3.1 Description of the model

An important development performed within the BEACON project is the first introduction of temperature effects in the double structure constitutive model that had been used in the analyses of the other benchmarks in the project. Although the incorporation of thermal effects is still at an early stage and requires further work (notably at integration algorithm and verification level), it has been decided to use if in the analysis of the NAGRA assessment because of its non-isothermal nature. For this reason, the results reported here should be viewed as provisional and subject to modification.

For conciseness, only the parts of the formulation and constitutive models affected by the introduction of temperature effects are included in this description. Special attention is paid to the mechanical constitutive model, the key ingredient in the issues addressed in the Beacon project. The full descriptions of the formulation and constitutive laws are provided in Deliverable 3.3 of the project: *Description of the constitutive models developed in the Beacon project - Final report from WP3*. Table 3.3-1contains the notation required to interpret the model equations.

Table 3.3-1 General variable notation for the mathematical description of the double porosity formulation

$(\dot{\blacksquare})$	Incremental (or rate) form of a generic variable.
$(\blacksquare)_\alpha$, $(\blacksquare)_\beta$, $(\blacksquare)_{\alpha\beta}$	Subscripts used to identify the structural level ("$\beta \equiv m$" for microstructure; "$\beta \equiv M$" for macrostructure) and/or phases ("$\alpha \equiv s$" for solid; "$\alpha \equiv l$" for liquid; "$\alpha \equiv g$" for gas).
$(\blacksquare)^\gamma$	Superscript used to identify the species present in the porous medium ("$\gamma \equiv s$" for solid grains (mineral); "$\gamma \equiv w$" for water; "$\gamma \equiv a$" for air).
V_s; $V_{\alpha\beta}$; V	Volume of the solid species/phase; volume of the α phase (liquid or gas) in the β-structural medium; total volume of the porous medium.
V_p; $V_{p,\beta}$	Total volume of pores in the soil; volume of pores in the β-structural medium.
$(\blacksquare)_\beta$; $\overline{(\blacksquare)}_\beta$	Variable evaluated respect to the volume occupied by the β-structural level; variable evaluated respect to the total volume of the soil.
ϕ; ϕ_β	Total porosity; porosity of the β-structural medium respect to its actual volume.
$\bar{\phi}_\beta$	Pore volume fraction of the β-structural medium.
ρ_s; $\rho_{\alpha\beta}$	Local density of the solid; local density of the α phase in the β-structural medium.
$\omega_{\alpha\beta}^\gamma$	Mass fraction of the γ species (solid, water or gas), in the α phase, in the β-structural medium.
$\theta_{\alpha\beta}^\gamma$	Partial density of the γ species, in the α phase, in the β-structural medium.

$m_{\alpha\beta}$; $m^{\gamma}_{\alpha\beta}$	Mass of the α phase in the β-structural medium; mass of the γ species (solid, water or gas), in the α phase, in the β-structural medium.
S_{α}; $S_{\alpha\beta}$	Degree of saturation of the α phase in the soil; degree of saturation of the α phase in the β-structural medium.
s_{β}	Suction at the β-structural level.
E_{α}	Specific internal energy of the α phase.
$\boldsymbol{j}'^{\gamma}_{\alpha\beta}$	Flux of the γ species, in the α phase, in the β-structural medium respect to the solid skeleton.
$\boldsymbol{q}_{\alpha\beta}$	Advective flux of the α phase in the β-structural medium.
$\boldsymbol{i}_c$	Conductive heat flux.
$\boldsymbol{\sigma}$, $\boldsymbol{\sigma}_{\beta}$; σ_t	Effective stress tensor for the whole porous medium and for the β-structural medium; total stress tensor.

Energy balance equation

In non-isothermal problems, it is necessary to consider an additional balance equation that expresses the conservation of energy.

The assumption of local thermal equilibrium among the phases implies that the equation for the internal energy balance is established for the porous medium as a whole by accounting for the energy stored in each phase. In the context of a double porosity approach and using the notation presented in Table 3.3-1, the energy balance equation reads:

$$\begin{aligned}\frac{D_s(E_s\rho_s)}{Dt}(1-\phi)+\frac{D_s\left(E_l\rho_{lm}S_{lm}+E_g\rho_{gm}S_{gm}\right)}{Dt}\bar{\phi}_m+\frac{D_s\left(E_l\rho_{lM}S_{lM}+E_g\rho_{gM}S_{gM}\right)}{Dt}\bar{\phi}_M\\ +\left(E_l\rho_{lm}S_{lm}+E_g\rho_{gm}S_{gm}\right)\dot{\bar{\varepsilon}}^{v}_{m}+\left(E_l\rho_{lM}S_{lM}+E_g\rho_{gM}S_{gM}\right)\dot{\bar{\varepsilon}}^{v}_{M}\\ +\quad\nabla\cdot\left(\boldsymbol{i}_c+E_l\rho_{lM}\boldsymbol{q}_{lM}+E_g\rho_{gM}\boldsymbol{q}_{gM}\right)\\ =\mathrm{f}^{Q}-\left(E_l\rho_{lm}S_{lm}+E_g\rho_{gm}S_{gm}-E_s\rho_s\right)(1-\phi)\frac{\dot{\rho}_s}{\rho_s}\end{aligned} \quad (1)$$

where E_{α} is the specific internal energy of the α phase; f^{Q} is an internal/external energy supply per unit volume of soil; $\boldsymbol{i}_c$ represents the heat flux by conduction through the porous medium and $\boldsymbol{q}_{lM}$, $\boldsymbol{q}_{gM}$ are the macro-structural advective fluxes of the liquid and gas phases with respect to the solid phase, respectively.

Thermal constitutive equations

Heat conduction through the soil ($\boldsymbol{i}_c$) is driven by temperature gradients (∇T) and described by Fourier's law according to:

$$\boldsymbol{i}_c = -\lambda \cdot \nabla T \tag{2}$$

where the global thermal conductivity of the porous medium (λ) is usually expressed as a function of the thermal conductivity of each phase in the soil (λ_α), porosity (ϕ) and degree of saturation (S_l), that is,

$$\lambda = f(\lambda_\alpha, \phi, S_l) \tag{3}$$

In double porosity media, the thermal conductivity becomes dependent not only on the water content in the two pore-structure domains but also on the pore volume fraction of each structural medium. Thus, the global thermal conductivity is evaluated in terms of an average degree of saturation (S_l), which is defined as:

$$S_l = \frac{\bar{\phi}_m}{\phi} S_{lm} + \frac{\bar{\phi}_M}{\phi} S_{lM} \tag{4}$$

Mechanical constitutive equation

A direct consequence of assuming the expansive clay as two distinct but interacting continuum media is the possibility of establishing distinct stress-strain constitutive relationships for each structural level. The coupling between these two porous media is accomplished through mass transfer processes and strain coupling mechanisms that account for the portion of macro-structural strains arising from the deformations that occur at particle level (microstructure).

The generalized stress-strain relationship for the β-structural domain can be expressed by:

$$\dot{\boldsymbol{\sigma}}_\beta = \left[\boldsymbol{D}_\beta\right]\dot{\boldsymbol{\varepsilon}}_\beta + \boldsymbol{h}_{l\beta}\dot{P}_{l\beta} + \boldsymbol{h}_{g\beta}\dot{P}_{g\beta} + \boldsymbol{h}_{T\beta}\dot{T} \tag{5}$$

where $\dot{\boldsymbol{\sigma}}_\beta$ is the constitutive stress rate vector, $\dot{\boldsymbol{\varepsilon}}_\beta$ is the strain rate vector, $\left[\boldsymbol{D}_\beta\right]$ is the constitutive stiffness matrix, $\boldsymbol{h}_{l\beta}$, $\boldsymbol{h}_{g\beta}$ are the generic constitutive vectors relating changes in liquid and gas pressures, respectively, to stress increments and $\boldsymbol{h}_{T\beta}$ is a constitutive vector relating stress to temperature changes.

It is assumed that the macro-pore structure can be affected by the micro-structural deformations. Consequently, it is reasonable to define a macro-structural strain component that expresses such a mechanical coupling ($\dot{\bar{\boldsymbol{\varepsilon}}}_{m\to M}$). In contrast, it is assumed that the micro-structural behaviour is not affected by the deformations of the macrostructure. Consequently, plastic changes in the soil fabric are caused by the

loading-collapse mechanism (LC mechanism) and by the micro-macro structural coupling mechanism (beta mechanism). Thus, the strain decomposition in the double structure media can be expressed as:

$$\dot{\boldsymbol{\varepsilon}} = \dot{\boldsymbol{\varepsilon}}^e + \dot{\boldsymbol{\varepsilon}}^p = \left(\dot{\boldsymbol{\varepsilon}}_m^e + \dot{\boldsymbol{\varepsilon}}_M^e\right) + \dot{\boldsymbol{\varepsilon}}_M^p \quad (6)$$

Elastic behaviour

Taking into account the strain decomposition given in (6), the elastic behaviour of the expansive soil is completely described by its micro-structural and macro-structural strain components. In the context of THM analyses, the elastic strain component associated with the microstructure, $\dot{\boldsymbol{\varepsilon}}_m^e$, can be split into a hydro-mechanical component, $\left(\dot{\boldsymbol{\varepsilon}}_m^e\right)_{\Delta\sigma,\Delta P_\alpha}$, and a thermal component, $\left(\dot{\boldsymbol{\varepsilon}}_m^e\right)_{\Delta T}$, as follows:

$$\dot{\boldsymbol{\varepsilon}}_m^e = \left(\dot{\boldsymbol{\varepsilon}}_m^e\right)_{\Delta\sigma,\Delta P_\alpha} + \left(\dot{\boldsymbol{\varepsilon}}_{m,}^e\right)_{\Delta T} \quad (7)$$

where

$$\left(\dot{\boldsymbol{\varepsilon}}_m^e\right)_{\Delta\sigma,\Delta P_\alpha} = [\bar{\boldsymbol{D}}_m^e]^{-1}\dot{\boldsymbol{\sigma}}_m = [\bar{\boldsymbol{D}}_m^e]^{-1}\dot{\boldsymbol{\sigma}} + \frac{1}{3\bar{K}_m}\cdot\mathcal{H}\left(S_{lm}, P_{lm}, P_{gm}, T\right)\boldsymbol{m} \quad (8)$$

$$\left(\dot{\boldsymbol{\varepsilon}}_{m,}^e\right)_{\Delta T} = \frac{1+e_m}{1+e}\cdot\left(\dot{\boldsymbol{\varepsilon}}_m^e\right)_{\Delta T} \quad (9)$$

In those expressions, $[\bar{D}_m^e]$ and $\dot{\boldsymbol{\sigma}}_m$ are the elastic constitutive stiffness matrix and the generalized Bishop effective stress vector for the microstructure; $\bar{K}_m$ is the volumetric elastic modulus of the micro-structural medium; $\dot{\boldsymbol{\sigma}}$ is the net effective stress vector (for the soil); $\mathcal{H}$ represents a non-linear function of temperature, saturation and fluid pressures in micro-pores; and $\boldsymbol{m} = [1 \quad 1 \quad 1 \quad 0 \quad 0 \quad 0]^t$ is an auxiliary vector. Equation (9) establishes the relationship between the thermal component of the micro-structural strain, $\left(\dot{\boldsymbol{\varepsilon}}_m^e\right)_{\Delta T}$, and the elastic thermal expansion of each clay particle/aggregate (microstructure), $(\dot{\boldsymbol{\varepsilon}}_m^e)_{\Delta T}$.

The elastic deformations of the solid skeleton (macrostructure), $\dot{\boldsymbol{\varepsilon}}_M^e$, can be also described by means of a hydro-mechanical component, $\left(\dot{\boldsymbol{\varepsilon}}_M^e\right)_{\Delta\sigma,\Delta P_\alpha}$, and a thermal strain component, $\left(\dot{\boldsymbol{\varepsilon}}_M^e\right)_{\Delta T}$:

$$\dot{\boldsymbol{\varepsilon}}_M^e = \left(\dot{\boldsymbol{\varepsilon}}_M^e\right)_{\Delta\sigma,\Delta P_\alpha} + \left(\dot{\boldsymbol{\varepsilon}}_M^e\right)_{\Delta T} \tag{10}$$

where

$$\left(\dot{\boldsymbol{\varepsilon}}_M^e\right)_{\Delta\sigma,\Delta P_\alpha} = [\bar{\boldsymbol{D}}_M^e]^{-1}\dot{\boldsymbol{\sigma}} + \frac{1}{3\bar{K}_s}\dot{s}_M\boldsymbol{m} + \left(\dot{\boldsymbol{\varepsilon}}_{m\to M}^e\right)_{\Delta\sigma,\Delta s_M} \tag{11}$$

$$\left(\dot{\boldsymbol{\varepsilon}}_M^e\right)_{\Delta T} = \left(\dot{\boldsymbol{\varepsilon}}_{m\to M}^e\right)_{\Delta T} = \dot{\boldsymbol{\varepsilon}}_{\Delta T}^e - \left(\dot{\boldsymbol{\varepsilon}}_m^e\right)_{\Delta T} \tag{12}$$

where $[\bar{D}_M^e]$ is the elastic constitutive matrix for the macrostructure; $\bar{K}_s$ is the volumetric elastic modulus related to changes in the macro-structural suction, $\dot{s}_M$; $\dot{\boldsymbol{\varepsilon}}_{\Delta T}^e$ is the elastic thermal expansion of the soil (as a whole), defined as:

$$\dot{\boldsymbol{\varepsilon}}_{\Delta T}^e = \frac{1}{3K_T}\dot{T}\boldsymbol{m} \tag{13}$$

where K_T is the thermal bulk modulus of the porous medium. The preliminary assumption of fully reversible thermal strains in the mathematical formulation of the present double porosity model imposes that the porous skeleton must undergo the same thermal expansion experienced by the solid particles (clay particle/aggregate) when temperature changes, i.e. $\dot{\boldsymbol{\varepsilon}}_{\Delta T}^e = (\dot{\boldsymbol{\varepsilon}}_m^e)_{\Delta T}$. Consequently, the macro-structural component of the elastic thermal strains in Equation (12) can be written as:

$$\left(\dot{\boldsymbol{\varepsilon}}_M^e\right)_{\Delta T} = \bar{\phi}_M\dot{\boldsymbol{\varepsilon}}_{\Delta T}^e = \frac{\bar{\phi}_M}{3K_T}\dot{T}\boldsymbol{m} \tag{14}$$

The elastic bulk moduli, $\bar{K}_M$, $\bar{K}_s$ and K_T, are defined by the following expressions:

$$\bar{K}_M = \frac{(1+e_M)p}{\bar{\kappa}_M} \tag{15}$$

$$\bar{K}_s = \frac{(1+e_M)(s_M+p_{atm})}{\bar{\kappa}_s} \tag{16}$$

$$K_T = \frac{1}{\alpha_0 + 2\alpha_2\Delta T} \tag{17}$$

where p is the net mean effective stress, p_{atm} is the atmospheric pressure and $\bar{\kappa}_M$, $\bar{\kappa}_s$, α_0 and α_2 are model parameters. It is important to remark that the "macro" void ratio parameter in such expressions (e_M) is estimated without taking into account the fraction of pores within the clay particles/aggregates, that is,

$$e_M = \frac{\bar{\phi}_M}{1 - \bar{\phi}_M} \tag{18}$$

The assumption of no fabric changes in the elastic range entails a geometrical restriction that links the elastic moduli of the microstructure ($\bar{K}_m$) and the macrostructure ($\bar{K}_M$). This coupling between elastic parameters leads to the following relationships:

$$K = K_m = \left(\frac{1+e}{1+e_m}\right)\bar{K}_m \tag{19}$$

$$K = \bar{\phi}_M \bar{K}_M \tag{20}$$

$$\bar{K}_m = \left(\frac{e - e_m}{1+e_m}\right)\bar{K}_M \tag{21}$$

where K and K_m are the bulk moduli of the expansive soil and the individual clay particle/aggregate, respectively.

Plastic Loading-Collapse mechanism

The plastic loading-collapse (LC) mechanism of the double porosity formulation is defined by the same set of equations and parameters that describe the single-porosity, thermo-elastoplastic Barcelona Basic Model (BBM). The yield surface for a general state, expressed in terms of the stress invariants (p, J, θ), is given by:

$$F_{LC} = 3J^2 - \left(\frac{g_F(\theta, \alpha_F)}{g_F\left(-\frac{\pi}{6}, \alpha_F\right)}\right)^2 \cdot M_F^2 \cdot (p + p_s) \cdot (p_0 - p) = 0 \tag{22}$$

where M_F is the slope of the critical state line, g_F is a function of Lode's angle (θ), α_F is a model parameter and p_s expresses the dependence of the shear strength on macro suction and temperature, according to:

$$p_s = p_{s0} + k_s \cdot s_M \cdot exp(-\rho_T \cdot \Delta T) \quad (23)$$

where p_{s0} is the tensile strength in saturated conditions; k_s and ρ_T are model parameters that control the dependence of p_s on the macro suction and temperature, respectively. The apparent unsaturated pre-consolidation pressure (p_0), that defines the locus of activation of irreversible deformations due to loading increments or macro-structural collapse, is given by:

$$p_0 = p_c \cdot \left(\frac{p_{0,T}^*}{p_c}\right)^{\frac{\lambda_{(0)} - \bar{\kappa}_M}{\lambda_{(s_M)} - \bar{\kappa}_M}} \quad (24)$$

where:

$$p_{0,T}^* = p_0^* + 2(\alpha_1 \cdot \Delta T + \alpha_3 \cdot \Delta T \cdot |\Delta T|) \quad (25)$$

$$\lambda_{(s_M)} = \lambda_{(0)} \cdot [r + (1 + r) \cdot exp(-\beta \cdot s_M)] \quad (26)$$

where $\lambda_{(0)}$ and $\lambda_{(s_M)}$ are the macro-structural compressibility at saturated conditions and for a given macro suction, s_M, respectively; p_0^* is the pre-consolidation pressure at saturation and p_c is a reference pressure. α_1 and α_3 are model parameters that control the size of the BBM surface for a temperature increment (ΔT); r and β are model parameters that express the dependence of the size and evolution of the LC curve on the macro suction. A three-dimensional representation of the BBM yield surface is presented in Figure 3.3-1.

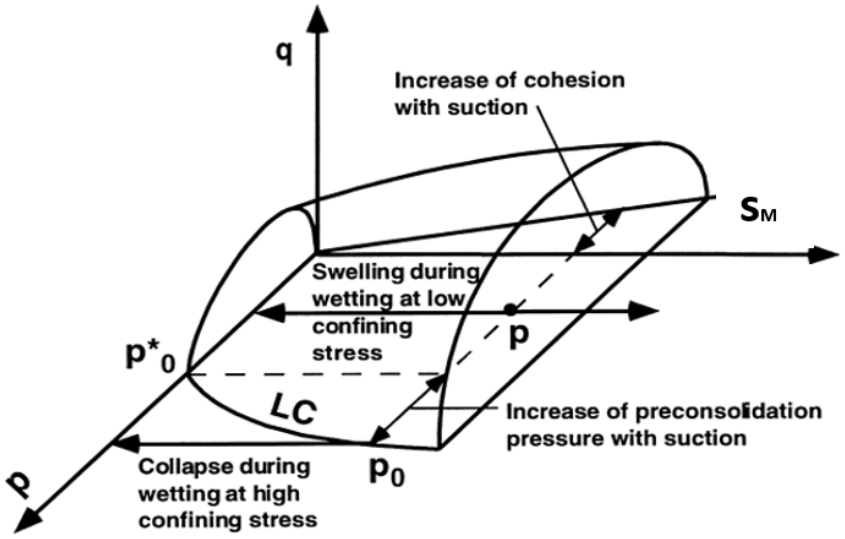

Figure 3.3-1 Three-dimensional representation of the BBM yield surface

The generation of macro-structural plastic deformations when the LC mechanism is activated is governed by the plastic flow rule, which is given by the following expression:

$$\dot{\boldsymbol{\varepsilon}}^{p}_{M,LC} = \dot{\lambda}_{LC} \frac{\partial G_{LC}}{\partial \boldsymbol{\sigma}} \tag{27}$$

where the magnitude of the plastic deformation rate is determined by the scalar plastic multiplier, $\dot{\lambda}_{LC}$. The plastic potential function of the LC mechanism, G_{LC}, is expressed as:

$$G_{LC} = 3 \cdot \alpha_{LC} \cdot J^2 - \left(\frac{g_F(\theta, \alpha_F)}{g_F\left(-\frac{\pi}{6}, \alpha_F\right)} \right)^2 \cdot M_F^2 \cdot (p + p_s) \cdot (p_0 - p) = 0 \tag{28}$$

where α_{LC} is the non-associativity parameter.

Plastic Beta (β) mechanism

It has been assumed that micro-structural behaviour is not affected by the macro-structural state. However, the volumetric deformations of microstructure may induce plastic strains at the macro-structural level. The magnitude of these macro-structural deformations ($\dot{\boldsymbol{\varepsilon}}^{p}_{M,\beta}$) is taken as proportional to the micro-structural elastic strains:

$$\dot{\boldsymbol{\varepsilon}}^{p}_{M,\beta} = f_{\beta} \cdot \dot{\boldsymbol{\varepsilon}}^{e}_{m} \tag{29}$$

where f_β represents a pair of micro-macro coupling functions that distinguishes between the stress paths characterized by a micro-structural contraction (MC paths) and those paths in which a micro-structural swelling (MS paths) occurs. The following general expression has been used in the current double porosity approach:

$$f_{\beta} = \begin{cases} f_{MC}^{(1)} + \left(f_{MC}^{(0)} - f_{MC}^{(1)}\right) \cdot \left(1 - \mu_{\beta}\right)^{n_{MC}} & if \quad \dot{p}_m > 0 \\ f_{MS}^{(1)} + \left(f_{MS}^{(0)} - f_{MS}^{(1)}\right) \cdot \left(1 - \mu_{\beta}\right)^{n_{MS}} & if \quad \dot{p}_m < 0 \end{cases} \tag{30}$$

where μ_β is a parameter that accounts for the degree of compactness of the macrostructure and $\dot{p}_m$ is the rate of the mean effective stress at the micro-structural domain. $f_{MC}^{(0)}$, $f_{MC}^{(1)}$, n_{MC} and $f_{MS}^{(0)}$, $f_{MS}^{(1)}$, n_{MS} are model parameters that define the structural coupling function in MC paths and MS paths, respectively. A general representation of the micro-macro coupling functions, including the main behaviour features expected during wetting and drying paths are shown in Figure 3.3-2.

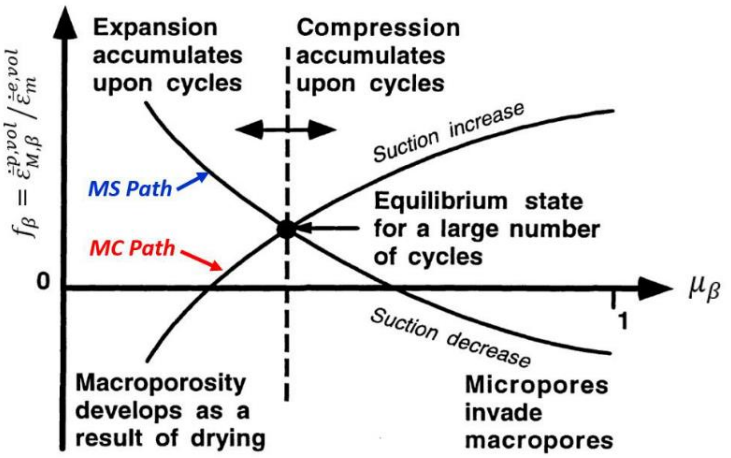

Figure 3.3-2 Micro-macro interaction functions

A modification of equation (29) is required to ensure the simplifying assumption of elastic thermal deformations at both structural levels in non-isothermal analyses. Under such conditions, the thermal expansion of the microstructure does not generate any irreversible structural changes (such as a thermal collapse) in the soil skeleton. Consequently, the thermal component of the micro-structural deformations must be discounted from the total micro-structural strains:

$$\dot{\boldsymbol{\varepsilon}}^{p}_{M,\beta} = f_{\beta} \cdot \left(\dot{\boldsymbol{\varepsilon}}^{e}_{m} - \left(\dot{\boldsymbol{\varepsilon}}^{e}_{m} \right)_{\Delta T} \right) \tag{31}$$

When isothermal analyses are performed, $\left(\dot{\boldsymbol{\varepsilon}}^{e}_{m} \right)_{\Delta T} = \mathbf{0}$, and equation (29) is recovered.

Hardening rule

Finally, the hardening of the double porosity medium is given by the evolution of the isotropic yield stress due to the contribution of both plastic mechanisms considered in the current formulation. Thus, the evolution of the saturated pre-consolidation pressure (the hardening parameter of this model), $\dot{p}_0^*$, is given as follows:

$$\dot{p}_0^* = p_0^* \cdot \left(\frac{1 + e_M}{\lambda_{(0)} - \bar{\kappa}_M} \right) \cdot \left(\dot{\varepsilon}^{p,v}_{M,LC} + \dot{\varepsilon}^{p,v}_{M,\beta} \right) \tag{32}$$

where $\dot{\varepsilon}^{p,v}_{M,LC}$ is the volumetric plastic strain induced by the yielding of macrostructure due to the LC mechanism and $\dot{\varepsilon}^{p,v}_{M,\beta}$ is the volumetric component of macro-structural strains due to the plastic β-mechanism.

In non-isothermal problems, the evolution of this hardening parameter, $\dot{p}^*_{0,T}$, can also become dependent on the temperature changes. In such conditions, the general expression for the hardening rule of the double structure model is given as follows:

$$\dot{p}^*_{0,T} = p^*_{0,T} \cdot \left(\frac{1 + e_M}{\lambda_{(0)} - \bar{\kappa}_M} \right) \cdot \left(\dot{\varepsilon}^{p,v}_{M,LC} + \dot{\varepsilon}^{p,v}_{M,\beta} \right) + 2(\alpha_1 \pm 2\alpha_3 \cdot \Delta T) \cdot \dot{T} \tag{33}$$

3.3.2 Geometry and discretization

A 2-D plane strain geometry, 100 m wide and 200 m high has been adopted to model the assessment case. The symmetry of the cross section has been considered. This modelled domain has been spatially discretized as a structured finite element mesh composed of 4,920 linear quadrilateral elements and 5,063 nodes, as illustrated in Figure 3.3-3. The geometry of the EBS specified in the NAGRA assessment case have been used in the generation of the mesh.

The tunnel in which the engineered barrier (EB) is emplaced has a circular cross section with a radius of 1.75 m. An excavated damage zone (EDZ) around the tunnel, with a thickness of 0.875 m (half of the tunnel radius), has been also incorporated in the geometry although with the same THM properties of the intact rock formation, except for its porosity and pore-air entry suction. A 10 cm-thick shotcrete and a concrete lining with a thickness of 25 cm have been emplaced around the tunnel wall immediately

after tunnel excavation. The metal canister, with an external radius of 52.5 cm, has been modelled as a very thin layer of finite elements with low porosity and very low water permeability and high stiffness. It constitutes the surface on which the thermal loading is applied. The canister rests on a pedestal made of compacted MX-80 bentonite. The void space between the canister, the pedestal and the concrete liner is filled with granular bentonite material (GBM). Three distinct zones inside the GBM have been incorporated in the mesh. It has been assumed that the construction of the compacted block, the canister and the GBM is performed instantaneously and simultaneously.

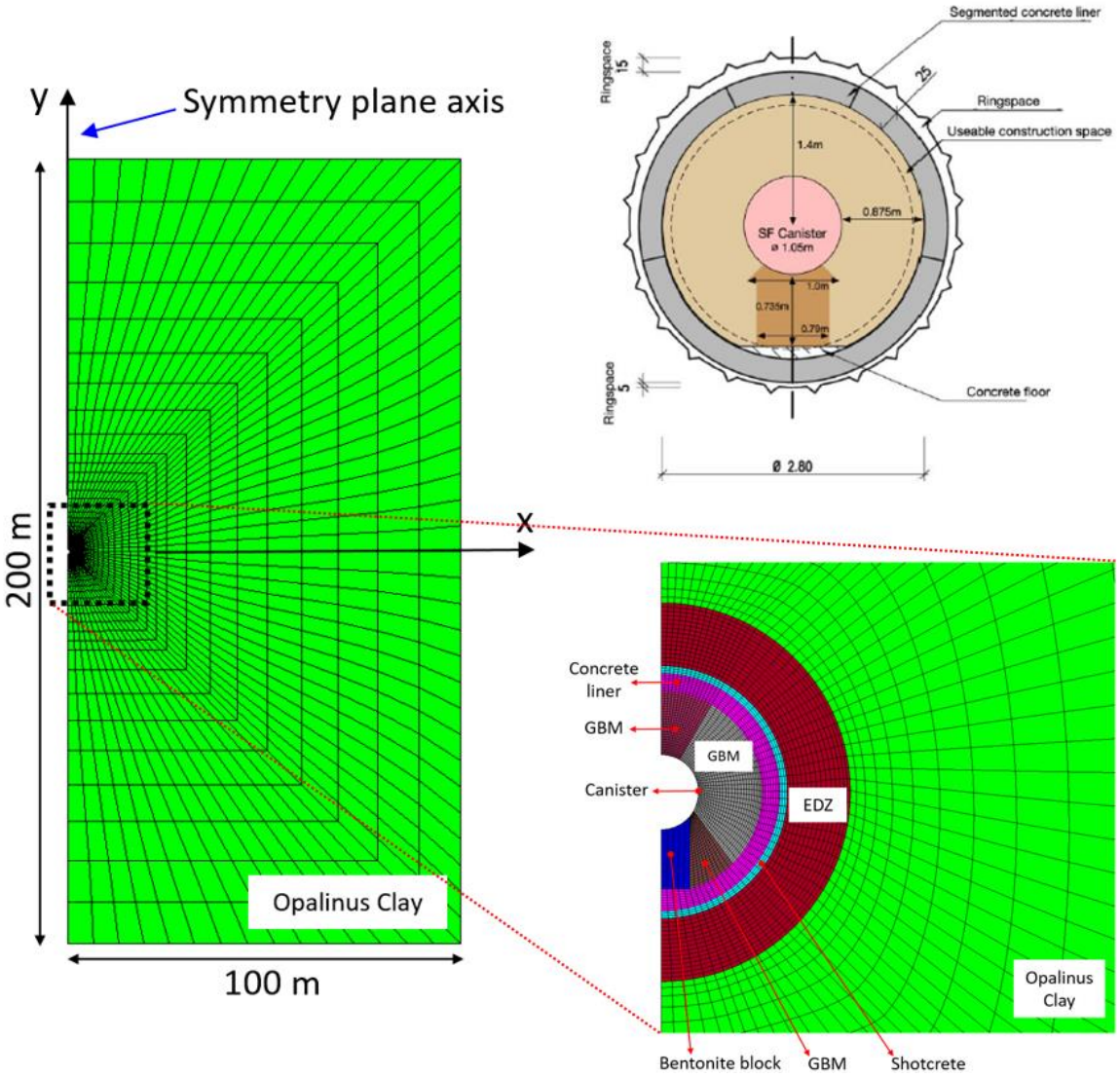

Figure 3.3-3 Finite element mesh (left) with a view of the proposed configuration for the NAGRA buffer concept (top right) and the EB model domain (bottom right).

3.3.3 Input parameters

Most of the input parameters for the bentonite-based materials (compacted blocks and the granular bentonite) have been derived from previous modelling tasks of the *in-situ* heating HE-E experiment, from laboratory experiments or estimated by back-calculation. The required parameters for the intact and the disturbed rock have been collected from the literature (see Gens, 2000; Muñoz *et al.*, 2003; Villar, 2007; Rothfuchs *et al.*, 2012; Gaus *et al.*, 2014), taking as reference the values provided during the *PEBS Project* (2010-2014) for the Opalinus Clay formation.

Temperature evolution in the EB and in the surrounding rock formation is mainly related to the conductive heat flux through the porous media, which, as indicated above, it is expressed by Fourier's law (equation (2)).

The thermal conductivity coefficient of the porous medium, λ, depends on porosity and the water content. In this case, this material property is expressed in terms of the global thermal conductivities at water-saturated (λ_{sat}) and dry (λ_{dry}) conditions. For the bentonite-based materials, the following relationship is used:

$$\lambda = \lambda_{sat}^{S_l} \cdot \lambda_{dry}^{1-S_l} \tag{34}$$

while the global thermal conductivity for the host rock (intact and disturbed), the concrete liner and the metallic canister is computed as:

$$\lambda = \lambda_{sat} \cdot \sqrt{S_l} + \lambda_{dry} \cdot \left(1 - \sqrt{S_l}\right) \tag{35}$$

where S_l is the global degree of saturation. Figure 3.3-4 shows the dependence of the thermal conductivity on saturation for some MX-80 bentonite materials together with the empirical functions defined in equation (34) for the GBM and the compacted bentonite block. The saturated and dry thermal conductivities for each material are given in Table 3.3-2.

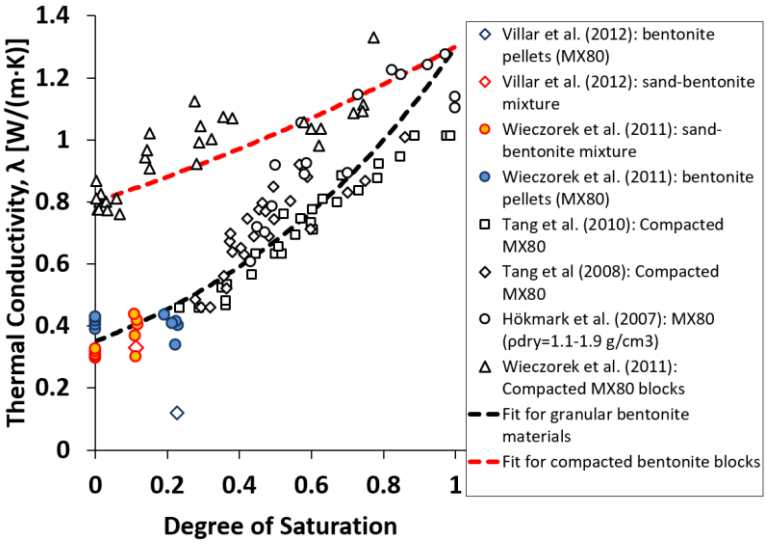

Figure 3.3-4 Dependence of thermal conductivity on degree of saturation of MX-80 bentonite materials and curves used in the calculations for the GBM and the compacted block.

Table 3.3-2 Saturated and dry thermal conductivities used in the calculations

	GBM	Bentonite block	Host rock (intact/EDZ)	Concrete (liner/shotcrete)	Canister
λ_{sat} [W/(m·K)]	0.35	0.81	1.20	1.00	52.5
λ_{dry} [W/(m·K)]	1.30	1.30	1.90	1.00	52.5

A modified form of the van Genuchten law (van Genuchten, 1980) has been used to represent the water retention curve (WRC). Its general expression is given by:

$$S_l = S_{l,r} + (S_{l,s} - S_{l,r}) \cdot \left(1 + \left(\frac{s}{P}\right)^{1/(1-\lambda_{rc})}\right)^{-\lambda_{rc}} \cdot \left(1 - \frac{s}{P_d}\right)^{\lambda_d} \quad (36)$$

where $S_{l,r}$, $S_{l,s}$ are the residual and the maximum water saturation, respectively; s is the current suction ($s = P_g - P_l$) and P is a material parameter related to the pore-air entry value (P_0) at a given temperature; λ_{rc}, λ_d are model parameters and P_d is a pressure related to the suction at dry conditions. The shape of the WRC for the host rock (Opalinus Clay) and the bentonite materials, together with some experimental data (see Gens, 2000; Muñoz *et al.*, 2003; Zhang & Rothfuchs, 2005; Villar, 2005, 2007; Rizzi *et al.*, 2012; Seiphoori *et al.*, 2014) are shown in Figure 3.3-5. The water retention parameters are given in Table 3.3-3.

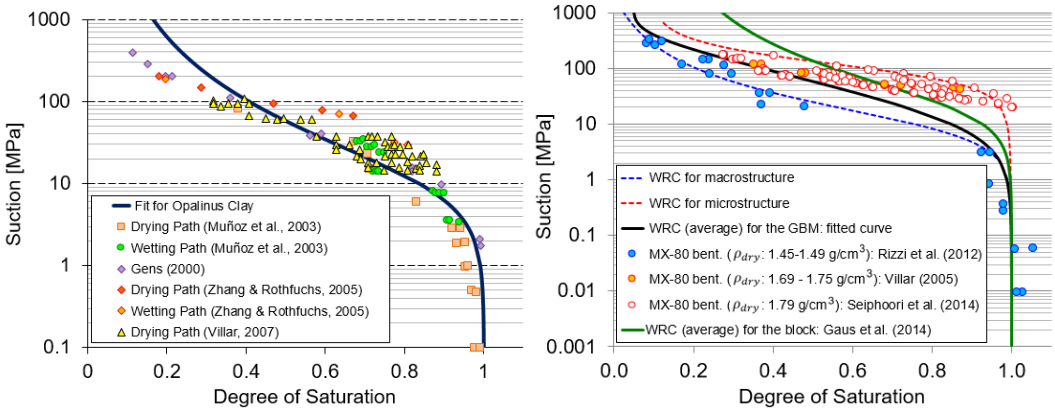

Figure 3.3-5 Retention curves (full lines) for the rock formation (left) and the bentonite-based materials (right). The symbols represent experimental data

Table 3.3-3 Input parameters for the WRC of the materials considered in the modelling

	GBM	Bentonite block	Host rock	Concrete (liner/shotcrete)
P_0 [MPa]	12.0	21.9	11.0	25.0
σ_0 [N/m]	7.2e-02	7.2e-02	7.2e-02	7.2e-02
λ_{rc} [-]	0.23	0.30	0.29	0.50
$S_{l,r}$ [-]	0.05	0.10	0.007	0.05
$S_{l,s}$ [-]	1.00	1.00	1.00	1.00
P_d [MPa]	2.0e03	1.0e27	1.0e27	1.0e27
λ_d [-]	8.50	0.00	0.00	0.00

The hydration of a clay barrier is also affected by the changes in its water permeability as the water content increases. Although the hydraulic conductivity tends to increase with the degree of saturation, in highly expansive clays under global volumetric restrictions, the hydration process may lead to a marked reduction in the liquid intrinsic permeability, (see Hoffmann *et al.*, 2007). This is a direct consequence of the evolution of the clay fabric. In the model, liquid intrinsic permeability is assumed to depend on the macrostructural pore volume fraction according to the empirical Kozeny's law that expresses such a dependence according to:

$$\boldsymbol{k} = \boldsymbol{k_0} \cdot \frac{\hat{\phi}^3}{\left(1-\hat{\phi}\right)^2} \cdot \frac{\left(1-\hat{\phi}_0\right)^2}{\hat{\phi}_0^3} \quad (37)$$

where $\boldsymbol{k}$ is the current intrinsic permeability tensor and $\boldsymbol{k_0}$ is the intrinsic permeability at a reference porosity, $\hat{\phi}_0$. In double-porosity approach, $\hat{\phi}$ is the macro-pore volume fraction. The evolution of the water permeability with the saturation state of the bentonite materials has been modelled by the following generalized power law:

$$k_{rl} = A_{kr} \cdot (S_{el})^{\lambda_{kr}} \quad (38)$$

while the van Genuchten model has been used to express the dependence on the saturation state of the rock formation as well as the concrete lining and the shotcretes:

$$k_{rl} = \sqrt{S_{el}} \cdot \left(1 - \left(1 - (S_{el})^{1/\lambda_{kr}}\right)^{\lambda_{kr}}\right)^2 \quad (39)$$

where k_{rl} is the relative permeability factor that accounts for the impact of the degree of saturation on the advective flow and A_{kr} and λ_{kr} are model parameters. The effective degree of saturation, S_{el}, is defined as:

$$S_{el} = \frac{S_l - S_{l,r}}{S_{l,s} - S_{l,r}} \quad (40)$$

The main hydraulic properties used in the calculations for modelling the water flow through the EB and the host rock are summarized in

Table 3.3-4. Figure 3.3-6 shows the dependence of the relative liquid permeability on the degree of saturation, according to the van Genuchten model (rock and concrete) and to a power law (bentonite-based materials).

Table 3.3-4 Hydraulic parameters required for modelling the advective flow of water through the EB and the host rock

	GBM	Bentonite block	Host rock	Concrete (liner/shotcrete)
k_0 [m²]	3.50e-20	2.50e-21	3.16e-20	1.00e-18
$\hat{\phi}_0$ [-]	0.285*	0.174*	0.137	0.200
A_{kr} [-]	1.0	1.0	-	-
λ_{kr} [-]	3.0	3.0	0.52	0.52
$S_{l,r}$ [-]	0.0	0.0	0.007	0.0
$S_{l,s}$ [-]	1.0	1.0	1.0	1.0

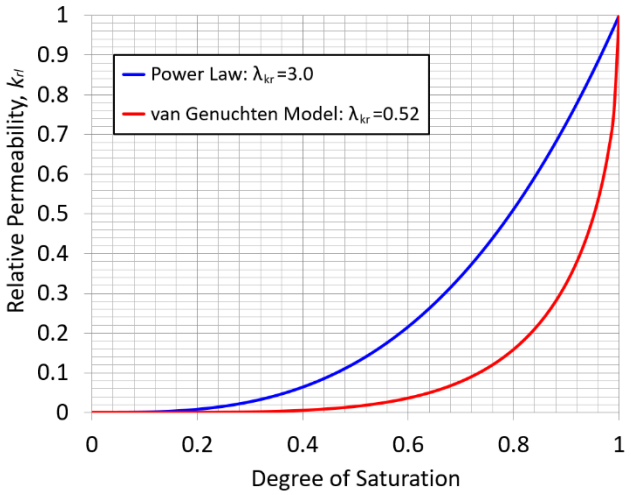

Figure 3.3-6 Dependence of the relative liquid permeability on the degree of saturation, according to the van Genuchten model (rock and concrete) and to a power law (bentonite-based materials).

The mechanical behaviour of the bentonite materials is described by the elastoplastic constitutive law described earlier. It has been assumed that elastic constitutive models can be used to model the mechanical response of the host rock, the concrete materials and the metallic canister. The mechanical parameters used in the simulations are given from

Table 3.3-5 to Table 3.3-8.

Table 3.3-5 Elastic parameters for the rock formation, the concrete materials and the metal canister

	Host rock (intact)	**Host rock (EDZ)**	**Concrete (liner/shotcrete)**	**Canister**
Young modulus [MPa]	3,570	3,570	10,000	210,000
Poisson's ratio [-]	0.33	0.33	0.24	0.24

Table 3.3-6 Elastic parameters for the bentonite materials

	GBM	**Bentonite block**
κ^M [-]	6.0e-03	2.0e-03
κ^m [-]	1.0e-03	1.0e-03
κ_s^M [-]	1.0e-02	5.2e-02

Poisson's ratio [-]	0.30	0.20

Table 3.3-7 Elastoplastic parameters for the plastic loading-collapse mechanism of the macrstructure (for bentonite materials)

		GBM	Bentonite block	Description
p_0^*	[MPa]	1.0	14	Pre-consolidation pressure at saturated conditions.
p_c	[MPa]	0.075	0.10	Reference pressure.
$\lambda(0)$	[-]	0.17	0.18	Slope of void ratio – mean stress at saturation.
r	[-]	0.60	0.75	Parameter defining the maximum soil stiffness.
β	[MPa^{-1}]	0.05	0.05	Parameter controlling the rate of increase of stiffness with suction.
p_{s0}	[MPa]	0.10	0.10	Tensile strength in saturated conditions.
k_s	[-]	0.1	0.1	Parameter that takes into account the increase of tensile strength due to suction.
M	[-]	1.3	1.0	Critical state line parameter.
ω	[-]	1.0	1.0	Non-associativity parameter.

Table 3.3-8 Elastoplastic parameters for the plastic micro-macro coupling mechanism (for bentonite materials)

		GBM	Bentonite block
f_{SD0}	[-]	-0.1	0.0
f_{SD1}	[-]	1.1	1.0
n_{SD}	[-]	3.0	3.0
f_{SI0}	[-]	-0.1	0.0
f_{SI1}	[-]	1.1	1.0

n_{SI}	[-]	0.45	0.45

The thermal impact on porewater viscosity and density is considered in the analysis. The dependence of water viscosity (μ_l) on is given by:

$$\mu_l = A \cdot e^{\left(\frac{B}{273.15+T}\right)} \quad (41)$$

where A = 2.1e-12 MPa·s and B = 1,808.5 K^{-1}.

The evolution of water density due to temperature changes is due to the thermal expansion of water. The volumetric thermal expansion coefficient for water, $\alpha(T)$, depends on temperature, as illustrated in Figure 3.4.7. A constant density value has been adopted for concrete materials and metal canister. Other relevant material properties used in the numerical calculations are listed in

Table 3.3-9.

The thermally-induced water phase exchange (evaporation and condensation), the expansion of the porous skeleton and the diffusive transport of water vapour_are also included in the analysis.

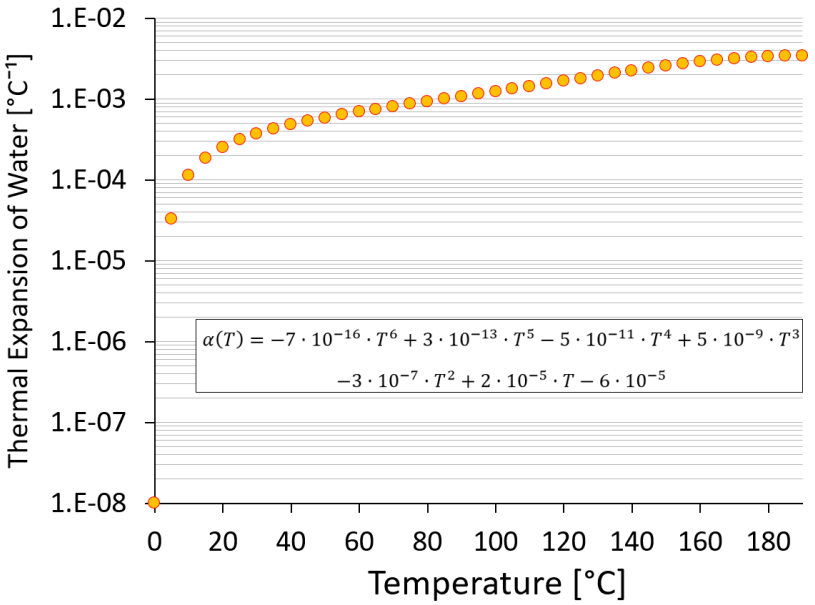

Figure 3.3-7 Volumetric thermal expansion coefficient for water as a function of temperature

Table 3.3-9 Physical parameters used in the analysis

	GBM	Bentonite block	Host rock	Concrete	Canister
Solid grain density [kg/m^3]	2,700	2.700	2,700	2,700	7,850
Specific heat (dry)[J/kg·K]	893	1,058	800	1,000	440
Linear thermal expansion for the solid grain [°C^{-1}]	2.5e-05	2.5e-05	1.7e-05	1.5e-05	1.2e-05
Thermal expansion for water [°C^{-1}]	*	*	*	3.4e-04	3.4e-04

*Value varies with temperature

3.3.4 Initial and boundary conditions

The modelling has been performed in two main steps. The first step corresponds to the excavation and ventilation of the tunnel and the construction of the EB and other components of the case such as lining, concrete and canister. The second step involves the thermal loading from the canister and the simultaneous hydration of the bentonite barrier from the host rock.

The excavation of the host rock has been simulated instantaneously through a relaxation of the total stress around the tunnel wall from its initial value to zero. The evolution of the pore water pressure in the vicinity of the tunnel section before the emplacement of the clay barrier has been modelled by prescribing liquid pressure changes at the internal boundary of the concrete liner in order to reach a suction value corresponding to the relative humidity (RH) of the ventilation period. The construction of the bentonite pedestal and the emplacement of the metallic canister and the granular bentonite material have been simulated in a single step. The thermal loading has been applied on the internal surface of the metal canister. The heating power function displayed in Figure 3.3-8 has been used to represent the long-term thermal impact of the canister, in accordance with the specifications described in Leupin *et al.* (2020). All these modelling steps are described in more detail below. A summary of the initial conditions for each material considered in the analysis is presented in Table 3.3-10.

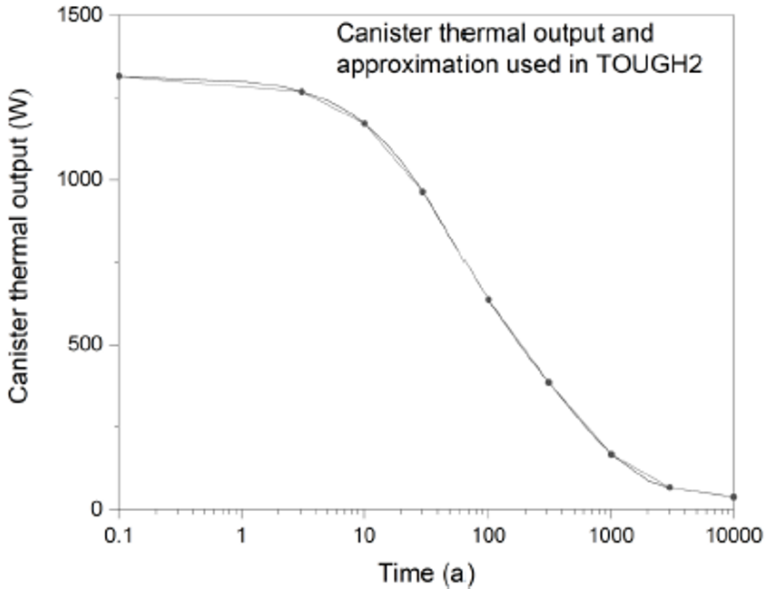

Figure 3.3-8 Specified heat decay curve

Table 3.3-10 Initial state of the materials considered in the modelling

	GBM	Bentonite block	Host rock	Concrete	Canister
σ [MPa] (isotropic)	-0.1	-4.5	-4.5	-0.1	-0.1
P_l [MPa]	-200	-21	2.1	-470	-200
T [°C]	18	18	18	18	18
p_0^* [MPa]	1.0	14	-	-	-
ϕ [-]	0.444	0.374	0.137	0.200	0.0001
$\bar{\phi}_m$ [-]	0.285	0.174	-	-	-
S_l [-] (average)	0.17	0.81	1.00	0.10	0.00

Initial and boundary conditions prior to tunnel excavation

No thermal, hydraulic or mechanical anisotropy in the material properties have been considered for the host rock. The initial water pressure has been set at 2.1 MPa throughout the model domain. An isotropic compression pressure of 4.5 MPa has been adopted to represent the initial stress state in the rock formation. The initial temperature in the host rock has been assumed to be 18°C. Consequently, a pore water pressure of 2.1 MPa and a constant temperature of 18°C have been prescribed at the upper and the lower horizontal boundaries and at the right vertical boundary,

representing the boundary conditions in the far field. Null vertical displacements have been imposed at the upper and the lower boundaries while null horizontal displacements have been applied on the right external boundary. The initial and boundary conditions in the host rock before the tunnel excavation are presented graphically in Figure 3.3-9.

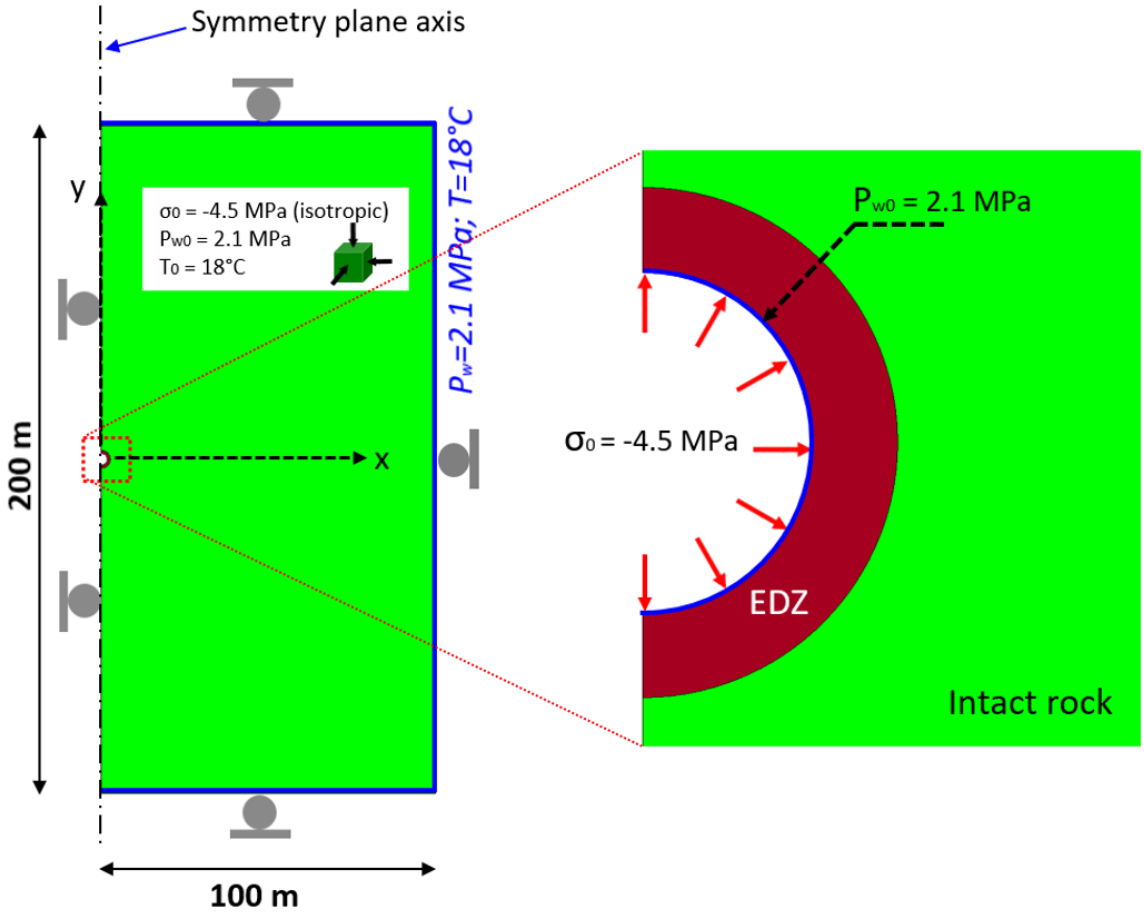

Figure 3.3-9 Geometry and initial and boundary conditions before the excavation of the tunnel

Tunnel excavation and ventilation period

As indicted before, the excavation of the tunnel has been performed by a relaxation of the initial total stresses at the boundary representing the tunnel wall. The liquid pressure on that boundary has been changed linearly from its initial value to zero during the excavation process. Some properties of the host rock close to the tunnel (the EDZ material) have been modified at the end of the excavation in order to take into account the mechanical disturbances caused by the excavation process. However, such changes have been restricted to a slight reduction of porosity (taking as reference the value in the intact rock) and to the adoption of a lower value for the

pore-air entry pressure. The shotcrete layer and the concrete liner have been constructed instantaneously after the tunnel opening.

The ventilation of the excavated tunnel has been simulated by changing linearly the liquid pressure at the internal boundary of the lining until reaching a suction value of about 68 MPa, which corresponds to a RH of 60%. Temperature inside the tunnel has been kept constant and equal to 18°C throughout the ventilation step. This value of has been prescribed at the internal boundary of the concrete lining. The open tunnel condition has been simulated for a period of two years (730 days). The THM boundary conditions prescribed at the tunnel wall after excavation and during the ventilation stage are shown in Figure 3.3-10.

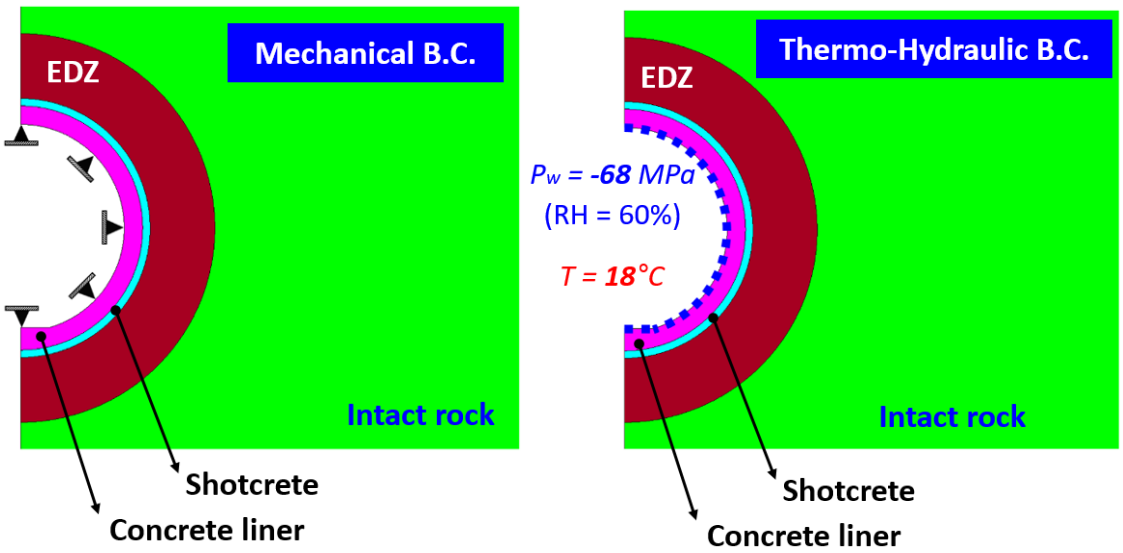

Figure 3.3-10 Mechanical (left) and thermo-hydraulic boundary conditions (right) after excavation and before the emplacement of the clay barrier

Emplacement of the canister and engineered barrier

The construction of the compacted bentonite block on which the canister rests, the canister itself and the granular bentonite material has been modelled in a single step, assuming that all such operations have occurred simultaneously. Suction values of 200 MPa and 21 MPa have been set to represent the initial hydraulic conditions of the GBM and the bentonite block, respectively. These suction values have been estimated from the average water retention curves shown in Figure 3.3-5, in accordance with the average values of their initial water content (5% for the GBM and 18% for the block) and dry density (1.50 g/cm^3 for the GBM and 1.69 g/cm^3 for the block). An initially homogenous GBM has been assumed. The initial stress state for the bentonite-based materials has been assumed as isotropic, with a stress value of 0.1 MPa. The metal canister has been modelled as a thin very rigid layer. A schematic representation of the boundary conditions after the EB construction and before the start of heating is shown in Figure 3.3-11.

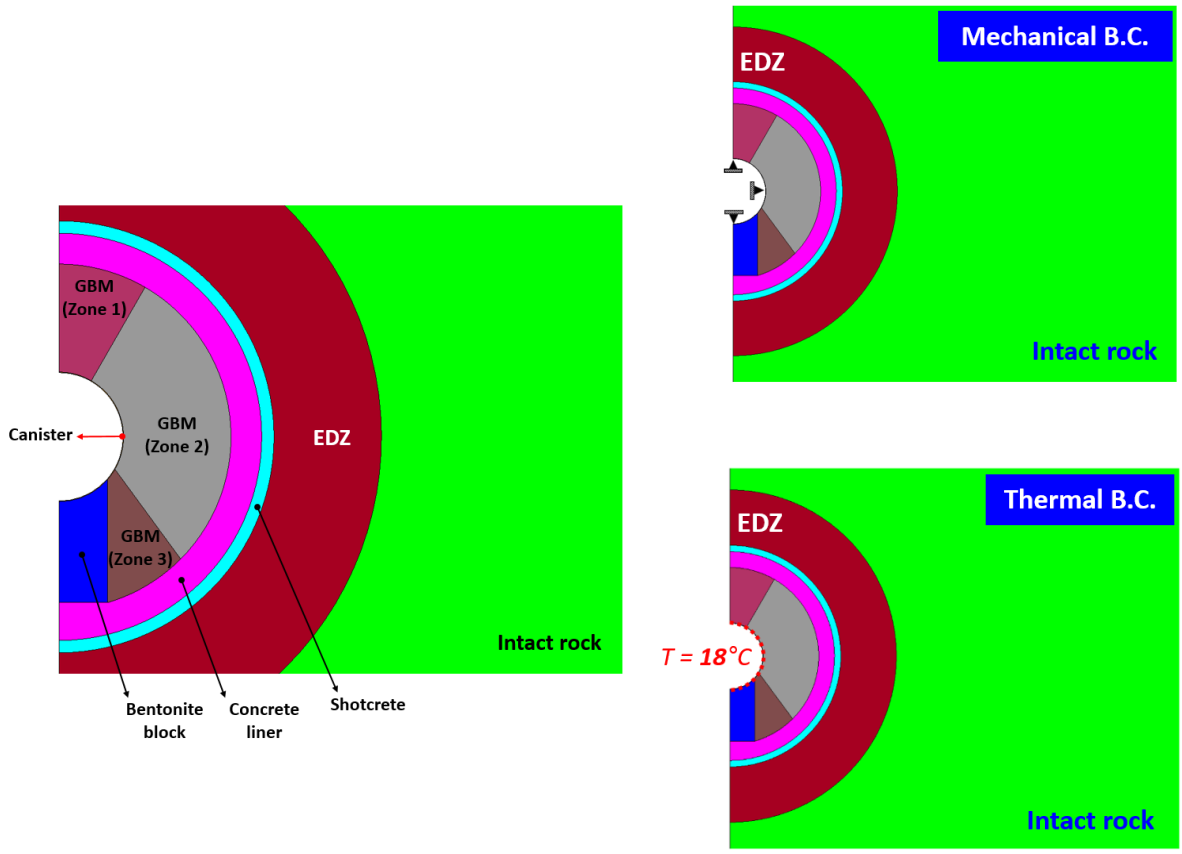

Figure 3.3-11 View of the clay barrier and the canister inside the tunnel (left) and mechanical and thermal boundary conditions immediately after EB emplacement and before the start of heating (right)

Heating stage

The thermal input of the analysis has been simulated by prescribing a heat flux at the inner boundary of the thin layer representing the canister in the modelled domain. The initial heating phase has been simulated as a linear increment of heat power from zero until reaching its maximum value. The time required to reach the target power on the canister surface was not defined in the specifications, suggesting that the initial heating should be applied instantaneously. However, it has been decided to apply it over 36 days in order to avoid convergence problems caused by an instantaneous temperature increase. Afterwards, the analysis follows the specified heat decay curve.

The adoption of a 2D plane strain geometry for representing the modelled domain implies that the separation between successive canisters is not taken into account in the simulation. Consequently, the actual thermal loading applied has been reduced to 75% of the nominal value (see Figure 3.3-12) in order to achieve a more realistic temperature field.

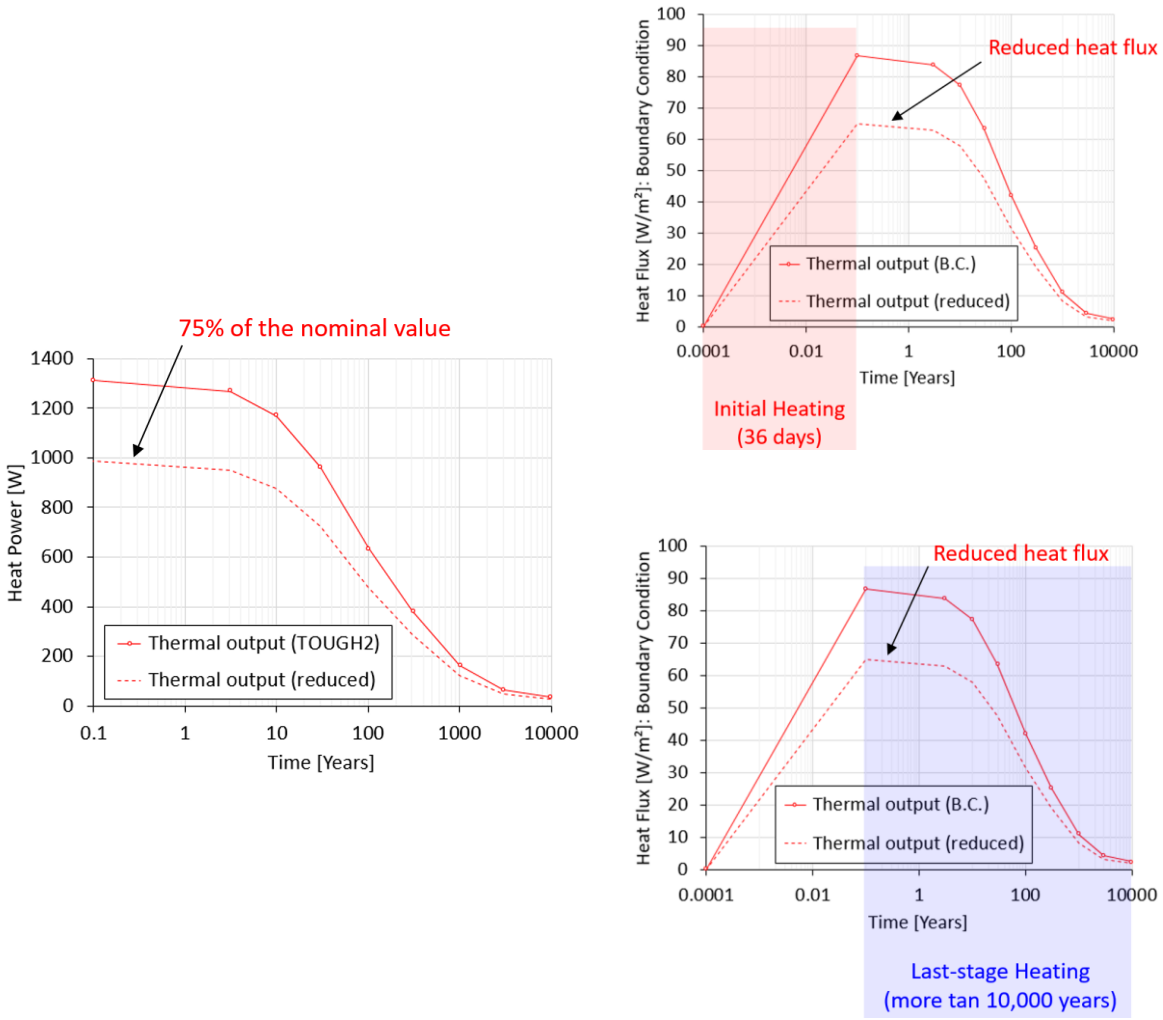

Figure 3.3-12 Nominal and applied heat power (left) and heat fluxes (right) prescribed on the canister inner surface (right).

3.3.5 Results

The results of the analysis in terms of temperature, saturation and density inside the bentonite barrier and in the vicinity of the EBS have been represented along seven radial profiles and at twelve selected points around the canister, as shown in Figure 3.3-13. The radial profiles follow a clock-like coding. Five profiles cross the EB zone filled with GBM (P-12h to P-04h), another one crosses the bentonite block (P-06h) and profile P-05h crosses both the bentonite pedestal and the GBM. The points for which the evolution of the different variables is plotted belong to radial profiles P-12h, P-03h and P-06h. Three of these points are located at a distance of 5 cm from the canister surface (A-12h, A-03h and A-06h) while other three are about 5 cm from the EB-lining interface (C-12h, C-03h and C-06h). Points B-12h, B-03h and B-06h are located in an intermediate location inside the buffer. Results are also evaluated at three points in the EDZ (D-12h, D-03h and D-06h), located about 25 cm into the rock formation. The coordinates of these evaluation points are given in Table 3.3-11.

The results along the radial profiles, for a specific time, are plotted against the distance from the canister surface. In all the charts displayed in this section, time "zero" corresponds to the beginning of heating. Because of optimization and convergence issues associated with the implementation and use of the new thermomechanical constitutive model, only the results for the first 10 years of heating are available at the present time.

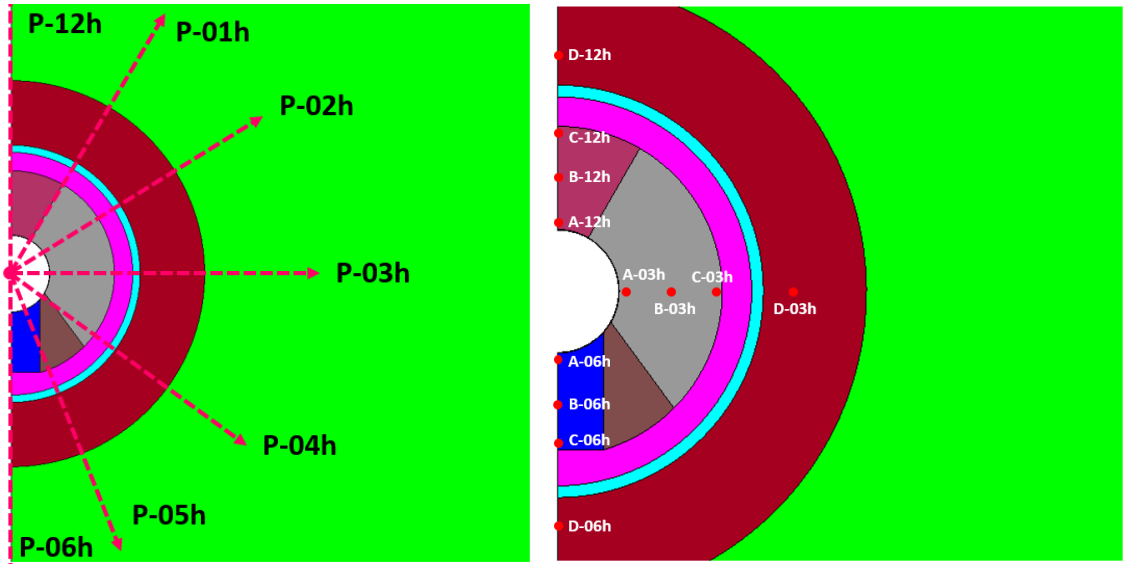

Figure 3.3-13 Radial profiles (left) and points (right) for presenting the results of the analysis

Table 3.3-11 Coordinates of the points selected for representing the results of the analysis

	Coord. X (m)	Coord. Y (m)
Tunnel Center	0.00	0.00
A-12h	0.00	0.575
A-03h	0.575	0.00
A-06h	0.00	-0.575
B-12h	0.00	0.96
B-03h	0.96	0.00
B-06h	0.00	-0.96
C-12h	0.00	1.35
C-03h	1.35	0.00
C-06h	0.00	-1.30
D-12h	0.00	2.00
D-03h	2.00	0.00
D-06h	0.00	-2.00

Tunnel ventilation

The evolution of the saturation around the open tunnel before the emplacement of the bentonite barrier occurs in response to the changes in suction applied on the internal boundary of the concrete lining during ventilation. As mentioned before, a suction of 68 MPa (RH≈60%) represents the condition in the open tunnel at the ventilation stage. Consequently, the initial pore pressure state around the tunnel (2.1 MPa along the profile P-03h) undergoes a noticeable reduction in the first meters into the host rock caused by the excavation and ventilation. The distribution of the liquid pressure around the open tunnel at the end of the ventilation period is shown in Figure 3.3-14, where it can be noted that the hydraulically affected zone extends up to 8-10 meters away from the tunnel wall.

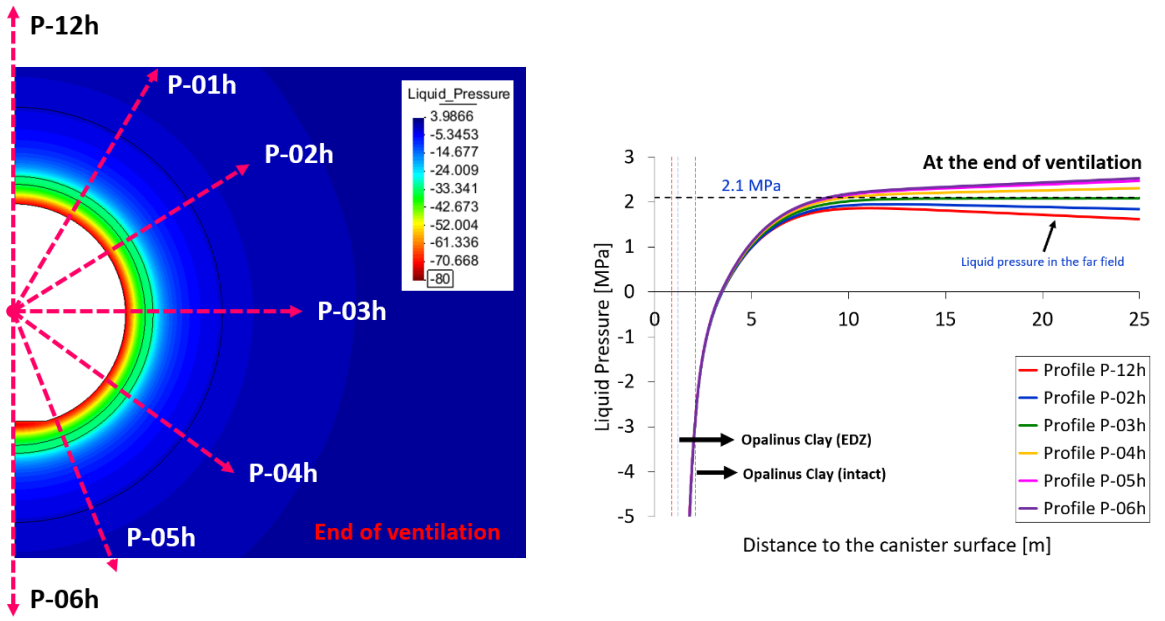

Figure 3.3-14 Liquid pressure distribution around the tunnel at the end of the ventilation step

The extension of the desaturation zone into the rock at the end of the ventilation is limited to about 0.8-1 m into the rock, as shown in Figure 3.3-15. This is quite consistent with the results reported in Gens & Garitte (2013) based on the controlled Ventilation Test (VE) carried out in a 1.3 m diameter tunnel excavated in Opalinus clay. Figure 3.3-16 presents the radial profiles of relative humidity at the end of the ventilation stage. Figure 3.3-16b shows that the results of the analysis are in remarkable agreement with the VE test observations, especially considering that the two cases are nor totally coincident; for instance, there was no lining in the VE experiment.

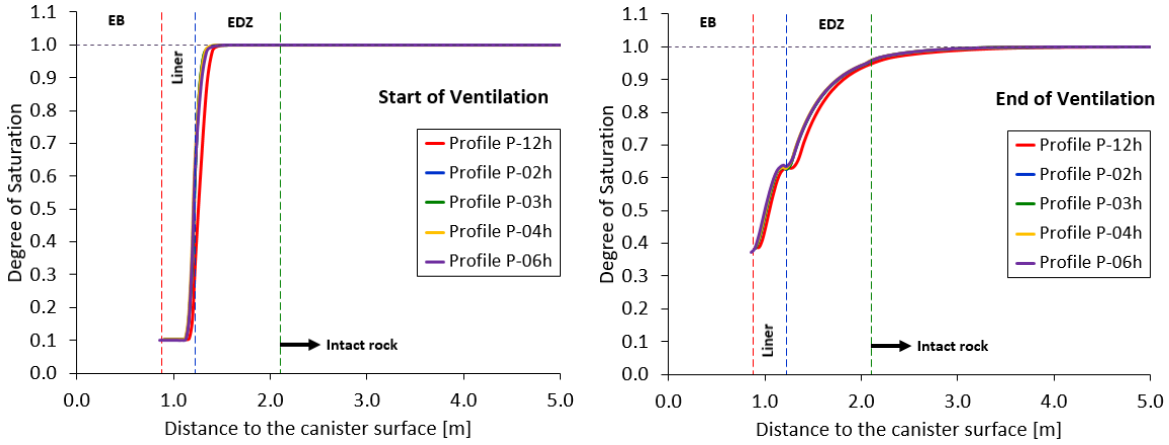

Figure 3.3-15 Radial profiles of degree of saturation at the beginning (left) and the end (right) of the ventilation period

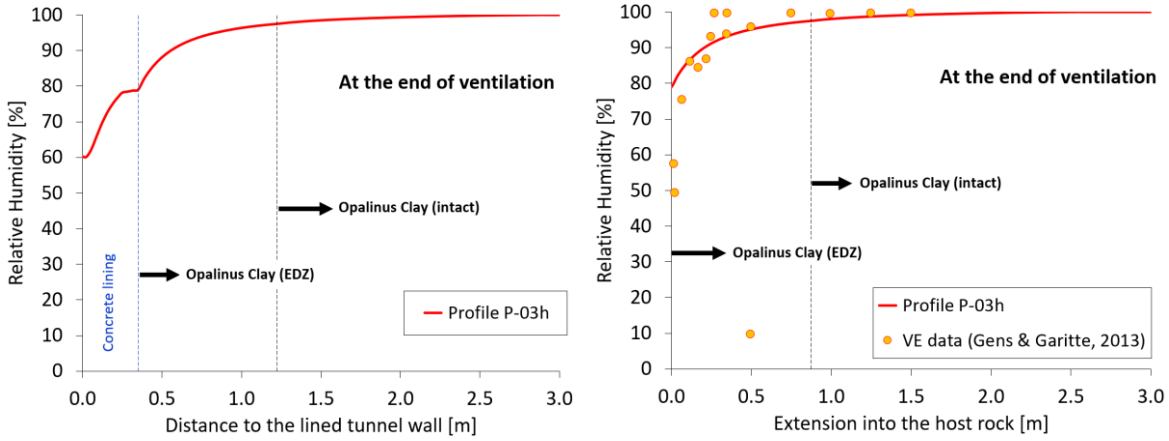

Figure 3.3-16 Radial profile (P-03h) of relative humidity at the end of the ventilation period.

Temperature

The spatial distributions of temperature in the near field for times equal to 36 days, 3 years and 10 years of heating are presented in Figure 3.3-17 while the evolutions of temperature at the selected points on radial profiles P-12h and P-06h during the first 10 years of heating are shown in Figure 3.3-18. It can be noted that temperature increases quickly around the canister during the initial heating stages generating a strong thermal gradient inside the EB. The initial low saturation of the GBM enhances the difference between the temperatures computed close to the heat source and those near the rock. However, the thermal differences among the radial profiles of temperature inside the bentonite barrier tend to reduce as the analysis progresses. Also, the extent of the heated zone increases as heat propagates from the EB to the rock formation. Thus, the increase in temperature is around 14°C after 10 years of heating at points located 10 m away from the canister surface.

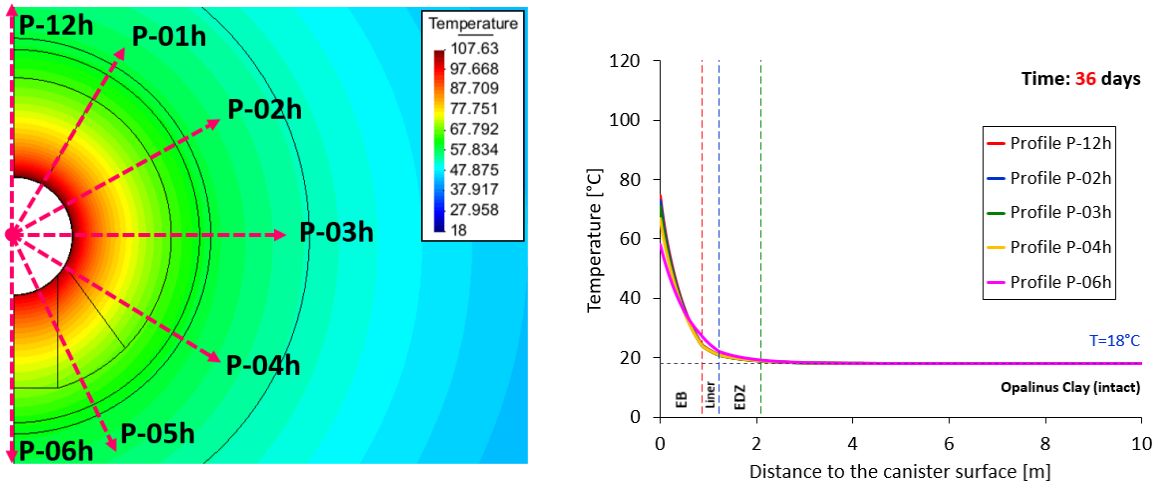

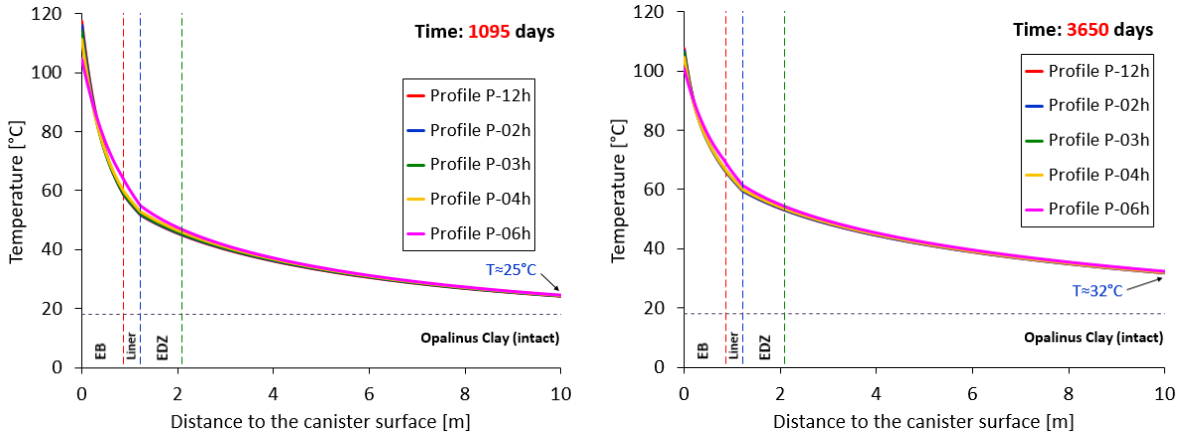

Figure 3.3-17 Temperature contours after 10 years of heating (top left) and radial distributions of temperature for 36, 1095 and 3650 days of heating.

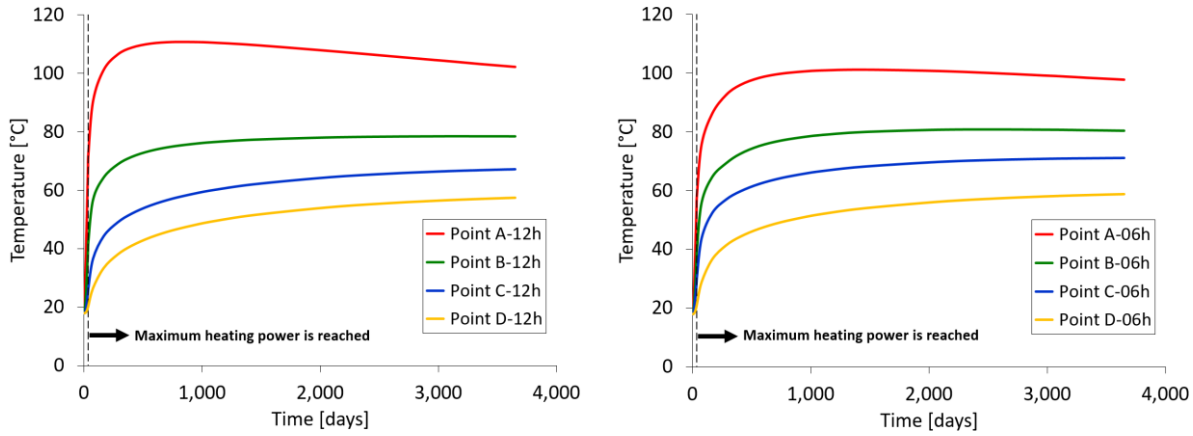

Figure 3.3-18 Evolution of temperature at the selected points in the radial profiles P-12h (left) and P-06h (right) during the first 10 years of heating

As Figure 3.3-18 shows, temperature continues to rise around the heat source for several years after the beginning of heating. For the evaluation point A-12h, located at 5 cm from the canister surface, a maximum temperature of about 108°C is reached after 936 days (≈ 2.6 years) The maximum temperature in the bentonite barrier (at a point immediately next to the canister surface) is about 118°C and occurs on the 750th day (≈ 2.1 years) after the start of heating.

It is interesting to note that the higher thermal conductivity of the bentonite pedestal explains the lower temperatures along profile P-06h in comparison to the values computed along the radial profiles crossing the granular material. Consequently, the amount of heat transferred to the host rock is higher along P-06h, which means that temperature is slightly higher in the part of the rock formation located at the bottom of the bentonite barrier. This can be inferred from the evolution of temperature at points A-12h, A-03h and A-06h (close to the heat source) and points D-12h, D-03h and D-06h (within the EDZ of the surrounding rock) plotted in Figure 3.3-19.

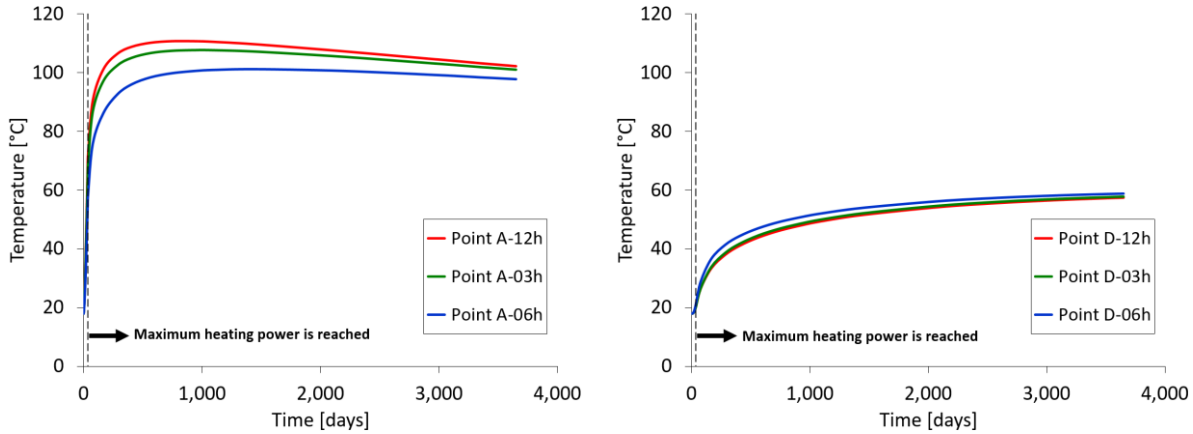

Figure 3.3-19 Temperature evolution of three points located 5 cm from the canister surface (left) and 25 cm into the surrounding rock (right).

Engineered barrier (EB) hydration

The evolution and spatial distribution of water content inside a bentonite barrier under thermal loading can be understood as the results of a combination of thermally-induced processes and natural hydration form the rock. Thermally-induced phenomena are predominant in the initial stages of heating, when the barrier is still very dry and the thermal gradient within the barrier is very large. In such stages, temperature close to the heat source generates vapour, the resulting vapour travels by diffusion from the hotter zones to the relatively cooler outer ones causing a thermally-induced drying near the heating element and an increase in the saturation state at the EB zones further away, where vapour condensates (Gaus et al., 2014; Gens & Vasconcelos, 2019). In addition, hydration processes are related to the advective flow of water from the surrounding rock formation into the bentonite barrier. This water mass transport is the main process controlling the long-term saturation of the barrier.

This account is confirmed by the results of the analysis presented in terms of radial profiles of suction at different times (Figure 3.3-20), the evolution of suction at the selected points in profiles P-12h and P-06h (Figure 3.3-21Figure 3.3-21) and the distribution of degree of saturation at different times (Figure 3.3-22). During the emplacement of the engineered barrier (and before the start of heating) a hydraulic interaction occurs between the bentonite and the concrete lining. A reduction in the initial suction of the granular material is computed close to the lining due to the hydration of the GBM by the water taken from the concrete. In contrast, the initial suction in the bentonite block (profile P-06h) is lower than the suction in the concrete liner at the end of the ventilation step and, therefore, the portion of the bentonite block near the lining dries. Once the heating phase starts, a thermally-induced hydration caused by the differential thermal expansion of water respect to the solid leads to a slight increase in saturation of the barrier around the canister. However, as the canister temperature continues to rise, the heated material closer to the heat source dries due to water evaporation in that zone. The suction heterogeneity in the bentonite materials at emplacement tends to disappear as heat is dissipated and natural hydration progresses. In such a context, the increase in the saturation state in zones far away from the canister surface can be attributed to the combination of the

condensation of vapour coming from the innermost zones of the barrier, the thermal expansion of water in pores and the advective water transport from the rock formation. Suction values ranging from 150 MPa to 180 MPa are predicted near the heat source and values around 19 MPa are obtained close to the buffer-lining interface after 10 years of heating.

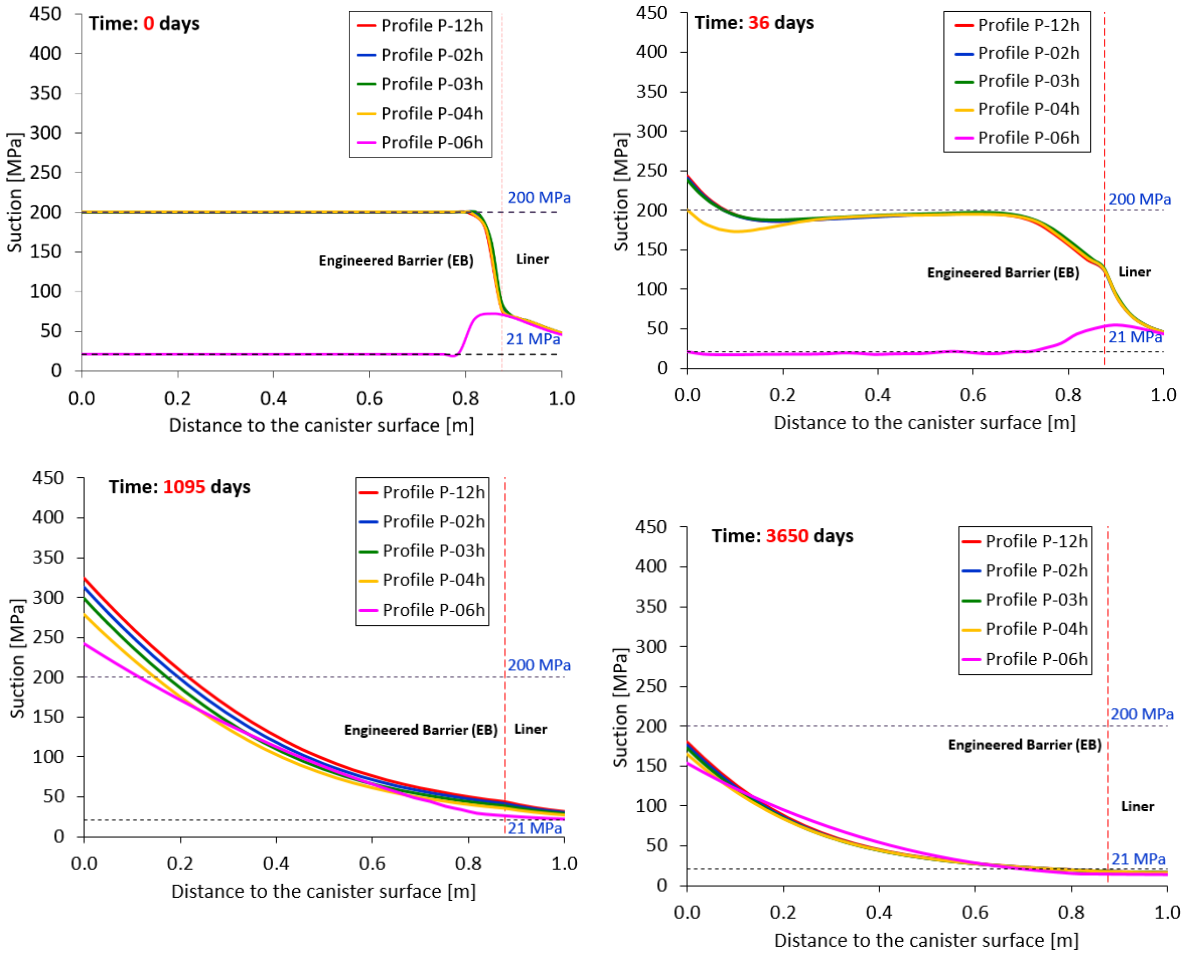

Figure 3.3-20 Radial distributions of suction within the bentonite barrier for 0, 36, 1095 and 3650 days

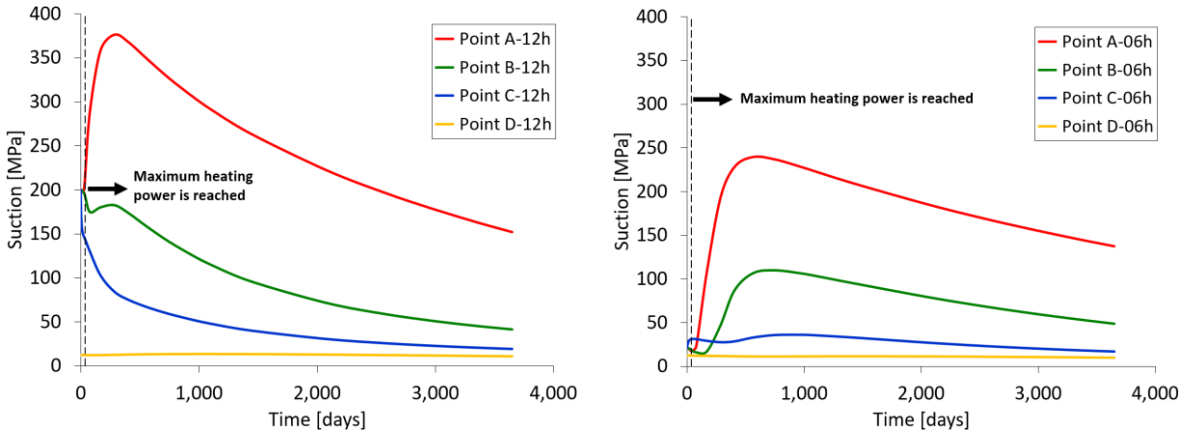

Figure 3.3-21 Evolution of suction at selected points in radial profiles P-12h (left) and P-06h (right) over 10 years of heating.

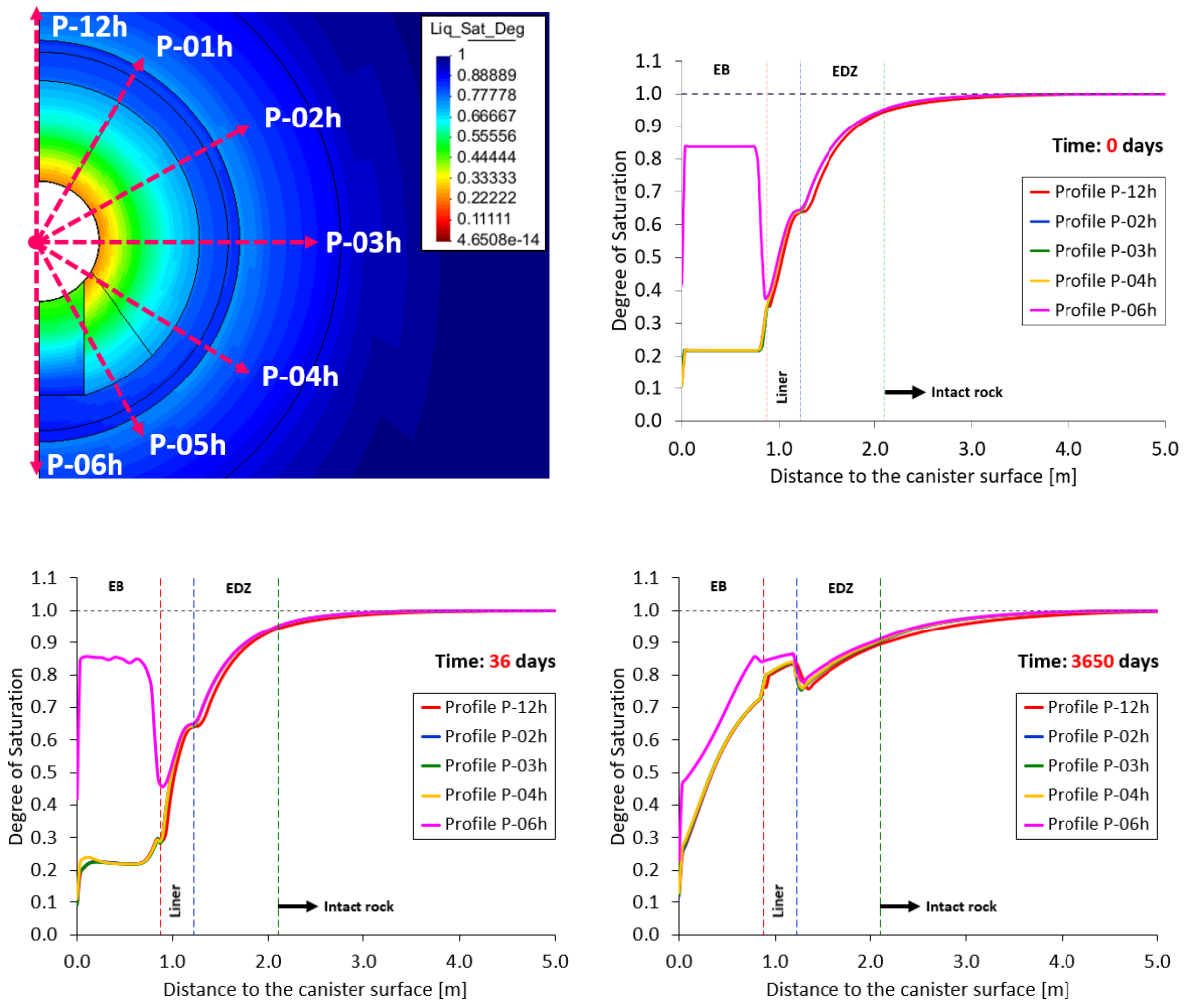

Figure 3.3-22 Degree of saturation contours after 10 years of heating (top left) and radial distributions of degree of saturation for 36, 1095 and 3650 days of heating.

Dry density and volume change

As discussed above, in the early stages of heating vapour will migrate from the inner part of the barrier to the cooler outer zones. Some hydration of the barrier closer to the lining is also due to water uptake form the rock, although it is quite limited due to the low permeability of the rock. This is confirmed by the results shown in Figure 3.3-23 and, in more detail, in Figure 3.3-24 for profile P-03h. Changes of density are of course related to volumetric strains; their evolution for three different points are plotted in Figure 3.3-25. It can be noted that the point closer to the lining undergoes an expansion compensated by the contraction at the point closer to the canister. Modelling time is too short, though, to provide information on the long-term distribution of dry density in the barrier.

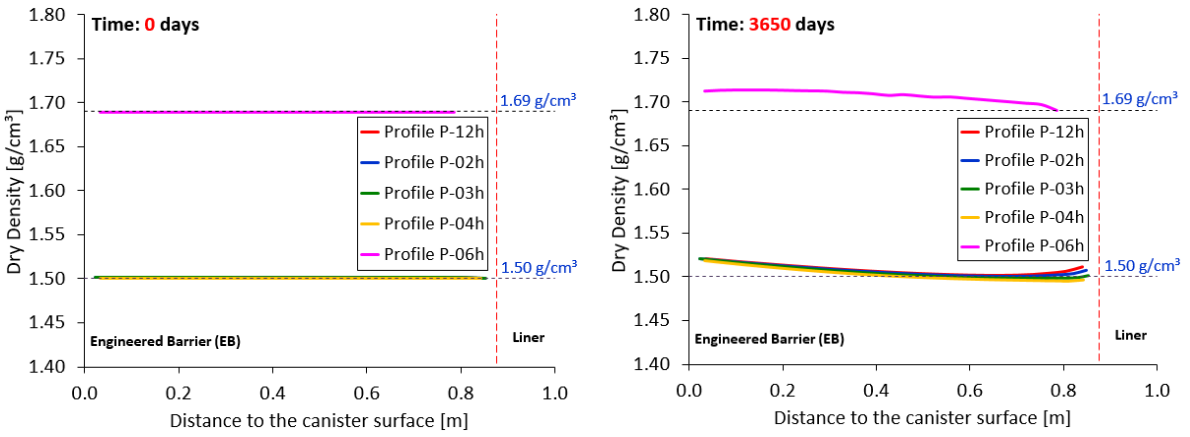

Figure 3.3-23 Radial distribution at the start of heating (left) and after 3650 of heating (right).

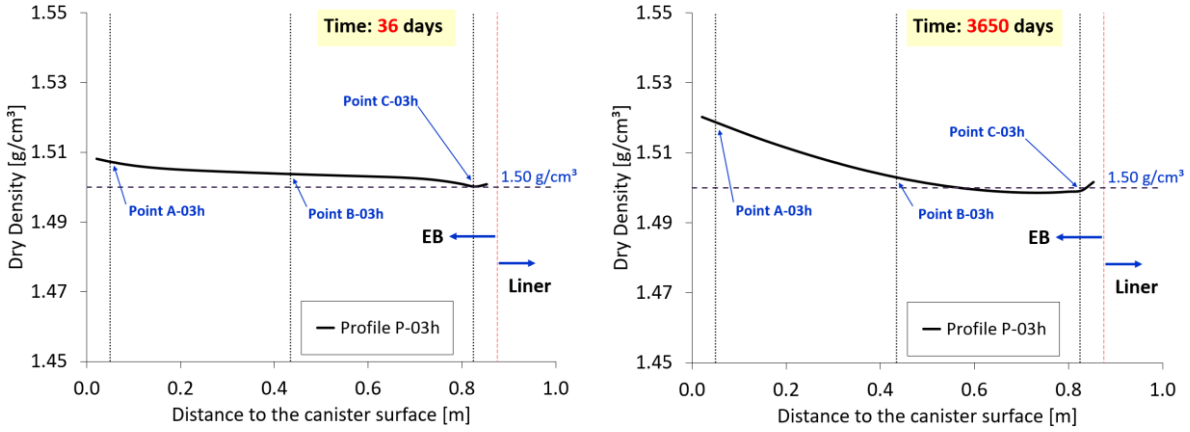

Figure 3.3-24 Radial distribution at the start of heating (left) and after 3650 of heating (right) for profile P-03h.

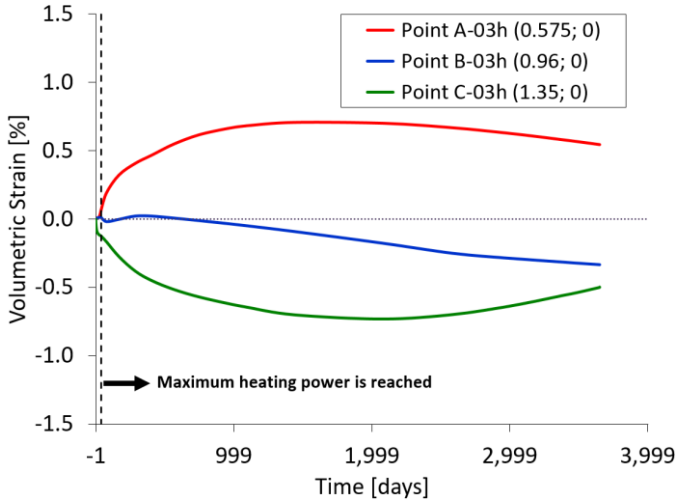

Figure 3.3-25 Evolution of the volumetric strains at three selected points in profile P-03h

Stresses in the EB

The changes in the density state of a bentonite barrier during the re-saturation process under global confinement conditions are associated with the changes in the stress state inside the barrier; in particular with the development of a swelling pressure in the bentonite materials. This mechanical behaviour is illustrated in Figure 3.3-26. It can be observed that there is an increase of stresses driven by the swelling of the outer part of the barrier that gets transferred to the other parts of the barrier. It is interesting to note, however, that at some point during the heating, mean stresses in the central and outer part of the barrier show a reduction suggesting a collapse of the GBM structure.

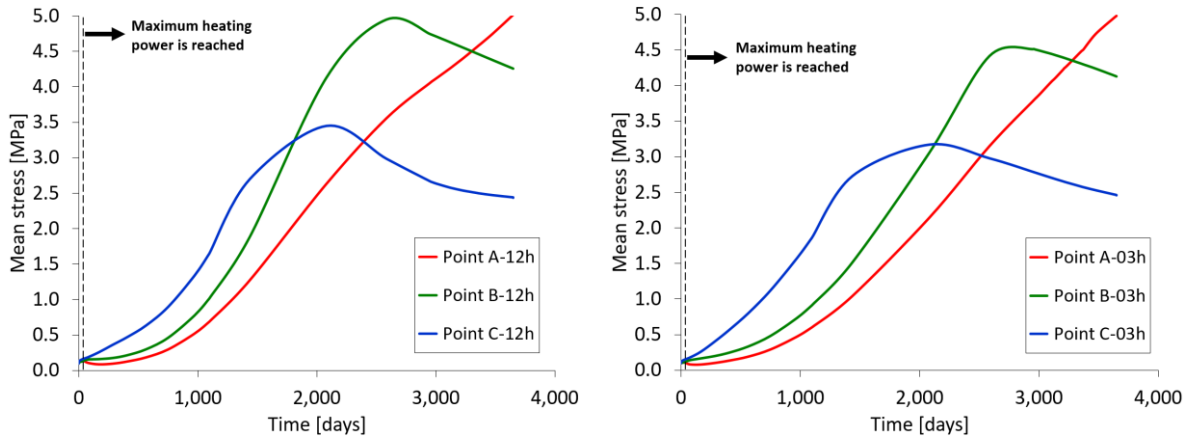

Figure 3.3-26 Evolution of the total mean stress at three selected points in profiles P-12h (left) and P-03h (right).

3.3.6 Discussion

The non-isothermal Nagra assessment case has been analysed using a recent development of a double structure model that incorporates thermal effects in a

consistent and rigorous manner. Although more work is still required in the verification and implementation of the model, it was decided to use it in this analysis for consistency with the modelling of the other Beacon benchmarks.

The boundary conditions have been carefully defined in order to reproduce all the stages of the case from excavation, through shotcrete, lining, barrier and canister installation to heating. Only 75% of the nominal heat power is applied in the analysis to obtain a more realistic temperature field. Particular attention has been given to the selection of model parameters based on existing information and laboratory results. Because of optimization and convergence issues associated with the implementation and use of the new thermomechanical constitutive model, the progress of the calculations has been protracted and only the results for the first 10 years of heating are available at the present time.

Based on physical considerations and on previous experience, it is possible to anticipate what is the expected behaviour of the barrier in the early stages of heating and hydration. The results obtained from the analysis correspond very well to this expected THM behaviour suggesting that the formulation and the constitutive law are performing satisfactorily so far. Modelling time, however, is too short to provide information on the long-term behaviour of the barrier and on its potential homogenization.

3.4 Synthesis of results – key lessons (Nagra + all participants in the Nagra test)

Three modelling teams participated to the Nagra assessment case. Among them only UPC used a double structure model. More details on the models can be found in deliverable D3.3 or in the previous paragraphs. Two configurations were proposed: a "homogeneous" case with a structure filled with granular bentonite material (GBM) distributed with the same dry density everywhere; a heterogeneous case where initial distribution of GBM is not uniform leading to local differences in dry density. For both cases initial heterogeneity is introduced in the field due to the presence of compacted blocks and pellets. The two cases have not been modelled by all the partners as can be seen in Table 3.4-1.

Table 3.4-1 Models used by each partner and treated cases

	UPC	BGR	EPFL
Code	Code_Bright/double structure	OpenGeoSys6/Elastoplasticity, linear swelling	Lagamine/ACMEG-TS Elastoplasticity
Homogeneous case	X		X
Heterogeneous case		X	X

The heterogeneity of dry density distribution in GBM was not introduced in the same way by BGR and EPFL. For BGR, the initial dry density distribution of the granular bentonite material is computed from measurements given in the specifications. For EPFL, the initial dry density is distributed by zones (see Figure 3.4-1).

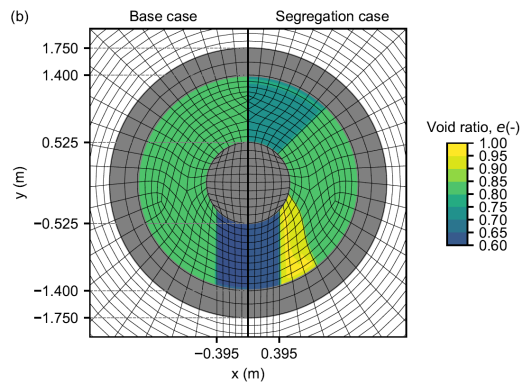

EPFL – initial void ratio - two initial state homogeneous (left) – heterogeneous (right)

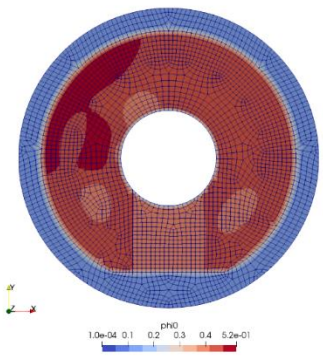

BGR – Initial porosity

Figure 3.4-1 Initial state in terms of void ratio distribution or porosity

Some ouputs have provided by each partners. The most relevant for this case in regards of the Beacon project is the final distribution of dry density over the bentonite domain. Other indicators are also interesting such as the swelling pressure or time to reach full saturation. It is important to notice that in this test the temperature is elevated due to the presence of a warm canister. Temperature at different locations will be compared and its influence on the hyromechanical responses will be analysed.

3.4.1 Time to reach full saturation

Full water saturation is reached with the four simulations between 50 and 80 years. The same trend is observed for all the approaches and consistent with what was expected. A faster saturation for the bentonite close to the host rock (points B, C Figure 3.4-2) than the bentonite in the vicinity of the canister. The rise in temperature results in a decrease in water saturation in the early stages around the canister. This decrease is of larger amplitude in the compacted block where the initial saturation is much higher than in the GBM. This can be seen on point A, B or G in Figure 3.4-2. The decrease of water saturation in the block could be also due to the large disequilibrium between block and GMB (only 20% of initial water saturation). The differences between the heterogeneous case and the homogeneous one are very small. This can be seen on the contributions from EPFL, the only teams that modelled the two situations. It should be noticed that the initial conditions considered by each team is different especially in the block part.

- About 80% in compacted block and 20% in GBM for UPC and EPFL
- About 60% in compacted block and 20% in GBM for BGR

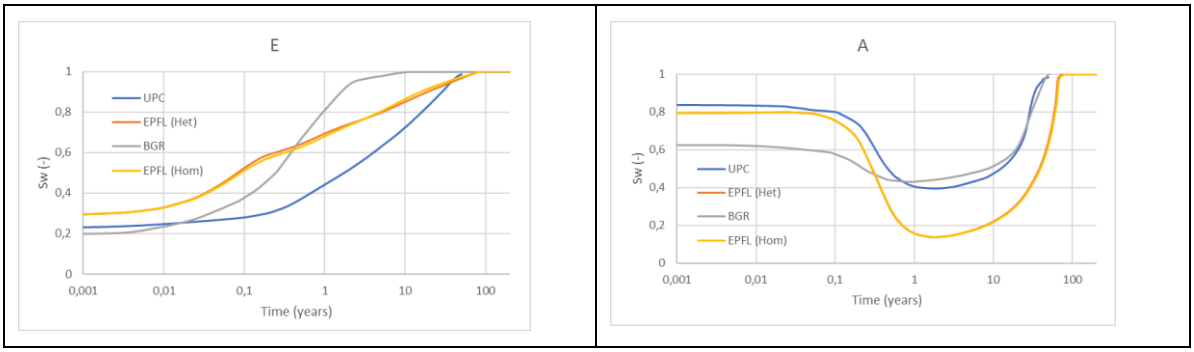

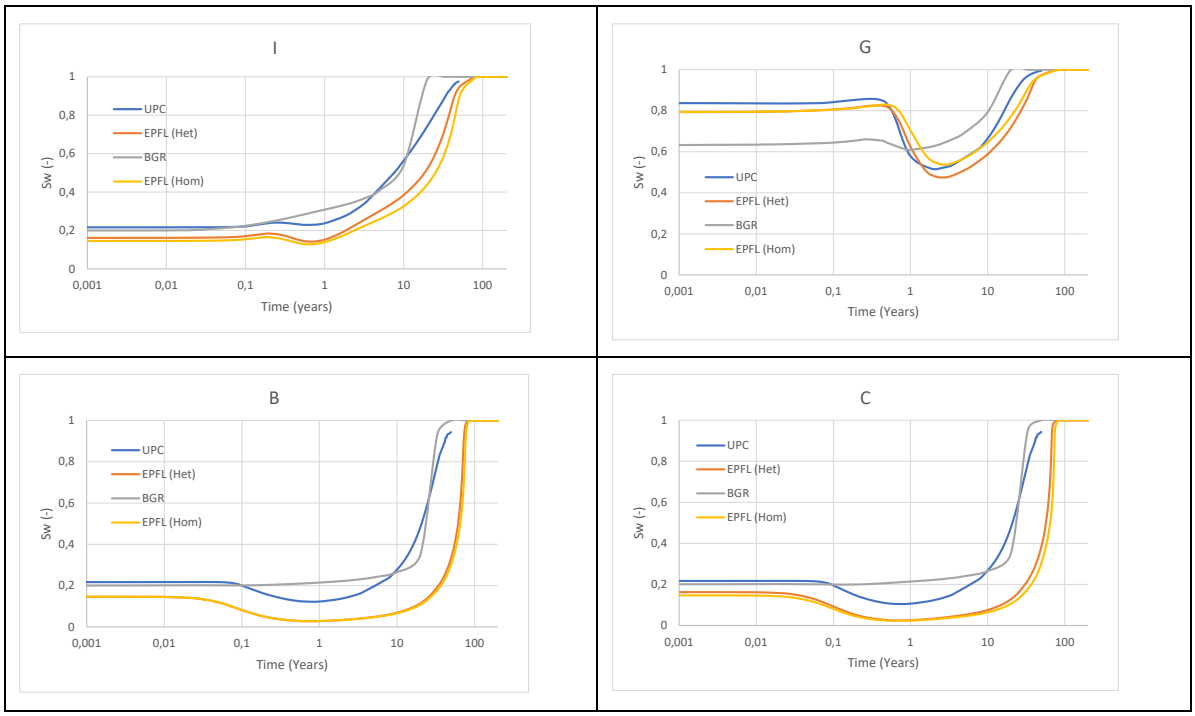

Figure 3.4-2 Comparison of water saturation evolution at 6 points (E, A, I, G, B, C)

As in most of the test cases performed in WP5, a large discrepancy is observed between the model when the transient phase is compared. This can be seen on horizontal water saturation profiles plot after 10 years (Figure 3.4-3).

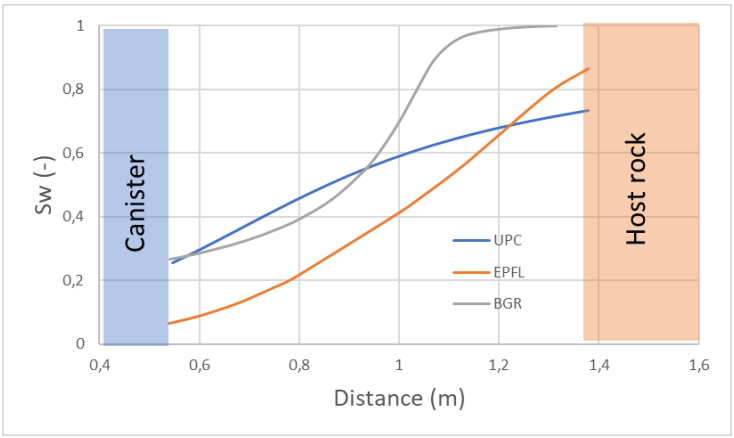

Figure 3.4-3 Horizonal profile of degree of saturation at t=10 years

3.4.2 Temperature evolution

A maximum of temperature between 110 and 115 °C is obtained close to the canister. At the interface with the host rock, the maximum of temperature is much lower between 70 and 80°C. Small differences are observed between the models on this

maximal level and the time of occurrence. This is mainly due to small differences in the way to consider the thermal source to adapt it to this reduce geometry. It is interesting to see that the initial distribution of dry density in the bentonite has a low influence on the results.

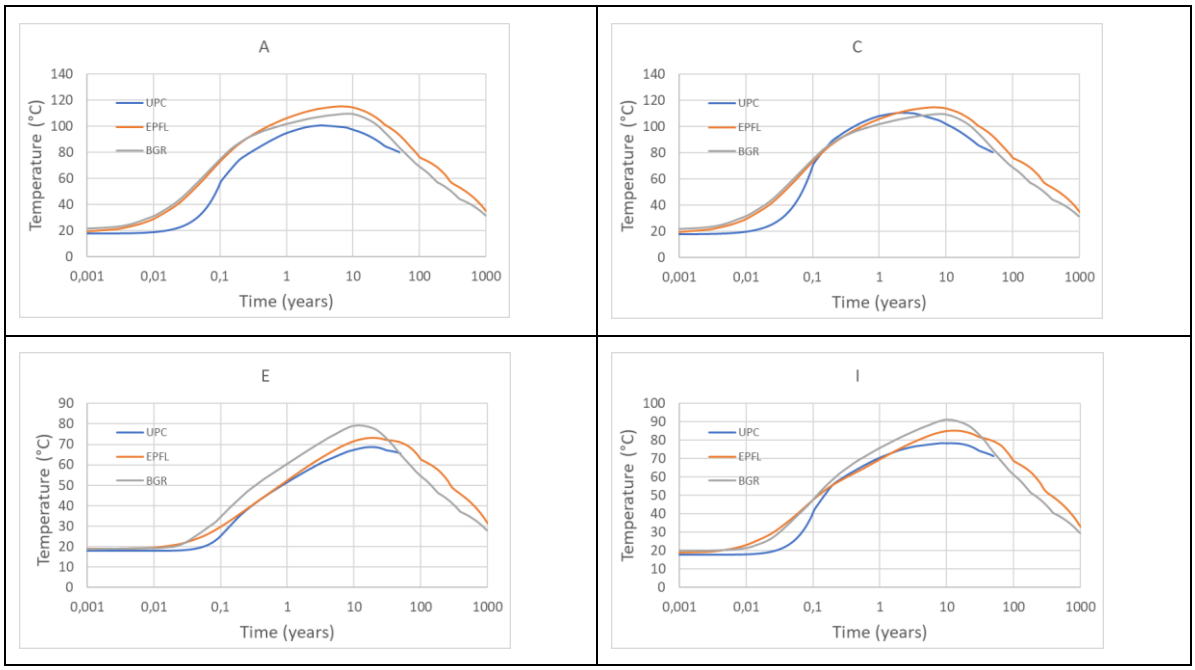

Figure 3.4-4 Temperature evolution for 4 points – close to the canister (A, C), close to the host rock (E), in the middle on GBM (I)

3.4.3 Dry density distribution

One of the most important indicators is the final distribution of dry density in the bentonite around the canister. Figure 3.4-5 shows the comparison of dry density evolution at several location (near the canister (A, B, C), near the host rock (D, E), in the middle of bentonite (G, H, I). Most of the time, a large discrepancy is observed between the models. The origin of the difference is certainly related to the initial dry density distribution that is different regarding the situation treated by each team. However, it can't explain all the differences observed. If a comparison is made between results from UPC and EPFL (homogeneous case) differences are visible despite the same initial distribution in bentonite. If the final state seems in the same range between UPC and EPFL, the pathway to reach it is quite different.

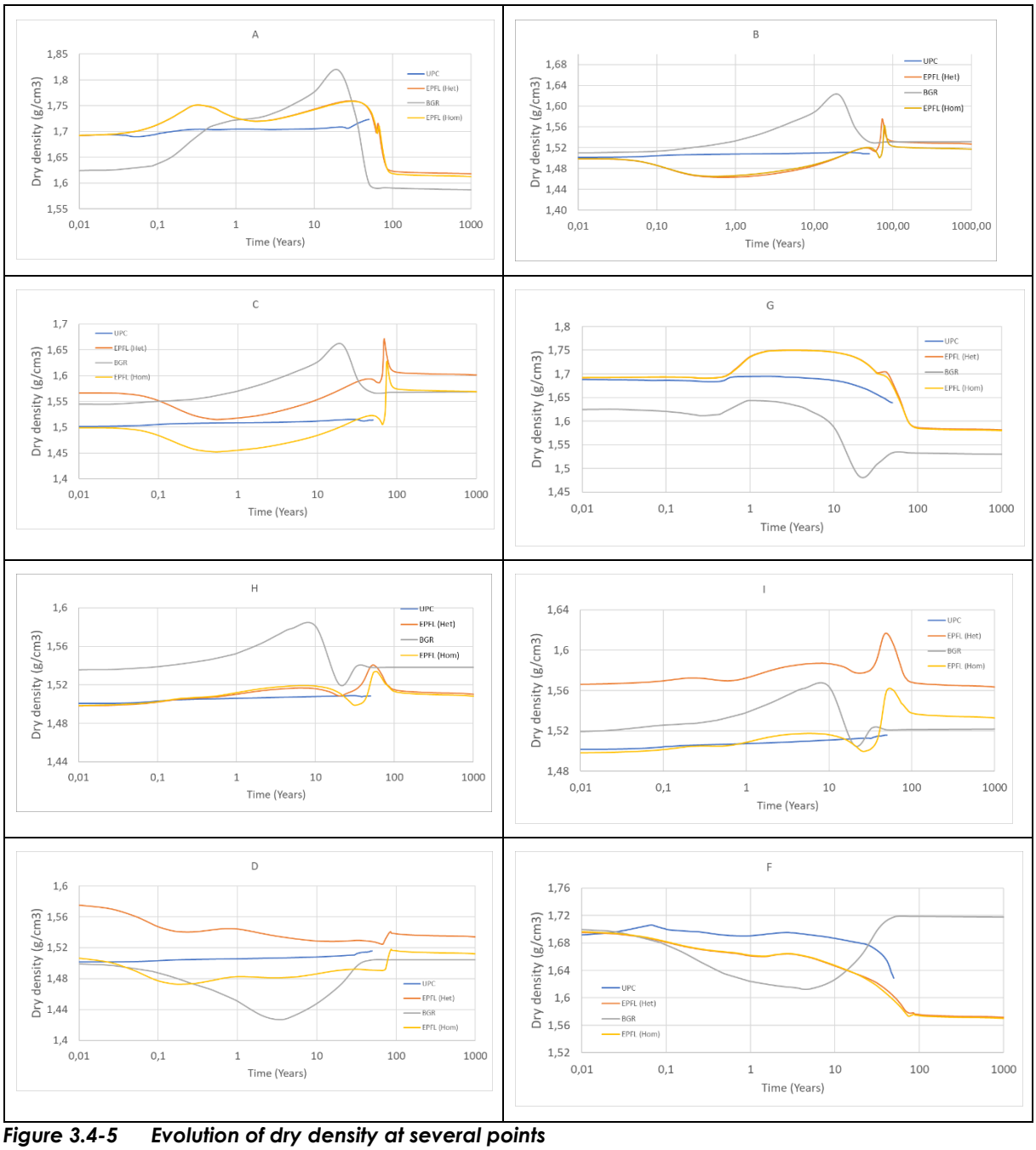

Figure 3.4-5 Evolution of dry density at several points

The comparison of the vertical dry density profiles illustrated clearly that the final state of the bentonite is heterogeneous. On all the results, the maximum dry density is obtained in contact of the canister (max value is just below in the block part). The lower values are obtained in the GBM on the top of the tunnel. Vertical profile plot at 50 years and 1000 years confirms the differences between the results obtained by the 3 teams as can be seen on the graphs (Figure 3.4-6).

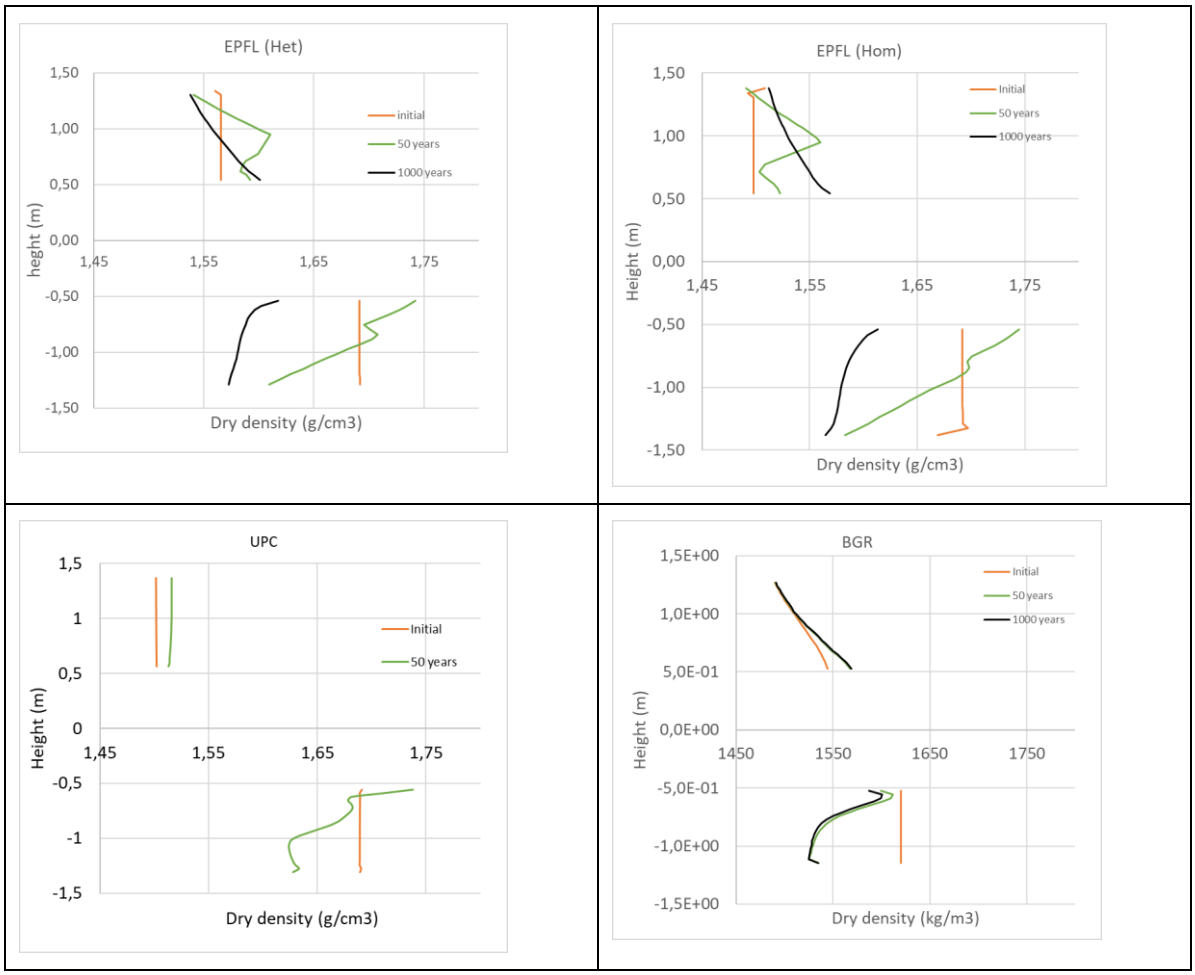

Figure 3.4-6 Vertical dry density profiles – initial, after 50 years, after 1000 years

3.4.4 Swelling pressure

The swelling pressure evolution is presented on Figure 3.4-7 and Figure 3.4-8 at six points. Three of them are at the interface between canister and bentonite, the others at the interface between bentonite and liner. Results are only available on the first fifty years for UPC. A first comparison is made at this date showing a large discrepancy in the results: between 1and 2 MPa for UPC; around 8MPa for BGR; between 2 and 5 MPa for EPFL for both initial situation heterogeneous or homogeneous. It should be notice that for EPFL, the stress field is far from the equilibrium at 50 years. As can be seen on Figure 3.4-8, the pressure stabilisation occurs after 1000 years.

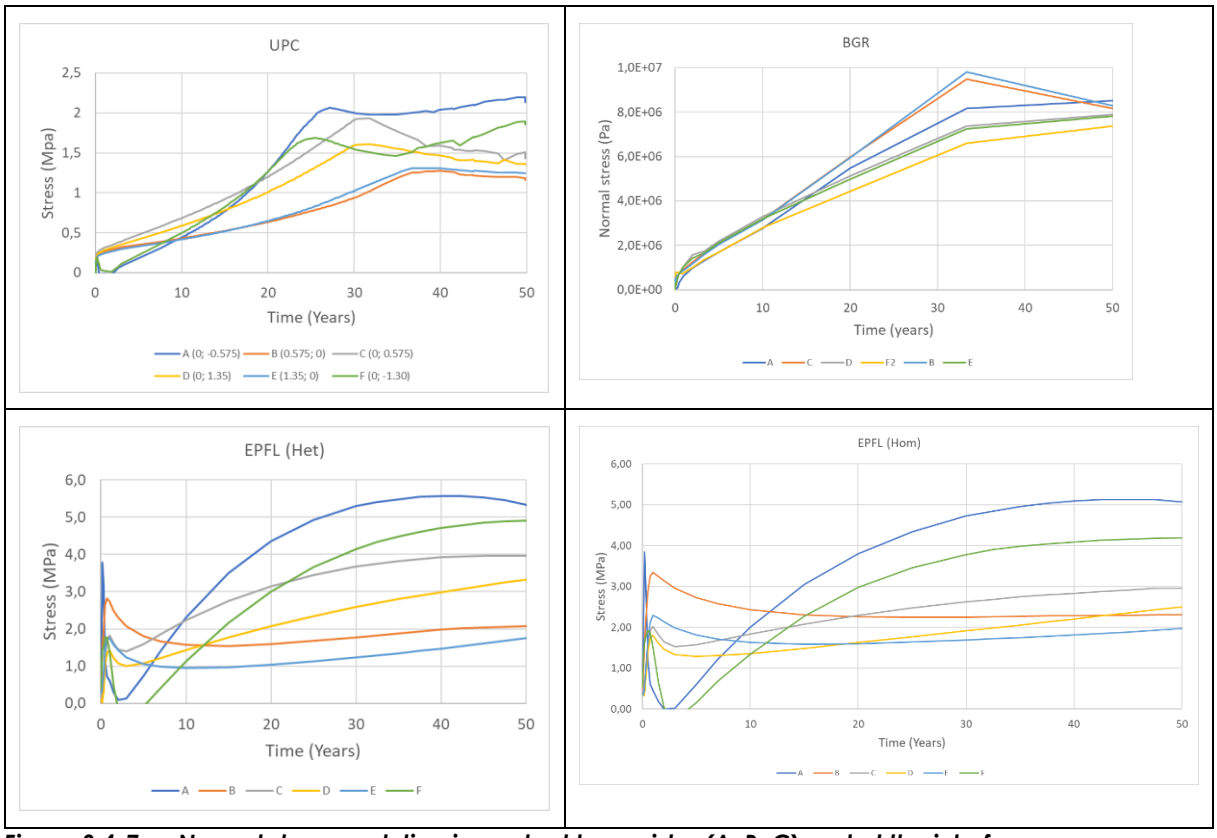

Figure 3.4-7 Normal stress evolution in contact to canister (A, B, C) and at the interface bentonite/liner (E, E, F) till 50 years

It can be observed on EPFL and UPC simulations that the pressure is maximum above and below the canister in the vertical direction which was expected due to the presence of compacted blocks.

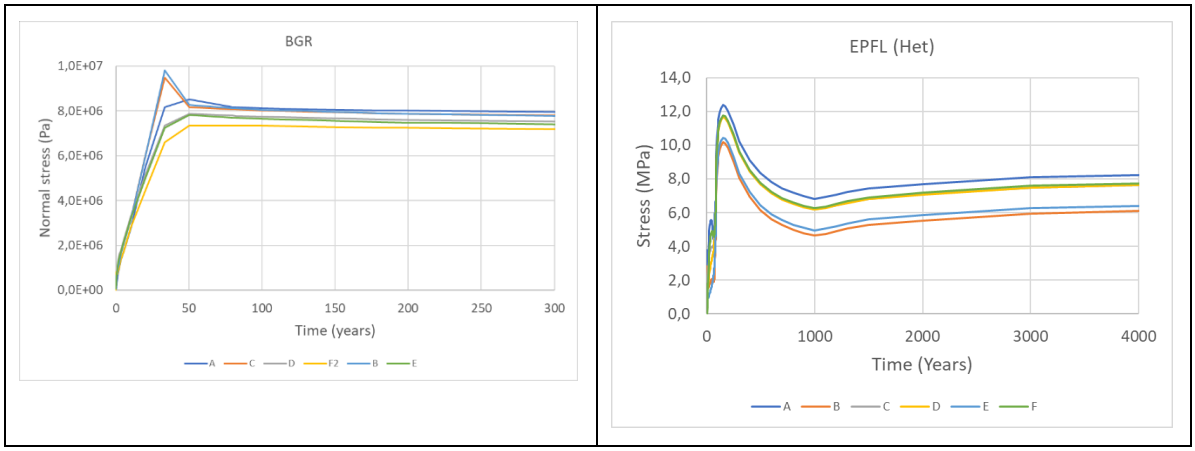

Figure 3.4-8 Normal stress evolution in contact to canister (A, B, C) and at the interface bentonite/liner (E, E, F) until stabilisation

A comparison can be made between swelling pressure and the dry density obtained in simulations and data obtained on samples. It can be seen a good consistency after

stabilization (close to hydromechanical equilibrium) for the long-term simulations performed by EPFL and BGR (see Figure 3.4-9). The final swelling pressure is estimated between 6 and 8 MPa (see Figure 3.4-8) corresponding to a range of drying density of 1.55 and 1.65 g/cm^3. This range is consistent with the mean dry density.

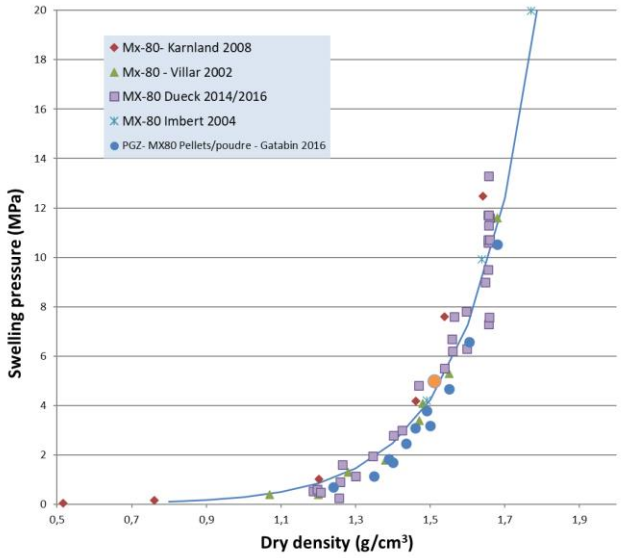

Figure 3.4-9 Swelling pressure function of dry density for MX-80 – compilation of measurements coming from several studies

3.4.5 Overall assessment

Three different models were used to simulate the Nagra assessment case. The main challenges of this assessment case are the different bentonite materials (blocks and granular bentonite), and the non-isothermal conditions. The Nagra case could be simulated by assuming an initially homogeneous distribution of granular bentonite or using the density distribution from the large-scale experiment FE.

Regarding resaturation the simulations of all three teams reach full saturation after 50 – 80 years[1] which is comparable to results from simplified TH modelling (Senger et al., 2016). The BGR team assumed different initial conditions with an initial water saturation of 60% for the bentonite blocks. The other two teams opted for 80 % as given in the assessment case description.

[1] Models assumed a permeability for the Opalinus Clay of 5×10^{-20} m^2 parallel to bedding and 10^{-20} m^2 normal to bedding, together with a constant boundary pore pressure of ~2.1MPa similar to that observed at the FE experiment.

Differences can be found in the rate of saturation: the saturation distribution for BGR shows a rather steep gradient from the outer part towards the inner part while for UPC and EPFL the curve is more linear and less steep. In terms of consistency in simulation results, it is important to note that full saturation is reached for all the models used after about a century which coincides with the closure of the repository. The time to full saturation is in Nagra's however not safety relevant.

The simulated temperature evolution peaked between 110 and 115 °C close to the canister. Only small differences are observed between the models regarding the time of occurrence. The simulated temperature range corresponds to the range of temperatures measured in large-scale experiments such as the FE. Unfortunately, the model results do not show whether the temperature below the canister are smaller due to the higher thermal conductivity of the bentonite blocks (which have a higher initial water saturation) as has been observed in the Large-scale experiment FE.

At the rock interface temperatures of between 70 – 80°C are reached. The temperatures are again in good agreement with the temperatures simulated by simplified TH models. From a safety point of view only the maximum temperature at the rock interface is of relevance which should not exceed the Opalinus Clay palaeotemperature of about 80-90°C.

The final distributions of dry density in the bentonite around the canister simulated by the three different teams vary greatly. The differences are certainly related to the different initial dry density assumed (BGR) but this does not explain all the differences observed. Comparing results from UPC and EPFL (homogeneous case) differences are visible despite assuming the same initial distribution. If the final state seems in the same range for UPC and EPFL, the pathways to reach it are quite different. The results of UPC are still preliminary and the authors indicated that the model was calibrated with data that lie outside the range of swelling pressures to be simulated in the frame the Nagra assessment case.

Obviously, the distribution of dry density is the most important indicator for the homogenization process. The results obtained by UPC and BGR would suggest that the minimum requirements formulated by Nagra would not be satisfied. Their results however do not align with expected results from lab scale experiments that would suggest higher swelling pressures (e.g. Karnland 2006) and further verification and/or validation of the codes used would certainly help in understanding the reasons for the observed deviation. The results from EPFL are consistent with literature data and measurements performed in large-scale experiments. These results indicate that both the degree of homogeneity and the swelling pressures comply with Nagra's safety related requirements for the bentonite buffer.

4 Andra assessment case

4.1 ULg

4.1.1 Description of the model

Argillite

The mechanical behaviour of the COx is considered elastoplastic with linear elasticity (PLASOL mechanical law), using the Van Eekelen yield surface (van Eekelen 1980).

Viscosity is not considered in this study.

The hydraulic model considers isotropic hydraulic permeability and defines the water adjective flow based on the Darcy's law.

The (van Genuchten 1980) water retention model is used [Eq. 1]:

$$S_{r,w} = S_{res} + (S_{max} - S_{res})\left[1 + \left(\frac{p_c}{P_r}\right)^{\frac{1}{1-m}}\right]^{-m} \qquad \textit{Eq. 1}$$

The water relative permeability is linked to the saturation degree via the following equation [Eq. 2].

$$k_{r,w} = \sqrt{S_{r,w}} + (1 - \left(1 - {S_{r,w}}^{1/m}\right)^{m})^2 \qquad \textit{Eq. 2}$$

Bentonite

Mechanical model

The complexity of the coupled multiphysical and multiscale phenomena taking place during bentonite hydration is well known. The Barcelona Basic Model (BBM) **Source spécifiée non valide.** is able to reproduce a wide range of phenomena occurring in unsaturated soils and, due to this, it is selected as mechanical constitutive model. The model is formulated adopting net stress $\boldsymbol{\sigma}$ [Eq. 3] and suction s as stress variables.

$$\boldsymbol{\sigma} = \boldsymbol{\sigma}_T - u_a \boldsymbol{I} \qquad \textit{Eq. 3}$$

With $\boldsymbol{\sigma}_T$ the total stress tensor, u_a the air pressure for $s>0$ and $\boldsymbol{I}$ the identity tensor.

According to the BBM, under isotropic stress conditions, the variation of volumetric elastic strain is associated to changes in mean net stress p and suction s [Eq. 4]. Moreover, in order to tackle the stress dependence of the swelling strain for change in suction underlined by [Eq. 4],[Eq. 5] is adopted.

$$d\varepsilon_v^e = \frac{\kappa}{1+e}\frac{dp}{p} + \frac{\kappa_s}{1+e}\frac{ds}{s+u_{atm}} \quad \textit{Eq. 4}$$

$$\kappa_s(p) = \kappa_{s0} * \exp(-\alpha_p * p) \quad \textit{Eq. 5}$$

The evolution of the preconsolidation pressure $p_0(s)$ is modelled consistently with the concept of increasing the elastic domain with increasing suction [Eq. 6] as well as the rate of increase of the soil stiffness with suction [Eq. 7].

$$p_0(s) = p_c\left(\frac{p_0^*}{p_c}\right)^{\frac{\lambda(0)-\kappa}{\lambda(s)-\kappa}} \quad \textit{Eq. 6}$$

$$\lambda(s) = \lambda(0)[(1-r)\exp(-\omega s) + r] \quad \textit{Eq. 7}$$

The mechanical constitutive law is based on the Barcelona Basic Model (Alonso, Gens, and Josa 1990).

Hydraulic model

The selected water retention model is formulated in terms of water ratio e_w [Eq. 8], which is expressed as the superposition of a contribution from the water stored in the micropores e_{wm} and a second contribution from the water contained in the macropores e_{wM} [Eq. 9].

$$e_w = S_r e \quad \textit{Eq. 8}$$

$$e_w = e_{wm} + e_{wM} \quad \textit{Eq. 9}$$

The model also considers the microstructure evolution occurring during saturation [Eq. 10].

$$e_m = e_{m0} + \beta_0 e_w + \beta_1 e_w^2 \quad \textit{Eq. 10}$$

Therefore, global degree of saturation is obtained by the sum of the microstructural and macrostructural degrees of saturation, weighed by the corresponding volumetric fractions [Eq. 9].

$$S_r = \frac{e_w}{e} = \frac{e_m}{e}S_{rm} + \frac{e_M}{e}S_{rM} \quad \textit{Eq. 11}$$

Dubinin's isotherm is adopted to describe the water retention behaviour of the microstructure, which is mainly stored by absorption [Eq. 12]. For the macrostructural water retention domain, the van Genuchten equation is selected [Eq. 13] replacing the void ratio e by macrostructural void ratio e_M =e-e_m. The parameter α is assumed to depend on the macrostructural void ratio representing the influence of the bentonite structure on the air-entry value [Eq. 14].

$$e_{wm}(s, e_m) = \mathrm{e}_m exp[-(C_{ads}s)^{n_{ads}}] \quad \textit{Eq. 12}$$

$$e_{wM}(s, e) = (e - e_m)\left[1 + \left(\frac{s}{\alpha}\right)^n\right]^{-m} \quad \textit{Eq. 13}$$

$$\alpha = \frac{A}{e - e_m} \quad \textit{Eq. 14}$$

Finally, in order to consider the double structure nature of compacted bentonite-based materials also in the water transfer mechanisms, the water permeability evolution is modelled considering an Extended Kozeny-Carman model [Eq. 15], in which the total porosity is substituted by the macrovoid ratio e_M.

$$K_w = K_{w0}\frac{e_M^{expn}}{(1 - e_M)^{expm}}\frac{(1 - e_{M0})^{expm}}{e_{M0}{}^{expn}} \quad \textit{Eq. 15}$$

4.1.2 Geometry and discretization

The Andra assessment configuration consists in a circular gallery excavation, of 10 m diameter. In this modelling strategy, plane strain conditions are taken into account and only half domain is considered, with a vertical symmetry axis coinciding with the plane cutting the buffer at the centre.

The considered domains host-rock is 100 m high and 50 m large. Such domain size is selected in order to avoid boundary influence (Figure 4.1-1).

The current modelling strategy accounts for two phases:

1. Gallery excavation in the Callovo Oxfordian host rock. It is worth of attention that the excavation in the host-rock itself strongly modifies the hydro-mechanical properties of the clay-rock causing stress modifications and damage propagation. It results, in fact, into the creation of an Excavation Damaged Zone (EDZ) developing close to the drift wall. In the present work, a simple modelling for the EDZ is also used to take into consideration its properties.
2. The activation and saturation of bentonite plug. An apical technological gap is expected on the top of the bentonite plug due to the emplacement procedure. As the bentonite sealing hydrates, it swells in quasi-free swelling conditions closing the gap. When the gap is closed isochoric hydration conditions are reached and swelling pressure is developed on the host-rock.

The technological apical gap is modelled via an interface element (Cerfontaine et al. 2015).

As the swelling deformation is prevented, a swelling pressure is generated, which is defined as the pressure needed to prevent the volume change.

The presence of the argillite is supposed to represent a mechanical obstacle in the swelling process. Hence, a new stress state is obtained at the interface between the different materials.

Moreover, the host rock is the major water source for the bentonite. A new hydraulic equilibrium state has to be defined as well as the stress one. Hence, swelling plug and host rock interact from both hydraulic and mechanical points of view.

The mesh consists in 5840 8-node isoparametric elements (Figure 4.1-2), which represent the COx (intact and damaged zone), the bentonite plug and linear elastic low stiffness virtual elements. Linear elastic low stiffness elements are considered at the place of the bentonite in the gallery during the excavation phase. Their modelling does not affect the hydro-mechanical response of the model. It is employed to assure numerical stability during the bentonite elements activation.

Distributed uniform forces are modelled in order to simulate the decreasing confining stress in the host-rock (LICHA).

This modelling strategy considers also 5 2-node isoparametric interface elements representing the gap itself. These elements model on the one hand the unilateral contact induced by swelling, and on the other hand a good water transmissivity (T = 10E-19)

Table 4.1-1 reports the number of elements of the mesh.

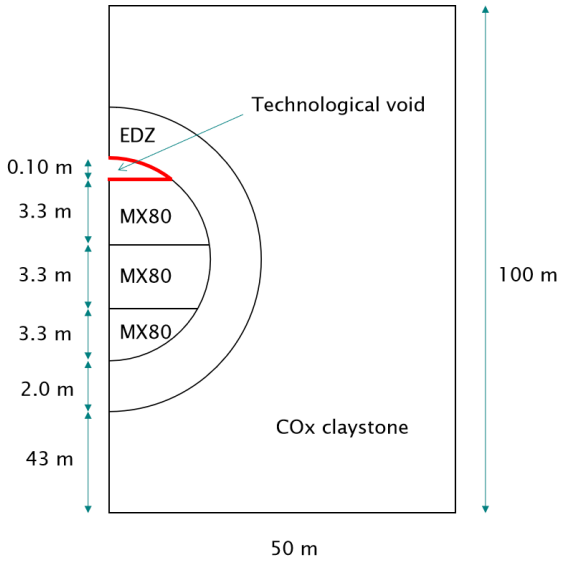

Figure 4.1-1 Domain dimensions.

Table 4.1-1 Number of elements of each component.

	Number of elements
Licha	150
Interface	5
Intact rock	210
EDZ	360
Bentonite	1435
Virtual element	1435
Total	5995

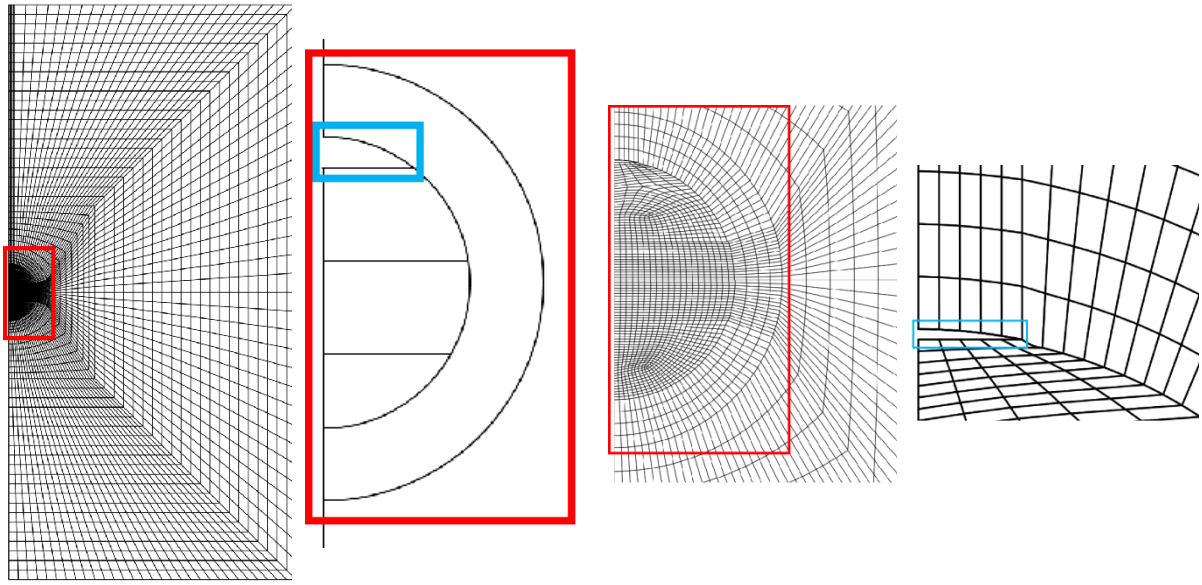

Figure 4.1-2 FE mesh of the modelled domain

4.1.3 Input parameters

Argillite

During galleries excavation, the boreholes cause stress modifications and damage propagation, resulting in an Excavation Damaged Zone (EDZ) developing close to the drift wall. The EDZ presents distributed damage and possible macro-fractures, encouraging the water flux in the rock that modifies the stress states in turn.

In this zone, the material mechanical performances are poorer and the permeability is higher with respect to the intact rock matrix one. The permeability is the highest close

to the drilling walls, where the material is highly disturbed and becomes lower as the distance from the excavation increases (Pardoen 2015).

Thus, the modelling of the EDZ is taken into account considering homogeneously distributed mechanical and hydraulic features in an equivalent radius presenting lower values with respect to the intact rock's ones.

Table 4.1-2 COx mechanical parameters.

	Young's modulus	**Friction angle**	**Cohesion**	**Poisson's ratio**	**Density**	**Biot's coefficient**
	E **[GPa]**	**φ** **[°]**	**c** **[MPa]**	**v** **[-]**	**ϱ** **[Kg/m³]**	**b** **[-]**
Intact rock	5	20	2	0.3	2300	0.6
EDZ	0.5	20	0.5	0.3	2300	0.6

The anisotropy of the argillite will not be considered in this analysis.

The selected hydro-mechanical model parameters of the Callovo Oxfordian claystone are reported in Table 4.1-2 and

Table 4.1-3.

Table 4.1-3 COx hydraulic parameters.

	Water permeability	**Water retention curve parameter**	**Water retention curve parameter**	**Residual saturation degree**	**Field saturation degree**	**Relative permeability curve parameter**
	K_w **[m^{-2}]**	**Pr** **[MPa]**	**m** **[-]**	**Sres** **[-]**	**Smax** **[-]**	**m** **[-]**
Intact rock	$2*10^{-20}$	15	1.49	0.01	1	0.32886
EDZ	$2*10^{-16}$	15	1.49	0.01	1	0.32886

Bentonite

The mechanical parameters are related to the MX-80 pellet mixture related to the experimental test analysed in WP5_1b (Table 4.1-4).

Table 4.1-4: Bentonite mechanical parameters.

EXPERIMENTAL TESTS		**WP5_1B**
κ	[-]	0.06
κ_s	[-]	0.07
a_p	[-]	2.6×10^{-7}
p_0^*	[MPa]	1.86
p_c	[MPa]	0.93
$\lambda(0)$	[-]	0.20
r	[-]	0.75
ω	[Pa^{-1}]	1.00×10^{-7}
φ	[°]	25
v	[-]	0.35
$c(0)$	[MPa]	0.10
k	[-]	0

The selected hydraulic input parameters are chosen due to model calibration on experimental observations for MX80 pellet mixture related to the experimental test analysed in WP5_1b. Double porosity water retention model and permeability evolution model are selected.

Table 4.1-5: Bentonite water retention curve parameters.

EXPERIMENTAL TESTS		**WP5_1B**
e_{m0}	[-]	0.31
β_0	[-]	0.1

β_1	[-]	0.48
C_{ads}	[MPa^{-1}]	0.0075
n_{ads}	[-]	0.2
n	[-]	3
m	[-]	0.45
A	[MPa]	0.2

Table 4.1-6: Bentonite permeability evolution parameters

EXPERIMENTAL TESTS		**WP5_1B**
C_k	[m^2]	1.8 ×10^{-20}
expm	[-]	1.5
expn	[-]	0.2
γ	[-]	4

4.1.4 Initial and boundary conditions

The first phase boundary conditions consist in imposed total stresses and pore pressures both in the inner (galley axis) and outer radius of the host rock (Figure 4.1-3).

An initial isotropic total confining pressure of 12.4 MPa and an initial pore water pressure of 4.7 MPa is considered in the host rock.

The excavation is simulated through the variation of boundary conditions on the drilling front (i.e. inner radius of the host-rock) via the evolution laws depicted in (Figure 4.1-5).

The variation of confining pressure develops in the first 28 days of the simulation time.

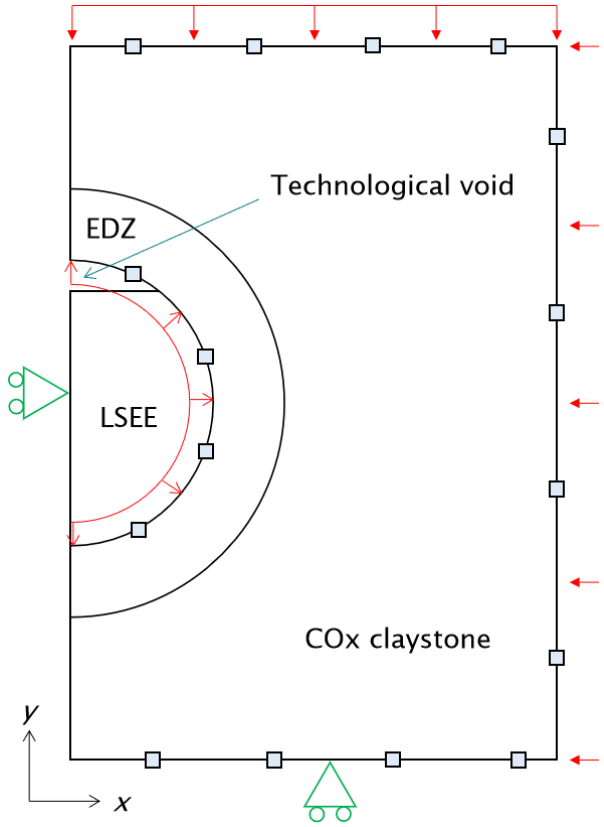

Figure 4.1-3 Excavation phase configuration

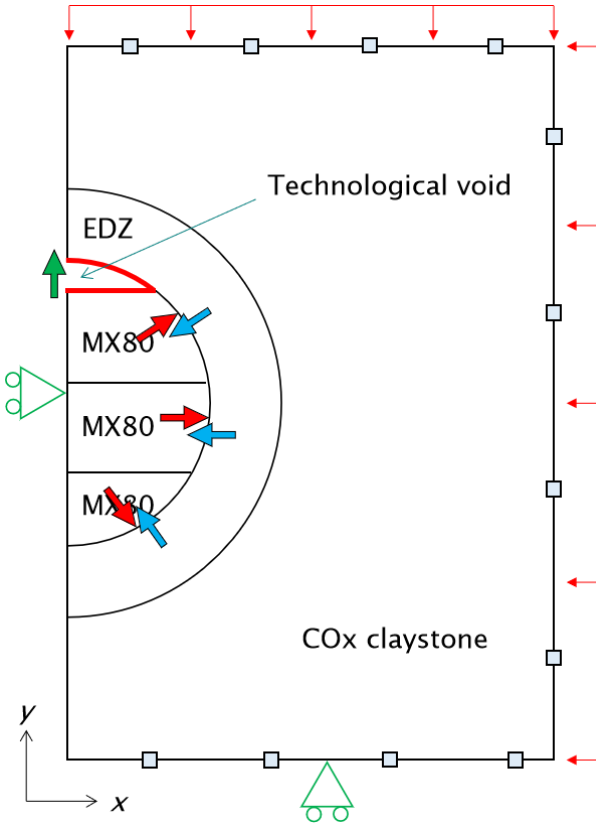

Figure 4.1-4: Saturation phase configuration

The variation of pore water pressure occurs in 2 days, between the 13th and the 15th day of the simulation time from the initial value of 4.7 MPa to 0 and between the 60th day and the 10th year of the simulation time from 0 to -100 MPa, which wants to simulate the ventilation period before the sealing.

On the outer boundary:

- on the vertical left axis horizontal displacement and water flux is prevented;
- on the right and top boundaries initial confining pressure and pore water pressure remain constant;
- on the bottom boundary vertical displacement is prevented and pore water pressure remain constant at its initial value.

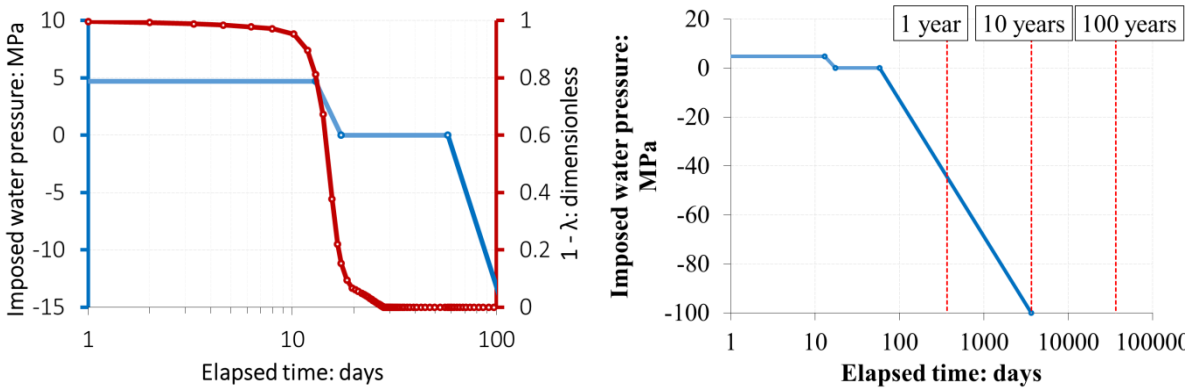

Figure 4.1-5 Confining pressure and pore water pressure evolving on the excavation wall

For the second phase, the addition of the bentonite plug is considered at the 100th year of simulation time.

The bentonite plug presents heterogeneous initial dry density (in layers), heterogeneous permeability (related to the initial dry density), uniform suction s=100 MPa and saturation degree close to Sr=29% (according to the selected water retention curve). Only the density and the permeability differ between the 3 layers, the other parameters are equal. So we didn't model a strong heterogeneity.

Location	Dry density
Layer	ρ_d
	[g/cm^3]
Top	1.48
Centre	1.55
Bottom	1.60

The pore water pressure of the host rock in contact with the bentonite is not fixed anymore (Figure 4.1-4) due to the hydration process of the core which develops water flux. The apical gap closes and then the stress state also varies due to the swelling pressure developed in the process.

A new equilibrium state is obtained after some time.

4.1.5 Results

Excavation phase

Gallery drilling simulated via confining stress and pore pressure decrease (respectively from 12.56 MPa to 0 and 4.7 MPa to 0) causes excavation wall convergence of about 8 cm in the first 28 days of the simulation time. When ventilation is applied (i.e. pore pressure decrease from 0 to -100 MPa) a partial recover of convergence is recorded of about 2 cm.

As ventilation is stabilised (i.e. constant suction from 10th year of the simulation time), pore pressure redistribution inside the clay-stone generates a further small deformation (Figure 4.1-6).

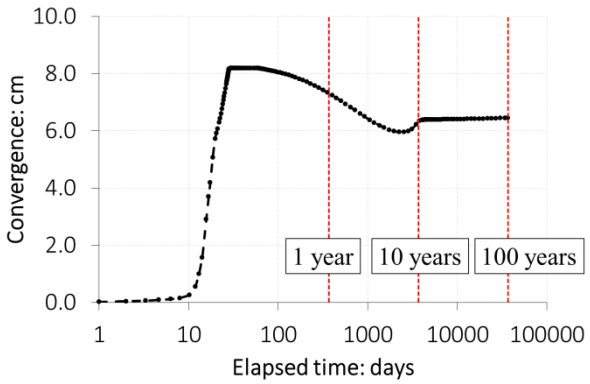

Figure 4.1-6 Convergence at the excavation wall during the first 100 years of the simulation time. Results concerning section in Figure 4.1-7.

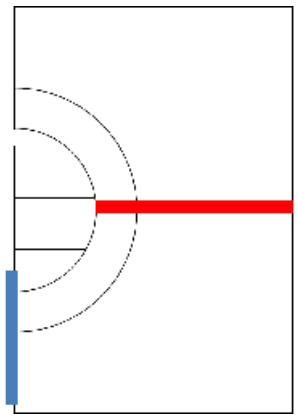

Figure 4.1-7 Analysed section in host rock.

Figure 4.1-8 and Figure 4.1-9 show the pore water pressure profile in the host-rock (Figure 4.1-7) with respect to several simulation times. The permeability contrast between the intact rock and the EDZ is evident. The latter one is particularly subjected to the initial pore-pressure decrease and consequential ventilation. The high permeability does not allow the formation of pore water pressure gradients, which are observable in the intact rock.

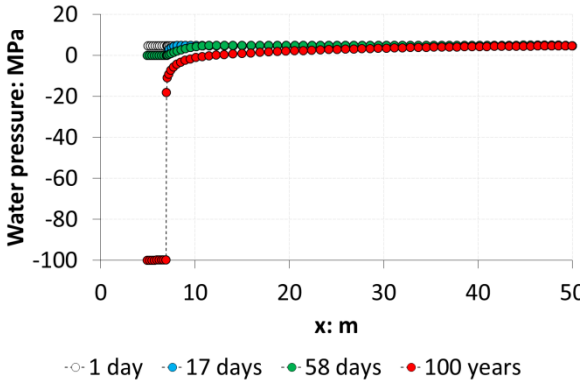

Figure 4.1-8 Pore water pressure in host-rock for several times. Results concerning section in Figure 4.1-7.

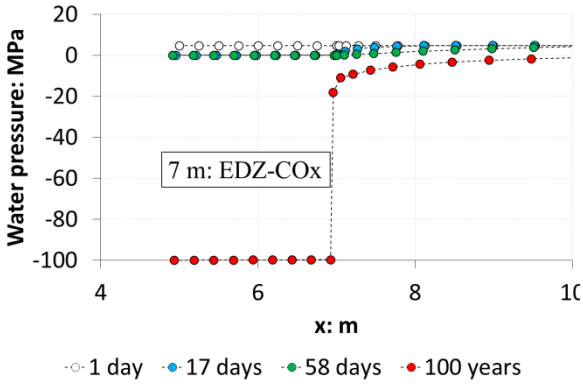

Figure 4.1-9 Pore water pressure in host-rock for several times, detail on EDZ. Results concerning section in Figure 4.1-7.

It is indeed possible to notice this occurrence from the pore-water pressure distribution (Figure 4.1-10). The EDZ presents uniform and homogeneous pore water pressure value equal to -100 MPa, whereas the pressure gradient in the intact rock develops for about 45 m. This possibly suggests that the domain should have an increased extension.

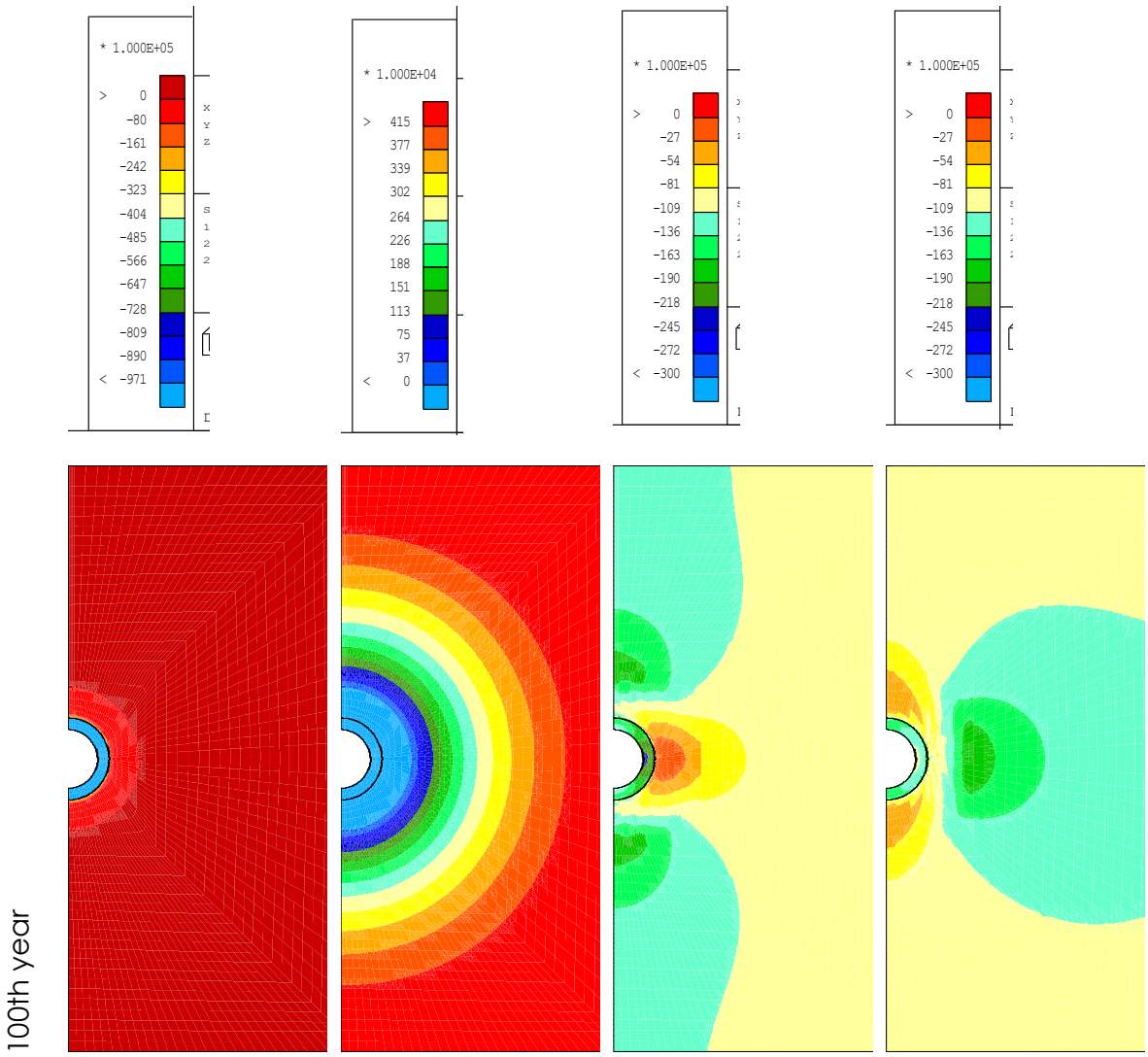

Figure 4.1-10 Host-rock iso-values for pore water pressure, horizontal stress and vertical stress.

Saturation phase

Bentonite

The following analysis refers to the bentonite portion reported in Figure 4.1-11.

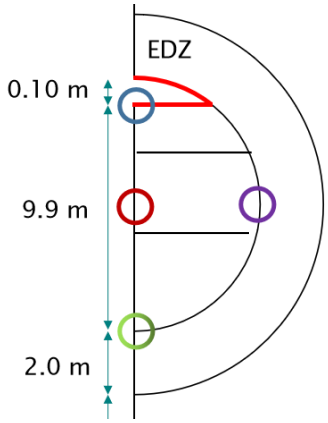

Figure 4.1-11 Analysed bentonite portion in time evolution plots.

Figure 4.1-12 shows the saturation time evolution of the considered bentonite portion. It is evident that the saturation is quicker on the top part of the sealing, where the gap is found. The trend of this point is slightly different from the one of the bottom and side portions, which are in direct contact with the COx and thus correspond. However, as soon as the gap is closed, the top material saturation evolution follows the same behaviour of the bottom and side material. Since the central part of the central layer is the farest from the water source (i.e. the rock), it is consequentially the last to reach full saturation, after about 3000 years.

However, buffer saturation takes place quite homogeneously as the saturation fields in Figure 4.1-13 suggest. The saturation isovalues are not homogeneous but underline the presence of different dry density distribution as this modelling strategy considers. The saturation is linked to the dry density via the selected dry density dependent water retention model.

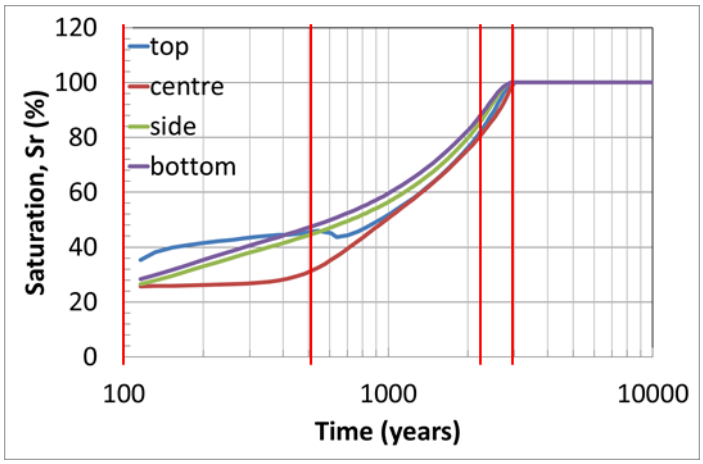

Figure 4.1-12 Saturation time evolution of four points in the bentonite.

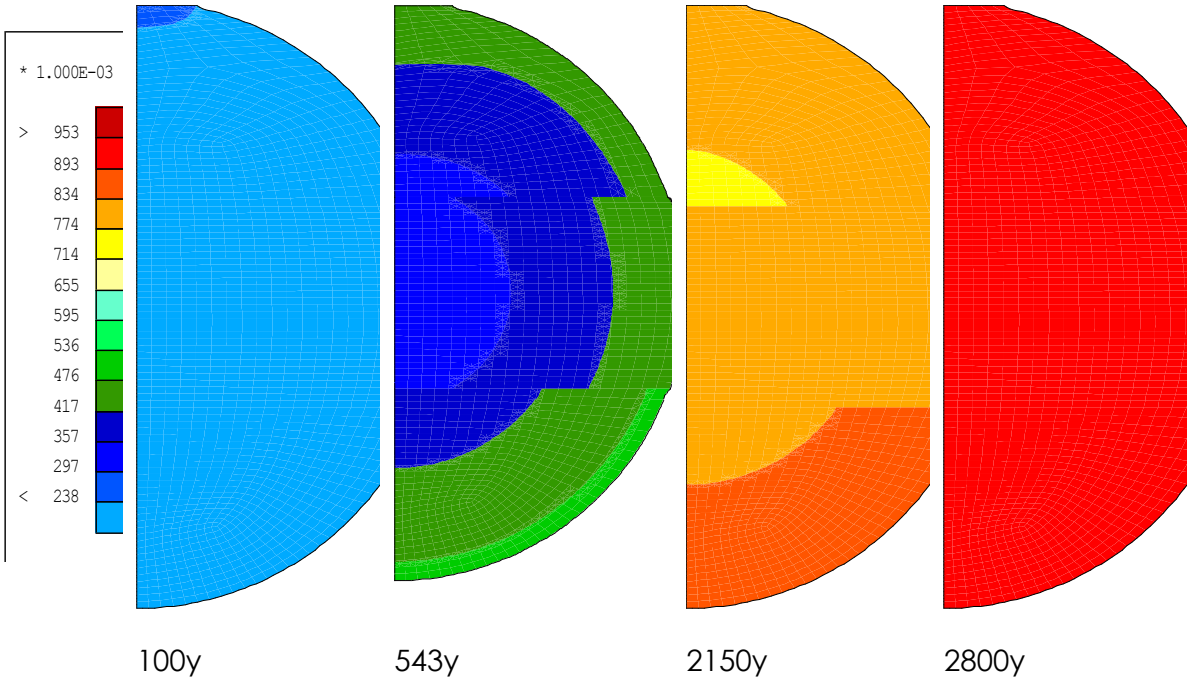

Figure 4.1-13 Saturation iso-values in the bentonite plug.

Accordingly, suction (Figure 4.1-14) firstly decreases on the top part with an immediate drop of about 40 MPa from the initial value of 100 MPa. Differences are more evident with respect to the saturation evolution. Similarly to saturation development, when the apical gap is closed (543 years), the suction trend of the top material starts to follow the ones of the side and bottom portions. The central part evidences a much slower suction decrease.

Suction field distributions at several times (Figure 4.1-15) describe the above mentioned trends. Initially, the top material immediately experiences suction decrease, while most material is still homogeneous. At the contact time (543 years),

an evident suction gradient can be observed. This gradient disappears as the saturation process progresses (i.e. 2150 and 2800 years of the simulation time).

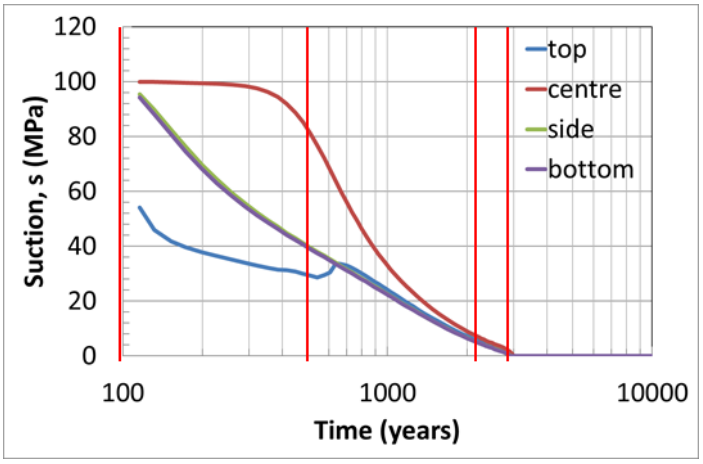

Figure 4.1-14 Suction time evolution of four points in the bentonite.

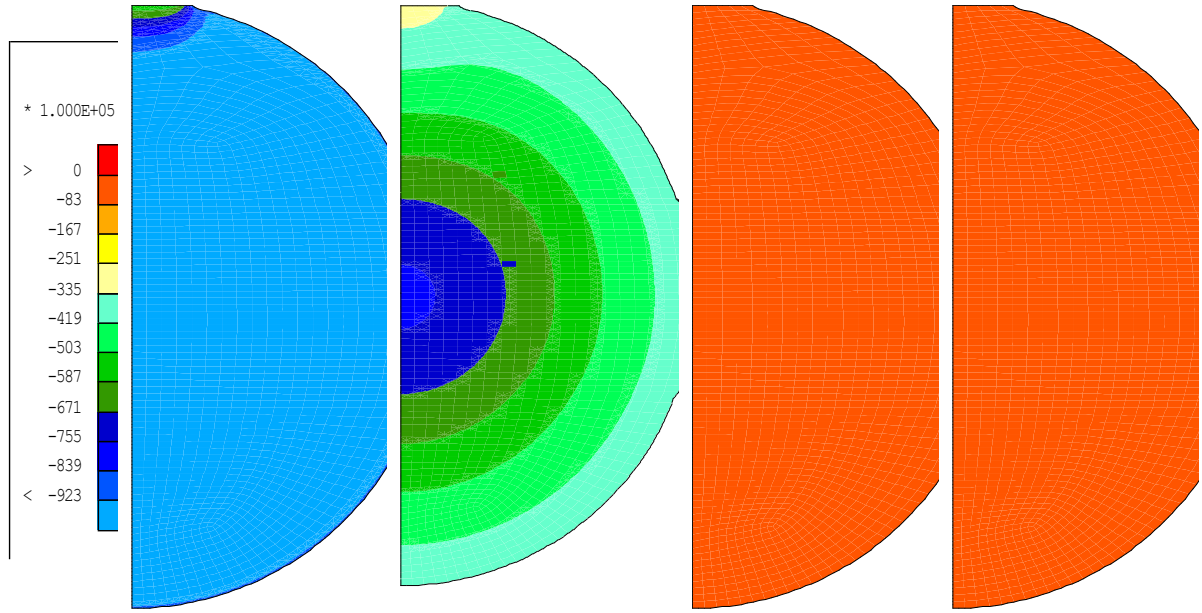

Figure 4.1-15 Suction iso-values in the bentonite plug (-Pa).

Figure 4.1-16 and Figure 4.1-18 show respectively the horizontal and vertical stresses time evolution. Swelling pressure starts to increase only when constant volume conditions are reached (i.e. 543 years, when the gap is closed). Before this stage, the top bentonite portion is able to swell almost freely. It is possible to see that the swelling pressure development is similar in both horizontal and vertical directions. Changes of slopes are not evident. One can be found for instance just before the full saturation

time (2800 year). Peak values are between 3 and 3.5 MPa, with maximum corresponding to the central core of the plug, which is the most compacted portion.

After full saturation, pressure drops are observed. Those drops are related to the transition from the unsaturated state to the saturated one. To those domains, net stress and effective stress representations correspond,

Horizontal and vertical stress field distributions (Figure 4.1-17 and Figure 4.1-19) show that swelling pressure increases homogeneously with the selected modelling strategy (i.e. stress dependent swelling capacity) (i.e. 2800th year of the simulation time).

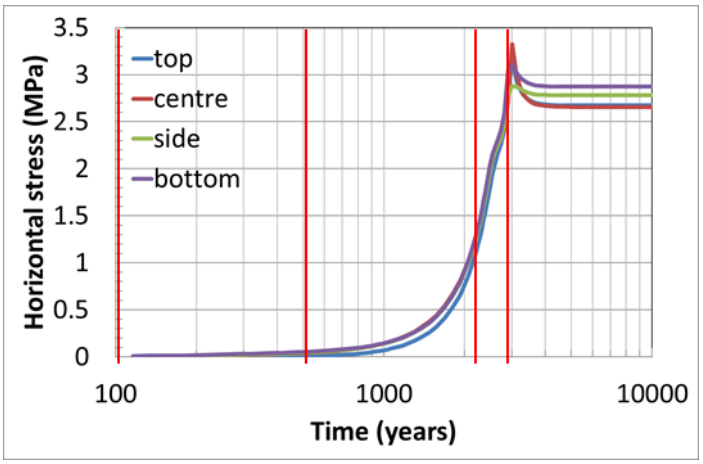

Figure 4.1-16 Horizontal stress time evolution of four points in the bentonite.

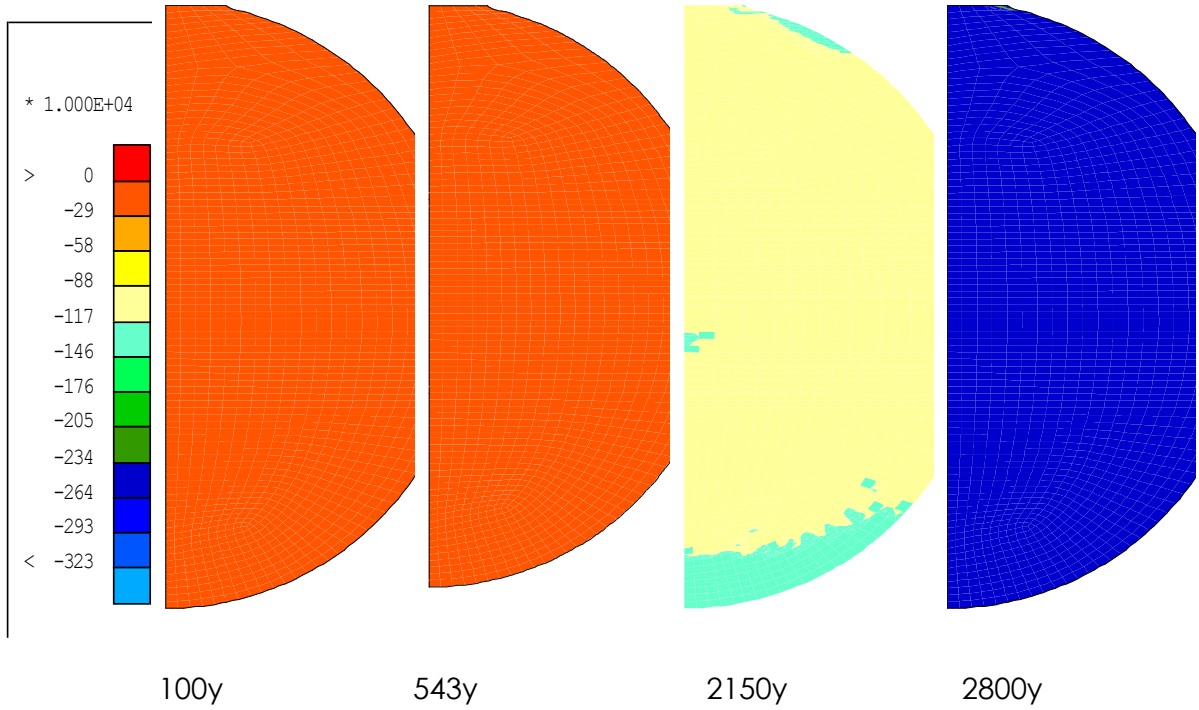

Figure 4.1-17 Horizontal stress iso-values in the bentonite plug (-Pa).

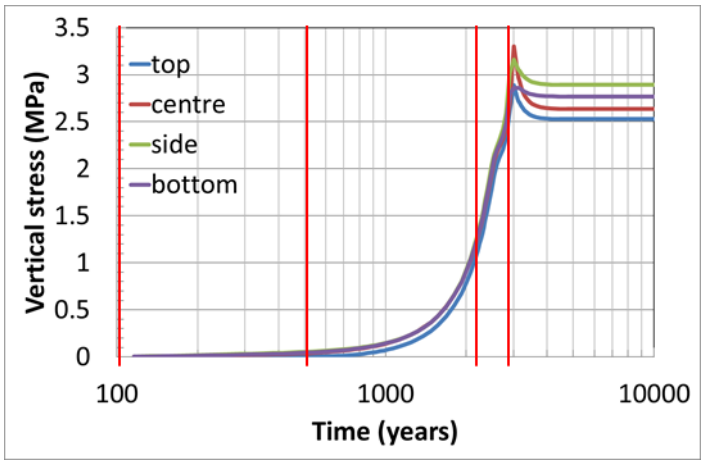

Figure 4.1-18 Vertical stress time evolution of four points in the bentonite.

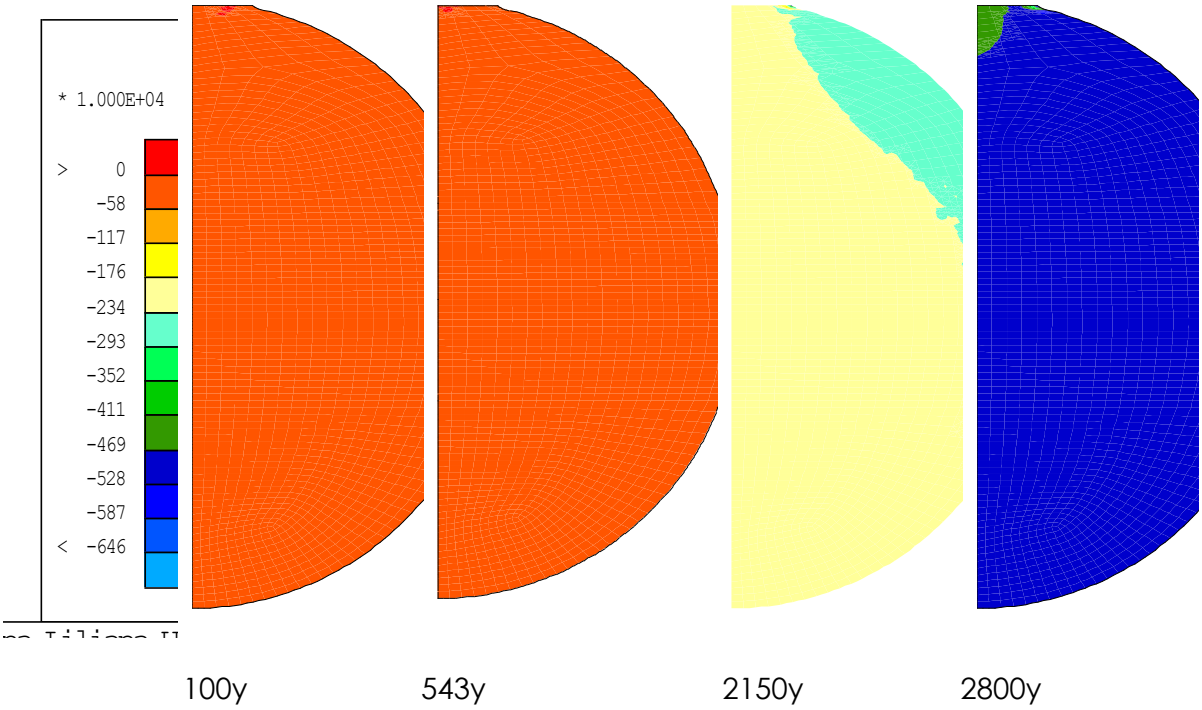

Figure 4.1-19 Vertical stress iso-values in the bentonite plug (-Pa).

Figure 4.1-20 and Figure 4.1-21give further insights with respect to the development of heterogeneities field into a bentonite plug. As previously mentioned, the top portion material (lowest dry density of the plug equal to 1.48 Mg/m^3) immediately swells. Its dry density decreases up to 1.44 Mg/m^3 at the contact with the top excavation wall time (543 year). The bottom and side portions remain quite constant, while compacting the central core of the central layer (from 1.55 to 1.6 Mg/m^3). After the gap closure, dry density in the top bentonite plug, decreases due to the swelling of the inner core. At the end of the saturation process, dry density is in general the loosest near the host rock and the densest in the central part of each layer. The initial swelling deformation, which caused a remarkable dry density decrease on the top of the seals is erased. Final dry density of the seal spans between 1.5 and 1.6 Mg/m^3.

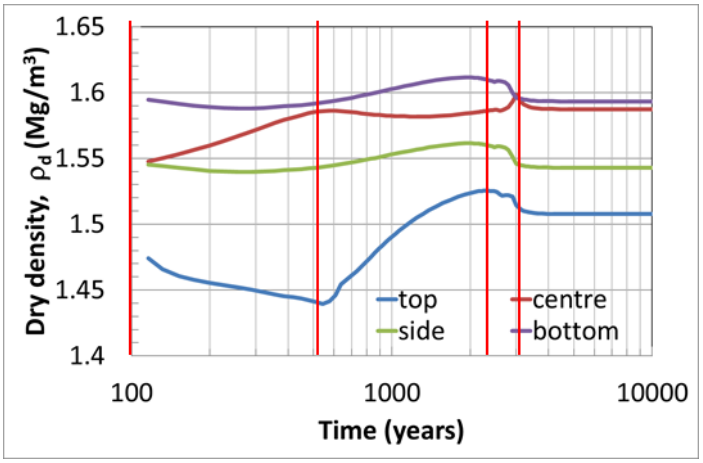

Figure 4.1-20 Dry density time evolution of four points in the bentonite.

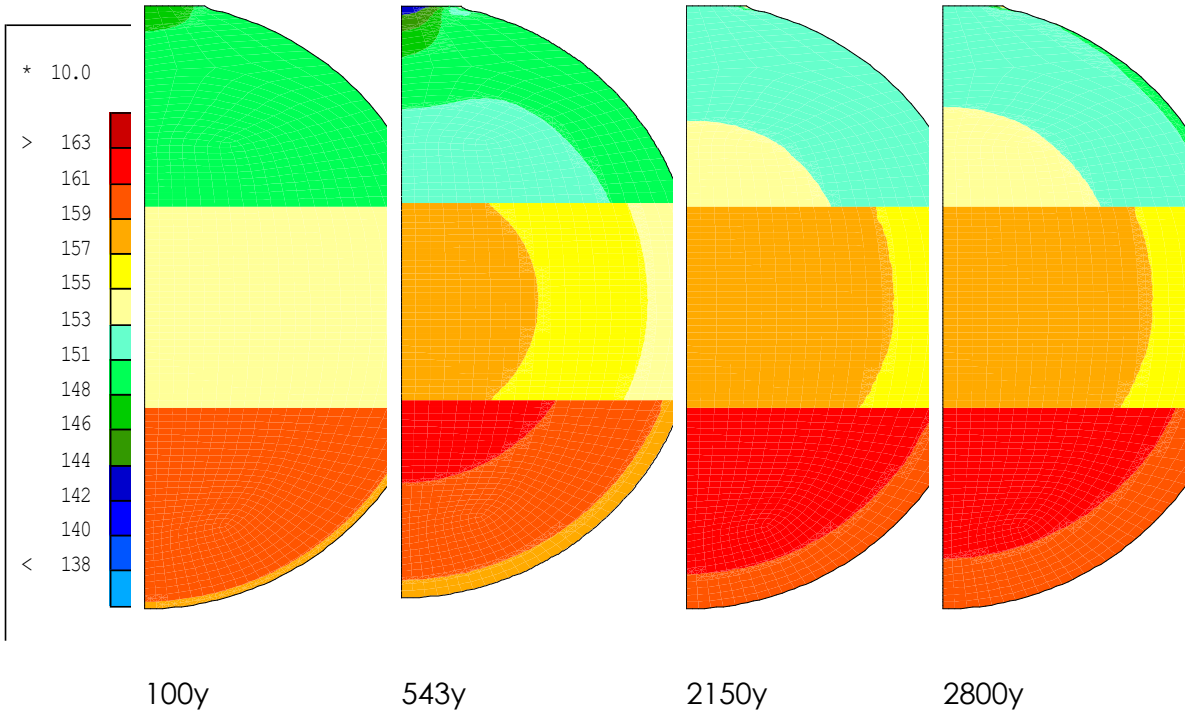

Figure 4.1-21 Dry density iso-values in the bentonite plug (kg/m3).

Dry density profiles at several time steps (Figure 4.1-22 and Figure 4.1-23) provide further insights on the development of additional heterogenity in the seal during saturation and, on the contrary, on homogenisation establishment. Vertical profile (Figure 4.1-22) shows that initial dry density heterogeneity is kept until the end of the saturation. However, dry density gradients can be observed still in the direction of hydration. On the bottom and top layers the losest dry density is found in the contact with the host rock (-6 and 6 m). The central layer presents the highest dry density in the central part. The horizontal profiles (Figure 4.1-23) are related to the central layer. Gradients are still found once again on the horizontal hydration direction. Thus, it can be concluded that heterogeneities are due not only to the hydration but also to the initial state of the barrier.

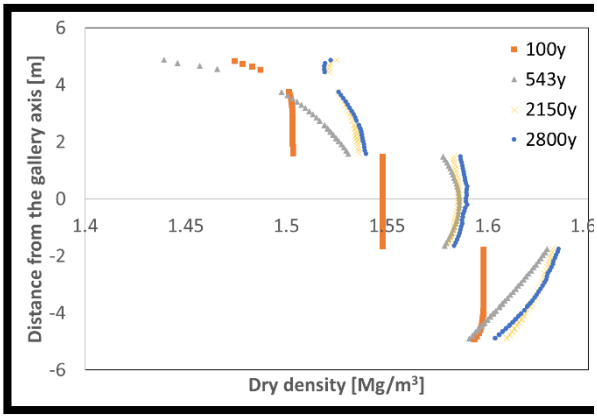

Figure 4.1-22 Dry density profiles at several time steps for the central vertical axis of the gallery.

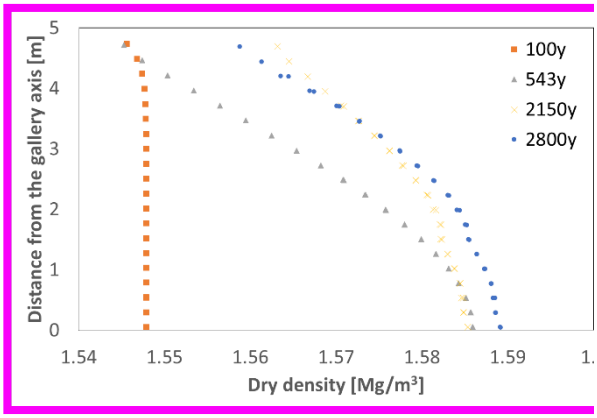

Figure 4.1-23 Dry density profiles at several time steps for the central horizontal axis of the gallery.

Also permeability heterogeneous initial distribution related to dry density and evolution is considered (Figure 4.1-24). The initial permeability values span between $3*10^{-20}$ m^2 (on the bottom layer, ρ_d=1.65 Mg/m^3) and $4.5*10^{-20}$ m^2 (on the top layer, ρ_d=1.48 Mg/m^3). On the top loosest part, as the dry density decreases and the saturation increases the permeability remains constant until the contact time (543th year), wherase it generally decreases for the middle and bottom layers. As the saturation is reached permeability is constant regardless discrepancies in dry density

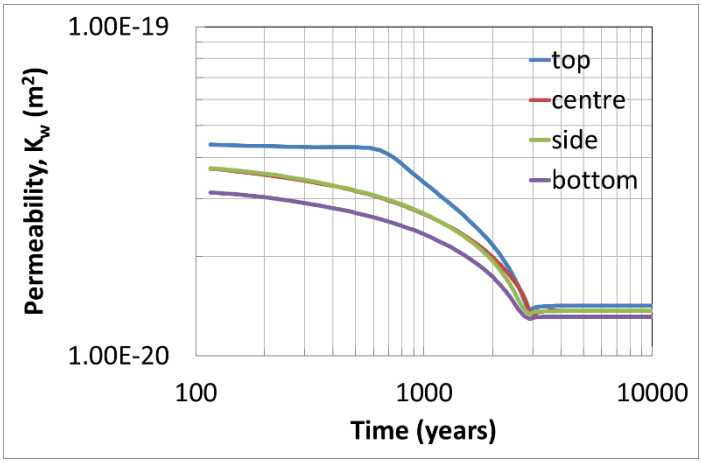

Figure 4.1-24 Permeabiliy time evolution of four points in the bentonite.

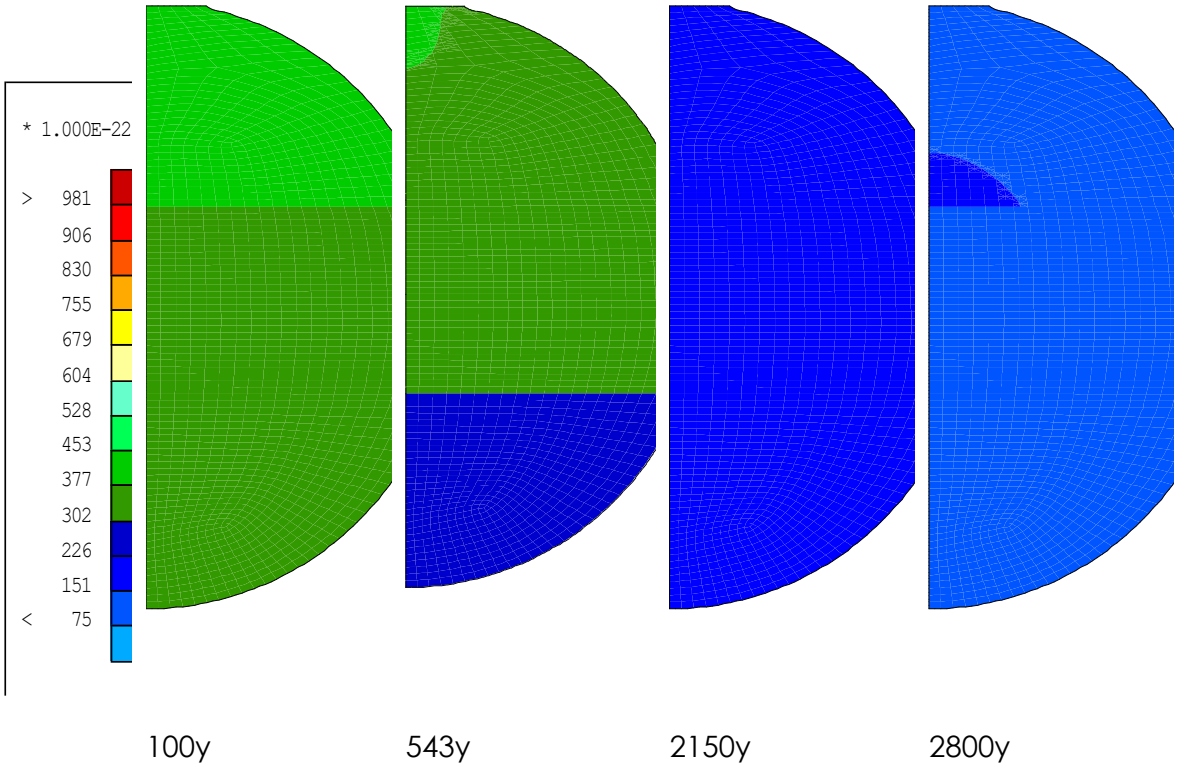

Figure 4.1-25 Permeability iso-values in the bentonite plug (m2).

Differently from dry density, permeability tends to homogenise (Figure 4.1-26 and Figure 4.1-27) reaching the constant homogeneous value of about $1*10^{-20}$ m^2 in all the directions.

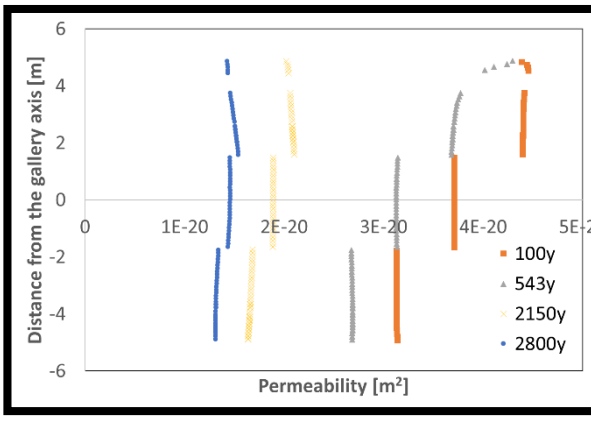

Figure 4.1-26 Permeability profiles at several time steps for the central vertical axis of the gallery.

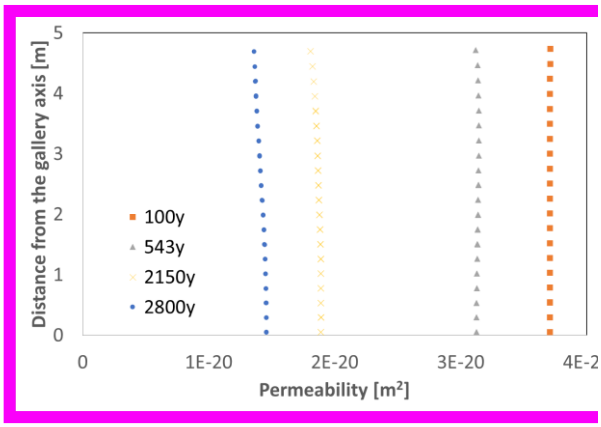

Figure 4.1-27 Permeability profiles at several time steps for the central horizontal axis of the gallery.

Figure 4.1-28 shows the apical gap time evolution on the top. The gap is initially 10 cm, but due to the host-rock convergence during excavation, it is reduced to 7 cm. Its complete closure takes place at the 543th year of the simulation time. Negative values are related to the "numerical interpenetration", which is linked to the penalty coefficient employed with the interface element. Given the very small dimension of the apical gap with respect to the whole bentonite structure, this interpenetration of 1 cm does not affect welling pressure results.

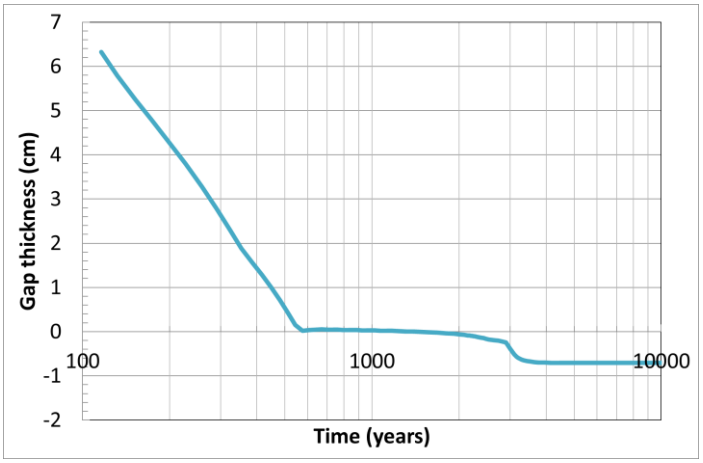

Figure 4.1-28 Apical gap time evolution.

Argillite

The activation of the bentonite plug in the gallery modifies the hydro-mechanical state of the host-rock. The host-rock initially presents on the inner radius pore water pressure equal to -100 MPa (suction s=100 MPa). As the bentonite plug hydrates, the hydraulic state of the rock evolves being the only water source for saturation. The pore water pressure on the excavation wall quickly increases as water is provided to the plug that saturates (Figure 4.1-29). Due to the fact that suction decreases, convergence at this location increases due to the decreasing effective stress (Biot coefficient equal to 0.6). This process causes bentonite plug dry density increase. At the 2090th year of the simulation time, the excavation wall convergence experiences a recover of deformation related to the swelling pressure exerted by the bentonite saturation. Indeed, the swelling pressure of the sealing structure experiences a slope variation and a more pronounced swelling pressure development (Figure 4.1-16 and Figure 4.1-18). The excavation wall reaches the 0 value of pore water pressure at the 3700th year of the simulation time. This further pore water pressure increases results in an effective stress decrease that would cause excavation wall convergence. The further convergence is prevented by the bentonite swelling.

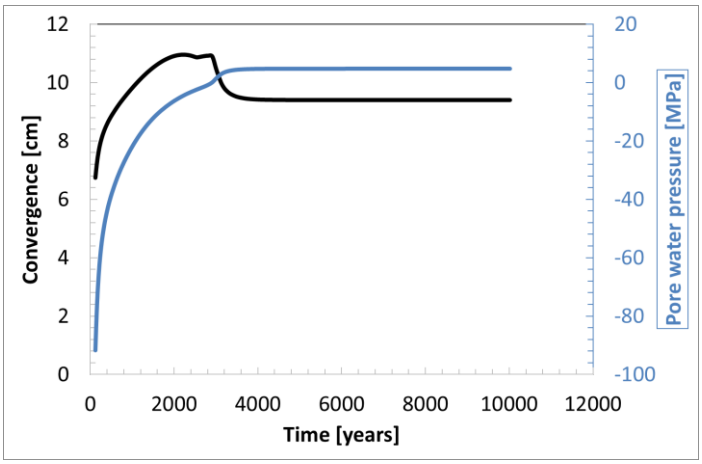

Figure 4.1-29 Convergence and pore water pressure at the excavation wall during the saturation phase (100y to 10000y). Results concerning section in Figure 4.1-30.

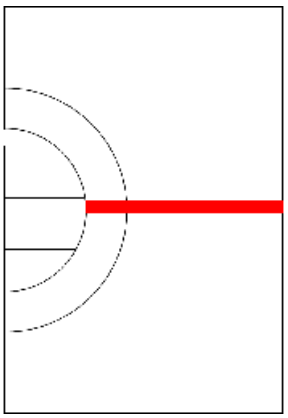

Figure 4.1-30 Analysed section in hostrock.

Figure 4.1-31 to Figure 4.1-33 present the pore water pressure, horizontal and vertical stresses profiles in the host-rock. The higher permeability and low stiffness of the EDZ remarkably affect the hydro-mechanical response of the model.

The lower pore water pressure (i.e. the higher suction) is translated into the higher effective stress in the EDZ. Whereas, in the intact rock, the effect of hydro-mechanical state modifications is still observable but less abrupt.

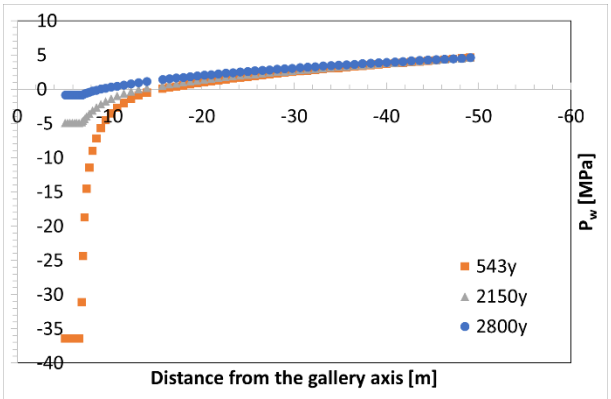

Figure 4.1-31 Host-rock pore water pressure profiles for several simulation times. Results concerning blue section in Figure 4.1-30.

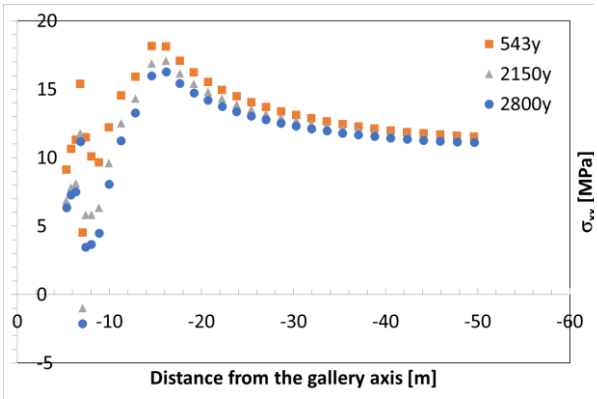

Figure 4.1-32 Host-rock horizontal stress profiles for several simulation times. Results concerning blue section in Figure 4.1-30.

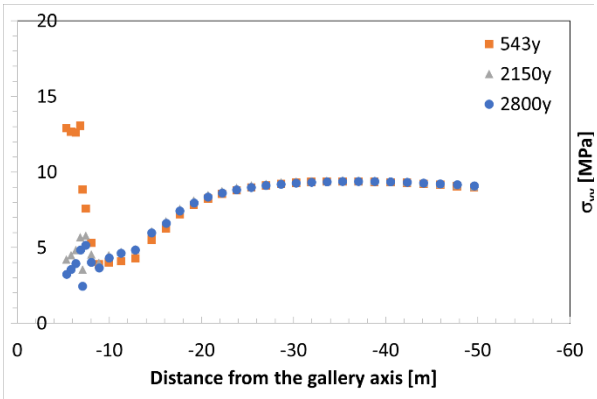

Figure 4.1-33 Host-rock vertical stress profiles for several simulation times. Results concerning blue section in Figure 4.1-30.

Figure 4.1-34 and Figure 4.1-35 show the pore water pressure, horizontal and vertical stress field distributions in the claystone. Pore-water pressure gradients are easily to distinguish and develop for the whole host-rock domain possibly suggesting an in-depth analysis of the domain dimension effect on the calculations.

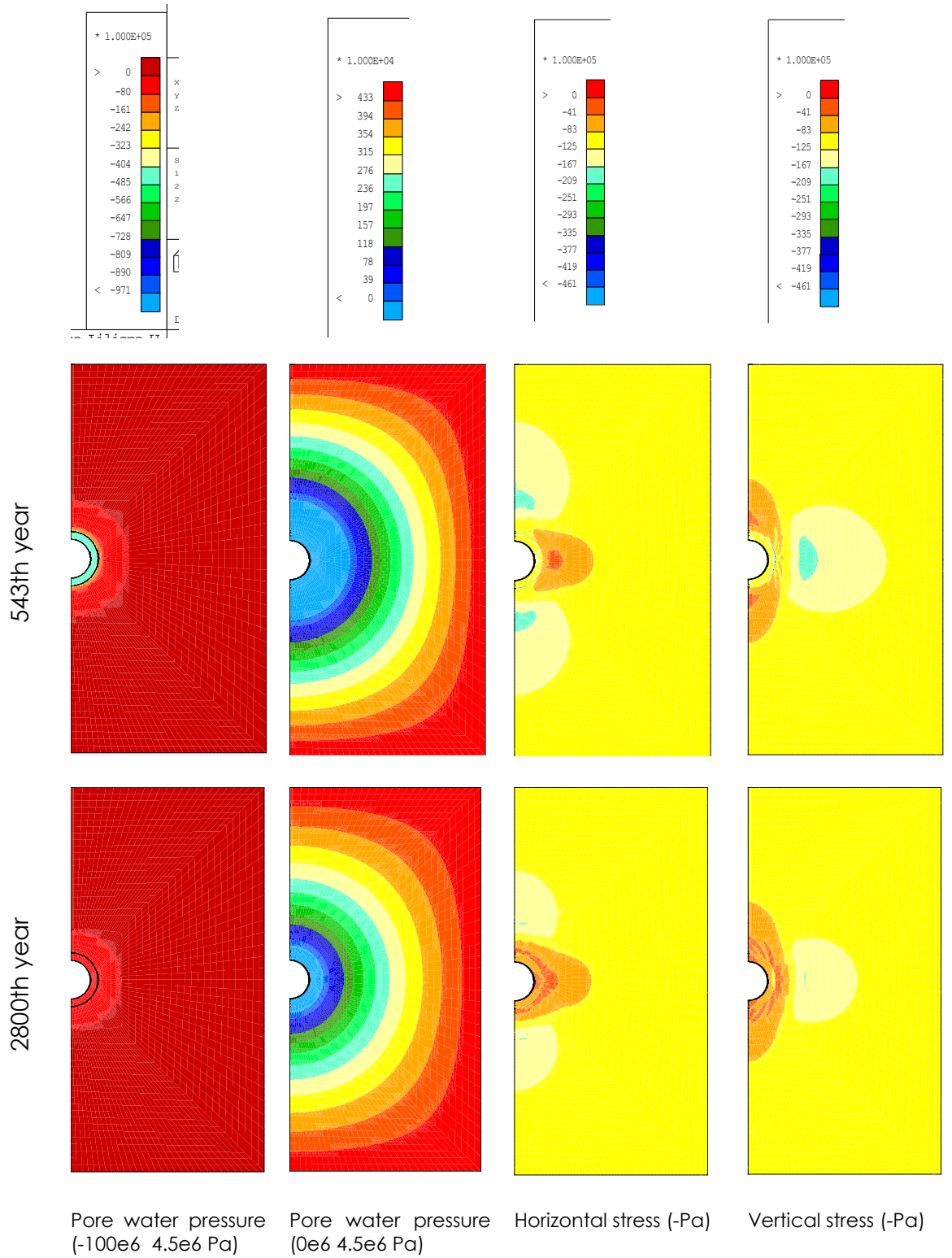

Figure 4.1-34 Host-rock iso-values for pore water pressure, horizontal stress and vertical stress.

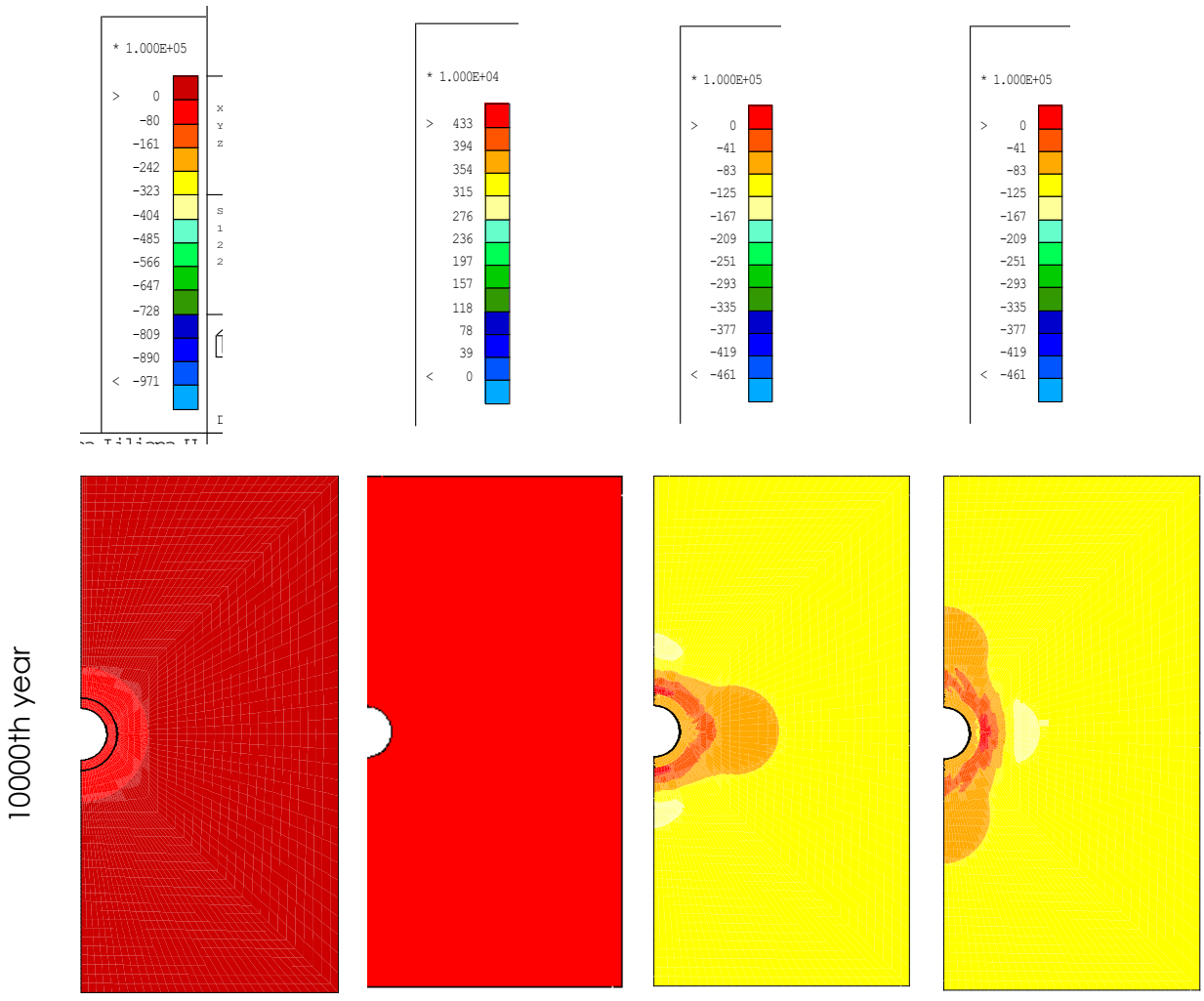

Pore water pressure (-100e6 4.5e6 Pa) | Pore water pressure (0e6 4.5e6 Pa) | Horizontal stress (-Pa) | Vertical stress (-Pa)

Figure 4.1-35 Host-rock iso-values for pore water pressure, horizontal stress and vertical stress.

4.1.6 Discussion

The model is able to account for the technological gap between the host-rock and the bentonite plug. It presents an evident effect in terms of swelling pressure development.

Indeed, swelling pressure starts to develop remarkably only when the technological gap is closed.

Dry density evolution is not only controlled by the hydration direction but also on the hydro-mechanical interaction with the host-rock. More precisely, dry density gradients are always found, also in the case of initially heterogeneous medium following saturation direction.

Finally, permeability has a key role in the whole hydro-mechanical process. However, the model shows that the selected double porosity dry density dependent permeability law evolution provides final homogeneous permeability.

The following Table 4.1-7 summarises some relevant results concerning the saturation phase.

Table 4.1-7 Summary table

At saturation	Min	Max
Horizontal stress (MPa)	3	3.5
Vertical stress (MPa)	3	3.5
Dry density (Mg/m^3)	1.5	1.6
Full saturation time (years)	4000	

Some warning

The numerical 2D plane strain simulation of the galley excavation and bentonite saturation is not a simple task. Some relevant issues encountered during this study are provided in the following:

- Interface element employment is far from simple. Both hydraulic and mechanic parameters are not easy to determine and have a huge impact on numerical convergence and results.
- Excavation phase computation is also really time demanding. It decreases the possibility to perform sensitivity analyses.
- Bentonite hydration phase is a very complex process from a physical, theoretical and numerical point of views. BBM, WRC, permeability evolution combination factors affect undeniably the numerical convergence.

4.2 Quintessa

4.2.1 Description of the models

Quintessa's THM bentonite model is described fully in Deliverable 3.3. For this model of the Andra assessment case, the bentonite seal is assumed to be at constant temperature so only a coupled hydro-mechanical model is required. The model is implemented in QPAC[2], a multi-physics finite volume/mixed element code.

4.2.2 Geometry and discretization

The objective of this task was to develop a model of a 2D cross-section of the bentonite, EDZ and Callovo-Oxfordian claystone (Figure 4.2-1). In discussion with other teams modelling the Andra assessment case, the geometry of the void region was simplified from an apical void to a circular segment to simplify the resulting mesh and avoid extreme small/acute elements that would be needed to discretise the ends of the void 'crescent' in the original geometry (Figure 4.2-1). Since the volume of the void (1.6 m^3 in the original geometry or 0.13 m^3 in the simplified geometry) is very small compared to the volume of the bentonite (77-78 m^3), this is not expected to have a significant impact on the results. The main purpose of its inclusion is to test the capability of modelling a void.

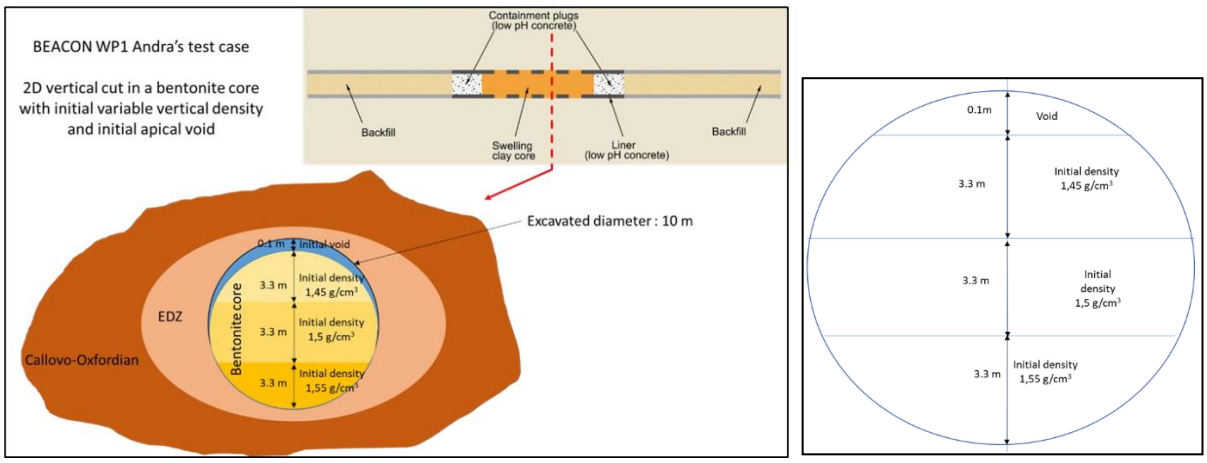

Figure 4.2-1: Geometry and simplified geometry (right) of the bentonite seal to be considered in initial modelling. (Note figure not to scale.)

In QPAC, the model geometry and mesh can only be directly defined using either a Cartesian or cylindrical coordinate system. It is therefore not possible to accurately

[2] https://www.quintessa.org/software/QPAC

represent the geometry shown in Figure 4.2-1; the circular domain cannot be represented in the Cartesian geometry and the internal boundaries between the bentonite layers cannot be represented in a cylindrical geometry. QPAC supports an alternative 'abstract' representation of the grid, which can be used to directly specify cell locations and cell-cell connection areas and distances to define an explicit unstructured grid.

As described in Deliverable 3.3, a preprocessor has been developed to allow unstructured 2-D grids developed using the Gmsh mesh generator[3] to be converted to QPAC abstract form. A 2-D mesh of the simplified bentonite geometry using quad elements is shown in Figure 4.2-2.

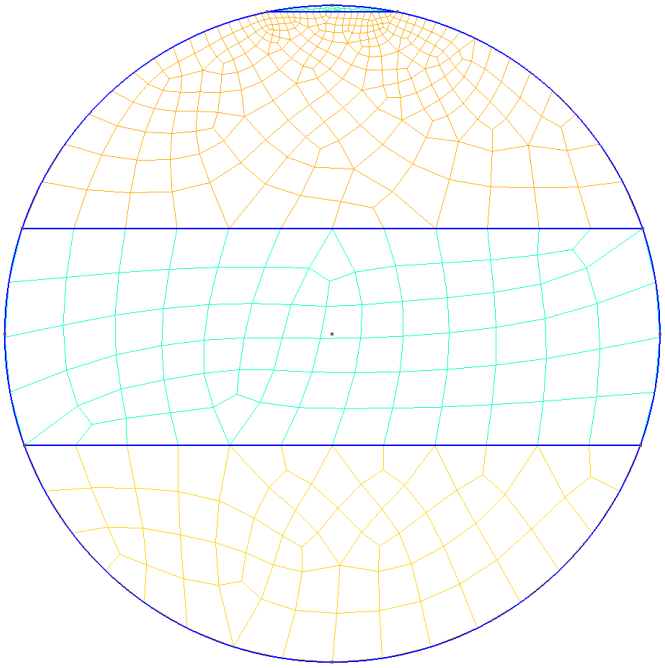

Figure 4.2-2 2D-meshing of the simplified bentonite seal geometry.

Gmsh is only used to define the discretisation of the bentonite seal. The influence of the surrounding EDZ and intact host rock on the bentonite is accounted for by defining mechanical and hydraulic boundary conditions on the outer surface of the bentonite. To parameterise the hydraulic boundary conditions, two separate QPAC models were run. Firstly, a model representing the EDZ during the ventilation phase was run and used to define the initial saturations and pressures in the EDZ. Secondly, a model representing the EDZ and a uniform-density bentonite seal was run and used to define the evolving water pressures in the EDZ at the boundary with the bentonite. These

[3] https://gmsh.info/

models are described further in Section 4.2.4. Each model uses a cylindrical geometry, with the EDZ assumed to be 2 m thick (Figure 4.2-3). A 180° segment is modelled with a symmetry boundary.

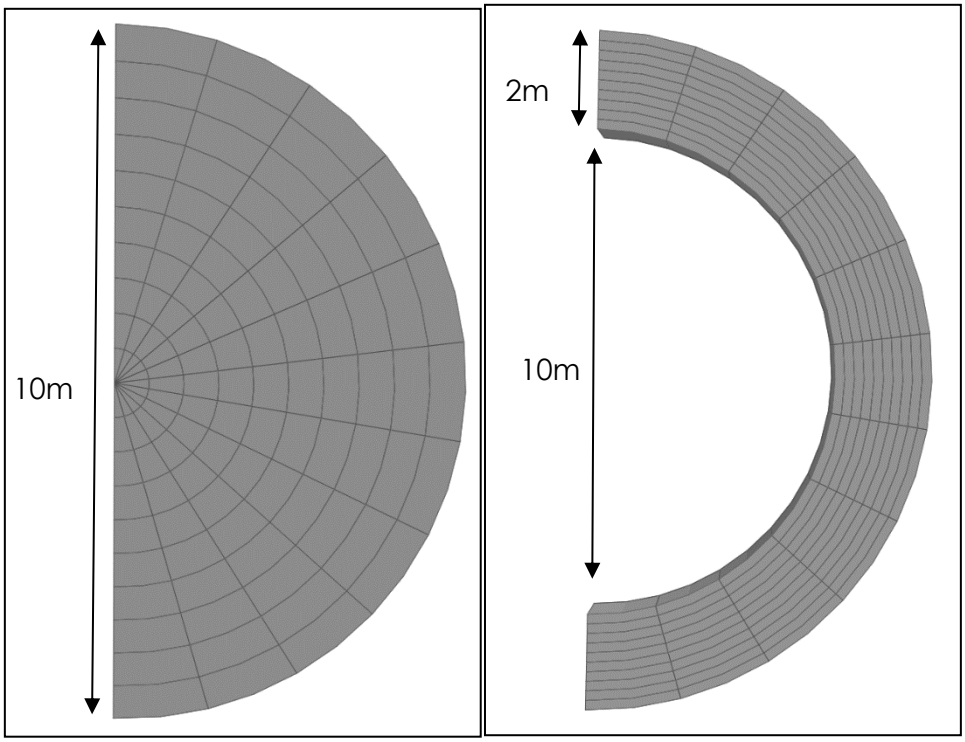

Figure 4.2-3: QPAC geometry and discretisation of the bentonite (left) and EDZ (right) in the model used to specify boundary conditions for the bentonite-EDZ interface.

4.2.3 Input parameters

Table 4.2-1 shows the input parameters for the bentonite. In Quintessa's Internal Limit Model, the retention curve is parameterised with the same constants as the swelling pressure – dry density curve and the plastic failure curve:

$$s = p_0 \exp\left(\frac{\rho_w}{\lambda\left(\theta + \frac{\rho_w}{\rho_g}\right)}\right)$$

where s is suction, ρ_w is water density [g/cm^3], θ is gravimetric water content [-], and p_0, λ, ρ_g are defined in Table 4.2-1.

The ILM parameters p_0 and λ are calibrated to the dry density – swelling pressure data supplied by Andra (for synthetic site water). The hydraulic conductivity – dry density relation is also calibrated to data supplied by Andra. Other material parameters are unchanged from those used to model MX-80 bentonite in previous Beacon tasks.

For simplicity, the void is also approximated as a porous medium modelled with the same equations as the bentonite. The void material is assumed to be highly permeable and compressible (Table 4.2-1). Since the void represents only a small volume, the

properties of this material are not expected to significantly affect the behaviour of the bentonite. In practice, there was some difficulty obtaining convergence with this model so for the results presented here, the void was instead represented as a mechanical boundary condition allowing free displacement of the bentonite into an apical void.

Table 4.2-1: Bentonite and void material parameters (hydraulic and mechanical)

Parameter	**Description [units]**	**Bentonite**	**Void**
p_0	ILM constant [MPa]	1.526 x 10^{-4}	1.526 x 10^{-4}
$1/\lambda$	ILM constant [cm^3/g]	6.738	6.738
ρ_g	Grain density [g/cm^3]	2.78	2.78
ξ	Poisson's ratio [-]	0.27	0.5
κ_0	Initial bulk modulus [MPa]	25	1 x 10^{-4}
κ_1	Bulk modulus scale factor [-]	30	30
M	Slope of critical state line [-]	1.25	1.25
K_0	Absolute hydraulic conductivity	$7 \cdot 10^{-10} \cdot e^{-5.733\rho_d}$	1.0 x 10^{-2}
k_r	Relative permeability	S_w^3	1

The EDZ is also modelled explicitly to provide hydraulic boundary conditions for the bentonite. For simplicity, mechanics are not modelled in the EDZ or intact rock; these are both assumed to be incompressible. The water retention curve in the EDZ is modelled with a Van Genuchten curve using parameters specified by Andra (

Table 4.2-2):

$$s = \left(1 + \left(\frac{S_w}{P_0}\right)^n\right)^{-\frac{1}{1-\frac{1}{n}}}$$

The intact rock is not modelled explicitly, but the intact rock permeability is used to define hydraulic boundary conditions at the outside of the EDZ.

Table 4.2-2: EDZ material parameters (hydraulic only)

Parameter	Description [units]	EDZ	Intact COx
ρ_g	Grain density [g/cm^3]	2.78	-
e	Porosity [-]	0.2	-
k_0	Intrinsic permeability	1 x 10^{-16}	1 x 10^{-20}
k_r	Relative permeability	S_w^3	-
P_0	Van Genuchten constant [MPa]	19.6	-
n	Van Genuchten constant [-]	1.5	-

4.2.4 Initial and boundary conditions

Three separate models are run to define the boundary conditions for the bentonite seal.

Firstly, the ventilation phase is simulated and used to specify the initial water pressure and water content in the EDZ at the time of bentonite emplacement. At the start of the excavation phase, the EDZ is assumed to be fully saturated. After instantaneous excavation, the unlined gallery is ventilated for 100 years with constant 50% air humidity (RH). This information is used to define a constant water pressure boundary condition at the inner surface of the EDZ:

$$P_w = \frac{\rho_w RT \ln(RH)}{M_v}$$

where R is the gas constant (8.314 J K^{-1} mol^{-1}), T is temperature (296 K), M_v is the molar mass of water vapour (18.02 g mol^{-1}). At the outer boundary of the EDZ, inflow from the intact rock is modelled with a specified water flux (q [m s^{-1}) boundary condition based on Darcy's law:

$$\frac{q}{A} = \frac{\rho_w k_{0,cox}}{\mu} \frac{(P_0 - P)}{x}$$

where μ is the viscosity of water (1 x 10^{-3} Pa s), A is the area of interface between the EDZ and the intact rock, P_0 is the water pressure at a distance x from the EDZ and P is the pressure at the EDZ boundary. The sealing is at 500 m depth, so P_0 is set to 5 MPa. x should be a distance sufficiently far from the tunnel that the water pressure is not affected by the excavation, so it is set to 50 m. The saturations and pressures in the EDZ after 100 years are generally insensitive to the parameters used in this boundary condition. Displacements are not calculated in the EDZ.

The water pressure and water content in the EDZ after 100 years are used to define the initial conditions in the EDZ for the next phase of the model. In this second model, the

water flows in the bentonite and EDZ are coupled. This is only possible using the QPAC cylindrical grid, in which the layers of different bentonite density cannot be modelled. In this phase of the model, the bentonite dry density is therefore set to 1.5 g cm^{-3}, equating to a porosity of 0.46. The bentonite has an initial suction of 100 MPa as prescribed in the specification, which equates to a saturation of 45% with the ILM retention curve. Mechanics are only modelled in the bentonite, which is assumed to have zero displacement at the boundary between the bentonite and EDZ. The void is not included in this model. This model is run for 10,000 years and used to specify the evolving water pressure in the EDZ at the boundary with the bentonite for the final Gmsh model.

In the final model, only the bentonite seal is modelled explicitly. Gmsh is used to generate the mesh shown in Figure 4.2-3. The initial bulk dry density of the bottom, middle and top layers of the bentonite is 1.55, 1.5 and 1.45 g cm^{-3} respectively, equating to initial porosities of 0.44, 0.46 and 0.48 and initial saturations of 50%, 47% and 43% respectively (with an initial suction of 100 MPa throughout the bentonite). The outer hydraulic boundary is set to a specified water pressure, equal to the evolving water pressure at the EDZ-bentonite boundary in the uniform-density bentonite model. This can be done instead of fully coupling the bentonite and the EDZ because the bentonite is relatively impermeable and has little influence on the flows in the EDZ; this was tested by running the second (coupled) model with uniform bentonite densities of 1.45 g cm^{-3} and 1.55 g cm^{-3} and ensuring that the water pressures in the EDZ did not significantly change. The outer mechanical boundary of the bentonite is set to zero displacement; this is equivalent to an incompressible rock, with no slippage allowed between the bentonite and rock surface. This is not likely to be truly representative of the bentonite-EDZ interface but further development is needed to implement more complex boundary conditions with the unstructured mesh.

The boundary conditions on the void region are the same as the boundary conditions on the bentonite. The void is given an initial dry density of 0.0278 g cm^{-3}, equating to a porosity of 99% and an initial suction of 100 MPa consistent with the bentonite suction (equating to a saturation of 0.4%).

The initial and boundary conditions are summarised in Table 4.2-3.

Table 4.2-3: Initial and boundary conditions

Condition	**Void**	**Bentonite**	**EDZ**
Model 1 – Ventilation Phase (EDZ only)			
Initial saturation	-	-	1
Hydraulic boundary	-	-	Inner (gallery): $P_w = -95[\text{MPa}]$ Outer (intact COx): Flow rate per unit area = $2 \cdot 10^{-16}(5[\text{MPa}] - P_w)$

Model 2 – Uniform bentonite (coupled EDZ and bentonite)			
Initial water content [-]	-	0.143	*From Model 1*
Initial dry density [g cm^{-3}]	-	1.5	-
Hydraulic boundary	-	- *(Coupled to EDZ)*	Outer (intact COx): Flow rate per unit area = $2 \cdot 10^{-16}(5[\mathrm{MPa}] - P_w)$
Mechanical boundary	-	Zero displacement	-
Model 3 – Heterogeneous bentonite (bentonite and void only)			
Initial water content [-]	0.143	0.143	-
Initial dry density [g cm^{-3}]	0.0278	Upper: 1.4 Middle: 1.5 Lower: 1.55	-
Hydraulic boundary	*From Model 2 (EDZ pressure)*	*From Model 2 (EDZ pressure)*	-
Mechanical boundary	Zero displacement	Zero displacement	-

4.2.5 Results

Two versions of the model were run: with and without representation of the void at the top of the bentonite.

Each version of the model was run until the bentonite had fully saturated and reached an equilibrium state at 8000 years after emplacement; there is little change in the bentonite after 7000 years (Figure 4.2-4). There is no significant difference between the evolution of saturation in the centre of the bentonite in the two models. Note that the final saturation reached is 101%, since the ILM does not enforce a strict limit of 100%.

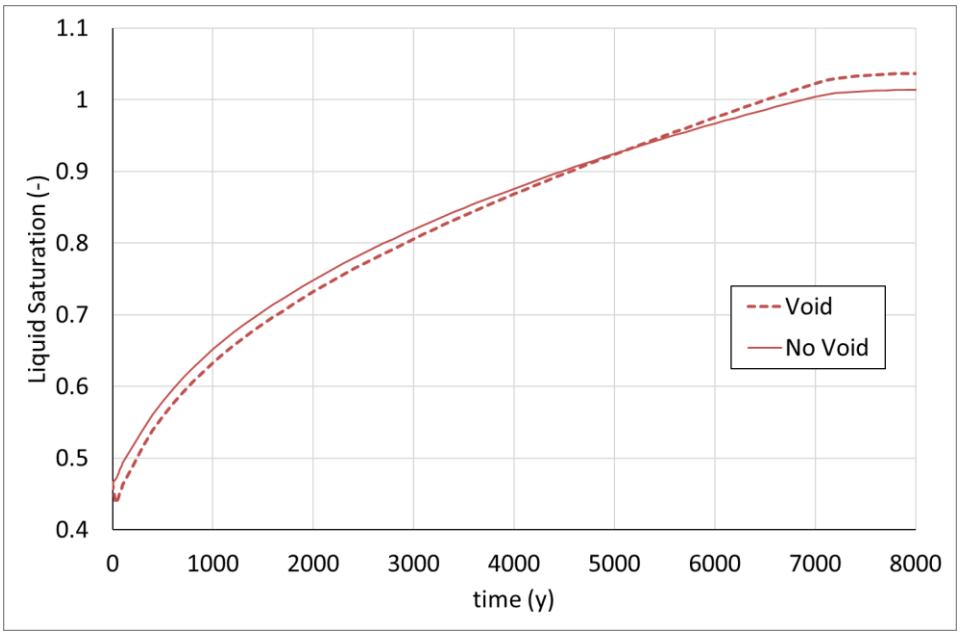

Figure 4.2-4 Evolution of saturation in the centre of the bentonite seal.

Figure 4.2-5 shows the development of swelling pressure in each layer of the bentonite seal. A similar final swelling pressure is reached in each of the layers, showing a significant degree of homogenisation. The final swelling pressure is reached by approximately 2000 years after bentonite emplacement; this is more rapid than the rate of saturation. This is a surprising outcome of the model since swelling is driven by water uptake, but appears to be caused by increasing plastic collapse in the bentonite opposing the increasing swelling expansion. The final swelling pressure reached in the bentonite is 3.75-3.83 MPa in the model without a void and 2.88-2.95 MPa in the model with a void. This is a direct result of the ILM swelling pressure-dry density curve (with the ~1 m^3 void, the average dry density decreases by ~0.02 kg m^{-3}) and illustrates the high sensitivity of the model to dry density.

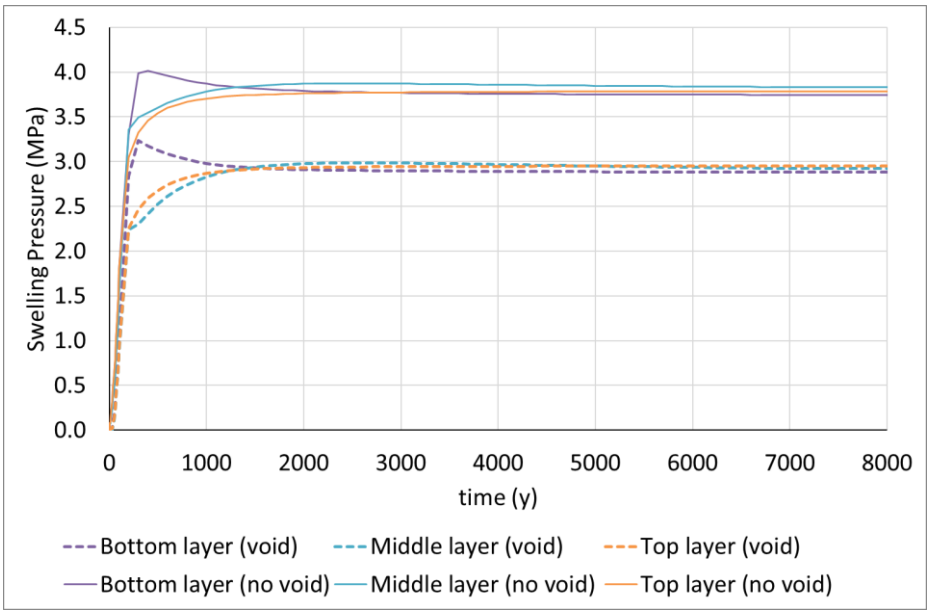

Figure 4.2-5 Evolution of swelling pressure development in the centre of the bottom (initial dry density 1.55 kg m^{-3}), middle (1.5 kg m^{-3}) and top (1.45 kg m^{-3}) layers of the bentonite seal.

Figure 4.2-6 shows vertical profiles of water content in the bentonite and Figure 4.2-7 and Figure 4.2-8 show vertical and horizontal profiles of dry density. There is an increase in the bentonite water content due to hydration from the rock from an initial constant value of 14.3% to 30-35%. Horizontal profiles of water content remain mostly flat, with some vertical variation. There is a significant degree of homogenisation of the dry density in the bentonite, although some gradient still remains. The void lowers the average dry density of the bentonite. The final horizontal profiles of dry density are mostly homogenous, but the dry density at the outside of the bentonite adjacent to the EDZ is generally lower, reflecting the larger amount of swelling.

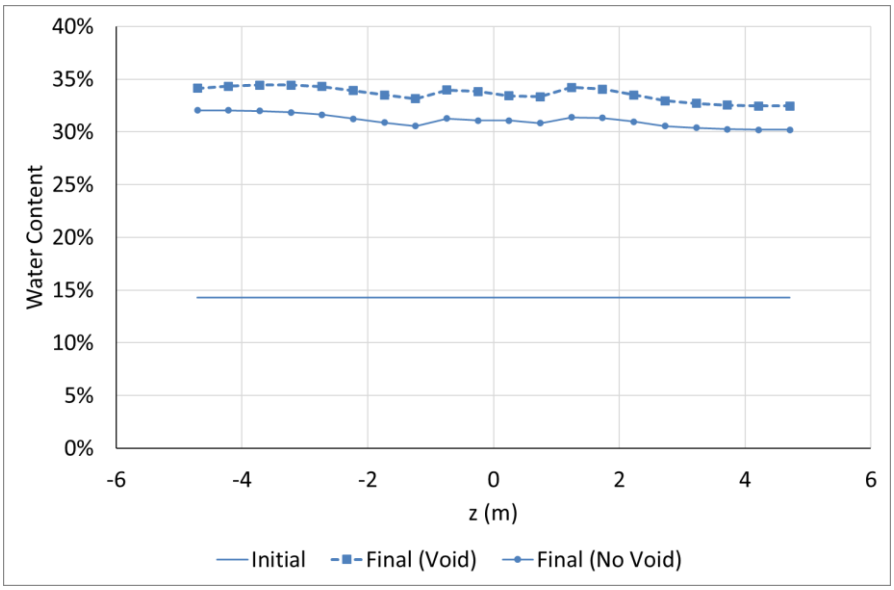

Figure 4.2-6 Initial and final vertical profiles of water content.

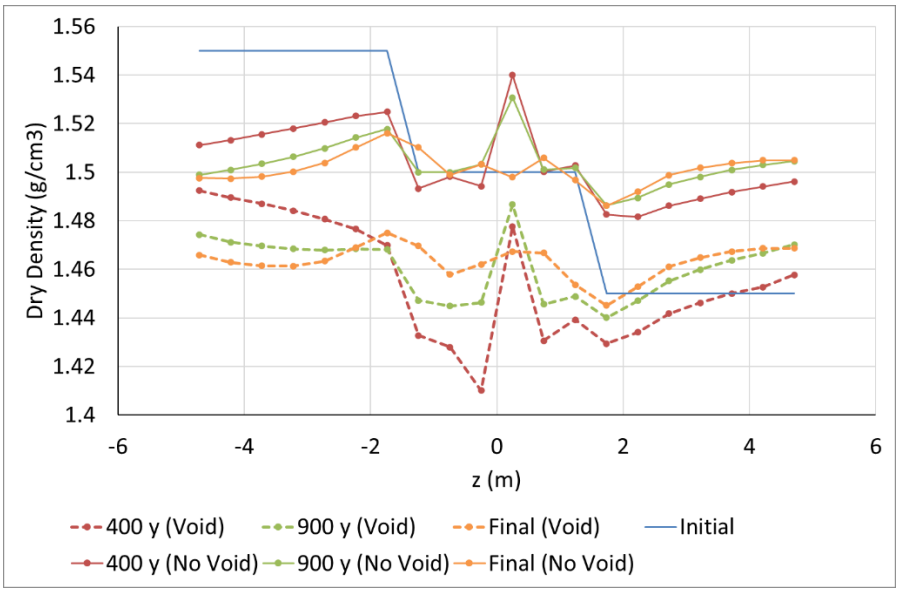

Figure 4.2-7 Initial, intermediate and final vertical profiles of dry density.

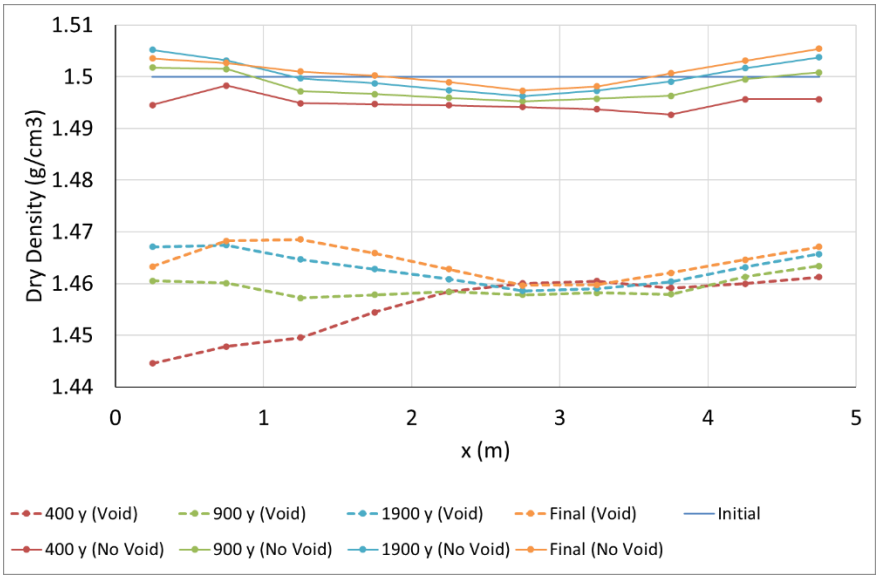

Figure 4.2-8 Initial, intermediate and final horizontal profiles of dry density.

4.2.6 Discussion

We are able to model most of the features of this assessment case, including the geometry and void, and interactions with the surrounding EDZ. However, some developments were required to the model to enable us to represent unstructured grids; these developments are not yet complete, so the choice of mechanical boundary conditions is restricted with these grids (we have not been able to explore the effects of friction between the bentonite and rock, for example). It would also be useful to further investigate representation of the void space; this can be represented as a porous medium but the model has difficulty in converging a solution. Alternatively,

it can be represented as a mechanical boundary condition allowing free swelling, but more work is needed to define appropriate hydraulic conditions at the boundary. Even though the volume of the void is small in comparison to the bentonite, it can result in significant differences in the predicted final values of swelling pressure.

The model has not considered a separate gas phase, or the impact of the groundwater chemistry. These could both be significant in an assessment case and could be useful to consider in future work.

4.3 Andra

4.3.1 Description of the models

A non-linear elastic approach is required for the mechanical model of bentonite. The hydro-mechanical behaviour of bentonite might be more precisely assessed with a double porosity model, but here a simple porosity model (modified BBM) is chosen. Plastic behaviour is not expected in such confined conditions (consolidation pressure not reached).

The clay rock is modelled with an elasto-plasticity model with a Mohr-Coulomb criterion and stress softening. Rock creep is not taken into account as a conservative hypothesis. The EDZ is modelled as a specific domain with different hydraulic properties. The initial apical void is modelled with a bilinear elastic model (becoming stiff as volumetric strain is enough negative).

4.3.2 Geometry and discretization

The geometry represents a 2D cross-section of the sealing surrounded by the geological clay rock with an extension of 50x100 m. Two concentric rings of damaged argillite are defined (connected fractured zone & diffuse fractured zone). Compared to the schematic representation of the problem, a simplified geometry is chosen for the apical void, which is assimilated as a thin layer with a maximum height of 10 cm. The hexaedric mesh is composed of 1340 nodes as a whole (Figure 4.3-1).

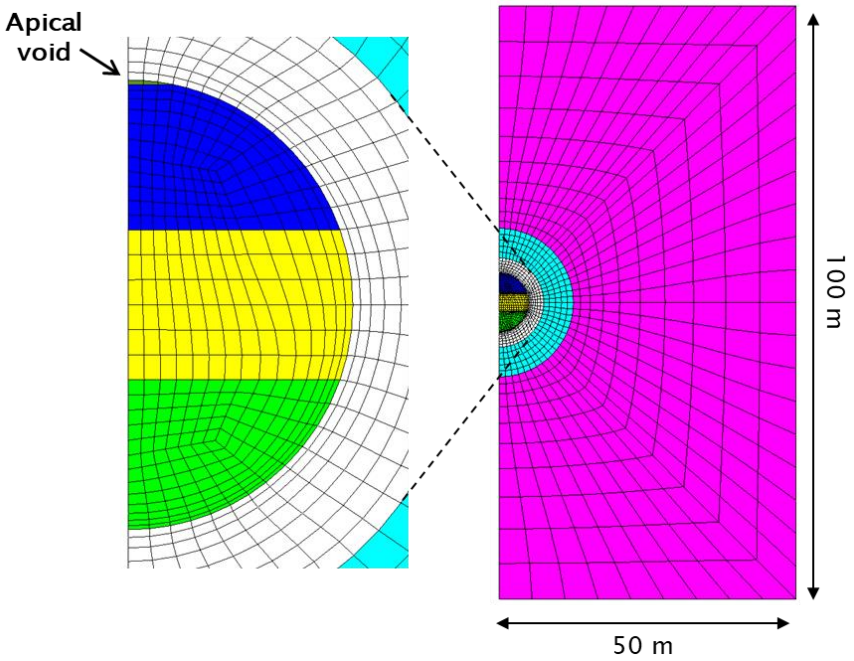

Figure 4.3-1 Geometry and mesh

4.3.3 Input parameters

The bentonite core has a constant and very low permeability (10^{-13} m/s). Each layer has a specific porosity consistent with its dry density (see initial values in Figure 4.3-3). The capillary pressure is expressed as a Van Genuchten's relationship (Figure 4.3-2). The relative permeability is expressed as a cubic law assigned to all clay components (including bentonite).

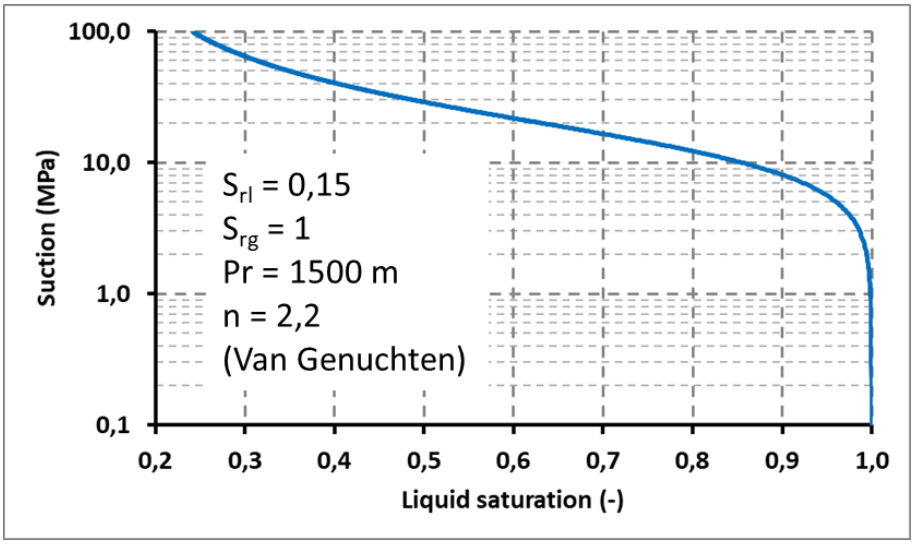

Figure 4.3-2 Suction properties for bentonite

Non-linear elasticity parameter values for bentonite are based on input target swelling pressure consistent with initial dry density (experimental evidence at constant volume conditions, see Figure 4.3-3).

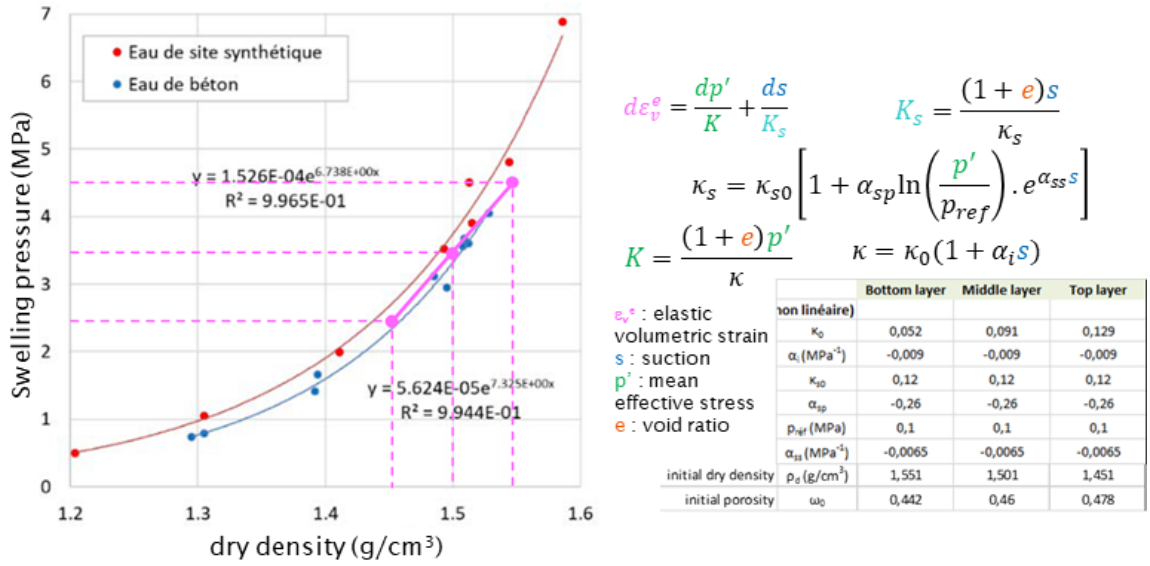

		Bottom layer	Middle layer	Top layer
non linéaire)				
	κ_0	0,052	0,091	0,129
	α_i (MPa^{-1})	-0,009	-0,009	-0,009
	κ_{s0}	0,12	0,12	0,12
	α_{sp}	-0,26	-0,26	-0,26
	p_{ref} (MPa)	0,1	0,1	0,1
	α_{ss} (MPa^{-1})	-0,0065	-0,0065	-0,0065
initial dry density	ρ_d (g/cm^3)	1,551	1,501	1,451
initial porosity	ω_0	0,442	0,46	0,478

Figure 4.3-3 Hydro-mechanical properties (modified BBM model) for bentonite

The apical void has a 99 % porosity, constant 10^{-9} m/s permeability and negligible stiffness until it is reduced down to 1 % of its initial volume (E = 10^{-4} MPa then 4000 MPa). Hydro-mechanical parameters for clay rock are presented in Table 4.3-1.

Table 4.3-1 Parameters for clay rock

		Intact rock	Diffuse fractured zone	Connected fractured zone
		COx-UA	**ZFD-UA**	**ZFC**
Porosity	ω (-)	18 %	18 %	20 %
Absolute perm.	K_{i0} (m^2)	$1 \cdot 10^{-20}$	$1 \cdot 10^{-18}$	$1 \cdot 10^{-16}$
Retention curve	P_0 (MPa)	19,6	19,6	19,6
	n (-)	1.6	1.5	1.5
	S_{res} (-)	0	0	0
Elasticity	E(GPa)	5	5	5 0,5 (sensitivity)
	ν(-)	0.3	0.3	0.3
Biot's coefficient	b (-)	0.8	0.8	0.8
Plasticity	c' (MPa)	2	1	0.5
	ϕ' (°)	20	20	20
	Ψ' (°)	20	20	20

4.3.4 Initial and boundary conditions

The bentonite core is an initially dry mixture (initial suction = 100 MPa). Initial porosity is specified for each layer in Figure 4.3-3.

Initial in situ stresses and liquid pressure in the clay rock vary linearly with depth, considering a homogeneous density of 2400 kg/m^3. The sealing is located at 500 m depth. Stresses are isotropic in the modelled 2D plane whereas the orthogonal stress is 30 % higher (major stress).

After instantaneous excavation (without set of a lining here), the gallery is ventilated during 100 years with an air of constant 50 % humidity level. Thereafter the sealing is supposed to be set instantaneously and natural resaturation begins from the clay rock. Boundary conditions are displayed in Figure 4.3-4. The dimensions of the model (50x100 m) have been determined so as not to influence the hydro-mechanical evolution of the sealing. Calculation has been run until hydraulic balance is reached (so after full resaturation of the sealing).

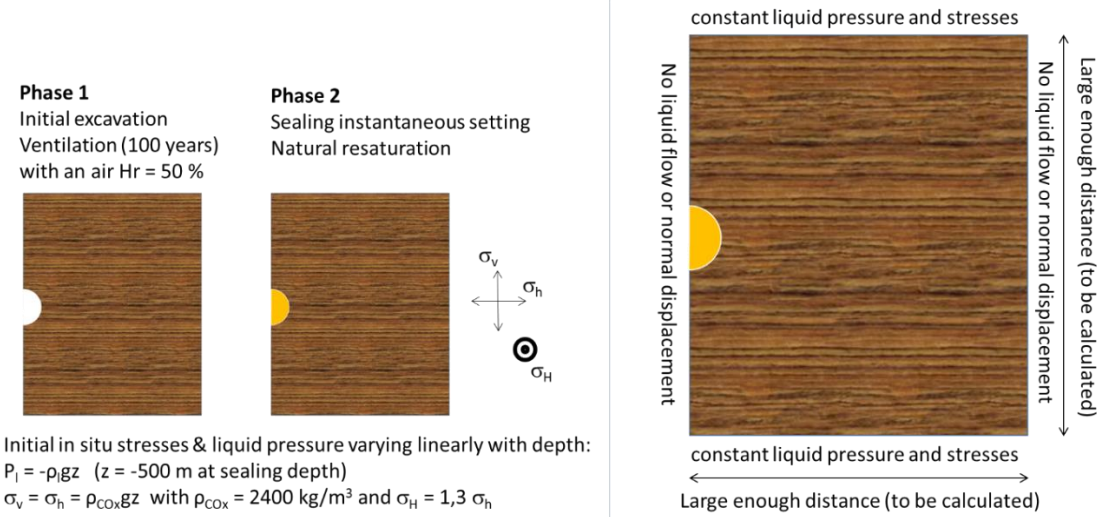

Figure 4.3-4 Initial and boundary conditions

4.3.5 Results

Hydraulic results evidence a complete resaturation of the bentonite core in ~6500 years and a total hydraulic recharge in an additional ~2000 years (Figure 4.3-5 and Figure 4.3-6). Saturation fields show a centripetal mode of hydration.

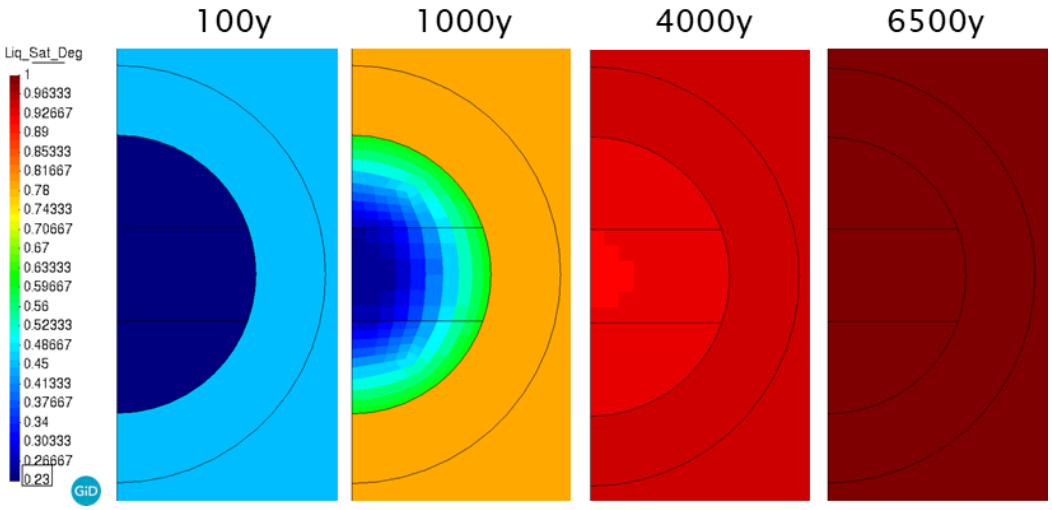

Figure 4.3-5 Water saturation field at several times

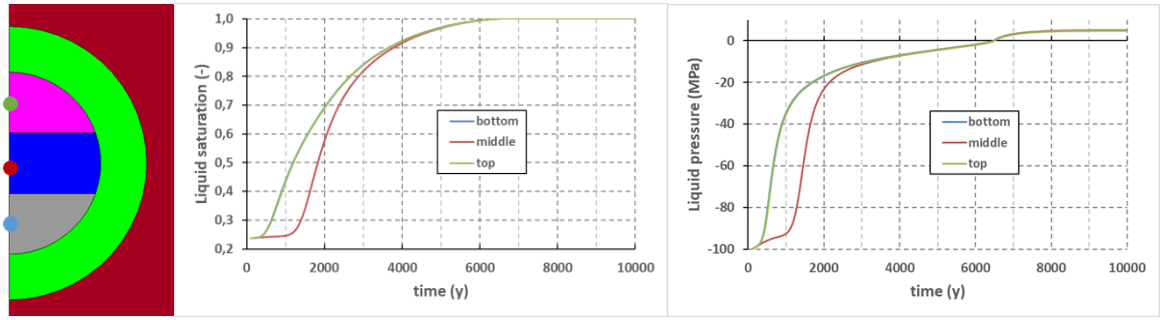

Figure 4.3-6 Water saturation and liquid pressure evolution

The initial dry density contrast between the bentonite layers decreases over time (Figure 4.3-7 and Figure 4.3-8) due to mechanical interaction as swelling pressure builds up (Figure 4.3-9). During the first 1000 years, the almost fully saturated outer part of the core expands radially and compresses its inner part while at the same time the lower part, which has a relatively high swelling potential, compresses the other two, and finally closes the apical void close to which dry density is *de facto* slightly lower. Afterwards, while the middle of the core swells in turn, the lower and middle parts of the core compress its upper part until the fully resaturation state. Finally, as water pressure increases in the fully saturated state, only small changes occur. Results without apical void are nearly the same except at the very top of the core (see graphs in Figure 4.3-10).

Overall, the vertical mechanical re-equilibration contributes to reduce the dry density contrast but the latter does not come close to zero because the horizontal net stresses, which are part of the swelling pressure, remain more contrasted than the vertical ones (Figure 4.3-9) due to the rock stiffness (the final global volumetric strain of the bentonite core is only ~0.4 %).

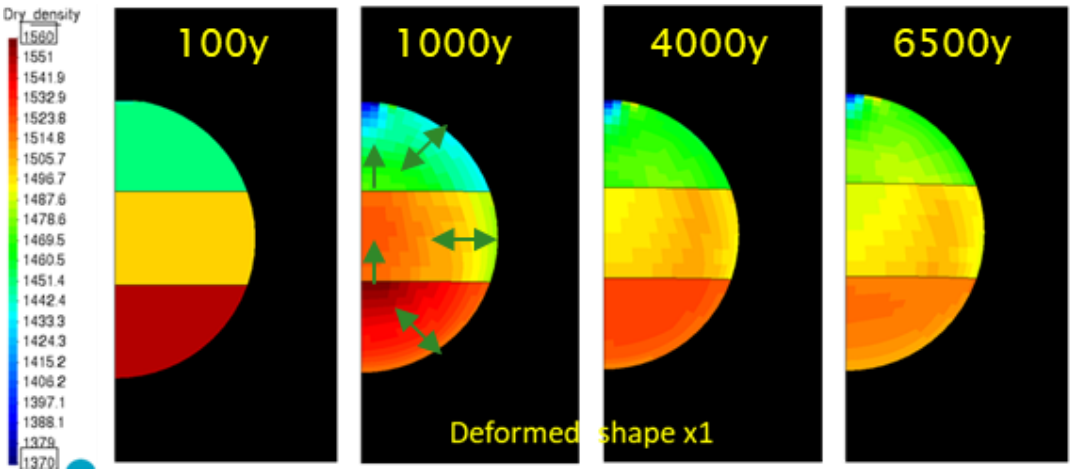

Figure 4.3-7 Dry density field at several times

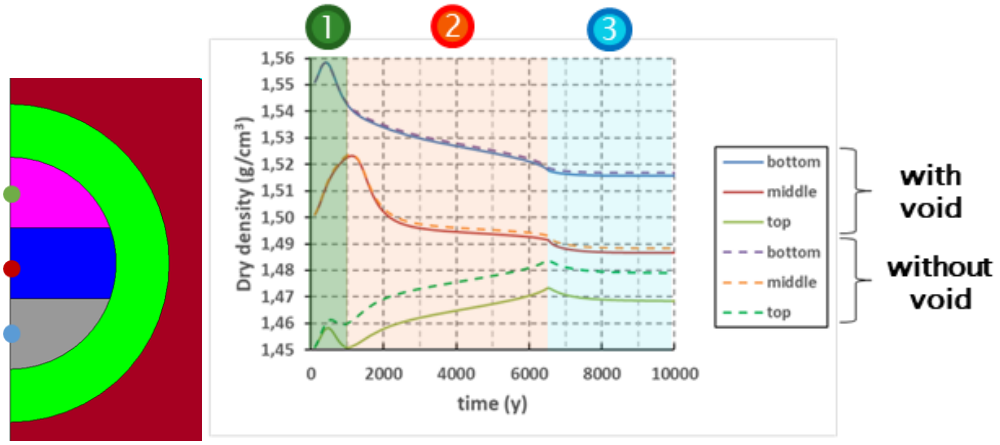

Figure 4.3-8 Dry density evolution with and without void

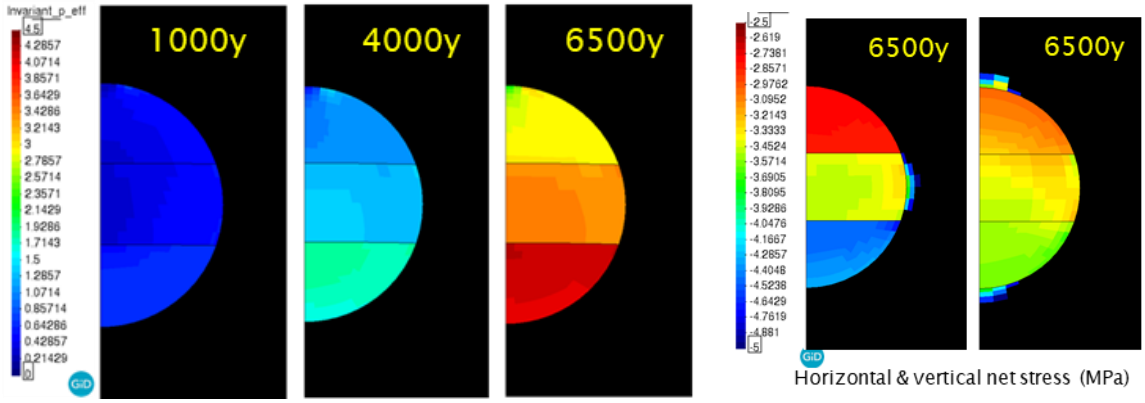

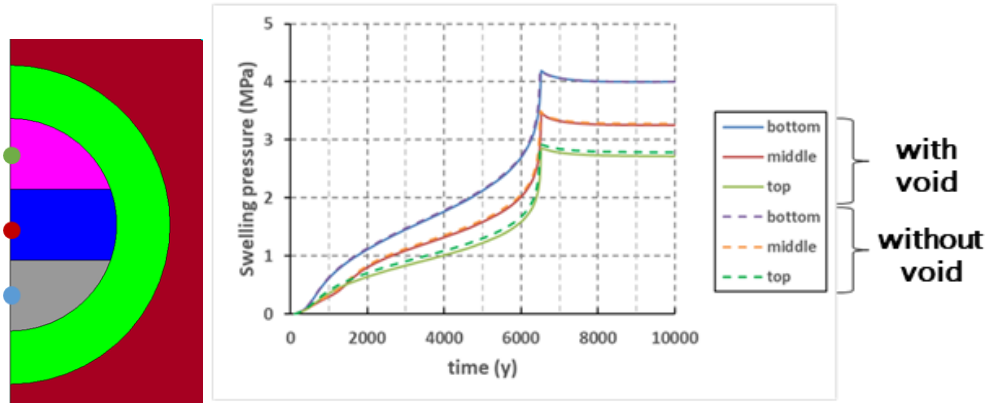

Figure 4.3-9 Swelling pressure evolution with and without void

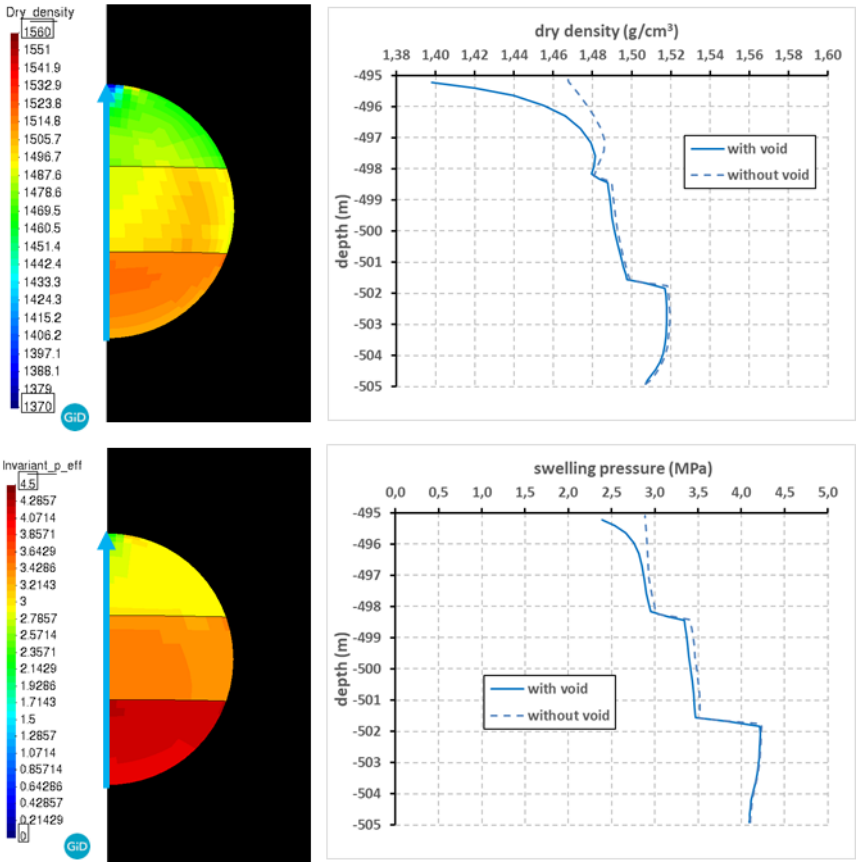

Figure 4.3-10 Final vertical profiles of dry density & swelling pressure

4.3.6 Discussion

The resaturation scheme of the bentonite core remains simple despite its initial heterogeneity and closely dependent on intact rock permeability because the latter is the only water provider. Hence, in the scope of a sensitivity analysis, the resulting resaturation time is proportionally inverse of rock permeability.

Besides the mechanical explanation, the remaining contrast of dry density and swelling pressure in the fully saturated state can also be explained by the modelled permanent perfect contact between bentonite and rock, which does not allow circumferential sliding.

In addition, the hydro-mechanical kinetics should be more realistic using a double porosity model (BExM) for bentonite, which would lead to faster short-term increase of swelling pressure and dry density changes.

4.4 Synthesis of results – key lessons (Andra + all participants in the Andra test)

Three teams participated to the assessment cases proposed by Andra. Details on the models can be found in deliverable D3.3 or in the previous paragraphs. The interest of this case was to introduce initial heterogeneities in bentonite from two origins. It was supposed (i) an initial segregation in the bentonite happening when installing. This was introduced by three layers with different initial dry densities. (ii) an initial gap on the top of the bentonite between the bentonite plug and the host rock representing a filling defect.

Two cases were proposed, one with an initial void and one without the initial void supposing that the gallery is fully filled at the beginning.

The two cases have not been modelled by all the partners as can be seen in Table 4.4-1.

Table 4.4-1 Models used by each partner and treated cases

	ULG	Quintessa	Andra
Code	Lagamine	QPAC/ILM	Code_Bright
No void case		X	X
Void case	X	X	X

It was suggested to simulate first the excavation of the host rock before having a 100 years period of ventilation. This will define the boundary condition around the bentonite plug that is putting in place after 100 years.

Two of the teams represented a full domain including the Callovo-Oxfordian claystone and the two phases of excavation and ventilation. One team modelled the EDZ alone during the 100 years period of ventilation and therefore used the results as a boundary condition for the bentonite.

It should be noticed that the initial apical void represents a very small volume (~0.13m3) compared to the volume of bentonite introduced in the tunnel (~78m3). This can be seen of Figure 4.2-2 from Quintessa meshing. Despite this difference of volume, it allows to evaluate the capacity of the numerical models to manage the void closure due to bentonite swelling.

In the test case proposed by Andra, representative of a seals placed in a tunnel, several situations have already encountered in previous WP5 tests. They are in line with the objectives of BEACON and the capacity of the model to deal with different kinds

of heterogeneities. The initial void closure and the final distribution of dry density are two indicators particularly important in terms of performance assessment.

4.4.1 Time to reach full saturation / gap closure

A comparison between the water saturation taken in the middle of the bentonite plug from the 3 different models shows a comparable time to reach full saturation for Andra and Quintessa (around 6000 years). ULG predicted a time to full saturation of half the times obtained by the other teams. This was analysed as due to the water permeability considered in the model for the host rock. The water permeability introduced by ULG in the model was two time higher than the specified one. The availability of water is more important in this case and could lead to a full saturation two times faster. Taking into account this difference on water permeability, the results are consistent with these obtained by the other teams (Figure 4.4-1).

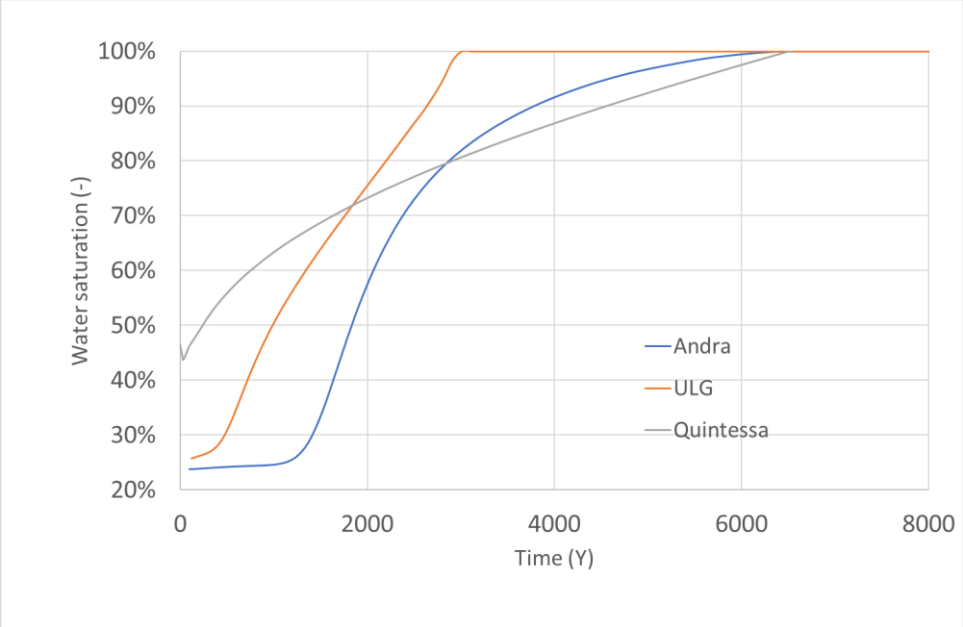

Figure 4.4-1 Evolution of water saturation in the middle of bentonite plug

Only few differences are observed on saturation time when void are considered or not. This can be seen on Figure 4.2-4 from Quintessa results.

The void on the top of bentonite plug closes in a consistency way with the evolution of saturation. It can be seen on Figure 4.4-2 that the models are able to predict the void closure. As for the full saturation time, the differences are due to the water permeability of the host rock introduced in the model. It can be seen that the void are closed early in the simulation before full saturation has been reached.

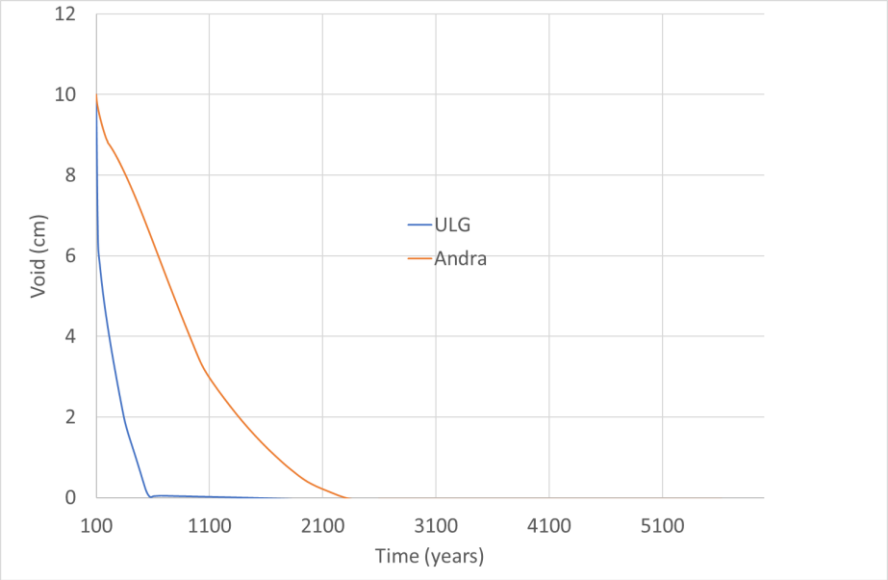

Figure 4.4-2 Evolution of void closure at the top of bentonite plug

4.4.2 Evolution of dry density

One of the main objectives of the test case is to evaluate how evolve the initial heterogeneities in bentonite during hydration and the consequence of these heterogeneities on the expected function of the bentonite component. For Andra, two specifications are considered for tunnel sealing:

- a low water permeability. This mean that the local dry density should be higher than a minimum value;
- a swelling capacity to fill the technological voids.

The results obtained by the modellers clearly indicate that after hydration and reaching a state of equilibrium, the dry density remains variable in the bentonite. This can be seen on Figure 4.4-3 and Figure 4.4-4 where horizontal et vertical profiles are presented for the initial state and at the end of the simulation. This is consistent with the previous simulations performed in WP5 and with the observations made on several experimental tests.

The results are quite different between the teams. It should be noticed that ULG introduced a higher dry density than the one specified. This could explain the difference on the final level of dry density. The origin of the differences is difficult to understand at this stage.

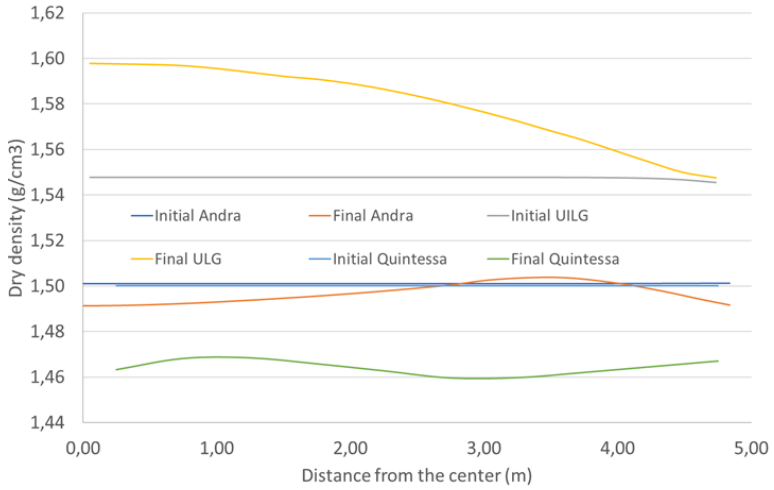

Figure 4.4-3 Comparison of horizontal profiles of dry density initial/final state

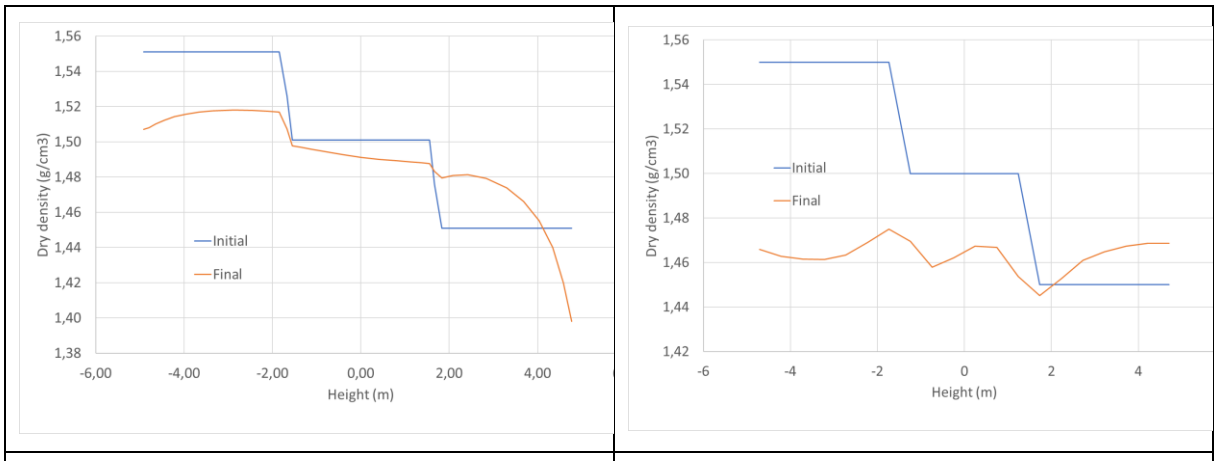

Andra	Quintessa

Figure 4.4-4 Vertical profile of dry density initial/final

The comparison on the profiles obtained by the 3 teams indicates a final dry density between 1.4 and 1.6 g/cm3 consistent with what it is expected from Andra specifications. In this range of dry density, the hydraulic conductivity is lower than 10^{-11} m/s as can be seen on the Figure 4.4-5. The lower dry density is obtained at the final state in the zone where voids were initially introduced (see Figure 4.4-6). A comparison between the simulation with and without initial voids clearly shows the difference at the final state on the upper part of the bentonite plug (1.4/1.47 for Andra and 1.47/1.51 for Quintessa). The results are consistent with the void closure observed on Figure 4.4-2.

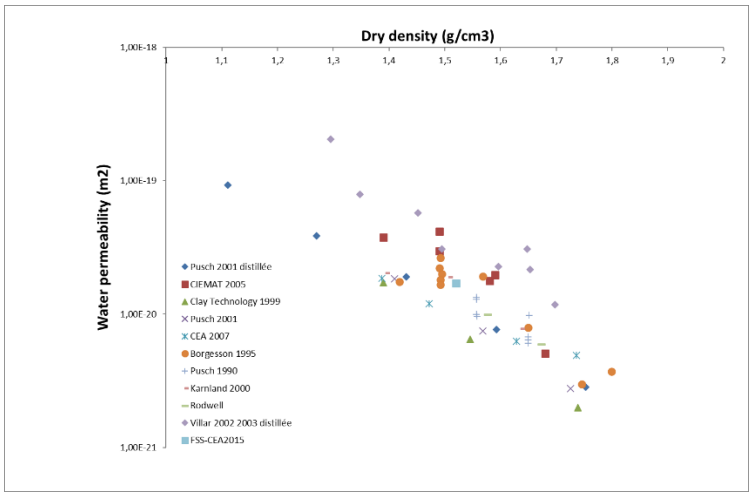

Figure 4.4-5 Water permeability function of dry density for pure MX80 – data from literature

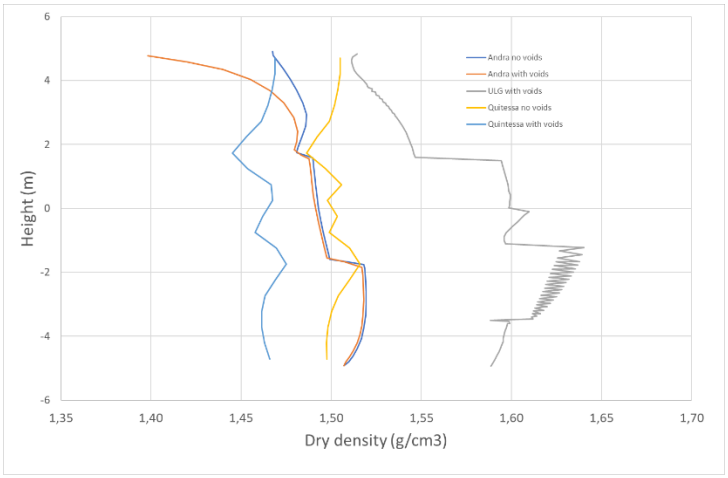

Figure 4.4-6 Comparison of vertical profiles of dry density final state with and without void

4.4.3 Swelling pressure

The final swelling pressure obtained by the three teams are in the same range around 3MPa ±0.4 (see Figure 4.4-7a). However as it was observed on previous simulations during the Beacon project, the way to reach the final state can be very different. A part of the differences can be explained by how the initial and boundary conditions are introduced in the model. For Quintessa, there is no real representation of the host rock. This could contribute to explain why the characteristic times are shorter than the others. For ULG, the initial dry density distribution is not the one specified and the water permeability of the host rock is higher inducing a faster transient phase. It is interesting to see the consistency of the model when representing on the same graph the void closure and the with a swelling pressure on the top of the bentonite. As it is expected the swelling pressure starts to increase after the void closure (Figure 4.4-7b).

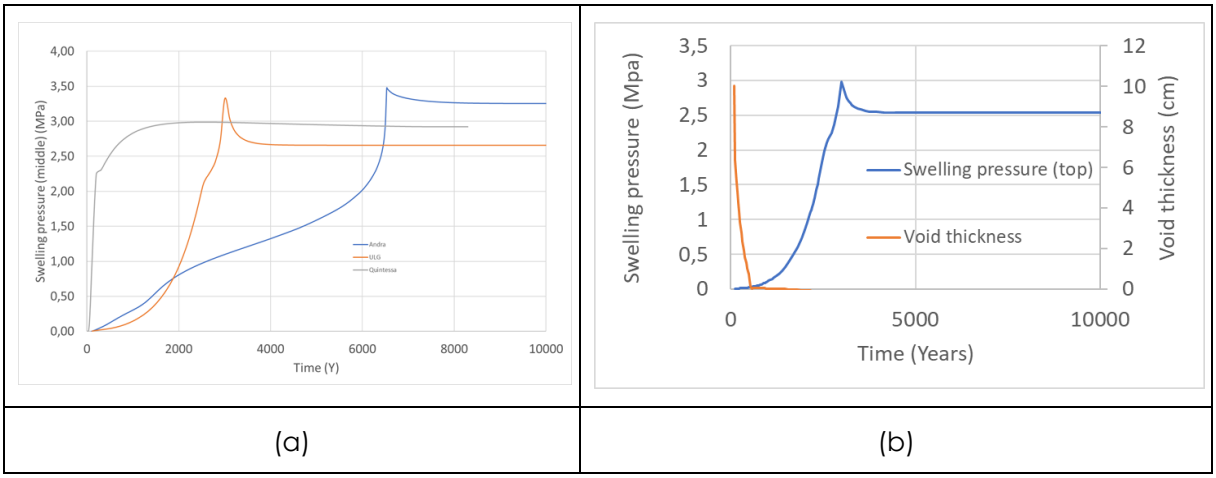

(a) (b)

Figure 4.4-7 (a) Swelling pressure evolution in the middle of bentonite plug, (b) evolution of gap thickness and swelling pressure on the top of bentonite plug (ULG)

4.4.4 Conclusion on Andra assessment case

The simulations performed with three different models have been succeeded to evaluate the evolution of a bentonite seal putting in place in a tunnel. The more advanced models are able to simulate the excavation, a period of ventilation and finally the hydration of the bentonite plug. All the models predict a final state with heterogeneous distribution of dry density resulting of the initial conditions in the bentonite. Two types of heterogeneities were introduced: variable dry density distribution to represent a potential segregation when a 10-diameter tunnel is filled with pellets; technological voids on the top of the bentonite between the bentonite plug and the host rock. The simulations indicated as expected that technological gaps are closed in the early times after repository closure. It is important to note the ability of the models to simulate the closure of the voids initially present and the overall consistency of the results. This situation is close to the one encountered in one of the first lab tests used in the first task of WP5 (test1a) and this certainly highlights the progress of the teams during the project.

As shown before on the other tasks of WP5, differences between the results obtained with the 3 models (still) appear mainly during the transient phase. It should be considered that a part of the differences could be attributed to the choice made by each team in term of initial conditions, boundary conditions or parameters retained for the simulations. This highlights the needs on such complex problem to carry out sensitivity analyses with a view to comparing the weight of different parameters or modelling choices on final results in regard to the assessment indicators.

The models used to simulate the Andra case are quite different even if these used by Andra and ULG are based on the BBM model. Among the three teams, only ULG considered a double structure and this is introduced only in the hydraulic part.

Despite the differences between the three models on some results and how they apprehend the transient phase, it is interesting to see that the final dry density

distribution is in accordance with the requirements issued by Andra. The range of dry density allows to reach hydraulic conductivities below 10^{-11}m/s. The other characteristic desired by Andra is the capacity of the material to fill technological voids and to have sufficient dry densities in these zones. The models all suggest that the voids will be closed and a sufficiently high dry density achieved.

The differences observed in the results highlight certainly that the representation of some processes should be improved to reenforce the demonstration of robustness of predictions made by the models. However, the global trend seems to be well captured as it was also shown before in the previous tasks when comparing experimental data and simulations. More complex models have been used during the project introducing micro/macro coupling for both mechanical and hydraulic part indicating good directions to improve the behaviour of bentonite taking into account the initial presence of heterogeneities.

5 New results from task5.1, task5.2 and task 5.3

5.1 LEI

LEI model development in WP3 proceeded gradually together with model applications for modelling experiments in tasks 5.1, 5.3 and 5.4 of WP5.

The preliminary modelling results of Test1a01 from task 5.1 (Talandier, 2018) obtained with very first LEI model formulation were presented in deliverable D5.1.2 (Talandier et al., 2019) in 2019. Preliminary results showed limited agreement with experimental data. By the end of the project, Test1a01 was re-run with the final LEI model formulation to present improvements in model capabilities and obtained results. The conclusion was made that the final model formulation in COMSOL Multiphysics led to better agreement with experimental data compared to preliminary results. However, the final model underestimated (to some extent) the void ratio and water content at different parts of the specimen and overestimated measured swelling pressure at step 1, but underestimated it for step 2.

The description of modelled experiment Test1a01, modelling assumptions and detailed comparison of preliminary and final results could be found in LEI contribution to BEACON WP3 deliverable D3.3.

5.2 EPFL

After the development of the new model in the WP3, EPFL has revisited the experimental campaign of Dueck et al (2011) that was proposed for task 5.1.

The previous results in terms of stresses are shown in Figure 5.2-1. the magnitude of swelling pressure could be captured with the model but a significant collapse was obtained during the saturation phase which overestimated the real measurements. This was one of the stress paths that revealed that the loading collapse curve formulation required a change. The reloading phase was qualitatively captured although the radial stress was overestimated.

The new formulation was used to model these tests using the same saturated state parameters that have been used for the Nagra assessment case. The loading collapse curve parameters have been calibrated for this specific dry density as shown in Figure 5.2-2. It can be observed that the new formulation can provide a better fit to the experimental results. It predicts a smoother transition to the saturated state while avoiding an excessive collapse.

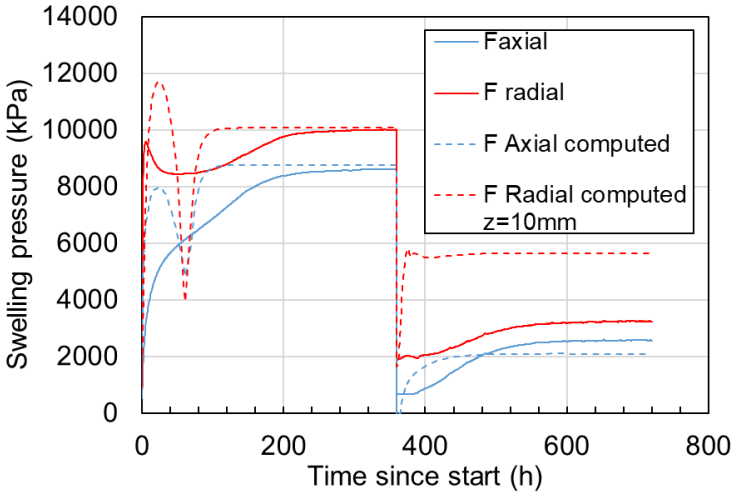

Figure 5.2-1 Previous results for task 1a using the model available at the start of the project.

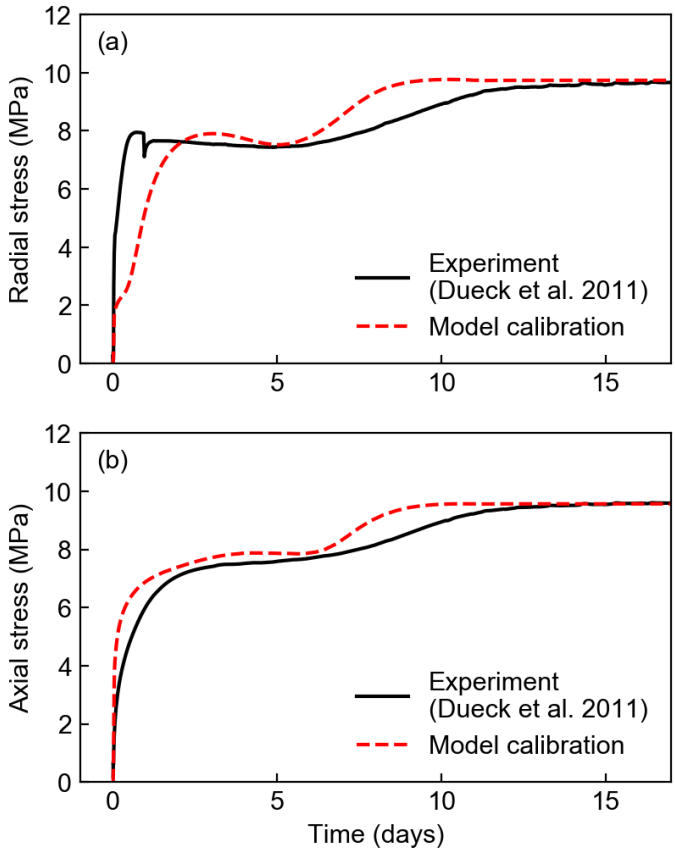

Figure 5.2-2 Calibration of the new constitutive model. In particular the parameters defining the block bentonite behaviour under unsaturated states against the swelling pressure. (a) Results in terms of radial stress and (b) results in terms of axial stress.

Once the loading collapse curve parameters were defined, the model was used to predict the unloading-reloading response of the bentonite. For this the results of a test in which the unloading and reloading was perform up to 5 times were used.

The results are shown in Figure 5.2-3. It can be seen that the model provides a good prediction of the reloading cycles even from a quantitative point of view in some of the cycles. Note that the time required to reach equilibrium for each cycle is also well predicted. The predicted dry density at the end of the test, as shown in Figure 5.2-4, is also in good agreement with the dismantling measurements. As the reloading cycles were performed under saturated states, this also validates the use of the same saturated states parameters for a given bentonite irrespectively of its initial state (we recall that these are the same that were used to model CEA tests reported by Bernachy Barbe et al. 2019).

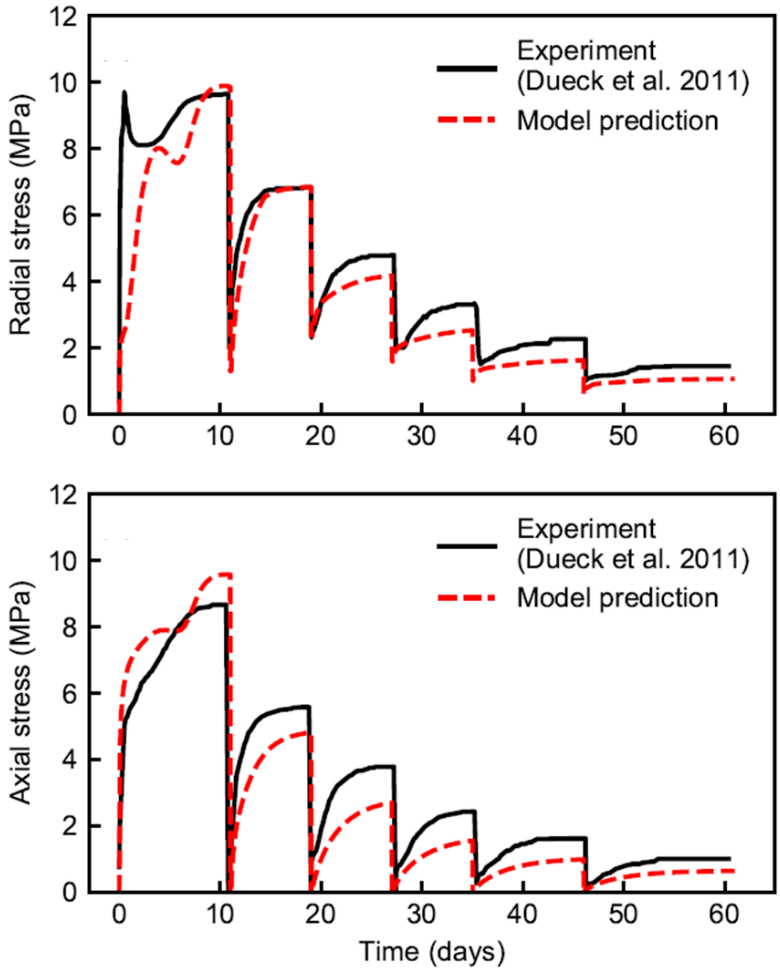

Figure 5.2-3 Predicted response of the new model against the results reported by Dueck et al. (2011). (a) radial stress and (b) axial stress.

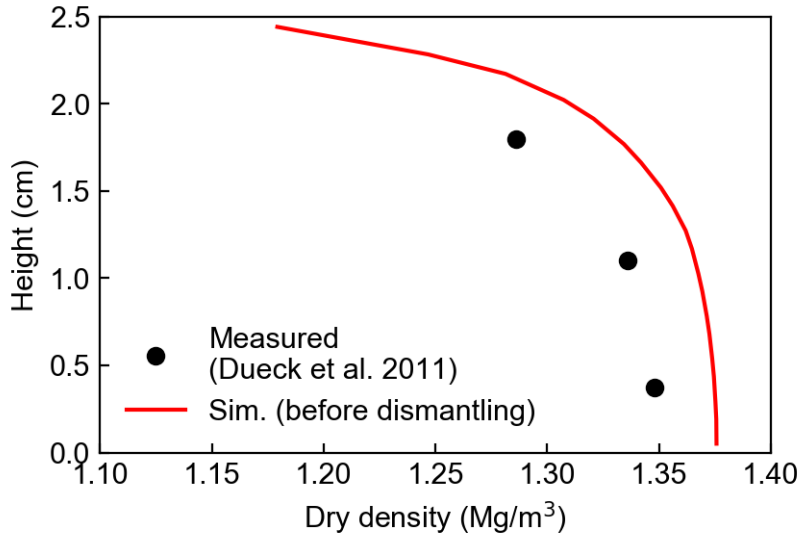

Figure 5.2-4 Final distribution of the dry density predicted by the new model compared to the measurements after dismantling of Dueck et al. (2011)

5.3 UPC, Task 5.3

Mainly due to the disruption caused by the pandemic, the modelling of task 5.3 by UPC was delayed and only partial results were reported in Deliverable 5.6: "Specifications for BEACON WP5: testing, verification and validation of models. Step 3-predictive test case". The modelling task has now been completed with new analyses performed for all the three tests: MGR22, MGR23 and MGR 27. The spirit of a predictive test case has been respected with the analysis of MGR27 being run with exactly the same parameters as those used for the calibration tests MGR22 and MGR 23. In this section, the main features and results of this modelling exercise are presented. In order to limit the extent of this addendum, the model used is not reported here, it has been fully described in Deliverable 5.6, section 3.9.1.

5.3.1 Geometry and discretization

For the numerical simulations, the solution of the governing coupled hydromechanical equations has been carried out using the Code_Bright software.

All the tests to be analysed have the same geometry, a cylinder of diameter 5 cm and 10 cm high. One half of the cylinder is occupied by granular bentonite (pellets) and the other half by a compacted block. Consequently, an axisymmetric domain has been used; it is discretised by 400 linear quadrilaterals with a total of 451nodes. A selective integration technique has been used to avoid locking of the linear finite elements. The mesh employed is shown in Figure 5.1.1. It can be observed that the finite element mesh is finer near the hydration surface and in the vicinity of the block/pellets contact surface. It should be noted, however, that, in the absence of

friction, the problem is in fact purely-one dimensional, so that a one-dimensional mesh would be sufficient to solve it. Such a mesh has been employed on occasions.

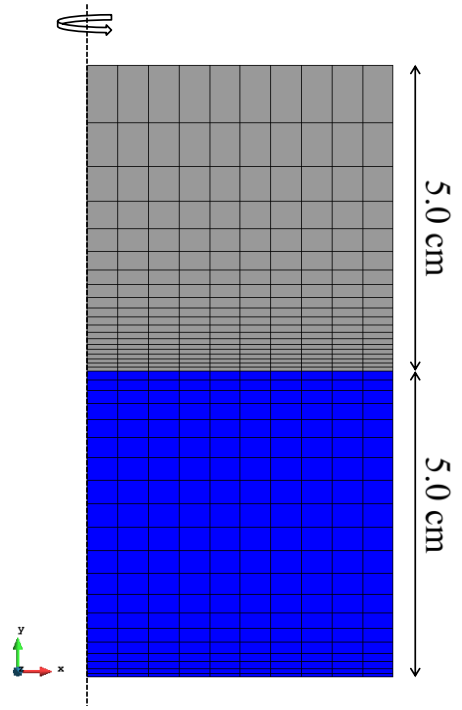

Figure 5.1.1 Analysis domain and discretization

5.3.2 Input parameters

Parameters were derived from available information on the Febex bentonite both as compacted blocks and as pellets (Alonso et al. (2011), ENRESA (2000), Hoffman et al. (2007) , Lloret et al. (2003), Villar & Gomez-Espina (2009) and the BEACON report D5.2.1 (2018)). Because of the conditions of the tests to be simulated, particular attention has been paid to the swelling pressure tests of Lloret et al (2003) for the compacted block and of Hoffman et al. (2007) for the pellets.

Figure 5.3-1 shows some of the most important constitutive relationships for the compacted block and for the pellets. The double-porosity model requires the definition of a different retention curve for each structural level. The overall retention curve of the specimen is given by the superposition of the micro and macro Van Genuchten curves, as shown in Figure 5.3-1a, b). Also, the mechanical micro-macro coupling (β-mechanism) was simulated by defining the shape of the interaction functions (f_β), plotted in Figure 5.3-1c, d). The parameters defining the initial LC curve (i.e. r, β, λ, p_0^*, p_c) result in the curve presented in Figure 5.3-1e, f) and the permeability parameters yield the curves of (Figure 5.3-1g, h). The non-linear elasticity parameters ($\bar{\kappa}$ and κ_s) were determined according to the results of laboratory swelling pressure tests. The Poisson ratio ν and the shear strength angle (ϕ) have been set to a value of 0.3 and 25 respectively. Finally, the initial macro and micropore volume were

determined from the MIP observations provided with the specifications. Initial hydraulic equilibrium between structural levels was assumed.

The same input parameters have been used in all the simulations reported here. Table 5.3-1 shows the input parameters and initial conditions common for all the tests for compacted bentonite and bentonite pellets considered in the analysis.

Table 5.3-1 Input parameters and initial conditions

INPUT PARAMETERS		COMPACTED BENTONITE	PELLETS BENTONITE
Bishop parameter microstructural level	p_k (-)	0.7	0.7
	q_k (-)	100	100
	$\bar{\kappa}$ (-)	0.0007	0.00015
Non-linear elasticity	κ_s (-)	0.028	0.03
	ν (-)	0.3	0.3
Mechanical interaction Macro-micro Interaction functions	f_{ms0} (-)	2	1
	f_{ms1} (-)	0	0
	n_{ms} (-)	7	2
	f_{mc0} (-)	0	0
	f_{mc1} (-)	2	1
	n_{mc}	5	2
Macro-structural level Plastic mechanism (BBM)	φ	25	25
	p_c	0.5	0.1
	λ_{sat}	0.25	0.25
	r	0.65	0.41
	β	0.25	0.025
	k_s	0.01	0.01
	α	1	1
Leakage parameter	γ	0.4E-5	0.4E-5

Water retention curve for micro-structural level	$(P_o)_m$	180	180
	σ_o	0.072	0.072
	$(\lambda_o)_m$	0.70	0.70
	$(S_l)_{rm}$	0.2	0.1
	$(S_l)_{sm}$	1	1
	$(P_d)_1$	2000	2000
	$(\lambda_d)_1$	3.0	3.0
Water retention curve for Macro-structural level	$(P_o)_M$	10	1
	σ_o	0.072	0.072
	$(\lambda_o)_M$	0.30	0.33
	$(S_l)_{rM}$	0.0	0.001
	$(S_l)_{sM}$	1	1
	$(P_d)_M$	1500	900
	$(\lambda_d)_M$	3.0	2.5
Intrinsic permeability	k_0 (m^2)	1.0e-20	0.6e-18
	b (-)	12	6
Initial conditions	$(\phi_{min})_M$	0.18	0.392
	P_o^* (MPa)	1.9	0.4
	ϕ (-)	0.402	0.526
	$\bar{\phi}_m$ (-)	0.222	0.134
	P_{Lm} (MPa)	-120	-114
	P_g (MPa)	0.1	0.1

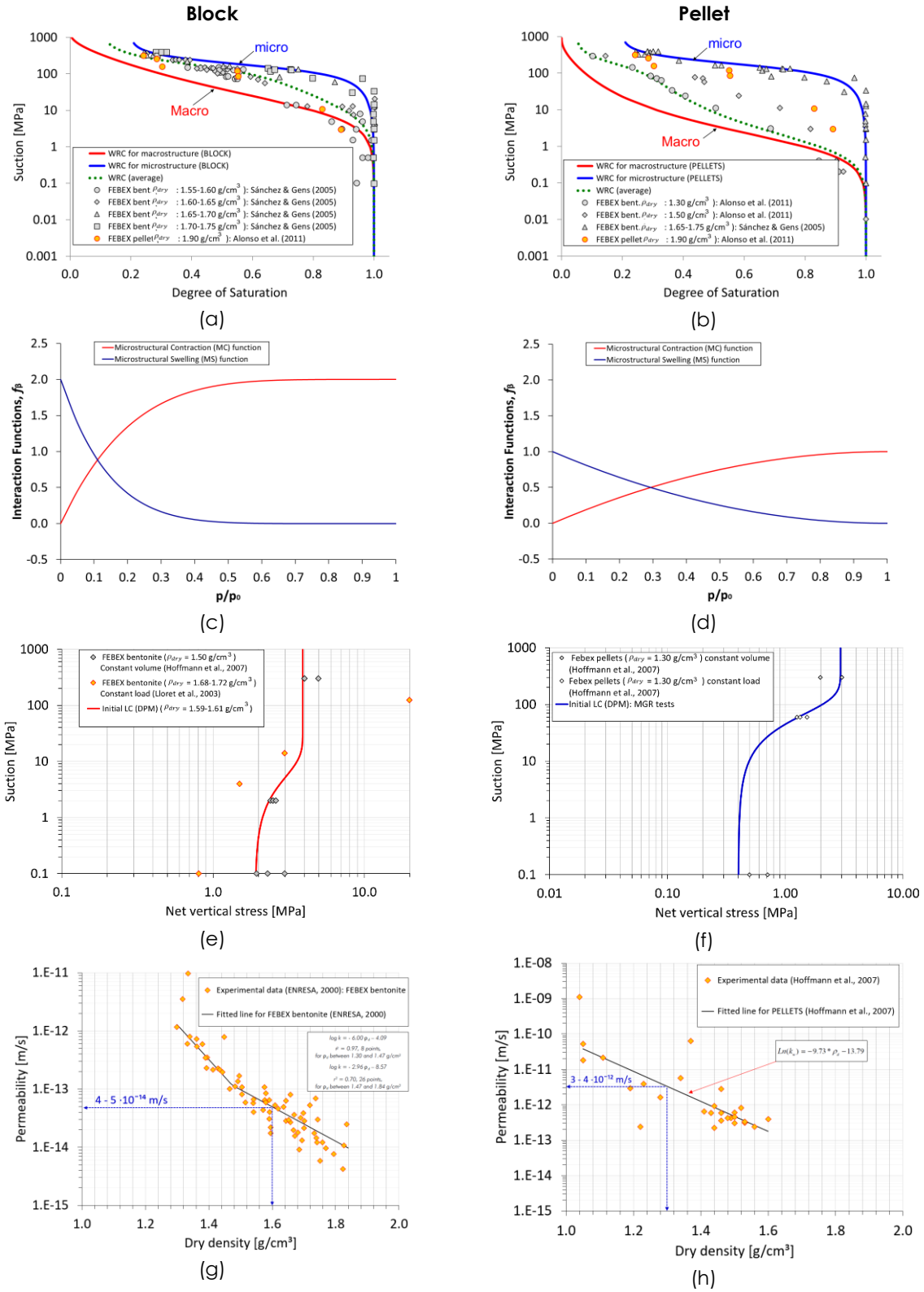

Figure 5.3-1 a, b) Water retention curve for macro and microstructure, c, d) Interaction functions, e, f) Initial LC curve, and g, h) Permeability

5.3.3 Specific initial and boundary conditions

Some initial conditions of the block and pellets bentonite vary from test to test according to the specifications. They are shown in Table 5.3-2. Due to some issues at the beginning of the simulation (applying the water pressure), the initial suction of the pellets in both MGR23 and MGR27 were changed to 120MPa. This is admissible as the effect of suction changes at very high values are slight.

Table 5.3-2 Specific initial conditions

MGR22			
	Block	Pellets	**Total**
w (%)	13.60	9.90	11.90
h (cm)	4.94	5.04	9.98
ρ_d (g/cm^3)	1.61	1.28	1.45
Sr (%)	55	25	37
Suction (MPa)	-120	-115	-118
MGR23			
	Block	Pellets	**Total**
w (%)	14.20	3.50	9.40
h (cm)	4.98	5.00	9.98
ρ_d (g/cm^3)	1.60	1.30	1.45
Sr (%)	56	9	29
Suction (MPa)	-120	-290	-205
MGR27			
	Block	Pellets	**Total**
w (%)	14.20	3.50	9.40
h (cm)	4.98	5.00	9.98
ρ_d (g/cm^3)	1.60	1.30	1.45
Sr (%)	56	9	29
Suction (MPa)	-120	-310	-215

The mechanical boundary conditions are illustrated in Figure 5.3-2. They are the same in all cases. The measurement of axial load is carried out at the top where zero vertical displacements are prescribed. It can be noted that for test MGR27 the locations of pellets and block have been exchanged.

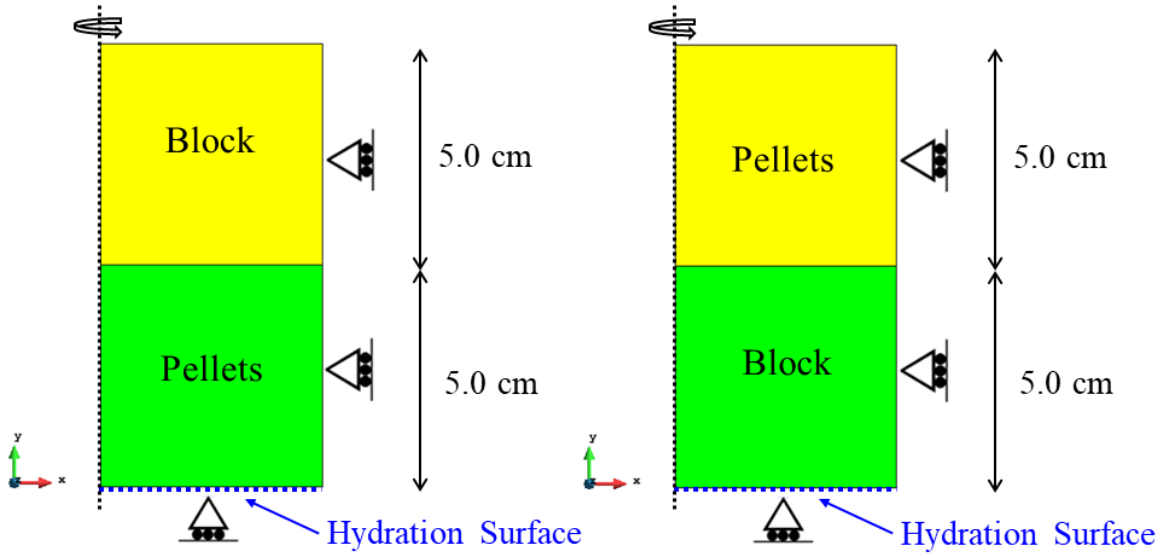

Figure 5.3-2 Mechanical boundary conditions. a) MGR 22 and MGR 23, b) MGR 27

Hydration is performed through the bottom boundary. In MGR22 a constant flow rate of 0.047 cm^3/h is applied whereas in MGR23 and MGR27 a constant water pressure of 15 kPa is applied. To avoid numerical convergence issues, the boundary water pressure is not applied instantaneously but over 1 day. Despite this, the solution at the start of the test is still somewhat unstable. In any case, from about 10 days on, the results can be considered sound and reliable.

5.3.4 MGR22 results

For the simulation of the MGR22 test, the real experimental protocol of the test has been followed as closely as possible including an initial period of 10 days without water inflow followed by a constant water injection of 0.047 cm^3/h.

The evolution of the water inflow (prescribed) and the calculated axial stress are presented in Figure 5.3-3 along with the experimental results.

It can be seen that the final swelling pressure is correctly reproduced. The variation in time is also quite satisfactory, although the initial rate of pressure increase calculated is faster than that observed, suggesting that the leakage parameter should be lower to delay the initial transfer of water from the macrostructure to the microstructure.

a)

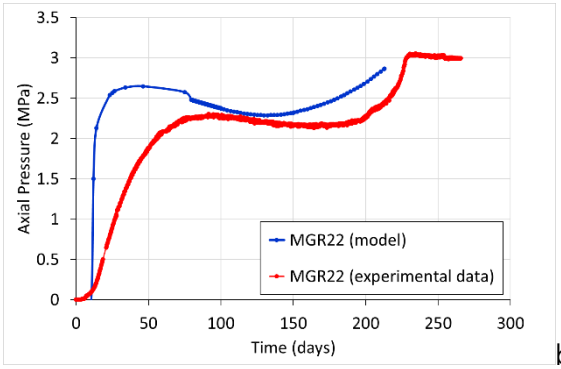

b)

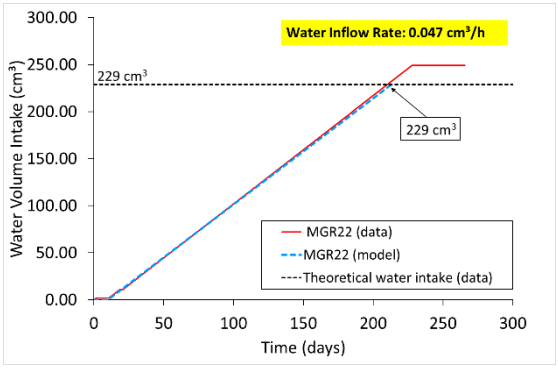

Figure 5.3-3 Comparison of the experimental observations with the results of the model. MGR22 test. a) Axial pressure, b) Water intake

The progress of homogenization in the analysis can be followed (Figure 5.3-4a) by plotting the evolution of global porosity at three different points. The point with coordinate y = 2.5 cm is located at the centre of the area of the pellets while the points with y = 7.5 cm and y = 10 cm correspond to the centre of the block and the top of the column, respectively.

It can be seen that the porosity in the pellet zone is reduced, while that of the block zone increases; its difference has reduced very significantly at the end of the test. It can also be observed that the reduction of the porosity in time is very similar throughout the bentonite block. More information on the variation of the porosity can be obtained by drawing the evolution of the void ratios of the two structural levels at the same points (Figure 5.3-4b, c and d). It can be noted that, locally, the microporosity (micro volume fraction) increases upon hydration and, as expected, a large reduction of the macro porosity of the pellets is predicted.

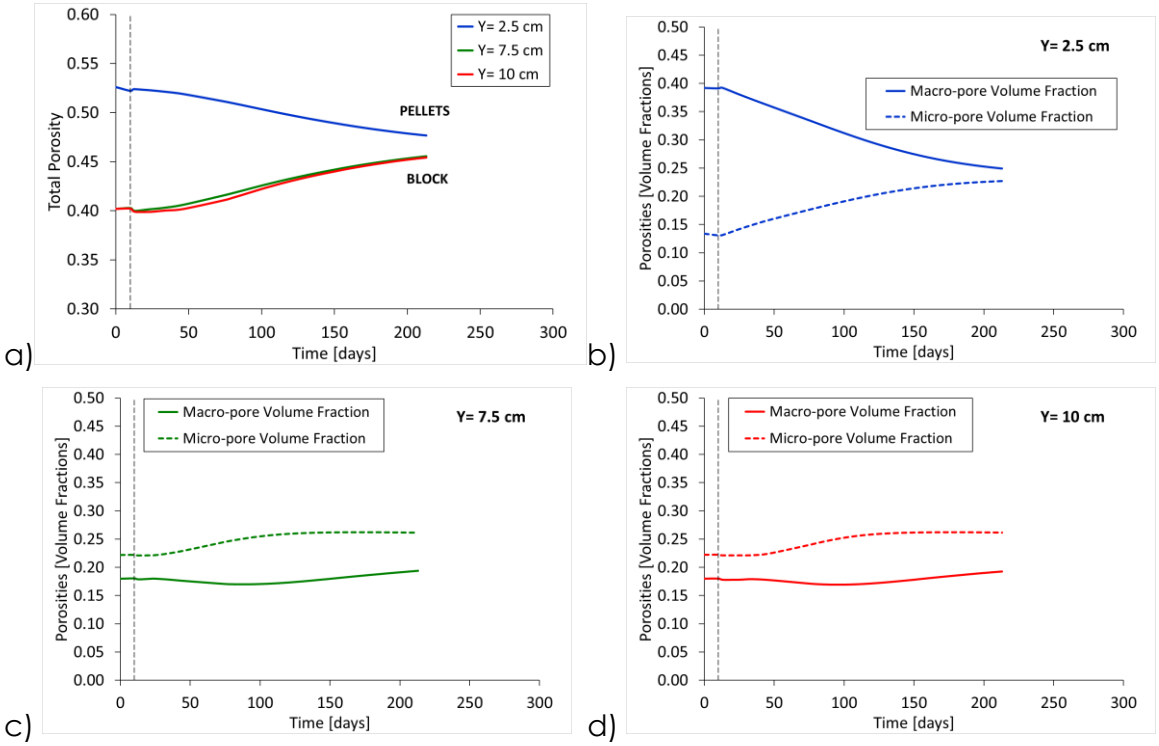

Figure 5.3-4 Test MGR22. a) Calculated evolution of the porosity of the pellets and of the bentonite block. b) Calculated macro and micro porosities (volume fractions) at y=2.5 cm, c) Calculated macro and micro porosities (volume fractions) at y=7.5 cm, d) Calculated macro and micro porosities (volume fractions) at y=10 cm. Coordinate y denotes the distance to the hydration boundary

The progress of hydration is illustrated by following the changes in the degrees of saturation calculated (global, micro and macro) in Figure 5.3-5 for the same points considered above. The graphs show that the column reaches saturation after approximately 200 days. During the test, the degree of macro saturation is always lower than the degree of micro saturation because its initial value is lower, especially in the pellet zone.

a)

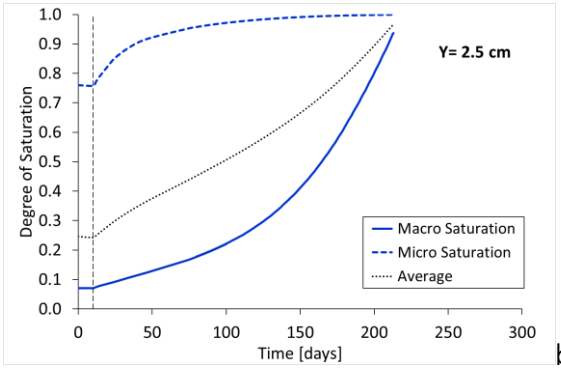

b)

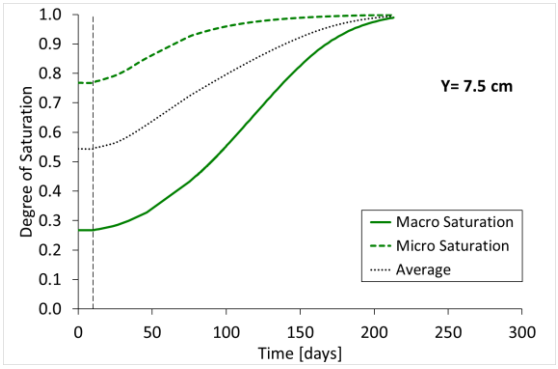

c)

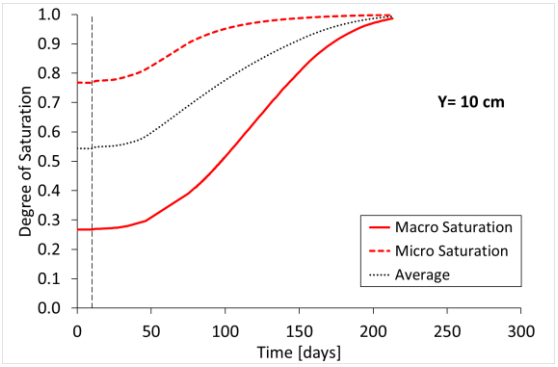

Figure 5.3-5 Calculated evolution of the degrees of micro, macro and global saturation. MGR22 test. a) centre of the pellet zone (y=2.5cm), b) centre of the block (y=7.5cm), c) top of the column (y=10cm)

The most significant result regarding the homogenization process is shown in Figure 5.3-6, which shows the dry density distribution along the column at the end of the test. It can be seen that a high degree of homogeneity has been achieved, especially if the initial large difference in densities (represented by the green vertical lines) is considered. It is important to note that the numerical simulation predicts a result very close to that observed, indicating that the formulation used is adequate to represent the homogenization process, at least in this case. As the material is saturated at the end of the test, the moisture distribution follows the same pattern as the dry densities.

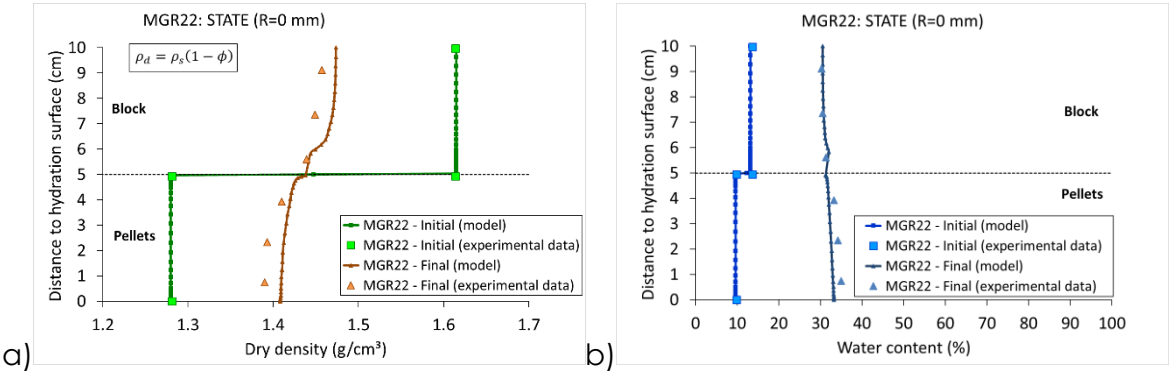

Figure 5.3-6 Comparison of the experimental observations with the results of the analysis. MGR22 test. a) Final distribution of dry density (green vertical lines correspond to the initial conditions, b) final distribution of water content (blue vertical lines correspond to the initial conditions)

Since MIP results are available for different specimens taken at the end of the test, it is interesting to compare the experimental observations with the results of the analysis of the double structure model. It can be observed that micro void ratio has increased both in the block and in the pellets due to the hydration of the clay minerals (Figure 5.3-7a). In contrast, the changes in macro void ratio (Figure 5.3-7b) differ in the two zones of the sample. In the block zone, there is an increase in macro void ratio because of the highly compacted state of the block. In contrast, in the pellets zone, there is a large reduction in macro void ratio that corresponds to the reduction of the large pores present initially in the pellet material. The remarkable agreement between experimental data and model calculations should be noted.

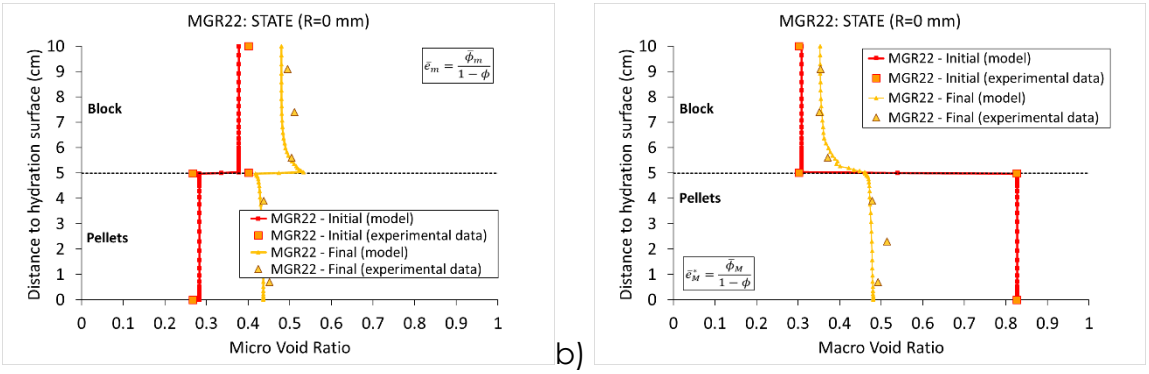

Figure 5.3-7 Comparison of the experimental observations with the results of the analyses. MGR22 test. a) Micro void ratio, b) Macro void ratio

5.3.5 MGR23 results

For the simulation of this test, the constant water pressure of 15 kPa has been applied to the lower face of the sample. To avoid numerical convergence problems the water pressure has not been applied instantaneously but in one day.

Figure 5.3-8 shows the evolution of the calculated and observed water inflow. It can be seen that the initial hydration rate is underestimated. Instead, the calculation overestimates the rate of increase of the axial stress. This difference in initial velocities suggests again that the water exchange parameter between structural levels should be lower. The final value of the swelling pressure is overestimated by 17% approximately.

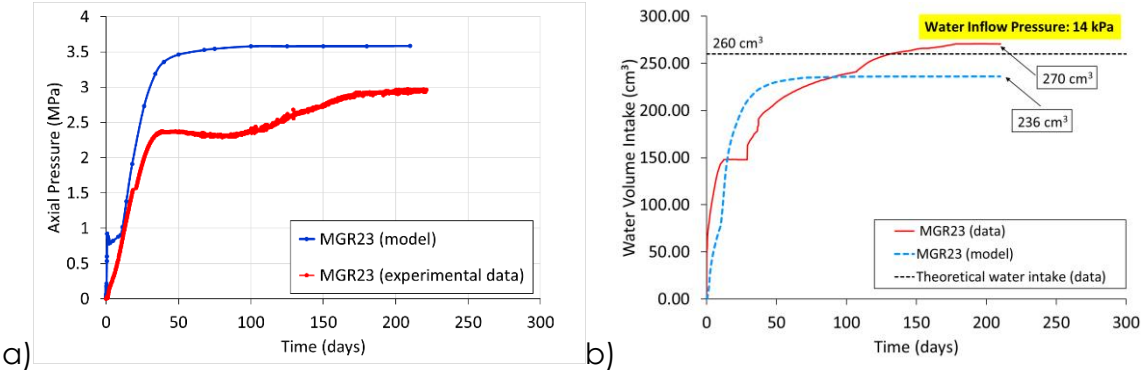

Figure 5.3-8 Comparison of the experimental observations with the results of the model. MGR23 test. a) Axial pressure, b) Water intake

The variation of porosity with time for the 3 selected points (Figure 5.3-9a) shows a final degree of homogenization similar to that of test MGR22 test despite its different hydration conditions. In this case, however, it appears that homogenization occurs earlier in the test. Again, the evolution of porosity is very similar throughout the block section. The pattern of computed micro and macro porosity evolution is quite similar to that of test MGR22 (Figure 5.3-9b, c, d).

As Figure 5.3-10 shows, the entire column is practically globally saturated at the end of the test.

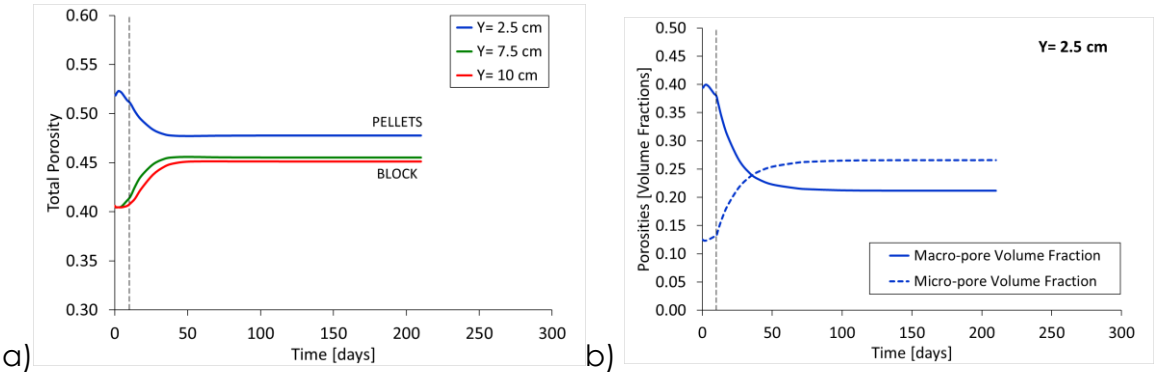

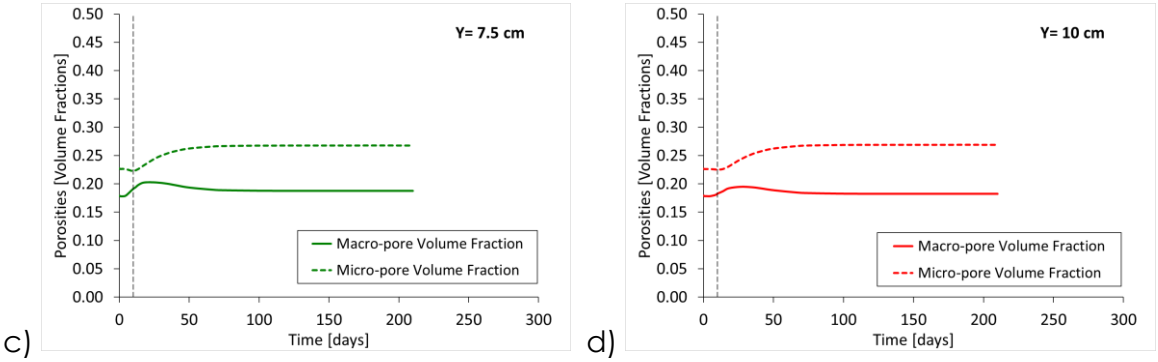

Figure 5.3-9 Test MGR23. a) Calculated evolution of the porosity of the pellets and of the bentonite block. b) Calculated macro and micro porosities (volume fractions) at y=2.5 cm, c) Calculated macro and micro porosities (volume fractions) at y=7.5 cm, d) Calculated macro and micro porosities (volume fractions) at y=10 cm. Coordinate y denotes the distance to the hydration boundary

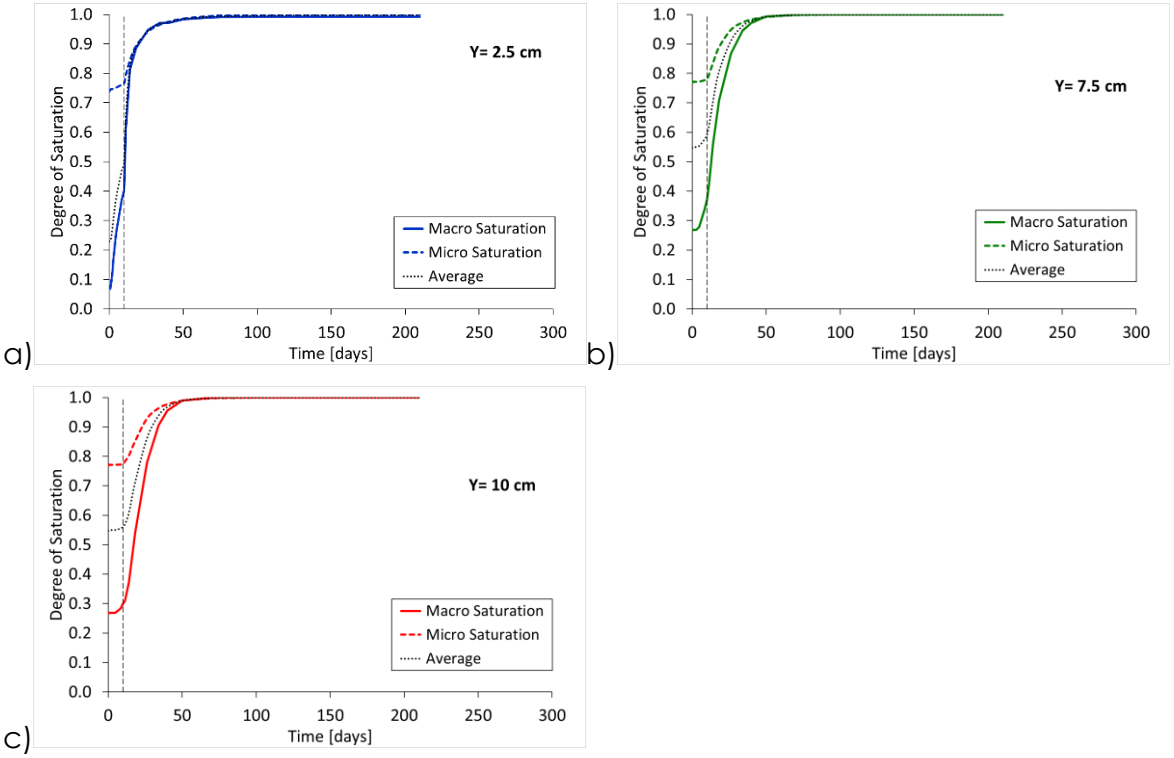

Figure 5.3-10 Calculated evolution of the degrees of micro, macro and global saturation. MGR23 test. a) centre of the pellet zone (y=2.5cm), b) centre of the block (y=7.5cm), c) top of the column (y=10cm), d) degree of saturation profile (initial and final state) and e) suction profile (initial and final state)

The calculated dry density distribution at the end of the test corresponds quite well to that determined experimentally (Figure 5.3-11a). Again, the formulation used can satisfactorily represent the intense homogenization observed in the test. The saturation state of the column at the end of the test implies that the moisture distribution follows

the variation corresponding to the dry density distribution, both experimental and calculated (Figure 5.3-11b).

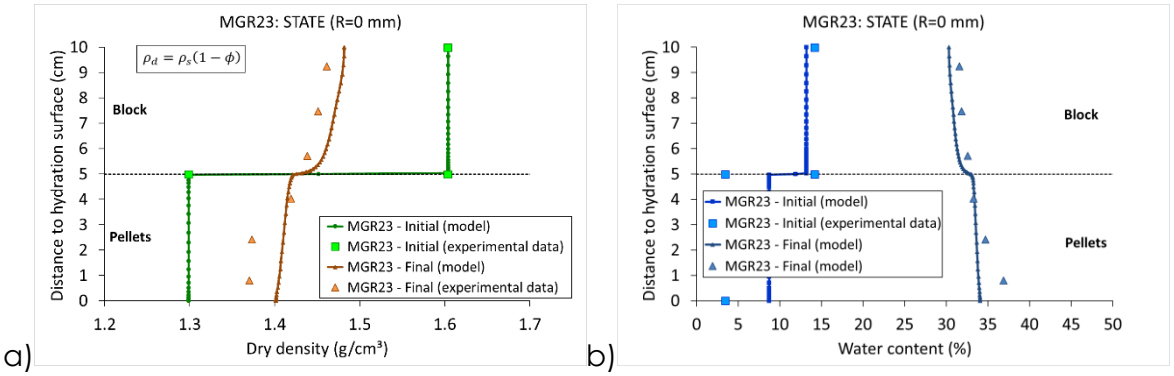

Figure 5.3-11 Comparison of the experimental observations with the results of the model. MGR23 test. a) Final distribution of dry density (green vertical lines correspond to the initial situation, b) final distribution of water content

The comparison between observed and computer macro and micro void ratio (Figure 5.3-12) follows the same pattern as for test MGR 22 and it is also quite satisfactory, except for the specimen quite close to the hydration boundary where the amount of microstructural swelling and of macrostructural contraction are underestimated.

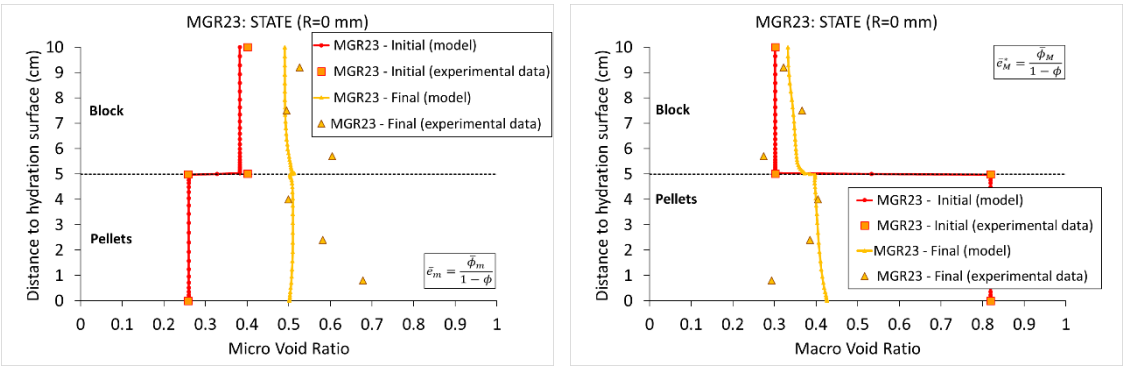

Figure 5.3-12 Comparison of the experimental observations with the results of the analyses. MGR23 test. a) Micro void ratio, b) Macro void ratio

5.3.6 MGR27 results

For the simulation of this test, a constant water pressure of 15 kPa has been applied to the lower face of the sample. Now the hydration is through the bentonite block that occupies then lower part of the specimen. Again, to avoid numerical convergence problems the water pressure has not been applied instantaneously but over one day. Keeping with the spirit of a predictive exercise, the input parameters used in the analysis of this test are exactly the same ones as for tests MGR22 and MR23.

Figure 5.3-13 shows the evolution of the calculated and observed water inflow. It can be seen that the transient behaviour is quite well matched although there is some overestimation of the initial rate of hydration. This difference in initial velocities suggests again that the water exchange parameter between structural levels should be lower. It is also noticeable that the swelling pressure is grossly overpredicted. As a matter of fact, the recoded value of swelling pressure is quite low considering the overall dry density of the sample at the end of the test. This suggests that such a low value is affected by the effects of lateral friction. Therefore, the difference between observed and computed swelling pressure is likely due to the fact that friction was not incorporated in the analysis

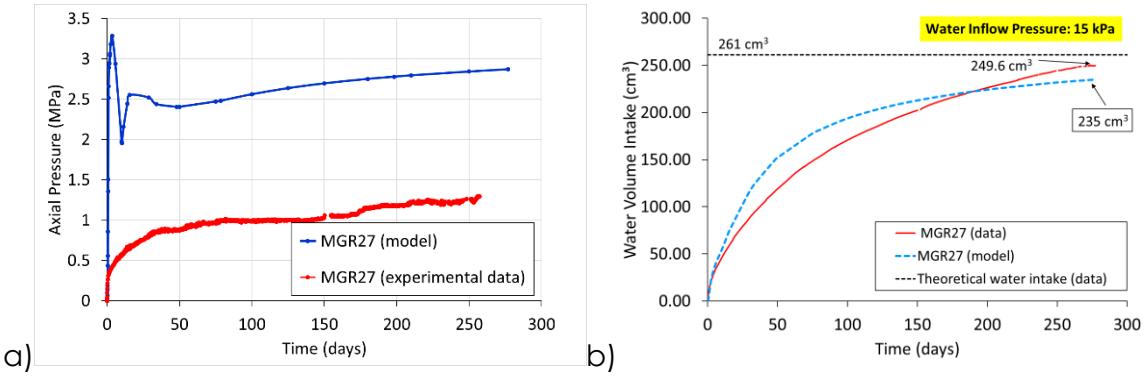

Figure 5.3-13 Comparison of the experimental observations with the results of the model. MGR27 test. a) Axial pressure, b) Water intake

Again, the progress of homogenization can be followed by drawing the evolution of global porosity (Figure 5.3-14a). Despite the location of pellets and block being exchanged, the porosity evolution is very similar to that of the previous tests, the difference in total porosity has reduced very significantly at the end of the test. Also, the pattern of local evolution of micro and macro porosities is also similar to that found in the analyses of the other tests (Figure 5.3-14b, c, d).

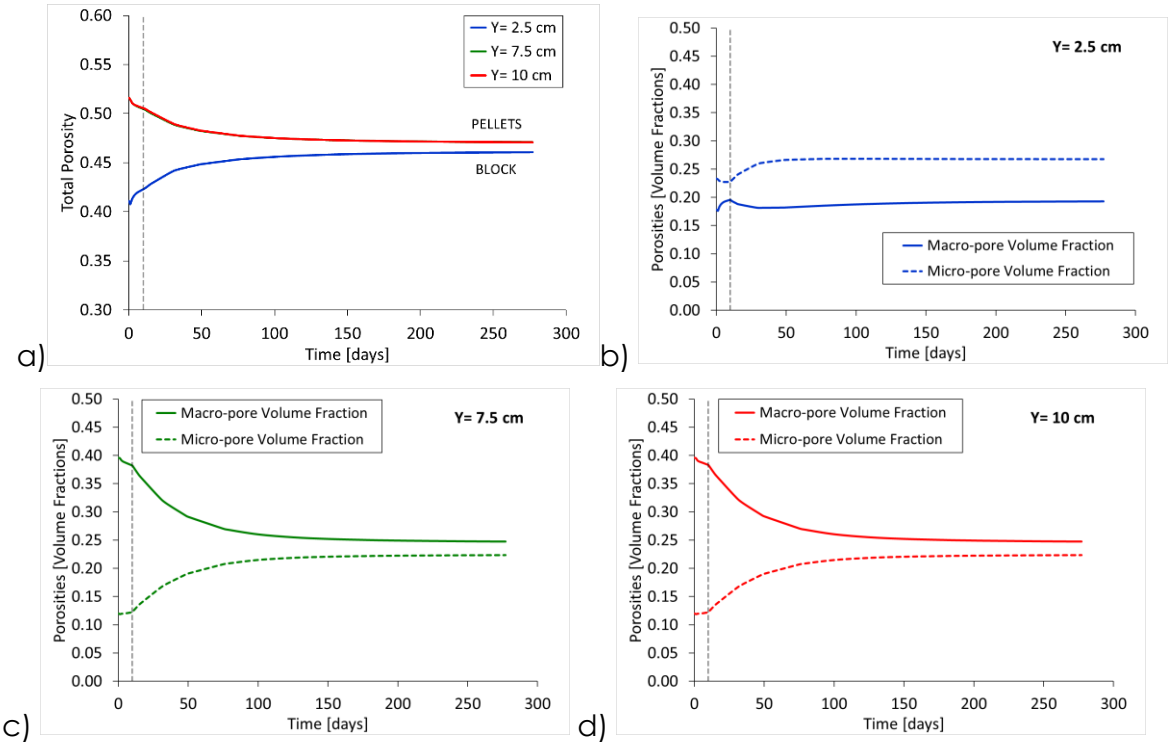

Figure 5.3-14 Test MGR27. a) Calculated evolution of the porosity of the pellets and of the bentonite block. b) Calculated macro and micro porosities (volume fractions) at y=2.5 cm, c) Calculated macro and micro porosities (volume fractions) at y=7.5 cm, d) Calculated macro and micro porosities (volume fractions) at y=10 cm. Coordinate y denotes the distance to the hydration boundary

The progress of hydration is illustrated again in Figure 5.3-15 by plotting the changes in the calculated degrees of saturation (global, micro and macro) the same points considered before. It can be observed that the macrostructure of the pellet zone still shows a certain unsaturation because, in its retention curve, a small suction corresponds to a not completely saturated state. This is an unintended consequence of not considering the effect of pore size changes in the retention curve. In any case the whole sample is quite close to saturation at the end of the test.

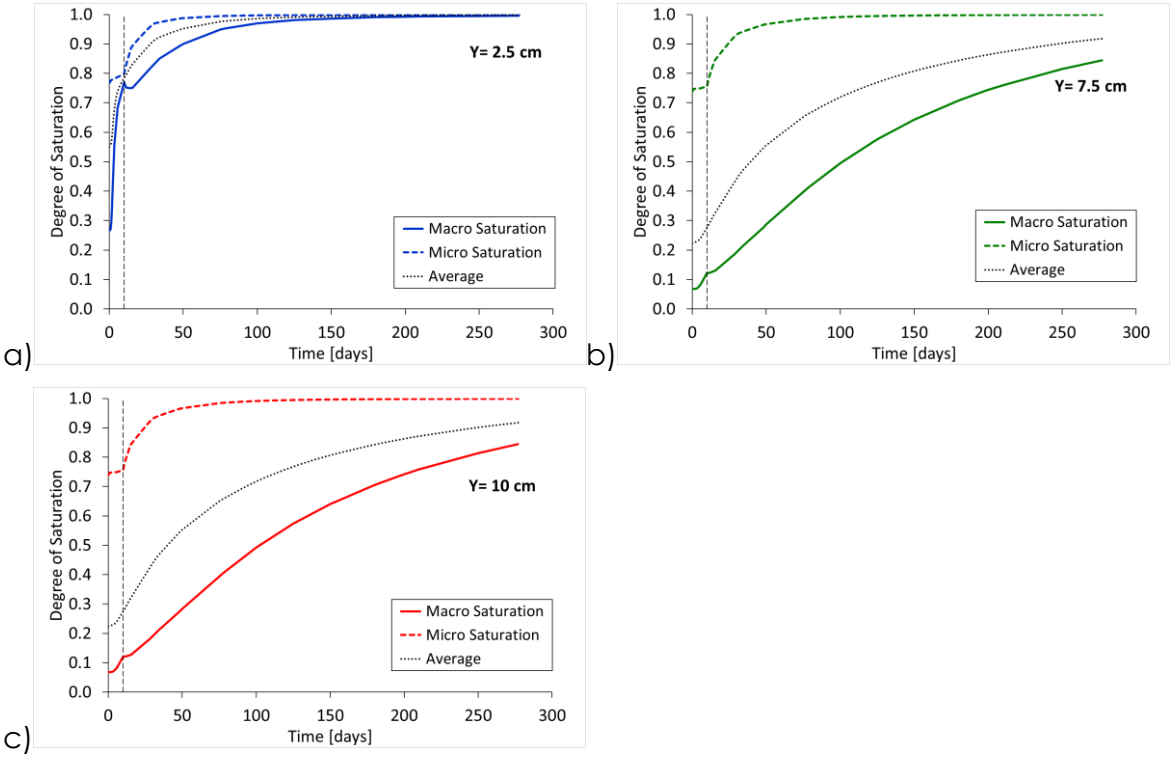

Figure 5.3-15 Calculated evolution of the degrees of micro, macro and global saturation. MGR27 test. a) centre of the pellet zone (y=2.5cm), b) centre of the block (y=7.5cm), c) top of the column (y=10cm), d) degree of saturation profile (initial and final state)

The calculated dry density distribution at the end of the test corresponds again well with that determined experimentally (Figure 5.3-16a). This is particularly satisfying given the predictive nature of the analysis. The saturated state of the column at the end of the test implies that the moisture distribution follows the variation corresponding to the dry density distribution, both experimental and calculated (Figure 5.3-16b)

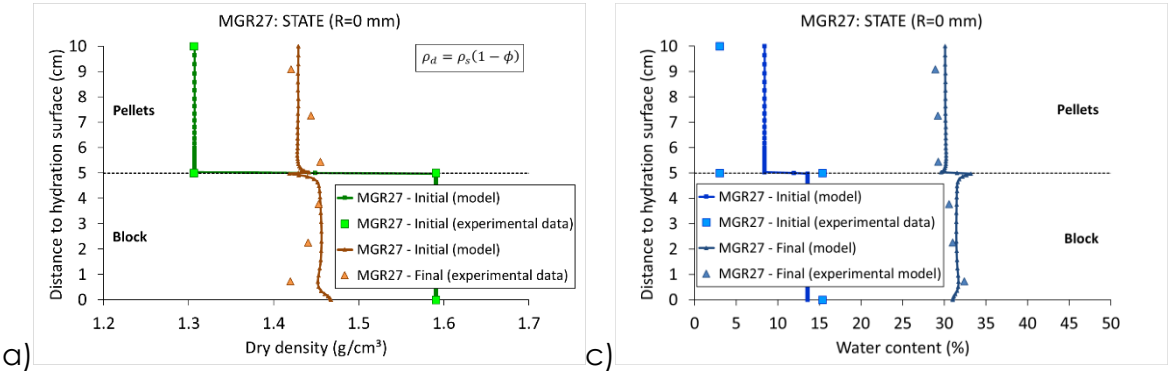

Figure 5.3-16 Comparison of the experimental observations with the results of the model. MGR27 test. a) Final distribution of dry density (green vertical lines correspond to the initial situation, b) final distribution of water content

The observed and computed micro and macro void ratios at the end of the test are shown in Figure 5.3-17. Both micro and macro void ratio changes in the compacted block are quite well reproduced by the analyses but the void ratio changes in the pellets section follow the correct trend but are underestimated.

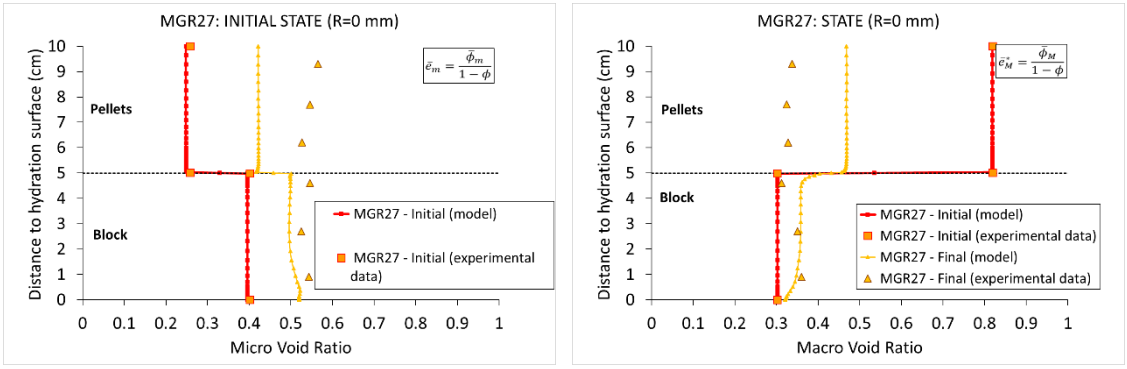

Figure 5.3-17 Comparison of the experimental observations with the results of the analyses. MGR27 test. a) Micro void ratio, b) Macro void ratio

5.3.7 Discussion

From the point of view of the Beacon main objective, a quite large degree of axial homogenization between pellets and blocks has been observed in all three tests under examination in spite of starting from very different initial dry densities. Importantly, the constitutive model is capable to capture very satisfactorily the final state of the sample in terms of dry density in all cases. The final saturated condition of the specimen is also reproduced by the analyses and the final value of swelling stress is reasonably well predicted except for test MGR27 because lateral friction has not been represented in the modelling.

In contrast, the observed transient behaviour is not so well matched by the calculations. Generally, the initial development of axial pressure is overestimated in the modelling suggesting that an analysis with a lower leakage parameter would

results in a better agreement. In any case, the general pattern of variation of axial pressure and water intake is realistically captured.

The adoption of a double structure model allows the examination of the hydration process with a broader perspective. Fortunately, al the specimens underwent MIP testing at the start of the experiments providing the necessary information on the partition of total porosity between micro and macro. The analyses yield predictions of the variations of degree of saturation and porosity at a micro, macro and overall scale. The results obtained are quite reasonable and in agreement with expected behaviour. More meaningfully, the MIP determinations made at the end of the tests provide data for comparison with the results of the analyses. It has been shown that, with few exceptions, observations and predictions are quite close.

In conclusion, the formulation and constitutive model have been proved very capable of simulating the large degree of axial homogenization achieved in these hydration tests. Of course, this does not prove that the same success would be obtained under different conditions but it is, on its own terms, a very encouraging result. The use of a double structure model provides interesting insights on the evolution of the test at a microstructural level. It I very significant that the partition between micro and macro porosities observed in MIP determinations at the end of the tests is very consistent with the model predictions.

6 Main lessons learned during the project in WP5

6.1 UPC

6.1.1 Model inputs

A characteristic feature of the UPC modelling has been the development (in the framework of generalized elasto-plasticity) and use of a double structure (or double porosity) constitutive model to represent the thermo-hydro-mechanical behaviour of bentonite materials. With this model, it is possible to obtain insights on the microstructural evolution of the material and, potentially, to achieve modelling more closely related to the physical reality. Basing modelling on sound physical principles is a good strategy if predictions for very long periods are required.

Adoption of a double structure constitutive model, however, implies an increase of complexity and a larger number of parameters that, even if they have a clear physical meaning, may be difficult to determine. Examples of parameters with a higher degree of uncertainty are: the partition between micro and macro porosity, the value of the leakage parameter controlling the water exchange between structural levels, the functions defining the micro-macro interactions and the retention curves for micro and macro structures.

So, for a sound application of the double structure constitutive model, it is necessary to have information on the distribution of pore sizes in the material to be modelled. This can be more readily achieved by performing MIP tests. Their use in experimental

programmes should be generalized both in the laboratory and in the field. This information leaves still unanswered the question of what criterion should be used to make the partition between micro and macro porosity. Generally, the distinction is clear cut in the initial state of compacted blocks or bentonite pellets but becomes more blurred as saturation progresses, as demonstrated in the Step 3 task. More research and calibration are required regarding this issue.

A reasonable estimate of the interaction functions can be derived from performing swelling tests under a range of applied stresses followed by compression loading whereas the leakage parameter would require the performance of hydration tests (preferably under isochoric conditions) using different values of inflow rates. Finally, retention curves for micro and macro structures can be derived from standard retention curve determinations performed on samples of a range of densities.

In summary, it is possible to design an experimental programme to determine most of the new parameters implicit in the double structure formulation but it is evident that it requires a significant experimental effort given their complexity and the long times required by the tests envisaged. Thus, a cost/benefit exercise should be undertaken when considering the application of a double structure model to a particular problem in order to adopt the most profitable approach.

The predictions of the transient hydraulic behaviour are generally subject to a higher degree of uncertainty due to the sensitivity of the outcome to small details of the formulation such as hydraulic conductivity, relative permeability and retention curves. The double structure model takes into account the variation of fabric during hydration by making hydraulic conductivity dependent on the value of the macro porosity. This is a rational assumption since advective flow takes place in the macropores. However, this is still insufficient to model accurately the hydraulic regime when there are fabric changes because hydraulic conductivity depends not only on the volume of the macropores but, even more critically, on the size of the pores, a variable that should be included in the model. Fortunately, pore size is an information that MIP tests provide and can be used.

From a wider perspective, it is apparent that, while compacted bentonite is quite well characterized over a wide range of conditions, information on pellets-based materials is scarcer, especially considering that a wider range of materials exist. There is a tendency to refer simply as "pellets" materials that have very different grading curves Thus, the experimental characterization of the (T)HM behaviour of different pellets-based materials should be undertaken (e.g. single-size pellets, well graded pellets (Fuller's curve), mixtures of pellets and powder) to identify the basic differences of behaviour between them. Naturally, priority should be given to materials being considered for design and/or testing.

It also noticeable that there are two bentonites that have been intensely studied and characterized: MX-80 and Febex. Fortunately, they have quite different cation content thus providing a range of conditions. However, other bentonites could be examined suing a few key reference tests for comparison with what have become standard bentonites.

6.1.2 Progress made during the project

In the initial stages of the project, a number of significant modifications were introduced to the existing double structure constitutive model formulation. The most salient ones are: a more consistent definition of porosity and volume fractions, the microstructure could be unsaturated, it is not assumed that there is hydraulic equilibrium between microstructure and macrostructure. The transfer of liquid (or, sometimes, gas) is governed by a linear law between flow and micro/macro potential difference at a rate controlled by a newly introduced leakage parameter. Subsequent developments have included the clarification of the physical meaning of the interaction functions via DEM simulations and the examination of the relationship between the micro and macro elastic components that lead to a direct relationship between the two sets of elastic parameters.

Model developments affected also the hydraulic component of the formulation. Variations of permeability depend only on the macro porosity, a more realistic assumption that, in addition, allows to examine the effect of evolving microstructure. This is consistent with the assumption introduced that advective flow tales place in the macrostructure. The exchange of water (or gas) between micro and macro levels occurs at a local level only; this has the added advantage that the potential (or suction) at micro level becomes a local variable, thus reducing the number of global degrees of freedom. Also, two separate retention curves are defined for each structural level, as the microstructure may now be unsaturated. Finally, there has been continuous work on the model implementation in the computer code (that it is still ongoing) to improve the convergence performance of the calculations.

UPC has contributed to the four steps around which WP5 is structured. All the analyses have been performed using the computed code CODE_BRIGHT. Step 1 includes a series of deceptively simple laboratory experiments structured in three different sets of tests: bentonite swelling into a void performed by Clay Technology (1a), a constant-volume swelling test on pellets mixture carried out by CEA (1b) and the hydration of a specimen composed by pellets poured on top of a bentonite block, performed by POSIVA (1c). The performance of the model was generally highly satisfactory not only in terms of the final state of the sample but also regarding its transient evolution. The main exception is the axial pressure of case 1c; as friction was not included in the analysis, the different axial pressures measured in the test at both ends of the sample, could not be reproduced.

Step 2 refers to large scale tests; UPC selected the EB experiment for analysis. The EB test involves the artificial hydration of an engineered barriers that include bentonite blocks and granular bentonite (pellets). The practically complete homogenization between blocks and pellets is successfully reproduced by the analysis. There are more differences between observations and model results regarding the transient hydration period. However, it should be pointed out that the degree of control of the process of artificial hydration was limited and the level of instrumentation in the barrier was rather

sparse. A sensitivity analysis was performed to check on the effects of two of the most uncertain components of the formulation: retention curve and interaction functions.

Step 3 is based on a series of isochoric oedometer hydration tests performed by CIEMAT on samples constituted by bentonite pellets placed on top of a compacted bentonite blocks. Different hydration conditions are applied. Three tests are selected for the step, two of them intended for calibration and the third one for blind prediction. The UPC work in this step was delayed because of the Covid-19 pandemic. It coincided with a change of personnel and the necessary training of new researchers was hindered by lockdown restrictions. For this reason, the UPC results of this step were only partially reported in Deliverable 5.6; the analyses of this step have now been completed and are reported in this Deliverable 5.7. The spirit of blind prediction has been kept by using for test MGR27 the same parameters as for the two calibration tests without any change. In all cases, there has been a quite large degree of axial homogenization between pellets and blocks that has been well captured by the analyses. The type of evolution and final value of the swelling pressure is also well reproduced by the model but there are significant departures concerning the time evolution of hydration and pressure development during the transient period. Also, the non-consideration of lateral friction prevents a good prediction of the swelling pressure value in the MGR27 test. The development of interface formulations for friction modelling is under way, based on thin finite elements, but they are not fully implemented yet. Micro and macro porosity results from the double structure model appear largely consistent with observations.

In the latter part of the project, the main activity has been related to the integration of thermal effects into the double structure constitutive law in a rigorous manner that has required the modification of a large proportion of the model formulation. The work is still ongoing but a first version incorporating the thermal expansion of constituents and of the overall medium is available. It has been applied to the non-isothermal assessment case proposed by Nagra that involves an engineered barrier made up of bentonite blocks and pellets subjected to heating and natural hydration from the rock. Because the development of the formulation is still not fully complete and requires considerable optimization in its numerical implementation, there are a number of convergence difficulties and the requested final time of the analysis has not been yet achieved at the time of writing this contribution.

In summary, the double structure constitutive law incorporating the modifications introduced at the start and during the project has proved capable of providing a good modelling performance especially regarding the bentonite homogenization processes, the central objective of the project. The thermal version is in a preliminary stage and requires further work.

At this point, it is possible to identify a number of further developments to improve the existing double structure model:

- review the adoption of Bishop effective stress for the microstructural behaviour in order to make more independent the effects of suction and stress changes

- development of a more constrained manner to determine and calibrate the interaction functions is required
- review and modification of the variation of permeability with fabric changes
- incorporation of irreversible thermal effects
- friction has proved to be significant, at least in some laboratory tests. It should be introduced in the formulation (this development is already ongoing)
- optimization of the integration algorithm especially for the non-isothermal formulation

Because of the number of benchmark cases and the need to submit results at the scheduled times, there has been little time and resources that could be used for performing sensitivity analyses. As a matter of fact, the only systematic sensitivity analyses carried out have been in the analysis of the EB test (step 2). Two of the most uncertain components of the model were selected for this exercise: interaction function and retention curves for the compacted blocks. The case involving the interaction functions is presented as an example here.

Figure 6.1-1 shows the two sets of alternative interaction function together with the functions used in the Base Case. One of the alternatives (Var 02) correspond to the case of interaction functions equal to zero, i.e. there is no interaction between the micro and macro structural levels. It can be observed (Figure 6.1-2) that the Var 02 case does not agree with experimental observations and the analysis underestimates severely the degree of homogenization observed in the field test. It is apparent that the interaction between micro and macro levels is essential to achieve a good representation of the real system and its homogenization. This is an illustrative example of the role of sensitivity analyses in enhancing understanding.

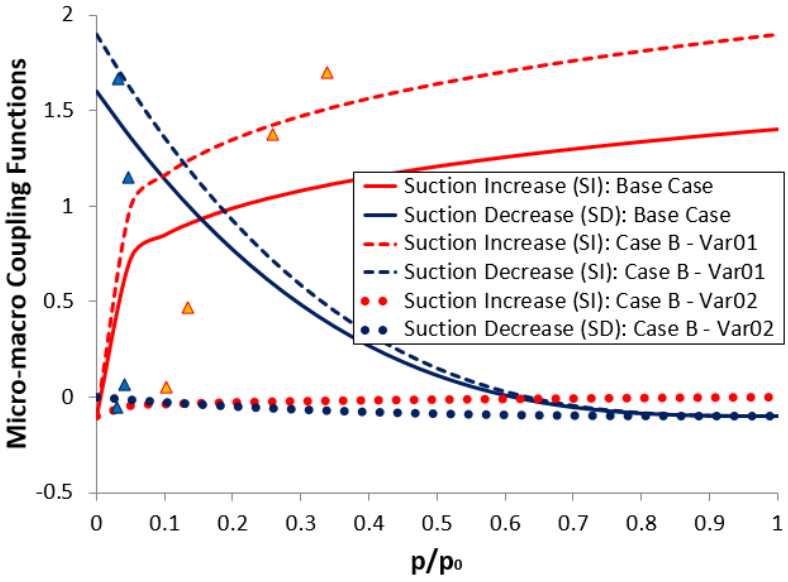

Figure 6.1-1 Alternative and Base Case micro-macro interaction functions for the compacted bentonite blocks

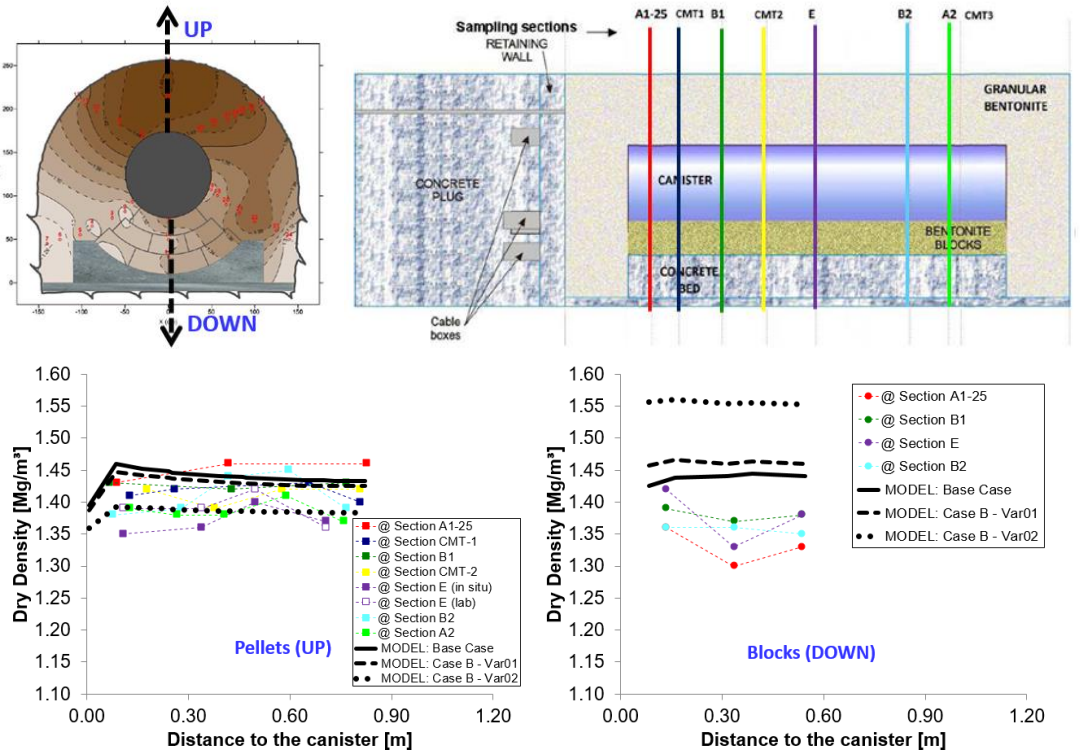

Figure 6.1-2 Radial profiles of dry density for points located in the upper section of the barrier (left) and inside the compacted blocks (right): Base Case vs. Case B with alternative interaction functions. Symbols correspond to observations.

6.1.3 Lessons and prospective activities

The overall impression of the activities performed within WP5 is that the current version of the formulation and constitutive model are able to simulate satisfactory the set of isothermal benchmarks that have been proposed. The final state of the specimens is correctly reproduced including the high degree of homogenization that has been observed in both laboratory samples and engineered barriers (EB test) that started form a highly heterogenous situation (presence of voids, combination of blocks and pellets). Final values of swelling pressure are also adequately predicted except in the cases where friction is dominant.

The adoption of a double structure model that distinguishes between microstructure and macrostructure allows a modelling closer to the physical reality and provides enlightening insights on the progress of the saturation of the bentonite and of the associated mechanical effects. Comparison with MIP data has confirmed that the model does follow the observed fabric change trends correctly.

The success in reproducing the transient behaviour of the bentonite is more variable, good agreement with experimental observations in some cases are in contrast with other instances that exhibit significant differences between predictions and test results. Since transient behaviour is largely controlled by hydraulic phenomena, it may be

simply the result of the high sensitivity of hydraulic processes to small variations of hydraulic conductivity, relative permeability and retention curves. This implies that perhaps more efforts should be made to determine precisely those model components. But it may also be necessary to accept that transient behaviour will be always be subject to a higher degree of uncertainty. Sensitivity analysis may be the best way to bound those uncertainties.

In the latter part of the project, the double structure model has been rigorously updated to incorporate thermal effects. This work still requires further development and optimization.

Considering the work in WP5 overall, it can be stated the formulation and constitutive model are both robust and operative. Against those advantages, it is necessary to weigh, however, the added complexity and cost of using a double structure model instead of a single porosity one. In this respect, the work performed and reported in the Beacon project provides relevant information for reaching a rational decision when designing the numerical analysis of a new problem.

The spirit of the Beacon proposal was to offer a wide range of benchmarks for analysis. This allows testing the capabilities of the models over a wide range of situations thus providing a good overview of the scope of applicability of the models. On the other hand, this limits the possibilities of spending more time and resources in performing sensitivity analyses and other activities on specific cases in order to enhance the understanding of the processes involved and to identify the relationship between model features and parameters with the outcome of the analyses. In this context, it has to be accepted that there are no firm conclusions regarding how homogenization relates to the features of the constitutive model and to the specific features of each particular case. Evidently, throughout the development of the project a better understanding of model capabilities and consequences has accrued but they have not been organised in a systematic and verifiable manner.

A similar conclusion can be drawn concerning the predictive capacity of the model that has not been explored in depth during the project. There has been a predictive exercise in WP5 that has met with a fair degree of success but the prediction case was quite similar to the tests used for calibration. The predictive power for other cases and across of a wider span of conditions remains basically unproved.

Consequently, future work on the modelling of the THM behaviour of bentonite materials should focus on the issues of understanding and assessment of predictive power. The number of cases to be analysed should be fewer and carefully selected to cover the areas of interest of end users. Prediction exercises should involve blind predictions organised in a systematic and structured manner allowing enough time to perform a number of successive iterations if necessary. Prediction exercises of cases quite different from the calibration tests should be envisaged. Well-designed laboratory tests should have priority over complex field experiments.

6.2 ICL

6.2.1 Model inputs

The hydro-mecahnical modelling tools summarised in Section 2.5 were used for all simulations performed as part of Beacon's WP3 and WP5. These have included a range of experiments, from laboratory to large scale in-situ tests, and two types of bentonite, MX80 and Febex.

Both mechanical (ICDSM) and hydraulic (SWR and permeability) models were calibrated from experimental evidence found in the literature for the two types of bentonite. Two derived sets of model parameters, one each for MX80 and Febex materials, were used throughout the project in their respective analyses. Adjustments were made mainly to micro-structural parameters and SWR curves in the relevant simulations, to reflect the changes in the initial dry density, ρ_d.

6.2.2 Progress made during the project

Simulations of laboratory tests

With respect to simulated laboratory tests, which involved only hydro-mechanical (HM) coupling and either confined or free swelling, the constitutive model ICDSM was shown capable of reproducing reasonably well the maximum values of swelling pressures (Tests 1a, 1b; Task 3.3). The model is isotropic in its formulation, hence predicting similar magnitudes of axial and radial swelling pressures measured in constant volume experiments, while the measurements showed these values to be different. It was difficult to assess whether measured data were a result of some inherent anisotropy in specimens of compacted bentonite (which is reasonable to expect to exist), as there also existed some uncertainty of the initial stresses in specimens before the start of their hydration. The simulations also under-estimated the initial rate of the swelling pressure rise (both axial and radial), which could be attributed to possible inadequate variation of permeability at the start of the experiment.

The post-mortem analyses of bentonite states at the end of laboratory tests showed that the model was capable of reproducing the correct trends and close magnitudes of the evolved void ratio / water content / dry density profiles interpreted experimentally.

Laboratory hydration tests under constant volume with mixed bentonite samples (half compacted block, half pellets, Test 1c, Task 5.3) showed fairly homogenised profiles of the evolved void ratio / water content / dry density at the end of experiments. The model was able to simulate the correct magnitudes of changes in these parameters (between the initial values and those at the end of the test) in both parts of the specimen (block and pellets), but still showing a distinction (jump-change) between the two parts. This was again attributed to inadequate permeability modelling especially at the start of the experiment.

Large scale in-situ tests

The large scale in-situ tests simulated as part of Task 5.2 (FEBEX and CRT) involved thermal coupling in addition to hydro-mechanical coupling. The constitutive model is not formulated in terms of temperature, but appropriate parameters for thermal conductivity and coefficients of thermal expansion were applied to bentonite buffer and the surrounding host rock, as well as appropriate temperature / thermal flux boundary conditions at the canister / buffer interface. In both cases the buffer was constructed from compacted bentonite blocks involving Febex bentonite in the Febex experiment and MX80 bentonite in the CRT experiment. The model parameters in both cases were the same as calibrated for the simulations of laboratory tests, the objective being to examine whether such model calibration can be extended for application to a large scale boundary value problem.

The numerical model was shown to reproduce very well the evolution of the temperature field in the buffer. The field tests involved essentially confined hydration (as buffer is entrapped between the canister and the host rock). The model reproduced very well the mobilised maximum swelling pressures measured at different cross-sections and in different rings of the buffer. The important part of comparison was also the interpretation of field measurements with respect to their operational time of the experiment, in particular in the case of the Febex test which spanned 18 years.

What was not well reproduced in simulations was the rate of wetting in the buffer rings interfacing the host rock, as near 100% relative humidity (RH) in those was measured within the first three years of the Febex experiment, whereas this was around nine years in the simulation. The agreement between the numerical results and measurements of RH evolution was improving for inner rings, given the scatter in measurements. Similar to laboratory experiments discussed above, this shortcoming of the simulation was attributed to inadequate permeability modelling at the start of the experiment.

The post-mortem examination of void ratio / water content / dry density radially across the buffer, after the Febex experiment was dismantled, showed very satisfactory agreement with measurements taken in different cross-sections of the buffer.

6.2.3 Lesson and prospective activities

The modelling approach at ICL was to firstly apply the Barcelona Basic single-structure type of a constitutive model (BBM) in the modelling of bentonite, which showed that such a model was not capable of reproducing the measured high swelling pressures. The adopted modelling framework was therefore changed to a double-structure extension of the BBM, introducing two distinct levels of micro and macro porosity in the form of an IC Double Structure Model (ICDSM).

For each of the bentonite types used in the actual experiments, the parameters for ICDSM were derived from model calibration on appropriate laboratory experiments found in literature, different from those simulated for Beacon. It should be noted that some parameters could not be derived directly from any experiments, but were instead derived from simulations of the experiments used in the calibration process.

The objective of this approach was to examine the predictive capabilities of such calibration, by employing independently derived model parameters in the simulations of experiments selected for various stages of the Beacon project. Additionally, appropriate initial stresses / void ratio / dry density in the bentonite material were initialised at the start of each simulation.

Analysing the results from simulations at all scales (laboratory and field) and recognising some of the modelling shortcomings, it was felt that the applied modelling approach was shown broadly capable of reproducing the observed patterns of bentonite's THM response and reasonable agreements between simulations and measurements. The principal challenge has been the experimental characterisation of permeability, both for compacted bentonite blocks and for different pellet assemblies, as well as adequate modelling of permeability changes during the process of bentonite hydration.

6.3 VTT/UCLM

6.3.1 Model inputs

The mechanical clay models should be based on direct measurements and not on fitting to more complicated experiments (such as the simulated experiments in Beacon) or on experiments which do not produce complete data on the mechanical behaviour (for example oedometric conditions or simple compression).

The evolution of the wetting profiles (water content-distance plots at various times) are poorly captured by the recent models. Better consistence between the models and experiments would likely require revisiting the model concepts.

In general, there is rather need for well instrumented simple experiments that would provide the model parameters as directly as possible than complicated experiments (with only few measurements), the modelling of which allows too many degrees of freedom in model parametrisation.

There is not too much experimental data or experience in simulating the behaviour of differently processed bentonite fills (pellet, pellet-grain mixtures, compacted granular fills, etc.). Such material should be focused on, if they become key materials in the disposal concepts.

In Beacon, there has been somewhat limited interest in chemical aspects of bentonite, even though chemistry (coupled to other phenomena) plays a critical role in the material understanding and performance.

To perform precise sensitivity analysis of bentonite behaviour, there should be statistical information on the model parameters, that is, not only one value without knowledge on the error.

6.3.2 Progress made during the project

During the time-line of the project, the main improvements to the existing models have been

- introduction of third level of porosity (between the pellet, or similar larger granule) to the previous double porosity models
- new model implementation and improved robustness of the implementation
- methodology and tools to perform sensitivity analysis.

Only part of the work has been carried out within Beacon (mainly sensitivity analysis related matters and performing various simulations with the model in WP5).

The progressing complexity in WP5.1 test cases from blocks to pellets and their mixtures resulted in realisation that a third porosity level is needed for 1) the model concept to better match the experiments and 2) double porosity model parameters to remain physically meaningful.

The SKB tunnel backfill assessment case demonstrated that it is difficult to evaluate the effect of different phenomena and parameters on the bentonite mechanical evolution without carrying out a statistically sound sensitivity analysis. The performed sensitivity analysis helped to identify the most important parameters for the density evolution of the assessment case and also direct the possible future work on the topic. The developed sensitivity analysis work process and tools would allow future use of such methods for more elaborated analysis and for other applications (for example, different simulations cases, but also design and analysis of experiments).

6.3.3 Lesson and prospective activities

- Use of sensitivity analysis in modelling gives rational means to identify the most important parameters with respect to specific applications
    - An elaborated sensitivity analysis would, however, require better statistical information on the varied input parameters, since currently the parameter ranges have to be guessed in many occasions.
    - The sensitivity analysis results could help to direct experiments to most effective directions.
- Use of sensitivity analysis and Design of Experiments methods could also help to plan experiments that cover many conditions.
- Many of the basic phenomena seen in the experiments are not captured by the current models. Resolving the issue likely requires simulations of well controlled, well instrumented relatively simple experiments, which allow as little model adjustments as possible (that is, the freedom to play with the model parameters and details should be kept minimal). Such simulation should be focused on with enough time and detailed discussion.

6.4 ULg

6.4.1 Lesson and prospective activities

BBM model performed well, surprisingly well compared to more complex models. However, some limitations invited to build a new constitutive model (that still need to be used and valorized!).

Double porosity models help understanding bentonite transient behavior. However, models with 2 porosity scale and experimental PSD curves are not easy to compare. Double porosity, mechanical aspects and water transfer aspects need to be considered. But how to demonstrate their added value?

Small heterogeneities, density varying of 0.05 to 0.10: how do the model parameters vary for such small density changes? Not clear presently! Constitutive models parameters: not easy to have data sets for various densities, including the initial density heterogeneity (in place before hydration). Need to improve this information, to elaborate.

Deviatoric stress paths are not enough explored experimentally: friction angle of bentonite? Depending on the saturation / suction or constant? Value? Also important for the experimental results analysis: deviatoric behavior will drive the radial stress development, which is a significant part of the friction mobilization.

Friction on interfaces has been modelled in some benchmark, and has proved to give improvement of results. In the French concept, seal friction on liner or on clay host rock is an important aspect of the mechanical answer. But what is the constitutive behavior or friction with variable suction? We lack of experimental data

Swelling at low level of suction / of stress: the BBM is not well designed for such state. Moreover, there is a lack of experimental data, which don't help to elaborate an improved model.

Granular bentonite (incl pellets) was modelled successfully with BBM, as well as bentonite block. Existing constitutive models may be used for such "new" material.

Permeability is not enough documented. Especially permeability of granular bentonite in the dry state (before wetting) is probably very high, while decreasing quickly at the wetting beginning. But this was difficult to quantify.

Moreover, transient behavior is less accurately modeled than final state. Efforts should be paid on transient behavior during a next research program. The MGR tests by Ciemat are of great interest as they provide intermediate results at early time, with a lot of details (experiments stopped at an early time, and post-mortem data available at theses early times).

Numerical simulations are expansive: the need a lot of modeler / engineer time, they are complex, strongly nonlinear and coupled. So not easy to manage! This don't help to do variation, sensitivity analysis, etc., while it would be really interesting.

6.5 BGR

6.5.1 Model inputs

In the last tasks of BEACON which were carried out with the double structure model combined with elasto-plasticity a lot of time was spent in calibrating the material model using parameters based on available literature values. In order to determine the yield stress, stiffness and hardening parameters additional data focusing only on the elasto-plastic material characterization would be beneficial. In the current stage of model development, such experiments provide more insights compared to experiments focusing on the saturation behavior. With such tests the mechanical behavior of bentonite in the absence of swelling could be studied further. If these tests were redone with different states of saturation the double structure model combined with elasto-plasticity could also be validated if the current hydro-mechanical model suitably represents the process of bentonite hydration.

6.5.2 Progress made during the project

When BEACON was started in 2017 the simulations with the porous media simulator OpenGeoSys5 were restricted to linear elasticity and only weakly (staggered) coupled thermo-hydro-mechanical problems. Furthermore the porosity evolution was not accounted rigorously. Now we switched the simulation environment to OpenGeoSys6 described in Bilke et al. (2019). Here the balance equations are coupled monolithically which allows a more stable solution behavior and better convergence of the non-linear solver. The porosity evolution is computed from mass balance of the solid phase and with the double structure porosity model also experimental data regarding the microstructure can be taken into account. Additionally the double porosity model allows for modelling time shifted swelling behavior as observed in the majority of experiments carried out. The swelling itself is now a process only active on the micro scale, where an orthotropic relationship between saturation and swelling strains was postulated.

Also the coupling of OpenGeoSys6 to the MFront environment after Helfer et al. (2015) ensures a simple introduction of non-linear elasto-plastic constitutive laws.

To illustrate the model improvements the simulation of Task 1a of work package 5 was redone. In Deliverable 5.1.2 this test case was reported. The model consists of a linear elastic hydro-mechanical model and was solved with the simulation environment OpenGeoSys5. Now this task is revised with the double porosity model and a modified Cam-clay constitutive model in OpenGeoSys6. The basic model properties where obtained from the Work Package 3 Test case 3. In Figure 6.5-1 the results of both simulations are shown together with the measured axial stress. The improvements of the model is not just the better match of the absolute axial stress. The porosity evolution gives additional insight into the model. During the first phase of the process the model is constrained to conserve the volume. But in Figure 6.5-1 we can see how the micro porosity increases and the macro pores are reduced due to swelling under conservation of total porosity. The second part of the test consist of removing the volume constraint at the top boundary. Since we assume full saturation at the end of

phase one, there is no additional driving force for further swelling. The only process visible in the simulations is therefore an elastic rebound.

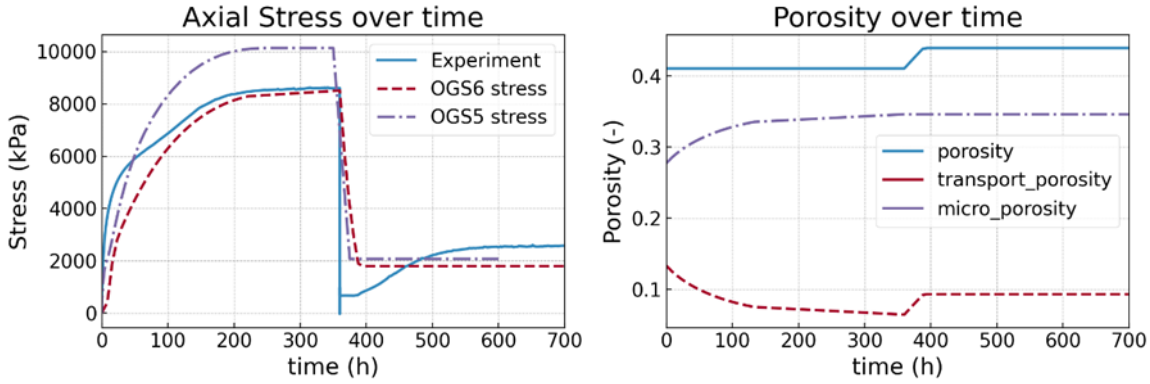

Figure 6.5-1 Comparison of axial stress between OGS5 and OGS6 (left) and simulated porosity evolution (right)

The macro porosity increases where the micro porosity is constant. Since we are not entirely sure what the reason is for measured increase of stress in the second phase - either a further swelling or the release of friction force or a combination of both, we limit our focus to the first phase. This is also the more important case for further assessment cases.

In Task 3.3 the stress path dependency of the model was studied in detail. The path dependency enters the model via the elasto-plastic constitutive equation. At the beginning of the BEACON project this path dependency couldn't be considered.

6.5.3 Lesson and prospective activities

During the BEACON project the mathematical models were extended and refined. With the current model the experiments of the previous BEACON tasks packages should be redone to get a better insight into the model behaviour and to gain confidence in the parameters describing the material behaviour. This process is ongoing and first results are presented in Section 6.5.2. We already identified some shortcomings of the model in Section 3.2.6 and therefore future investigations will be aimed at improving these deficiencies. We can identify three distinct points to improve or assure the quality of the presented results.

First the mathematical model for the underlying thermo-hydro-mechanical process needs additional improvements reflecting the mentioned short comings.

- The current double porosity hydro-mechanical model needs to be extended to a fully coupled thermo-hydro-mechanical process.
- The separation of initial suction in hydraulic potential and mechanical effective suction for effective stress concept in partially saturated states.
- The amount of swelling is not yet related to the dry density of the material. A specimen with low dry density will produce the same swelling stress in the porous

media as a specimen with high dry density but identical initial saturation. This should be revised.
- The yield function of the modified Cam-clay model is not saturation dependent. Different attempts of BEACON partners show promising results and should be investigated in our model.
- Implementation of non-linear pressure dependent elasticity.

As a second point of ongoing investigations a sensitivity analysis with respect to the model parameters is planned. With this the robustness of the solution with respect to its model parameters is studied. The third and the last point is an analysis of the influence of the model assumptions to the solution e.g.: What roles do initial and boundary conditions play and is a 2D plane strain representation a valid assumption?

6.6 ClayTechnology

6.6.1 Model inputs

In this section variables/functions/parameters included in the mechanical constitutive formulation of the Hysteresis Based Material (HBM) model are reviewed. The review is structured around four of the quantities included in the mechanical formulation: the clay potential functions $\tilde{\Psi}_M(e_\mu)$ and $\tilde{\Psi}_\Delta(e_\mu)$, the path dependent variable $\boldsymbol{f}$, the contact area fraction α, and the micro void ratio e_μ. A description of the HBM model is given in D3.3 and will not be repeated here. The micro void ratio is, however, frequently occurring in the expressions below and to get a chance to understand some discussions better its relation to the gravimetric water content $w = \rho_w/\rho_s\, e_\mu$ can be held in mind. First, short descriptions of how the expressions/functions were selected and fitted to data are given. Then, tests which are relevant for the quantity in question are listed and discussed.

The clay potential functions

$$\boldsymbol{\Psi} = \tilde{\Psi}_M(e_\mu)\mathbf{1} + \tilde{\Psi}_\Delta(e_\mu)\boldsymbol{f} \tag{6-1}$$

$$\tilde{\Psi}_\beta(e_\mu) = {\Psi_\beta}^0 \exp\left(c_0^\beta + c_1^\beta e_\mu + c_2^\beta {e_\mu}^2 + c_3^\beta {e_\mu}^3\right) \tag{6-2}$$

The clay potential functions $\tilde{\Psi}_M(e_\mu)$ and $\tilde{\Psi}_\Delta(e_\mu)$ are fitted to experimental data. The data used is the retention for wetting and drying conditions, swelling pressure, and deviatoric stress at failure. Oedometer loading/unloading tests could also be useful here, but data is scarce. The clay potential functions, expressed in terms of micro void ratio, follows an "exponential form" and several different functions have been used to parameterize it. Equation (6-2) shows one example of such a parametrization where

the constants c_0, c_1, c_2 and c_3 are determined from the experimental data and has to be set for the bentonite type being modelled.

Tests related to the clay potential functions:

- Retention for wetting and drying conditions, swelling pressure tests, deviatoric stress at failure (obtained from triaxial tests, uniaxial unconfined compression tests), and loading/unloading oedometer tests.
- The clay potential functions are expressed in terms of the micro void ratio which can have very low values at dry conditions. Data corresponding to these conditions are quite hard to find. Especially so for bentonites other than MX-80.
- Oedometer loading/unloading data is very limited. More data would be beneficial.

The path dependent variable

$$\boldsymbol{f}: d\boldsymbol{f} = \frac{\partial \boldsymbol{f}}{\partial \boldsymbol{\varepsilon}} d\boldsymbol{\varepsilon} \tag{6-3}$$

$$\frac{\partial f_{ij}}{\partial \varepsilon_{kl}} = -K_{\alpha\beta}\left(f_{ij} - {f^{lim}}_{ij}\right)\,\mathrm{sgn}(\dot{\varepsilon}_{kl}) \tag{6-4}$$

$${f_p}^2 + {f_q}^2 = R^2 \tag{6-5}$$

The form of expression (6-4), which defines the evolution of the path dependent variable $\boldsymbol{f}$, was chosen to obtain a path dependent behavior of the clay potential which emulates what is seen for the scanning curves in measured retention and loading/unloading curves in oedometer tests.

Without going into details (which can be found in D3.3), equation (6-5) provides a condition from which ${f^{lim}}_{ij}$, a limiting value of f_{ij}, is obtained. The parameter R sets the "strength" of the condition and the value of R was set from analysing simulations using HBM in COMSOL of laboratory tests and obtaining the sought behaviour.

The modulus $K_{\alpha\beta}$ governs how "fast" $\boldsymbol{f}$ goes towards the limiting value and have two different values, $K_{\alpha\beta} = K_{aa}$ for the compressive/tensile components such as df_{11}, and

$K_{\alpha\beta} = K_{ab}$ for the shear components such as df_{12}. K_{aa} was obtained by fitting the solution of the model against strain-deviator stress evolutions in triaxial tests. K_{ab} was calculated by expressing a given strain state in two different coordinate systems. This resulted in a tensile/compressive representation and a shear representation from which the ratio K_{ab}/K_{aa} could be obtained.

Tests related to the path dependent variable:

- Wetting and drying retention, deviatoric stress at failure (strain-deviator stress evolutions), and oedometer loading/unloading tests.
- Oedometer loading/unloading data is very limited. More data would be beneficial.
- More data where the retention scanning curves are characterized would be beneficial.
    - The shape of the scanning curves and how they relate to the limiting wetting/drying curves are not fully understood.
    - There also seems to be indications of a direction dependency of the scanning curves, e.g. that the behavior is different during wetting as compared to during drying, something that is not currently captured in HBM.

The contact area fraction

$$\alpha = \tilde{\alpha}(e, e_\mu) = \left(\frac{1 + e_\mu}{1 + e}\right)^\gamma \qquad (6\text{-}6)$$

The contact area fraction has been assumed to be related to the ratio between the saturated volume $(1 + e_\mu)$ and the total volume $(1 + e)$. A power law of this volume ratio was adopted for representing the contact area fraction. The value of the exponent γ was obtained by observing that it gave a fairly realistic behavior in the performance calculations reported in D3.1.

Tests related to the contact area fraction:

- The alpha-function could be calibrated/validated by comparing simulations against data from
    - swelling pressure build up,
    - oedometer tests with constant water content
    - swelling/shrinkage tests at constant load
    - uniaxial unconfined compression tests at different water contents

These tests should be carried out for both block, as well as granular and pellets materials

- It would be beneficial to investigate the behavior of α for large ranges in void ratio
- If simulating slots filled with pellets or granular filling, it is likely that $\tilde{\alpha}(e, e_\mu)$ will have to be changed. The tests mentioned above would give indications about what changes to be made.

The micro void ratio

$$e_\mu : de_\mu = \frac{\partial e_\mu}{\partial e} de + \frac{\partial e_\mu}{\partial s} ds \tag{6-7}$$

$$\frac{\partial e_\mu}{\partial e} = \tilde{\alpha}(e, e_\mu) \tag{6-8}$$

$$\left(\frac{\partial e_\mu}{\partial s}\right) = \begin{cases} \dfrac{(e - e_\mu)\tilde{\Psi}_M(e_\mu)}{s} \dfrac{1}{(e - e_\mu)\dfrac{\partial \tilde{\Psi}_M}{\partial e_\mu} - \tilde{\Psi}_M(e_\mu)} & \text{if } \dot{s} < 0 \\ \dfrac{-e_{step}}{\left|s - \tilde{\Psi}_M(e_\mu - e_{step})\right|} & \text{otherwise} \end{cases} \tag{6-9}$$

The differential with respect to void ratio is in the current formulation chosen to be taken as the contact area function. The differential with respect to suction is formulated using $\tilde{\Psi}_M(e_\mu)$ and, for positive suction rates, a parameter e_{step} which sets the shrinkage limit of the material.

Tests related to the micro void ratio:

- e_{step} can be calibrated by comparing simulations against shrinkage tests where the shrinkage limit can be evaluated.
- swelling pressure build up
- oedometer tests with constant water content
- swelling/shrinkage tests at constant load

6.6.2 Progress made during the project

At the start of the project the HBM model was only formulated for very limited conditions. The water mass balance was not solved for, i.e. the hydraulic process (water uptake and transport) could not be simulated. The model had not been written on a format suitable for implementation in a general numerical solver such as Comsol Multiphysics (a cross-platform finite element analysis, solver and multiphysics simulation software) and had, consequently, not been implemented in such software either.

With the described starting point in mind, the most important progress made during Beacon is therefore the ability to perform the simulations of the test cases. When the test cases demanded a new "feature" (general mechanical states, unsaturated conditions, etc.), the model was extended to include this. After reformulation of the model on a suitable format, the model was implemented in Comsol, and numerical settings were tested to obtain a solution of the new problem. The progress of the HBM implementation in Comsol is described below and listed in Table 6.6-1.

- In WP5.1 the first Comsol implementation was used for some of the modelling concerning saturated states. MathCad (a computer algebra software) was used for the most part when unsaturated states were solved.
- When modeling the Febex test in WP5.2 significant development and improvements had been made. An unsaturated formulation was used, and vapor transport was included as well. The vapor transport required an extension of the water mass balance, solution of the energy balance and the introduction of further constitutive models. A new interaction function (in terms of the evolution law for micro void ratio) was formulated and implemented as well. New clay potential functions were formulated and fitted against data for Febex bentonite. The implementation technique in COMSOL had also been significantly changed as compared to previously, to implement the unsaturated formulation.
- In WP5.3 two different materials, compacted block and a granular filling (crushed pellets), were represented in the same simulation. The original HBM model was intended for representing bentonite at relatively high dry density, for example in form of compacted blocks, and was altered when used to represent the granular filling. Formulation of an "interface material" between the block and granular filling was also developed to circumvent unwanted effects of the solver setup and enhance the numerical performance. This consisted of a thin layer of non-porous linear elastic material transmitting force and water flow.

During the project a significant part has been dedicated towards reformulating the mathematical description of the material model to implement it in COMSOL. A mix of COMSOL's built-in physics modules (e.g. Solid Mechanics, "Darcy's Flow" and Heat Transport in Solids) and our own parts (solid mass balance, water mass balance, constitutive relations), implemented as user defined differential equation, has been used.

The implementation strategy has changed significantly over time. At the beginning HBM was implemented as an external material (as a linked C-code library called by COMSOL), and then through a combination of COMSOL's built-in Solid Mechanics module and user defined domain ode interfaces (DODE).

Table 6.6-1 Progress of the HBM implementation in Comsol.

Test Case	Feature in Comsol
WP5.1	• principal stress states • saturated conditions
WP5.2	• new implementation strategy in Comsol • general stress states • unsaturated conditions • new interaction function • new evolution equation for micro void ratio • vapor included (new water mass balance, energy balance)
WP5.3	• two materials in one model • new area fraction function for granular filling • interface representation between materials

6.6.3 Lesson and prospective activities

One of the main lessons learned when carrying out the exercises is that HBM in general seems to be well suited to represent bentonite subjected to very different conditions using one set of parameters. It is however important to test this further by comparing the model response to experimental data from additional test such as swelling pressure build up, oedometer tests with constant water content and swelling/shrinkage tests at constant load. This would confirm that the model is up for the task as it is or would give new knowledge about how to improve the formulation.

Another lesson learnt is the high impact of the clay potential on the HBM model response. To obtain representative solutions, the clay potential functions must be properly parametrized and fitted to consistent experimental data of high quality. And, for the model to produce representative responses both mechanically and hydraulically, fitting to both types of experimental data should be performed as well. This can be considered both a strength and a weakness. When properly set up, the model generates responses which agree well with experimental data. To achieve a proper parametrization can, however, be quite difficult.

The HBM solutions of WP5.3 show that the model produces final dry density profiles that in total agree well with the measurements. The transition between block and granular

filling is, however, not as gradual as is expected from experimental findings. This is a property of HBM which could be improved upon. To achieve this, changes of the contact area fraction function, the void ratio dependent part of the micro void ratio evolution and the path dependent variable evolution could be tested.

To enhance the predictive capacity of HBM, the numerical performance of the implementation must be improved. To do this, however, one must first determine where the difficulty in achieving convergence comes from. Several possibilities can be found, some of these are:

- The implementation technique
- Incorrect solver settings
- The nonlinearity/non-smoothness of the current formulation

Development of a new, smoother, formulation of the evolution equation for the path dependent variable $\boldsymbol{f}$ could for example be a way forward to achieve increased numerical efficiency.

For some systems wall friction can significantly affect the homogenization process and it should therefore be included to improve the predictive capacity. In the present project we have not been able to include friction, mainly due to difficulties with convergency.

It would also be beneficial to improve our understanding how to select suitable parametrizations and determine the parameter values in the model. Due to the coupling between different parts of the model, using the clay potential function and contact area fraction in the micro void ratio evolution, it is somewhat difficult to separate the effects from different parts.

We were also asked to comment on the use of systematic sensitivity studies to enhance our understanding of the homogenization process. First, if a system is simulated using an improper model, systematic sensitivity studies would not give valuable information, one should concentrate on improving the model. If the material model used for representing the system is well designed, however, sensitivity studies could offer insight into where it is important to have high precision in the input to obtain a small spread in output. Furthermore, they could also be used to understand the spread/uncertainty in the output given a spread/uncertainty of the input data. One could, for example, think of the influence from wall-friction or spread in permeability as suitable cases for performing sensitivity analyses. For the HBM model the sensitivity to variation in the clay potential could be a suitable case.

6.7 LEI

6.7.1 Model inputs

Within the BEACON project the collaborative efforts were put to collect a database of experiments of different scale and conditions designed for the studies of bentonite heterogeneities. This indeed is a very valuable source of data for model validation for different types of bentonite, different hydrating water, density, etc. Sustainability and

public access of such database will play a significant role in further model development.

During the mechanical model development there is a demand of various parameters characterising behaviour under external stress of the material of different type, density, form, different saturation, i.e. parameters from basic mechanical tests (oedometric tests, triaxial tests, etc.), measured water retention data. Some of those data could be found in published papers and separate reports over decades, potentially are compiled internally by different teams. However, the list of aspects playing an important role in overall bentonite behaviour is quite large, thus it was difficult to assess the scope, comprehensiveness and representativeness of available data. The sustainable database of bentonite material mechanical characterisation data in well-defined structure would be very beneficial for further model development and for assessment of needs for further experimental measurements (type, form, solution composition, boundary conditions, etc.).

6.7.2 Progress made during the project

The preliminary linear elastic hydro-mechanical model was applied for the task 5.1 tests in WP5 at the beginning of BEACON project. Limited agreement with experimental data was obtained with the first model formulation. During the project the model was developed further and finally evolves to non-linear elastic hydro-mechanical model. The final model formulation was used to re-run Test1a01 from task 5.1. The results were compared and better agreement with experimental data (compared to preliminary results) were obtained. Final formulation was also applied to test EPFL test case in WP3 and SKB assessment case in task 5.4.

The main improvement in the hydraulic part of the model was related to description of water retention curve. Water retention curve based on van Genuchten formulation with void ratio dependent air entry pressure was applied for particular tests. The tests where sample undergoes large deformations (free swelling) the need of suitable WRC was indicated and implementation of other forms than van Genuchten model was necessary.

The main improvement in the mechanical part of the model was related to definition of Young's modulus and swelling coefficient and their evolution. The comparison of modelling results and experimentally measured data indicated the trend that values of these parameters should be related to changes of saturation or/and porosity/void ratio changes instead of constant values.

6.7.3 Lesson and prospective activities

The variability of modelling results of transitional phase during resaturation could be explored further by performing more experiments with the same set-up and identical samples. Within WP3 EPFL test was performed with 3 identical samples and transient swelling pressure evolution differed among the samples to some extent. Thus, it would be reasonable goal for numerical model to provide output within the range of experimental data. Nevertheless, the experimental procedure of sample preparation

and test running have to be thoroughly followed and reported, measurement uncertainty should be reported too.

The obtained results within WP3 and WP5 showed that LEI model's predictive capabilities are limited for some analyzed cases. The model output could be treated more as indicatory of trends (e. g., full saturation time under same hydration conditions, tendency of occurrence/absent of homogenization) but not the absolute values. In order to increase the predictive capacity of the model, the hydromechanical behavior of bentonite under different material layouts, hydration conditions should be explored further experimentally and numerically. Further model developments are needed with the main focus of the consideration of friction (for laboratory scale experiments), the representation of irreversible strains.

6.8 Quintessa

6.8.1 Model inputs

The key assumption underlying the ILM is that the same equation can be used to parameterise the void ratio-vertical stress data from oedometer tests, unconfined water retention data, and swelling pressure vs dry density data. This has been tested with datasets for MX-80 (Wang et al., 2012) and FEBEX bentonites (Lloret et al, 2005). It would be useful to have further complete datasets including for different bentonites, to build confidence in the ILM and to help define uncertainty ranges for the model parameters.

Modelling of small-scale laboratory tests during Beacon has demonstrated the significant impact that friction can have on the swelling behaviour and stresses in experiments of this size. Friction is often not directly measured or is assumed to be negligible, so additional experiments to quantify the friction coefficient and to investigate ways of minimizing its impact would be useful to constrain models of laboratory experiments. This is not expected to be as significant for full-scale tests but may nonetheless improve our understanding of the comparisons between modelling and lab-scale experimental results.

In general, it would be useful to have a greater understanding of the uncertainty and variability in experimental results. When comparing modelling results with experimental data, it is not always clear which features of the data are reproducible and which are artefacts of a particular experiment (due to e.g. unquantified heterogeneities in the bentonite, the initial preparation of the sample, or the measuring equipment used). For example, in WP5 Task 3, one of the tests was repeated three times with slightly different measured axial stresses – with particular difference in the transient behaviour. It would be interesting if several different teams could conduct an identical experiment on a sample of the same bentonite and compare the results. This would help us to understand what level of agreement between models and data should be reasonably expected.

6.8.2 Progress made during the project

Through WP3 and WP5 of Beacon, Quintessa has developed our model through:

- Applying the model to different bentonite types (MX-80 and FEBEX bentonites) and forms (blocks, pellets and powder), enabling us to test the performance of the model and develop a more widely-applicable and better-constrained dataset;
- Applying the model to different geometries, including development of a preprocessor to allow representation of complex geometries with unstructured grids;
- Applying the model to different boundary conditions, including development of a friction model and testing different approaches to modelling voids (including boundary conditions and modelling the void as a porous medium);

- Testing parameter and process sensitivities, including alterations to the swelling model to represent pellets, sensitivity to friction and voids, and sensitivity to other key parameters.

The benchmark tests in WP5 have been very useful for developing understanding of our model processes, testing sensitivities, and evaluating the performance of the model. It has been useful to have measurements of both axial and radial stresses, to constrain our mechanical model. It has also been useful to have measurements of water intake to constrain the swelling model and allow comparison of the rate of water uptake with the rate of development of swelling pressure. For example, in Test 1b, a delay was observed between the water inflow and the development of axial stress. This highlighted that our representation of pellets as a homogeneous bulk material was unable to reproduce that behaviour, so we tested the concept of introducing a further 'delay' term to represent water entering the voids between pellets.

Measurements of axial stress at different heights within a sample have highlighted the importance of friction in small samples (causing a difference in stresses between the top and bottom of the sample). Introducing friction to our model produced much better results in Test 1c, for example. We were then able to use this development in our blind predictions for Test 3, resulting in a better prediction of stresses. Including a blind prediction benchmark test was useful to test the predictive capabilities of our model, without calibration.

6.8.3 Lesson and prospective activities

Modelling of the benchmark tests has demonstrated that the ILM is capable of making good predictions for the behaviour of block bentonite in confined geometries. We are generally able to model final values of saturation, swelling pressure and dry density well but have more difficulty in reproducing the transient behaviour. In particular, for experiments with large voids and initial heterogeneities such as pellets, the simplified single-porosity assumptions of the ILM are not able to fully capture the transient evolution of the bentonite. The benchmark tests have also demonstrated that there is a reasonable amount of variability in transient behaviour (water intake and stress development) between experiments, which makes comparison with the modelling results more uncertain. The transient behaviour is largely controlled by the rate of water uptake and hence the bentonite permeability; the comparison of results from WP5 Task 4 showed that teams were using a range of different permeabilities in their models, so it would be interesting to compare results when teams were using an identical fixed permeability. Any further experimental data to constrain the permeability-porosity relationship for different bentonites would be useful.

One of the strengths of the ILM is its minimal number of required parameters. This ensures that the model requires minimal calibration which should make it more useful as a predictive tool. Additional experimental data and uncertainty ranges to support the choice of values for key parameters (ILM coefficients, Young's modulus, permeability, thermal parameters) would be valuable. The ILM is particularly sensitive to dry density because of the exponential curve it is based on; small uncertainties in dry density can lead to significant variations in swelling pressure. The accuracy of

predictions of swelling pressure or stress compared to experimental measurements is therefore highly affected by any heterogeneities in the bentonite density close to the measurement device, or any small void spaces in the sample. Interestingly, we were able to produce better results modelling large-scale in-situ experiments like the FEBEX experiment than some well-controlled small lab experiments; this may be because small heterogeneities in the bentonite and boundary conditions are less significant on a larger scale.

In conclusion, we have demonstrated that Quintessa's model is capable of representing the types of processes, materials, geometry and conditions required for modelling bentonite in repository concepts. However, there is scope for further refinement and testing of our model; in particular, representation of swelling into voids, and representation of granular bentonite. Quintessa plans to use the set of swelling experiments conducted by BGS during Beacon WP4 as a future modelling exercise to help understand the behaviour of bentonite at voids.

We would also like to improve our understanding of the interactions between elastic and plastic behaviour in our model since the timing and extent of plastic failure is often important in the transient development of stresses. WP3 Task 3 was a useful exercise in testing the model against a very simple experiment looking at different stress paths. These 'single-cell' experiments are a useful starting point for understanding the fundamental processes controlling bentonite behaviour, before looking at more complex experiments like those involving pellets.

Finally, further development is required to our model to allow us to model complex geometries using an unstructured grid in coordination with a wider range of mechanical boundary conditions.

6.9 CU/CTU

The CU/CTU team has actively participated in tasks 5.1, 5.2, and 5.3 (not in task 5.4). During the course of the project, and with the increasingly complexity of the tasks, various challenges have been faced and some have been addressed. With the journey coming to an end, it has become apparent that the team's modelling approach and performance have improved. A good part of the merit goes to the interaction with other teams during the periodic workshops and the invaluable work of the WP leader in collating, interpreting and providing feedback on the teams' results. Some lessons learnt from the performed tasks and recommendations for future activities are summarized below.

6.9.1 Model inputs

The laboratory-scale behaviour of bentonite subject to thermo-hydro-mechanical forcing has been the object of extensive research. Field-scale testing is being performed too, yet the complexity associated with the larger scale makes experimental results rarer but at the same time more precious. Field tests are done, in particular, on material assemblies, geometries, and boundary conditions that closely mimic the expected operational conditions. Flexibility on their setup is, therefore, limited. Nonetheless, they are an invaluable resource for confirming the lessons learned on laboratory-scale tests, and a way to explore how uncertainties build up in response of the model complexities. On the other hand, laboratory tests offer superior flexibility in exploring specific processes and material assemblies.

Overall, our numerical simulations provided reasonable outputs. Nevertheless, we realize the need to (better) assess the impact of the following parameters and processes:

- lateral friction during swelling/swelling pressure tests: our simulations did not account for lateral friction; therefore, differences in pressure between the top and bottom faces of the samples could not be assessed;
- homogenization of layered samples (bentonite pellets, compacted bentonite): our simulations showed insufficient homogenization owing to an underestimation of volume changes and water flows near or at saturation, caused by difficulties in the numerical implementation;
- lack of a triple-structure framework for bentonite pellets: our model has a double-structure formulation that is well-suited for the simulation of compacted bentonite but can be insufficient for the simulation of the homogenization of pellet assemblies; in fact, numerical issues arise if the assembly has an overall low dry density (despite the high dry density of the individual pellets), as well as difficulties in the correct modelling of permeability (initially large in the macro voids between pellets but small within the pellets);
- voids: our numerical implementation encountered some difficulties in presence of finite voids (gaps) that were filled by the bentonite during swelling owing to the sudden change in boundary conditions once the void was filled.

The above points could be addressed by further developing the constitutive and numerical model implementations on the basis of already available experimental results. Nevertheless, it seems reasonable to further study the response of heterogeneous (layered) samples in order to obtain additional insights into the homogenization process and the development (variable in space and time) of the lateral friction across the whole height of the walls. In addition, further experiments with variable boundary conditions (e.g., with gaps, elastic constraints, time-dependent hydraulic pressures or flows, and time-dependent temperature or heat flows) could be valuable in order to further test and improve the model performance. Laboratory experiments with simultaneous presence of compacted bentonite, pellets, and non-compacted powder also could be useful to test the model implementation in the presence of large variations of dry density and/or degree of saturation. Finally, we have noticed (task 5.3) the strong control on the saturation and swelling pressure development exerted by the layer in closest proximity to the water source. This caused a mismatch between predicted and actual values and trends in most simulations owing to the inability to finely calibrate the material response when the layer was, on the contrary, far from the water source. More experiments could be performed using the logic of permutating the position of layers of different nature (pellets, blocks, powder) or conditions (in terms of initial dry density, degree of saturation) in order to analyze the model's capability of performing predictions on the basis of data obtained with different layer positions, which could represent an important plus when implementing real-scale simulations with complex spatial variations in properties.

In all the cases mentioned above, test replicates could be precious to evaluate the repeatability of the experimental results and hence provide a more robust reference for the numerical simulations.

6.9.2 Progress made during the project

Our constitutive model and its numerical implementation have been the object of continuous development throughout the project duration. We recognize the following key improvements that provided an advantage during the simulations: (i) a better representation of the water retention curve, (ii) an improved numerical stability upon saturation; (iii) an increased computational speed, particularly through the use of a fully-coupled approach; and (iv) the use of a saturation-dependent permeability.

All our simulations were carried out using a coupled thermo-hydro-mechanical double-structure constitutive framework for expansive clays based on the theory of hypoplasticity (Mašín, 2013, 2017). In the model, the hydro-mechanical coupling is accounted for at both structural levels (micro-structure and macro-structure). The water retention behaviour and the effective stress definition also are specified for both levels, and they are linked to each other through double-structure coupling functions. The model can also account for the effect of variations of temperature at both structural levels.

The general model formulation can be expressed as:

$$\dot{\boldsymbol{\sigma}}^{M} = f_s[\boldsymbol{\mathcal{L}}:(\dot{\boldsymbol{\varepsilon}} - f_m\dot{\boldsymbol{\varepsilon}}^{m}) + f_d\boldsymbol{N}\|\dot{\boldsymbol{\varepsilon}} - f_m\dot{\boldsymbol{\varepsilon}}^{m}\|] + f_u(\boldsymbol{H}_s + \boldsymbol{H}_T) \qquad (1)$$

where: $\boldsymbol{\mathcal{L}}$, $\boldsymbol{N}$, $\boldsymbol{H}_s$, and $\boldsymbol{H}_T$ are hypoplastic tensors; f_s, f_d, and f_u are hypoplastic scalar factors; $\dot{\boldsymbol{\varepsilon}}$ is the Euler stretching tensor; $\dot{\boldsymbol{\sigma}}^M$ is the objective effective stress rate of the macrostructure; and $\dot{\boldsymbol{\varepsilon}}^m$ is the microstructural strain rate. In the model, an anisotropic mechanical response of the macrostructure is permitted, while the microstructure can only deform isotropically.

The water retention behaviour of the macrostructure has been initially modelled using a bilinear hysteretic relationship between the suction and the degree of saturation (Mašín, 2013):

$$S_r^M = \chi^M = \begin{cases} 1 & \text{for} \quad s < s_e \\ \left(\frac{s_e}{s}\right)^\gamma & \text{for} \quad s \geq s_e \end{cases} \tag{2}$$

where: S_r^M is the degree of saturation of the macrostructure, χ^M is the effective stress parameter of the macrostructure, s is the suction, s_e is the air entry/expulsion value of suction, and γ is a soil parameter that can be assumed equal to 0.55 for any soil and represents the slope of the main drying/wetting curve in a $\ln S_r^M - \ln s$ plane. Conversely, the microstructure has been assumed to remain saturated at any value of suction.

The improvement focused on the reformulation of the water retention model for the macrostructure. In the basic model by Mašín (2017), which follows that of Mašín (2013) and Wong and Mašín (2013), a bi-linear formulation of the water retention curve of Brooks and Corey (1964) type was used, as described in **Eq. (2)**. The resulting water retention curve is sketched in Figure 6.9-1. It is clear that the water retention curve is C-0 continuous only, which means that derivatives $\partial S_r^M / \partial s$ change abruptly at the intersection of the main wetting/drying curves with the scanning curve and at the air entry/expulsion value of suction. These discontinuities are by-products of the simplification adopted while defining the model equations, as real soil shows non-linear dependency of S_r^M on suction. In addition, they lead to problems in numerical performance of the model when implemented into a finite element code. Last, this bilinear formulation, which resembles the response of an elasto-plastic constitutive model, is in contrast to the general formulation of the THM constitutive model, which is hypoplastic and thus inherently nonlinear.

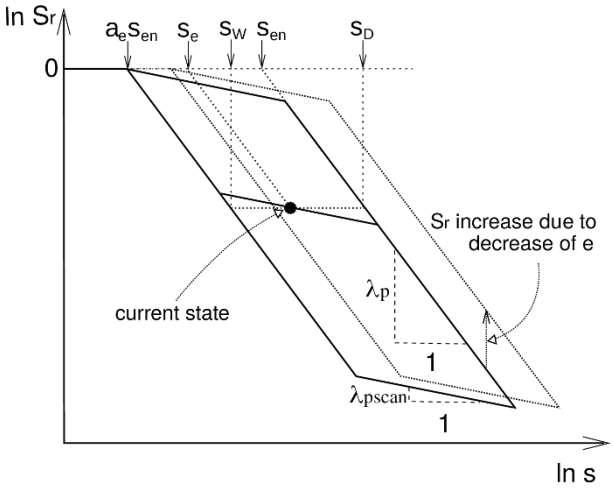

Figure 6.9-1 Hysteretic water retention model for the macrostructure adopted in the hypoplastic THM model for expansive soils.

In redefining the water retention curve to be C-1 continuous, we used the r_λ formulation proposed by Wong and Mašín (2013). Using this approach, the complete bilinear water retention curve (not only the main wetting and drying curves) was defined as

$$S_r^M = \begin{cases} 1 & \text{for } s \leq a_e s_{en} \\ \left(\frac{s_e}{s}\right)^{\lambda_p} & \text{for } s > a_e s_{en} \end{cases} \quad (3)$$

where the meaning of variable s_e is clear from **Fig. 1**. It is calculated as

$$s_e = s_{en}(a_e + a_{scan} + a_e a_{scan}) \quad (4)$$

where a_{scan} defines the position of the current state along the scanning curve, such that $a_{scan} = 0$ on the main drying curve and $a_{scan} = 1$ on the main wetting curve:

$$s_D = \frac{s - s_W}{s - s_D} \quad (5)$$

For the meanings of s_W and s_D see **Fig. 1**. The rate of variable a_{scan} is given by

$$\dot{a}_{scan} = \frac{1 - r_\lambda}{s_D(1 - a_e)} \dot{s} \quad (6)$$

where r_λ represents the ratio of the scanning curve slope (in $\ln s$ vs. $\ln S_r$ plane) and the slope of the main drying and wetting curves. For the original model, this ratio is given by

$$r_\lambda = \begin{cases} 1 & \text{for } s = s_D \text{ and } \dot{s} > 0 \\ 1 & \text{for } s = a_e s_D \text{ and } \dot{s} < 0 \\ \frac{\lambda_{pscan}}{\lambda_p} = 0.1 & \text{otherwise} \end{cases} \quad (7)$$

The slopes λ_p and λ_{pscan} are indicated in Figure 6.9-1.

In the improved model, the discrete value of r_λ from **Eq. (7)** was modified such that the slope of the scanning curve smoothly varied between the main drying and wetting curves. The modification uses three parameters, which are aimed to be internal (hidden from the user) such that the parameters of the complete THM model to be user-calibrated do not change between the two formulations. These internal parameters are denoted as $p_{scan} = 3$, $S_{lim} = 0.75$ and $p_{wett} = 1.1$. In the formulation, a new factor f_{scan} is used, defined as

$$f_{scan} = \begin{cases} a_{scan} & \text{for } \dot{s} > 0 \\ 1 - a_{scan} & \text{for } \dot{s} < 0 \end{cases} \quad (8)$$

The smoothed WRC formulation is then achieved by redefining r_λ from **Eq. (7)** to

$$r_\lambda = \begin{cases} 0 & \text{for } s < a_e s_{en} \text{ and } \dot{s} > 0 \\ \left(\frac{1-S_r^M}{1-S_{lim}}\right)^{p_{wett}} & \text{for } S_r^M > S_{lim} \text{ and } \dot{s} < 0 \\ {f_{scan}}^{p_{scan}} & \text{otherwise} \end{cases} \quad (9)$$

A comparison of predicted water retention curves with the original and redefined models is shown in Figure 6.9-2. Clearly, the updated model provides a smooth WRC curve while keeping the reference main wetting and drying curves as asymptotic targets. The subsequent figures present results of constant volume cyclic wetting-drying test expressed in terms of various state variables adopted in the THM hypoplastic model. These figures demonstrate that, apart from the smoothing of the WRC formulation, other properties of the model (in this case, the evolution of the proportion of microstructural and macrostructural void ratios and their effect on the position of the main drying and wetting branches of water retention curve) are not compromised.

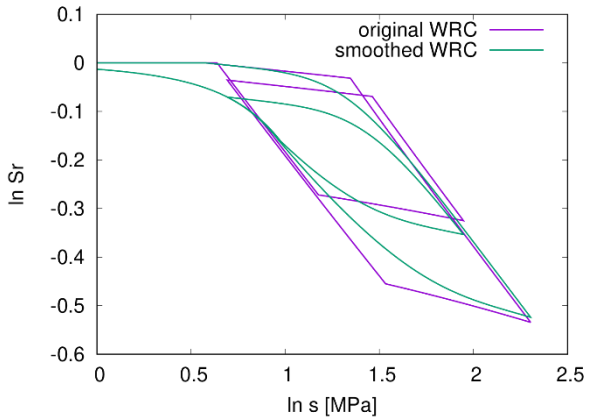

Figure 6.9-2 Comparison of water retention curves predicted with the original and modified macrostructural WRC formulations.

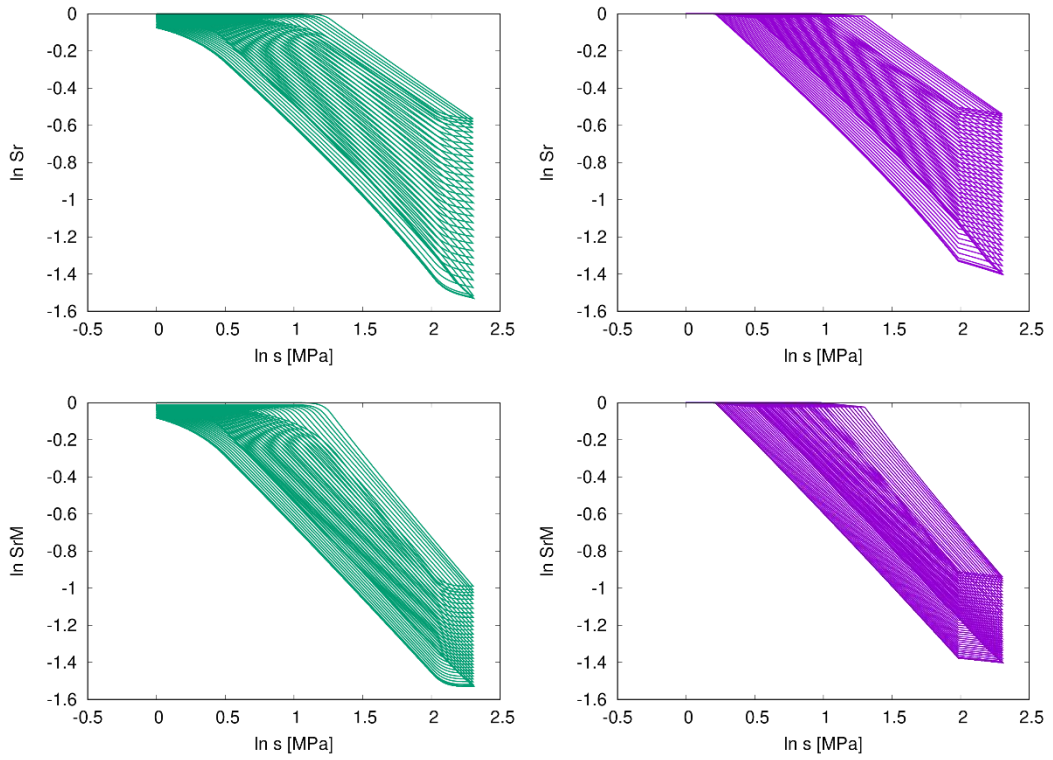

Figure 6.9-3 Comparison of hysteretic behaviours in wetting-drying cycles with the original (left) and improved (right) formulations of the WRC, with respect to the global (top row) and macrostructural (bottom row) degree of saturation as a function of suction.

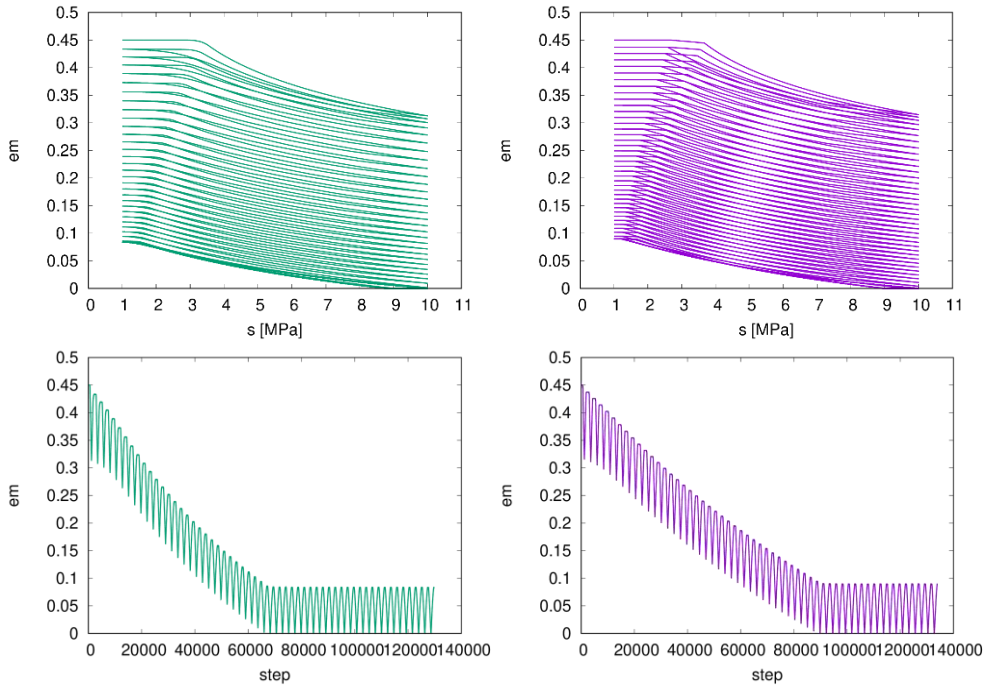

Figure 6.9-4 Comparison of hysteretic behaviours in wetting-drying cycles with the original (left) and improved (right) formulations of the WRC, with respect to the microstructural void ratio as a function of suction (top row) and the number of cycles (bottom row).

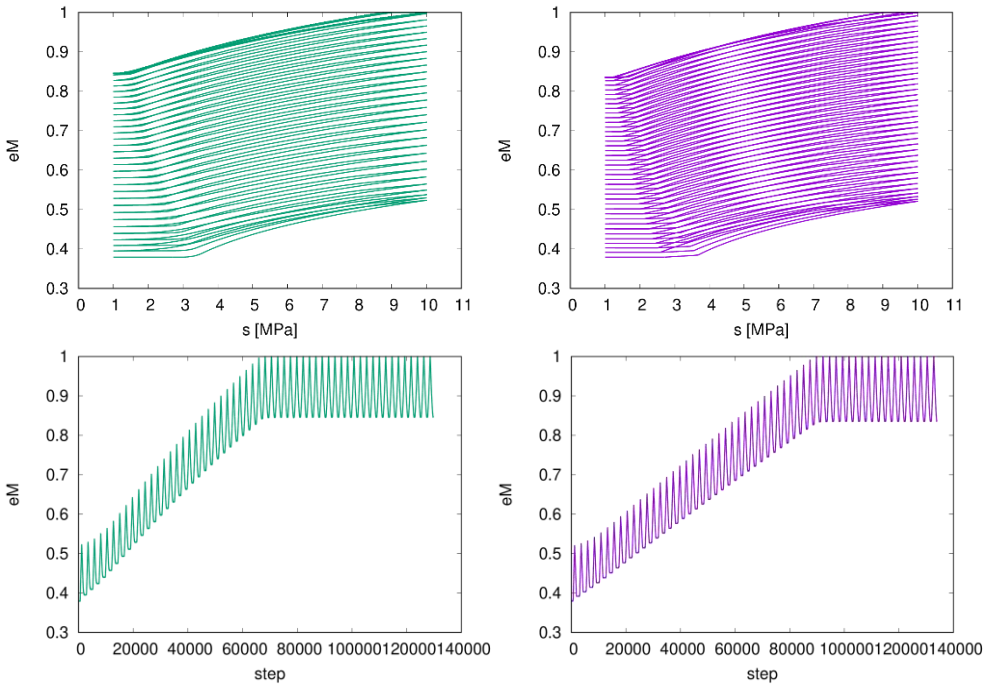

Figure 6.9-5 Comparison of hysteretic behaviours in wetting-drying cycles with the original (left) and improved (right) formulations of the WRC, with respect to the macrostructural void ratio as a function of suction (top row) and the number of cycles (bottom row).

In order to simulate the laboratory experiments, the single-element numerical implementation of the hypoplastic model written in C++ language has been plugged into the inhouse finite element code SIFEL. The integration of the rate formulations of the hypoplastic model was performed using a set of Runge-Kutta-Fehlberg schemes (e.g., Koudelka et al., 2017). The time-dependent problem was solved in SIFEL using a Newton-Raphson algorithm. The finite element code allows for both partly-coupled and fully-coupled solving of the hydraulic and mechanical components of the model. This feature has been improved during the simulations, so that, while test 1a and 1b in Task 5.1 were solved with the partly-coupled approach, test 1c was solved in a fully-coupled manner. Further improvements deriving from the adoption of a smoothed water retention curve are reflected in the delivered final results of all tests as opposed to the preliminary ones of test 1a, obtained with the bilinear formulation. Improved approaches for the calculation of the stiffness matrix and for accelerating the convergence during the iterative calculation were also produced during the simulations. In particular, the construction of the stiffness matrix was carried out either by approximation with the linear part of the THM hypoplastic model, or by numerical estimation of the stiffness matrix using perturbation. The Newton-Raphson scheme was implemented in two ways: by updating the system matrix at every iteration, which makes the implementation time consuming, or by using the same system matrix for several steps, with matrix factorisation being carried out only when the matrix is updated.

Task 5.1, test 1a

The main challenge of this test was the need of simulating a variable boundary condition: initial constant volume followed by swelling into a limited void. This caused numerical instability; therefore, the first phase of test 1a01 was simulated under constant volume condition by introducing a spring element with very high stiffness. To allow for swelling in the second phase of the test, the stiffness of the spring was reduced to (almost) zero. This reduction was achieved gradually to prevent numerical instability. In test 1a02, the entire simulation was conducted at constant volume using a very stiff spring element. The simulation proved successful in capturing the swelling pressure in the first phase of test 1a01 both in the axial and in the radial directions (Figure 6.9-6). A sudden increase of pressure after ~220 days of simulation was observed during the preliminary runs, caused by the chosen bilinear formulation of the water retention curve, which presents a discontinuity upon saturation. This has been resolved in subsequent simulations by adopting the smoothed formulation. In the second part of the simulation of test 1a02, the swelling pressures were underpredicted because the sample did not swell enough to reach the top boundary at its new location. The lower-than-expected swelling was be attributed to the isotropic deformation of the microstructure predicted by the hypoplastic model, which is inconsistent with the one-dimensional deformation in the experimental condition. Overcoming this issue is a direction of future research. The smaller swelling capability of the model was also reflected in the results of test 1a02, which showed a swelling pressure developing later than expected in axial direction, due to slower swelling, and remaining at smaller values than those measured experimentally. Similarly, in radial direction, even though the time evolution of the pressure could be captured with an

appropriate choice of the value of permeability, the simulated values remained smaller than the measured ones at all times.

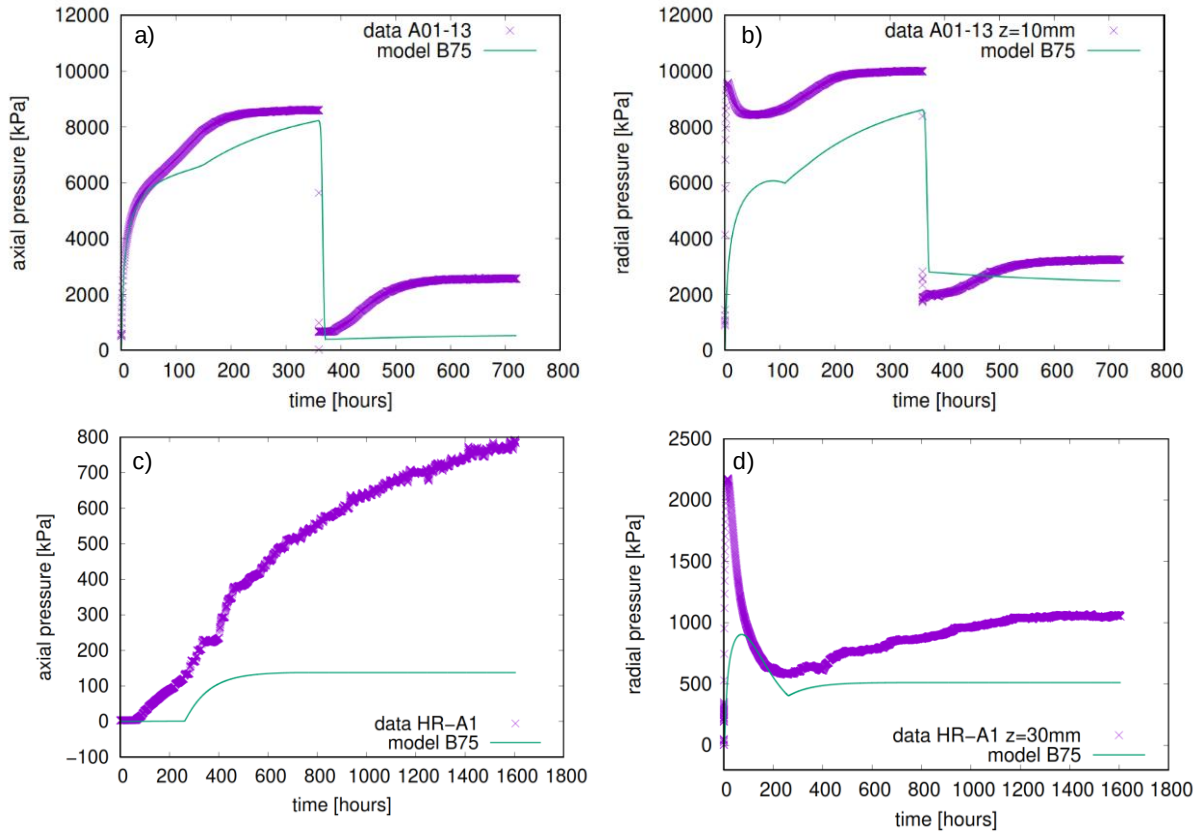

Figure 6.9-6 Summary of the results of test 1a: a) axial pressure, and b) radial pressure at 10 mm from the bottom of the sample in test 1a01; c) axial pressure, and d) radial pressure at 30 mm from the bottom of the sample in test 1a02.

Task 5.1, test 1b

In this test, the challenge was represented by the need to simulate a pellet assembly. In our implementation, the pellets were not simulated individually. Instead, an equivalent, homogeneous double-structure medium was used. As shown in Figure 6.9-7, the simulation was able to capture the final values of both the axial and the radial pressures. However, the development of the pressure through time could not be captured together with the evolution of the relative humidity. In fact, a low value of permeability was necessary to simulate the development of the swelling pressures satisfactorily, but such value provided, at the same time, low and unrealistic values of relative humidity. Conversely, satisfactory values of permeability to simulate the evolution of relative humidity would result in a very quick (within days) development of swelling pressures.

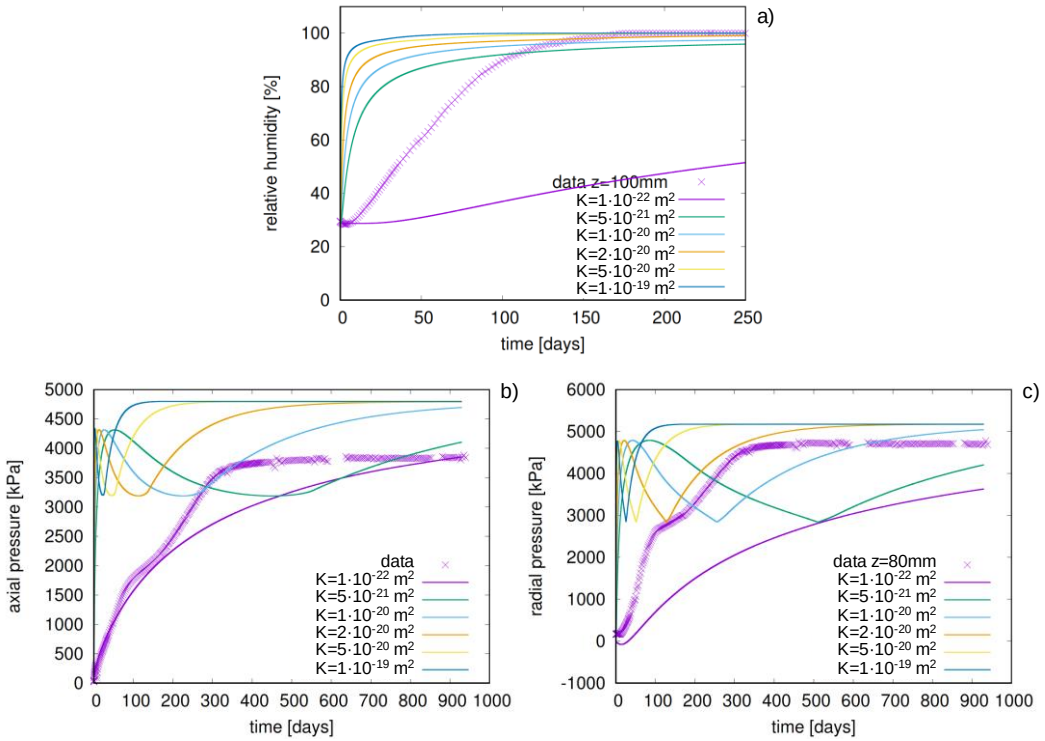

Figure 6.9-7 Summary of the results of test 1b: a) relative humidity as a function of the chosen intrinsic permeability K; b) axial, and c) radial pressure at 80 mm from the bottom of the sample.

Task 5.1, test 1c

Also in this test, the pellets were not simulated individually. An equivalent, homogeneous double-structure medium was chosen to simulate the pellet layer. For this layer, it was not possible to assign, to the void ratio, an initial value comparable to that of the experimental condition. The required high value would have lied outside of the state boundary surface prescribed by the hypoplastic formulation, and modelling would not have been possible. The largest admissible void ratio in the simulation ($e = 1.30$) was assigned to the pellet layer as the initial value, together with an initial suction ($s = -60\ \mathrm{MPa}$) to approach the initial degree of saturation in the experimental condition. With the appropriate choice of initial condition to overcome the significantly different initial void ratio that had to be assigned to the pellet layer, the results of the simulation matched with the experimental ones satisfactorily (Figure 6.9-8). Since the model could not account for the friction between the sample and the lateral boundary of the experimental device, the axial pressures at the top and at the bottom of the sample coincided. In the delivered result, the simulation was tuned so as to match the axial pressure at the sample bottom. At the same time, a good match with the radial pressure in the top layer could be achieved, while that in the bottom layer was significantly overpredicted. Among the many trials preformed, a ratio between the permeabilities in the two layers of 200:1 and a value of permeability in the bentonite block set at $5 \cdot 10^{-22}\ \mathrm{m}^2$ provided the best results in terms of the shape of the temporal evolution of the pressures. Notably, negative radial pressures were recorded in the initial phase of the simulation, which in reality would correspond to a

null pressure with detachment of the sample from the lateral walls of the experimental device. This was expected on the basis of the high initial void ratio of the simulated material, which would undergo an initial collapse upon wetting. This behavior was not recorded in the experiment, since the actual void ratio of the pellets was much smaller (while the overall void ratio was larger), thus the pellets quickly swelled into the inter-pellet voids and generated swelling pressures.

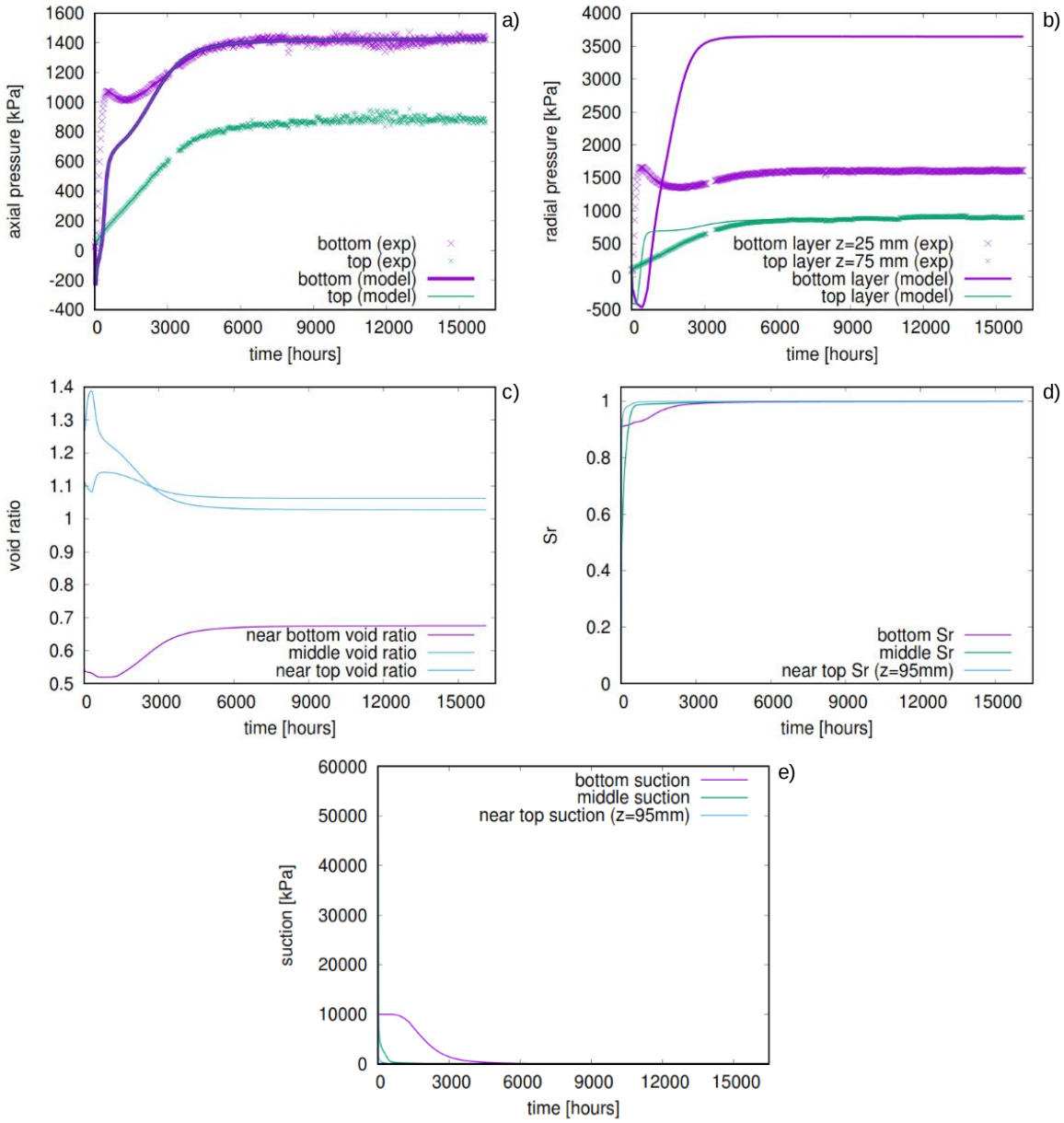

Figure 6.9-8 Summary of the results of test 1c: a) axial pressure at the top and at the bottom of the sample; b) radial pressure at 25 mm from the bottom (in the bentonite block layer) and at 75 mm from the bottom of the sample (in the pellet layer); c) void ratio, d) degree of saturation, and e) suction near the bottom of the sample (in the bentonite block layer), in the middle (at the base of the pellet layer), and near the top of the sample (in the pellet layer).

Task 5.2, CRT simulation

We constructed a finite-element geometry in SIFEL according to the specifications of the CRT reference case (deliverable D.5.2.1§4.6), i.e. the entire buffer was simulated. Using the experience gained from the previous task, we modelled four different regions – and material types/characteristics – corresponding to the ring-shaped bentonite blocks, the cylinder-shaped bentonite blocks, the bentonite bricks, and the bentonite pellets loosely installed in the outer gap, between the blocks and the host rock. However, we did not model the prescribed inner gap between the ring-shaped blocks and the cannister in order to avoid numerical issues. To simulate the anchors holding the plug on top of the cylinder-shaped blocks, a spring element was introduced with appropriate stiffness.

The model parameters were calibrated from experimental results relative to the MX-80 bentonite. Experiments on the Czech B75 bentonite were also used, as it was shown that its behaviour is reasonably similar to that of the MX-80 bentonite. The calibration of most of the THM hypoplastic model parameters was performed using the element test driver TRIAX. Reasonable values of φ_c and υ were assumed, and the reference values s_r, e_0^M, and T_r were chosen to be in the range relevant to the experiments. In fact, these values can be selected arbitrarily, together with e_{r0}^m, which can be adjusted to optimise the water retention behaviour. The parameter κ_m was chosen so as the swelling behaviour could be predicted. The results of isotropic compression tests on MX-80 bentonite were used to calibrate the parameters of the basic hypoplastic model λ^* and κ^*; then, N, n_s, n_T, and l_T were corrected to predict the INCL correctly, as well as of heating-induced volume changes. The parameter α_s was calibrated from heating tests under high suction, while s_{e0} and a_e, having little effect on the behaviour under high suction, were simply assumed. The values of a and b also were assumed under the simplification that the effect of T on water retention capacity is caused only by changes of surface tension of water. A Lewis and Schrefler's model with mechanical coupling (simplified two-phase transport, i.e. neglecting transport through gas) was implemented in the finite-element model.

The initial conditions were assigned to the model according to the specifications. The only adjustment concerned the porosity of the pellet-filled gap. In fact, while the pellets themselves were made of well-compacted bentonite, they were installed in the gap loosely, resulting in an overall very low dry density and hence high porosity. Once again, the lack of a third level of structure resulted in the need of implementing an equivalent double-structure homogeneous medium. The chosen value of porosity (n = 0.49) was the maximum allowed by the THM hypoplastic model to run successfully. Obviously, this introduced some differences compared to the experiments, as the dry mass of the pellets was overestimated, with resulting overestimation of the possible swelling of the layer. As for the boundary conditions, the water pressure protocol was used as per specifications while the heater power protocol was not used; instead, experimental values of some of the temperature sensors were used to set the thermal boundaries at the interfaces with the cannister and with the host rock. This solution was preferred as it was simpler to implement than by setting an energy flux.

In general, the numerical simulation was rather smooth, with only some adjustments in the solver parameters to ensure better and faster convergence of the iterative processes (12-24 hours to simulate 1877 days using a 12-core desktop computer). This is an important plus of the updated model implementation, that would allow comparatively easy and fast long-term simulations of large and complex domains. Some challenges were brought by the spring element simulating the anchors, which in some cases caused numerical convergence issues. However, it was found that the value of the stiffness and hence the swelling allowed could be changed in a reasonable range without causing significant changes in the results, but at the same time improving the numerical performance significantly. Some key results of the simulations are shown in Figure 6.9-9 and Figure 6.9-10.

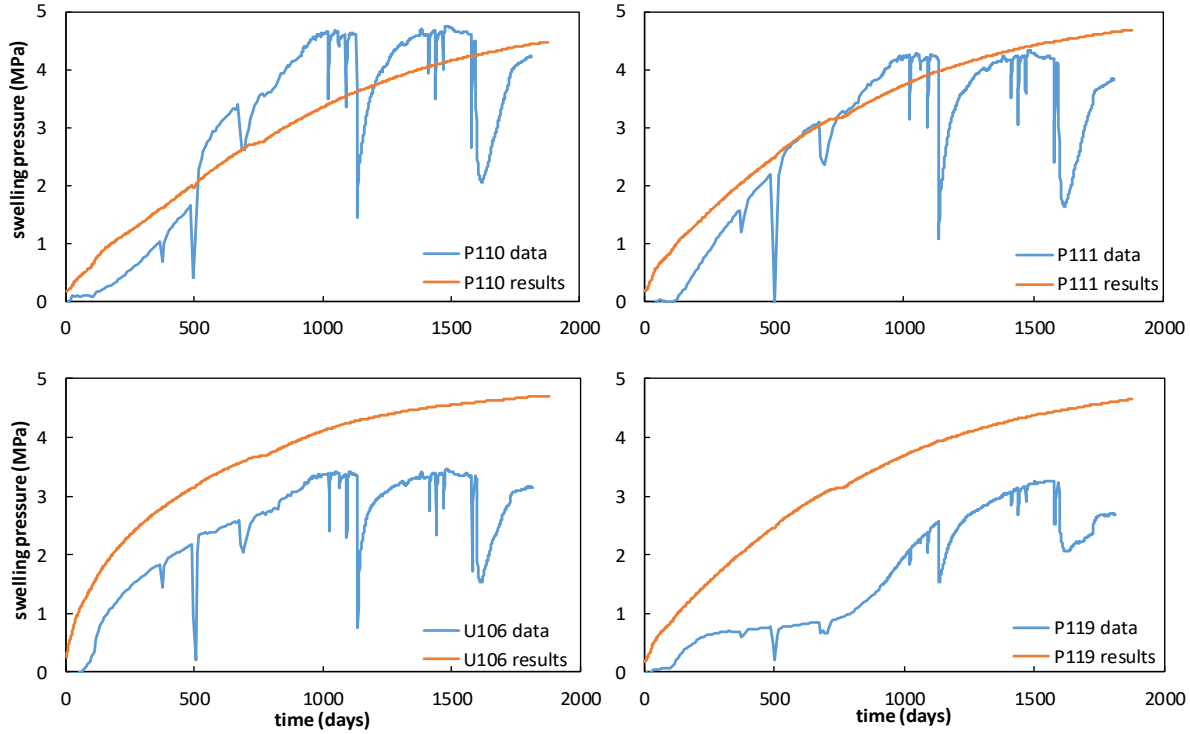

Figure 6.9-9 Simulated (results) and experimental (data) values of swelling pressure at four locations in the simulated domain. The sensors P110, P111, and U106 were located in the ring-shaped bentonite block n.5 (R5), at 2.75 m of height from the bottom of the domain, at radii 0.585, 0.685, and 0.785 m, respectively; P119 was located in the ring-shaped bentonite block n.10 (R10), at 5.25 m of height from the bottom of the domain, at 0.685 m radius.

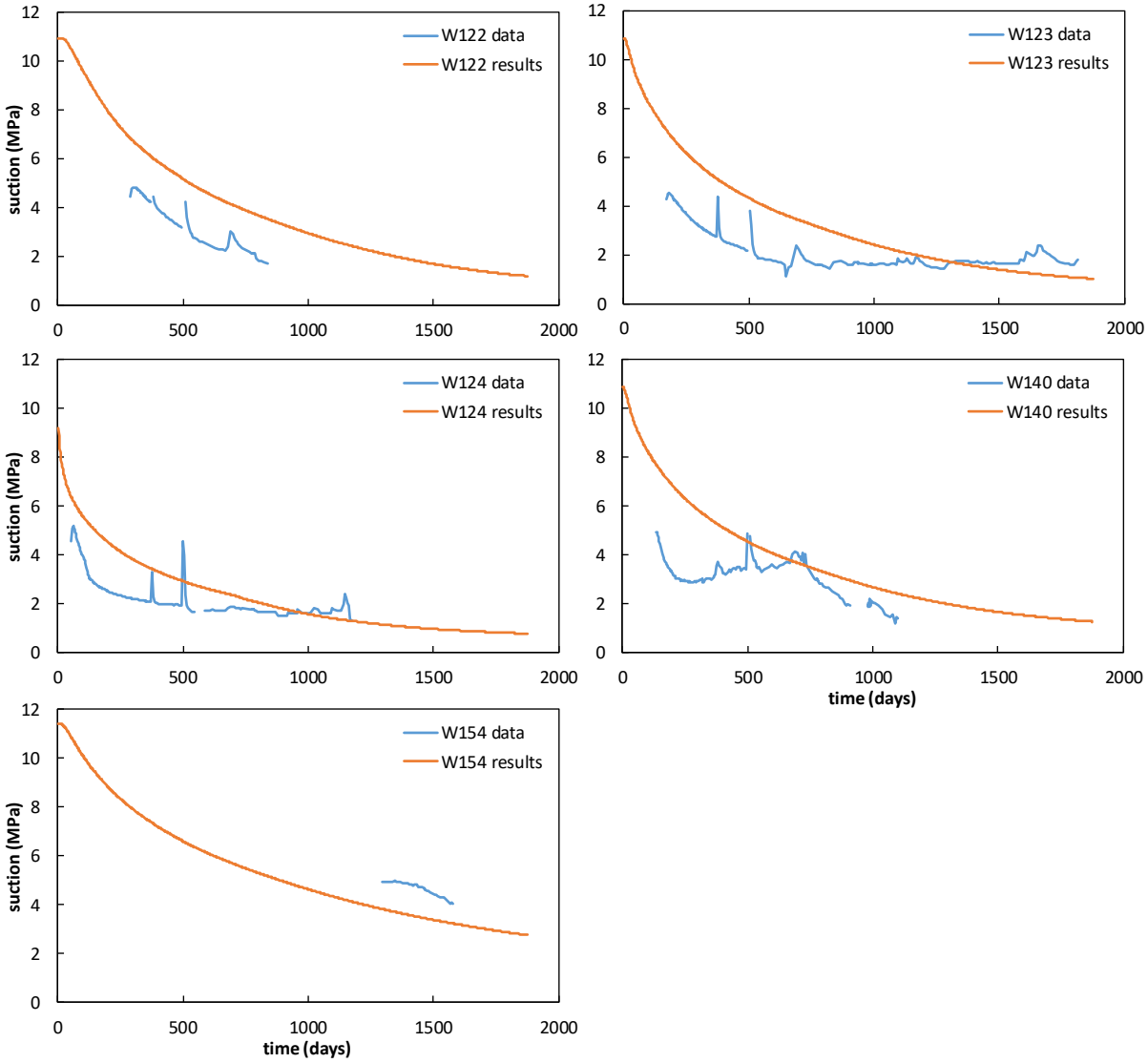

Figure 6.9-10 Simulated (results) and experimental (data) values of suction at five locations in the simulated domain. The sensors W122, W123, and W124 were located in the ring-shaped bentonite block n.5 (R5), at 2.75 m of height from the bottom of the domain, at radii 0.585, 0.685, and 0.785 m, respectively; W140 was located in the ring-shaped bentonite block n.10 (R10), at 5.25 m of height from the bottom of the domain, at 0.685 m radius; W154 was located in the cylinder-shaped bentonite block n.3 (C3), at 6.25 m of height from the bottom of the domain, at 0.585 m radius.

The results of the simulation were generally in good agreement with the experimentally measured quantities. The trend of swelling pressure development was well captured, both in terms of time evolution and values, suggesting that the swelling parameters and the hydraulic conductivity were well calibrated. Furthermore, the experimental results suggested that the thermal (inner) boundary exerted a stronger control than the hydraulic (outer) boundary on the development of swelling pressures; however, the numerical model showed more or less equal importance of the two boundaries.

The model did not show much homogenization of the bentonite (Figure 6.9-11). While most of the domain reached saturation or near-saturation by the end of the simulation, the dry density crystallized during the last year of simulation (note the small differences between the values at 1400 days and those at 1877 days) while significant gradients were still present. The case of section C3 was rather emblematic, as it showed that the differences in dry density along the section remained almost unchanged throughout the simulation. In this respect, the model underestimated the homogenization which, even though it was incomplete, did take place in a more significant way in the actual experiment.

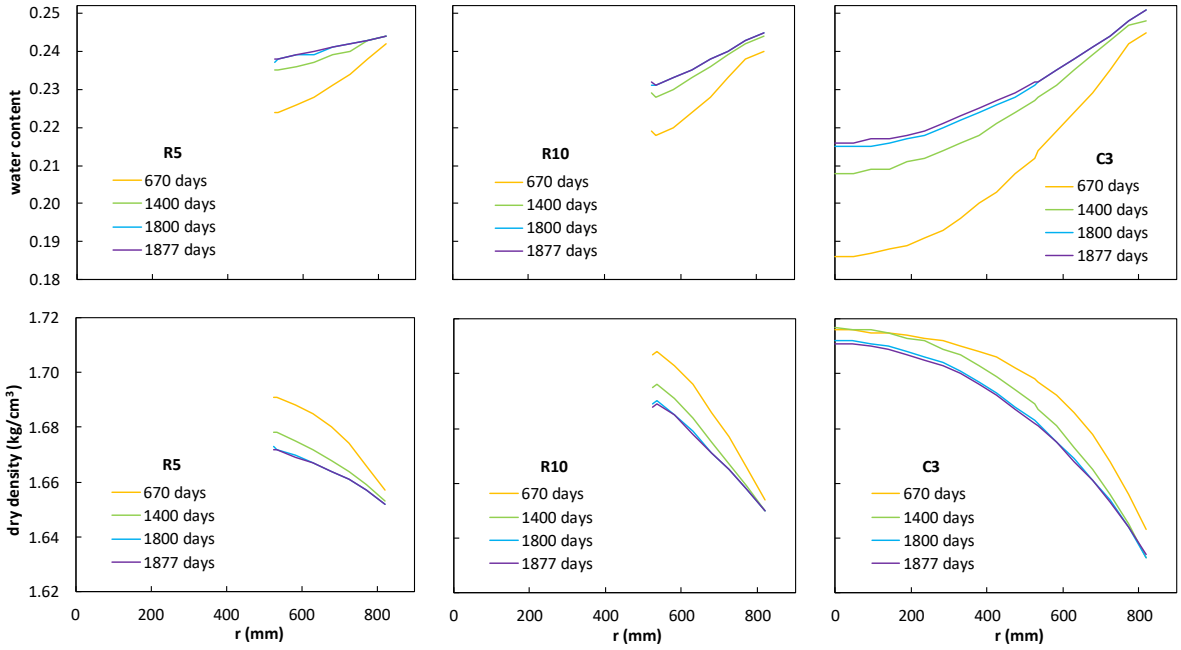

Figure 6.9-11 Simulated values of water content (top) and dry density (bottom) across three sections of the experimental domain (R5 – 2.75 m, R10 – 5.25 m, C3 – 6.25 m from the bottom) at various times during the simulation.

We used this simulation setup to get some insight into the sensitivity of the numerical model to some of the parameters. We explored three values of air-entry value (s_{e0} parameter in the hypoplastic models), i.e. 1, 2.7, and 6 MPa. The intrinsic permeability of the bentonite blocks and bricks was changed in the range 0.5–10·10^{-19} m^2, keeping a ratio of 10 between the (equivalent) permeability of the pellet-filled gap and that of the blocks. The stiffness of the anchors also was changed, as it was found that it could affect the convergence and success of the simulation even though it did not affect the results in terms of swelling pressures and suctions significantly. Most of the successful simulations were obtained using comparatively high values of stiffness, corresponding to very little swelling of the top cap. On the other hand, more realistic values, providing values of swelling in line with the experimental result, often resulted in numerical issues that need to be addressed. An overview of all the simulations that were conducted is provided in Figure 6.9-12, which shows all the successful simulations (100% on the horizontal axis), as well as all the simulations that were interrupted at some point due to numerical issues.

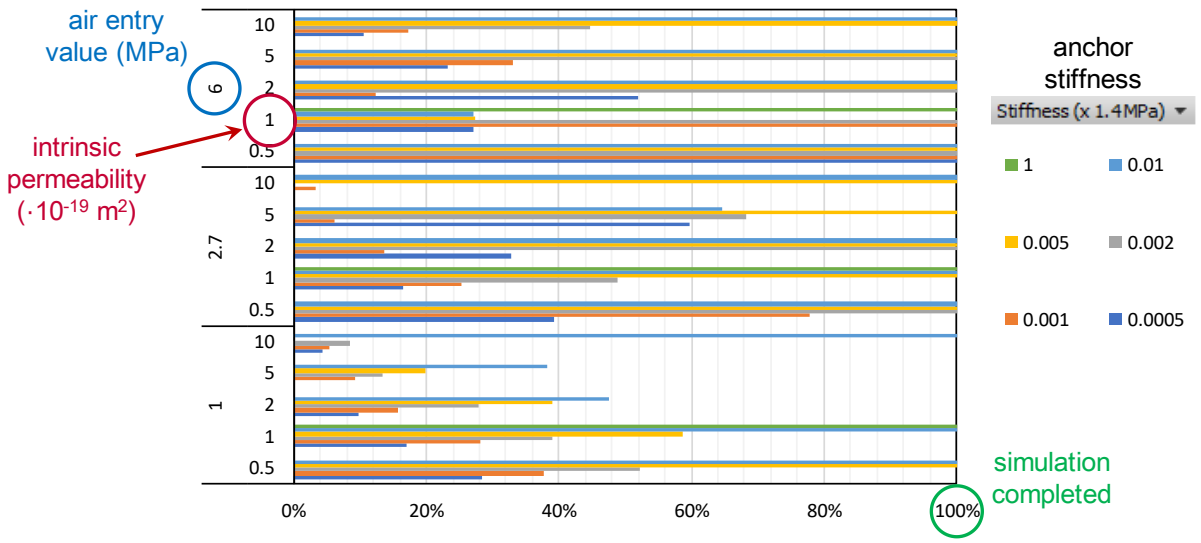

Figure 6.9-12 Sensitivity analyses – completed and unsuccessful simulations according to the choice of parameters.

For a quantitative comparison of the results of the various simulations, the normalised mean error (NME) and the normalised root mean square error (NRMSE) were used as the error metrics because of their simplicity:

$$NME = \frac{\frac{1}{n}\sum_i^n (S_i - E_i)}{\frac{1}{n}\sum_i^n E_i};\ NRMSE = \frac{\sqrt{\frac{1}{n}\sum_i^n (S_i - E_i)^2}}{\frac{1}{n}\sum_i^n E_i}$$

where S_i and E_i represent simulated and experimental values at corresponding times (i), respectively, and n is the number of experimental observations that were considered.

These error metrics were computed in relation to data series of 9 sensors: 4 swelling pressure sensors (P110, P111, U106, P119) and 5 suction sensors (W122, W123, W124, W140, W154). To obtain comprehensive metrics, the data series were combined assigning weights corresponding to their degree of completeness. For instance, if a sensor was functional during 75% of the experiment, a weight of 0.75 was assigned to the data series.

In Figure 6.9-13, groups of vertical bars indicate successful simulations performed with the same set of parameters except for the stiffness of the anchors, which is confirmed to not play a significant role in the investigated range. On the other hand, the figure shows that the trends of NRMSE are not monotonic with respect the intrinsic permeability, while they are less affected by the choice of air-entry value. By looking at the results in terms of NRMSE and NME comprehensively, it is possible to identify some sets of parameters that provide the best performance (smaller square error, smaller over/underestimation). It is clear, however, that there is not a unique set of parameters that optimises the simulation results both in terms of suctions and swelling pressures, and a trade-off is therefore necessary. This is the reason why, earlier in this section, the simulation with air-entry value of 2.7 MPa and intrinsic permeability of $2 \cdot 10^{-19}$ m^2 was

chosen as the representative one, even though it provides some overestimation of suctions and, in smaller proportion, also of swelling pressures. By choosing a smaller value of permeability, for instance, the error in terms of swelling pressures would have been minimised, but at the expenses of a much larger overestimation of suctions.

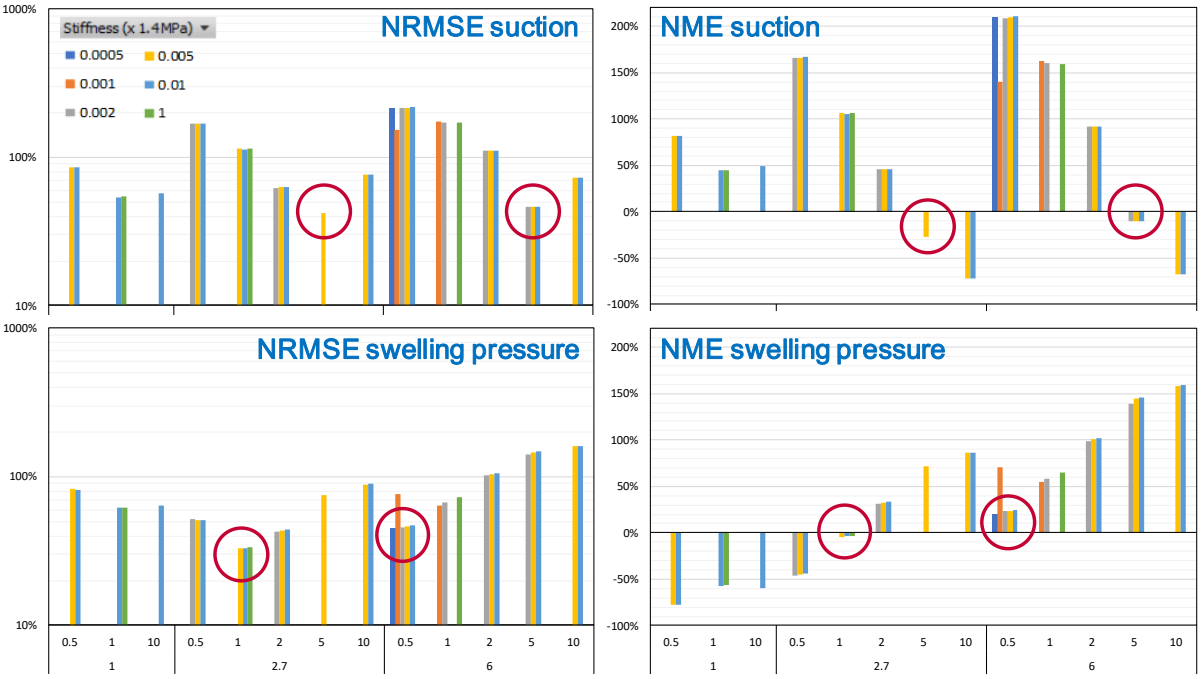

Figure 6.9-13 Normalised root mean square error (NRMSE) and normalised mean error (NME) relative to experimental data from suction and swelling pressure sensors for all successful simulations (100% completed) as a function of the chosen air-entry value of suction (1, 2.7, 6 MPa), intrinsic permeability (0.5–10·10^{-19} m^2), and anchor stiffness (0.0005–1 ·1.4 MPa). Red circles indicate the simulation or group of simulations with the lowest NRMSE or NME values.

Task 5.3, MGR tests

These tests were performed using a version of the THM double-structure hypoplastic model for expansive clays, which had been updated in BEACON and described in Deliverable 3.2. The hypoplastic parameters were calibrated from experimental results on FEBEX bentonite, available in the BEACON deliverables and in the literature. Concerning the calibration of the input parameters, it should be noted that we differentiated the values for the two sub-domains (block and pellets) and used a back-analysis of the swelling pressure time-evolution curves to finally evaluate a lower permeability to the pellets in consideration of their higher internal dry density (despite the overall lower dry density of the assembly). Again, we did not consider the triple-structure of the pellet zone and we must note that the selected permeability is relevant for representation of swelling pressure evolution (which is controlled by pellet swelling), rather than to representation of water flow through the pellet zone (which is controlled by macropores between the pellets). In the simulations, we first used a constant value of permeability, then explored the effect of a variable permeability, defined as a function of total suction.

Also note that the initial suction values were chosen based on the initial water contents so as to be reasonable in the light of published experiments on the FEBEX bentonite. In fact, our calculations which were bound to experimental water retention curves led either to an overestimation of the suction with unreasonable values (in the order of several GPa) or to an overestimation of the initial water content. In our simulations, we were considering initial suction as the initial condition and thus the initial water content has been somewhat overpredicted). Consequently, we also need a smaller water intake to reach saturation, which is reflected in smaller water flows.

As for the hydraulic boundary condition, we could not impose a constant water flow from the bottom of the domain as this option has not been available in SIFEL finite element package used in simulations. For that reason, we have specified a constant pressure at the bottom boundary (15 kPa in all tests). This value was set such that the water flow could be well approximated over the experiment duration. However, by this procedure we have overpredicted the water flow at the beginning of the experiments.

Key results of tests MGR22 (back-analysis), MGR23 (back-analysis), and MGR27 (prediction) are shown in Figure 6.9-14, Figure 6.9-15 and Figure 6.9-16. In Figure 6.9-17, we show the effect of a variable permeability function as opposed to a constant permeability independent of suction/saturation. An improvement in the initial part of the test can be seen, in that the initial development of swelling pressure is slower and hence better captured.

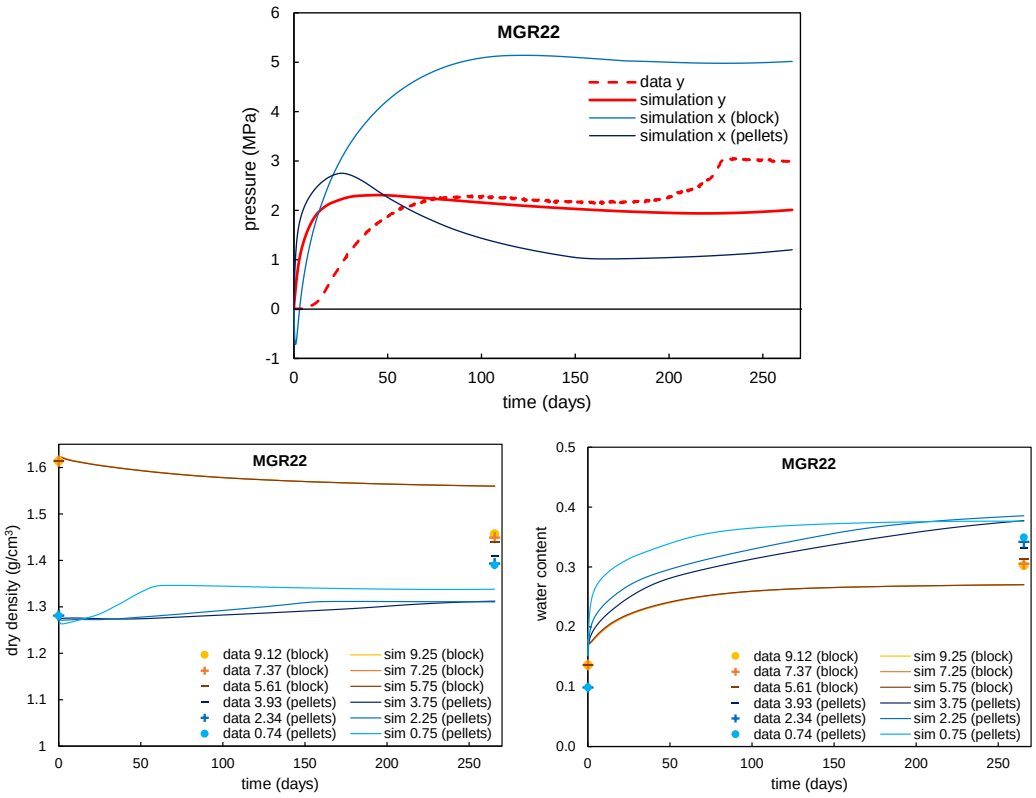

Figure 6.9-14 Simulated results of test MGR22 compared with experimental results.

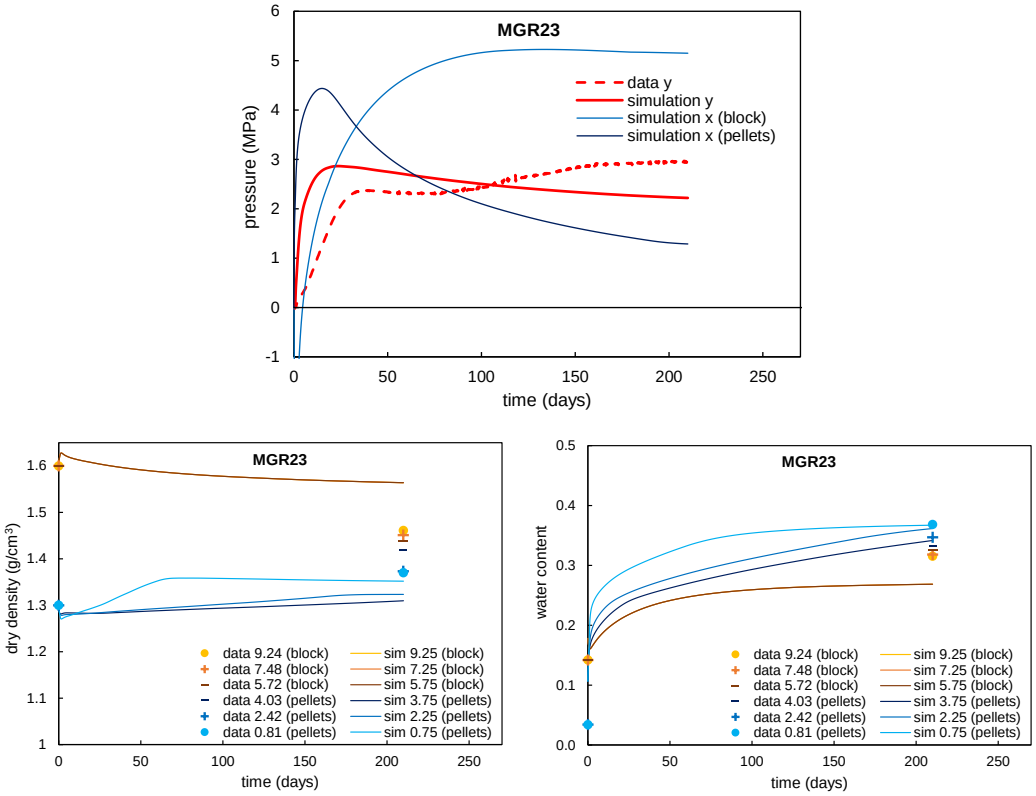

Figure 6.9-15 Simulated results of test MGR23 compared with experimental results.

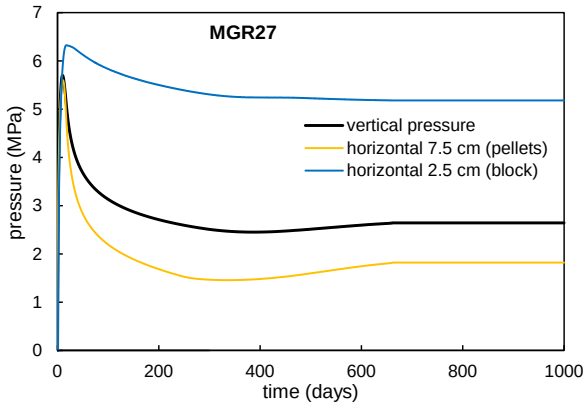

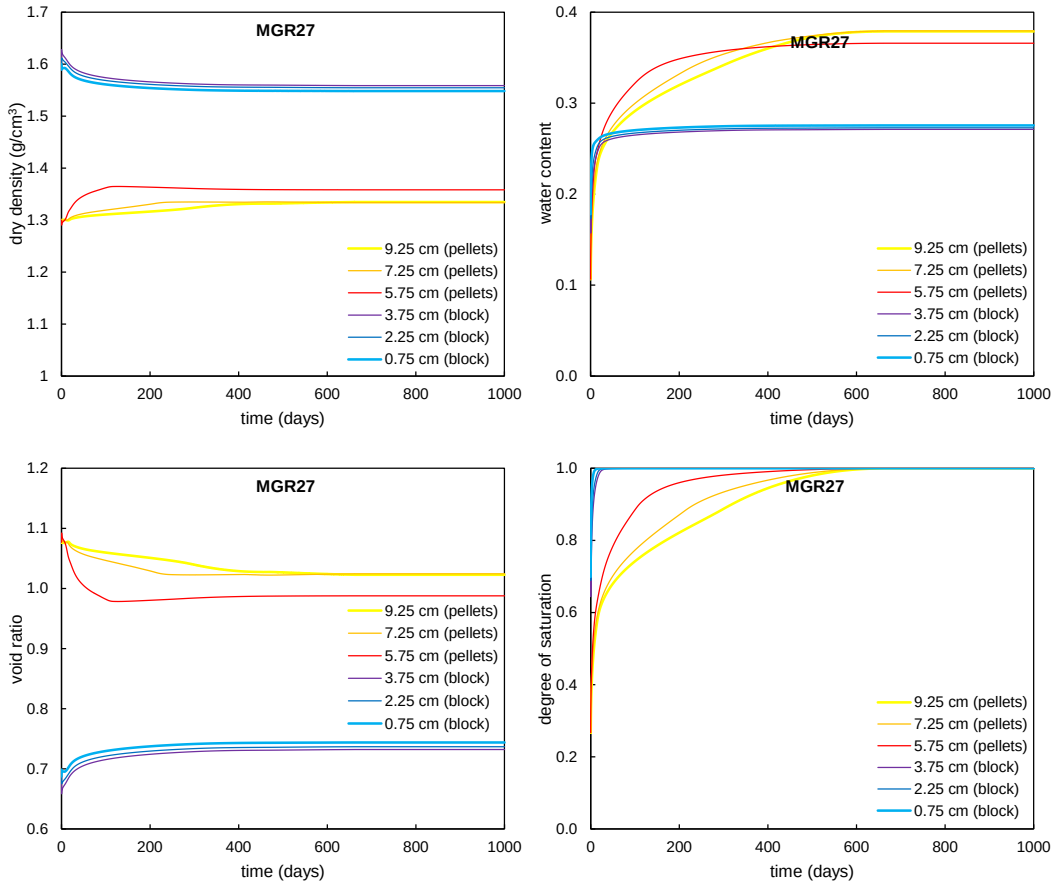

Figure 6.9-16 Simulated results of test MGR27.

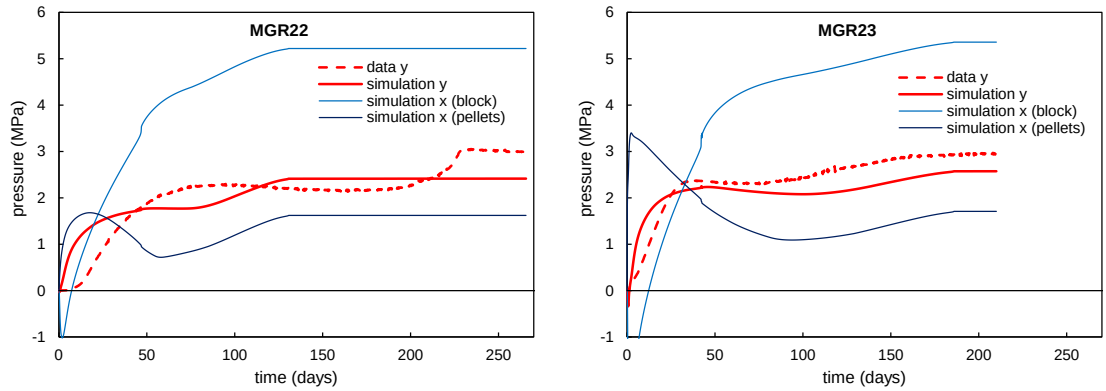

Figure 6.9-17 Swelling pressure as a function of time in MGR22 (left) and MGR23 (right) after implementing a variable permeability function (compare the charts with those shown in Figs. 14 and 15.

Overall, we judge the simulation results for MGR22 and MGR23 satisfactory as we could capture the magnitude and, partly, also the trends of swelling pressures. However, we recognise a number of shortcomings that should be addressed in further developments of the model.

- We were unable to fit, at the same time, the initial suction and initial water content on the basis of our calibration on FEBEX experimental data. We chose to keep reasonable values for suction, but this came with an overestimation of the initial water contents and underestimation of the fluxes.
- At first, we could not assign a constant water flow condition for MGR22 due to software limitation and we had to assign a constant pressure condition as in the other tests. However, we could overcome this issue through a model update but this caused some numerical issues that are still under investigation.
- Similarly to past simulations, we were able to get a trend in homogenisation, but the final homogenisation was less pronounced than in the experiment. The more porous domain did not shrink enough under the swelling pressure of the less porous one, and the less porous one did not swell enough owing to the constraints by the more porous one. Some improvement could be obtained by adjusting the model parameters, but it came at the expenses of the overall fit to the experimental values during calibration, thus it was discarded.
- Finally, we note that the simulation results were quite sensitive to the permeability of the bottom layer (the pellets in MGR22 and MGR23) while they were much less sensitive to the permeability of the top layer (the block in MGR22 and MGR23). Consequently, we could well back-analyse the permeability of the block layer but not of the pellet layer, which was critical in MGR27 simulations where the order of layers was switched. This might influence our accuracy of time-evolution of variables in the MGR27 test.

6.9.3 Lesson and prospective activities

The simulation of specific experiments by several teams has been extremely valuable in that it pointed out strengths and weaknesses of the various modelling approaches and provided suggestions on best strategies that could be implemented by different teams (such as the consideration of lateral friction, the use of various water retention functions, and the use of various saturation-dependent permeability functions).

With respect to our modelling approach, we recognize its inability to correctly represent a triple-structure material such as a (compacted or non-compacted) assembly of pellets. This limitation results in numerical issues when attempting to simulate the response of an overall loose assembly, with very low initial dry density despite a high dry density of the individual pellets. Furthermore, it results in an incorrect definition of the permeability, as it differs by orders of magnitude, at least initially, between the inter-pellet macrovoids and the intra-pellet microvoids (inter-aggregate and intra-aggregate). Our solution to model pellets assemblies was to either overestimate the initial dry density or to correct the initial suction / moisture content in order to obtain reasonable bulk values, i.e., by treating the pellets assembly as an equivalent bentonite block. However, even though this solution allowed us to overcome the numerical issues, is not adequate as it cannot correctly represent all the important variables of the process simultaneously (saturation, water intake, swelling or swelling pressure). A triple-structure constitutive model can be a matter to look into, even though it is anticipated that it could bring additional complexity to the model implementation. Alternatively, the additional structural layer could be provided

directly in the numerical implementation in the form of finite-element domains, but this would increase the complexity in defining the geometry and discretization of the domain of interest, or via a superimposed continuum (e.g., regulated by a parameter such as the inter-pellet porosity) that would control the macro-scale response in a fashion similar to that of the classic framework implemented to account for the solid and fluid components in single-structure materials.

The model's inability to represent the lateral friction in swelling pressure tests has resulted in mismatches between simulated and actual values of pressure on the top and bottom faces of the sample. This would not be a problem if the walls exerted little friction. However, as the experimental results have shown, this friction can be important and lead to an important difference between the top and bottom pressures. This is certainly a point to look into during further model development (in this case, this does not concern the constitutive equations but the finite-element implementation and should not pose particular problems).

Our model showed an insufficient ability to reproduce the homogenization of layered samples owing to numerical issues arising upon full saturation, after which only little changes are predicted despite the presence of remaining differences (in density, water content) between layers that should keep sustaining further strains and flows. Even though some improvements were made during the project, we are committed to further looking into this issue.

Notwithstanding the aforementioned limitations, our model implementation was capable of reproducing experimental trends reasonably well and with the correct magnitude. In particular, the improved numerical stability – through a better definition of the water retention response and the full coupling between the mechanical and hydraulic components of the finite-element implementation – allowed reasonable running times with reasonable convergence and time steps in most cases.

Simulation of heterogeneous (layered) domains, particularly in "predictive mode", that is using calibrations based on different spatial arrangements or material characteristics has proven to be the most difficult task. In particular (see task 5.3) it has been difficult to make predictions owing to the inability of finely calibrate the response of the key layer (i.e., the one closest to the water source) that occupied a different position in the experiments used for calibration. A strategy to overcome this issue would be to systematically perform sensitivity analyses in order to quantify the importance of certain parameters and predict their effect when the layers are arranged in different configurations. Even in absence of a predictive need, sensitivity analyses could be precious for evaluating the need (or lack of need) of fine-tuning certain input parameters rather than others (also depending on the test configuration), which could also be translated in the need of deepening the knowledge of the role of these parameters via targeted experiments.

Nonetheless, systematic sensitivity analyses can be time-consuming; therefore, is seems reasonable to propose the introduction of machine-based solutions for model calibration. These are relatively unexplored but may offer interesting performances, particularly in relation to the ability of these models to continuously learn from a progressively increasing dataset of experimental/simulation results.

Finally, a suggestive option for optimizing the simulation performance could be that of model mashups, that is the possibility of using more than one model approach (sequentially or for different spatial domains), selecting the most suited/best performing according to the process of interest. Of course, such an approach would only be feasible if the different models could operate on the same platform (e.g., a finite-element framework) and had a set of common parameters/variables that could be used to exchange information across the models.

6.10 EPFL

6.10.1 Model inputs

- In a hydro-mechanical coupled model, the calibration of the water retention curve is fundamental and should include a dependency on the current void ratio. Furthermore, consideration of adsorbed water allows to fit the water content at high suctions with few additional parameters.
- The position of the normal compression line at saturated states is very similar for a given bentonite regardless of the initial as-compacted form. This is important as it dominates the swelling pressure and the void ratio at saturation
- To enhance the model and its calibration, basic tests (of single materials) in which suction is measured during the experiments are needed in order to confidently obtain the mechanical parameters without the influence of flow rates. In this regard, the monitoring of radial stress is essential in order to understand the stress paths developed during saturation.

6.10.2 Progress made during the project

Within the WP3 a new model has been developed based on the detected pitfalls of the previous version. Especially regarding the water retention and loading collapse relationships. As shown in section 5, the test 1a of the WP5 has been reviewed and analysed with the new model, achieving a better reproduction of the experimental evidence and increasing process understanding by verifying the hypothesis made during the development and calibration of the constitutive model. Of particular interest that the adsorbed water leads to better fit at low degrees of saturation and that the final state of saturation the material state lies close to the normal compression line. This has been verified with the large scale tests such as Febex and the block-pellets homogenisation. Further work needs to be done to improve the model response during saturation of pellets mixtures at low densities.

These results illustrate the progress made not only in the model development but also on the process understanding, as for instance, the same saturated state parameters can be used between different compacted forms of the same bentonite type.

6.10.3 Lesson and prospective activities

The model can be calibrated using the same saturated state parameters regardless of the initial as-compacted form and this leads to a good prediction of the final profile of dry density. However, the swelling pressure at equilibrium is more sensitive because of its exponential relationship with dry density, which implies that small variations of dry density lead to large variations of swelling pressure. Thus the range of uncertainty increases with increasing dry density.

A major source of uncertainty is the development of swelling pressure during saturation. With the model, it is necessary to have previous tests using the same bentonite form in order to determine the loading collapse (unsaturated state) parameters. The model has high predictive capabilities in terms of the dry density redistribution after saturation as demonstrated after revisiting the test 1a and the blocks-pellets homogenization test presented by CIEMAT. Our model works well for dry densities higher than 1.4 Mg/m3. For lower dry densities, high collapse is predicted during swelling pressure tests, as shown for instance in the CIEMAT tests. While the swelling pressure development is sensitive to the saturation rate, its impact on the final distribution of dry density after saturation is very low.

References

Abed A., M. Laitinen, J. Lamsa, T. Harjupetana, W. T. Solowski. Hydro-mechanical modelling of MX-80 bentonite: one dimensional study. In Proceedings of the 3rd European Conference on Unsaturated Soils – E-UNSAT, 2016.

Åkesson, Mattias, Lennart Börgesson, and Ola Kristensson. 2010. "SR-Site Data report. THM modelling of buffer, backfill and other system components."

Åkesson M. et al. SR-Site Data report. THM modelling of buffer, backfill and other system components. SKB report TR-10-44, 2010.

Åkesson M. et al. THM modelling of buffer, backfill and other system component. Critical processes and scenarios. SKB report TR-10-11, 2010.

Alonso E.E., Vaunat J., Gens A. (1999). Modelling the mechanical behaviour of expansive clays. Engineering Geology 54(1), pp. 173-183.

Alonso E.E., Romero E., Hoffman C. (2011). Hydromechanical behaviour of compacted granular expansive mixtures: experimental and constitutive study. Géotechnique 6(4), pp. 329-344.

Ballarini, E, B Graupner, and S Bauer. 2017. "Thermal–hydraulic–mechanical behavior of bentonite and sand-bentonite materials as seal for a nuclear waste repository: Numerical simulation of column experiments." *Applied Clay Science* 135: 289-299.

Bernachy-Barbe, F. (2021). Homogenization of bentonite upon saturation: Density and pressure fields. *Applied Clay Science*, *209*, 106122.

Bilke, Lars, Bernd Flemisch, Thomas Kalbacher, Olaf Kolditz, Rainer Helmig, and Thomas Nagel. 2019. "Development of Open-Source Porous Media Simulators: Principles and Experiences." *Transport in Porous Media*.

Bosch J.A., Baryla P., Ferrari A. (2019). BEACON project. Modelling specifications for Task 3.3: Performance of constitutive models developed in the project. EPFL, July 2019.

Bosch, J.A., Ferrari, A., and Laloui, L., (2021). Coupled hydro-mechanical analysis of compacted bentonite behaviour during hydration. *Computers and Geotechnics, vol. 140,* 104447.

Bossart, P., & Thury, M. (2008). Mont Terri Rock Laboratory. Project, programme 1996 to 2007 and results. Wabern: Reports of the Swiss Geological Survey no. 3.

Brooks, R., Corey, A. (1964). Hydraulic properties of porous media. Hydrology paper no.3. Colorado State University.

Callari, Carlo, F Auricchio, and E Sacco. 1998. "A finite-strain Cam-clay model in the framework of multiplicative elasto-plasticity." *International Journal of Plasticity* 14 (12): 1155-1187.

Charlier, R. (1987) : Approche unifiée de quelques problèmes non linéaires de mécanique des milieux continus par la méthode des éléments finis. PhD Thesis, Université de Liège in Department ArGEnCo, Liège, Belgium.

Collin, F. (2003) : Couplages thermo-hydro-mécaniques dans les sols et les roches tendres partiellement saturés. PhD Thesis, Université de Liège in Department ArGEnCo, Liège, Belgium.

Collins, I.F. and Kelly, P.A., 2002. A thermomechanical analysis of a family of soil models. Geotechnique, 52(7), pp.507-518.

Crisci, E., Ferrari, A., Giger, S. B., & Laloui, L. (2019). Hydro-mechanical behaviour of shallow Opalinus Clay shale. *Engineering Geology*, *251*, 214-227.

Dueck A. & Nilsson U. (2010). Thermo-Hydro-Mechanical properties of MX-80 - Results from advanced laboratory tests. SKB, Technical Report TR-10-55. December 2010.

Dueck, A., Goudarzi, R., & Börgesson, L. (2011). Buffer homogenisation, status report (No. SKB-TR--12-02). SKB technical report.

Dupray, F., & Laloui, L. (2016). Numerical analysis of canister movements in an engineered barrier system. *Acta Geotechnica*, *11*(1), 145-159.

Favero V, Ferrari A, Laloui L (2016a) On the hydro-mechanical behaviour of remoulded and natural Opalinus Clay Shale. Eng Geol 208:128–135

ENRESA 2000, FEBEX project. Full-scale engineered barriers experiment for a deep geological repository for high level radioactive waste in crystalline host rock. *Final report. ENRESA, Madrid*

Gaus, I., Garitte, B., Senger, R., Gens, A., Vasconcelos, R., Garcia-Sineriz, J.-L., Trick, T., Wieczorek, K., Czaikowski, O., Schuster, K., Mayor, J.C., Velasco, M., Kuhlmann, U. & Villar, M.V., 2014. The HE-E experiment: layout, interpretation and THM modelling. *NAGRA Arbeitsbericht NAB 14-53.* Wettingen, Switzerland.

Gens, A., 2000**.** HE Experiment: complementary rock laboratory tests. *Technical Note 2000-47. Mont Terri Project.*

Gens, A. & Garitte, B., 2013**.** Ventilation effects in an argillaceous rock tunnel examined via unsaturated soil mechanics, In: *Advances in Unsaturated Soils – Caicedo et al. (eds), Taylor & Francis Group, London, ISBN 978-0-415-62095-*6, pp. 33-40.

Gens, A. & Vasconcelos, R., 2019**.** HE-E Experiment: modelling of the HE-E test. *Mont Terri Project TN 2019-43 – Mont Terri Project (Phase 24).* Barcelona, Spain.

Gens A. & Alonso E.E. (1992). A framework for the behaviour of unsaturated expansive clays. Canadian Geotechnical Journal 29(6), pp. 1013-1032.

Georgiadis K., Potts D.M., Zdravkovic L. (2005). Three-dimensional constitutive model for partially and fully saturated soils. International Journal of Geomechanics 5 (3), pp. 244–255.

Ghiadistri G.M. (2019). Constitutive modelling of compacted clays for applications in nuclear waste disposal. PhD Thesis, Imperial College London, UK.

Ghiadistri G.M., Potts D.M., Zdravkovic L., Tsiampousi A. (2018). A new double structure model for expansive clays. 7th Int. Conf. on Unsaturated Soils, E-UNSAT 2018, 3-5 August, 2018, Hong Kong.

Helfer, Thomas, Bruno Michel, Jean-Michel Proix, Maxime Salvo, Jérôme Sercombe, and Michel Casella. 2015. "Introducing the open-source mfront code generator: Application to mechanical behaviours and material knowledge management within the PLEIADES fuel element modelling platform." *Computers & Mathematics with Applications* 70 (5): 994-1023.

Hoffman C., Alonso E.E., Romero E. (2007). Hydro-mechanical behaviour of bentonite pellet mixtures. Physics and Chemistry of the Earth 32, pp. 832-849.

Jobmann, Michael. 2019. *MONTANARA - Monitoring von Endlagern für hochradioaktive Abfälle mit Blick auf die Langzeitsicherheit und im Kontext der Partizipation.* BGE TECHNOLOGY GmbH; (Peine).

Karnland, O., Nilsson, U., Weber, H., & Wersin, P. (2008). Sealing ability of Wyoming bentonite pellets foreseen as buffer material–laboratory results. *Physics and Chemistry of the Earth, Parts A/B/C*, *33*, S472-S475.

Koudelka T, Krejčí T, Kruis J., 2017. Numerical modelling of expansive clays. In: Fuis V (Ed.), Engineering Mechanics 2017, 23rd Intl. Conf., Brno University of Technology, Brno, Czech Republic, ISBN 978-80-214-5497-2.

Laloui, L. and Cekerevac, C., 2003. Thermo-plasticity of clays: an isotropic

yield mechanism. *Computers and Geotechnics*, *30*(8), pp.649-660.

Laloui L, Francois B. 2009 ACMEG-T: Soil Thermoplasticity Model. Journal of Engineering Mechanics; 135(9):932–944.

Müller, H. R., Garitte, B., Vogt, T., Köhler, S., Sakaki, T., Weber, H., ... & Cloet, V. (2018). Implementation of the full-scale emplacement (FE) experiment at the Mont Terri rock laboratory. In *Mont Terri Rock Laboratory, 20 Years* (pp. 289-308). Birkhäuser, Cham.

Leupin O., Talandier J., Sellin P., Lanyon G.W. (2020). BEACON project. Assessment cases for the evaluation of the degree of heterogeneity, August 2020.

Lloret A., Villar, M. V., Sanchez, M., Gens, A., Pintado, X. and Alonso, E. E. 2003. Mechanical behaviour of heavily compacted bentonite under high suction changes. *Geotechnique* 53 (1), pp. 27-40.

Marcial D., Delage P., Cui Y.J. (2008). Hydromechanical couplings in confined MX80 bentonite during hydration. 1st Eur. Conf. on Unsaturated Soils, E-UNSAT 2008, 2-4 July 2008, Durham, UK.

Martin, CD, and GW Lanyon. 2003. "Measurement of in-situ stress in weak rocks at Mont Terri Rock Laboratory, Switzerland." *International Journal of Rock Mechanics and Mining Sciences* 40 (7-8): 1077-1088.

Mašín D, 2013. Coupled Thermohydromechanical Double-Structure Model for Expansive Soils. J. Eng. Mech. 143(9):04017067.

Mašín D, 2017. Double structure hydromechanical coupling formalism and a model for unsaturated expansive clays. Eng. Geol. 165:73-88.

Mašín, D., and Khalili, N. (2016). Swelling phenomena and effective stress in compacted expansive clays. Can. Geotech. J., 53(1), 134–147.

Melgarejo Corredor M.L. (2004). Laboratory and numerical investigations of soil retention curves. PhD Thesis, Imperial College, University of London, UK.

Müller, Herwig R, Benoit Garitte, Tobias Vogt, Sven Köhler, Toshihiro Sakaki, Hanspeter Weber, Thomas Spillmann, Marian Hertrich, Jens K Becker, and Niels Giroud. 2018. "Implementation of the full-scale emplacement (FE) experiment at the Mont Terri rock laboratory." In *Mont Terri Rock Laboratory, 20 Years*, 289-308. Springer.

Muñoz, J.J., Lloret, A. & Alonso, E.E., 2003. VE Experiment. Laboratory Report: Characterization of hydraulic properties under saturated and non saturated conditions. *Technical Report, Project Deliverable D4*.

NAGRA (2019) Implementation of the Full-scale Emplacement Experiment at Mont Terri: Nagra Design, Construction and Preliminary Results. Technical Report 15-02, NAGRA, Wettingen, Switzerland.

A. Narkuniene, P. Poskas, D. Justinavicius. The modeling of laboratory experiments with COMSOL Multiphysics using simplified hydromechanical model. Minerals, 2021; 11(7):754.

Nuth, M. & Laloui, L. (2008). Effective stress concept in unsaturated soils: Clarification and validation of a unified framework. International Journal for Numerical and Analytical Methods in Geomechanics 32, 771–801. doi:10.1002/nag.645.

Nyambayo V.P. & Potts D.M. (2010). Numerical simulation of evapotranspiration using root water uptake model. Computers & Geotechnics 37, pp. 175-186.

Nguyen, Son, Jing Lanru, Lennart Boergesson, Masakazu Chijimatzu, Petri Jussila, and Jonny Rutqvist. 2007. *DECOVALEX-THMC Project. Task A. Influence of near field coupled THM phenomena on the performance of a spent fuel repository. Report of Task A1: Preliminary scoping calculations.* Swedish Nuclear Power Inspectorate.

Olsson S., Jensen V., Johannesson L.E., Hansen E., Karnland O., Kumpulainen S., Kiviranta L., Svensson D., Karnbranslehantering S., Hansen S., Linden J., Akademi A. (2013). Prototype Repository - Hydro-mechanical, chemical and mineralogical characterization of the buffer and tunnel backfill material from the outer section of the Prototype Repository. SKB, Technical Report TR-13-21. September 2013.

Philip, JR, and DA De Vries. 1957. "Moisture movement in porous materials under temperature gradients." *Eos, Transactions American Geophysical Union* 38 (2): 222-232.

Potts D.M. & Zdravkovic L. (1999). Finite element analysis in geotechnical engineering: theory. Thomas Telford Publishing, London, UK.

Pusch, R. (1980). *Swelling pressure of highly compacted bentonite* (No. SKBF/KBS-TR--80-13). Svensk Kaernbraenslefoersoerjning AB.

Pusch, R., Bluemling, P., Johnson, L.H., 2003. Performance of strongly compressed MX-80 pellets under repository-like conditions. Appl. Clay Sci. 23, 239–244.

Richards, Lorenzo Adolph. 1931. "Capillary conduction of liquids through porous mediums." *Physics* 1 (5): 318-333.

Rizzi, M., Seiphoori, A., Ferrari, A., Ceresetti, D. & Laloui, L., 2012. Analysis of the behaviour of granular MX-80 bentonite in THM processes. *Nagra-Aktennotiz AN 12-102*. Wettingen, Switzerland.

Rothfuchs, T., Czaikowski, O., Hartwig, L., Hellwald, K., Komischke, M., Miehe, R. & Zhang, C.-L., 2012. Self-sealing barriers of sand/bentonite mixtures in a clay repository. *SB Experiment in the Mont Terri Rock Laboratory. Final Report, GRS-302*. Braunschweig, Germany.

Rutqvist, J, L Börgesson, M Chijimatsu, A Kobayashi, Lanru Jing, TS Nguyen, J Noorishad, and C-F Tsang. 2001. "Thermohydromechanics of partially saturated geological media: governing equations and formulation of four finite element models." *International journal of rock mechanics and mining sciences* 38 (1): 105-127.

Seiphoori A., Ferrari A., Laloui L. (2014). Water retention behaviour and microstructural evolutions of MX-80 bentonite during wetting and drying cycles. Géotechnique 64(9), pp. 721-734.

A. Seiphoori et al. Water retention behaviour and microstructural evolution of MX-80 bentonite during wetting and drying cycles. Geotechnique, 2014; 64(9): 721–734.

Sellin P., Akesson M., Kristensson O., Malmberg D., Borgesson L., Birgersson M., Dueck A., Karnland O., Hernelind J. (2017). Long re-saturation phase of a final repository - Additional supplementary information. SKB, Technical Report TR-17-15. November 2017.

Senger, R, A Papafotiou, and P Marschall. 2014. "Thermo-hydraulic simulations of the nearfield of a SF/HLW repository during early-and late-time post-closure period." *Nagra Working Report NAB*: 14-11.

Shepard, Donald. 1968. "A two-dimensional interpolation function for irregularly-spaced data." 1968.

Talandier J. Specifications for BEACON WP5: testing, verification and validation of models. Step 1- verification cases. BEACON deliverable report D5.1.1, 2018.

Talandier J. et al. Synthesis of the results obtain of test cases from task 5.1. BEACON deliverable report D5.1.2, 2019.

Tang A.M. & Cui Y.J. (2010). Experimental study on hydro-mechanical coupling behaviours of highly compacted expansive clay. Journal of Rock Mechanics and Geotechnical Engineering 2(1), pp. 39-43.

Tang, A. M., Cui, Y. J., & Le, T. T. (2008). A study on the thermal conductivity of compacted bentonites. *Applied Clay Science*, *41*(3-4), 181-189.

Toprak E., Olivella S., Pintado X. (2020). Modelling engineered barriers for spent nuclear fuel repository using a double-structure model for pellets. Environmental Geotechnics 7(1), pp. 72-94.

E. Toprak, N. Mokni, S. Olivella, X. Pintado. Thermo-hydro-mechanical modelling of buffer. Posiva report 2012-47, 2013.

Tsiampousi A., Zdravkovic L., Potts D.M. (2013). A new Hvorslev surface for critical state type unsaturated and saturated constitutive models, Computers & Geotechnics 48, pp. 156–166.

Van Eekelen, H.A.M., 1980. Isotropic yield surfaces in three dimensions for use in soil mechanics. International Journal for Numerical and Analytical Methods in Geomechanics, 4(1), pp.89-101.

Van Genuchten, M Th. 1980. "A closed-form equation for predicting the hydraulic conductivity of unsaturated soils." *Soil science society of America journal* 44 (5): 892-898.

Vilarrasa, V., Parisio, F. and Laloui, L., 2017. Strength evolution of geomaterials in the octahedral plane under nonisothermal and unsaturated conditions. International Journal of Geomechanics, 17(7), p.04016152.

Villar, M. V. (2005). *MX-80 Bentonite. Thermal-Hydro-Mechanical Characterisation Performed at CIEMAT in the Context of the Prototype Project* (No. CIEMAT--1053). Centro de Investigaciones Energeticas.

Villar, M.V., 2007. Retention curves determined on samples taken before the second drying phase. *Technical Report M2144/5/07*. Madrid, Spain.

Villar M.V. and Gómez-Espina R 2009. Report on Thermo-Hydro-Mechanical Laboratory Tests Performed by CIEMAT on Febex Bentonite 2004-2008. *CIEMAT report 1178, Madrid*

Villar, M.V., Martín, P.L., Gómez-Espina, R., Romero, F.J. & Barcala, J.M., 2012. THM cells for the HE-E test: setup and first results. *PEBS Report D2.2-7.1. CIEMAT Technical Report CIEMAT/DMA/2G10/02/2012.* Madrid, Spain.

Wieczorek, K., Miehe, R. & Garitte, B. (2011): Measurement of thermal parameters of the HEE buffer materials. PEBS Deliverable D2.2-5

Wong, K. S. and Mašín, D. (2014). Coupled hydro-mechanical model for partially saturated soils predicting small strain stiffness. Computers and Geotechnics 61, 355-369.

Zhang, C.L. & Rothfuchs, T., 2005. Report on instrument layout and pre-testing of large lab VE-tests. *NFPRO Deliverable 4.3.11*

Zhou, A.N., Sheng, D., Sloan, S.W. and Gens, A., 2012. Interpretation of unsaturated soil behaviour in the stress–saturation space, I: volume change and water retention behaviour. Computers and Geotechnics, 43, pp.178-18

Appendix 1 – Element on sensitivity analysis developed by VTT for SKB assessment case

Methodology

When carrying out experiments, or in this case numerical simulations, with varying parameter value combinations but not using a systematic way to sample from the parameter space, the regression coefficients are generally aliased (confounded). This means that a particular coefficient of a multiple regression estimated by OLS depends on the correlations between the input parameter corresponding to the regression coefficient, and all the other input parameters, as well as on the correlation between all the other input parameters and the output variable. Therefore, the effects of different parameters on the output variable cannot be separated, which clearly compromises the sensitivity analysis.

In addition, a model misspecification, such as, for example, omitting an influential second-order term from the regression equation and instead estimating a linear main effects model only, generally causes the regression coefficients to be biased ("omitted variable bias", Wooldridge, 2012). This bias depends on the regression coefficient associated with the omitted variable and the correlation between the variables included in the regression model and the one(s) omitted form the regression model.

To avoid aliased regression coefficients and to minimize the needed number of simulation runs, a number of sensitivity analysis designs (Designs of Experiments, DoE) have been suggested. One type of such designs, Definite Screening Designs (DSD, Jones & Nachtsheim, 2011, 2013) consider parameters at three different values (and therefore allows for a deterministic sensitivity analysis), that is, at the low and the high end of the considered parameter value range and in the centre between these two extremes. The parameter value ranges can differ from parameter to parameter and besides continuous parameters, categorical parameters can be included. The DSD prescribes a sampling scheme for a certain number of parameters.

Parameter columns of a DSD including only continuous variables are all uncorrelated with each other and with the second-order effect columns (i.e., the design is orthogonal for main effects). Hence, carrying out the simulations according to the DSD allows for the unbiased estimation of the regression coefficients associated with linear model terms (and thus, of the main effects), whether or not the specification of the regression model is correct. This is a desired property for the sensitivity analysis, since then each regression coefficient determines the sensitivity of the output variable with respect to the associated input parameter.

However, it is important to note that the inclusion of binary categorical variables in addition to continuous variables into the DSD results in small but non-zero correlations between the categorical and the continuous variables and thus, the design is no longer orthogonal.

Note also that in theory, the main effect estimates are aliased with third- and higher-order terms but these have been assumed to be negligible (effect hierarchy).

Table 6.10-1 shows the DSD for 6 continuous (x1-x6) and 1 categorical (x7) parameters. This design is used the performed sensitivity analysis and requires 19 model runs. The design contains only the main effect columns. The second-order effect columns are obtained from elementwise multiplication of the different design columns considering all possible combinations (two-factor interactions or 2fi's) and squaring each design column elementwise (quadratic terms).

Table 6.10-1. Definitive screening design (DSD) for testing 6 continuous parameters and one categorical parameter (x_7),

Run	x_1	x_2	x_3	x_4	x_5	x_6	x_7
1	0	1	1	1	1	1	1
2	0	-1	-1	-1	-1	-1	-1
3	1	0	-1	-1	1	-1	1
4	-1	0	1	1	-1	1	-1
5	1	1	0	-1	-1	1	-1
6	-1	-1	0	1	1	-1	1
7	1	1	1	0	-1	-1	1
8	-1	-1	-1	0	1	1	-1
9	1	-1	1	1	0	-1	-1
10	-1	1	-1	-1	0	1	1
11	1	1	-1	1	1	0	-1
12	-1	-1	1	-1	-1	0	1
13	1	-1	1	-1	1	1	1
14	-1	1	-1	1	-1	-1	-1
15	1	-1	-1	1	-1	1	1
16	-1	1	1	-1	1	-1	-1
17	0	0	0	0	0	0	1
18	0	0	0	0	0	0	-1

Statistical analysis

Commonly, effects are presented as standardized effects, that is, the regression coefficients are divided by the respective standard error (which is the t-statistic). Generally, the standard error of a particular regression coefficient depends on the correlations between the input parameter corresponding to the regression coefficient and all the other input parameters. Since these correlations are zero for the main effects, the standard errors can be estimated independently from each other.

However, the small correlations present when categorical variables are included in the study need to be born in mind. In addition, note that the standard error depends also on the mean squared residuals (residual = difference between observed output variable and fitted value) and thus, on the number of terms included in the regression model. Therefore, the t-statistic differs for different regression model specifications.

The obtained regression models are evaluated for their statistical significance with various statistical tests. The main tests and related concepts are described in the following.

F-test

F-test evaluates the significance of the regression model as whole. It tests if the fitted regression model explains the data better than a naive regression model with zero regression coefficients. The test passes if the p-value associated with the F-test is less than a significance level α (Montgomery, 2012). A significance level of $\alpha = 0.05$ is used for all hypothesis tests.

t-test

The two-sided t-test evaluates the significance of any individual regression coefficient. It tests if the fitted regression coefficient explains the data better than zero coefficient. The test passes if the p-value associated with the t-test is less than a significance level α (Montgomery, 2012).

Box-Cox transformation, normality plots, Anderson-Darling test

The application of both the F-test and t-test are based on the assumption that the errors of the regression model are independent and normally distributed with a mean of zero and a constant variance. Consequently, the output variable is independently and normally distributed (Montgomery, 2012). Therefore, Box-Cox transformation (Box & Cox, 1964) of the output variable is performed to find an optimal exponent λ that transforms a non-normal distribution into an approximately normal shape.

The assumption of normality of the residuals and the output variable is checked using normal probability plots and performing Anderson-Darling (AD) test (Nelson, 1998; Stephens, 1974). AD test passes if the associated p-value is larger than the significance level α.

Residuals-vs-fitted value plots, residual symmetry plots

In addition, the analysis of residuals is crucial with regard to detecting possible violations of the underlying assumptions of OLS. The assumptions are that the independent variables (i.e., the parameters included in the regression model) are uncorrelated with the error (zero conditional mean assumption) and that the errors have a constant variance (homoscedasticity assumption) (Montgomery, 2012; Wooldridge, 2012). The zero conditional mean assumption holds if the residuals are normally distributed. Consequently, the normality is checked from normality plots and by performing AD test for the residuals. The homoscedasticity assumption is checked by seeking symmetry patterns in the residuals-vs-fitted-values plots, which would indicate violation of the assumption

Since for a DSDs are orthogonal (except for small correlations between categorical and continuous parameters), the regression coefficients estimated using OLS remain unbiased even if the zero conditional mean assumption is not upheld (e.g., due to a model misspecification).

A violation of the homoscedasticity assumption results in biased standard errors and thus, in unreliable t-statistics, which compromises the screening of important parameters based on standardized effects.